Study of the Bloch-Torrey equation associated to diffusion magnetic resonance imaging

Nicolas Moutal

INSTITUT POLYTECHNIQUE DE PARIS

NNT : 2020IPPAX031

Thèse de doctorat

ÉCOLE POLYTECHNIQUE

IP PARIS

Study of the Bloch-Torrey equation associated to diffusion magnetic resonance imaging

Thèse de doctorat de l'Institut Polytechnique de Paris
préparée à École Polytechnique

École doctorale n°626 École Doctorale de l'Institut Polytechnique de Paris (ED IP paris)
Spécialité de doctorat: Physique

Thèse présentée et soutenue à Palaiseau, le 30/06/2020, par

M. NICOLAS MOUTAL

Composition du Jury :

M. Jean-Marie Bonny Directeur de Recherche, INRAE	Président
M. Valerij Kiselev Professeur, University Medical Center Freiburg	Rapporteur
M. Pierre Levitz Directeur de Recherche, CNRS	Rapporteur
M. Denis Le Bihan Directeur de Recherche, CEA	Examinateur
M. Ludovic De Rochefort Chargé de Recherche, CNRS	Examinateur
M. Denis Grebenkov Chargé de Recherche, École Polytechnique	Directeur de thèse
M. Bernard Helffer Professeur Émérite, Université de Nantes	Invité

This page is unintentionally left not blank.

Remerciements

Il est difficile d'exprimer par écrit avec justesse toute l'admiration que j'éprouve pour mon directeur de thèse Denis Grebenkov. Au cours de mes trois années de thèse, j'ai pu apprécier la qualité exceptionnelle de son encadrement, sa compétence, et le temps considérable qu'il a investi dans nos échanges et dans mon travail. Il est évident que la qualité de ma thèse lui doit beaucoup et je l'en remercie très chaleureusement.

En second lieu, j'aimerais remercier mon jury de thèse pour son investissement dans mon travail, et tout particulièrement les rapporteurs Pierre Levitz et Valerij Kiselev pour avoir pris le temps de décortiquer mon manuscrit de thèse.

Bien que mon travail de thèse ait été un travail théorique, j'ai pu bénéficier de collaborations expérimentales, qui furent cruciales pour valider nos résultats. J'aimerais donc remercier les personnes avec qui j'ai travaillé à ces occasions : J.-M. Bonny, S. Clerjon, G. Pagès, D. Topgaard, M. Nilsson, I. I. Maximov, T. A. Kuder, K. Demberg.

Plus proche géographiquement, je remercie le laboratoire PMC qui m'a accueilli pendant trois ans et m'a fourni un soutien scientifique, logistique, administratif. Je profite de cette occasion pour souhaiter une belle réussite à tous les doctorants du laboratoire, notamment à mes camarades de troisième année.

Enfin, j'aimerais remercier ma famille et mes amis pour leur soutien pendant ma thèse et pour la relecture partielle ou totale de mon manuscrit. Plus particulièrement, un grand merci à Antoine Chrisment pour nos innombrables discussions sur nos sujets de thèse et pour m'avoir dit un jour, l'air de rien : "Et pourquoi tu ne ferais pas un triangle ?" (cf. Figs. 1.8 et 1.10). Je remercie aussi chaleureusement Marion Fumaroli pour son soutien dans mes choix professionnels et pour nos discussions autour de l'enseignement de la physique qui m'ont offert une bulle d'air dans le milieu parfois un peu trop spécialisé de la recherche. Enfin, je ne peux conclure sans remercier ma femme Eva, qui m'a rappelé constamment qu'après tout, il n'y a pas que la science dans la vie.

Résumé

L'imagerie de réonance magnétique nucléaire pondérée par diffusion (dMRI) est une technique expérimentale qui a pour but d'identifier les propriétés microstructurales d'un échantillon bien en-dessous de la résolution conventionnelle de l'IRM "classique". Cette technique repose sur la mesure de la dispersion de phase de spins portés par des molécules qui diffusent dans un champ magnétique inhomogène. Bien que la trajectoire individuelle de chaque molécule soit inaccessible expérimentalement, la dispersion de phase qui en résulte conduit à une diminution du signal d'IRM qui, à son tour, permet de remonter aux caractéristiques des trajectoires diffusives. Bien que cette technique ait été introduite et appliquée dans divers contextes depuis plusieurs décennies, de nombreux éléments théoriques restent à élucider, et ce d'autant plus avec l'amélioration constante des appareils d'imagerie et des techniques expérimentales. Notablement, les mécanismes de formation du signal d'IRM aux forts gradients sont encore largement incompris, malgré une tendance "naturelle" à l'augmentation des gradients pour sonder des échelles structurales de plus en plus fines.

Nous revisitons dans un premier temps les effets d'anisotropie géométrique. Tandis que l'anisotropie aux échelles micro- et macroscopiques a été l'objet de beaucoup d'attention ces dernières années, l'échelle intermédiaire, "mésoscopique", n'avait pas encore été étudiée systématiquement. Dans ce régime, l'effet des frontières du domaine se traduit par une diminution apparente du coefficient de diffusion proportionnelle au rapport surface-volume du domaine. Ce résultat classique depuis près de trente ans a été énoncé sous la forme de la formule de Mitra, qui ignore les effets d'anisotropie et se restreint à un profil de gradient très particulier. Nous avons obtenu une généralisation de la formule de Mitra qui tient compte de ces effets. Ainsi, elle permet d'améliorer significativement l'estimation du rapport surface-volume de domaines arbitraires quelle que soit la séquence de gradient utilisée. De plus, elle nous a permis de mettre à jour un nouveau critère d'isotropie pour les séquences de gradient, qui diffère du critère réalisé par les séquences dites d'encodage sphérique.

Dans un second temps, nous étudions les effets de perméabilité, qui sont cruciaux pour les applications biomédicales. Une première situation est celle de petits compartiments plongés dans un milieu homogène, avec des frontières perméables. Nous proposons une analyse critique de trois modèles classiques de l'effet de l'échange sur le signal d'IRM de diffusion. Puis nous étudions une deuxième situation où le milieu est segmenté par une collection de membranes perméables parallèles. Nous formulons une méthode numérique et théorique générale et flexible pour étudier la diffusion à travers ces membranes et nous mettons en évidence plusieurs lois d'échelles.

Le dernier chapitre constitue le coeur de la thèse et aborde l'étude non perturbative de l'équation de Bloch-Torrey qui régit l'évolution du signal d'IRM de diffusion. Aux forts gradients, nous montrons théoriquement, numériquement, et expérimentalement l'universalité du phénomène de localisation, qui ouvre des perspectives prometteuses pour augmenter la sensibilité du signal d'IRM à la microstructure. Ce phénomène de localisation est encore largement ignoré dans la communauté scientifique, probablement à cause de la technicité mathématique associée et de ses conséquences paradoxales au regard des phénomènes qui se produisent aux faibles gradients. Nous proposons une explication qualitative du régime localisation, point qui jusqu'alors manquait et témoignait de notre imparfaite compréhension de ce régime. Par ailleurs, nous présentons une extension de résultats déjà connus et clarifions certaines questions théoriques. Un des résultats les plus inattendus au vu de l'état actuel des connaissances est l'existence du régime de localisation dans des milieux non bornés (dans la thèse nous étudions en détail le cas des milieux périodiques). Tous ces résultats suggèrent la nécessité d'un changement de paradigme dans les approches théoriques actuelles, majoritairement basées sur le régime des faibles gradients, afin de tirer pleinement parti des possibilités offertes par l'IRM de diffusion.

Abstract

Diffusion magnetic resonance imaging (dMRI) is an experimental technique which aims at unraveling the microstructural properties of a sample well below the conventional spatial resolution of "classic" MRI. This technique relies on the measurement of phase dispersion of spins carried by molecules which diffuse in an inhomogeneous magnetic field. The individual trajectory of molecules is itself inaccessible experimentally, however the resulting phase dispersion leads to a reduced MRI signal which in turn allows one to recover some properties of diffusive motion. Although this technique has been proposed and applied in various contexts for several decades, many theoretical points remain to be clarified, even more with the permanent improvement of MRI scanners and experimental protocols. Notably, the understanding of the signal formation at high gradients is largely incomplete, in spite of the "natural" tendency to increase the gradient in order to probe finer and finer structural scales.

We first revisit anisotropy effects. While micro- and macroscopic anisotropy have been largely studied over past years, the intermediate, "mesocopic" scale had not been investigated systematically. In this regime, the boundaries of the domain produce an apparent reduction of the diffusion coefficient which is proportional to the surface-to-volume ratio of the domain. This result is well-known and was formulated through Mitra formula, while ignoring anisotropy effects and focusing on a particular gradient profile. We have obtained a generalized Mitra formula which improves significantly surface-to-volume ratio estimations for arbitrary domains and gradient waveforms. Moreover, this generalization allowed us to exhibit a new isotropy criterion for gradient waveforms, which differs from the one realized by "spherical encoding" sequences.

In a second chapter, we investigate permeability effects, that are crucial for biomedical applications. We first treat the situation of small compartments contained in a homogeneous medium and exchanging through permeable boundaries. We critically revise three classical models of exchange for dMRI. Then we turn to a second situation where a medium is segmented by an array of parallel planar boundaries. We formulate a general numerical and theoretical method to study diffusion trough these membranes and we exhibit several scaling laws.

The last chapter is the heart of the thesis and contains a non-perturbative study of Bloch-Torrey equation governing the dMRI signal. At high gradient strength, we reveal theoretically, numerically, and experimentally the universality of the localization phenomenon, which opens promising perspectives to improve the sensitivity of the signal to the microstructure. The localization phenomenon is still largely ignored in the scientific community, probably because of mathematical technicity and "anormal" behavior compared to the low-gradient

case. We propose a qualitative explanation for the localization regime. To us, this point was missing and reflects the current lack of understanding of the localization regime. Moreover, we extend several results and clarify important theoretical points regarding the localization regime. One of the most unexpected (given the present knowledge in the field) results is the existence of the localization regime even in unbounded domains (we treat the case of periodic domains in full detail). Our results suggest the need of a paradigm shift in the current theoretical approaches, mostly based on perturbative low-gradient expansions, in order to take full advantage of the possibilities of diffusion MRI.

Foreword

During three years of PhD, a student has two main goals: to understand the scientific field around his subject, and to produce original research works. The outline of this thesis follows these two goals. It begins with a presentation of the field of diffusion magnetic resonance imaging (dMRI), with increasing details and technicity. This presentation is neither comprehensive, nor objective. Rather, it reflects my own interests and the viewpoint of a theoretical physicist. I wrote it while having in mind my first steps into the field of dMRI. In a second part, research works, in which some specific aspects of dMRI are explored and studied in much detail, are presented in a thematic order. With my supervisor, we explored several interesting questions that form independent chapters of this thesis. In a sense, the aforementioned two goals merged as one: me trying to understand the field of dMRI led us to revisit various areas in the classical theoretical knowledge of the field.

List of publications

1. N. Moutal, M. Nilsson, D. Topgaard, and D. S. Grebenkov, "The Kärger vs bi-exponential model: Theoretical insights and experimental validations," *J. Magn. Reson.*, vol. 296, pp. 72–78, 2018.

2. N. Moutal, I. Maximov, and D. S. Grebenkov, "Probing surface-to-volume ratio of an anisotropic medium by diffusion NMR with general gradient encoding," *IEEE Trans. Med. Imag.*, vol. 38, pp. 2507–2522, 2019.

3. N. Moutal and D. S. Grebenkov, "Diffusion Across Semi-permeable Barriers: Spectral Properties, Efficient Computation, and Applications," *J. Sci. Comput.*, vol. 81, pp. 1630–1654, 2019.

4. N. Moutal, K. Demberg, D. S. Grebenkov, and T. A. Kuder, "Localization regime in diffusion NMR: theory and experiments," *J. Magn. Reson.*, vol. 305, pp. 162–174, 2019.

5. N. Moutal, A. Moutal, and D. S. Grebenkov, "Diffusion NMR in periodic media: efficient computation and spectral properties," *J. Phys. A*, 2020 (accepted).

6. N. Moutal and D. S. Grebenkov, "The localization regime in a nutshell," *J. Magn. Reson.*, 2020 (submitted).

7. Y. Lanoiselée, N. Moutal, and D. S. Grebenkov, "Diffusion-limited reactions in dynamic heterogeneous media," Nature Commun., vol. 9, 4398, 2018.

Conference proceedings

7. N. Moutal, D. S. Grebenkov, S. Clerjon, G. Pages, and J.-M. Bonny, "Diffusion MRI in muscles at high b-values: towards a quantification of microscopic organelles," *International Society of Magnetic Resonance in Medicine*, 2018.

8. N. Moutal, D. S. Grebenkov, S. Clerjon, G. Pages, and J.-M. Bonny, "Quantifying the mitochondrial content with diffusion MRI," *International Conference on Magnetic Resonance Microscopy*, 2019.

9. N. Moutal, I. I. Maximov, and D. S. Grebenkov, "Probing surface-to-volume ratio in anisotropic media," *International Conference on Magnetic Resonance Microscopy*, 2019.

10. N. Moutal, I. I. Maximov, and D. S. Grebenkov, “An accurate surface-to-volume ratio estimation by general diffusion gradient waveform,” *International Society of Magnetic Resonance in Medicine*, 2019.

11. N. Moutal, I. I. Maximov, and D. S. Grebenkov, “Optimized diffusion gradient waveforms for estimating surface-to-volume ratio of an anisotropic medium,” *International Society of Magnetic Resonance in Medicine*, 2019.

List of notations

As a general rule, bold symbols ($\mathbf{r}$, $\mathbf{J}$, etc.) denote vectors in real space, sans-serif symbols (D, S, etc.) denote matrices and tensors, calligraphic symbols ($\mathcal{B}$, $\mathcal{G}$, etc.) denote differential operators and their Green functions, tilded symbols ($\tilde{G}$, $\tilde{\mathbf{r}}$, etc.) denote quantities that have been rescaled to be dimensionless. The symbol $\sim$ shall be used as "is proportional to", and $\approx$ means "is approximately equal to". The notation ∂_x stands for partial derivative with respect to x.

In the table below, we give a short description of each symbol, its unit (1 means dimensionless, – means no unit), and a reference to a part of the text where it is defined (generally its first occurrence in the text).

Symbol	Description	Unit	Reference
a	Lattice step of a discrete random walk	m	Sec. 3.1.1
a_x, a_y, a_z	Spatial period of a periodic medium	m	Sec. 4.4
a_n	Zeroes of the derivative of Airy function	1	Sec. 4.2.1
$A(t,x)$	Amplitude of magnetization in an amplitude-phase representation	1	Sec. 4.1
$\mathsf{A}(\tilde{G})$	Projection of the Bloch-Torrey operator at a spectral bifurcation	–	Sec. 4.3
b	Diffusion weighting strength	$\mathrm{s/m^2}$	Eq. (1.46b)
$\mathbf{B_0}$, $\mathbf{B_1}$	Magnetic fields employed in magnetic resonance	T	Sec. 1.1.3
B_x, B_y, B_z, $\mathsf{B}_{y,p}$, $\mathsf{B}_{z,p}$	Matrices employed for numerical solution of Bloch-Torrey equation by spectral method	m	Sec. 1.1.5 and App. C.10
$\mathcal{B}$	Bloch-Torrey operator	$\mathrm{s^{-1}}$	Sec. 1.2.4
B	Diffusion weighting tensor	$\mathrm{s/m^2}$	Sec. 2.2.1
c	Semi-axis along the revolution axis of a spheroid	m	Sec. A.2
$c_{n,n'}$	Coefficients of spectral decomposition	$\mathrm{m}^{d/2}$	Sec. 4.3.3
$c_k(f,h)$	Coefficients of short-time expansion of heat kernel	$[f][h]\mathrm{m}^{-k}$	Sec. A.1

to be continued on following page

table continued from previous page

Symbol	Description	Unit	Reference
$C_{\text{latt}}(\mathbf{q})$, $C_{\text{pore}}(\mathbf{q})$	Structure factor of lattice and pore	1	Sec. 1.2.3
$C_{p,n}(q)$	Generalized structure factor in a periodic medium	1	Sec. 4.4
$C\left(\frac{t-t'}{\tau_{\text{n}}}\right)$	Two-point correlation function of noise	1	App. D
$\mathbb{C}$	Set of complex numbers	–	–
d	Dimensionality of the medium under study	1	Sec. 1.1.2
$\mathrm{d}(\cdot, \partial\Omega)$	Distance to the boundary of the domain	m	Sec. 2.3.1
D_0	Intrinsic diffusion coefficient	m^2/s	Sec. 1.1.2
D_0	Intrinsic diffusion tensor	m^2/s	Sec. 2.1
D	Effective diffusion coefficient probed by dMRI	m^2/s	Sec. 1.2.2
D_∞	Effective diffusion coefficient in the long-time (tortuosity) limit	m^2/s	Sec. 1.2.2
D_{MSD}	Effective diffusion coefficient defined through mean-squared displacement	m^2/s	Sec. 2.1
D_{MSD}	Effective diffusion tensor defined through mean-squared displacement	m^2/s	Sec. 2.1
$\mathcal{D}$	Time-evolution operator of the diffusion equation	1	Sec. 4.3.3
$\mathbf{e}_{\mathbf{x}}$, $\mathbf{e}_{\mathbf{y}}$, $\mathbf{e}_{\mathbf{z}}$	Unit vectors associated to Cartesian coordinates x, y, z	1	Sec. 1.1.4
$\mathbf{e}_{\mathbf{r}}$, $\mathbf{e}_\theta$, $\mathbf{e}_\phi$	Unit vectors associated to spherical coordinates r, θ, ϕ	1	App. A.2
$\mathbf{e}_{\mathbf{z}}$, $\mathbf{e}_\rho$, $\mathbf{e}_\theta$	Unit vectors associated to cylindrical coordinate z, r, θ	1	App. A.2
$\mathbf{e}$	Gradient direction	1	Sec. 2.2.2
erf	Error function	1	Sec. 2.3.1

to be continued on following page

table continued from previous page

Symbol	Description	Unit	Reference
erfcx	Scaled complementary error function	1	Sec. 3.1.2
$\mathbb{E}[\cdot]$	Expectation value	–	–
E_+, E_-	Zeeman energy levels of a spin	J	Sec. 1.1.3
f	Generic intensive quantity carried by diffusing particles	$[f]$	Sec. 1.1.2
	Correction to the mean-squared displacement near a planar boundary	1	Sec. 2.3.1
$f_1, \ldots, f_k$	Basis functions to optimize a gradient sequence with linear or bilinear conditions	1	Sec. 2.3.4
F	Dawson function	1	Sec. 2.3.3
$F_c(t)$	Fraction of particles that has crossed a permeable boundary	1	Sec. 3.1.2
$F(\lambda) = 0$	Transcendental eigenvalue equation	–	Sec. 3.4.2
$F_r(\tilde{x})$, $F_l(\tilde{x})$	Fundamental solutions of the one-dimensional time-independent dimensionless Bloch-Torrey equation	1	Sec. 4.2.1
$\mathcal{F}(T, x_0, x)$	Green function of one-dimensional Bloch-Torrey equation	$\mathrm{m}^{-\mathrm{d}}$	App. C.2
$\hat{\mathcal{F}}(T, x_0, x)$	Green function of one-dimensional Bloch-Torrey equation in Laplace domain	$\mathrm{m}^{-\mathrm{d}}\mathrm{s}$	App. C.2
g	Magnetic field gradient	T/m	Sec. 1.1.4
$g_{l_1}(y_1)$	Lateral eigenmode of Bloch-Torrey operator at a curved boundary	$\mathrm{m}^{-1/2}$	Sec. 4.2.2
$\mathbf{G}$, G	Larmor precession rate gradient	$\mathrm{s}^{-1}\mathrm{m}^{-1}$	Sec. 1.1.4
$\tilde{G}$	Dimensionless gradient	1	Sec. 4.3
$\hat{G}(t)$	Sampled gradient profile	$\mathrm{s}^{-1}\mathrm{m}^{-1}$	Sec. 4.4
$\mathcal{G}(T, \mathbf{r_0}, \mathbf{r})$	Diffusion propagator from $\mathbf{r_0}$ to $\mathbf{r}$ at time T	m^{-d}	Sec. 1.1.2
$\hat{\mathcal{G}}(s, x_0, x)$	Diffusion propagator in Laplace domain	$\mathrm{m}^{-\mathrm{d}}\mathrm{s}$	Sec. 3.4.2

to be continued on following page

table continued from previous page

Symbol	Description	Unit	Reference
$h_{l_2}(y_2)$	Lateral eigenmode of Bloch-Torrey operator at a curved boundary	$\mathrm{m}^{-1/2}$	Sec. 4.2.2
h	Relative precision of numerical computations	1	Sec. 4.4.4
$H(x)$	Heaviside function (integrated Dirac distribution)	1	Sec. 3.4.2
$H_l(z)$	Hermite polynomial	1	Sec. 4.2.2
H	Hamiltonian of field-spin interaction	J	Sec. 1.1.3
H	Mean curvature	m^{-1}	Sec. 4.2.2
i	Imaginary unit	1	–
	Generic index	–	–
I	Unit (or identity) matrix	1	Sec. 2.1
$\mathbb{I}$	Indicator function of a set	1	Sec. 3.1.1
$I_1, I_2, \ldots$	Nested subintervals	–	App. B.2.2
j	Generic index	–	–
$\mathbf{J}, J$	Diffusive flux of the intensive quantity f	$[f]\mathrm{m/s}$	Sec. 1.1.2
$J_\nu(z)$	Bessel function of the first kind	1	Sec. 1.2.3
k_B	Boltzmann constant	J/K	Sec. 1.1.3
k	Generic index	–	–
K	Parameter of Watson distribution	1	Sec. 2.3.3
K, $\mathsf{K}_{i,i+1}$	Matrix associated to a permeable barrier	1	Sec. 3.4.2
$\mathcal{K}$	Integral operator associated to temporal tensors	$\mathrm{s}^{1/2}$	App. A.3
$K(t-t')$	Kernel of the integral operator $\mathcal{K}$	$\mathrm{s}^{-1/2}$	App. A.3
$\hat{K}(\omega)$	Fourier transform of the kernel K	$\mathrm{s}^{1/2}$	App. A.3
ℓ_{mfp}	Mean free path of diffusing particles	m	Sec. 1.1.2
ℓ_{d}, ℓ_δ, ℓ_Δ	Diffusion length	m	Sec. 1.1.2

to be continued on following page

table continued from previous page

Symbol	Description	Unit	Reference
ℓ_s	Structural length of the medium	m	Sec. 1.2
ℓ_g	Gradient length	m	Sec. 1.2
ℓ_q	Phase pattern period	m	Sec. 1.2
ℓ_κ	Permeability length	m	Sec. 3.1.2
l	Generic index	–	–
l_i, l_a, l_h	Barrier spacings, arithmetic mean value, harmonic mean value	m	Sec. 3.4.2
L	Slab width, spacing between localization pockets	m	Sec. 4.3.3
L	Affine mapping related to to micro-anisotropy	1	Sec. 2.3.6
L_k	Fourier transform vector	m	Sec. 3.4.5
$m(T, \mathbf{r})$	Transverse magnetization density	1 ([a])	Sec. 1.1.4
m	Projection of the magnetization onto the Laplacian eigenbasis	$\mathrm{m}^{d/2}$ ([a])	Sec. 1.1.5
m	Number of subintervals	1	Sec. 3.4.2
$\mathbf{M}$	Magnetic moment of a spin	$\mathrm{A.m}^2$	Sec. 1.1.3
M	Transition matrix of a subinterval	1	Sec. 3.4.2
M	Subperiod of a bi-periodic geometry	1	App. B.3.3
n	Generic index	–	–
$\mathbf{n}$	Inward (from boundary to pore space) normal vector at the boundary of the domain	1	Sec. 1.1.2
N	Generic counter	–	–
N	A nilpotent matrix	1	App. C.5
$O(\cdot)$	At most of the same order as $\cdot$	–	–

to be continued on following page

table continued from previous page

Symbol	Description	Unit	Reference
	Structural disorder exponent	1	Sec. 1.2.2
p	Generic index	–	–
	Pseudo-periodicity wavenumber	m^{-1}	Sec. 4.4
$p_i(\mathbf{r})$	Projection along $\mathbf{e_i}$	m	App. A.1
P	Fine sampling parameter	1	Sec. 4.4
$\mathcal{P}_x$	Generic x-parity transformation	1	Sec. 1.2.4
$\mathbb{P}(\cdot)$	Probability	–	–
$P(\Delta, \mathbf{r})$	Averaged propagator	m^{-d}	Sec. 1.2.3
$P_x(\tilde{t}, \tilde{\kappa})$	Scaled first exit time tail distribution	1	App. B.2
$P(\cdot)$	Tail distribution of a random variable	1	App. B.1.2
$P(X)$	Polynomial function	1	App. B.3.5
$\mathbf{q}$, q, q_0	Wavevector/wavenumber associated to a gradient pulse	m^{-1}	Sec. 1.2.3
$\tilde{\mathbf{q}}$, $\tilde{q}$	Rescaled wavevector/wavenumber	1	Sec. 3.4.5
$q(t/T)$	Rescaled Q-profile	m^{-1}	App. A.3
$\mathbf{Q}$, Q	Time-integrated gradient profile	m^{-1}	Sec. 1.1.4
$\hat{Q}$	Sampled Q-profile	m^{-1}	Sec. 4.4
$Q(X)$	Polynomial function	1	Sec. B.3.5
$\mathbf{r}$	Position vector	m	Sec. 1.1.2
$\mathbf{r}_t$	Random diffusive trajectory	m	Sec. 1.1.2
r_i, r_e	Intra- and extra-cellular decay rates of magnetization	s^{-1}	Sec. 3.2
r, $r_{i,i+1}$	Permeable barrier resistance (inverse permeability)	s/m	Sec. 3.4.2
$\tilde{r}$	Rescaled barrier resistance	1	Sec. 3.4.2

to be continued on following page

table continued from previous page

Symbol	Description	Unit	Reference
$\mathbf{R}$	Displacement vector	m	Sec. 1.2.3
$\mathbf{R_i}$	Lattice vector	m	Sec. 1.2.3
R	Radius of a cylinder, sphere, curvature radius	m	Sec. 1.2.3
R, R_i	Rotation matrix	1	Sec. 2.1
$R(X)$	Polynomial function	1	App. B.3.5
$\mathbb{R}$	Set of real numbers	–	–
	Non-normalized signal	m^3 ([a])	Sec. 1.1.4
s	Laplace variable	s^{-1}	Sec. 3.4.2
	Generic integration variable	–	–
sinc	Sinus cardinal function	1	Sec. 1.2.3
surf$(\cdot)$	Area of a (two-dimensional) surface	m^2	Sec. 2.3.2
$\mathbf{S}$	Spin	$kg.m^2/s$	Sec. 1.1.3
S	Normalized signal	1	Sec. 1.1.4
S	Symmetry matrix	1	Sec. 3.4.2
t	Generic time variable	s	–
$\tilde{t}$	Rescaled time	1	Sec. 3.4.5
T	Echo time	s	Sec. 1.1.3
	Temperature	K	Sec. 1.1.3
T_1, T_2, $T_2^\dagger$	Magnetic resonance relaxation times	s	Sec. 1.1.3
$\mathcal{T}$	Tortuosity factor	1	Sec. 1.2.2
$\mathsf{T}^{(m)}$	Temporal tensors	1	Sec. 2.3.2
T	Transition matrix associated to a permeable barrier array	1	Sec. 3.4.2
T_x	Random first exit time	s	App. B.2

to be continued on following page

table continued from previous page

Symbol	Description	Unit	Reference
u	Generic variable	–	–
u_n	Laplacian eigenmodes	$\mathrm{m}^{-d/2}$	Sec. 1.1.5
$u_n^{(k)}$	Small-$\tilde{G}$ expansion coefficient of BT eigenmodes	1	Sec. 4.3.1
$u_{p,n}$	p-Pseudo-periodic Laplacian eigenmodes	$\mathrm{m}^{-d/2}$	Sec. 4.4
$\mathbf{u}$	Orientation of microdomain	1	Sec. 2.1
U, U_m	Energy potential for Langevin equation	J	App. D
$\mathbf{v}_t$	Velocity of diffusing particles	$\mathrm{m/s}$	Sec. 1.1.2
v_n	Bloch-Torrey eigenmodes	$\mathrm{m}^{-d/2}$	Sec. 1.2.4
$\mathrm{vol}(\cdot)$	Volume of a (three-dimensional) domain	m^3	Sec. 1.1.4
$\mathbb{V}[\cdot]$	Variance	–	–
w	Generic complex variable	–	–
$\mathbf{W}_t$	Brownian motion (Wigner process)	$\mathrm{s}^{1/2}$	Sec. 1.1.2
W	Wronskian matrix	1	Sec. 3.4.2
x, y, z	Cartesian coordinates	m	–
z	Generic complex variable	–	–
$\mathbb{Z}$	Set of integers	–	–

to be continued on following page

table continued from previous page

Symbol	Description	Unit	Reference
α	Flipping angle performed by radio-frequency pulses	1	Sec. 1.1.3
	Time-independent decrease of intracellular signal in the motional narrowing regime	1	Eq. (3.47)
	Interpretation parameter of Langevin equation	1	App. D
	Dimensionless square-root of eigenvalue for the 1D geometry with permeable barriers	1	Sec. 3.4.3
α_n	Zeroes of the derivative of the spherical Bessel function	1	Eq. (3.28b)
β_n	Normalization factor of eigenmodes	$\mathrm{m}^{-d/2}$	Secs. 3.4.2 and 4.2
$\beta_{n,n'}$	Generalized overlapping factor of Bloch-Torrey eigenmodes	1	Sec. 4.3.3
γ	Gyromagnetic ratio	$\mathrm{T}^{-1}\mathrm{s}^{-1}$	Sec. 1.1.3
$\Gamma^x_{p\to p+q_0}$	Gradient pulse matrices in a periodic medium	1	Sec. 4.4
$\delta(\cdot)$	Dirac distribution	s^{-1}	Sec. 1.1.2
δ	Gradient pulse duration in the PGSE sequence	s	Fig. 1.6
Δ	Inter-pulse duration in the PGSE sequence	s	Fig. 1.6
$\epsilon(d)$, $\epsilon'(d)$	Numerical prefactor for Debye-Porod formula	1	Eqs. (1.62) and (1.66)
ϵ	Barrier crossing probability	1	Sec. 3.1.1

to be continued on following page

table continued from previous page

Symbol	Description	Unit	Reference
ϵ_n	Symmetry factor of Laplacian eigenmodes in 1D geometry	1	Sec. 3.4.2
	Correction factor for the center of symmetry of 1D Bloch-Torrey eigenmodes	1	App. C.2
$\varepsilon(\theta, \phi)$	Weak perturbation of spherical shape	1	App. A.2
$\varepsilon_0(\mathbf{r})$	Generalized eigenmode at a spectral bifurcation	$\mathrm{m}^{-d/2}$	App. C.5
ζ_{-1}	Motional narrowing numerical coefficient	1	Sec. 1.2.2
ζ_i	Number of neighbors of subinterval i	1	Sec. 3.4.2
	Bloch-Torrey eigenvalue for the radial part at a curved boundary	s^{-1}	Sec. 4.2.2
ζ	Damping coefficient of Langevin equation	kg/s	App. D
η	Numerical correction factor to Mitra formula	1	Sec. 2.3.2
η_n	Symmetry factor of Laplacian eigenmodes in 1D geometry	1	Sec. 3.4.2
θ	Polar angle in spherical coordinate system	1	–
	Azimuthal angle in cylindrical coordinate system	1	–
Θ	Orientation order parameter	1	Sec. 2.1
κ	Surface relaxivity	m/s	Sec. 1.1.4
	Permeability	m/s	Sec. 3.1.1
$\tilde{\kappa}$	Scaled permeability	1	Sec. 3.4.2
κ_α	Generalized permeability for any Langevin interpretation	$\mathrm{m}^{2\alpha-1}/\mathrm{s}^{\alpha}$	App. D

to be continued on following page

table continued from previous page

Symbol	Description	Unit	Reference
λ_n	Laplacian eigenvalues	s^{-1}	Sec. 1.1.5
$\lambda_n^{(k)}$	Small-$\tilde{G}$ expansion coefficient of BT eigenvalues	1	Sec. 4.3.1
$\lambda_{p,n}$	Laplacian eigenvalues with p-pseudo-periodic boundary conditions	s^{-1}	Sec. 4.4
$\{\lambda\}$	Set of structural lengths in a multiscale domain	m	Sec. 1.2
λ	Period of slowly modulated microscopic potential	m	App. D
Λ	Matrix version of the diffusion operator for numerical computations	s^{-1}	Sec. 1.1.5
Λ_p	Matrix version of the p-pseudo-periodic diffusion operator	s^{-1}	Sec. 4.4
μ, μ_n	Bloch-Torrey eigenvalues	s^{-1}	Sec. 1.2.4
ν	Index of Bessel function	1	Sec. 1.2.3
ξ	Quantification of restricted diffusion during a gradient pulse	1	Sec. 3.2
	Abstract change of variables in Bloch-Torrey equation	1	Sec. 4.2.1
	Inertia relaxation rate in a viscous fluid	s^{-1}	App. D
$\Xi_n(\ell_g/\ell_s)$	Scaling form of Bloch-Torrey eigenvalues	1	Sec. 1.2.4
$\Xi(t,t')$	Integrated relaxation rate	1	App. D
$\Pi(\tilde{G})$	Projector associated to the Bloch-Torrey operator at a spectral bifurcation	–	–
ρ	Water fraction of interior space	1	Sec. 3.2
	Radius in cylindrical coordinate system	m	App. A.2
σ	Surface-to-volume ratio	m^{-1}	Sec. 1.2

to be continued on following page

table continued from previous page

Symbol	Description	Unit	Reference
$\tilde{\sigma}$	Effective scaled surface-to-volume ratio of a permeable boundary	1	Sec. 3.4.5
$\sigma(\mathcal{A})$	Spectrum of a differential operator $\mathcal{A}$	–	App. C.11
σ_{n}	Standard deviation of noise in the Langevin equation	$\mathrm{s}^{-1/2}$	App. D
τ_{mfp}	Mean time between two collisions	s	Sec. 1.1.2
τ	Narrow-pulse duration	s	Sec. 1.1.5
	Time step of a discrete random walk	s	Sec. 3.1.1
τ_κ	Intrinsic crossing time of a permeable barrier	s	Sec. 3.1.2
τ_{e}	Global exchange time of a compartment with the exterior	s	Sec. 3.1.2
τ_K, $\tau_{i\to e}$, $\tau_{e\to i}$	Exchange times between compartments	s	Sec. 3.2
$\tau^{(m)}$	Numerical prefactor of the temporal tensors	1	Sec. 2.3.4
τ_{i}	Inertial relaxation time of a massive particule under a damping force	s	App. D
τ_{n}	Correlation time of colored noise	s	App. D
ϕ	Random phase acquired by spin-bearing diffusing particles	1	Sec. 1.1.4
	Azimuthal angle in spherical coordinates	1	App. A.2
$\phi(s,x)$	A fundamental solution of the diffusion equation in an array of permeable barriers	1	Sec. 3.4.2
$\varphi_m(\cdot,\cdot)$	Bilinear form associated to temporal matrices $\mathsf{T}^{(m)}$	1	Sec. 2.3.4
φ_{m}	Mitochondrial volume fraction	1	Sec. 3.3

to be continued on following page

table continued from previous page

Symbol	Description	Unit	Reference
$\varphi(t,x)$	Phase of the magnetization in an amplitude-phase representation	1	Sec. 4.1
φ	Free volume fraction in the Lorentz gas model	1	App. D.3.1
$\Phi^{(m)}$	Matrix form of the bilinear form $\varphi_m(\cdot,\cdot)$	1	Sec. 2.3.4
χ	Random threshold of local crossing time of a reflected Brownian motion	s	Sec. 3.1.1
$\chi(X)$	Prefactor of equilibrium distribution in a slowly modulated potential	m^{-1}	App. D
ψ	Wavenumber for the finite periodic array of permeable barriers	1	Sec. 3.4.2
$\psi(s,x)$	A fundamental solution of the diffusion equation in an array of permeable barriers	1	Sec. 3.4.2
Ψ	Correction of the velocity autocorrelator to the Brownian motion result	s^{-1}	Sec. 1.1.2
ω_0, $\omega(\mathbf{r})$	Larmor precession rate	s^{-1}	Sec. 1.1.3
ω	Generic Fourier transform variable	–	–
Ω, Ω_1	Geometric domain under study	–	–
$\partial\Omega$	Boundary of Ω	–	–

[a] By convention

This page is unintentionally left not blank.

Contents

This page is unintentionally left not blank.

This page is unintentionally left not blank.

Chapter 1

Presentation of diffusion magnetic resonance imaging

1.1 Introduction

1.1.1 General description

Diffusion magnetic resonance imaging (dMRI) is an experimental technique that relies on the magnetic resonance (MR) phenomenon and magnetic resonance imaging (MRI) devices to probe diffusion. In other words, it is an imaging technique where diffusion plays the role of a contrast mechanism. The baseline is that areas where diffusion of the spin-bearing molecules is fast appear darker (i.e., less signal) than areas where diffusion is slow. Beyond the intrinsic interest of measuring diffusion coefficients, this technique aims to go beyond the spatial resolution of MRI images and infer microstructural properties of the medium.

Let us explain the reasoning behind this goal on the example of water inside a kitchen sponge. A sponge, as one can easily check at home, is a porous material made of multiple round cavities of various sizes that are mostly connected together. If the pores are smaller than the spatial resolution of the MRI image (for most scanners this is about 1 mm but it depends on many acquisition parameters), it is simply impossible to observe the pores, measure their sizes and their distribution, study their connectivity, and so on. How can the measurement of diffusion solve this issue? The diffusion of water inside the sponge is directly related to the microstructural properties of the sponge: at short times, water diffuses inside individual pores and the diffusion motion is controlled by the pore diameter; at long times, water diffuses across several pores and the diffusion motion is controlled by the distance between pores and overall connectivity of the medium. Thus, measuring the diffusive properties of water inside the sponge

gives informations about its microstructure (that could be interesting to infer its water absorption capabilities, for example). In practice, this example is unrealistic because the pores would have to be 10 to 100 times smaller to be probed by water diffusion, as we shall see. With this intuitive picture of a sponge, one can imagine many other porous media such as sedimentary rocks from which oil is extracted, or biological organs such as lungs or liver, whose microstructure can be accessed by dMRI.

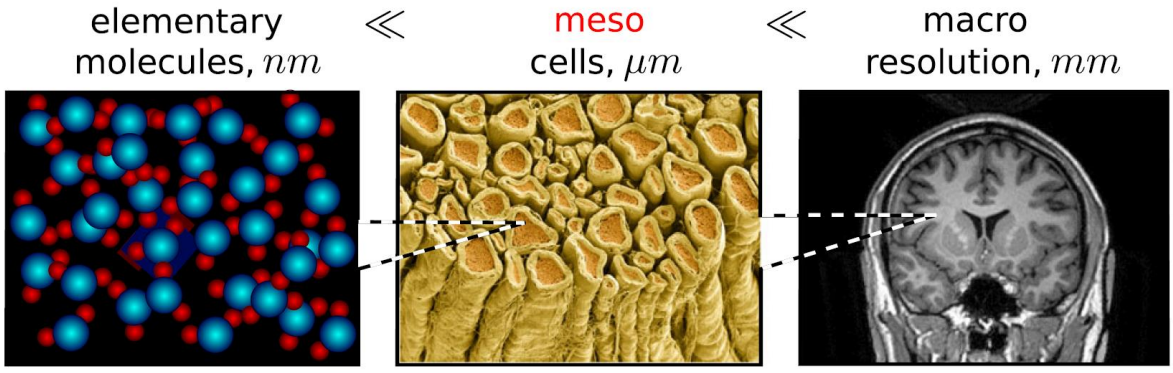

Figure 1.1: Illustration of the separation between the microscopic, mesoscopic, and macroscopic scales in the brain, from Ref. [10].

We stress that, as in the above example, the motivation behind the diffusion MRI technique is that the microstructural details are finer than the spatial resolution of the image so that one cannot see them directly. More precisely, diffusion MRI involves an important separation of scales that is illustrated on Fig. 1.1 (reproduced from [10]). The diffusion length traveled by particles defines a "mesoscopic" scale at which microstructure is probed. This scale is intermediate between the molecular scale and the macroscopic scale defined by the spatial resolution of images (i.e., the voxel size). For the same reason, one cannot observe directly the diffusive motion of spin-bearing particles.

By applying a diffusion-weighting protocol, one measures the MR signal inside one voxel (volumic equivalent of a pixel) as a function of various experimental parameters (for example, the diffusion time). The dependence of the signal on those parameters, *combined with a model for the medium*, yields the desired microstructural properties. In the above example of the sponge, one would model the medium as, say, a lattice of spherical pores connected by channels or by random hopping. If the measured signal fits well with this model, one can extract the diameter of the pores and their spacing. A more sophisticated model could account for e.g. non-spherical pore shape or structural disorder, but would require more experimental data to extract all model parameters and would be more likely

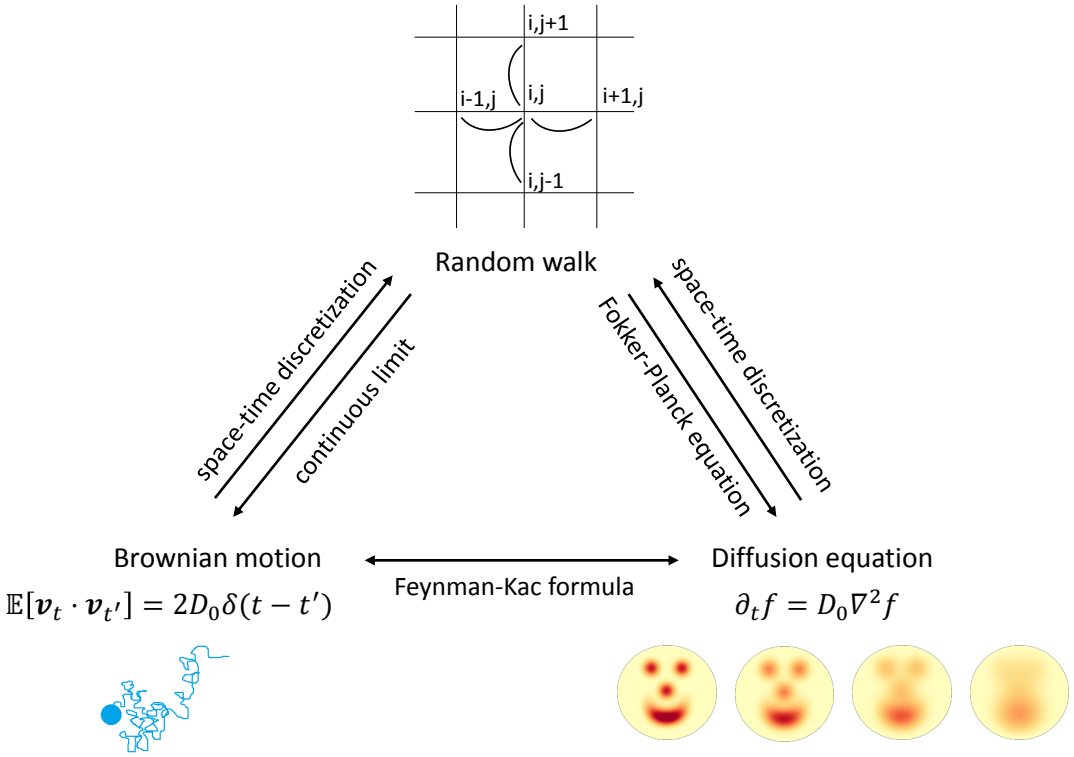

Figure 1.2: Schematic representation of different models of diffusion and their relations.

to fail compared to a coarser model that somewhat averages the complexity of the medium.

In the following subsections we are going to present the dMRI technique in more details. First, we recall some basic properties of diffusion, which makes up one half of the story. The second half, namely MRI, is then presented. We mainly focus on magnetic resonance itself and not imaging. Finally both parts are combined to give the Bloch-Torrey equation that governs the dynamics of dMRI.

1.1.2 Diffusion

The phenomenon of diffusion can be understood from two different points of view, the "molecular" point of view and the "continuum" point of view. These two points of view lead to two different but equivalent mathematical descriptions of the same phenomenon, which is very useful. Throughout this thesis we shall switch between molecular and continuum points of view depending on our needs.

At the molecular scale, particles are in constant motion due to thermal equi-

librium and they interact with each other through "collisions". By collision one means a short-duration, short-range interaction between two particles. Thus the trajectory of a given molecule can be approximated as a sequence of straight lines (free motion), separated by abrupt changes in direction (collisions). The number of collisions in the typical time scales of interest is very large: about 10^8 collisions in 1 ms, and most dMRI experiments involve diffusion times longer than 1 ms. Therefore the random walk $\mathbf{r}_t$ becomes in the continuous limit a Brownian motion (or Wiener process) $\mathbf{W}_t$ scaled by a diffusion coefficient determined by the mean free path ℓ_{mfp} and the time between two collisions τ_{mfp} [275, 281]:

$$\mathbf{r}_t = \sqrt{2D_{\text{mic}}}\,\mathbf{W}_t \;, \tag{1.1}$$

$$D_{\text{mic}} = \frac{\ell_{\text{mfp}}^2}{\tau_{\text{mfp}}} \;. \tag{1.2}$$

The fundamental property of the Brownian motion $\mathbf{r}_t$ is that its velocity $\mathbf{v}_t = \mathrm{d}\mathbf{r}_t/\mathrm{d}t$ is a Gaussian white noise, i.e. a Gaussian stochastic process with no time-correlations:

$$\mathbb{E}[\mathbf{v}_t \otimes \mathbf{v}_{t'}] = 2D_{\text{mic}}\mathsf{I}\delta(t - t') \;, \tag{1.3}$$

where we have introduced the notation for outer product: if $\mathbf{a}$ and $\mathbf{b}$ are vectors, then $\mathbf{a} \otimes \mathbf{b}$ is a matrix with elements

$$(\mathbf{a} \otimes \mathbf{b})_{ij} = \mathrm{a}_i \mathrm{b}_j \;. \tag{1.4}$$

Furthermore, $\delta(\cdot)$ denotes here the Dirac distribution and I is the identity matrix. For a liquid with low viscosity such as water, the above relation (1.2) yields $D_{\text{mic}} \sim 1\ \mu\text{m}^2/\text{ms}$. In a gas, the mean free path is much larger that yields a value about 10^4 times larger, that is $D_{\text{mic}} \sim 0.01\ \text{mm}^2/\text{ms}$. As we will see throughout this thesis, these orders of magnitude are essential to understand the scales that are probed by dMRI. In the following, we always use the notation $\mathbf{r}_t$ to denote the stochastic trajectory of a diffusing particle.

On the other hand, at the continuum scale, the random motion of all particles is averaged and one describes any intensive quantity f "carried" by the diffusing particles (particle density, temperature, or magnetization, for example) as a continuous function. Let us denote by Ω a spatial domain representing a voxel of interest. The evolution of f is then governed by a partial differential equation ("diffusion equation") on Ω [12, 13]:

$$\partial_t f = D_{\text{mac}} \nabla^2 f \;, \tag{1.5}$$

where D_{mac} is the diffusion coefficient of the particles under study inside the domain Ω. The above equation may be written in the form of a conservation

equation that makes the diffusive flux $\mathbf{J}$ appear explicitly

$$\partial_t f + \nabla \cdot \mathbf{J} = 0 \,, \qquad \mathbf{J} = -D_0 \nabla f \,. \tag{1.6}$$

The molecular and continuum points of view coincide because the probability density function of a Brownian motion and the propagator of Eq. (1.5) in free space (i.e., its solution with a Dirac peak as initial condition) are the same function

$$\mathcal{G}(T, \mathbf{r_0}, \mathbf{r}) = \frac{1}{(4\pi D_0 T)^{d/2}} \exp\left(-\frac{(\mathbf{r}-\mathbf{r_0})^2}{4D_0 T}\right) \,, \tag{1.7}$$

where d is the dimensionality of the domain where diffusion takes place and $D_0 = D_{\text{mic}} = D_{\text{mac}}$ unifies both values of the diffusion coefficient. Furthermore, as depicted in Fig. 1.2, one can derive both the Brownian motion and the diffusion equation descriptions from a random walk description where particles make discrete jumps on a lattice. Finally, using the mathematical formalism of stochastic differential equations, one can derive the Feynman-Kac formula that makes a bridge between stochastic processes such as the Brownian motion and partial differential equations such as the diffusion equation [280].

The above Gaussian distribution depends on a single parameter

$$\ell_{\text{d}} = \sqrt{D_0 T} \,, \tag{1.8}$$

that can be interpreted as the typical length traveled by diffusing particles during the measurement time T. For instance, the variance of displacement of particles is $\mathbb{V}\left[\mathbf{r}_T\right] = 2d\ell_{\text{d}}^2$ and the variance of displacement along a given direction $\mathbf{e}$ is $\mathbb{V}\left[(\mathbf{e}\cdot\mathbf{r}_T)\right] = 2\ell_{\text{d}}^2$, whereas its mean value is equal to its initial position: $\mathbb{E}\left[\mathbf{r}_T\right] = \mathbf{r}_0$. For liquid or gas diffusion and typical experimental times, one obtains

$$\text{liquid}: \quad 1\text{ ms} \leq T \leq 100\text{ ms} \quad \rightarrow \quad 1\ \mu\text{m} \leq \ell_{\text{d}} \leq 10\ \mu\text{m} \,, \tag{1.9a}$$

$$\text{gas}: \quad 1\text{ ms} \leq T \leq 100\text{ ms} \quad \rightarrow \quad 0.1\text{ mm} \leq \ell_{\text{d}} \leq 1\text{ mm} \,. \tag{1.9b}$$

Note the considerable upscaling (by a factor of about 100) of gas diffusion compared to liquid diffusion, due to the much larger diffusion coefficient.

In the presence of miscrostructure (obstacles, boundaries), the stochastic motion $\mathbf{r}_t$ becomes a reflected Brownian motion that introduces time-correlations in the velocity $\mathbf{v}_t$:

$$\mathbb{E}[\mathbf{v}_t \otimes \mathbf{v}_{t'}] = 2D_0 \mathrm{I}\delta(t-t') + 2D_0 \Psi(|t-t'|) \,, \tag{1.10}$$

where $\Psi(\cdot)$ is a matrix of smooth functions that decay at ∞ and that depend on the geometry of the medium. In turn, the formula for the diffusion propagator

$\mathcal{G}(T, \mathbf{r_0}, \mathbf{r})$ is modified compared to the free space result (1.7). In parallel, the diffusion equation (1.5) has to be supplemented with boundary conditions over $\partial\Omega$. One often assumes perfectly reflecting boundaries, that yields the no-flux or Neumann boundary condition:

$$\mathbf{n} \cdot D_0 \nabla f|_{\partial\Omega} = 0 \,, \tag{1.11}$$

where $\mathbf{n}$ is the inward normal vector at the boundary (from boundary to pore space). Other boundary conditions that take into account relaxation or permeation will be discussed later in the text.

1.1.3 Magnetic Resonance

In this section we recall some basic results about nuclear magnetic resonance (refer to books [1, 2] for a complete introduction). The phenomenon of magnetic resonance results from the interaction between magnetic fields and spins. Particles with a spin $\mathbf{S}$ indeed possess a magnetic moment $\mathbf{M}$ given by

$$\mathbf{M} = \gamma \mathbf{S} \,, \tag{1.12}$$

where γ is the gyromagnetic ratio of the particle. The theoretical value of the gyromagnetic ratio of a given particle involves sophisticated quantum electrodynamics computations, however one usually gets a reasonable *order of magnitude* with the classical formula $\gamma = q/(2m)$ for a rotating particle of charge q and mass m. For example, the gyromagnetic ratio of the proton is $\gamma = 2.675 \cdot 10^8 \ \mathrm{T^{-1}s^{-1}}$ and the classical formula yields $q/(2m) = 0.479 \cdot 10^8 \ \mathrm{T^{-1}s^{-1}}$. Throughout this thesis, we consider only *nuclear* magnetic resonance, i.e. spins from nuclei. Among all spin-bearing nuclei, the hydrogen nucleus is probably the most common one, especially because of its abundance in biological and mineral samples in the form of water or hydrocarbon molecules. Additionnally, we restrict ourselves to 1/2-spins that represent most of experimental works in the field, including the ones presented in this thesis. In fact, water diffusion probed by hydrogen resonance and gas diffusion probed by Xenon 129 resonance both involve 1/2-spins.

Thus, the interaction of a spin $\mathbf{S}$ and a magnetic field $\mathbf{B_0}$ results from the Hamiltonian

$$\mathsf{H} = -\mathbf{M} \cdot \mathbf{B_0} = -\gamma \mathbf{S} \cdot \mathbf{B_0} \,. \tag{1.13}$$

with eigenvalues

$$E_\pm = \pm \gamma \hbar B_0 / 2 \tag{1.14}$$

corresponding to a spin aligned with the field (E_-) or anti-aligned with the field (E_+).

For example, protons in a 10 T field yield the energy splitting:

$$E_+ - E_- = \gamma\hbar B_0 \approx 1.4 \cdot 10^{-25}\ \text{J} \approx 3.3 \cdot 10^{-5} k_B T \tag{1.15}$$

at room temperature ($T = 300$ K). Thus, a strong magnetic field produces a relatively weak magnetization, very far from saturation. More precisely, the small energy splitting compared to $k_B T$ implies that the magnetization density m_0 of a population of spin is proportional to the external magnetic field according to Curie's Law

$$m_0 = \frac{n\gamma^2\hbar^2 B_0}{4k_B T}\ , \tag{1.16}$$

where n is the density of spin-bearing particles. As the density of a gas is about 10^3 smaller than that of a liquid, the magnetization produced by a gas at thermal equilibrium is generally very close to the noise level that would prevent any experiments on gas diffusion. To circumvent this difficulty, the technique of spin-exchange optical pumping is used to "hyperpolarize" the gas and reach magnetization levels up to 10^4 higher than at thermal equilibrium [133–135]. Thus, the signal from hyperpolarized gas is of the same order of magnitude than liquids at thermal equilibrium. In practice, the gas is hyperpolarized then injected into the sample of interest (for example, inhaled by a patient to probe the structure of his/her lungs) and the measurement is then performed. This technique is *a priori* limited by the time (usually denoted by T_1) after which the magnetization of the sample returns to its thermal equilibrium value (1.16). In Xenon 129 gas, relaxation times T_1 are generally of the order of dozens of minutes (it depends on the chemical composition of the gas, its pressure, the applied magnetic field) that is much longer than the typical duration of one measurement (< 1 s).

Now we turn to the out-of-equilibrium situation and study the dynamics of a spin inside the external magnetic field $\mathbf{B_0}$. We will adopt a "semi-classical" point of view where the quantum operator $\mathbf{S}$ is replaced by a vector that represents its expectation value. There are three main reasons for this choice: (i) it provides the correct result for the evolution of the expectation value of the operator, which is sufficient if the detailed knowledge of each quantum states is not required; (ii) for $1/2$ spins, there is an equivalence between the quantum description and the geometrical description (Bloch sphere); (iii) the evolution of the spin is expressed in terms of the evolution of a vector instead of a quantum operator, which is geometrically more intuitive. In this geometrical description, one can show that the evolution of a spin follows the laws of mechanics on angular momentum

$$\frac{d\mathbf{S}}{dt} = \mathbf{M} \times \mathbf{B_0} = \gamma \mathbf{S} \times \mathbf{B_0}\ . \tag{1.17}$$

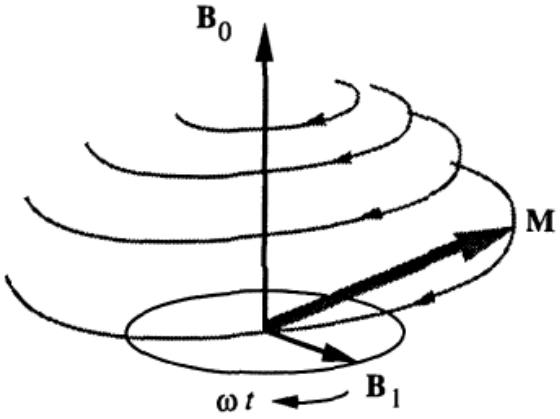

Figure 1.3: Schematic representation of magnetic resonance

The solution of this equation is a precession motion around $\mathbf{B_0}$ at the Larmor angular frequency

$$\omega_0 = \gamma B_0 \ . \tag{1.18}$$

This means that the component of the magnetization along the field $\mathbf{B_0}$ remains constant whereas its transverse component rotates at the angular frequency ω_0. In most MR devices, B_0 is of the order of several teslas, so that ω_0 is in the radiofrequency range.

Let us switch on another magnetic field $\mathbf{B_1}$, orthogonal to $\mathbf{B_0}$ and rotating at the Larmor frequency ω_0. In the rotating frame attached to $\mathbf{B_1}$, the Larmor precession of $\mathbf{S}$ around $\mathbf{B_0}$ is cancelled and the motion of $\mathbf{S}$ is merely a precession around the (fixed) field $\mathbf{B_1}$ at angular frequency $\omega_1 = \gamma B_1$. Going back to the laboratory frame, the motion of $\mathbf{S}$ is the superposition of a precession around $\mathbf{B_0}$ at angular frequency ω_0 and a nutation at angular frequency ω_1, hence a typical spiralling motion (see figure). The duration during which $\mathbf{B_1}$ is switched on controls directly the nutation angle of $\mathbf{S}$ with respect to the main field $\mathbf{B_0}$ so that one can apply a "α-pulse" for any desired angle α (experimentally, the most common angles are $\alpha = 90°$ and $\alpha = 180°$). In particular, from the thermal equilibrium situation where the net magnetization is aligned with the magnetic field, one can apply a 90°-pulse to flip the magnetization to the transverse plane and detect its precession by induction in a nearby coil.

If one applies a 180°-pulse, then the magnetization is flipped so that the interaction energy with the external field goes from negative (aligned spins) to positive (anti-aligned spins). In other words, there is an energy transfer from the oscillating field $\mathbf{B_1}$ to the spin population, thus the name magnetic *resonance*. In the language of quantum mechanics, the splitting between two eigenstates of the hamiltonian (1.13) corresponds to an angular frequency $(E_+ - E_-)/\hbar = \gamma B_0$, i.e.

the Larmor frequency associated with the field B_0. Thus, it is possible to trigger a transition between the "aligned" and "anti-aligned" state by applying a perturbation at angular frequency ω_0. The consistency between the purely quantum description and the semi-classical one confirms the validity of the latter.

In the above description, the interaction between spins was discarded. It is interesting to compute an order of magnitude of the magnetic field created by the spin magnetization (1.16) in the case of water (where the spin-bearing particles are hydrogen nuclei) at room temperature: $B_{\text{spin}} = \mu_0 m_0 \approx 2 \cdot 10^{-9} B_0$. This computation indicates that spin-spin interactions are a very weak correction to the hamiltonian (1.13). In a liquid or a gas, the dipole interaction between spins is modulated by the fast rotational tumbling of molecules that creates a time-dependent perturbation of the Hamiltonian (1.13) and therefore leads to the relaxation of magnetization towards its thermal equilibrium state. This relaxation mechanism actually involves two processes with different rates. The first one is longitudinal relaxation that governs the return to thermal equilibrium magnetization parallel to the applied magnetic field. As we mentioned above, one usually denotes the associated relaxation time by T_1. The second relaxation process is transverse relaxation that governs the decay of magnetization perpendicular to the applied magnetic field, with relaxation time denoted by T_2. In the early days of NMR, Bloembergen, Purcell and Pound [16] computed the theoretical relaxation rates from the combined effect of dipole interaction and molecular tumbling. They showed that $T_2 < T_1$ in general, and that they coincide in the limit of very fast tumbling rate compared to Larmor precession rate.

A complete theory of relaxation involves many additional mechanisms that we shall not describe here [1]. However, it is interesting to draw a distinction between so-called "homogeneous" and "inhomogeneous" relaxation effects. Whereas the former are caused by short-range and fluctuating interactions between spins, the latter are caused by magnetic field inhomogeneities that broaden the spectrum of Larmor frequencies (1.18) and destroy transverse magnetization by fast dephasing between spins. One usually emphasizes this distinction by writing the total transverse relaxation rate as $1/T_2^* = 1/T_2 + 1/T_2^\dagger$, where $1/T_2$ denotes the homogeneous relaxation rate and $1/T_2^\dagger$ the inhomogeneous one.

Two typical examples of inhomogeneous broadening are chemical shift and magnetic impurities. In the first example, the chemical environment surrounding a spin slightly changes the magnetic field felt by the spin. For instance, for a given applied magnetic field $\mathbf{B_0}$, the Larmor frequency of water hydrogens is not the same as the one of fatty acids hydrogens. Therefore, the chemical composition of a sample may affect its relaxation properties. In the second example, magnetic impurities, e.g. iron atoms, are polarized by the external field $\mathbf{B_0}$ and produce a relatively strong local perturbation to this field, therefore causing neighboring

spins to precess at a different rate. The same phenomenon occurs with internal gradient or susceptibility differences in the medium. Contrary to homogeneous relaxation effects, inhomogeneous broadening involves no increase in entropy and can be "negated" by spin echoes, as we shall see in the next section.

Throughout this thesis, we discard all relaxation effects except when stated otherwise. Despite their importance, we focus here on different aspects such as interplay between microstructure, diffusion, and phase encoding. We shall mention relaxation times occasionnally because they may impose limitations on the duration of diffusion experiments.

1.1.4 Diffusion + magnetic resonance, Bloch-Torrey equation

Now we shall see how one can probe the diffusive motion of spin-bearing particles with magnetic resonance. From a population of spins initially aligned with the constant magnetic field $\mathbf{B_0}$, we apply a 90°-pulse so that all spins are flipped to the transverse plane at time $t = 0$. In this plane, spins can be represented by a complex number

$$M = M_0 e^{i\phi} \,, \tag{1.19}$$

where ϕ denotes the angle that they have turned from their initial position at time $t = 0$. Therefore, the measured MR signal, which is proportional to the net magnetization in the sample, can be represented as a sum over all spins

$$s = \sum M_0 e^{i\phi} \,. \tag{1.20}$$

In the following, except when explicitly said otherwise, we will always normalize the signal with respect to its value at time $t = 0$, when all spins are aligned with the same angle $\phi = 0$. Therefore the normalized signal can be represented as

$$S = \mathbb{E}[e^{i\phi}] \,. \tag{1.21}$$

The notation for expectation value instead of a spatial average may be unexpected at this point. As we shall see in the next paragraph, the combination of diffusion and precession implies that the phase of a spin ϕ is a random variable that depends on the random trajectory of the spin-bearing particle. Because of the very large number of particles, the sum over all spins can be replaced by the average over all possible diffusive trajectories in the medium, hence Eq. (1.21). We emphasize that this average is computed at a fixed time T, at which the measurement is performed. Throughout the text, we keep the convention of lower-case s for non-normalized signal and upper-case S for normalized signal.

The fundamental ingredient of dMRI is an *inhomogeneous* $\mathbf{B_0}$ field, and the most common case is a magnetic field gradient that is generally time-dependent:

$$\mathbf{B_0} = (B_0 + \mathbf{g}(t) \cdot \mathbf{r})\mathbf{e_z} \, , \tag{1.22}$$

where the direction of the magnetic field is unchanged and its amplitude is a linear function of position. Note that the null-divergence property of magnetic fields would constrain the gradient to be orthogonal to the direction of the magnetic field. In practice, since $|\mathbf{B_0}|/|\mathbf{g}|$ is much larger than the voxel size, the gradient can take any direction by allowing a slight variation of the magnetic field direction. The magnetic field gradient (1.22) translates into a Larmor precession rate gradient $\mathbf{G}(t) = \gamma \mathbf{g}(t)$:

$$\omega(\mathbf{r}) = \omega_0 + \mathbf{G}(t) \cdot \mathbf{r} \, . \tag{1.23}$$

In the following, we discard the constant ω_0 as it is a constant precession effect that has no effect on the measured signal. Because of the gradient $\mathbf{G}$, spins in different positions precess at different angular frequencies and a phase difference is accumulated as time increases

$$\phi_1 - \phi_2 = \int_0^T \mathbf{G}(t) \cdot (\mathbf{r_{1}}_t - \mathbf{r_{2}}_t) \, \mathrm{d}t \, . \tag{1.24}$$

Let us denote by L the size of the voxel in which the experiment is performed. We recall that the voxel is much larger than the length explored by diffusing particles over the time T, i.e. $L \gg \ell_\mathrm{d}$. Therefore, under a constant gradient $\mathbf{G}$, the width $\Delta\phi$ of the phase distribution over the voxel can be estimated simply by considering two particles at opposite ends of the voxel, that yields

$$\Delta\phi = GLT \, . \tag{1.25}$$

This behavior is unwanted for two main reasons. First, because of this increasing dephasing, the signal (1.21) decays very rapidly with increasing time and/or gradient strength. In particular, any uncontrolled magnetic field inhomogeneity leads to a fast decay of the signal even in the absence of externally applied magnetic field gradient. The second point is that the decay of the signal is not related to diffusion of particles but simply to their difference in position. In other words, in this setting, the constant gradient $\mathbf{G}$ is a *position-encoding* mechanism and not a *motion-encoding* mechanism. As a side remark, magnetic resonance imaging is essentially based on this principle.

An elegant solution to both of these issues is the use of spin echoes, that were invented in 1950 by Hahn [17] and have been at the heart of magnetic

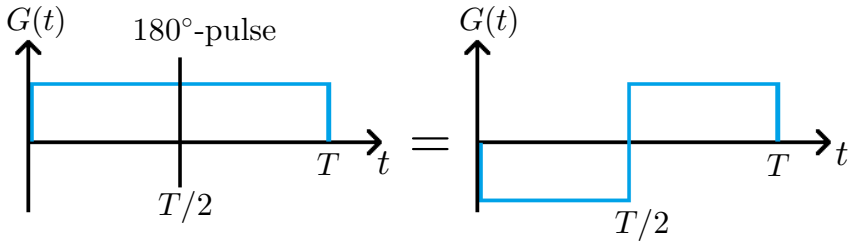

Figure 1.4: (left) A schematic gradient sequence with a refocusing 180° pulse at $t = T/2$. (right) The effective gradient description takes into account the effect of refocusing 180° pulses into the sign of the gradient by reversing the gradient before the pulse.

resonance ever since. The principle of spin echo is to apply a 180°-pulse at time $T/2$ that reverses all spins with respect to the $\phi = 0$ axis. In other words, this pulse reverses the sign of all phases ϕ, i.e., it effectively reverses the effect of all magnetic fields applied between $t = 0$ and $t = T/2$. One can see immediately that it solves the first issue of signal decay due to field inhomogeneity. Indeed, the uncontrolled effect of field inhomogeneities is reversed at time $T/2$ and cancels exactly at time T. Experimentally, the signal that is destroyed by fast dephasing of spins is reformed at time T and forms an "echo". About the second issue of position-encoding versus motion-encoding, it is useful to introduce the notion of "effective" gradient that takes into account the effect of the refocusing 180° pulse through a sign change in the gradient (see Fig. 1.4). In the following, the gradient $\mathbf{G}(t)$ is implicitly the effective gradient. One can see that the effect of the recofusing pulse is equivalent to imposing

$$\int_0^T \mathbf{G}(t)\,\mathrm{d}t = \mathbf{0}\ . \tag{1.26}$$

With this condition, the phase of spins become independent of their absolute position, i.e., a particle that does not move is not dephased by the gradient. A particle that diffuses gets dephased by

$$\phi = \int_0^T \mathbf{G}(t)\cdot\mathbf{r}_t\,\mathrm{d}t \tag{1.27a}$$

$$= \int_0^T \mathbf{G}(t)\cdot(\mathbf{r}_t-\mathbf{r}_0)\,\mathrm{d}t = \int_0^T \mathbf{G}(t)\cdot(\mathbf{r}_t-\mathbf{r}_T)\,\mathrm{d}t \tag{1.27b}$$

$$= -\int_0^T \mathbf{Q}(t)\cdot\mathbf{v}_t\,\mathrm{d}t\ , \tag{1.27c}$$

where we have introduced the integrated gradient profile

$$\mathbf{Q}(t) = \int_0^t \mathbf{G}(t')\,\mathrm{d}t'\ . \tag{1.28}$$

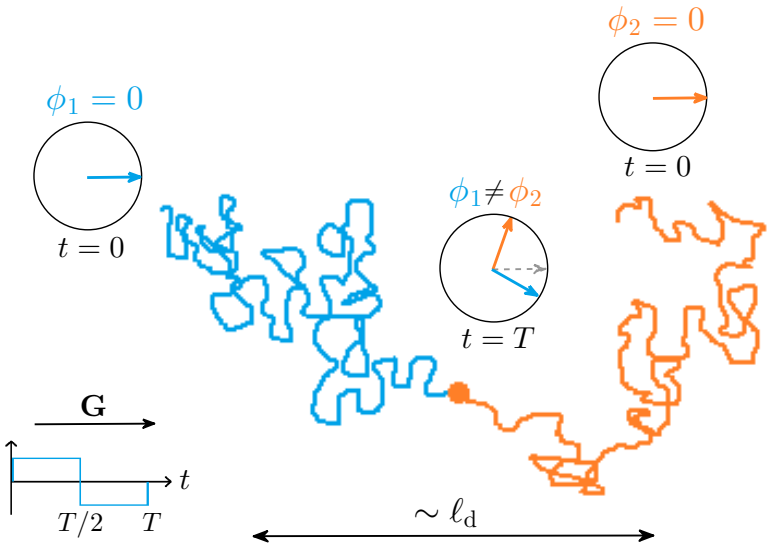

Figure 1.5: Illustration of diffusion encoding by the gradient. Two particles that meet each other at position $\mathbf{r}$ at the measurement time T have different histories that lead to different accumulated phases ϕ_1 and ϕ_2 (see Eq. (1.27b)). In turn, the resulting phase dispersion leads to signal decay according to Eq. (1.21).

The formulas (1.27b) and (1.27c) stress that a particle dephases because of its *motion* during the gradient sequence. Because of time-reversal symmetry, any trajectory going from the position $\mathbf{r}_1$ to the position $\mathbf{r}_2$ is equally probable to the trajectory traveled in opposite sense, going from $\mathbf{r}_2$ to $\mathbf{r}_1$, therefore

$$\mathbb{E}[\phi] = 0 \,. \tag{1.29}$$

and more generally all odd moments of ϕ are zero, and the signal (1.21) is real. All previous results hold for *any* gradient profile that satisfies the refocusing condition (1.26).

To summarize, to any random trajectory $\mathbf{r}_t$ is associated a random phase ϕ through Eq. (1.27b) because of encoding by the gradient (see Fig. 1.5). The measured signal is the superposition of all possible phases according to Eq. (1.21) and can be seen as the characteristic function of the random variable ϕ. This molecular point of view leads one to study individual random trajectories and derive the behavior of the signal from the properties of ϕ.

Now we turn to the continuum point of view where one studies the dynamics of the local transverse magnetization density $m(t, \mathbf{r})$. In complex notation, the

effect of the magnetic field gradient without diffusion is simply:

$$\partial_t m = i(\mathbf{G}(t) \cdot \mathbf{r})m \ . \tag{1.30}$$

The joint effect of diffusion and precession is then the superposition of both effects and yields the Bloch-Torrey (BT) equation introduced by Torrey in 1956 [19]:

$$\partial_t m = D_0 \nabla^2 m + i(\mathbf{G}(t) \cdot \mathbf{r})m \ . \tag{1.31}$$

If one takes into account surface relaxation due to magnetic impurities or susceptibility induced internal gradients, the boundary condition on $\partial\Omega$ takes the general Robin form

$$\mathbf{n} \cdot D_0 \nabla m - \kappa m|_{\partial\Omega} = 0 \ , \tag{1.32}$$

where κ is the surface relaxivity of the boundary. Neumann boundary condition (1.11) corresponds to no relaxivity, i.e. $\kappa = 0$ and the opposite limit of infinite relaxivity yields Dirichlet boundary condition: $m|_{\partial\Omega} = 0$. Finally, one often assumes that the transverse magnetization at $t = 0$ (i.e. right after the 90°-pulse) is uniform, that yields the initial condition:

$$m(t = 0, \mathbf{r}) = 1 \ . \tag{1.33}$$

Due to lack of spatial resolution, the transverse magnetization is not accessible experimentally, and one measures its average value over the voxel Ω at the echo time T:

$$S = \frac{1}{\mathrm{vol}(\Omega)} \int_\Omega m(T, \mathbf{r}) \, \mathrm{d}^3\mathbf{r} \ . \tag{1.34}$$

In this representation, one studies the behavior of the signal through a partial differential equation. The Feynmann-Kac formula shows that both representations coincide: Eqs. (1.21) and (1.27a) are equivalent to Eqs. (1.31) to (1.34). Note that one can define the local magnetization in terms of ϕ through

$$m(T, \mathbf{r}) = \mathbb{E}\left[e^{i\phi} | \mathbf{r}_T = \mathbf{r}\right] \ , \tag{1.35}$$

where the average is performed only on trajectories that end at position $\mathbf{r}$ at time T.

Having two representations of the same phenomenon is very helpful from a theoretical point of view because it provides more mathematical tools and more insight into the phenomenon.

1.1.5 Numerical techniques

In this section we provide a brief overview of three main numerical schemes to solve the Bloch-Torrey equation (1.31).

PDE solving by finite element or finite difference method

The Bloch-Torrey equation may be solved with standard numerical PDE solver using finite difference (regular mesh) or finite element (geometry-adapted mesh) methods [30–33, 195, 272]. The main limitations of this technique is the size of the mesh (i.e., number of nodes) that may become extremely large, especially in three dimensions.

Monte-Carlo simulations

By adopting the "molecular" point of view, i.e. Eq. (1.21), the solution of the Bloch-Torrey equation may be simulated with Monte-Carlo simulations [34, 35, 58, 192]. One draws randomly N particles inside the domain, and simulates for each particle a random walk, where the phase ϕ is accumulated at each time step according to Eq. (1.27a). Interestingly, this numerical method gives directly access to the phase distribution. In turn, the computation of the signal from the numerical phase distribution may be inaccurate if the signal is very low, because of the slow $1/\sqrt{N}$ convergence of the empirical average to the mathematical expectation value.

Spectral methods (matrix formalism)

The idea behind this third class of numerical techniques is that the complexity of the Bloch-Torrey equation is mainly contained in the Laplace operator and the boundary condition (1.32). Therefore, one solves the equation in two steps: (i) to solve the Laplace equation with the same boundary conditions; (ii) to incorporate the effect of the gradient [3, 36–38, 40]. .

Step (i) is performed by looking for Laplacian eigenmodes u_n and eigenvalues λ_n over the domain Ω of interest, i.e.

$$-D_0 \nabla^2 u_n = \lambda_n u_n \,, \tag{1.36a}$$

$$\mathbf{n} \cdot D_0 \nabla u_n - \kappa u_n|_{\partial\Omega} = 0 \,. \tag{1.36b}$$

Step (ii) is achieved by projecting the gradient term $i(\mathbf{G}\cdot\mathbf{r})$ onto the Laplacian eigenbasis, i.e. by computing the matrix elements

$$[\mathrm{B}_x]_{n,n'} = \int_\Omega x\, u_n(\mathbf{r}) u_{n'}(\mathbf{r})\, \mathrm{d}^3\mathbf{r} \,, \tag{1.37a}$$

$$[\mathrm{B}_y]_{n,n'} = \int_\Omega y\, u_n(\mathbf{r}) u_{n'}(\mathbf{r})\, \mathrm{d}^3\mathbf{r} \,, \tag{1.37b}$$

$$[\mathrm{B}_z]_{n,n'} = \int_\Omega z\, u_n(\mathbf{r}) u_{n'}(\mathbf{r})\, \mathrm{d}^3\mathbf{r} \,. \tag{1.37c}$$

This allows one to project the Bloch-Torrey equation onto the Laplacian eigenbasis:

$$\partial_t \mathsf{m} = \left[-\Lambda + i(G_x(t)\mathsf{B}_x + G_y(t)\mathsf{B}_y + G_z(t)\mathsf{B}_z)\right] \mathsf{m}\,, \tag{1.38}$$

where m is a vector with components $m_n(t) = \int_\Omega m u_n$ and Λ is a diagonal matrix with elements λ_n. Note that the boundary condition is "automatically" ensured by the choice of the basis $\{u_n(\mathbf{r})\}$. Since the Laplacian eigenbasis is complete, the knowledge of $m(t,\mathbf{r})$ is equivalent to the knowledge of the (infinite-dimensional) vector $\mathsf{m}(t)$. For numerical purpose, a finite truncation threshold $n \leq N$ has to be chosen. Since Λ and $\mathsf{B}_x, \mathsf{B}_y, \mathsf{B}_z$ matrices do not commute, one cannot integrate Eq. (1.38) straightforwardly if $G_x(t), G_y(t), G_z(t)$ are not constant. In order to solve the equation, two main approximations were proposed.

1. The continuous-time gradient profile is replaced by narrow and intense pulses during which diffusion may be neglected [36, 38]. The evolution of the magnetization results from the succession of gradient pulses without diffusion and diffusion without gradient. The application of a gradient pulse corresponds to left-multiplication by a matrix of the general form $\exp(i\tau[G_x\mathsf{B}_x + G_y\mathsf{B}_y + G_z\mathsf{B}_z])$, where τ is the pulse duration. In turn, diffusion without gradient corresponds to left-multiplication by a matrix of the general form $\exp(-\tau\Lambda)$, where τ is the diffusion step duration. We shall see a new application of this idea for simulating the Bloch-Torrey equation in periodic media in Sec. 4.4.

2. The continuous-time gradient profile is replaced by a piecewise-constant profile [3, 37, 40]. A step with constant gradient G_x, G_y, G_y and duration τ corresponds then to left-multiplication by the matrix $\exp(\tau[-\Lambda + i(G_x\mathsf{B}_x + G_y\mathsf{B}_y + G_z\mathsf{B}_z)])$. This method is more general and accurate than the above one because it is better suited to extended gradient pulses while being able to deal with narrow and intense gradient pulses.

Once the matrices Λ, $\mathsf{B}_x, \mathsf{B}_y, \mathsf{B}_z$ are known, the computation of the magnetization requires only matrix multiplications, which are very fast and accurate. Computing the Laplacian eigenbasis is generally a difficult and time-consuming numerical problem, except in some basic shapes (slab, disk, sphere, annulus, etc.) [14] where they are explicitly known. In such domains, spectral methods are extremely fast and accurate compared to other methods.

Note on numerical simulations in unbounded domains

Unbounded domains (that can model extracellular space or connected porous media, for example) often present a numerical challenge. In fact, numerical simulations in unbounded domains require adding a virtual outer boundary to the

domain with convenient boundary conditions (e.g., Dirichlet boundary condition). To ensure that the effect of this boundary is negligible, the boundary should be sufficiently far away from the area of interest so that very few particles can diffuse from one to the other. As such, the computational domain can be much bigger than the area of interest, especially in long diffusion time simulations, which makes the technique inefficient. In Sec. 4.4 we will present a numerical technique to solve the Bloch-Torrey equation in a periodic medium without this limitation.

1.1.6 Empirical versus theoretical approach to the problem

The aim of dMRI is to infer microstructural properties of the medium Ω from the signal S. In the Bloch-Torrey formulation, the microstructure of the medium enters through the boundary condition (1.32). Therefore, there is no explicit dependence of the signal on the properties of Ω and one is faced with an *inverse* problem. The existence of this thesis more than 60 years after the first publication of the Bloch-Torrey equation is probably a good indication of the difficulty of this problem.

Although a bit artificial, one can draw a distinction between two general attitudes in front of such a problem (see e.g. Ref. [111]). The first one would be the one of theoretical physicists. By studying simple geometries, one can identify and understand the main regimes of dMRI. In turn, this understanding may give rise to experimental protocols that allow one to recover interesting microstructural properties. The second attitude would be that of radiologists. Because of the overwhelming complexity of real-life samples (biological tissues for example), one adopts an empirical or statistical approach to the problem. For instance, if a significant difference in the signal behavior between healthy and sick people is measured, then the protocol can be used to detect the disease, regardless of the mechanisms at play.

In essence, these two attitudes reflect the difference between fundamental science and applications. Both have advantages and drawbacks but above all they have different short-term priorities. Naturally, this distinction is artificial because scientists are often somewhat between the two. The field of dMRI is special in that regard because the spectrum of researchers in the field is extremely broad, ranging from mathematicians to physicians and MRI engineers. As it is mentioned in the foreword, this thesis is written from the sole point of view of a theoretical physicist, with a strong focus on the understanding of fundamental mechanisms.

1.2 Main theoretical approaches and regimes

The main experimental parameter in the BT equation (1.31) is the gradient sequence. By changing the gradient sequence (duration, amplitude, profile) and measuring the variation in the signal, one aims at recovering microstructural information about the medium. Because of intrinsic mathematical difficulties associated to this equation, several theoretical approaches have been developed. We present them below, from perturbative (i.e., the gradient term is treated as a perturbation of a diffusion problem) to non-perturbative ones. To these theoretical approaches are associated various regimes of the dMRI signal that we will discuss and explain.

Naturally, these regimes depend on the geometry (domain Ω and boundary conditions (1.32)) in which diffusion takes place and it would take too much space and too much patience from the reader to provide here a comprehensive list of all theoretical knowledge and results in the field for all possible geometries (see Refs [2–5, 7, 9, 111, 116]). For this reason, we make the choice to base the discussion on a sponge-like porous medium, where we assume that pores have a typical diameter ℓ_s. The surface-to-volume ratio of the domain, that we denote by σ, scales therefore as $\sigma \sim \ell_s^{-1}$. As we shall see, at long diffusion times the behavior of the magnetization in bounded and unbounded domains may differ significantly. When it is the case, we shall discuss separately the case of isolated pores (i.e., bounded domain) and connected pores (i.e., unbounded domain).

This simplified setting allows us to discuss the competition between a single "structural" length scale ℓ_s and two experimental length scales, namely (i) the diffusion length ℓ_d and (ii) the gradient length ℓ_g (for extended-gradient pulses) or the phase pattern period ℓ_q (for narrow-gradient pulses). Multiscale domains with a wide spectrum of geometrical lengths $\{\lambda\}$ are much harder to study and to classify. Often, one performs a cut-off, or coarse-graining, that averages the effect of any length scale below the "mesoscopic scale" $\lambda \ll \ell_d$. In this way, one can reduce a complex medium to a simpler one where our discussion may be valid.

The aim of this section is to give a partial overview of the state of theoretical knowledge in dMRI. It is also the occasion to introduce fundamental concepts that will be deepened in the second part of this thesis devoted to research works. First, we introduce the length scales ℓ_g and ℓ_q and provide physical interpretations for these quantities, then we turn to a more systematic description of theoretical approaches and results.

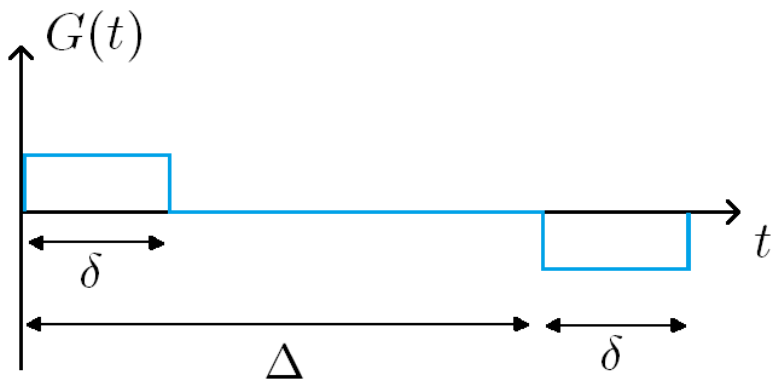

Figure 1.6: Schematic representation of the pulsed-gradient spin-echo (PGSE) sequence with conventional notations for the pulse and inter-pulse durations [20].

1.2.1 Length scales associated to the gradient

In this subsection, we introduce with qualitative arguments two fundamental length scales associated to the gradient, the gradient length ℓ_g and the phase pattern period ℓ_q. These two length scales have different physical interpretation and are somewhat "exclusive": while ℓ_g is better suited to discuss the behavior of extended-gradient pulse experiments, ℓ_q is better suited to the opposite case of narrow-gradient pulse experiments. The case of arbitrary gradient profiles is briefly discussed at the end of this subsection.

Gradient length ℓ_g

Let us consider two particles that meet each other at time T and position $\mathbf{r}$. Therefore, they are initially spaced by a distance of the order of the diffusion length ℓ_d (see Fig. 1.5). We assume that the pore diameter is much larger than this distance, i.e. $\ell_\mathrm{d} \ll \ell_\mathrm{s}$, and that the particles diffuse far away from the boundaries of the medium so that we neglect their influence. Furthermore, we assume a constant gradient amplitude G. The random phase difference (1.24) accumulated by these two particles until they meet is of the order

$$|\phi_2 - \phi_1| \sim GT\ell_\mathrm{d} = (\ell_\mathrm{d}/\ell_g)^3 \,, \tag{1.39}$$

where we have introduced the so-called gradient length

$$\ell_g = D_0^{1/3} G^{-1/3} \,. \tag{1.40}$$

Equivalently, the variance of ϕ at position $\mathbf{r}$ scales as

$$\mathbb{V}[\phi|\mathbf{r}_T = \mathbf{r}] \sim D_0 G^2 T^3 = (\ell_\mathrm{d}/\ell_g)^6 \,. \tag{1.41}$$

This quantity describes the phase dispersion at a given position, note that is position-independent because of the hypothesis of negligible influence of boundaries. If $\ell_\mathrm{d} \ll \ell_g$ the typical phase difference is small so that the spins have strongly correlated phases. In other words, two different trajectories yield close values of ϕ and we call this situation *weak diffusion encoding*. In contrast, if $\ell_\mathrm{d} \gtrsim \ell_g$, the typical phase difference is large and the spins have almost uncorrelated phases. This is the opposite regime of *strong diffusion encoding* where two different trajectories yield very different values of ϕ.

Therefore, one can interpret the gradient length ℓ_g as the typical length traveled by particles under the gradient G before they have decorrelated phases with other spins at the same position, *provided that they do not reach any boundary*. At this point, one understands that the signal attenuation after an extended-gradient pulse depends strongly on the competition between ℓ_g, ℓ_d, and the confining length ℓ_s. This interplay and the resulting regimes are detailed in Sec. 1.2.4. For liquid or gas diffusion and typical magnetic field gradient strengths, one obtains the following orders of magnitude for ℓ_g:

$$\text{liquid}: \quad 1\ \mathrm{mT/m} \leq g \leq 1\ \mathrm{T/m} \quad \longrightarrow \quad 20\ \mu\mathrm{m} \geq \ell_g \geq 2\ \mu\mathrm{m}\,, \tag{1.42a}$$

$$\text{gas}: \quad 1\ \mathrm{mT/m} \leq g \leq 1\ \mathrm{T/m} \quad \longrightarrow \quad 1\ \mathrm{mm} \geq \ell_g \geq 0.1\ \mathrm{mm}\,, \tag{1.42b}$$

where inequalities are reversed because the gradient length decreases with increasing gradient strength. Similarly to the diffusion length (see Eqs. (1.9a) and (1.9b)), there is a considerable upscaling with gas experiments because of the much larger diffusion coefficient. Note that the transition between medical imaging scanners and research scanners is around 50 mT/m.

The above reasoning is still valid if the gradient profile is made of two extended-gradient pulses with no diffusion time inbetween them, such as the profile shown on Fig. 1.6 with $\Delta - \delta = 0$. Indeed, the first (positive) gradient pulse induces a stronger dephasing than the second (negative) one because particles are further apart during the first pulse. However, it fails if the pulses are separated by a diffusion time that is significantly longer than the duration of the pulses, i.e., $\Delta \gg \delta$ with the notations of Fig. 1.6. Indeed, the diffusion step with no gradient mixes particles from different areas and thus increases dephasing between spins at a given position. This is especially the case in the narrow-gradient regime where the length ℓ_q, that we describe below, provides more insight into the formation of the signal.

Phase pattern period ℓ_q

The gradient length is an effective way of quantifying the dephasing acquired by diffusing particles because of their random motion, in other words, the variance

of ϕ. In contrast, let us consider the average phase at a given position $\mathbf{r}$ after a single gradient pulse of amplitude G and duration δ, such as on Fig. 1.6. We assume again that the effect of boundaries can be neglected. To compute the average value of ϕ, one cannot use Eq. (1.27b) or (1.27c) because they were derived under the hypothesis of a refocused gradient sequence, whereas we consider here a single constant-gradient pulse. Therefore, one uses Eq. (1.27a) and gets

$$\mathbb{E}[\phi] = \delta \mathbf{G} \cdot \mathbf{r}_0 \ . \tag{1.43}$$

This implies that the gradient pulse produces a phase pattern with wavevector $\mathbf{q}$ or equivalently with period ℓ_q (up to a 2π factor):

$$\mathbf{q} = \delta \mathbf{G} \ , \quad \text{and} \quad \ell_q = q^{-1} \ . \tag{1.44}$$

Note that in addition to this phase pattern, one should take into account the random dephasing computed above that attenuates the magnetization during the gradient pulse.

Let us consider the limit of narrow-gradient pulses: $\delta \longrightarrow 0$ and $\mathbf{q}$ is constant. The above estimation (1.41) of the variance of ϕ just after the pulse shows that it tends to zero in that limit, therefore the effect of a narrow-gradient pulse is simply to multiply the magnetization by the phase pattern $e^{i\mathbf{q}\cdot\mathbf{r}}$ with no attenuation. In other words, the attenuation of the magnetization is solely caused by the subsequent diffusion step of duration Δ that "blurs" the phase pattern of period ℓ_q. The competition between ℓ_q, ℓ_d and the confining length ℓ_s yields a rich variety of regimes that is detailed in Sec. 1.2.3. For liquid or gas diffusion and typical magnetic field gradient strengths with a 1 ms pulse duration, one obtains the following orders of magnitude for ℓ_q:

$$\text{liquid/(gas)} : \quad 1 \text{ mT/m} \leq g \leq 1 \text{ T/m} \quad \longrightarrow \quad 3 \text{ mm} \geq \ell_q \geq 3 \ \mu\text{m} \ , \tag{1.45}$$

where inequalities are reversed because the phase pattern period decreases with increasing gradient strength. As stated previously, the transition between medical imaging scanners and research scanners is around 50 mT/m. Contrary to the gradient length, the length ℓ_q does not depend on the diffusion coefficient, hence one gets the same order of magnitude for liquid and gas. However, the condition of narrow-gradient pulse may be much harder to achieve with gas diffusion. In fact, the large diffusion length during 1 ms (see Eq. (1.9b)) implies that one most likely has to take into account attenuation during the pulse. In contrast, gradient pulses shorter than 1 ms may be technically challenging because of finite slew-rate of gradient coils. Moreover, because of gradient strength limitations, shorter pulses reduce the range of accessible q-values.

General gradient profile

The length scales ℓ_g and ℓ_q are well-suited to describe extended-gradient and narrow-gradient experiments, respectively. In the general situation of arbitrary gradient profile, one cannot *a priori* use either of them. To our knowledge, almost all works with complex gradient profiles were done under the assumption of low gradient amplitude where, as we shall see, the signal can be expressed in terms of the first moments of ϕ, especially its variance. That situation corresponds to weak diffusion encoding by the gradient, where the behavior of the signal is solely controlled by the competition between the diffusion length ℓ_d and the structural scale ℓ_s. The next section starts with a description of this regime that provides universal results in the weak encoding limit for any gradient sequence. Then we turn to narrow-gradient sequences and finally to extended-gradient sequences. For reference we recall the four length scales that we have introduced so far:

Name	Symbol	Interpretation
Diffusion length	$\ell_\mathrm{d} = \sqrt{D_0 T}$	Typical distance traveled by diffusing particles during the experimental time T
Structural length	ℓ_s	Scale of microstructural features of the sample (e.g., pore diameter)
Gradient length	$\ell_g = D_0^{1/3} G^{-1/3}$	Length traveled by spin-bearing particles before their phases become decorrelated (diffusion encoding length)
Phase pattern period	$\ell_q = G^{-1}\delta^{-1}$	Period (up to a 2π factor) of the phase pattern produced by a narrow gradient pulse (position encoding length)

Table 1.1: Fundamental length scales of dMRI.

1.2.2 Low-gradient, cumulant expansion

As discussed in the previous subsection, the low-gradient perturbative approach is based on the assumption of weak dephasing between spins, i.e., weak phase encoding by the gradient. For an arbitrary gradient sequence, Eqs. (1.27c) and

(1.3) yield for free diffusion [17–20]:

$$\mathbb{V}[\phi] = 2bD_0 \,, \tag{1.46a}$$

$$b = \int_0^T \mathbf{Q}^2(t)\,\mathrm{d}t \,. \tag{1.46b}$$

One can check that this result is consistent with Eq. (1.41). In a sense, bD_0 is a generalization of the ratio $(\ell_\mathrm{d}/\ell_g)^6$ and measures the strength of diffusion encoding by the gradient if the effect of boundaries can be neglected.

Particles that diffuse close to a boundary are reflected on it, that reduces the range of exploration and in turn the discrepancies between two random trajectories. In other words, the effect of boundaries is to reduce the value of $\mathbb{V}[\phi]$ and one often defines an effective[1] diffusion coefficient $D < D_0$ [26] by analogy with the free diffusion formula (1.46a):

$$D(\mathbf{r}) = \frac{1}{2b}\mathbb{V}[\phi|\mathbf{r}_T = \mathbf{r}] \,, \tag{1.47a}$$

$$D = \frac{1}{2b}\mathbb{V}[\phi] \,. \tag{1.47b}$$

We emphasize that the effective diffusion coefficient D depends *a priori* on the gradient profile and therefore cannot be straightforwardly interpreted as a measure of displacement of particles inside the domain. Note that it does not depend on the overall amplitude of the gradient because b and $\mathbb{V}[\phi]$ both are quadratic functions of the gradient profile.

Another effect of boundaries is that the "local" expectation value of ϕ is not zero (although its "global" expectation value is zero, see Eq. (1.29)): $\mathbb{E}[\phi|\mathbf{r}_T = \mathbf{r}] \neq 0$. To see why this is the case, let us consider Fig. 1.5 and imagine that there is a boundary that limits exploration to the left of $\mathbf{r}$. Then all trajectories that end at $\mathbf{r}$ come from the right side, that leads to a non zero average value of ϕ. From a more mathematical point of view, the presence of a boundary breaks left-right symmetry, and Eq. (1.27b) shows that left-right symmetry is equivalent to $\phi \leftrightarrow -\phi$ (symmetries are studied in more detail later in Sec. 1.2.4). A consequence of the non-zero local expectaction value of ϕ is that the "global" effective diffusion coefficient D is not the spatial average of the "local" effective diffusion coefficient $D(\mathbf{r})$ but contains an additional term:

$$D = \frac{1}{\mathrm{vol}(\Omega)}\int_\Omega D(\mathbf{r}) + \frac{\mathbb{E}[\phi|\mathbf{r}_T = \mathbf{r}]^2}{2b}\,\mathrm{d}^3\mathbf{r} \tag{1.48}$$

In the weak diffusion encoding regime, i.e. $bD \ll 1$, the characteristic function of ϕ, i.e. the signal (1.21), can be computed perturbatively from the first

[1] One also finds the terminology "apparent diffusion coefficient" (ADC) in the literature.

moments or cumulants of the distribution of ϕ. Therefore, the magnetization and signal are given to the first order by

$$m(T,\mathbf{r}) \approx \exp\left(i\,\mathbb{E}[\phi|\mathbf{r}_T=\mathbf{r}] - \frac{1}{2}\mathbb{V}[\phi|\mathbf{r}_T=\mathbf{r}]\right) \tag{1.49a}$$

$$= \exp\left(i\,\mathbb{E}[\phi|\mathbf{r}_T=\mathbf{r}]\right)\exp(-bD(\mathbf{r}))\,, \tag{1.49b}$$

$$S \approx \exp\left(-\frac{1}{2}\mathbb{V}[\phi]\right) = \exp(-bD)\,, \tag{1.49c}$$

and the signal is a Gaussian function of the gradient amplitude through the variable b [25, 26]. In the above formula, b is an experimental parameter that is controlled by the choice of gradient profile, amplitude, and duration. By varying the b-value and fitting the signal with Eq. (1.49c), one can extract the effective diffusion coefficient D that contains *a priori* microstructural informations [25–28, 109–112, 138, 139].

Since these formulas are exact if ϕ is a Gaussian random variable, this regime is called "Gaussian phase approximation" (GPA) in the litterature[2]. In particular, these formulas are true for free diffusion without any restriction on the gradient strength because ϕ is Gaussian as a sum of independent Gaussian variables (see Eq. (1.27c)). Naturally, D is equal to the intrinsic diffusion coefficient D_0 in that case. Although free diffusion is not very interesting from a microstructural point of view, it is worth noting that one can measure the intrinsic diffusion coefficient D_0 of spin-bearing particles with dMRI. This is already an interesting application because the measurement of diffusion coefficients with other methods generally requires sophisticated experimental protocols. Therefore this method has been used since the 60s and was shown to be sensitive to a wide range of diffusion coefficients [20, 45, 46].

In contrast, restricted diffusion leads to three main regimes under the GPA, that are controlled by the ratio of diffusion length ℓ_d and pore diameter ℓ_s:

Short-time regime $\ell_\mathrm{d} \ll \ell_\mathrm{s}$. Diffusing particles can be split into two populations: the ones that stay away from boundaries and the ones that interact with the boundaries during the gradient sequence. Geometrically, we split the pore space in two parts: the bulk, and a boundary layer of thickness $\sim \ell_\mathrm{d}$. In the bulk, the effect of the boundary is negligible and the local effective diffusion coefficient $D(\mathbf{r})$ is equal to D_0. In contrast, near the boundaries there is far less

[2]This terminology may be misleading as it suggests that the phase is approximately Gaussian, whereas Eq. (1.49c) simply follows from a low-bD Taylor expansion, without any assumption on the phase distribution. See Refs [11, 126] for a more detailed discussion of misinterpretation of the GPA.

phase dispersion, which corresponds to $D(\mathbf{r}) < D_0$. Therefore, taking the average over the whole domain, one deduces that D differs from D_0 by a quantity that is proportional to the fraction of particles affected by the boundary, hence to the surface-to-volume ratio σ of the domain:

$$\frac{D_0 - D}{D_0} \sim \ell_d \sigma \ . \tag{1.50}$$

Mitra *et al.* obtained the numerical coefficient for an isotropic domain and a narrow-pulse sequence in [47–49] and we discuss this regime in much more detail in Sec. 2.3.

Long time regime $\ell_s \ll \ell_d$ in unbounded domain. The condition $\ell_d \gg \ell_s$ implies that all particles have diffused across multiple pores and that the microstructural complexity of the medium has been averaged out by diffusion. By upscaling the medium by a factor ℓ_d/ℓ_s, the diffusive motion of particles is similar to a Brownian motion in free space with a reduced diffusion coefficient $D_\infty = D_0/\mathcal{T}$, where the tortuosity coefficient $\mathcal{T}$ depends on the connectivity of the porous medium in which diffusion takes place. In general, the effective diffusion coefficient D approaches this limit at long time as a power law:

$$\frac{D - D_\infty}{D_\infty} \sim \left(\frac{\ell_s}{\ell_d}\right)^{d+p} , \tag{1.51}$$

where d is the dimensionality of the medium and p is the structural exponent that quantifies disorder in the medium (roughly speaking, weak disorder corresponds to $p \geq 0$ whereas stronger disorder yields $p < 0$). This universal behavior was first revealed by Novikov *et al.* in [68, 69] and we explain it in more details in the next subsection for the particular case of narrow-gradient pulses.

Long time regime $\ell_s \ll \ell_d$ in bounded domain. This corresponds to the situation of an isolated pore of diameter ℓ_s. The condition $\ell_s \ll \ell_d$ implies that each particle explores the domain multiple times during the gradient pulse, so let us denote by $n_{\text{expl}} = (\ell_d/\ell_s)^2 \gg 1$ the average number of domain explorations per particle. To compute the dephasing acquired by spins during one domain exploration, one can use the results of free diffusion recalled above, assuming that during one domain exploration, the particles have little interaction with the boundaries of the medium and that the gradient remains constant. Of course, this is not valid over the course of multiple domain explorations. Therefore, if one denotes by $\phi_{\text{expl}}(t)$ the phase acquired by a particle during one domain

exploration around time t, the free diffusion case (1.41) shows that it is of the order of

$$\mathbb{V}[\phi_{\text{expl}}(t)] \sim (\ell_s/\ell_g)^6 \sim G(t)^2 \ell_s^6 / D_0^2 \,. \tag{1.52}$$

In the following, we assume that $\ell_s/\ell_g \ll 1$ at all times so that the above dephasing is small. This assumption is necessary to ensure a weak attenuation of the bulk signal. Otherwise, the signal is dominated by the contribution from rare trajectories that remain close to the boundaries at all times. This is the localization regime that is explored in details later. After one domain exploration, the position of the particle is almost uncorrelated from its starting point so that the dephasings $\phi_{\text{expl}}(t)$ at different times can be seen as independent from each other (in the limit $n_{\text{expl}} \to \infty$). Therefore, one can see the total dephasing after n_{expl} domain explorations as a sum of independent variables so that

$$\mathbb{V}[\phi] \sim \frac{n_{\text{expl}}}{T} \int_0^T \mathbb{V}[\phi_{\text{expl}}(t)] \, \mathrm{d}t \sim \frac{\ell_s^4}{D_0} \int_0^T G(t)^2 \, \mathrm{d}t \,. \tag{1.53}$$

The above relation provides the correct scaling; an exact computation shows that it is true up to a numerical prefactor usually denoted by ζ_{-1} that depends on the geometry of the pore. For example, $\zeta_{-1} = 1/120$ for a slab, $\zeta_{-1} = 7/1536$ for a cylinder, and $\zeta_{-1} = 1/350$ for a sphere (where ℓ_s denotes the diameter of the pore). Therefore, the magnetization is uniform and the signal is given by

$$S = \exp\left(-\zeta_{-1} \frac{\ell_s^4}{D_0} \int_0^T G(t)^2 \, \mathrm{d}t\right) \,. \tag{1.54}$$

This is the motional narrowing regime, where fast position averaging by diffusion effectively reduces the Larmor precession rate dispersion [79–81]. A larger diffusion coefficient implies more explorations of the domain in the same amount of time, that increases the position averaging effect and in turn leads to less attenuated signal. The size of the pore contributes through ℓ_s^4, implying a strong discrimination between small and large pores. Although the numerical coefficient ζ_{-1} is generally unknown, the measurement of the signal for various gradient amplitudes or durations allows to recover a reasonable estimate of ℓ_s. This regime is revisited in terms of Bloch-Torrey eigenmodes in Sec. 1.2.4 and is studied in more detail in Secs. 3.2 and 4.3.1.

1.2.3 Narrow-gradient pulse, averaged diffusion propagator

The previous approach treated the gradient as a perturbation by ensuring a low amplitude. In that case the behavior of the signal is governed by the variance of ϕ,

therefore reducing the study of the Bloch-Torrey equation to a diffusion problem. Another way to perform such a reduction is by mean of narrow-gradient pulses: the gradient does not have a low amplitude but is localized in time, so that its effect can be separated from that of diffusion. More precisely, we consider a gradient profile such as the one on Fig. 1.6, with $\delta \longrightarrow 0$ and $\mathbf{q} = \delta\mathbf{G}$ is constant [20, 22]. Note that here T and Δ coincide; in the following we use the notation Δ for consistency with the literature.

Narrow pulses effectively encode the starting point and arrival point of each particle, so that their phase is simply related to their displacement along the gradient direction:

$$\phi = \mathbf{q} \cdot (\mathbf{r}_0 - \mathbf{r}_\Delta) \,, \tag{1.55}$$

and the magnetization and signal are given by integrals over all possible displacement $\mathbf{R} = \mathbf{r}_\Delta - \mathbf{r}_0$:

$$m(\Delta, \mathbf{r}) = \int e^{i\mathbf{q}\cdot\mathbf{R}} \mathcal{G}(\Delta, \mathbf{r}, \mathbf{r} + \mathbf{R}) \, \mathrm{d}^3\mathbf{R} \,, \tag{1.56a}$$

$$S = \int e^{i\mathbf{q}\cdot\mathbf{R}} P(\Delta, \mathbf{R}) \, \mathrm{d}^3\mathbf{R} \,, \tag{1.56b}$$

where $P(\Delta, \mathbf{R})$ is the average of the diffusion propagator $\mathcal{G}(\Delta, \mathbf{r}, \mathbf{r} + \mathbf{R})$ over all starting points $\mathbf{r}$:

$$P(\Delta, \mathbf{R}) = \frac{1}{\mathrm{vol}(\Omega)} \int_\Omega \mathcal{G}(\Delta, \mathbf{r}, \mathbf{r} + \mathbf{R}) \, \mathrm{d}^3\mathbf{r} \,. \tag{1.57}$$

Note that we used the symmetry of diffusion propagator related to time-reversal symmetry, i.e. $\mathcal{G}(\Delta, \mathbf{r}, \mathbf{r} + \mathbf{R}) = \mathcal{G}(\Delta, \mathbf{r} + \mathbf{R}, \mathbf{r})$ to write Eq. (1.56a) in a more convenient form. The signal appears as the Fourier transform of the averaged diffusion propagator $P(\Delta, \mathbf{R})$, that can in principle be recovered if a sufficient number of measurements is performed. However, the diffusion propagator itself is not available because of the limited spatial resolution of dMRI.

The b-value (1.46b) associated to the narrow-gradient pulse sequence is equal to

$$bD_0 = (\ell_\mathrm{d}/\ell_q)^2 \,. \tag{1.58}$$

The interpretation for free diffusion is rather straightforward. Indeed, the ratio between diffusion length and phase pattern period ℓ_d/ℓ_q can be interpreted as a measure of the "blurring" of the phase pattern by diffusion. In turn, this is consistent with the interpretation of bD_0 as a measure of diffusion encoding by the gradient in the free diffusion case. For restricted diffusion, one can identify several different regimes depending on the ratios of phase pattern period ℓ_q, diffusion lengh ℓ_d, and structural length ℓ_s. Those regimes are summarized graphically at the end of this subsection on Fig. 1.8.

Short-time and weak blurring: $\ell_d \ll \ell_s$ and $\ell_d \ll \ell_q$. Since $\ell_d \ll \ell_q$, this corresponds to the low b-value (GPA) regime described above where the signal decays as $\exp(-bD)$ with an effective diffusion coefficient D (see Eq. (1.49c) and related discussion). Moreover, $\ell_d \ll \ell_s$ implies that the effective diffusion coefficient is given by the Mitra formula (1.50).

Short-time and strong blurring: $\ell_d \ll \ell_s$ and $\ell_q \ll \ell_d$. Contrary to the previous case, one cannot rely on the GPA to obtain the expression of the signal because of the strong blurring hypothesis. The short-time hypothesis $\ell_d \ll \ell_s$ implies that each diffusing particle explores a small fraction of the domain. Therefore, one can split the domain Ω in small independent "blobs" of diameter ℓ_d and the signal is the sum of contributions from all blobs. The strong blurring hypothesis implies that the bulk magnetization is strongly attenuated so that the signal is dominated by boundary contributions. To obtain the expression of the signal, let us first compute the effect of a single impermeable boundary in a one-dimensional setting (the barrier is placed at $x = x_b$). At very large ℓ_d/ℓ_q, Eq. (1.56b) yields after integration by parts the following formula for the (non-normalized) signal contribution from the boundary:

$$s_b = -\ell_q^2 \,\mathrm{vol}(\Omega) \frac{\partial P}{\partial x}\bigg|_{x=x_b} = \ell_q^2 \,\mathcal{G}(\Delta, x_b, x_b) \ . \tag{1.59}$$

The return-to-the-barrier probability $\mathcal{G}(\Delta, x_b, x_b)$ is simply equal to twice the Gaussian probability density (1.7) at the origin because of the "folding" created by the boundary. This yields directly

$$s_b = \frac{1}{q^2\sqrt{\pi D \Delta}} = \frac{\ell_q^2}{\ell_d \sqrt{\pi}} \ . \tag{1.60}$$

The physical interpretation of Eq. (1.59) is that the signal is dominated by trajectories that start and end at a distance less than $\sim \ell_q$ from the boundary. The reason why only these trajectories matter is figuratively explained on Fig. 1.7

If the gradient makes the angle θ with the normal to the boundary, the attenuation of the signal results from the independent contribution of the normal and parallel part of the gradient. The normal part is the same as above with $\ell_q \to \ell_q/\cos\theta$, and the parallel part follows the free diffusion formula with $\ell_q \to \ell_q/\sin\theta$:

$$s_b = \frac{1}{\cos^2\theta} \frac{\ell_q^2}{\ell_d \sqrt{\pi}} \exp(-\sin^2(\theta)\, \ell_d^2/\ell_q^2) \ . \tag{1.61}$$

The above formula has to be modified at $\theta \approx \pm\pi/2$ because the assumption $\ell_q/\cos\theta \ll \ell_d$ is not valid anymore, however the strong decay from the exponential factor $\exp(-\sin^2(\theta)\, \ell_d^2/\ell_q^2)$ makes this correction negligible in practice. From

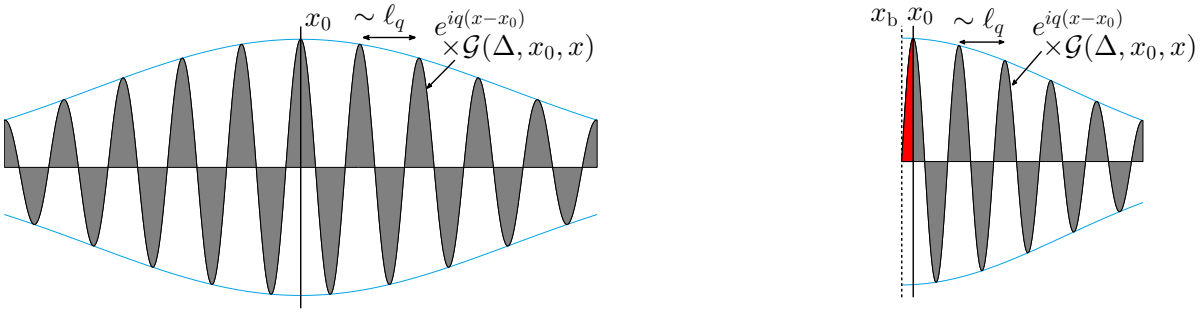

Figure 1.7: Schematic plot of $F(\mathbf{r}_0, \mathbf{r}) = e^{i\mathbf{q}\cdot(\mathbf{r}-\mathbf{r}_0)}\mathcal{G}(\Delta, \mathbf{r}_0, \mathbf{r})$ in 1D and in the limit $\ell_q \ll \ell_d$. The magnetization at position $\mathbf{r}_0$ (i.e. x_0 in 1D) is given by the integral of F, that is represented by the shaded area. (left) In the bulk, the left-right symmetry leads to positive and negative parts of F cancelling each other and a very weak magnetization. (right) Close to a boundary, there is a symmetry breaking and the integral of F is equal to the bulk integral plus a small contribution from an area of size $\sim \ell_q$ close to the boundary (shown in red). Therefore, the magnetization close to boundaries is more intense and gives the contribution (1.59) to the signal.

this result, one can easily compute the normalized signal from a d-dimensional isotropic medium by averaging over all possible orientations of the boundary with respect to the gradient:

$$S = \epsilon(d)\frac{\sigma \ell_q^{1+d}}{\ell_d^d}\,, \tag{1.62}$$

where $\epsilon(1) = 1/\sqrt{\pi}$, $\epsilon(2) = 1/\pi$, and $\epsilon(3) = 1/(2\sqrt{\pi})$. This is the analogous of Debye-Porod law for wave diffraction at large wavector $\mathbf{q}$ inside a d-dimensional disordered medium [82–84]. In particular, the scaling $S \sim \ell_q^{1+d}$ is universal at large values of ℓ_s/ℓ_q and simply results from the general properties of Fourier transform of functions with discontinuities in dimension d. In turn, the prefactor is modified if the short-time hypothesis is not valid, as we show in the next paragraph.

Long-time: $\ell_s \ll \ell_d$ in a bounded domain. In the long-time limit, the diffusion propagator $\mathcal{G}(\Delta, \mathbf{r}, \mathbf{r}+\mathbf{R})$ in a single pore Ω_1 becomes independent of time and equal to the two-point correlation function of the pore:

$$\mathcal{G}(\Delta, \mathbf{r}, \mathbf{r}') = \mathbb{I}_{\Omega_1}(\mathbf{r})\mathbb{I}_{\Omega_1}(\mathbf{r}') = \begin{cases} \frac{1}{\mathrm{vol}(\Omega_1)} & \text{if } \mathbf{r}, \mathbf{r}' \in \Omega_1\,, \\ 0 & \text{otherwise.} \end{cases} \tag{1.63}$$

The magnetization is uniform inside the pore and the signal is equal to the squared absolute value of the form factor $C_{\rm pore}(\mathbf{q})$ of the pore:

$$S = \left|C_{\rm pore}(\mathbf{q})\right|^2 = \left|\frac{1}{\mathrm{vol}(\Omega_1)}\int_{\Omega_1} e^{i\mathbf{q}\cdot\mathbf{r}}\,\mathrm{d}^3\mathbf{r}\right|^2 . \tag{1.64}$$

For illustration, here are the formulas for the form factor of an interval, a disk, and a sphere, where R denotes here the half-diameter of the pore:

$$\text{interval}: \quad C_{\rm pore}(q) = \mathrm{sinc}(qR)\,, \tag{1.65a}$$

$$\text{disk}: \quad C_{\rm pore}(q) = 2\,\frac{J_1(qR)}{qR}\,, \tag{1.65b}$$

$$\text{sphere}: \quad C_{\rm pore}(q) = 3\,\frac{\cos(qR) - \mathrm{sinc}(qR)}{(qR)^2}\,, \tag{1.65c}$$

where $\mathrm{sinc}(z) = \sin(z)/z$ and $J_\nu(z)$ is the Bessel function of the first kind. The form factor typically displays maxima and minima as a function of $\mathbf{q}$, separated by $\sim \ell_{\rm s}^{-1}$. This is the so-called diffusion-diffraction phenomenon for bounded domains where the dMRI signal is identical to that of wave diffraction by the pore Ω_1. It is interesting to note that at large values of qR, the signal (1.64) is the product of an oscillating function and a power law $q^{-(1+d)}$ that follows the Debye-Porod formula (1.62). Note that by reproducing the first computational step (1.59) in dimension d and replacing the return-to-the-barrier probability by its long-time limit σ, one obtains the general formula

$$S \approx \epsilon'(d)\frac{\sigma\ell_q^{1+d}}{\mathrm{vol}(\Omega_1)}\,, \tag{1.66}$$

where $\epsilon'(1) = 1$, $\epsilon'(2) = 2$ and $\epsilon'(3) = 2\pi$, and one recovers the same numerical prefactor as the large-qR asymptotic behavior of formulas (1.65a), (1.65b) and (1.65c) (squared and with averaged oscillations).

The diffusion-diffraction phenomenon was discovered by Callaghan *et al.* and stimulated a lot of interest as the patterns displayed by the signal could be directly related to the pore size [85–88]. However, if the domain Ω is made of several isolated pores of various shapes and diameters, the signal is the superposition of the contribution (1.64) from all pores that leads in general to a blurring of the diffusion-diffraction pattern.

Long-time: $\ell_{\rm s} \ll \ell_{\rm d}$ in unbounded domain. In this limit, each particle explores several pores many times each so that the diffusive motion can be described as the superposition of a discrete random walk over the lattice of pore

sites and a fast diffusive averaging inside each pore. The diffusion propagator can then be represented as:

$$\mathcal{G}(\Delta, \mathbf{r_1}, \mathbf{r_2}) = \mathbb{I}_{\Omega_1}(\mathbf{r_1} - \mathbf{R_1})\mathbb{I}_{\Omega_1}(\mathbf{r_2} - \mathbf{R_2})P_{\mathrm{rw}}(\Delta, \mathbf{R_1}, \mathbf{R_2}) \,, \tag{1.67}$$

where $\mathbf{R_i}$, $i = 1, 2$ denotes the center of mass of the pore containing $\mathbf{r_i}$, and P_{rw} denotes the discrete random walk propagator. The above formula assumes that all pores have identical shapes (described by the function $\mathbb{I}_{\Omega_1}(\mathbf{r})$) for simplicity. At long diffusion times, P_{rw} is the product of the lattice correlation function and a Gaussian envelope (1.7) with the tortuosity diffusion coefficient $D_\infty = D_0/\mathcal{T}$. This yields for the signal (1.56b):

$$S = \left|C_{\mathrm{pore}}(\mathbf{q})\right|^2 \left[C_{\mathrm{latt}}(\mathbf{q}) * \exp\left(-\frac{q^2\ell_{\mathrm{d}}^2}{\mathcal{T}}\right)\right] \,, \tag{1.68}$$

where $*$ denotes convolution and C_{latt} is the structure factor of the lattice

$$C_{\mathrm{latt}}(\mathbf{q}) = \sum_{\mathbf{R}} e^{i\mathbf{q}\cdot\mathbf{R}} \,, \tag{1.69}$$

where the sum is performed over all lattice sites.

For weak position encoding, i.e. $\ell_{\mathrm{s}} \ll \ell_q$, the pore form factor is nearly constant and equal to 1 and the lattice structure factor is reduced in a first approximation to a Dirac peak $\delta(\mathbf{q})$ at $\mathbf{q} = \mathbf{0}$. The signal is then reduced to the GPA formula in the tortuosity limit:

$$S = \exp(-bD_\infty) \,. \tag{1.70}$$

In general, the structure factor of the lattice follows the low-q asymptotics:

$$C_{\mathrm{latt}}(\mathbf{q}) - \delta(\mathbf{q}) \underset{q\to 0}{\sim} q^p \,, \tag{1.71}$$

with an exponent $p > -d$. This asymptotic behavior can be understood as follows: $C_{\mathrm{latt}}(\mathbf{q})$ is the Fourier transform of the two-point correlation function of the lattice and therefore encodes the set of correlation lengths $\{\lambda\}$ in the medium through the wavevector $\mathbf{q}$. A periodic (i.e., perfectly ordered) lattice with period ℓ_{s} has a discrete set of correlation lengths $\{\lambda\} \sim \ell_{\mathrm{s}}\mathbb{Z}^3$ and $C_{\mathrm{latt}}(\mathbf{q})$ displays intense peaks at the reciprocal lattice vectors $\mathbf{q} \in 2\pi\ell_{\mathrm{s}}^{-1}\mathbb{Z}^3$. In contrast, a disordered lattice possess a continuous range of correlation lengths and the structure factor $C_{\mathrm{latt}}(\mathbf{q})$ is in turn continuous. The disorder "strength" can be quantified by looking at long-range correlations, i.e. low-q behavior. The larger p is, the faster C_{latt} decays to zero at low-q and the weaker the long-range disorder. Note that

$p \leq -d$ corresponds to non self-averaging disorder with a non-integrable lattice structure factor. We discard such situations that generally lead to "anormal" long-time diffusion behavior [307, 308].

By combining Eqs. (1.68) and (1.71), one gets

$$\begin{aligned} S &= \exp(-bD) \ , \\ \frac{D - D_\infty}{D_\infty} &\sim \left(\frac{\ell_\mathrm{s}}{\ell_\mathrm{d}}\right)^{d+p} \ , \end{aligned} \tag{1.72}$$

that is a particular case of the general result of Novikov *et al.* on the long-time asymptotics of effective diffusion coefficient in disordered media [69].

In contrast, the strong position encoding case, i.e. $\ell_q \lesssim \ell_\mathrm{s}$ yields a complex signal that results from (i) the pore form factor, and (ii) the lattice structure factor, broadened by the Gaussian envelope resulting from the finite number of lattice sites visited by each diffusing particle. This yields a "double" diffusion-diffraction pattern, one from the pore shape and one from the pore lattice. As time increases, the pattern from the lattice structure factor becomes sharper, whereas the pore form factor is unchanged. The first experimental observation of this double diffusion-diffraction pattern was performed by Callaghan *et al.* in a spectacular work [85]. By modeling a packing of monodisperse micrometric polystyrene beads by a periodic lattice of spherical pores, they were able to extract physical parameters of the packing such as the diameter of the beads. For clarity, we emphasize that in this system the pores are the inter-beads spaces. Therefore, the assumption of spherical pores is crude, but may be justified by the orientational averaging effect caused by the random packing.

In the previous paragraph, we showed that the signal from an isolated pore is analogous to that of wave diffraction by the pore. In the case of connected pores, one can see a strong analogy with wave diffraction by a grating [2]. In particular, the width of the Gaussian envelope in Eq. (1.68) is equal to $(\ell_\mathrm{d}^2/\mathcal{T})^{-1}$, that is the inverse of the typical diffusion length probed by particles in the porous medium. This is equivalent to the situation of wave diffraction by a grating, where the width (in $\mathbf{q}$ space) of the diffraction peaks scales as the inverse of the size of the illuminated portion of the grating.

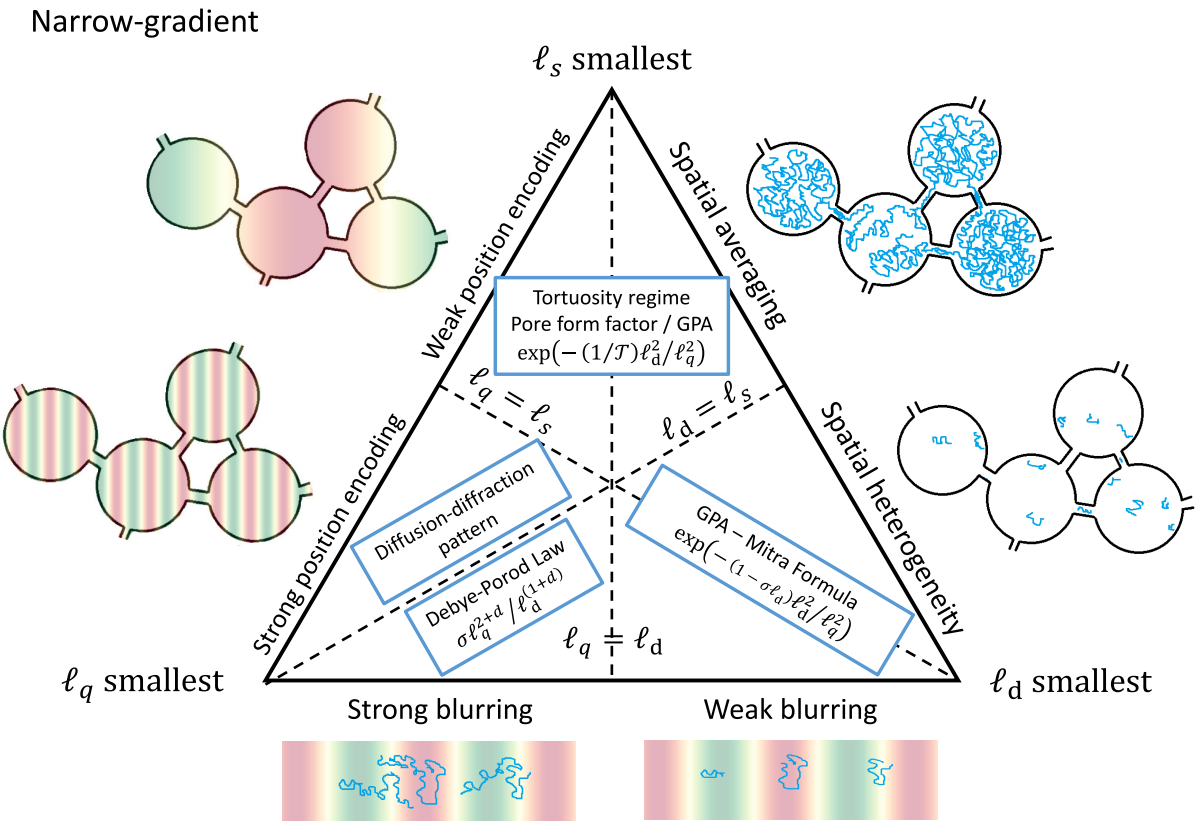

Figure 1.8: Schematic representation of different regimes of dMRI for the narrow-gradient pulse experiment. Refer to Table 1.1 for the definition of the length scales ℓ_d, ℓ_s, ℓ_q.

1.2.4 Extended-gradient pulse, Bloch-Torrey operator

After having presented the two main "perturbative" approaches to the Bloch-Torrey equation, namely low gradient amplitude and short gradient duration, we turn to the non-perturbative study of the Bloch-Torrey equation. For clarity, we consider a PGSE sequence (see Fig. 1.6) with no diffusion time between two pulses (i.e. $\Delta - \delta = 0$) and the gradient is in the x direction with positive then negative amplitude $\pm G$. The right-hand side of the Bloch-Torrey equation during the first gradient pulse is the Bloch-Torrey operator[3]

$$\mathcal{B} = -D_0\nabla^2 - iGx \,, \tag{1.73}$$

and the application of a constant gradient pulse of duration δ can be written formally as

$$m(\delta, x, y, z) = \exp(-\delta\mathcal{B})m(0, x, y, z) \,. \tag{1.74}$$

One way to give some operational meaning to the above relation is through the eigenmodes of $\mathcal{B}$. In fact, it is a very often employed formulation in quantum mechanics where the evolution of a wavefunction results from the evolution of the eigenstates of the Hamiltonian. However, although the BT operator is formally similar to a Schrödinger operator, the imaginary "potential" iGx makes the operator non-Hermitian. Therefore, the existence and *a fortiori* the completeness of eigenmodes of $\mathcal{B}$ is far from trivial. As we shall see throughout this thesis, the non-Hermitianity of the BT operator is at the heart of the variety of regimes of dMRI and of the transition from perturbative to non-perturbative, i.e., low-gradient to high-gradient behavior of the magnetization and the signal.

Let us assume that the Bloch-Torrey has a complete set of eigenmodes $v_n(x, y, z)$ with eigenvalues μ_n:

$$\mathcal{B}v_n = \mu_n v_n \,, \tag{1.75a}$$

$$\mathbf{n} \cdot D_0\nabla v_n - \kappa v_n|_{\partial\Omega} = 0 \,, \tag{1.75b}$$

This is always the case if the domain Ω is bounded because the gradient term can be seen as a bounded perturbation of the Laplacian [95]. Although this perturbation may be large, this is enough to ensure the completeness of $\{v_n\}_{n\geq 1}$ as well as the continuity of the spectrum as $G \longrightarrow 0$ (i.e., continuous transition from Bloch-Torrey spectrum to Laplacian spectrum). The formal equation (1.74) may then be rewritten as

$$m(\delta, x, y, z) = \sum_n \alpha_n v_n(x, y, z) \exp(-\delta\mu_n) \,, \tag{1.76}$$

[3] From a mathematical point of view, the Bloch-Torrey operator contains also the boundary condition (1.32) through the definition of the Laplace operator ∇^2.

where α_n are some complex coefficients and we show below how to compute them from the initial magnetization $m(0, x, y, z)$. At long times, only eigenvalues with the lowest real part contribute significantly to the above formula and the magnetization is represented by a few numbers of eigenmodes, whereas its time-evolution is controlled by their corresponding eigenvalues. Thus, the study of the eigenmodes and eigenvalues of the BT operator provides another viewpoint to understand the formation of the signal.

Basic properties of the Bloch-Torrey operator

In this section, we present the most basic properties of the Bloch-Torrey operator and of its eigenmodes and eigenvalues. We expect that most readers are unfamiliar with this operator and this is a good opportunity to introduce some simple results that we will use later in this thesis. Moreover, we will see that even very simple computations and considerations about symmetry or scaling already carry some interesting physical interpretation.

Projection: Although the BT operator is not Hermitian, it is symmetric, i.e. for any functions f_1, f_2 that satisfy the boundary condition (1.75b) on $\partial\Omega$, one has

$$\int_\Omega f_1(\mathcal{B}f_2) = \int_\Omega f_2(\mathcal{B}f_1) \ . \tag{1.77}$$

Therefore, if we denote by $(\cdot|\cdot)$ the real "scalar product"

$$(f_1|f_2) = \int_\Omega f_1 f_2 \ , \tag{1.78}$$

then we obtain

$$(v_n|v_{n'}) = 0 \quad \text{if } \mu_n \neq \mu_{n'} \ . \tag{1.79}$$

As we work with complex functions, the bilinear form $(\cdot|\cdot)$ is not a scalar product because it is not positive definite. Equation (1.79) and the completeness of eigenmodes imply that one can project any function f onto the family $\{v_n\}_{n\geq 1}$ with the following formula

$$f(x, y, z) = \sum_n \frac{(f|v_n)}{(v_n|v_n)} v_n(x, y, z) \ , \tag{1.80}$$

provided that all eigenvalues μ_n are simple[4]. We shall see that this is generally the case except for some exceptional values of the gradient amplitude G. At these

[4] If the eigenmode family is complete and all eigenvalues are simple, then $(v_n|v_n) \neq 0$ otherwise v_n would be orthogonal to any linear combination $\sum_{n'} \alpha_{n'} v_{n'}$ and thus would be orthogonal to the whole space $L^2(\Omega)$.

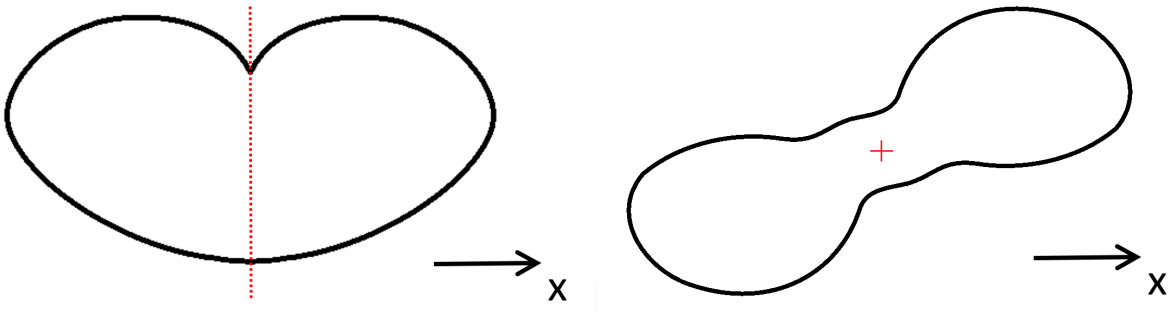

Figure 1.9: Illustration of two domains that are symmetric under x-parity: (left) the domain is symmetric under mirror symmetry indicated by red dotted line; (right) the domain is symmetric under central symmetry indicated by red cross.

"bifurcation" or "branching" points, two eigenvalues and eigenmodes coalesce into a Jordan block of dimension 2, and the resulting eigenmode is orthogonal to itself with respect to $(\cdot|\cdot)$. This peculiar behavior and the generalization of Eq. (1.80) are investigated in details in Sec. 4.3. Outside these special values, we shall always assume that the eigenmodes v_n are normalized in the sense that $(v_n|v_n) = 1$.

Interpretation of the real and imaginary part of eigenvalues. Multiplying Eq. (1.75a) by v_n^* and integrating yields

$$\mathrm{Re}(\mu_n) = \frac{D_0 \int_\Omega |\nabla v_n|^2 + \kappa \int_{\partial\Omega} |v_n|^2}{\int_\Omega |v_n|^2} \geq 0 \,, \tag{1.81a}$$

$$\mathrm{Im}(\mu_n) = -G \frac{\int_\Omega x|v_n|^2}{\int_\Omega |v_n|^2} \,, \tag{1.81b}$$

where we used the Robin boundary condition (1.75b) and Green's formula to write the first relation. One can see that the conventional minus sign in the definition of the BT operator (1.73) ensures eigenvalues with positive real part. If the integrals in the above formulas are well-defined (that is always the case for bounded domains), then the BT eigenmode v_n is localized and its mean position is given by $-\mathrm{Im}(\mu_n)/G_x$. Moreover, if the surface relaxivity κ is zero, then the typical scale of variation of the mode is given by $\sqrt{D_0/\mathrm{Re}(\mu_n)}$. We shall see in Sec. 4.2.1 and Appendix C.2 that Bloch-Torrey eigenmodes generally exhibit a fast oscillating behavior that dominates the value of $\mathrm{Re}(\mu_n)$.

Symmetry properties First, one can note that reversing the gradient direction is equivalent to applying a complex conjugation to the BT operator (and as

a result to v_n and μ_n). As a side remark, it shows that the (real) signal after a refocused gradient sequence is not affected by the gradient reversal. Now let us assume that the domain Ω is bounded and invariant by an isometric transformation that reverses the x-axis (i.e., π rotation around an axis orthogonal to $\mathbf{e_x}$ or mirror symmetry with respect to the plane orthogonal to $\mathbf{e_x}$), see Fig. 1.9. We call this transformation x-parity in short and we denote it generically by $\mathcal{P}_x$. In Sec. 4.4 we investigate the case of periodic media and we shall see that the following discussion requires more care, hence the assumption of bounded Ω here. The BT operator is then invariant under the combination x-parity plus complex conjugation

$$\mathcal{P}_x \mathcal{B}^* = (-\nabla^2 - iG(-x))^* = \mathcal{B} \,, \tag{1.82}$$

and this property translates for the eigenmodes into the following: if v_n is an eigenmode with eigenvalue μ_n, then $\mathcal{P}_x v_n^*$ is an eigenmode with eigenvalue μ_n^*. This leads to two possible situations.

(i) the eigenvalue μ_n is real (and simple), so that $v_n = \pm \mathcal{P}_x v_n^*$. In that case, the eigenmode v_n is "symmetric" in the sense that $|v_n|$ is invariant by x-parity. Note that this is consistent with the previous paragraph: the imaginary part of μ_n is zero and the mode is centered around $x = 0$.

(ii) two eigenvalues μ_n and $\mu_{n'}$ form a complex conjugate pair, so that $v_{n'} = \mathcal{P}_x v_n^*$. This means that the mode $v_{n'}$ is the "symmetric" of v_n if one considers their absolute value. Following the conclusion of the previous paragraph, each mode is localized on one side of the domain (given by the sign of $\mathrm{Im}(\mu_n) = -\mathrm{Im}(\mu_{n'})$).

Scaling properties For clarity, let us assume that the domain Ω is an isolated pore of diameter ℓ_s, and let us perform the rescaling

$$\tilde{\mathbf{r}} = \mathbf{r}/\ell_g \,, \tag{1.83}$$

where we recall that ℓ_g is the gradient length given by Eq. (1.40). The BT operator becomes then

$$\mathcal{B} = \frac{D_0}{\ell_g^2} \left(-\tilde{\nabla}^2 - i\tilde{x} \right) \,. \tag{1.84}$$

Therefore, the eigenmodes v_n of the BT operator in a pore of diameter ℓ_s are (up to rescaling) the eigenmodes of the dimensionless BT operator $\tilde{\mathcal{B}} = -\tilde{\nabla}^2 - i\tilde{x}$ in a rescaled pore of diameter ℓ_s/ℓ_g. Thus, if the pore shape is prescribed (e.g., spherical), the eigenmodes of the BT operator are controlled by a single parameter ℓ_s/ℓ_g. Following the same reasoning, the eigenvalues μ_n can be written in the following form:

$$\mu_n T = \frac{\ell_\mathrm{d}^2}{\ell_g^2} \, \Xi_n(\ell_g/\ell_\mathrm{s}) \,, \tag{1.85}$$

where $\Xi_n(\cdot)$ are dimensionless functions.

In Sec. 1.2.2, we explained that the competition between the diffusion length ℓ_d and the gradient length ℓ_g controls the strength of diffusion encoding by the gradient pulse, i.e. the width of the phase distribution after the gradient sequence. In that regard, strong gradients correspond to strong diffusion encoding, i.e. $\ell_g \ll \ell_\mathrm{d}$. Here, the study of eigenmodes and eigenvalues of the BT operator reveals a new competition, namely between ℓ_g and ℓ_s. At low gradient $\ell_\mathrm{s} \ll \ell_g$, the BT eigenmodes and eigenvalues are close to the Laplacian ones. In contrast, high gradient corresponds to $\ell_g \ll \ell_\mathrm{s}$ where the gradient term dominates.

Regimes of dMRI for extended-gradient pulses

The previous paragraphs allow us to write the magnetization after the full PGSE sequence as an eigenmode decomposition. Naturally we assume that the eigenmodes exist and form a complete basis. As we explained above, this is ensured in bounded domains, for example. Furthermore, we assume that eigenmodes are normalized in the sense that $(v_n|v_n) = 1$. Finally, we recall that the initial condition for the magnetization is a uniform magnetization $m(0,\mathbf{r}) = 1$. We present below the time-evolution of the magnetization in terms of spectral projection over the Bloch-Torrey eigenbasis:

$$m(0,\mathbf{r}) = \sum_n (1|v_n) v_n(\mathbf{r}) \,, \tag{1.86a}$$

$$m(\delta,\mathbf{r}) = \sum_n (1|v_n) v_n(\mathbf{r}) e^{-\delta\mu_n} \,, \tag{1.86b}$$

$$m(\delta,\mathbf{r}) = \sum_{n'} \sum_n (1|v_n)(v_n|v^*_{n'}) v^*_{n'}(\mathbf{r}) e^{-\delta\mu_n} \,, \tag{1.86c}$$

$$m(T=2\delta,\mathbf{r}) = \sum_{n'} \sum_n (1|v_n)(v_n|v^*_{n'}) v^*_{n'}(\mathbf{r}) e^{-T(\mu_n+\mu^*_{n'})/2} \,, \tag{1.86d}$$

$$S = \frac{1}{\mathrm{vol}(\Omega)} \sum_{n'} \sum_n (1|v_n)(v_n|v^*_{n'})(v^*_{n'}|1) e^{-T(\mu_n+\mu^*_{n'})/2} \,, \tag{1.86e}$$

where we used that the eigenmodes and eigenvalues for reversed gradient are the complex conjugates of v_n and μ_n. Although the full expression (1.86d) is more complicated than the single-pulse expression (1.76) as it involves couplings between v_n and $v^*_{n'}$, it still reduces to a small number of terms in the long-time limit where the magnetization behavior is controlled by the eigenmodes with the lowest eigenvalue in real part.

Therefore in general there are three possible regimes for the magnetization after extended-gradient pulses that are controlled by the three length scales ℓ_s,

ℓ_d, and ℓ_g. We have already discussed the short-time, weak diffusion encoding regime ($\ell_d \ll \ell_s$ and $\ell_d \ll \ell_g$) in the first subsection: the signal is given by Eqs. (1.49c) and (1.50) as a consequence of the narrow phase distribution produced by the gradient sequence. For a bounded domain, the motional narrowing regime can be revisited in terms of the BT eigenmodes. Finally we discuss the localization regime that emerges at strong gradients.

Motional narrowing regime revisited: $\ell_s \ll \ell_d$ and $\ell_s \ll \ell_g$. As we explain above, the assumption $\ell_s \ll \ell_g$ implies that the gradient can be treated as a small perturbation of the Laplace operator, that yields for μ_n an expansion in powers of $iG \sim i(\ell_s/\ell_g)^3$. The zero-order term yields the n-th Laplacian eigenvalue of the domain (denoted η_n), the first-order term is imaginary and yields the average Larmor frequency shift (we assume that it is set to zero by suitable coordinate change), therefore one has:

$$\Xi_n(\ell_g/\ell_s) \underset{\ell_g \gg \ell_s}{\approx} (\ell_g/\ell_s)^2 \left(\eta_n + \eta_n'(\ell_s/\ell_g)^6 + \dots\right) , \tag{1.87a}$$

$$\mu_n T \underset{\ell_g \gg \ell_s}{\approx} \eta_n \frac{\ell_d^2}{\ell_s^2} + \eta_n' \frac{\ell_d^2 \ell_s^4}{\ell_g^6} + \dots , \tag{1.87b}$$

where η_n' are geometry-dependent dimensionless coefficients (see Sec. 4.3.1). Since we assumed impermeable boundaries, the first Laplacian eigenmode is constant and the first Laplacian eigenvalue is zero, i.e. $\eta_1 = 0$, so that one has

$$\mu_1 T \underset{\ell_g \gg \ell_s}{\approx} \eta_1' \frac{\ell_d^2 \ell_s^4}{\ell_g^6} , \qquad \mu_2 T \underset{\ell_g \gg \ell_s}{\approx} \eta_2 \frac{\ell_d^2}{\ell_s^2} , \tag{1.88}$$

and the assumption $\ell_d \gg \ell_s$ allows us to truncate the expansion (1.86e) to the first term, that yields (after identifying η_1' to ζ_{-1}):

$$S = \exp\left(-\zeta_{-1} \frac{\ell_s^4 \ell_d^2}{\ell_g^6}\right) , \tag{1.89}$$

where the prefactor 1 is given by $|(1|v_1)|^2 (v_1|v_1^*)/\mathrm{vol}(\Omega)$ since v_1 is nearly constant and equal to $\mathrm{vol}(\Omega)^{-1/2}$. Furthermore, the magnetization profile is given by v_1, i.e. uniform, as expected from the fast diffusive averaging inside the pore.

Localization regime: $\ell_g \ll \ell_s$ and $\ell_g \ll \ell_d$. We shall provide two interpretations of this regime. Although very different in nature, they provide two complementary viewpoints on both magnetization and signal behavior. The first one

relies on the spectral properties of the BT operator and the second one follows from the study of the dephasing acquired by individual particles. We emphasize that these interpretations are somewhat qualitative. The localization regime is the object of Chapter 4.

Because of the assumption $\ell_g \ll \ell_s$, the gradient is a strong perturbation of the BT operator and deeply affects its spectral properties. Qualitatively, there is a competition between the delocalized eigenmodes of the Laplace operator and the Dirac peak eigenmodes of the gradient term. At large gradient strength, eigenmodes are thus localized. As the only relevant length scale in this limit, ℓ_g appears as the typical localization scale of these modes and Eq. (1.81a) implies that

$$\mu_n T \sim \frac{\ell_d^2}{\ell_g^2} , \tag{1.90}$$

and the signal decays as

$$-\log S \sim \ell_d^2/\ell_g^2 . \tag{1.91}$$

The above equation (1.90) may be restated as $\Xi_n(\ell_g/\ell_s)$ having a finite limit for $\ell_g/\ell_s \to 0$. The exact limit $\Xi_n(0^+) = -e^{-i\pi/3}a_n$ was obtained by Stoller *et al.* in 1991 in [98], where the coefficients a_n are the zeros of the derivative of the Airy function: $a_1 \approx -1.019$, $a_2 \approx -3.248$, $a_3 \approx -4.820$, etc.

Another way to understand this regime is to go back to the interpretation of ℓ_g in terms of dephasing acquired by diffusing particles. Because of the assumption of strong diffusion encoding ($\ell_g \ll \ell_d$), particles that diffuse far away from boundaries are strongly dephased with one another and the bulk magnetization vanishes. In contrast, particles that remain close to boundaries are dephased less. This effect is the strongest for boundaries that are perpendicular to the gradient. Since any particle that diffuses further than a distance ℓ_g will have strong phase differences with its neighbor, one deduces that the threshold between "far away from boundaries" and "close to boundaries" is given by ℓ_g.

Therefore, the magnetization at long times and large gradient is localized over the length ℓ_g near boundaries that are perpendicular to the gradient. As time increases, the magnetization decay is due to the increasing dephasing between spins close to the boundaries as well as the decreasing number of particles staying near the boundaries (see Sec. 4.1 for a more detailed qualitative description of the emergence of the localization regime).

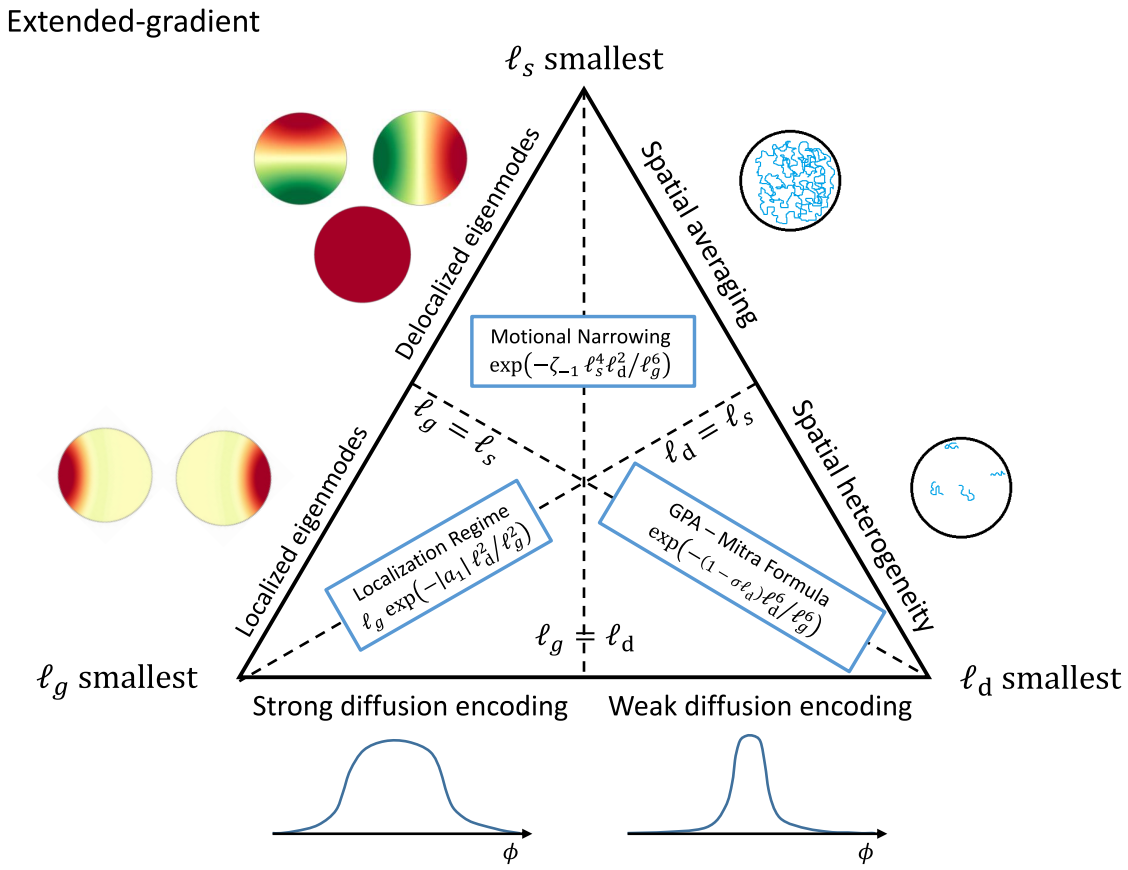

Figure 1.10: Schematic representation of different regimes of dMRI for the extended-gradient pulse experiment. Refer to Table 1.1 for the definition of the length scales ℓ_d, ℓ_s, ℓ_g.

This page is unintentionally left not blank.

Chapter 2

Anisotropy

An interesting property of diffusion MRI is that the random motion of particles is encoded along a prescribed gradient direction. Since the seminal work by Stejskal [21] in 1965, researchers in the field quickly appreciated that this could be used to probe diffusive properties of a medium in different directions and therefore to detect the anisotropy of the medium [106, 132, 145–148, 226]. As we already discussed in the introduction, the diffusion length ℓ_d allows one to distinguish between three different scales, namely microscopic, mesoscopic, and macroscopic. In the first section, we discuss how anisotropy may arise at these different scales. The study of microscopic anisotropy with dMRI stimulated many works in the past years and we briefly present this field of research. Then we turn to the less explored mesoscopic anisotropy and we show how one can generalize Mitra's formula for the short-time behavior of the effective diffusion coefficient. This last part is largely drawn from our publication [344].

2.1 Anisotropy at different scales

Isotropy is defined as "uniformity in all directions", or equivalently "invariance by spatial rotations". In terms of microstructure, no medium is, strictly speaking, isotropic. Indeed, one may go to a fine enough scale where the microstructure is locally non-invariant by rotations. The keyword here is *scale*. As one goes to larger and larger scales, the properties of the microstructure are averaged and the anisotropy of the medium may change. A common example of this phenomenon is found in optics. A piece of transparent material at the molecular scale is locally non-isotropic because of spatial arrangements of molecules. When one goes to the macroscopic scale, two distinct behaviors are observed: either the material is a glass (i.e. amorphous, disordered, hence macroscopically isotropic), that leads to the usual refractive behavior; or the material is a crystal (i.e. ordered, hence

macroscopically anisotropic), that generally leads to birefringence properties.

In the context of diffusion, we shall see in this section that anisotropy manifests itself differently depending on its scale with respect to the diffusion length. Since the diffusion length quantifies the size of the region explored by individual particles, one distinguishes three main scales: (i) microscopic scale, where the anisotropy is averaged out by diffusion into an anisotropic diffusion tensor; (ii) mesoscopic scale, where the diffusion behavior is complex, time-dependent, and anisotropy generally arises in the time-dependence of diffusive properties; (iii) macroscopic scale, where anisotropy arises as a statistical (or ensemble) average of micro- and meso-anistropy of independent micro-domains. The discussion below is summarized graphically on Fig. 2.1.

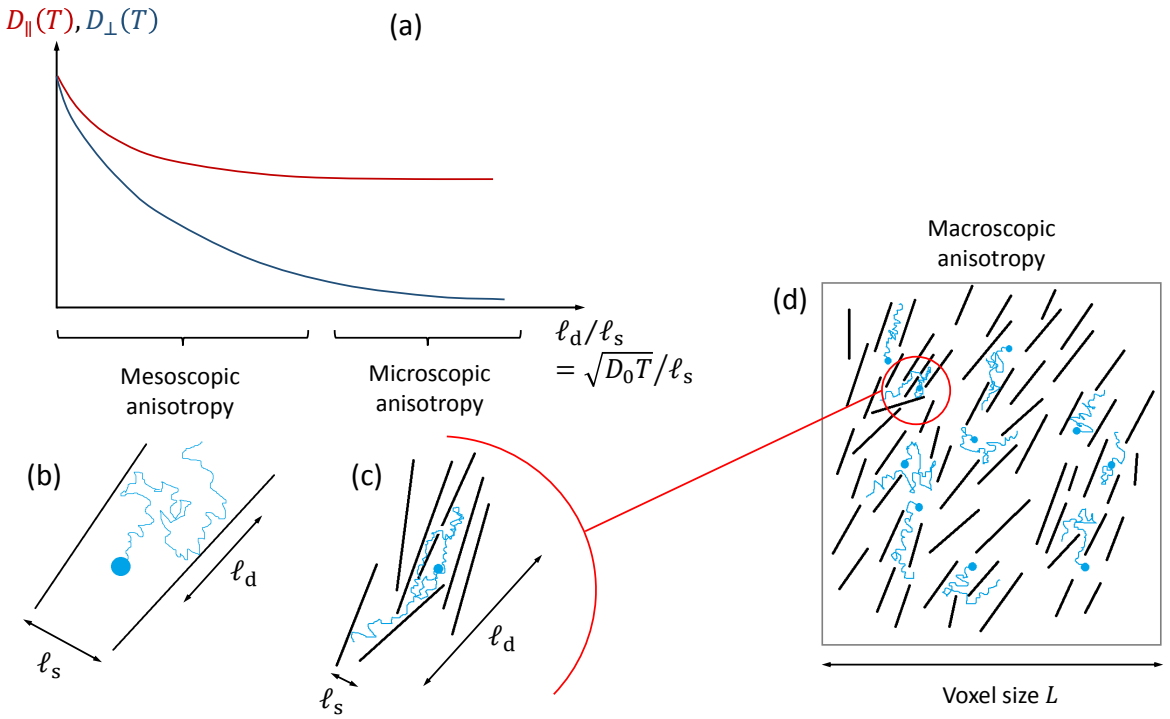

Figure 2.1: Schematic representation of different scales of anisotropy. (a) If diffusion takes place between fibers spaced by ℓ_s, the diffusive motion may be modeled as two time-dependent diffusion coefficients: $D_\parallel(T)$ in the direction parallel to the fibers and $D_\perp(T)$ in the direction perpendicular to the fibers. (b) The mesoscopic scale corresponds to ℓ_s being of the same magnitude as the diffusion length ℓ_d. Both coefficients $D_\parallel$, $D_\perp$ vary with time and the motion may be modeled by a time-dependent diffusion tensor. (c) The microscopic scale corresponds to $\ell_s \ll \ell_d$: both coefficients $D_\parallel$, $D_\perp$ have reached a stationary value and the diffusive motion may be modeled by a constant diffusion tensor (i.e., the diffusion motion is effectively "free"). (d) Macroscopic anisotropy results from a coherent alignment of anisotropic microdomains at the scale of a voxel.

2.1.1 Microscopic scale

The microscopic scale refers to any structure much smaller than the diffusion length ℓ_d. For water diffusion and typical diffusion times (1.9a), this corresponds to any structure smaller than ~ 1 μm. At this scale, the microstructural complexity is averaged by diffusion and one may model the complex diffusive motion by a coarse-grained effective Brownian motion. For example, one may think of water diffusion inside a living cell. Although the cytoplasm is a very complex medium that is filled with macromolecules of various sizes, one usually discards this complexity and reduces it to a single number, namely the diffusion coefficient D_0 inside the cytoplasm. In turn, the large-scale structure of the cell (membrane, organelles, etc.) would be incorporated via boundary condition. Here we discard these effects. In that case, the coarse-grained diffusion is effectively free diffusion.

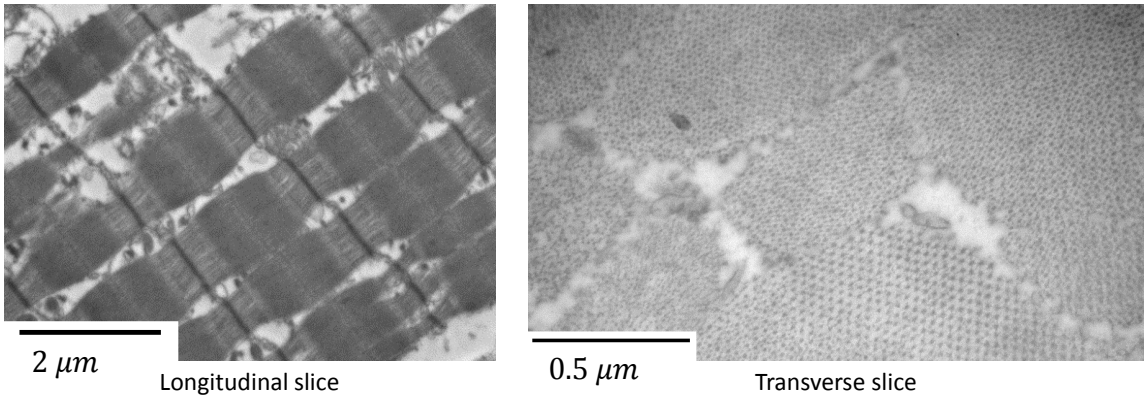

Figure 2.2: The structure of muscle fibers at the sub-micrometric scale. The images were obtained with TEM microscopy by T. Astruc from QuaPa (UR370 Inra).

In a microstrure that is anisotropic, such as oriented muscle fibers (see Fig. 2.2), neuronal fibers, the coarse-graining yields an anisotropic diffusion *tensor* D_0 [141–144, 148]. One can provide two equivalent definitions for the diffusion tensor, that generalizes the scalar diffusion coefficient. The first one is the generalization of Eq. (1.6) and relates the diffusive flux $\mathbf{J}$ to the gradient of the quantity f of interest:

$$\mathbf{J} = -\mathrm{D}_0 \nabla f \ . \tag{2.1}$$

In the anisotropic case, the flux $\mathbf{J}$ is generally not parallel to the gradient ∇f. Another way to define the anisotropic diffusion tensor is through the velocity autocorrelator (1.10):

$$\mathbb{E}[\mathbf{v}_t \otimes \mathbf{v}_{t'}] = 2\mathrm{D}_0 \delta(t - t') \ . \tag{2.2}$$

Equivalently, one has

$$\mathbb{E}[(\mathbf{r}_T - \mathbf{r}_0) \otimes (\mathbf{r}_T - \mathbf{r}_0)] = 2\mathsf{D}_0 T \ . \tag{2.3}$$

The diffusion tensor is symmetric hence it can be diagonalized. Let us assume that our axes x, y, z are chosen so that D_0 is in diagonal form:

$$\mathsf{D}_0 = \begin{bmatrix} D_{xx} & 0 & 0 \\ 0 & D_{yy} & 0 \\ 0 & 0 & D_{zz} \end{bmatrix} . \tag{2.4}$$

In that case its interpretation becomes simple: each diagonal element of the tensor represents a one-dimensional diffusion coefficient along each axis. The diffusion is anisotropic if the diagonal elements are not equal to each other: there are axes of faster diffusion and axes of slower diffusion. For instance, in Fig. 2.2, one expects that diffusion parallel to the fibers is faster than diffusion in the orthogonal plane. The opposite situation of isotropic diffusion corresponds to

$$\mathsf{D}_0 = D_0 \mathsf{I} \ , \tag{2.5}$$

where I denotes the identity tensor. Any tensor that is proportional to the identity is invariant by any spatial isometry (rotation or symmetry) and thus we call such tensors "isotropic" throughout the text.

Note that the mean-squared displacement does not distinguish between isotropic and non-isotropic diffusion:

$$\mathbb{E}[(\mathbf{r}_T - \mathbf{r}_0)^2] = 2dD_0 T \ , \tag{2.6}$$

where

$$D_0 = \frac{1}{d}\mathrm{Tr}(\mathsf{D}_0) \tag{2.7}$$

is the average diffusivity and coincides with the scalar diffusion coefficient for isotropic diffusion. At this point, a mathematical remark is in order: because the trace $\mathrm{Tr}(\cdot)$ is the only linear operation on a tensor that is invariant by spatial isometries (rotations and symmetries), it appears naturally whenever one performs orientational averages or computes rotation-invariant quantities related to the diffusion tensor. In particular, one has

$$\left\langle \mathsf{R}\mathsf{D}_0\mathsf{R}^\dagger \right\rangle = \frac{\mathrm{Tr}(\mathsf{D}_0)}{3}\mathsf{I} \ , \tag{2.8}$$

where the average $\langle\cdot\rangle$ is performed here over all possible rotation matrices R (with isotropic integration measure). We shall see several examples of this result in the following.

2.1.2 Mesoscopic scale

The mesoscopic scale corresponds to structures with sizes similar to ℓ_d (i.e., $\sim 10 - 100$ μm for water diffusion). As we have discussed in Sec. 1.2.2 and as we show later (see Sec. 2.3 for the short-time limit), such structures typically lead to a formula for the mean-squared displacement of the form

$$\mathbb{E}[(\mathbf{r}_T - \mathbf{r}_0)^2] = 2dD_{\mathrm{MSD}}(T)T\,, \tag{2.9}$$

where the average is performed over all trajectories and $D_{\mathrm{MSD}}(T)$ is a time-dependent effective diffusion coefficient. The index MSD emphasizes that it is defined through the mean-squared displacement. At short times, the effect of the boundaries of the structure is negligible and $D_{\mathrm{MSD}} = D_0$. At longer times, D_{MSD} decreases and tends to the tortuosity limit D_∞ (note that $D_\infty = 0$ in bounded domains). Compared to the microscopic scale discussed above where one has only access to the tortuosity limit, the time-variation of diffusivity at the mesocopic scale contains *a priori* much more microstructural information.

If the medium structure is anisotropic at the mesoscopic scale (for example, diffusion inside prolate cells or outside large fiber arrangements), then the diffusion process, that is isotropic at short times, becomes anisotropic at longer diffusion times. Hence Eq. (2.9) is not sufficient to describe the time-dependence of diffusivity and one generalizes it to a tensorial form:

$$\mathbb{E}[(\mathbf{r}_T - \mathbf{r}_0) \otimes (\mathbf{r}_T - \mathbf{r}_0)] = 2\mathrm{D}_{\mathrm{MSD}}(T)T\,. \tag{2.10}$$

The short-time behavior of $\mathrm{D}_{\mathrm{MSD}}$ is investigated in Sec. 2.3.

2.1.3 Macroscopic scale

The macroscopic scale corresponds to the size of the voxel. Practically, it is much larger than the diffusion length ($\gtrsim 100$ μm for water diffusion) so that a negligible amount of particles actually travels through the medium over this scale. Therefore at the macroscopic scale one can split the medium into independent "microdomains" and the result of a measurement is the superposition of results from all microdomains. The relevance of this scale in the context of dMRI is related to the lack of spatial resolution that leads one to measure the signal from a voxel that is typically 100 times larger (in length) than the diffusion length ℓ_d. Note that each microdomain would have a typical size of $\gtrsim 10\ell_d$.

Let us assume that each microdomain is anisotropic at the microscopic scale, but with different orientations with respect to each other. Note that the following discussion extends straightforwardly to mesoscopic anisotropy but we focus on

microscopic anisotropy for clarity. The voxel is then characterized at the macroscopic scale by a distribution of anisotropic diffusion tensors D_0. For example, if the anisotropy is caused by a fiber-like structure such as on Fig. 2.2, the distribution of D_0 is related to the macroscopic distribution of fiber orientation. Thus, the medium is macroscopically anisotropic if there is a coherent orientation of microdomains at the macroscopic scale. In that case, the ensemble average of diffusion tensors yield an anisotropic tensor whose axes are related to the average microdomain orientation. In the opposite case of a macroscopically isotropic medium (e.g., fully random microdomain orientation), the ensemble average of diffusion tensors yields an isotropic tensor [154–156].

Let us illustrate this effect on the simplest possible example: diffusion inside thin cylinders in 3 dimensions. Thin cylinders may model muscle fibers [226–228] or alveolary ducts [151] in the long-time regime where diffusion transverse to the cylinder axis is fully restricted. Inside a cylinder, diffusion is anisotropic with diffusion tensor equal to $\mathrm{D}_0 = D_0\, \mathbf{u} \otimes \mathbf{u}$, where $\mathbf{u}$ is a unit vector oriented along the axis of the cylinder. To show this, it is sufficient to note that (i) the formula is correct if $\mathbf{u} = \mathbf{e_x}$, and that (ii) both sides of the formula are (contravariant) tensors with respect to spatial isometries. We shall use this argument again later in the text. We denote by θ and ϕ the spherical coordinates of $\mathbf{u}$, so that the diffusion tensor has elements

$$\mathrm{D}_0 = D_0 \begin{bmatrix} \sin^2\theta\cos^2\phi & \sin^2\theta\cos\phi\sin\phi & \sin\theta\cos\phi\cos\theta \\ \sin^2\theta\cos\phi\sin\phi & \sin^2\theta\sin^2\phi & \sin\theta\sin\phi\cos\theta \\ \sin\theta\cos\phi\cos\theta & \sin\theta\sin\phi\cos\theta & \cos^2\theta \end{bmatrix}. \tag{2.11}$$

The ensemble average of D_0 is then governed by the distribution of the orientation of the cylinder (i.e. distribution of θ, ϕ) over the voxel. To simplify further, we assume that the distribution of cylinder orientation is axially symmetric around z, that yields

$$\langle \mathrm{D}_0 \rangle = \frac{D_0}{3} \begin{bmatrix} 1-\Theta & 0 & 0 \\ 0 & 1-\Theta & 0 \\ 0 & 0 & 1+2\Theta \end{bmatrix}, \tag{2.12}$$

where

$$\Theta = \langle (3\cos^2\theta - 1)/2 \rangle \tag{2.13}$$

is the so-called "orientation order parameter" of the angular distribution of fiber orientation [154–156] and results from the average of the second Legendre polynomial weighted by the angular distribution of θ. One can make the following observations: (i) the orientation distribution is reduced to a single parameter $-1/2 \leq \Theta \leq 1$; (ii) the value $\Theta = 0$ corresponds to an isotropic averaged

tensor $\langle \mathrm{D}_0 \rangle$ with diffusivity $D_0/3$. Note that this diffusivity is exactly equal to $\mathrm{Tr}(D_0\, \mathbf{u} \otimes \mathbf{u})/3$, that is another application of Eq. (2.8). We emphasize that the average diffusivity is one third of the intrinsic diffusion coefficient D_0 because of the one-dimensional character of cylinders.

2.2 Interplay between micro- and macro-anisotropy in dMRI

In this section, we briefly investigate the effect of micro- and macro-anisotropy on the dMRI signal. To simplify the discussion and emphasize the most interesting mechanisms, we discard the effect of obstacles, boundaries, etc., at the mesoscopic scale. In other words, we assume that diffusion is well represented by a local diffusion tensor D_0. First we present the case of macroscopically anisotropic medium where one may recover structural information such as fiber orientation at the scale of the voxel. This corresponds to diffusion tensor imaging [141–144], a technique that was invented in the 90s and showed spectacular results in the brain [140], among others. Then we turn to macroscopically isotropic medium, that recently renewed interest in the design of a new family of gradient profiles generically called "spherical encoding" profiles [153, 158–163, 168].

2.2.1 Diffusion tensor imaging

As we have shown in Sec. 1.2.2, in the free diffusion regime, the signal is governed by the variance of the phase ϕ acquired by diffusing particles, according to Eq. (1.49c) that we reproduce here

$$S = \exp\left(-\frac{1}{2}\mathbb{V}[\phi]\right) . \tag{2.14}$$

For isotropic free diffusion, we already obtained the simple formula (1.46a) for the variance of ϕ. Using Eqs. (1.27c) and (2.2), one deduces immediately the generalization to anisotropic free diffusion:

$$\mathbb{V}[\phi] = 2\int_0^T \mathbf{Q}(t)\cdot \mathrm{D}_0\mathbf{Q}(t)\,\mathrm{d}t . \tag{2.15}$$

This formula may be rewritten in a convenient form by introducing the B-tensor [141–143], that generalizes the b-value (1.46b):

$$\mathrm{B} = \int_0^T \mathbf{Q}(t)\otimes\mathbf{Q}(t)\,\mathrm{d}t . \tag{2.16}$$

Note in particular that $\mathrm{Tr}(\mathrm{B}) = b$. In terms of the B-tensor, the above equation becomes:

$$\mathbb{V}[\phi] = 2\,\mathrm{Tr}(\mathrm{B}\mathrm{D}_0) . \tag{2.17}$$

Mathematically, the variance of ϕ may be seen as a scalar product between two symmetric tensors B and D_0. Whereas the tensor D_0 is a property of the medium

under study and is generally unknown, the B-tensor is fully under control of the experimentalist. Therefore, one may choose different gradient sequences that produce different B. In particular, if B spans a basis of symmetric tensors, the measurement of $\mathbb{V}[\phi]$ through the signal (1.49c) allows one to recover the diffusion tensor D_0. This is the basic principle of diffusion tensor imaging (DTI) [141].

Symmetric matrices form a 6-dimensional vector space, therefore at least 6 different B-tensors are required to extract the diffusion tensor. A commonly employed scheme is to apply the same gradient temporal profile in 6 "non-collinear" spatial directions[1]. Below we give an example of such 6 directions with the associated B-tensors, and one can check that they indeed form a basis of symmetric tensors:

$$\begin{aligned}
\mathbf{e}_x+\mathbf{e}_y &\to \begin{bmatrix} 1 & 1 & 0 \\ 1 & 1 & 0 \\ 0 & 0 & 0 \end{bmatrix}, & \mathbf{e}_x-\mathbf{e}_y &\to \begin{bmatrix} 1 & -1 & 0 \\ -1 & 1 & 0 \\ 0 & 0 & 0 \end{bmatrix}, \\
\mathbf{e}_y+\mathbf{e}_z &\to \begin{bmatrix} 0 & 0 & 0 \\ 0 & 1 & 1 \\ 0 & 1 & 1 \end{bmatrix}, & \mathbf{e}_y-\mathbf{e}_z &\to \begin{bmatrix} 0 & 0 & 0 \\ 0 & 1 & -1 \\ 0 & -1 & 1 \end{bmatrix}, \\
\mathbf{e}_z+\mathbf{e}_x &\to \begin{bmatrix} 1 & 0 & 1 \\ 0 & 0 & 0 \\ 1 & 0 & 1 \end{bmatrix}, & \mathbf{e}_z-\mathbf{e}_x &\to \begin{bmatrix} 1 & 0 & -1 \\ 0 & 0 & 0 \\ -1 & 0 & 1 \end{bmatrix}.
\end{aligned} \tag{2.18}$$

In order to improve the quality of tensor reconstruction that may be altered by noise, one may employ more than 6 gradient directions [149].

As we explained in the previous section, the recovery of the diffusion tensor D_0 is only possible at the scale of a voxel, therefore it is useless if the medium is macroscopically isotropic. In other words, the above technique gives access to new informations only in ordered samples where the orientation of microscopic structures is coherent at the scale of a voxel. The most emblematic and spectacular example is probably neuronal tracts in the brain (see Fig. 2.3) [140]. Although neuronal fibers are too small to be resolved by MRI images, the diffusion anisotropy reveals their orientation. By "connecting" continuously results from neighboring voxels, one may then reconstruct whole fiber tracts in the brain. We emphasize that this can be done *in vivo* and *non-invasively*. This achievement

[1]Note that "non-collinear" is mathematically absurd here, however it is the term in usage in the field.

stimulated numerous research works in a field now known as “tractography”. This is also a part of the so-called functional MRI that plays the crucial role in neurosciences (see Refs [113, 114] for a review).

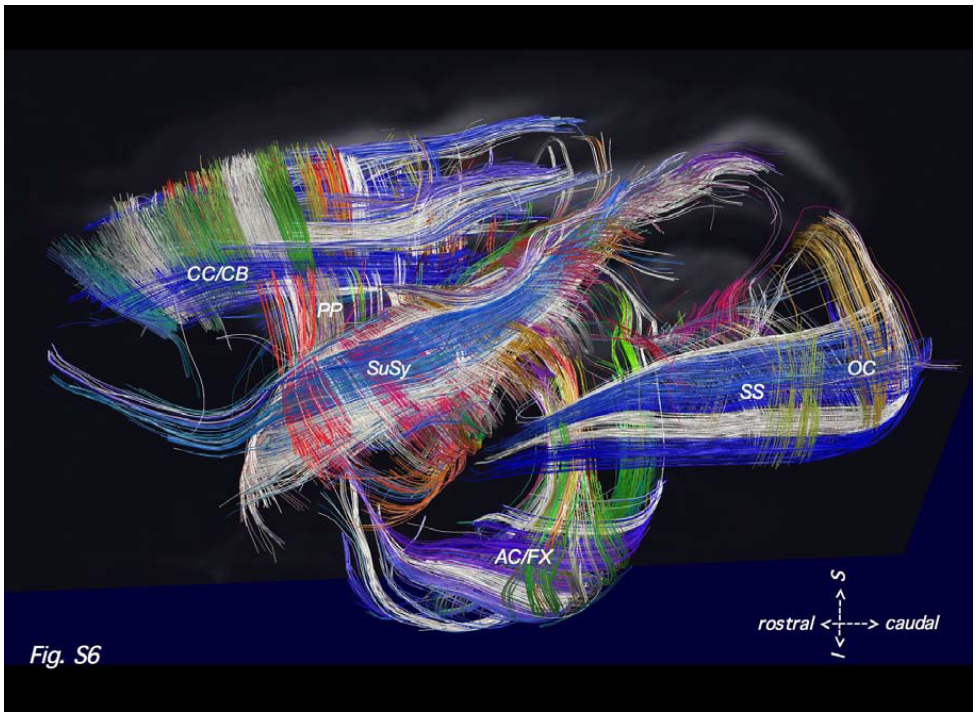

Figure 2.3: Left lateral view of an owl monkey cerebral hemisphere. Lines represent neuronal tracts obtained *in vivo, non-invasively* with diffusion tensor imaging (colors were used to guide the eye and help visualization of large-scale structures). The figure reveals sheets of interwoven fibers that are continuous at the scale of the whole hemisphere. Note that the thickness of one line is determined by the spatial resolution of the scanner (here, about 0.5 mm) that is much larger than the actual diameter of axons (a few microns). Figure from Ref [140].

2.2.2 Spherical encoding

The previous paragraph showed how one can recover the diffusion tensor D_0 from the measurement of the dMRI signal. The fundamental requirement is that the average of the microscopically anisotropic tensor D_0 is not isotropic (i.e., $\langle D_0 \rangle$ is not proportional to I), that would result from e.g. uniformly oriented fibers over the voxel of interest. To avoid any confusion, “uniformly oriented” means here “randomly oriented with a uniformly distributed orientation”. Now we examine the opposite situation of macroscopic isotropy. We take this opportunity to rephrase some previous considerations about the interplay between micro- and macro-anisotropy.

To simplify notations, we assume that the voxel is made of several identical microdomains that are uniformly oriented. Let us choose one microdomain in the voxel and denote by D_0 its local diffusion tensor. Then the local diffusion tensor at any other microdomain is given by an expression of the form $\mathrm{R}\mathrm{D}_0\mathrm{R}^\dagger$, where R denotes a rotation matrix that accounts for the orientation of the microdomain of interest with respect to our reference. The averaged diffusion tensor over the whole voxel is given by

$$\langle \mathrm{R}\mathrm{D}_0\mathrm{R}^\dagger \rangle = \frac{\mathrm{Tr}(\mathrm{D}_0)}{3}\,\mathrm{I}\,. \tag{2.19}$$

Now let us consider a gradient sequence with the gradient in a fixed direction $\mathbf{e}$. The B-tensor is given by

$$\mathrm{B} = b\,\mathbf{e}\otimes\mathbf{e}\,. \tag{2.20}$$

The signal from an individual microdomain with diffusion tensor $\mathrm{R}\mathrm{D}_0\mathrm{R}^\dagger$ is given by Eqs. (2.14), (2.17), and (2.20):

$$s = s_0 \exp\left(-b\mathrm{Tr}\left[(\mathbf{e}\otimes\mathbf{e})\mathrm{R}\mathrm{D}_0\mathrm{R}^\dagger\right]\right) = s_0\exp(-b\,\hat{\mathbf{e}}\cdot\mathrm{D}_0\hat{\mathbf{e}})\,, \tag{2.21}$$

where we denoted $\hat{\mathbf{e}} = \mathrm{R}^\dagger\mathbf{e}$, and s_0 is the non-normalized signal from the microdomain without gradient encoding. This fomula has a straightforward interpretation: the signal from a microdomain rotated by R is the same as the original microdomain if the gradient direction $\mathbf{e}$ is rotated by the inverse transformation, $\mathrm{R}^\dagger$. The average of the signal over the whole voxel gives two different behaviors depending on the strength of diffusion weighting. Note that averaging over the voxel is equivalent to averaging over all rotations R. In turn, this is equivalent to averaging over all possible orientations of $\hat{\mathbf{e}}$ on the unit sphere S^2:

$$S = \frac{1}{4\pi}\int_{S^2}\exp(-b\,\hat{\mathbf{e}}\cdot\mathrm{D}_0\hat{\mathbf{e}})\,\mathrm{d}^2\hat{\mathbf{e}}\,. \tag{2.22}$$

In the weak diffusion weighting regime, i.e. $b\,\mathrm{Tr}(\mathrm{D}_0)/3 \ll 1$, the orientational average can be performed inside the argument of the exponential[2], that yields:

$$S \approx \exp\left(-b\,\mathrm{Tr}(\mathrm{D}_0)/3\right)\,. \tag{2.23}$$

Two conclusions can be drawn from this first case. (i) The direction of the gradient has disappeared. This is expected because the voxel over which the measurement is performed is macroscopically isotropic. In other words, it is invariant by rotation, therefore the signal does not depend on the direction of the gradient. (ii) The anisotropic diffusion tensor D_0 is reduced to its trace, therefore the

[2]One linearizes $\exp(-x) \approx 1-x$, performs the average, then puts $1-\langle x\rangle$ in exponential form $\exp(-\langle x\rangle)$.

signal in this regime does not distinguish the micro-anisotropy of the medium [101, 153–155, 169].

We consider now the strong diffusion encoding regime: $b\mathrm{Tr}(\mathrm{D}_0)/3 \gtrsim 1$. In that case one cannot perform the average inside the argument of the exponential because its first order asymptotic expansion is not a good approximation anymore. In order to compute the signal (2.22), let us denote by $\lambda_1, \lambda_2, \lambda_3$, and $\mathbf{e_1}, \mathbf{e}_2, \mathbf{e}_3$ the eigenvalues and corresponding eigenvectors of D_0. We assume further that $\lambda_1 < \lambda_2, \lambda_3$. At large b-values, the signal (2.22) becomes dominated by the lowest values of $\hat{\mathbf{e}} \cdot \mathrm{D}_0 \hat{\mathbf{e}}$, i.e. $\hat{\mathbf{e}} \approx \mathbf{e_1}$. One can apply the Laplace method to find the approximate expression of the signal:

$$S \approx \frac{\exp(-\lambda_1 b)}{4b\sqrt{(\lambda_3 - \lambda_1)(\lambda_2 - \lambda_1)}} \,. \tag{2.24}$$

Since $\lambda_1 < \mathrm{Tr}(\mathrm{D}_0)/3$, this yields a slower decay with b than the low-b expression (2.23) (we assume here that the factor $1/b$ varies much slower than the exponential factor). Therefore, the signal deviates from the mono-exponential free diffusion decay at large b-values, which is a direct consequence of the micro-anisotropy of the medium. A strong micro-anisotropy leads to a large discrepancy between eigenvalues $\lambda_1, \lambda_2, \lambda_3$, and in turn a large deviation between the low-b and high-b decay. However, a non-mono-exponential signal is a not a definite proof of anisotropy. Indeed, it could result from, e.g., the existence of several independent compartments with different isotropic diffusivities.

An elegant way to reveal non-ambiguously the effect of microscopic anisotropy is to perform the same measurement but with a gradient sequence such that all microscopic domains yield the same, mono-exponential, signal decay [153]. This is ensured if $\mathrm{Tr}(\mathrm{BD}_0)$ does not depend on the orientation of the microstructure, i.e. if B is an isotropic tensor:

$$\mathrm{B} = \frac{b}{3}\mathrm{I} \,. \tag{2.25}$$

Such sequences are called "isotropic diffusion weighting" or "spherical encoding" sequences and involve a varying gradient direction during the measurement. In that case the signal from an individual microdomain with diffusion tensor $\mathrm{RD}_0\mathrm{R}^\dagger$ is given by

$$s = s_0 \exp(-\mathrm{Tr}(\mathrm{BRD}_0\mathrm{R}^\dagger)) = s_0 \exp(-b\mathrm{Tr}(\mathrm{D}_0)/3) \,, \tag{2.26}$$

that is indeed independent of R, i.e. of the orientation of the microstructure. The total signal follows the mono-exponential decay (2.23) even for strong diffusion encoding. The difference in the decay of the signal between the sequence

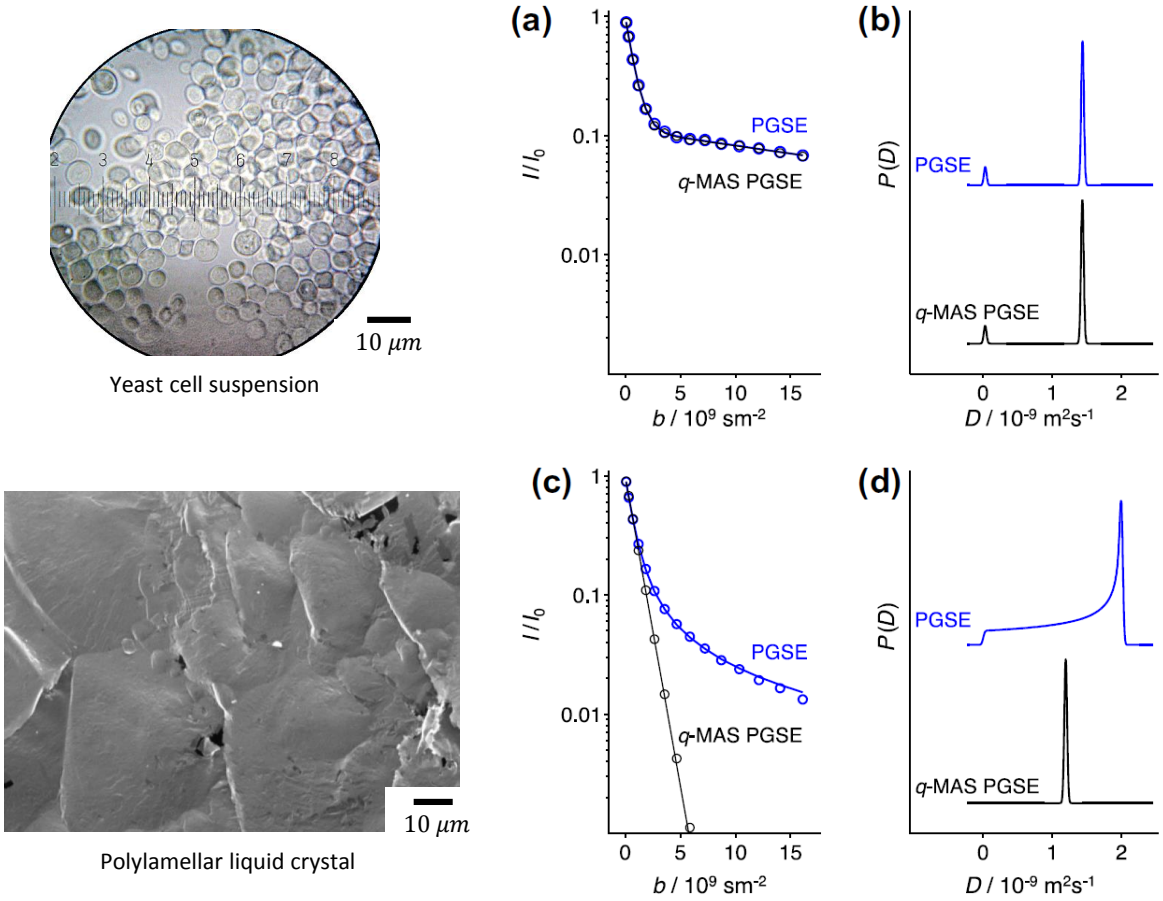

Figure 2.4: The dMRI signal from two different systems acquired with two different gradient sequences, as well as diffusion coefficient distribution obtained from inverse Laplace transform of the signal. The "q-MAS PGSE" sequence satisfies the isotropy condition (2.25), whereas the standard PGSE sequence satisfies Eq. (2.20) (Figure and data adapted from Ref. [153]). (top) experiments on a yeast cell suspension (optical microscopy image by Bob Blaylock under Creative Commons Attribution-Share Alike 3.0 Unported license). (a,b) The signal is bi-exponential that can be attributed to unrestricted extracellular diffusion and restricted intra-cellular diffusion with almost no exchange. The system is microscopically isotropic and both gradient sequences yield the same signal. (bottom) experiments on a lamellar liquid crystal with randomly oriented anisotropic microdomains (SEM image adapted from Ref. [150]). (c,d) While the PGSE sequence yields a non-mono-exponential decay associated to a broad distribution of effective diffusion coefficients, the q-MAS PGSE sequence yields a purely mono-exponential decay and therefore reveals the micro-anisotropy of the system.

with (2.20) and the one with (2.25) is an unambiguous marker of microscopic anisotropy. This is shown on Fig. 2.4 that was adapted from Ref. [153], where this finding was first reported. Although spherical encoding sequences and their ability to average microscopic anisotropy were well-known for more than 20 years, it was the first time that they were used in addition to a standard PGSE sequence to investigate the presence of micro-anisotropy.

To summarize, the B-tensor controls diffusion encoding of each particle trajectory. If it is anisotropic (e.g., Eq. (2.20)), trajectories are encoded along a preferential direction and the magnetization inside one microdomain results from the interplay of the anisotropy of B and the anisotropy of the microdomain through D_0. In turn, the total signal results from a statistical average over all microdomains, i.e. all values of D_0, that generally leads to a superposition of exponential functions and a complex signal decay. In contrast, if the B-tensor is isotropic (2.25), then trajectories are encoded isotropically, and the magnetization in each microdomain is given by the free diffusion decay with scalar diffusivity $\mathrm{Tr}(D_0)/3$. The signal is thus mono-exponential.

2.3 Mesoscopic anisotropy probed in the short-time limit

The previous sections gave an overview of the study of micro-anisotropy in the field of dMRI. However, only recently, anisotropy at the mesoscopic scale has attracted considerable attention [157]. The question is the following: how does the anisotropy of microstructural features of size ℓ_s comparable to the diffusion length ℓ_d affect the dMRI signal? In this section we investigate this effect in the short-time ($\ell_d \ll \ell_s$) and weak diffusion-encoding ($bD_0 \ll 1$) regime. In Sec. 1.2.2, we explained that in this regime, the signal may be described by the formula for free diffusion, with a reduced effective diffusion coefficient that depends on the surface-to-volume ratio σ of the domain (see Eq. (1.50) and related discussion). This result, first obtained by Mitra *et al.* in [47], was exclusively derived for isotropic structures and basic gradient sequences. We present a simplified pedagogical derivation of their formula in Sec. 2.3.1.

As we showed in the previous section, the use of three-dimensional gradient sequence may bring additional insights into the study of anisotropy. The extension of Mitra's formula to arbitrary geometry and gradient profiles is discussed in much detail in Sec. 2.3.2 and the following. We show that the form (1.50) is still valid provided a different prefactor in front of σ should be modified. Ignoring such a correction may lead to gross misestimation of σ. Our results introduce a new family of tensors that generalize the B-tensor, and we show that a new isotropy condition should be ensured to average mesoscopic anisotropy to the first order in ℓ_d (i.e., $T^{1/2}$). These results were published in [344].

2.3.1 Mitra formula for the mean-squared displacement

In this subsection we reproduce the computation performed by Mitra *et al.* in [48]. For pedagogical reasons, we focus on the first-order term, that makes the derivation simpler. In particular, it allows one to reduce the computation to a one-dimensional system where all computations can be done analytically. Besides the interest of closed and exact formulas, we believe that this simple computation sheds some light on the rather technical derivation of Mitra *et al.*. A general and systematic computation to any order in time and any geometry is presented in Sec. A.1 and relies on mathematical methods presented in [3, 330, 331].

We wish to obtain, in the short-time limit, the expression of the mean-squared displacement of particles in the presence of boundaries. As we explained in Sec. 1.2.2, the short-time limit corresponds to $\ell_d \ll \ell_s$ where each particle probes a region of size ℓ_d much smaller than the pore diameter ℓ_s. If the pore boundary is smooth, it can be replaced at first order in ℓ_d/ℓ_s by a planar boundary over a

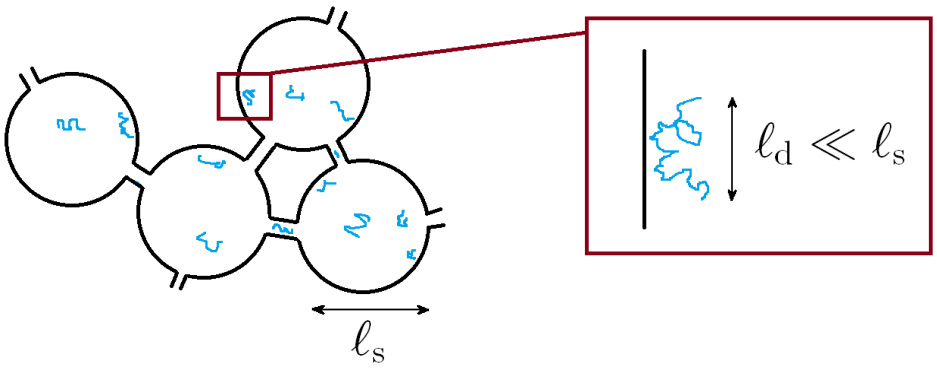

Figure 2.5: If the diffusion length ℓ_d is much smaller than the pore diameter ℓ_s, then the local boundary element probed by diffusing particles may be approximated by a flat surface. Note that here we neglect the effect of throats as they represent a vanishingly small volume fraction of the medium.

region of size ℓ_d. Therefore we compute the effect of a single planar boundary on the mean-squared displacement of particles, then we integrate over the pore boundary. We further assume that the surface relaxivity of the boundary is zero. This reduction is illustrated on Fig. 2.5.

We choose axes such that the boundary is parallel to (y, z), located at $x = 0$, and diffusion occurs in the $x \geq 0$ half-space. In that case the diffusive motion can be factorized in the three independent directions x, y, z that yields for the diffusion propagator:

$$\mathcal{G}(T, \mathbf{r_0}, \mathbf{r}) = \mathcal{G}_\mathrm{1D}(T, x_0, x) \frac{1}{4\pi\ell_\mathrm{d}^2} \exp\left(-\frac{(y-y_0)^2}{4\ell_\mathrm{d}^2}\right) \exp\left(-\frac{(z-z_0)^2}{4\ell_\mathrm{d}^2}\right) , \qquad (2.27)$$

where $\mathcal{G}_\mathrm{1D}$ denotes the one-dimensional propagator on the line with a reflecting condition at $x = 0$. We recall that $\ell_\mathrm{d} = \sqrt{D_0 T}$. In turn, the mean-squared displacement is the sum of contributions from x, y and z:

$$\mathbb{E}[(\mathbf{r}_T - \mathbf{r_0})^2] = \mathbb{E}[(x_T - x_0)^2] + 4\ell_\mathrm{d}^2 . \qquad (2.28)$$

To avoid any confusion, we emphasize that in the above formula, $\mathbf{r}_T$ is the random variable averaged while the starting point $\mathbf{r}_0$ of the trajectory is treated as a parameter. In the following we shall examine how the mean-squared displacement depends on the starting point $\mathbf{r}_0$ providing some insight into the Mitra formula.

The propagator $\mathcal{G}_\mathrm{1D}$ is computed with the method of images: by adding a virtual source at position $x = -x_0$, one automatically ensures the no-flux condition at $x = 0$. Naturally, this trick relies on the linearity of the diffusion equation (1.5) that allows one to make linear combinations of solutions to produce another

solution. Thus, one obtains the formula

$$\mathcal{G}_{1\mathrm{D}}(T, x_0, x) = \frac{1}{2\ell_\mathrm{d}\sqrt{\pi}}\left[\exp\left(-\frac{(x-x_0)^2}{4\ell_\mathrm{d}^2}\right) + \exp\left(-\frac{(x+x_0)^2}{4\ell_\mathrm{d}^2}\right)\right] . \tag{2.29}$$

To compute the mean-squared displacement along x, we simply compute the first moments $\mathbb{E}[x]$ and $\mathbb{E}[x^2]$. Since the above formula for the propagator is a sum of two terms, each moment involves a sum of two terms, denoted generically by A and B. However, the computations are simplified if one notices that B is obtained from A by reversing the sign of x_0.

$$A = \frac{1}{2\ell_\mathrm{d}\sqrt{\pi}}\int_0^\infty x \exp\left(-\frac{(x-x_0)^2}{4\ell_\mathrm{d}^2}\right) \mathrm{d}x \tag{2.30a}$$

$$= \frac{x_0}{2}\left[1 + \operatorname{erf}\left(\frac{x_0}{2\ell_\mathrm{d}}\right)\right] + \frac{1}{2\ell_\mathrm{d}\sqrt{\pi}}\int_0^\infty (x-x_0)\exp\left(-\frac{(x-x_0)^2}{4\ell_\mathrm{d}^2}\right) \mathrm{d}x \tag{2.30b}$$

$$= \frac{x_0}{2}\left[1 + \operatorname{erf}\left(\frac{x_0}{2\ell_\mathrm{d}}\right)\right] + \frac{\ell_\mathrm{d}}{\sqrt{\pi}}\exp\left(-\frac{x_0^2}{4\ell_\mathrm{d}^2}\right) . \tag{2.30c}$$

By summing A and B, we obtain directly

$$\mathbb{E}[x_T] = x_0 \operatorname{erf}\left(\frac{x_0}{2\ell_\mathrm{d}}\right) + \frac{2\ell_\mathrm{d}}{\sqrt{\pi}}\exp\left(-\frac{x_0^2}{4\ell_\mathrm{d}^2}\right) . \tag{2.31}$$

One can check that $\mathbb{E}[x_T] \approx x_0$ if $\ell_\mathrm{d} \ll x_0$. In the opposite limit, $\mathbb{E}[x_T] \approx 2\ell_\mathrm{d}/\sqrt{\pi}$. In a similar way, one can perform the computation of the second moment:

$$A = \frac{1}{2\ell_\mathrm{d}\sqrt{\pi}}\int_0^\infty x^2 \exp\left(-\frac{(x-x_0)^2}{4\ell_\mathrm{d}^2}\right) \mathrm{d}x \tag{2.32a}$$

$$= \frac{x_0^2}{2}\left[1 + \operatorname{erf}\left(\frac{x_0}{2\ell_\mathrm{d}}\right)\right] + \int_0^\infty \frac{(x-x_0)(x+x_0)}{2\ell_\mathrm{d}\sqrt{\pi}}\exp\left(-\frac{(x-x_0)^2}{4\ell_\mathrm{d}^2}\right) \mathrm{d}x \tag{2.32b}$$

$$= \frac{x_0^2}{2}\left[1 + \operatorname{erf}\left(\frac{x_0}{2\ell_\mathrm{d}}\right)\right]$$
$$- \frac{\ell_\mathrm{d}}{\sqrt{\pi}}\left(\left[(x+x_0)\exp\left(-\frac{(x-x_0)^2}{4\ell_\mathrm{d}^2}\right)\right]_0^\infty - \int_0^\infty \exp\left(-\frac{(x-x_0)^2}{4\ell_\mathrm{d}^2}\right) \mathrm{d}x\right) \tag{2.32c}$$

$$= \left(\frac{x_0^2}{2} + \ell_\mathrm{d}^2\right)\left[1 + \operatorname{erf}\left(\frac{x_0}{2\ell_\mathrm{d}}\right)\right] + \frac{x_0\ell_\mathrm{d}}{\sqrt{\pi}}\exp\left(-\frac{x_0^2}{4\ell_\mathrm{d}^2}\right) . \tag{2.32d}$$

The summation of A and B yields the simple result

$$\mathbb{E}[x_T^2] = x_0^2 + 2\ell_\mathrm{d}^2 \ . \tag{2.33}$$

As expected from an unbounded system, in the long-time limit the classical result $\mathbb{E}[x_T^2]/\ell_\mathrm{d}^2 \to 2$ is recovered. From the above result, one can easily compute the mean-squared displacement:

$$\mathbb{E}[(x_T - x_0)^2] = 2\ell_\mathrm{d}^2 \left(1 + f(x_0/\ell_\mathrm{d})\right) \ , \tag{2.34a}$$

$$f(u) = u^2 \left[1 - \mathrm{erf}(u/2)\right] - \frac{2u}{\sqrt{\pi}} \exp\left(-u^2/4\right) \ . \tag{2.34b}$$

The correction $f(x_0/\ell_\mathrm{d})$ to the free diffusion result is negative and tends to zero when the ratio x_0/ℓ_d goes either to zero or to infinity (for $x_0/\ell_\mathrm{d} = 4$ it is smaller than a 1% correction). Indeed, a particle starting on the boundary simply performs a Brownian motion reflected with respect to $x = 0$, therefore its mean-squared displacement is the same as a Brownian motion without boundary. The opposite limit is clear as the effect of the boundary becomes negligible if the starting point x_0 is very far from it. Therefore, there is a layer of size $\sim \ell_\mathrm{d}$ where the mean-squared displacement is significantly lower than its free diffusion value (see Fig. 2.6).

To obtain the effect of the boundary on the mean-squared displacement of all particles, one should then average over the whole domain. Since the half-line is unbounded, the term $2\ell_\mathrm{d}^2$ in Eq. (2.34a) yields an infinite integral. However, the correction term yields a finite value, which proves that the reduction of the mean-squared displacement is a surface effect:

$$\int_0^\infty \left(\frac{\mathbb{E}[(x_T - x_0)^2]}{2\ell_\mathrm{d}^2} - 1 \right) \mathrm{d}x_0 = -\frac{4}{3\sqrt{\pi}} \ell_\mathrm{d} \ . \tag{2.35}$$

Note that one may perform the same computation by studying the properties of the one-dimensional velocity v_t^x. In that case, one obtains a formula in the form of Eq. (1.10) with a correlation function that depends on the position with respect to the boundary. After integration over the whole domain, one obtains the simple formula for the boundary correction term

$$\Psi_{xx}(t - t') = \int_\Omega \left(\frac{\mathbb{E}[\mathrm{v}_t^x \mathrm{v}_{t'}^x]}{2D_0} - \delta(t - t') \right) \mathrm{d}x_0 = -\frac{1}{2\sqrt{\pi}} \frac{\sqrt{D_0}}{\sqrt{|t - t'|}} \ . \tag{2.36}$$

The negative sign of the correction term here agrees with the negative sign of the correction of mean-squared displacement (2.35). An interpretation is that

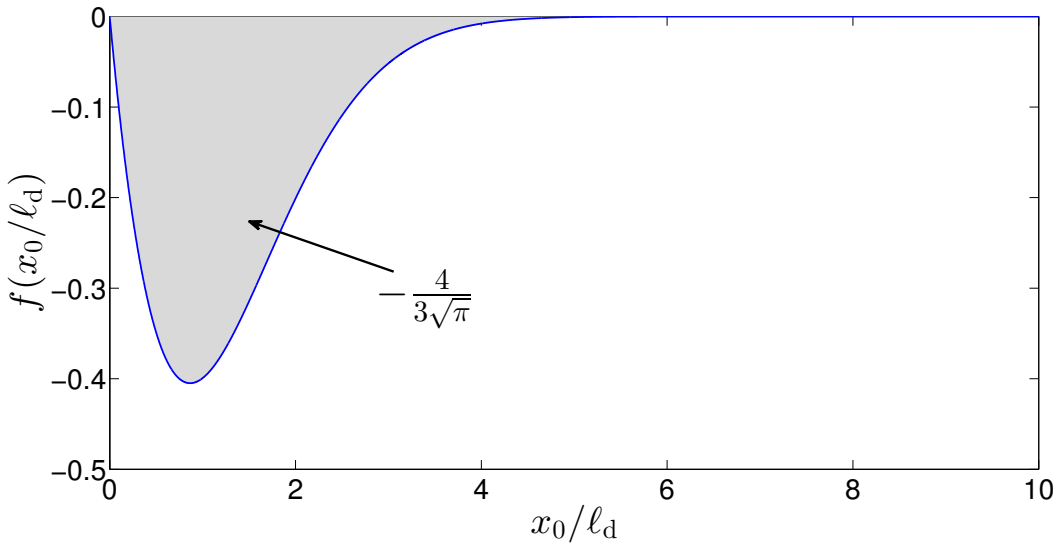

Figure 2.6: The correction term $f(x_0/\ell_\mathrm{d})$ from Eq. (2.34a) that represents the relative decrease in the one-dimensional mean-squared displacement close to a boundary as a function of starting position. The shaded area represents the integral of this correction term and yields the numerical prefactor $4/(3\sqrt{\pi})$ that was first computed by Mitra *et al.* in the context of dMRI. The fact that the integral is finite expresses that the correction is a surface effect.

particles reflecting on the boundary introduce a negative correlation between their velocity before reflection and their velocity after reflection. This approach is presented in more detail and generality in Ref. [61], where the velocity autocorrelator in an arbitrary geometry is expressed through the propagator between boundary points.

Using Eq. (2.28), one can reformulate the above results in terms of an effective diffusion coefficient $D_\mathrm{MSD}(T, \mathbf{r_0})$ (see Eq. (2.9)). If one returns to the original porous geometry, Eq. (2.34a) remains valid, where x_0 should be replaced by $\mathrm{d}(\mathbf{r_0}, \partial\Omega)$, the distance between the point of interest and the boundary:

$$D_\mathrm{MSD}(T, \mathbf{r_0}) = D_0 \left(1 + f(\mathrm{d}(\mathbf{r_0}, \partial\Omega)/\ell_d)/d\right) \ , \tag{2.37}$$

and the spatial average over the whole domain

$$D_\mathrm{MSD}(T) = \frac{1}{\mathrm{vol}(\Omega)} \int_\Omega D_\mathrm{MSD}(T, \mathbf{r_0}) \, \mathrm{d}^3\mathbf{r_0} \tag{2.38}$$

yields to the first order:

$$D_\mathrm{MSD}(T) = D_0 \left(1 - \frac{4}{3d\sqrt{\pi}} \sigma \ell_\mathrm{d}\right) \ , \tag{2.39}$$

where we recall that σ denotes the surface-to-volume ratio of the porous medium. To obtain Eq. (2.39), the integral over $\mathbf{r_0}$ is first restricted to the vicinity of $\partial\Omega$ then decomposed as a product of an integral along the surface and an integral perpendicular to it. This is Mitra's formula that was obtained in [48].

2.3.2 Application to effective diffusion coefficient probed by gradient encoding

The above computation allowed us to re-derive the seminal result of Mitra *et al.* on mean-squared displacement of particles in the short-time limit. The main result is the first-order, short-time expansion for the quantity D_{MSD} (2.39). However, a bridge is missing: the relation with the effective diffusion coefficient D probed by dMRI. For convenience, we reproduce here the formulas (1.49c), (1.47b), (1.46b), and (1.27b), (1.27c):

$$S \underset{bD\ll 1}{=} \exp(-bD)\,, \qquad b = \int_0^T \mathbf{Q}^2(t)\,\mathrm{d}t\,,$$
$$D = \frac{1}{2b}\mathbb{V}[\phi]\,, \qquad \phi = \int_0^T \mathbf{G}(t)\cdot(\mathbf{r}_t-\mathbf{r}_0)\,\mathrm{d}t = -\int_0^T \mathbf{Q}(t)\cdot\mathbf{v}_t\,\mathrm{d}t\,.$$

We shall now explain that the effective diffusion coefficient D differs from D_{MSD} on two aspects that lead us to the generalized Mitra formula.

Relative orientation of the gradient and the boundary

While the phase ϕ, and in turn the coefficient D, results from encoding of the motion along the direction of the gradient, the mean-squared displacement, hence D_{MSD} results from an average over all directions. As we discussed in Sec. 2.1, the correct description of mesoscopic anisotropy should involve a diffusion tensor $\mathsf{D}_{\mathrm{MSD}}$ that contains information about diffusion in all directions. Let us denote by $\mathbf{n}$ the inward normal vector (from the boundary to the pore space) at the boundary $\partial\Omega$. The above computation was done with $\mathbf{n} = \mathbf{e_x}$. The considerations of independence of motions along x, y, and z allow us to rewrite Eq. (2.35) in the tensorial form

$$\int_0^\infty \left(\frac{\mathbb{E}[(\mathbf{r}_T-\mathbf{r}_0)\otimes(\mathbf{r}_T-\mathbf{r}_0)]}{2\ell_{\mathrm{d}}^2} - \mathsf{I}\right)\mathrm{d}x_0 = -\frac{4}{3\sqrt{\pi}}\ell_{\mathrm{d}}\,\mathbf{n}\otimes\mathbf{n}\,. \tag{2.40}$$

The formula is true for $\mathbf{n} = \mathbf{e_x}$ and both sides are contravariant tensors with respect to spatial rotations, hence the formula is valid for any orientation of $\mathbf{n}$.

Similarly, one can rewrite the expression (2.36) the velocity autocorrelator for a planar boundary with inward normal vector $\mathbf{n}$:

$$\Psi(t-t') = -\frac{1}{2\sqrt{\pi}} \frac{\sqrt{D_0}}{\sqrt{|t-t'|}} \mathbf{n}\otimes\mathbf{n} \,. \tag{2.41}$$

For example, if the motion of the particle is probed along a direction $\mathbf{e}$, then the correction to the 1D mean-squared displacement is given by the projection of $\mathbf{e}$ over $\mathbf{n}$ according to

$$-\frac{4}{3\sqrt{\pi}}\ell_d \left(\mathbf{e}\cdot(\mathbf{n}\otimes\mathbf{n})\mathbf{e}\right) = -\frac{4}{3\sqrt{\pi}}(\mathbf{e}\cdot\mathbf{n})^2 \,. \tag{2.42}$$

After integration over the whole boundary $\partial\Omega$, one obtains the generalization of Eq. (2.39):

$$\mathsf{D}_{\mathrm{MSD}}(T) \approx \frac{D_0}{d}\left(\mathsf{I} - \frac{4}{3\sqrt{\pi}}\sigma\ell_d \mathsf{S}^{(3)}\right) \,, \tag{2.43}$$

with the following "structural" tensor $\mathsf{S}^{(3)}$ (the reason behind the superscript "$^{(3)}$" will appear later)

$$\mathsf{S}^{(3)} = \frac{1}{\mathrm{surf}(\partial\Omega)} \int_{\partial\Omega} \mathbf{n}\otimes\mathbf{n}\,\mathrm{d}\sigma \,. \tag{2.44}$$

One can also integrate the velocity autocorrelator over the whole boundary and get

$$\Psi(t-t') \approx -\frac{2}{\sqrt{\pi}} \frac{\sqrt{D_0}}{\sqrt{|t-t'|}} \sigma \mathsf{S}^{(3)} \,. \tag{2.45}$$

While Eqs. (2.40) and (2.41) are exact for a planar boundary, the integrated formulas (2.43) and (2.45) involve an approximation where the boundary $\partial\Omega$ is locally replaced by flat boundary elements over the scale ℓ_d.

Encoding by the gradient profile

The MSD measures the square of $\mathbf{r}_T - \mathbf{r}_0$, that is the squared distance between endpoints of the trajectory. In contrast, the phase ϕ results from the continuous encoding of the trajectory by the gradient profile $\mathbf{G}(t)$. If we discard anisotropy effects discussed above, one can see that D and D_{MSD} would coincide only for a narrow-gradient pulse experiment (see Eq. (1.55)), as it was explicitly stated by

Mitra *et al.*. In general, one can compute the variance of ϕ from:

$$\mathbb{V}[\phi] = \mathbb{E}\left[\int_0^T\int_0^T (\mathbf{Q}(t)\cdot\mathbf{v}_t)\,(\mathbf{Q}(t')\cdot\mathbf{v}_{t'})\,\mathrm{d}t\,\mathrm{d}t'\right] \tag{2.46a}$$

$$= \int_0^T\int_0^T \mathrm{Tr}\left[\mathbb{E}[\mathbf{v}_t\otimes\mathbf{v}_{t'}](\mathbf{Q}(t)\otimes\mathbf{Q}(t'))\right]\,\mathrm{d}t\,\mathrm{d}t' \tag{2.46b}$$

$$= 2D_0\int_0^T\int_0^T \mathrm{Tr}\left[(\delta(t-t')\mathsf{I}+\Psi(t-t'))(\mathbf{Q}(t)\otimes\mathbf{Q}(t'))\right]\,\mathrm{d}t\,\mathrm{d}t'\,, \tag{2.46c}$$

that yields from the above expression of the velocity autocorrelator (2.45):

$$\mathbb{V}[\phi] = 2bD_0\left(1-\frac{4}{3\sqrt{\pi}}\sigma\ell_\mathrm{d}\,\mathrm{Tr}(\mathsf{T}^{(3)}\mathsf{S}^{(3)})\right)\,, \tag{2.47}$$

with the following tensor $\mathsf{T}^{(3)}$:

$$\mathsf{T}^{(3)} = \frac{3}{8b\sqrt{T}}\int_0^T\int_0^T \frac{\mathbf{Q}(t)\otimes\mathbf{Q}(t')}{\sqrt{|t-t'|}}\,\mathrm{d}t\,\mathrm{d}t'\,. \tag{2.48}$$

After integration by parts, we can rewrite it in the following way

$$\mathsf{T}^{(3)} = -\frac{T}{2b}\int_0^T\int_0^T \mathbf{G}(t)\otimes\mathbf{G}(t')\left|\frac{t-t'}{T}\right|^{3/2}\,\mathrm{d}t\,\mathrm{d}t'\,. \tag{2.49}$$

A more systematic computation shows that higher-order terms are of the form $\ell_d^{m-2}\,\mathrm{Tr}(\mathsf{T}^{(m)}\mathsf{S}^{(m)})$, $m = 4, 5, \ldots$, with the generalized "temporal" matrices

$$\mathsf{T}^{(m)} = -\frac{T}{2b}\int_0^T\int_0^T \mathbf{G}(t)\otimes\mathbf{G}(t')\left|\frac{t-t'}{T}\right|^{m/2}\,\mathrm{d}t\,\mathrm{d}t'\,, \tag{2.50}$$

and where the matrices $\mathsf{S}^{(m)}$ encode geometrical properties of the boundaries such as curvature, surface relaxation, or permeability (see Sec. A.1 and Refs [3, 48–53]). However, these properties do not affect the first-order term in (2.51), on which we focus in this section. The computation and study of the ℓ_d^2 (i.e., D_0T) term is presented in Sec. 2.3.6. Note that with these notations $\mathsf{T}^{(2)}$ is actually the B-tensor renormalized by the b-value [141–143] (see Sec. A.1 from Eq. (A.19) to Eq. (A.24) for a detailed computation).

Therefore, we have generalized the Mitra formula (2.39) as

$$D(T) = D_0\left(1-\eta\frac{4}{3\sqrt{\pi}}\sigma\ell_d + O(T)\right)\,, \tag{2.51}$$

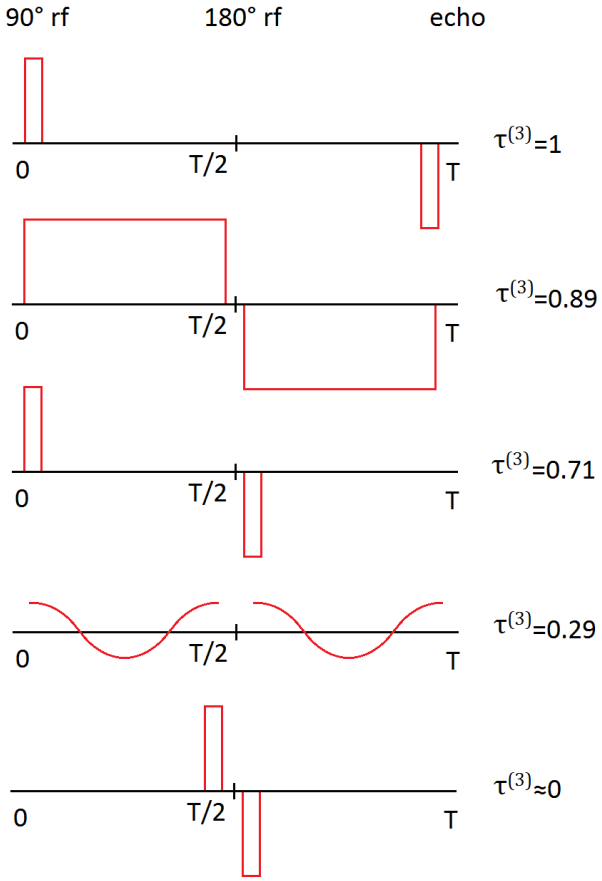

Figure 2.7: Illustration of some gradient profiles for spin echo experiments. We stress that these gradient profiles are "effective" in the sense that the gradients are reversed after $T/2$ to include the effect of the 180° rf pulse. The corresponding values of $\tau^{(3)}$ introduced in Sec. 2.3.4 are given for each profile. Note that $\tau^{(3)} = 1$ for the narrow pulses-case (first panel), which corresponds to Mitra's formula (2.39).

by introducing the dimensionless prefactor η that depends both on the structure of the medium and on the gradient waveform:

$$\eta = \mathrm{Tr}(\mathrm{S}^{(3)}\mathrm{T}^{(3)}) \ . \tag{2.52}$$

This correction factor is the result of an intricate coupling between the medium structure and the gradient sequence, which is expressed through a simple mathematical relation between $\mathrm{S}^{(3)}$ and $\mathrm{T}^{(3)}$. We recall that dependence on the waveform through $\mathrm{T}^{(3)}$ implies that one cannot, strictly speaking, interpret $D(T)$ as a measure of mean-squared displacement of randomly diffusing molecules, except for the theoretical case of two infinitely narrow gradient pulses.

We emphasize that the dependence of $\mathbb{V}[\phi]$ on $\mathrm{T}^{(3)}$ instead of $\mathrm{T}^{(2)} = \mathrm{B}/b$ in Eq. (2.47) prevents one from writing the generalized Mitra formula (2.51) in

the form of an effective diffusion tensor. Indeed, if one were to obtain an effective diffusion tensor $\mathsf{D}(T)$, then the variance of the phase would follow Eq. (2.17), i.e. $\mathbb{V}[\phi] = 2\,\mathrm{Tr}(\mathsf{B}\mathsf{D}(T))$, which would involve the $\mathsf{T}^{(2)}$ tensor and not $\mathsf{T}^{(3)}$. This observation contrasts with the diffusion tensor (2.43) defined through mean-squared displacement $\mathsf{D}_{\mathrm{MSD}}(T)$.

Several remarks are in order about the newly introduced $\mathsf{S}^{(m)}$ and $\mathsf{T}^{(m)}$ matrices. First, we emphasize that $\mathsf{S}^{(m)}$ and $\mathsf{T}^{(m)}$ are tensors in the sense that under a spatial rotation or symmetry described by a matrix R, $\mathsf{S}^{(m)}$ and $\mathsf{T}^{(m)}$ are transformed according to $\mathsf{S}^{(m)} \to \mathsf{R}\mathsf{S}^{(m)}\mathsf{R}^{-1}$ and $\mathsf{T}^{(m)} \to \mathsf{R}\mathsf{T}^{(m)}\mathsf{R}^{-1}$. Finally, all $\mathsf{S}^{(m)}$ and $\mathsf{T}^{(m)}$ tensors are dimensionless. As a consequence, η is invariant under dilatation of the gradient waveform, dilatation of the time interval $[0, T]$ and dilatation of the domain Ω.

Mitra's formula (2.39) was derived for PGSE experiments with (infinitely) short gradient pulses, where $T = \Delta$ is the inter-pulse time. We emphasize that for general gradient profiles, Δ is not defined anymore, and we use instead the echo time T in our generalized formula (2.51). If we compare the general formula (2.51) to the one for narrow-gradient pulses (2.39) (which corresponds to the profile shown on the first panel in Fig. 2.7), we see that Mitra's formula corresponds to the simple expression

$$\eta_{\mathrm{Mitra}} = 1/d \ . \tag{2.53}$$

Below we generalize this relation to arbitrary medium structures (Sec. 2.3.3) and gradient profiles (Sec. 2.3.4).

2.3.3 Dependence on the structure

Simple shapes

For any bounded domain Ω, the tensor $\mathsf{S}^{(3)}$ is symmetric, positive-definite, with $\mathrm{Tr}(\mathsf{S}^{(3)}) = 1$. For example, if Ω is a sphere, one gets $\mathsf{S}^{(3)}_{\mathrm{sphere}} = \mathsf{I}/3$, which is invariant under any spatial rotations of the medium, as expected. Let us recall that we call such matrices, that are proportional to the 3×3 unit matrix I, "isotropic". However, the same result holds if Ω is a cube, i.e. the cube is also qualified as isotropic by the $\mathsf{S}^{(3)}$ tensor. Clearly, the tensor $\mathsf{S}^{(3)}$ does not uniquely characterize the shape of Ω.

Let us now consider the example of a rectangular parallelepiped. We align its sides with the axes $(\mathbf{e_x}, \mathbf{e_y}, \mathbf{e_z})$ and denote their lengths by a, b, c. Then the normal vector $\mathbf{n}$ is either $\pm\mathbf{e_x}$, $\pm\mathbf{e_y}$, or $\pm\mathbf{e_z}$ depending on the facet of the parallelepiped,

and by integrating over each facet we get

$$\mathsf{S}^{(3)} = \frac{1}{bc + ca + ab} \begin{bmatrix} bc & 0 & 0 \\ 0 & ca & 0 \\ 0 & 0 & ab \end{bmatrix} . \tag{2.54}$$

This simple example shows that, by varying a, b, c, and applying rotations, the matrix $\mathsf{S}^{(3)}$ can be *any* symmetric positive-definite tensor with unit trace.

In the limit when one side of the parallelepiped (say, c) tends to infinity (or is much bigger than the other two), the rectangular parallelepiped transforms into a cylindrical domain with a rectangular cross-section and the $\mathsf{S}^{(3)}$ tensor becomes

$$\mathsf{S}^{(3)} = \frac{1}{a + b} \begin{bmatrix} b & 0 & 0 \\ 0 & a & 0 \\ 0 & 0 & 0 \end{bmatrix} . \tag{2.55}$$

Note that in the special case $a = b$ (cylindrical domain with square cross-section), one obtains the same result as for a circular cylinder of axis $\mathbf{e}_z$: $\mathsf{S}^{(3)}_{\text{cyl}} = (\mathsf{I} - \mathbf{e}_z \otimes \mathbf{e}_z)/2$. In the opposite limit where a and b are much bigger than c, the parallelepiped transforms into a slab perpendicular to $\mathbf{e}_z$ and the $\mathsf{S}^{(3)}$ tensor becomes $\mathsf{S}^{(3)}_{\text{slab}} = \mathbf{e}_z \otimes \mathbf{e}_z$.

One recognizes in the previous examples the factor $1/d$ of Mitra's formula (2.53): $1/3$ for a sphere, $1/2$ for a circular cylinder, and 1 for a slab. However, even in these basic cases, the factor η remains affected by the gradient waveform, as discussed in Sec. 2.3.4. In Appendix A.2, we provide additional computations of $\mathsf{S}^{(3)}$ for slightly non-spherical domains (perturbative computation) and for spheroids (exact computation). Such domains may be more accurate models of anisotropic pores in pathological tissues such as prostate tumor [64] than cylinders.

The effect of orientation dispersion

Now we consider a random medium consisting of infinite circular cylinders with random orientations and random radii. Cylinders are archetypical anisotropic domains and we choose them to illustrate in an explicit way the effect of orientation dispersion of the domains. They can also serve as a model for alveolary ducts in lungs [151] or muscle fibers [226–228]. For the sake of simplicity, we assume the radius of each cylinder to be independent from its orientation. Equations (1.49c) and (2.51) describe the signal on the mesoscopic scale (one cylinder).

Within the scope of small b-values ($bD_0 \ll 1$), the macroscopic signal formed by many cylinders is:

$$S \approx \langle \exp(-bD(T)) \rangle \approx \exp(-b\langle D(T) \rangle) \,, \tag{2.56}$$

where $\langle \cdots \rangle$ denotes the average over the voxel. Coming back to Eqs. (2.51) and (2.52), we see that the average of $D(T)$ is obtained through the average of the $\mathsf{S}^{(3)}$ matrices of the cylinders, that we now compute.

From the previous section, the $\mathsf{S}^{(3)}$ tensor of a cylinder oriented along any direction $\mathbf{u}$ (where $\mathbf{u}$ is a unit vector) is

$$\mathsf{S}^{(3)}_{\text{cyl}}(\mathbf{u}) = \frac{1}{2}\left(\mathsf{I} - \mathbf{u} \otimes \mathbf{u}\right) \,. \tag{2.57}$$

Moreover, for one cylinder of radius R, one has $\sigma = 2/R$, thus the voxel-averaged effective diffusion coefficient reads

$$\langle D(T) \rangle = D_0 \left(1 - \frac{4\ell_{\text{d}}}{3\sqrt{\pi}} \left\langle \frac{2}{R} \right\rangle \text{Tr}(\langle \mathsf{S}^{(3)} \rangle \mathsf{T}^{(3)}) + O(T)\right) . \tag{2.58}$$

The averaged tensor $\langle \mathsf{S}^{(3)} \rangle$ depends on the angular distribution of the cylinder orientations. Following a computation in Sec. 2.1, a distribution with a rotation symmetry around the z-axis yields

$$\langle \mathsf{S}^{(3)} \rangle = \frac{1}{6} \begin{bmatrix} 2+\Theta & 0 & 0 \\ 0 & 2+\Theta & 0 \\ 0 & 0 & 2-2\Theta \end{bmatrix} , \tag{2.59}$$

where Θ is the orientation order parameter of the medium (see Eq. (2.13)). The parameter Θ can take any value from $-1/2$ (all the cylinders are in the $x-y$ plane) to 1 (all the cylinders are aligned with $\mathbf{e_z}$). The special value $\Theta = 0$ corresponds to an isotropic tensor $\mathsf{S}^{(3)} = \mathsf{I}/3$ and can be obtained, for example, with a uniform distribution [154–156].

The orientation order parameter has direct analogies with other diffusion models describing the water diffusion in strongly anisotropic medium. For instance, if randomly oriented fibers obey a Watson distribution of parameter K [107], then one can compute [108]

$$\Theta = \frac{3}{4\sqrt{K}\,\mathrm{F}(\sqrt{K})} - \frac{3}{4K} - \frac{1}{2} \,, \tag{2.60}$$

where F is the Dawson function: $\mathrm{F}(u) = \int_0^u e^{t^2-u^2}\,\mathrm{d}t$. In the limits of K going to $-\infty$, 0, and $+\infty$, we obtain $\Theta = -1/2$, 0, and 1, respectively.

An important consequence of the above computations is that experiments at short diffusion times and small-amplitude gradients are unable to distinguish the mesoscopic anisotropy (the anisotropy of each cylinder) inside a macroscopically isotropic medium (uniform distribution of the cylinders). Therefore, regimes with longer diffusion times or higher gradients are needed for extracting mesoscopic diffusion information [101, 154, 155, 169]. This observation may be related to Sec. 2.2.2 about micro-anisotropy and spherical encoding sequences. In a similar way, we shall see that one can perform sequences with an isotropic encoding condition that would help to reveal mesoscopic anisotropy by producing an orientation-independent exponential decay.

2.3.4 Dependence on the gradient waveform

In this section we investigate the dependence of the correction factor η (and of higher-order terms) on the gradient waveform captured via the $\mathsf{T}^{(m)}$ tensors. We begin with the simpler case, the so-called linear gradient encoding, where the gradient $\mathbf{G}(t)$ has a fixed direction and each $\mathsf{T}^{(m)}$ tensor is reduced to a scalar. We show that significant deviations from the classical formula (2.39) arise depending on the chosen waveform.

Next, in Sec. 2.3.4, we study how the correction factor is affected in the most general case when both gradient amplitude and direction are time dependent. In particular, we show that recently invented spherical encoding sequences [153, 161] do not provide the *full mixing* effect in the sense that η still depends on the orientation of the (anisotropic) medium. In order to resolve this problem we describe in Sec. 2.3.4 a simple and robust algorithm to design diffusion gradient profiles with desired features and constraints.

Linear encoding

If we set $\mathbf{G}(t) = G(t)\mathbf{e}$, with a constant unit vector $\mathbf{e}$, the $\mathsf{T}^{(m)}$ tensors become

$$\mathsf{T}^{(m)} = \tau^{(m)}\, \mathbf{e} \otimes \mathbf{e}\,, \tag{2.61}$$

with the scalar

$$\tau^{(m)} = -\frac{T}{2b} \int_0^T \int_0^T G(t)G(t') \left|\frac{t-t'}{T}\right|^{m/2} \mathrm{d}t\, \mathrm{d}t'\,. \tag{2.62}$$

For clarity, we emphasize that $\tau^{(3)}$ is positive, as it is proven in Sec. A.3. The correction factor η becomes

$$\eta = \tau^{(3)} \left(\mathbf{e} \cdot \mathsf{S}^{(3)}\mathbf{e}\right)\,. \tag{2.63}$$

By keeping the same profile $G(t)$ and only changing the direction of the applied gradient $\mathbf{e}$, the factor $\tau^{(3)}$ is unchanged and the factor $\left(\mathbf{e}\cdot \mathrm{S}^{(3)}\mathbf{e}\right)$ allows one to probe the whole $\mathrm{S}^{(3)}$ tensor, and thus microstructural information on the domain. For this purpose, one can transpose standard diffusion tensor imaging reconstruction techniques (see Sec. 2.2.1 and Ref. [141]) to our case. Bearing in mind that $\mathrm{S}^{(3)}$ is symmetric positive-definite matrix with trace one, one needs at least 6 diffusion directions to estimate 5 independent coefficients of the $\mathrm{S}^{(3)}$ tensor and the surface-to-volume ratio σ.

For a $\mathrm{S}^{(3)}$ tensor such as the one of a parallelepiped in Eq. (2.54), the factor η takes different values depending on the gradient direction $\mathbf{e}$. Note that the extremal values of $\left(\mathbf{e}\cdot \mathrm{S}^{(3)}\mathbf{e}\right)$ are given by the minimal and maximal eigenvalue of $\mathrm{S}^{(3)}$. In other words, the relative difference between the extremal eigenvalues of $\mathrm{S}^{(3)}$ indicates the magnitude of the induced error on the estimation of σ. For instance, if one applies the gradient in a direction perpendicular to the smallest facets of parallelepiped, one probes the surface of these facets, not of the whole structure (see Eq. (2.54)). Although this example is specific, the conclusion is general: the mesoscopic anisotropy of a confining domain, captured via the tensor $\mathrm{S}^{(3)}$, can significantly bias the estimation of the surface-to-volume ratio. This circumstance was ignored in some former studies with application of the classical Mitra's formula, which is only valid for isotropic domains. While spherical encoding scheme aims to resolve this issue by mixing contributions from different directions, we will see in Sec. 2.3.4 that this mixing is not perfect for formerly proposed spherical encoding sequences.

In the remaining part of this subsection, we consider the particular case of isotropic (e.g., spherical) domains with $\mathrm{S}^{(3)} = \mathrm{I}/3$ so that the structural aspect is fully decoupled from the temporal one. In this case, Eq. (2.52) yields

$$\eta = \frac{\tau^{(3)}}{3}\,, \tag{2.64}$$

and we can focus on the temporal aspect (gradient waveform) captured via the factor $\tau^{(3)}$. Note that the original Mitra's formula corresponds to $\tau^{(3)} = 1$ (see Eq. (2.53)).

Figure 2.7 shows several examples of temporal profiles and the corresponding values of $\tau^{(3)}$. The maximum attainable value of $\tau^{(3)}$ is slightly over 1 (around 1.006), see Appendix A.3 for more details. Counter-intuitively, the maximal value of $\tau^{(3)}$ is not 1 while the profile with infinitely narrow pulses does not provide its maximum. The infimum of $\tau^{(3)}$ is 0; in fact, one can achieve very small values of $\tau^{(3)}$ by using very fast oscillating gradients. Indeed, for sinusoidal gradient waveforms of angular frequency ω, one has $\tau^{(3)} \sim \omega^{-1/2}$, in the limit $\omega T \gg 1$ (see Appendix A.3 and Refs. [59, 60]).

This finding has an important practical consequence: if one ignores the factor $\tau^{(3)}$ and uses the original Mitra's formula (for which $\tau^{(3)} = 1$), one can significantly underestimate the surface-to-volume ratio (by a factor $1/\tau^{(3)}$) and, thus, overestimate the typical size of compartments.

Isotropy and spherical encoding

As we discussed in Sec. 2.1 and 2.2.2, microscopic anisotropy is usually modeled via an anisotropic diffusion tensor D_0, and the expression of the diffusion signal becomes (see Eqs. (2.14) and (2.17)):

$$S \approx \exp\left(-b\mathrm{Tr}\left(\mathsf{T}^{(2)}\mathsf{D}_0\right)\right) . \tag{2.65}$$

Typical spherical encoding sequences [153, 158–161, 165, 168] aim to average out the microscopic anisotropy of the medium by applying an encoding gradient with time-changing direction. Mathematically, the goal is to obtain an isotropic $\mathsf{T}^{(2)}$ matrix, $\mathsf{T}^{(2)} = \mathsf{I}/3$, so that the signal in Eq. (2.65) depends only on the trace $\mathrm{Tr}(\mathsf{D}_0)$ and thus yields the same result for any orientation of microdomains inside the medium. We recall that throughout the thesis, we call a matrix isotropic if it is proportional to the unit matrix I (in other words, its eigenvalues are equal to each other).

Mesoscopic anisotropy manifests itself in the $\mathsf{S}^{(3)}$ matrix of individual compartments, as we explained in Sec. 2.3.3. Thus, from Eq. (2.51) we can deduce that mesoscopic anisotropy is averaged out (at the order $\sqrt{D_0 T}$) by the gradient sequence *only* if $\mathsf{T}^{(3)}$ is isotropic. In this case, the factor η does not depend on the orientation of the mesoscopically anisotropic medium nor on its actual shape, and one can estimate precisely the surface-to-volume ratio of the medium. Moreover, from Eq. (2.52) we see that in this case, η can be read directly from the expression of $\mathsf{T}^{(3)}$:

$$\mathsf{T}^{(3)}_{\mathrm{iso}} = \eta\,\mathsf{I} . \tag{2.66}$$

Similarly, the isotropy condition for the matrices $\mathsf{T}^{(4)}, \mathsf{T}^{(5)}, \ldots$ would be needed if the higher-order terms of expansion (2.51) were considered.

Hence, the natural question arises: "Do the former spherical encoding sequences that were designed to get an isotropic $\mathsf{T}^{(2)}$ (or B) tensor, produce isotropic $\mathsf{T}^{(m)}$ tensors (or at least $\mathsf{T}^{(3)}$)?". For instance, for the q-Space Magic-Angle-Spinning (q-MAS) sequence [153, 161] we obtain

$$\mathsf{T}^{(3)} = \begin{bmatrix} 0.14 & 0 & 0 \\ 0 & 0.28 & 0.10 \\ 0 & 0.10 & 0.17 \end{bmatrix} . \tag{2.67}$$

This matrix has eigenvalues $0.11, 0.14, 0.33$ and is thus not isotropic. Similarly, a triple diffusion encoding (TDE) sequence [168] (where three identical PGSE sequences are applied along three orthogonal direction in space) yields

$$\mathsf{T}^{(3)} = \begin{bmatrix} 0.19 & 0.08 & 0.05 \\ 0.08 & 0.19 & 0.08 \\ 0.05 & 0.08 & 0.19 \end{bmatrix}, \tag{2.68}$$

with eigenvalues $0.10, 0.14, 0.34$. Note that, although the diagonal elements of the matrix are identical, it is not isotropic because of the off-diagonal elements. The above matrix corresponds to a TDE sequence where each PGSE sequence is made of infinitely narrow pulses with spacing $\Delta = T/3$. One could also consider the FAMEDcos sequence [164], for which we get

$$\mathsf{T}^{(3)} = \begin{bmatrix} 0.13 & 0 & 0.012 \\ 0 & 0.11 & 0 \\ 0.012 & 0 & 0.10 \end{bmatrix}, \tag{2.69}$$

which is also not isotropic (with eigenvalues: $0.09, 0.11, 0.13$). All spherical encoding schemes that we could find in the literature produce anisotropic $\mathsf{T}^{(3)}$ matrices.

In order to illustrate the errors induced by such sequences in the estimation of the surface-to-volume ratio, let us apply the q-MAS sequence for the case of an infinite circular cylinder. We denote by $(\mathbf{e_1}, \mathbf{e_2}, \mathbf{e_3})$ the orthogonal basis of eigenvectors and by $(\lambda_1, \lambda_2, \lambda_3) = (0.11, 0.14, 0.33)$ the corresponding eigenvalues of the $\mathsf{T}^{(3)}$ matrix in Eq. (2.67) (see Fig. 2.8 for the orientation of these axes with respect to the $\mathbf{Q}$-space plot of the sequence). If the cylinder is oriented along $\mathbf{e_3}$, one obtains $\eta = (\lambda_1 + \lambda_2)/2 = 0.13$. However, if the cylinder is oriented along $\mathbf{e_1}$, then $\eta = (\lambda_2 + \lambda_3)/2 = 0.24$, which is nearly twice as large. In other words, the estimated σ ratio is twice as large in the second situation than in the first one. This artifact is a direct consequence of the differences between the eigenvalues of the $\mathsf{T}^{(3)}$ matrix, i.e. its anisotropy.

How to obtain isotropic matrices?

The question in the subsection title can be restated in an algebraic language: how to find three functions $G_x(t), G_y(t), G_z(t)$ with zero mean (see Eq. (1.26)) that are mutually "orthogonal" and have the same "norm" for a given set of symmetric bilinear forms φ_m, $m = 2, 3, \ldots$, with

$$\varphi_m(f_1, f_2) = -\frac{\gamma^2 T}{2b} \int_0^T \int_0^T f_1(t) f_2(t') \left| \frac{t - t'}{T} \right|^{m/2} \mathrm{d}t \, \mathrm{d}t' \,. \tag{2.70}$$

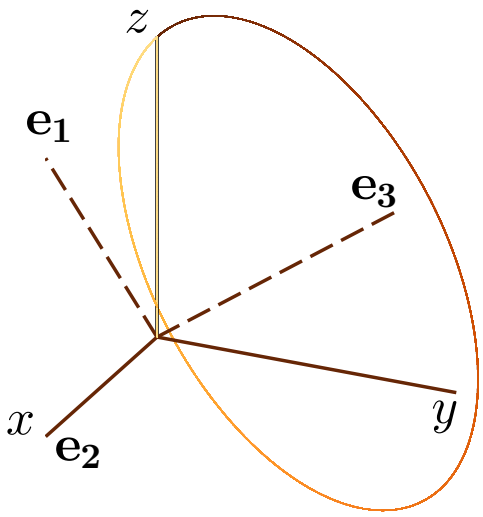

Figure 2.8: Plot of $\mathbf{Q}(t)$ for the q-MAS sequence. The color encoding of the trajectory represents time, from $t = 0$ (light yellow) to $t = T$ (dark brown). The additional axes are directed along the eigenvectors $(\mathbf{e}_1, \mathbf{e}_2, \mathbf{e}_3)$ of the $\mathsf{T}^{(3)}$ matrix (2.67) of the sequence.

Since the space of functions with zero mean is infinite-dimensional, we can be confident in finding such three functions. However, Eq. (2.70) involves a non-integer power of time that prevents us from getting analytical solution for this problem. Thus, we design a simple algorithm for generating the gradient sequences that satisfy these conditions.

The idea is to choose a family of functions $(f_1, f_2, \ldots, f_k)$ (for example, sines or polynomials, possibly with sign jumps at $T/2$) and to search for $G_x(t), G_y(t), G_z(t)$ as linear combinations of the basis functions. This is a generalization of the classical sine and cosine decomposition which was already used in the context of waveform optimization [161]. Mathematically, this means that

$$\begin{pmatrix} G_x(t) \\ G_y(t) \\ G_z(t) \end{pmatrix} = \mathsf{X} \begin{pmatrix} f_1(t) \\ f_2(t) \\ \vdots \\ f_k(t) \end{pmatrix}, \tag{2.71}$$

where X is a $3 \times k$ matrix of coefficients to be found. Now we define the $k \times k$ matrices $\Phi^{(m)}$ by

$$\Phi^{(m)}_{i,j} = \varphi_m(f_i, f_j)\,, \quad m = 2, 3, \ldots \tag{2.72}$$

In this way, one can compute directly the $\mathsf{T}^{(m)}$ matrices according to

$$\mathsf{T}^{(m)} = \mathsf{X}\Phi^{(m)}\mathsf{X}^{\dagger}\,. \tag{2.73}$$

The problem is then reduced to an optimization problem for the matrix X, which can be easily done numerically. In other words, one searches for *a* matrix X that ensures the isotropy of the matrix $\mathsf{T}^{(3)}$. In the same way, one can generate a sequence with both isotropic $\mathsf{T}^{(2)}$ and $\mathsf{T}^{(3)}$ matrices, or any other combination of isotropic $\mathsf{T}^{(m)}$ matrices. At the same time, we prove in Appendix A.4 that there is no gradient sequence that produces isotropic $\mathsf{T}^{(m)}$ matrices simultaneously for all integers $m \geq 2$.

The optimization algorithm can include various additional constraints. On one hand, one has a freedom to choose an appropriate family $(f_1, f_2, \ldots, f_k)$, for example, to ensure smoothness of the resulting gradient profile. Similarly, the refocusing condition can be achieved by choosing zero-mean functions. On the other hand, it is also possible to add some constraints as a part of the optimization problem. This is especially easy if the constraints can be expressed as linear or bilinear forms of the gradient profile $\mathbf{G}(t)$. For instance, each $\mathsf{T}^{(m)}$ matrix in (2.50) is a bilinear form of the gradient profile allowing one to express them as the simple matrix multiplication (2.73). Another example of additional conditions consists in imposing zeros to the designed gradient profiles. Indeed, for practical reasons, it is often easier to manipulate gradients that satisfy

$$\mathbf{G}(0) = \mathbf{G}(T/2) = \mathbf{G}(T) = \mathbf{0}\,. \tag{2.74}$$

This is a linear condition on the gradient profile. If one denotes by V the $k \times 3$ matrix

$$\mathsf{V} = \begin{bmatrix} f_1(0) & f_1(T/2) & f_1(T) \\ f_2(0) & f_2(T/2) & f_2(T) \\ \vdots & \vdots & \vdots \\ f_k(0) & f_k(T/2) & f_k(T) \end{bmatrix}, \tag{2.75}$$

then Eq. (2.74) becomes

$$\mathsf{XV} = \begin{bmatrix} 0 & 0 & 0 \\ 0 & 0 & 0 \\ 0 & 0 & 0 \end{bmatrix}. \tag{2.76}$$

In the following, we impose the above condition to produce our gradient waveforms.

It is worth to note that one can also generate flow-compensated gradients, or more generally, motion artifacts suppression techniques, by imposing linear conditions on the gradient profile

$$\int_0^T t^p \mathbf{G}(t)\,\mathrm{d}t = \mathbf{0}\,, \quad p = 1, 2, \ldots, P\,, \tag{2.77}$$

where $p = 1$ corresponds to the flow compensation, and higher values of p account for acceleration, pulsatility, etc. [29, 62]. This condition can be rewritten in the matrix form $\mathsf{XM} = 0$, where the $k \times P$ matrix M is defined by

$$\mathsf{M}_{i,p} = \int_0^T t^p f_i(t)\,\mathrm{d}t\,, \quad p = 1, 2, \ldots, P\,. \tag{2.78}$$

Another type of optimizaton constraints can be based on hardware limitations such as a need to minimize heat generation during the sequence execution which amounts to minimizing the following quantity

$$\langle \mathbf{G}, \mathbf{G} \rangle = \int_0^T |\mathbf{G}(t)|^2\,\mathrm{d}t\,, \tag{2.79}$$

which is a bilinear form of the gradient profile. Similar to representation (2.73) for $\mathsf{T}^{(3)}$, one can define a matrix $\mathsf{H}_{i,j} = \langle f_i, f_j \rangle$ to write Eq. (2.79) as $\langle \mathbf{G}, \mathbf{G} \rangle = \mathrm{Tr}\left(\mathsf{XHX}^\dagger\right)$, and then to include it into the optimization procedure.

The previous examples showed how linear and bilinear forms of the gradient profile can be simply expressed in terms of the weights matrix X, which allows one to perform very fast computations. The matrix corresponding to each condition (for example, $\Phi^{(3)}$, V, H) has to be computed only once, then optimization is reduced to matrix multiplications. The size of the matrices involved in the computations is defined by the size of the chosen set of functions $(f_1, \ldots, f_k)$. Note that the set size is independent of the numerical sampling of the time interval $[0, T]$ that controls accuracy of the computations.

Some properties of the designed gradients do not fall into the category of aforementioned linear or bilinear forms, e.g., "max" amplitude-function (i.e., one cannot impose the maximal gradient constraint in this way). They can be included in the optimization, however one cannot apply the previous techniques in order to speed up the computation.

We have to emphasize that the "optimal" solution is not unique and it depends on the choice of the set $f_1, \ldots, f_k$. Moreover, if the set is sufficiently large and the number of degrees of freedom is greater than the number of constraints, then the algorithm will likely yield different solutions depending on the initial choice of X for an iterative solver. This property can be advantageous in practice, as one can design many optimal solutions. The described optimization algorithm was implemented in Matlab (The MathWorks, Natick, MA USA). It concatenates all the chosen constraints in a single matrix-valued function $f(\mathsf{X})$ of the weight matrix X, in such a way that the constraints are expressed by the condition $f(\mathsf{X}) = 0$. This equation is then solved numerically with the Levenberg-Marquardt algorithm.

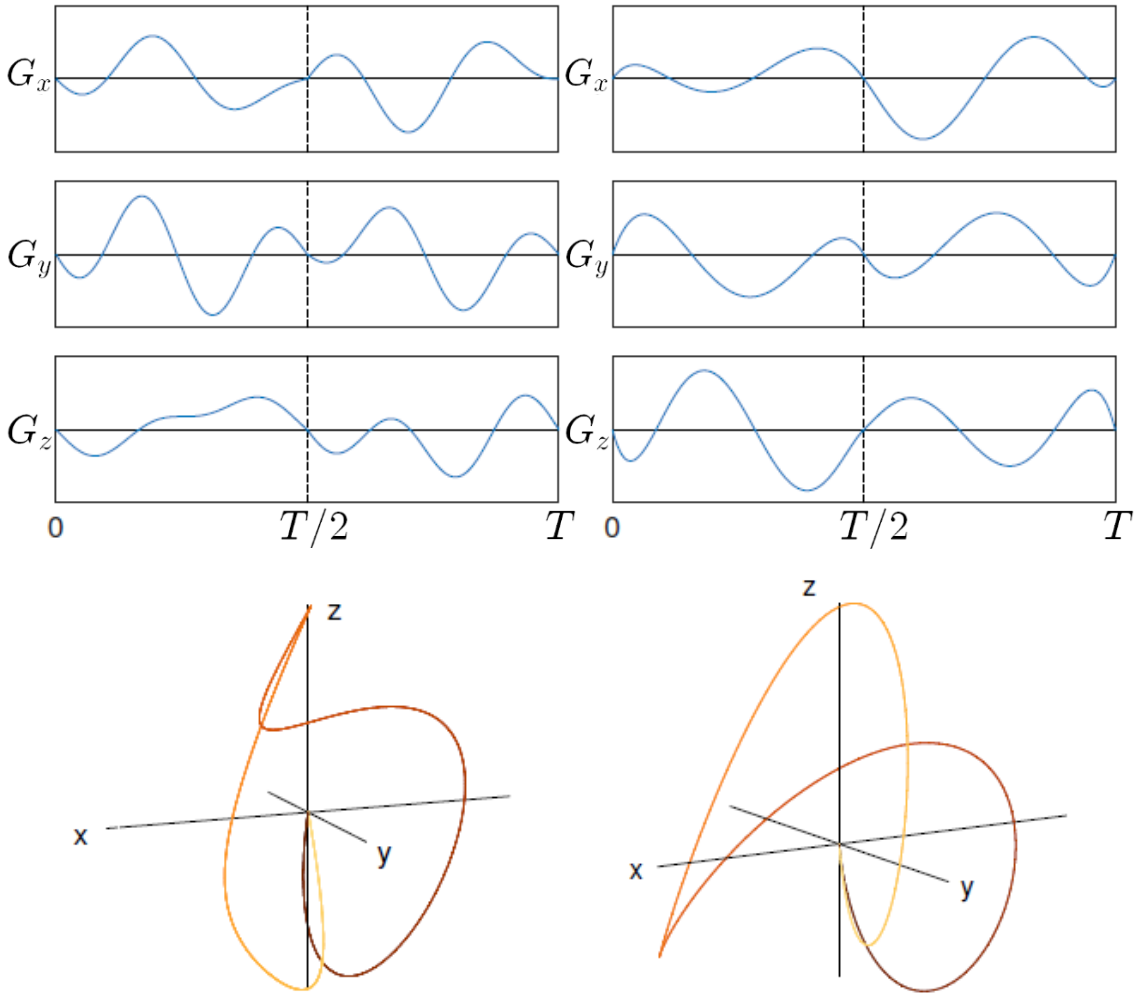

Figure 2.9: Two examples of gradient waveforms that produce an isotropic $\mathsf{T}^{(3)}$ matrix and that satisfy Eq. (2.74). Note that the gradients are "effective" gradients in the sense that we reversed them after the 180° rf pulse at $T/2$. The bottom figure shows the corresponding $\mathbf{Q}(t)$. The color encoding of the trajectory represents time, from $t = 0$ (light yellow) to $t = T$ (dark brown). (left) the profiles are combination of 9 piecewise sine and cosine functions with frequencies up to $6/T$, and in addition they satisfy isotropy of $\mathsf{T}^{(2)}$; (right) the profiles are piecewise polynomials of order 5, and they satisfy $\mathsf{T}^{(4)} = 0$.

Figure 2.9 shows two examples of gradient waveforms that produce an isotropic $\mathsf{T}^{(3)}$ matrix. These profiles were obtained from two sets with $k = 9$ functions. The first set was composed of $\cos(\pi jt/T)$ with $j = 1,\dots,5$; $\sin(\pi jt/T)$ with $j = 2,4,6$; and $\varepsilon(t)\sin(4\pi t/T)$ where $\epsilon(t)$ is a piecewise constant function that is equal to 1 on $[0,T/2]$ and -1 on $(T/2,T]$. We also imposed the condition of isotropy of $\mathsf{T}^{(2)}$. The second set was composed of a mixture of monomials, symmetrized odd monomials and antisymmetrized even monomials, with zero mean: $(t-T/2)$, $(t-T/2)^2 - T^2/12$, $(t-T/2)|t-T/2|$, $(t-T/2)^3$, $|t-T/2|^3 - T^3/32$, $(t-T/2)^4 - T^4/80$, $(t-T/2)^3|t-T/2|$, $(t-T/2)^5$, $|t-T/2|^5 - T^5/192$. In this case, we imposed the condition of vanishing $\mathsf{T}^{(4)}$. Although the combination of symmetric and antisymmetric functions helped us to increase the number of basis functions while keeping low degree monomials or slowly oscillating sines, one could alternatively use just monomials, polynomials, or other basis functions as well. Note that there is no need to impose the orthogonality of the basis functions $f_1,\dots f_k$.

Let us consider the waveform obtained in the left panel of Fig. 2.9. The condition of isotropy for both matrices $\mathsf{T}^{(2)}$ and $\mathsf{T}^{(3)}$ yields $5+5$ equations on the components of matrix X. Besides of matrices $\mathsf{T}^{(2,3)}$, condition (2.74) adds another 9 equations on the components of X. Moreover, we imposed the b-value so that the algorithm satisfied 20 conditions with $3k = 27$ degrees of freedom.

The gradient waveform corresponds to $\eta \approx 0.1$ and the dimensionless b-value is $b/(G_{\max}^2 T^3) \approx 0.006$ (with $G_{\max}$ being the maximum gradient amplitude). Hence the b-value is about three times smaller than what one can achieve with only the condition on the isotropy of $\mathsf{T}^{(2)}$ [161]. Instead of only constraining $\mathsf{T}^{(3)}$ to be isotropic, one can in addition impose a precise value of η by using Eq. (2.66). However we observed that the algorithm could not produce gradient waveforms with arbitrary values of η: there were bounds for η-values outside of which the optimization process did not converge. This behavior was expected, because even in the linear encoding case, there were mathematical limitations for the parameter η (see Sec. 2.3.4 and Appendix A.3). These bounds can be extended by adding more basis functions (i.e., by increasing the size k of their set). Another way to extend the bounds is to reduce the number of constraints, for example, by dropping out the condition of isotropic $\mathsf{T}^{(2)}$ matrix and only keeping the condition on $\mathsf{T}^{(3)}$. Indeed, the isotropy of $\mathsf{T}^{(2)}$ is only required in the case of a microscopically anisotropic medium, which we did not assume here (see Appendix 2.3.6).

Interestingly, the $\mathsf{T}^{(4)}$ matrix presents a special case: integrating by parts in Eq. (2.50) one can show that

$$\mathsf{T}^{(4)} = \left(\int_0^T \mathbf{Q}(t)\,\mathrm{d}t\right) \otimes \left(\int_0^T \mathbf{Q}(t)\,\mathrm{d}t\right) . \tag{2.80}$$

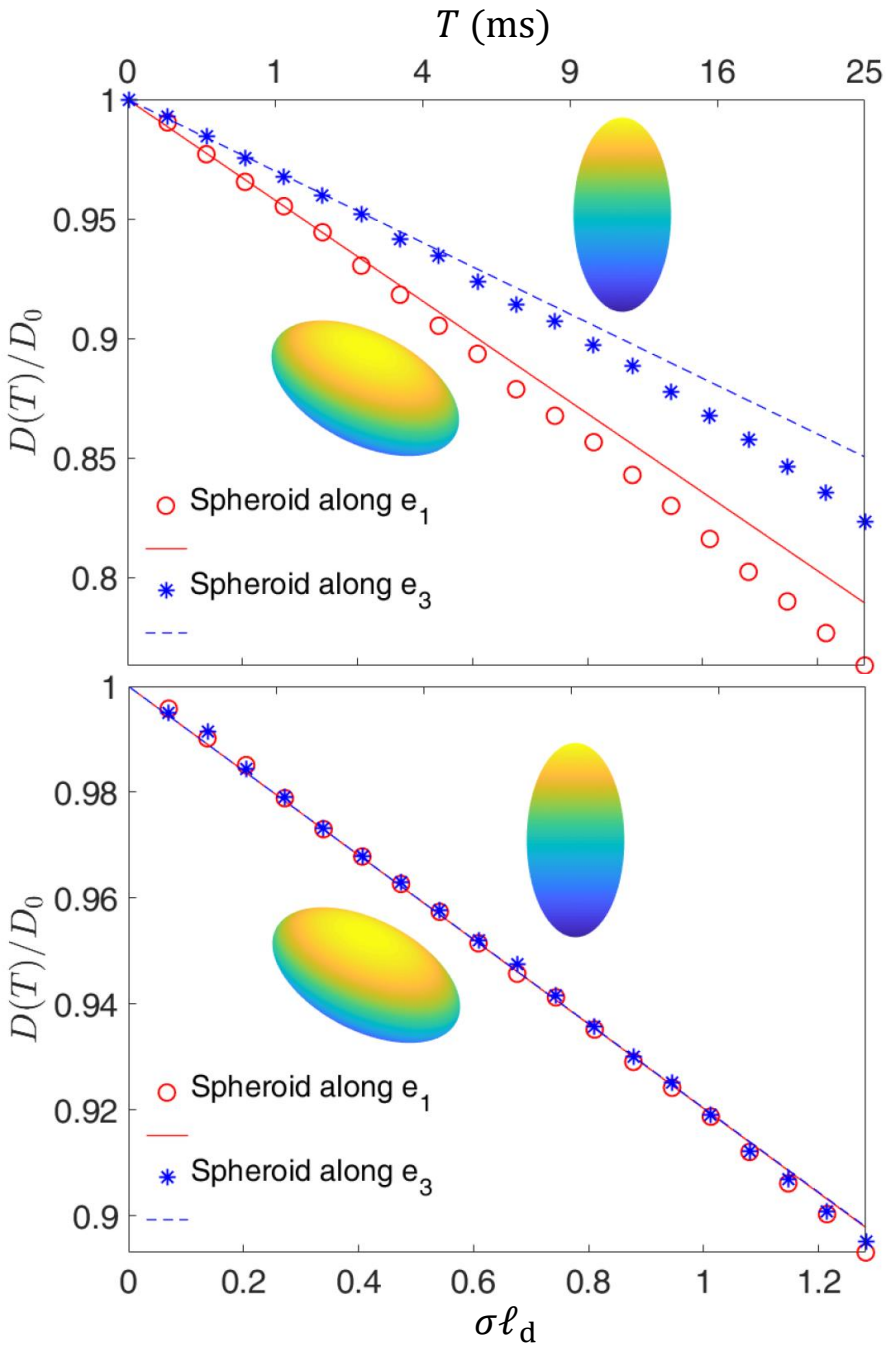

Figure 2.10: Effective diffusion coefficient $D(T)/D_0$ plotted against $\sigma\ell_\mathrm{d} = \sigma\sqrt{D_0 T}$ inside a prolate spheroid with semi-axes 10 μm and 5 μm for two gradient sequences and two orientations of the spheroid. The intrinsic diffusivity is $D_0 = 1$ $\mu\mathrm{m}^2/\mathrm{ms}$. The simulation results are shown as symbols and the generalized Mitra formula is plotted as line. (top) q-MAS sequence: different orientations of the domain produce different $D(T)$ curves. (bottom) Optimized sequence with isotropic $\mathsf{T}^{(3)}$ and zero $\mathsf{T}^{(4)}$: the $D(T)$ curves are the same for different orientations of the domain because of the condition on $\mathsf{T}^{(3)}$. Moreover, the condition on $\mathsf{T}^{(4)}$ extends the range of validity of the theoretical formula to about 20 ms.

This implies that the matrix has rank one, so it cannot be proportional to the unit matrix unless it is null, that occurs under the simple condition

$$\int_0^T \mathbf{Q}(t)\,\mathrm{d}t = \mathbf{0}\ . \tag{2.81}$$

This condition can be easily included in our optimization algorithm. This is the case for the designed profile shown on the right panel in Fig. 2.9. As a consequence, the corresponding term (of the order of D_0T) vanishes in the expansion (2.51).

The property of vanishing D_0T-order term is well-known for cosine-based waveforms with an integer number of periods [63], and, indeed, such functions automatically satisfy to Eq. (2.81). However, this property is not exclusive to cosine functions (for example, the right panel of Fig. 2.9 was obtained with polynomial functions). It is also easy to show that Eq. (2.81) is equivalent to condition (2.77) for $p = 1$. In other words, flow-compensated gradient profiles automatically cancel the $(\sigma\ell_\mathrm{d})^2$-order correction term in the generalized Mitra's expansion, as it was pointed out earlier in [62].

2.3.5 Monte Carlo simulations

We performed Monte Carlo simulations to illustrate our theoretical results. The confining domain Ω is a prolate spheroid with major and minor semi-axes equal to 10 μm and 5 μm. The intrinsic diffusion coefficient D_0 is 1 $\mu\mathrm{m}^2/\mathrm{ms}$ and the echo time T ranges from 0 to 25 ms. Reflecting conditions were implemented at the boundary of the domain and the interval $[0, T]$ was divided into 200 time steps of equal duration. For each value of T, we generated about $5{\cdot}10^6$ trajectories, applied the gradient sequence and computed the effective diffusion coefficient $D(T)$ from the variance of the random dephasing ϕ of the particles: $D(T) = \mathbb{V}[\phi]/(2b)$. In order to generate random initial positions for the particles inside the spheroid, we generated random positions inside a larger parallelepiped then discarded the particles that were outside the spheroid. We checked that the randomness in the effective number of particles was very small relatively to the number of particles (less than 0.1%).

We chose two different gradient sequences: the q-MAS sequence [153, 161] and an optimized sequence with isotropic $\mathsf{T}^{(3)}$ and zero $\mathsf{T}^{(4)}$ such as the one in the right panel of Fig. 2.9. Note that we could have replaced the q-MAS sequence by any other 3D gradient sequence from the present literature, such as triple diffusion encoding (TDE) [168]. For each sequence, we chose two different orientations of the spheroid that yielded maximal and minimal value of η. This can be done by finding numerically the eigenvectors $(\mathbf{e}_1, \mathbf{e}_2, \mathbf{e}_3)$ of the $\mathsf{T}^{(3)}$ matrix

(sorted by increasing eigenvalue) and then orienting the spheroid along $\mathbf{e}_1$ and $\mathbf{e}_3$, respectively (see for example Fig. 2.8). The $D(T)$ curves are presented on Fig. 2.10. The $\mathsf{S}^{(3)}$ matrix of a spheroid can be computed exactly (see Appendix A.2) and we plotted simulation results alongside analytical results.

The comparison between the two graphs reveals several important features. First, as we argued in the previous section, the q-MAS sequence is not isotropic with respect to mesoscopic anisotropy studied with short-time experiments. Different orientations of the spheroid yield different values of η (0.15 and 0.22, respectively) and thus, different $D(T)$ curves. In turn, if one does not know *a priori* what is the orientation of the spheroid, then it is impossible to recover its σ ratio from one $D(T)$ curve, as η depends on this orientation. In this case, one may estimate η from its average over different orientations of the domain: $\eta \approx \mathrm{Tr}\left(\mathsf{T}^{(3)}\right)/3$. For the q-MAS sequence this would yield $\eta \approx 0.20$.

On the other hand, sequences with isotropic $\mathsf{T}^{(3)}$ produce the same coefficient η independently of the shape or orientation of the domain. Thus, one obtains the same $D(T)$ curve for the two orientations of the spheroid that allows one to recover its surface-to-volume ratio σ from a single measurement.

Another important point lies in the range of validity of the first-order generalized Mitra formula (2.51). One can clearly see the effect of zero $\mathsf{T}^{(4)}$ matrix that extends the range of validity from about 5 ms to about 20 ms. This comes at the price of a lower η (here, $\eta = 0.11$), meaning a slower decay of $D(T)$, which is however compensated by the extension of the range of T. Note that this extension of the range of T may also compensate for a smaller b-value. In all these cases, the η values are significantly different from $1/3$ given by Mitra's original formula (see Eq. (2.53)).

2.3.6 Extensions

In this section we examine several extensions of our results. First we investigate in more details the next order, D_0T, term of expansion (2.51). Then we turn to the case where the medium is microscopically anisotropic, i.e. the diffusivity is a tensor D_0. Finally we discuss the effects of multiple compartments with different pore shapes and/or intrinsic diffusivities D_0.

Order D_0T term

From the short-time expansion of heat kernels [332–334] one can compute the next-order term of $D(T)$ as

$$\frac{D(T)}{D_0} = 1 - \eta\frac{4}{3\sqrt{\pi}}\sigma\ell_\mathrm{d} - \eta^{(4)}\frac{1}{2}H_0\sigma\ell_\mathrm{d}^2 + O(T^{3/2}), \tag{2.82}$$

where $\eta^{(4)}$ is a dimensionless parameter defined as

$$\eta^{(4)} = \mathrm{Tr}\left(\mathsf{S}^{(4)}\mathsf{T}^{(4)}\right) \ . \tag{2.83}$$

In the above formula, the structural matrix $\mathsf{S}^{(4)}$ is

$$\mathsf{S}^{(4)} = \frac{1}{H_0\,\mathrm{surf}(\partial\Omega)} \int_{\partial\Omega} H\,\mathbf{n}\otimes\mathbf{n}\,\mathrm{d}s \ , \tag{2.84}$$

where H is the local mean curvature of the surface, i.e. $H = (R_1^{-1} + R_2^{-1})/2$, where R_1 and R_2 are the local principal radii of curvature of the boundary $\partial\Omega$ of the domain. The integral is normalized by the average curvature of $\partial\Omega$:

$$H_0 = \frac{1}{\mathrm{surf}(\partial\Omega)} \int_{\partial\Omega} H\,\mathrm{d}s \ . \tag{2.85}$$

Note that this normalization ensures that the matrix $\mathsf{S}^{(4)}$ has unit trace.

Thus, one can potentially probe the curvature of the boundary of the domain by measuring the $\ell_\mathrm{d}^2 = D_0 T$ correction term in the short-time expansion of $D(T)$. Note that, as we mentioned in Sec. 2.3.4, the $\mathsf{T}^{(4)}$ matrix has rank one so that one would need at least three measurements (for example, the same linear gradient sequence in three orthogonal directions) in order to average out the anisotropy of $\mathsf{S}^{(4)}$ and recover H_0. We recall that we ignore permeation and surface relaxation that manifest in the $D_0 T$ term as well.

Tensor diffusivity

In this work, we specifically focused on mesoscopic anisotropy and excluded the effect of microscopic anisotropy by choosing a scalar diffusivity D_0. However, some of our results may be extended to a tensor diffusivity D_0. Let us assume that the eigenvectors of D_0 are directed along $\mathbf{e_x}$, $\mathbf{e_y}$, $\mathbf{e_z}$, with D_{xx}, D_{yy}, D_{zz} being the corresponding eigenvalues. The mean diffusivity is $D_0 = \mathrm{Tr}(\mathsf{D}_0)/3$. Let us denote by $\mathsf{S}^{(2)}$ the matrix defined by $\mathsf{S}^{(2)} = \mathsf{D}_0/D_0$.

By applying the affine mapping of matrix $\mathsf{L} = \sqrt{\mathsf{S}^{(2)}}^{-1}$, i.e. a spatial dilatation by the factor $\sqrt{D_0/D_{ii}}$ for each direction $i = x, y, z$, one transforms the anisotropic diffusion tensor D_0 into the isotropic diffusion tensor $D_0\mathsf{I}$. The domain and the gradient are also affected by this transformation and we denote by prime the new quantities. For instance, spheres are transformed in ellipsoids by this transformation. As the gradient is also affected by the matrix L^{-1}, one has $\mathsf{T}^{(m)\prime} = \mathsf{L}^{-1}\mathsf{T}^{(m)}\mathsf{L}^{-1}$. While the new volume is $\mathrm{vol}(\Omega') = \det(\mathsf{L})\mathrm{vol}(\Omega)$, there is

no simple formula for the surface-to-volume ratio σ' and the $\mathsf{S}^{(3)\prime}$ tensor. Applying our results on isotropic diffusivity to this new case, we get for the effective diffusion coefficient in the original system

$$D(T) = D_0 \left(\mathrm{Tr}(\mathsf{S}^{(2)}\mathsf{T}^{(2)}) - \eta' \frac{4}{3\sqrt{\pi}} \sigma' \ell_\mathrm{d} + O(T) \right) , \tag{2.86}$$

where

$$\eta' = \mathrm{Tr}(\mathsf{S}^{(3)\prime}\mathsf{T}^{(3)\prime}) = \mathrm{Tr}(\mathsf{L}^{-1}\mathsf{S}^{(3)\prime}\mathsf{L}^{-1}\mathsf{T}^{(3)}) . \tag{2.87}$$

From the above equation we obtain that $D(T)$ does not depend (to the order $\sqrt{D_0 T}$) on the orientation of the gradient sequence with respect to the medium if $\mathsf{T}^{(2)}$ and $\mathsf{T}^{(3)}$ are isotropic. As we mentioned before, the condition of isotropy of the temporal tensor $\mathsf{T}^{(2)}$ is equivalent to the isotropy of the B-tensor. Thus it is not surprising to obtain the condition of isotropic $\mathsf{T}^{(2)}$ (see Sec. 2.2.2).

Multiple compartments

Our results were derived under the assumption of a spatially homogeneous intrinsic diffusivity. Moreover, except in Sec. 2.3.3 where we investigated the effect of orientation dispersion of the confining pores, we implicitly assumed that all confining pores are identical. Here we present an extension to a medium that is composed of two or more non-communicating (isolated) compartments (for example, intra- and extra-cellular spaces) with different diffusion coefficients and/or different confining pores.

Inside each compartment, the diffusivity is constant and the pore shapes are identical, so that our formula (2.51) for $D(T)$ is valid, with parameters D_0, η, σ that depend on the compartment. The signal can be computed as a voxel-average of signals from individual compartments. In the regime of small b-values ($bD_0 \ll 1$), one has, in analogy to Eq. (2.56),

$$S \approx \langle \exp(-bD(T)) \rangle \approx \exp(-b\langle D(T) \rangle) , \tag{2.88}$$

where the average is weighted by the relative volume of each compartment, and

$$\langle D(T) \rangle = \langle D_0 \rangle - \frac{4}{3\sqrt{\pi}} \left\langle \eta\sigma {D_0}^{3/2} \right\rangle \sqrt{T} + O(T) . \tag{2.89}$$

We keep this general form of the voxel average which depends on the specific configuration of compartments, pore shapes, diffusivities, etc.

In the above reasoning, the hypothesis of non-communicating compartments is crucial and further modifications would be needed in order to include exchange between compartments when a nucleus can experience different diffusion coefficients during the measurement.

2.3.7 Conclusion

We presented a generalization of Mitra's formula that is applicable to any gradient waveform and any geometrical structure. This generalized formula differs from the classical one by a correction factor in front of the surface-to-volume ratio σ. In the case of linear encoding schemes, we showed that this factor can significantly affect the estimation of σ and lead to overestimated size of compartments.

We also discussed in detail the effect of anisotropy of the medium and the use of spherical encoding schemes. In particular, we showed that in order to estimate the surface-to-volume ratio of a mesoscopically anisotropic medium, the gradient should satisfy the isotropy condition ($\mathsf{T}^{(3)} \propto \mathsf{I}$) that is different from the usual one ($\mathsf{T}^{(2)} \propto \mathsf{I}$). In particular, common spherical encoding schemes do not satisfy this new condition. We presented a simple and flexible algorithm that allows fast optimization of gradient waveforms and is well-suited for design of diffusion weighted sequences with specific features such as isotropy of $\mathsf{T}^{(3)}$, flow compensation, heat limitation, and others.

The developed extension of Mitra's formula is expected to have a significant practical impact due to temporal diffusion encoding parametrization [60, 164], in particular, in medical applications [56, 65, 66]. The proposed approach characterizes the underlying microstructure via novel quantitative metrics such as $\mathsf{S}^{(3)}$-tensor and more accurate surface-to-volume ratio.

This page is unintentionally left not blank.

Chapter 3

Permeability

The aim of diffusion MRI is to unravel the microstructure of a sample through the diffusive motion of spin-bearing particles. The most prominent microstructural features of a sample are boundaries that restrict the diffusive motion. In the previous chapter we studied the effective reduction of the diffusion coefficient at short times due to impermeable boundaries. However, in biological samples the hypothesis of impermeable boundaries is often not valid as exchange of molecules between compartments (cells, organelles, extracellular medium, blood vessels, etc.) plays a major role in living organisms [8]. The actual mechanism of exchange may be passive (a small molecule goes through a membrane), facilitated by selective channel proteins, or even mediated by active (i.e., that involve consumption of chemical energy) processes. Moreover, biological membranes[1] usually are not equally permeable to all molecules, creating osmotic pressure effects. Throughout this chapter, we simplify greatly the analysis by discarding the detail of the permeation mechanism and by considering a single chemical species (water).

We show in Sec. 3.1 how one can define the permeability κ of a boundary and we exhibit natural time and length scales associated to permeability. In Sec. 3.2, we study how exchange between small compartments and an external medium affects the measured dMRI signal. Experimental data from this section was obtained by M. Nilsson and D. Topgaard at Lund University, and we published these results in [345]. Then we extend this approach to the study of mitochondria inside muscles, in collaboration with J.-M. Bonny, S. Clerjon, and G. Pagès at AgroResonance (QuaPA unit of INRA). Finally, in Sec. 3.4, we turn to the problem of diffusion through multiple barriers in a one-dimensional setting and we obtain scaling laws at short and long diffusion time for the dMRI signal. Those results were published in [346].

[1] We shall use "boundary", "membrane", and "barrier" as synonyms throughout this chapter.

3.1 General properties

3.1.1 One concept, many approaches

The permeability κ of a boundary can be introduced in different ways. We shall present four definitions that are equivalent with each other despite the variety of viewpoints, providing additional insights into the concept of permeability. For simplicity we consider a flat boundary but all the following considerations are applicable to any smooth boundary.

As an intermediate between impermeable boundary and no boundary

Let us denote by f a generic intensive quantity "carried" by diffusing particles (for example, the magnetization). A planar boundary $x = 0$ splits the medium in two parts with two different diffusion coefficients: D_- for $x < 0$ and D_+ for $x > 0$. The continuity of the flux J should be ensured between these two parts, yielding a first condition

$$J(0) = -D_- \partial_x f(0^-) = -D_+ \partial_x f(0^+) \ . \tag{3.1}$$

Note that this equation requires to adopt the Hänggi-Klimontovitch (or "isothermal") interpretation of Langevin equation (see Appendix D). At this point, the value of the flux $J(0)$ is not prescribed, nor the values of $f(0^-)$ and $f(0^+)$. One can distinguish three situations, illustrated on Fig. 3.1.

1. Impermeable boundary: the half spaces $x < 0$ and $x > 0$ are independent from each other and there is no flux at the boundary, i.e. $J(0) = 0$.

2. No boundary: there is continuity between two half-spaces, i.e. $f(0^-) = f(0^+)$.

3. Permeable boundary: As a natural intermediate case, $f(x)$ is discontinuous at the boundary and the jump is proportional to the flux:

$$J(0) = -\kappa(f(0^+) - f(0^-)) \ , \tag{3.2}$$

where the proportionality coefficient κ is the permeability of the boundary [53, 268–270, 273]. The larger κ, the larger the flux for a given discontinuity in f, that corresponds intuitively to a more permeable boundary. In particular, the impermeable boundary is obtained in the limit $\kappa \to 0$, whereas the limit $\kappa \to \infty$ is equivalent to no boundary.

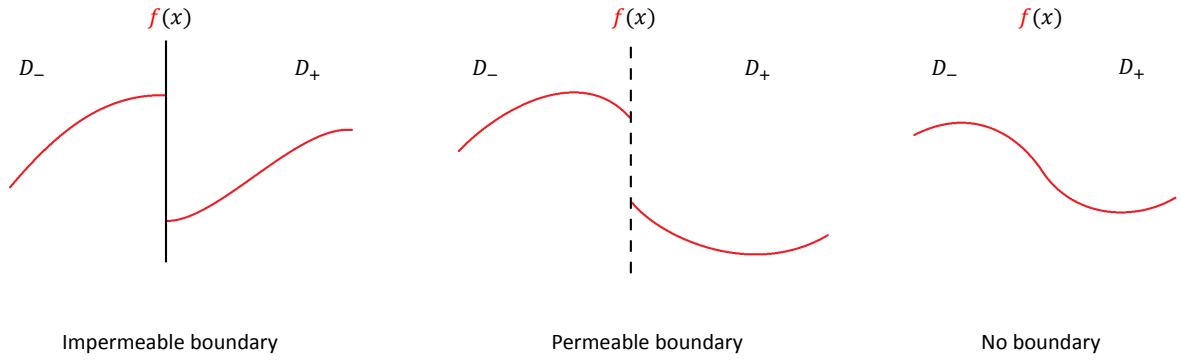

Figure 3.1: The permeable boundary appears as an intermediate case between impermeable boundary and no boundary.

The permeability κ has the dimension of a length divided by a time. Equation (3.2) suggests an interpretation of κ as a velocity. In fact, one can see the flux $J(0)$ as the result of the difference between the flux from left-to-right and the flux from right-to-left:

$$J(0) = J_{-\to+} - J_{+\to-} \qquad J_{-\to+} = \kappa f(0^-) \,, \qquad J_{+\to-} = \kappa f(0^+) \,. \tag{3.3}$$

These relations make κ appear as the velocity at which particles cross the boundary (keeping in mind that the process remains diffusive on both sides).

As an infinitely thin, weakly diffusive layer

Another point of view is illustrated on Fig. 3.2. Let us consider a thin layer $-e/2 \leq x \leq e/2$ of thickness e. The diffusion coefficient inside it is D_e. In the limit of infinitely small e, one gets that the flux is constant through the layer and equal to

$$J(0) = -D_- \partial_x f(-e/2) = -D_e \partial_x f(0) = -D_+ \partial_x f(e/2) \,. \tag{3.4}$$

In turn, the jump of f between two sides of the layer is equal to

$$f(e/2) - f(-e/2) = e\partial_x f(0) = -\frac{e}{D_e} J(0) \,. \tag{3.5}$$

One recovers the above boundary condition (3.2) if $D_e/e \underset{e\to 0}{\to} \kappa$ [9]. Note that this relation may be rewritten as $\kappa = e(e^2/D_e)^{-1}$, i.e., thickness of the layer divided by typical diffusion time through the layer. This is consistent with the above interpretation of κ as a boundary crossing velocity.

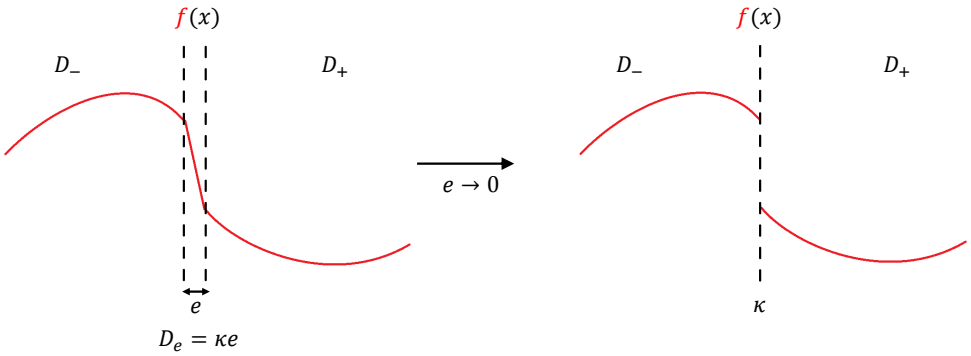

Figure 3.2: The permeable boundary appears as the limit of an infinitely thin layer of very low diffusivity. The permeability of the resulting membrane is the ratio between diffusion coefficient and thickness.

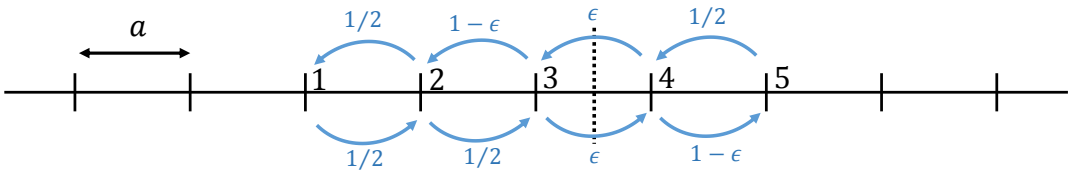

Figure 3.3: In the context of random walks, the permeable boundary (dotted line) is modeled by a small transition probability ϵ.

As a crossing probability

Let us replace the continuous Brownian motion by a discrete random walk on a cubic lattice (as the sum of three independent one-dimensional random walks). The step of the lattice is denoted by a, the time steps of the walk are denoted by τ. We recall that a random walk yields a Brownian motion in the continuous limit $a, \tau \longrightarrow 0$ if the diffusion coefficient $D_0 = a^2/(2\tau)$ remains constant. For simplicity of notations we assume here that the diffusion coefficient on both sides of the boundary is the same but the extension to different diffusion coefficients poses no difficulty. We introduce a permeable barrier as a small transition probability ϵ between the two half spaces, as shown on Fig. 3.3.

Let us compute the net flux between sites 1 and 2, with the convention that a flux from left-to-right is positive. We get simply

$$J_{1\to 2} = \frac{a}{\tau}\left(\frac{1}{2}f_1 - \frac{1}{2}f_2\right) = -\frac{a^2}{2\tau}\frac{f_2 - f_1}{a}\,, \tag{3.6}$$

where we recognize the formula $\mathbf{J} = -D_0\nabla f$. Then we compute the flux between

sites 2 and 3, 3 and 4, 4 and 5:

$$J_{2\to3} = \frac{a}{\tau}\left(\frac{1}{2}f_2 - (1-\epsilon)f_3\right) , \qquad J_{3\to4} = \frac{a}{\tau}\left(\epsilon f_3 - \epsilon f_4\right) , \tag{3.7a}$$

$$J_{4\to5} = \frac{a}{\tau}\left((1-\epsilon)\epsilon f_4 - \frac{1}{2}f_5\right) . \tag{3.7b}$$

One can see that the flux between 2 and 3 (or between 4 and 5) has a different expression than the one between 1 and 2 because of the reflection probability $1-\epsilon$. In particular, the equality $J_{2\to3} = J_{3\to4}$ yields $f_3 = f_2/2 + \epsilon f_4$ that may be very different from f_2. In other words, the discontinuity between sites 3 and 4 spreads to sites 2 and 5. Therefore, to compute the flux, we perform a weighted average of the flux from site 2 to 5 to cancel the contributions from sites 3 and 4 (alternatively, one can simply solve a system of linear equations):

$$\begin{aligned} J &= \left[J_{2\to3} + \frac{1-\epsilon}{\epsilon}J_{3\to4} + J_{4\to5}\right]\left(2 + (1-\epsilon)/\epsilon\right)^{-1} \\ &= \frac{D}{a}\frac{f_2 - f_5}{2 + (1-\epsilon)/\epsilon} . \end{aligned} \tag{3.8}$$

Then we relate f_2 and f_5 to $f(0^-)$ and $f(0+)$ through the slope of f, which is given by $-J/D_0$:

$$f_2 - f_5 = \left(f(0^-) - f(0^+)\right) + \frac{3aJ}{D_0} , \tag{3.9}$$

and by combining this relation with the formula for J, one obtains

$$J = -\frac{\epsilon}{1-2\epsilon}\frac{D_0}{a}\left(f(0^+) - f(0^-)\right) . \tag{3.10}$$

The identification with Eq. (3.2) yields

$$\kappa = \frac{D_0}{a}\frac{\epsilon}{1-2\epsilon} , \qquad \epsilon = \frac{\kappa a}{D_0 + 2\kappa a} . \tag{3.11}$$

Note that the permeability is infinite for $\epsilon = 1/2$, as it should be (no barrier). Interestingly, this formula differs from the case of a relaxing boundary where the factor $1-2\epsilon$ in the denominator is replaced by $1-\epsilon$, see Ref. [285]. In the continuous limit ($a, \tau \to 0$), the crossing probability goes to zero. In parallel, the motion becomes infinitely fast so that the number of times that the particle hits the boundary in a given amount of time goes to infinity. As we show in Appendix B.1.1, these effects compensate in the continuous limit.

As the local stopping rate of a reflected Brownian motion

In a sense, this formalism corresponds to the continuous limit of the previous description. We shall briefly describe it and we invite the interested reader to refer to books [279–281, 284] for a more complete introduction. We emphasize that all results here are classical. A reflected Brownian motion inside a domain Ω is described by a set of two stochastic processes, the position $\mathbf{r}_t$ and the local time[2] ℓ_t, that obey

$$\mathrm{d}\mathbf{r}_t = \sqrt{2D_0}\mathrm{d}\mathbf{W}_t + \mathbb{I}_{\partial\Omega}(\mathbf{r}_t)\,\mathbf{n}(\mathbf{r}_t)\,\mathrm{d}\ell_t\,, \tag{3.12}$$

with the conditions that $\mathbf{r}_t \in \Omega$ at all time t and ℓ_t increases only if $\mathbf{r}_t \in \partial\Omega$ [274, 282, 283]. In the above equation, $\mathbf{n}$ is the inward normal vector at the boundary and $\mathbb{I}_{\partial\Omega}$ is the indicator function of $\partial\Omega$, i.e. it is zero everywhere except on $\partial\Omega$, in which case it is equal to 1 (note that $\mathbf{n}(\mathbf{r}_t)$ is ill-defined but $\mathbf{n}(\mathbf{r}_t)\mathbb{I}_{\partial\Omega}(\mathbf{r}_t)$ is well-defined). This process describes diffusion inside a domain Ω with impermeable boundaries $\partial\Omega$.

Although a bit counter-intuitive, this formulation is self-consistent. Indeed, the condition that the trajectory does not leave the domain implies that $\mathrm{d}\ell_t$ has to "compensate" for the Brownian motion $\sqrt{2D_0}\mathrm{d}\mathbf{W}_t$ if $\mathbf{r}_t \in \partial\Omega$. In turn, ℓ_t stops increasing as soon as the particle leaves the boundary. If one has in mind a discrete random walk, when the particle is at the boundary, it has a $1/2$ chance to make the "wrong" jump that would make it cross the barrier, in which case ℓ_t has to compensate this wrong step by increasing by one step size a. This reasoning leads to the Levy formula

$$\ell_t = \lim_{a\to 0} \frac{D_0}{a} \int_0^t \mathbb{I}_{\mathrm{d}(\mathbf{r},\partial\Omega)<a}(\mathbf{r}_t)\,\mathrm{d}t\,, \tag{3.13}$$

that yields an interpretation for ℓ_t/a as the number of crossings of a layer of thickness a at the boundary before time t (alternatively, ℓ_t/D_0 would be a time per unit length spent in the vicinity of the boundary). Consistently with Levy formula, one can easily compute the local time for diffusion in a half space with a boundary at $x = 0$ by using the reflection principle:

$$\ell_t = D_0 \int_0^t \delta\left(x_0 + \sqrt{2D_0}(\mathbf{W}_{t'}\cdot\mathbf{e}_\mathbf{x})\right)\,\mathrm{d}t'\,. \tag{3.14}$$

To take into account the permeability of the boundary, the reflected Brownian motion is conditioned to stop at a random time T_c, at which it starts again on the other side of the boundary (i.e., the reflected Brownian motion now takes place

[2] Despite the historical terminology "local time", ℓ_t has dimensions of a length.

in the complementary of Ω). The random stopping time T_c is in turn related to the time spent at the boundary, i.e. the local time ℓ_t, by

$$T_c = \inf\{t \mid \ell_t \geq \chi\} , \tag{3.15}$$

where χ is a random variable that follows an exponential law with rate κ:

$$\mathbb{P}(\chi \geq u) = \exp(-\kappa u) . \tag{3.16}$$

The interpretation is as follows: depending on the permeability of the membrane, a random stopping local time χ is drawn out of an exponential distribution. As the particle meets the boundary, the local time ℓ_t increases; the trajectory is stopped when ℓ_t reaches the stopping time χ. In other words, the crossing events are modeled as independent events occuring at a constant rate κ, not in "real" time t, but in local time ℓ_t. As we show in Appendix B.1.1, the distribution of T_c is far from exponential because the local time is conditioned by the diffusive process. In particular, T_c has an infinite expectation value because of exceptional trajectories that perform very long excursions far away from the boundary before crossing it, and that dominate the distribution at long times.

3.1.2 Diffusion control versus permeation control

Let us consider a bounded compartment of size ℓ_s (e.g., a spherical pore) and surface-to-volume ratio σ, with permeability κ, and diffusion coefficient D_0. From these quantities, one can form two "new" time scales: the intrinsic crossing time τ_κ that is the typical time taken by a particle near the boundary to cross it; and the global exchange time τ_e that describes the typical time after which the compartment has fully equilibrated its content with outside. We shall see that both of these scales are relevant depending whether diffusion or permeation effect dominates, i.e. depending on the kinetically limiting process. Furthermore, the transition from one regime to the other is controlled by a single dimensionless parameter ℓ_s/ℓ_κ, where

$$\ell_\kappa = \frac{D_0}{\kappa} \tag{3.17}$$

is the "permeability length" [274, 276–278]. In Sec. 3.4 we shall use the notation $\tilde{\kappa} = \ell_s/\ell_\kappa$ for brevity.

Diffusion control, intrinsic crossing time τ_κ

We first assume diffusion to the barrier as being the limiting process in the kinetics of barrier crossing. In other words, a particle starting at a random point in the

compartment takes much more time to diffuse to the boundary than to cross the boundary after the first hit. Under these conditions, we shall see that the typical crossing time for a particle starting on the boundary is given by

$$\tau_\kappa = \frac{D_0}{\kappa^2} \, . \tag{3.18}$$

Therefore the "diffusion control" regime corresponds to the condition $\tau_\kappa \ll \ell_s^2/D_0$, or equivalently $\ell_\kappa \ll \ell_s$. The length ℓ_κ appears here as the diffusion length associated to τ_κ, i.e. $\ell_\kappa = \sqrt{D_0 \tau_\kappa}$, and represents the typical exploration length along the boundary by a particle before crossing it [274, 276–278]. Note that τ_κ is the result of a coupling between the diffusive process that brings the particle multiple times to the boundary and the permeation process that lets the particle cross the boundary after a sufficient "number of attempts".

The formula (3.18) for τ_κ may be obtained with the following reasoning. Let us denote by f the density inside the compartment and let us assume that it is initially uniform and equal to f_0. We assume that particles inside the compartment are labeled (or colored) differently than particles outside so that $f = 0$ outside the compartment. This hypothesis allows us to neglect permeation from outside, at least at short times. At time $t = 0$, there is a permeation flux from inside to outside:

$$J(t = 0) = \kappa f_0 \, . \tag{3.19}$$

We assume that at short times, the value of f near the boundary is not modified too much by this flow so that the above equation remains valid. Therefore after time t, the number of particles that have leaked outside per unit area is $Jt = \kappa f_0 t$. In parallel, the number N of particles per unit area that have actually hit the boundary at least once is $N \sim \sqrt{D_0 t} f_0$ (in the short-time limit $\sqrt{D_0 t} \ll \ell_s$). The ratio between these two quantities yields the fraction F_c of particles that have crossed the boundary among the ones that actually hit the boundary

$$F_c \sim \frac{\kappa \sqrt{t}}{\sqrt{D_0}} \sim \sqrt{\frac{t}{\tau_\kappa}} \, . \tag{3.20}$$

To summarize, at short time t, there is a thin layer of size $\sqrt{D_0 t}$ where particles hit the boundary and possibly cross it. Because of crossings, the particle density is lower in this layer than in the rest of the compartment. To know how much lower it is, one has to compute the fraction of particles that have crossed the barrier: this is given by F_c. Equation (3.20) makes τ_κ appear as the typical crossing time for particles starting close to the boundary. Stricly speaking, this expression is only valid at $t \ll \tau_\kappa \ll \ell_s^2/D_0$ since the previous computations were done under the assumption that (i) the density is weakly affected by permeation through the

boundary, i.e. $F_c \ll 1$, and (ii) few particles hit the boundary so that their number is well approximated by $N \sim \sqrt{D_0 t} f_0$.

Note that one can compute the exact distribution of crossing time through a planar boundary using a random walk approach or the reflected Brownian motion formalism [274, 284]. The assumption of planar boundary results from the short-time approximation $t \ll \ell_s^2/D_0$, similarly to Sec. 2.3.1. The computations and results are presented in Appendix B.1.1, and we show that the "survival probability" for a particle starting at the boundary is given by

$$S_c(t) = \mathrm{erfcx}(t/\tau_\kappa) \,, \tag{3.21}$$

that makes the scaling t/τ_κ appear explicitly (erfcx is the scaled complementary error function). The short-time behavior of $S_c(t)$ is given by

$$S_c(t) \underset{t \ll \tau_\kappa}{=} 1 - \sqrt{\frac{t}{\pi \tau_\kappa}} \,, \tag{3.22}$$

that is consistent with the behavior (3.20) obtained with qualitative arguments.

We have seen in Sec. 3.1.1 that κ is related to the rate (probability) of crossing the barrier in a continuous (or discrete) random walk description (see e.g. Eq. (3.11)). Therefore one would expect the typical crossing time to scale as the inverse of this rate (or probability), and the scaling as $1/\kappa^2$ in (3.18) might come as a surprise. As shown in Appendix B.1.1, the distribution of crossing times has infinite expectation value, caused by the infinite return-to-the-origin mean time. This leads to "non self-averaging", a phenomenon discussed in Appendix B.1.2. In a bounded domain, the mean return time is not infinite because the size of the compartment ℓ_s creates a "cut-off" at time ℓ_s^2/D_0 in the distribution of return times. Although this cut-off has negligible effect in the regime $\tau_\kappa \ll \ell_s^2/D_0$ just evoked, it becomes the dominant effect in the opposite regime. This is the object of the next paragraph.

Permeation control, global exchange time τ_e

For several reasons, the above discussion fails if $\tau_\kappa \gg \ell_s^2/D_0$. One can note already that the interpretation of ℓ_κ as a typical exploration length is invalid because $\ell_\kappa \gg \ell_s$. The time taken by a particle to cross the boundary is so large that the particle explores the compartment several times. Therefore the derivation in Appendix B.1.1 for a single planar boundary fails to describe the behavior for a bounded compartment. In the same way, the formula (3.20) for F_c reveals that $F_c \ll 1$ even at $t \sim \ell_s^2/D_0$, at which the hypotheses behind the computation are grossly invalid.

In this regime, called "permeation control", "pore equilibration" [85], or "barrier-limited exchange" [192, 193] , the relevant time scale is the global exchange time

$$\tau_{\mathrm{e}} = \frac{\ell_s}{\kappa} \sim \frac{1}{\sigma\kappa} \ . \tag{3.23}$$

This time scale represents the typical time before the compartment has fully equilibrated its content with the outside. Therefore, the permeation control regime emerges in the limit $\ell_{\mathrm{s}}^2/D_0 \ll \tau_{\mathrm{e}}$, or equivalently for $\ell_{\mathrm{s}} \ll \ell_\kappa$. This regime is characteristic of weakly permeable membranes and small compartments.

To obtain Eq. (3.23), we consider, as in the previous section, that particles initially inside the compartment are labeled so that the particle density f equal to f_0 inside the compartment, and equal to 0 outside. We assume all particles explore the compartment multiple times before crossing the boundary so that the leakage is homogeneous inside the compartment and f is uniform at all times. Finally, we neglect reentry of particles. This may be ensured by a weak permeability hypothesis (few particles have leaked so that the re-entry flux is much smaller than the leakage flux) or by an infinite outside medium (most particles diffuse far away from the compartment). Under these hypotheses, the evolution of the density is controlled by the leakage flux J:

$$\partial_t f \approx -J\sigma = -\kappa\sigma f \ , \tag{3.24}$$

that yields the simple expression

$$f(t) \approx f_0 e^{-\kappa\sigma t} \approx f_0 e^{-t/\tau_{\mathrm{e}}} \ . \tag{3.25}$$

This last expression makes τ_{e} appear as the typical exchange time between the compartment and the outside medium, as claimed above.

3.2 Exchange between small compartments and exterior medium probed by dMRI

3.2.1 Introduction

In this section we consider an unbounded "exterior" medium that contains small compartments (e.g., small cells or organelles) with permeable boundaries. Throughout the section we discard any effect that would result from different relaxation times between interior and exterior medium. We shall denote by ρ the volume fraction of the interior space, and by D_e and D_i the diffusion coefficients of spin-bearing particles in the exterior and the interior media, respectively. Intuitively, one understands that the dMRI signal may obey two distinct regimes depending on the ratio between experimental time T and the exchange time τ_e. If $T \ll \tau_\mathrm{e}$, one may neglect exchange and the signal is the sum of "interior" and "exterior" contributions. Inside small compartments, diffusion is significantly restricted even at short times leading to motional narrowing regime and a slow decay of intra-compartment magnetization (see Sec. 1.2.2 and Eq. (1.54)). Therefore, the signal is well represented by a bi-exponential model, which yields "fast" and "slow" effective diffusion coefficients [115, 120–125]. In contrast, at long times $T \gg \tau_\mathrm{e}$, most particles have diffused multiple times inside and outside compartments and the medium may be replaced by an effective medium with a coarse-grained diffusion coefficient $D_0 = \rho D_i + (1-\rho) D_e$. Thus, in principle the crossover between these two regimes allows one to probe the exchange time τ_e with dMRI. However, it is *a priori* unclear how the signal would behave at intermediate times.

In order to account for exchange between the two pools of spins, Kärger introduced in [186, 187] a model that was then developed to study diffusion NMR signals in the narrow-gradient pulse regime [188–191]. The main idea consists in characterizing diffusion in the complex structure of the medium by macroscopic quantities, namely diffusion coefficients and exchange times. This is a coarse-graining approach that relies on two hypotheses, as was shown in [192]: (i) the diffusion length ℓ_d is much larger than the correlation length of the medium ℓ_s, and (ii) exchange between compartments is in the permeation control regime, i.e., permeability length ℓ_κ is much larger than ℓ_s. This allows one to treat any complex medium as a "homogeneous" one where the exchange takes place at every point in space. This is the fundamental hypothesis of the Kärger model.

In the case of small compartments, the validity of the narrow-gradient pulse approximation, and in turn of the Kärger model, is not ensured. Indeed, one should take into account restriction by boundaries during each gradient pulse. In [194, 195] the Kärger model was rigorously extended to finite pulses, but the resulting ordinary differential equations need to be solved numerically. A "mod-

ified" Kärger model in which the slow effective diffusion coefficient is set to zero was also proposed in order to account for restricted diffusion [196]. Note that the derivation in [194, 195] yields the same modified Kärger model with zero intracellular effective diffusion coefficient (see Eqs. (20-29) from Ref. [195]).

In the following, we critically revise the derivation of three models (bi-exponential, Kärger model and modified Kärger model). Then we apply them to analyze pulsed-gradient stimulated spin-echo experiments with yeast cells. The Kärger model and the modified Kärger model are shown to be very close to each other in the relevant range of parameters, whereas the bi-exponential model exhibits some deviations at low gradients. All three models fit the data well and give access to the exchange time across the cell membranes.

In the next section, we shall apply the same modeling to mitochondria in muscle tissues. Compared to a well-controlled yeast cell suspension, muscles are much more complex and we shall see that interpretations are less clear.

3.2.2 Three Models

For the sake of clarity and being motivated by experiments with yeast cells, we consider a medium that contains spherical cells of radius R, and spin-bearing particles are water molecules. The gradient sequence is a standard PGSE sequence with two rectangular pulses of duration δ and an off-gradient duration $\Delta - \delta$ between two pulses. We recall that the signal from free diffusion with diffusivity D_0 would decay as

$$S = \exp(-bD_0) \,, \qquad b = G^2\delta^2 t_d \,, \qquad t_d = \Delta - \delta/3 \,. \tag{3.26}$$

In contrast, restricted diffusion exhibits a slower decay, as we discussed in Sec. 1.2. In order to quantify restriction of intracellular diffusion during the gradient pulses, we introduce the dimensionless quantity

$$\xi = \frac{D_i \delta}{R^2} \,. \tag{3.27}$$

Note that the total diffusion time $\Delta + \delta$ is *a priori* independent from ξ.

Under the Gaussian phase approximation (GPA), i.e. weak dephasing and weak signal decay, and in the absence of exchange, Neuman derived in [81] the decay of the intracellular signal:

$$S_i \approx \rho \exp(-D_s b) \,, \tag{3.28a}$$

$$D_s = \frac{4R^2}{\xi t_d} \sum_{n=1}^{\infty} \frac{1 - \frac{1}{{\alpha_n}^2 \xi} F_n(\xi, \Delta/\delta)}{{\alpha_n}^4 ({\alpha_n}^2 - 2)} \,, \tag{3.28b}$$

$$F_n(\xi, \Delta/\delta) = 1 - e^{-{\alpha_n}^2 \xi} + 2e^{-{\alpha_n}^2 \xi \Delta/\delta} \sinh^2({\alpha_n}^2 \xi/2) \,, \tag{3.28c}$$

where α_n are the zeroes of the derivative of the spherical Bessel function j_1: $\alpha_1 \approx 2.08, \alpha_2 \approx 5.94, \ldots$. The coefficient D_s is thus the apparent "slow" diffusion coefficient probed by dMRI. When ${\alpha_1}^2\xi \gtrsim 1$ one can rewrite (3.28b) with a very good approximation as:

$$D_s \approx \frac{16R^2}{175\xi t_d}\left(1 - \frac{F_1(\xi, \Delta/\delta)}{{\alpha_1}^2\xi}\right) . \tag{3.29}$$

In the limit $\xi \to \infty$ one recovers the well-known motional narrowing formula (see Eq. (1.54)):

$$D_s \underset{\xi\gg 1}{\approx} \frac{16R^4}{175 D_i \delta t_d} . \tag{3.30}$$

Equations (3.28a) to (3.30) rely on the GPA, that is a low-gradient approximation. More precisely, one should distinguish between two situations depending on the value of ξ. At low ξ, the effect of boundaries is weak during the encoding pulse and the narrow-gradient pulse regime is a good approximation. Figure 1.8 and the related discussion shows that the GPA, and thus Eq. (3.28b), is valid as long as

$$\ell_q = (G\delta)^{-1} \gg R , \qquad (\xi \ll 1) , \tag{3.31}$$

where we assumed that compartments are small so that $\ell_\mathrm{d} > R$, otherwise the condition is given by $\ell_q \gg \ell_\mathrm{d}$, i.e. $bD_i \ll 1$ (that would correspond to Mitra regime). If condition (3.31) is not respected, then the signal exhibits a diffusion-diffraction pattern controlled by the radius of cells R.

In contrast, if $\xi \gtrsim 1$, there is strong restriction by boundaries during each encoding pulse and one should refer to Fig. 1.10 that shows the regimes associated to extended-gradient pulses. In that case, one can see that Eq. (3.29) and *a fortiori* Eq. (3.30) are valid if

$$\ell_g = (G/D_0)^{-1/3} \gg R , \qquad (\xi \gtrsim 1) . \tag{3.32}$$

Note that this last condition may be rewritten as $\ell_q \gg R/\xi$, and is therefore less restrictive than condition (3.31). If condition (3.32) is not respected, the signal exhibits "abnormal" dependence on the b-value, $-\log(S) \sim b^{1/3}$, in the localization regime (see Chapter 4 and Refs [6, 79, 99, 100, 102]).

In typical experiments with biological samples, $D_i \sim 1\ \mu\mathrm{m}^2/\mathrm{ms}$, $\delta \sim 1-10$ ms and $R \sim 1-5\ \mu$m which makes the condition $\xi \gg 1$ difficult to achieve. Therefore one generally has to carefully check the validity of the GPA, especially for the small values of ξ (i.e., δ).

In the absence of exchange across cell membranes, the complete signal can then be written in a bi-exponential form [120, 122, 130]:

$$S = (1-\rho)\exp(-D_f b) + \rho \exp(-D_s b) , \tag{3.33}$$

where D_f is the apparent "fast" diffusion coefficient, which is smaller than the intrinsic D_e because the extracellular diffusion is hindered by the cells[3]. This involves already an approximation because the complex problem of diffusion in the crowded extracellular medium is reduced to an apparent diffusion coefficient, ignoring for example high-gradient localization effects at the cell boundaries [98–100, 102]. As we discussed in Sec. 1.2.2, D_f may decrease slowly with diffusion time t_d (generally as a power law) and reach the "tortuosity limit" at long times [53, 69, 70]. The short-time behavior, that was studied in depth in the previous chapter, is not relevant here because of small compartments compared to typical diffusion lengths. Now we investigate the effect of exchange accounted via three models.

Bi-exponential model with time-dependent water fractions

The most simple idea is to keep the bi-exponential form (3.33) but to consider time-dependent intracellular water fraction ρ. In the regime of permeation control, and neglecting re-entry into the same cell, the fraction of water that remains inside the same cell during the experimental duration T follows from the discussion of Sec. 3.1.2:

$$\rho = \rho_0 \exp(-T/\tau_{i\to e}) \,, \tag{3.34}$$

where $\tau_{i\to e}$ is the global exchange time (3.23) of the compartment and the indices emphasize that it describes exchange from interior to exterior of the cell. For a sphere of radius R the expression of $\tau_{i\to e}$ is given by the simple expression (and for an arbitrary shape of diameter $2R$ the result is always smaller):

$$\tau_{i\to e} = \frac{R}{3\kappa} \,. \tag{3.35}$$

The validity of this approach relies on several assumptions. (i) The encoding is sufficiently short to neglect the effect of permeability during pulses, i.e. $\delta \ll \tau_{i\to e}$. (ii) Exchange is permeation controlled, i.e. $\tau_{i\to e} \gg R^2/D_i$, or equivalently $R \ll D_i/\kappa$. (iii) Cells are spatially disordered, therefore there is no diffusion-diffraction effects due to water traveling from one cell to the other. (iv) Entry

[3] Note that the bi-exponential formula has been proposed as a robust phenomenological representation for the signal in complex samples such as brain tissue [111, 115]. On the other hand, it has been argued in [128] that the bi-exponential fit may be unstable because of a too large number of parameters compared to a Taylor expansion of the signal, that is more "universal" at low b-values. Furthermore, the danger of misinterpretation of biexponential fitting was highlighted in [11]. Those considerations do not apply to our work, since the bi-exponential form of the signal (3.33) is a *model* that relies on microscopic assumption on the studied sample, and not a mere convenient fit.

of spin-bearing molecules from the outside is neglected, that requires either a strong decay of extracellular magnetization during one pulse, or that particles from the outside have diffused from sufficiently far away so that their phase dispersion leads to a very weak contribution to the intracellular signal. One can see that the second condition, $D_f \tau_{i\to e} \gg \ell_q^2$ is much less restrictive than the first one, $D_f \delta \gg \ell_q^2$, that can thus be discarded.

In the restricted diffusion regime ($\xi \gtrsim 1$) that is the case considered here, (i) automatically implies (ii). Note that this corresponds to the conditions of applicability of the Kärger model discussed in Sec. 3.2.1. Moreover, it allows one to replace the total diffusion time $T = \delta + \Delta$ by $t_d = \Delta - \delta/3$ in Eq. (3.35), so that ρ decays as:

$$\rho = \rho_0 \exp(-t_d/\tau_{i\to e}) \ . \tag{3.36}$$

Kärger Model

The classical model for treating exchange between two compartments with different diffusion coefficients is the Kärger model [188, 189]. Roughly speaking, this is an extension of the bi-exponential model with an additional parameter: an exchange time τ_K which is the time-scale of the leakage from one compartment to the other. More precisely,

$$\tau_{i\to e} = \rho_0 \tau_K \qquad \text{and} \qquad \tau_{e\to i} = (1-\rho_0)\tau_K \tag{3.37}$$

are respectively the mean times for crossing the membranes from the inside to the outside and from the outside to the inside. Note that the dependence on ρ_0 is simply related to mass conservation in intra- and extra-cellular compartments.

As we discussed in Sec. 3.2.1, the Kärger model relies on a coarse-graining approach that allows one to treat the exchange between intra- and extra-cellular water pools as occuring at every point in space. Moreover, one assumes that the encoding and decoding gradient pulses are infinitely short. Therefore, the evolution of each pool of magnetization results from decay and exchange:

$$\begin{cases} \dfrac{\mathrm{d}S_i}{\mathrm{d}t} = -r_i S_i - S_i/\tau_{i\to e} + S_e/\tau_{e\to i} \ , & \text{(3.38a)} \\[2ex] \dfrac{\mathrm{d}S_e}{\mathrm{d}t} = -r_e S_e - S_e/\tau_{e\to i} + S_i/\tau_{i\to e} \ , & \text{(3.38b)} \end{cases}$$

where r_i and r_e are intra- and extra-cellular decay rates of the magnetization. All the geometric complexity of the medium is coarse-grained into the coefficients τ_K, r_i and r_e, that reduces the Bloch-Torrey partial differential equation to the

above system of ordinary differential equations. In the absence of exchange, each magnetization pool decays as

$$S_i = \rho_0 \exp(-D_s q^2 t_d) \,, \qquad S_e = (1-\rho_0) \exp(-D_f q^2 t_d) \,, \tag{3.39}$$

that yields by identification with the above system

$$r_i = D_s q^2 \,, \qquad r_e = D_f q^2 \,, \tag{3.40a}$$

$$S_i(t=0) = \rho_0 \,, \qquad S_e(t=0) = 1-\rho_0 \,. \tag{3.40b}$$

The Kärger model relies on the assumption that $\delta \ll \tau_K$, which allows one to neglect the effect of exchange during the encoding and decoding gradient pulses. This means that, as far as the exchange is concerned, one can use $t_d = \Delta - \delta/3$ instead of, say, $\Delta + \delta$, as the total time during which the exchange takes place. As a matter of fact, in the case of long-exchange times, it was shown that using this form of t_d as the total time improves the accuracy of the Kärger model to the first order in δ/Δ [198, 199]. In addition, it makes the comparison with the bi-exponential model easier.

Solving the system of differential equations on the intra- and extracellular signals

$$\begin{cases} \dfrac{\mathrm{d}S_i}{\mathrm{d}t} = -D_s q^2 S_i - S_i/\tau_{i\to e} + S_e/\tau_{e\to i} & \text{(3.41a)} \\[2ex] \dfrac{\mathrm{d}S_e}{\mathrm{d}t} = -D_f q^2 S_e - S_e/\tau_{e\to i} + S_i/\tau_{i\to e} & \text{(3.41b)} \end{cases}$$

and the initial conditions

$$S_i(t=0) = \rho_0 \,, \qquad S_e(t=0) = 1-\rho_0 \,, \tag{3.42}$$

one gets the Kärger formula

$$S = P_1 \exp(-D_1 q^2 t_d) + P_2 \exp(-D_2 q^2 t_d) \,, \tag{3.43}$$

where P_1, P_2, D_1, D_2 are functions of q given by

$$D_{1,2} = \frac{1}{2}\left(X_e + X_i \mp \sqrt{(X_e - X_i)^2 + \frac{4}{q^4 \tau_{e\to i}\tau_{i\to e}}} \right) \,, \tag{3.44a}$$

$$X_e = D_f + \frac{1}{q^2 \tau_{e\to i}} \,, \qquad X_i = D_s + \frac{1}{q^2 \tau_{i\to e}} \,, \tag{3.44b}$$

$$P_1 = \frac{D_2 - \rho_0 D_s - (1-\rho_0) D_f}{D_2 - D_1} \,, \tag{3.44c}$$

$$P_2 = \frac{\rho_0 D_s + (1-\rho_0) D_f - D_1}{D_2 - D_1} \,. \tag{3.44d}$$

Note that some authors [196, 200] claimed using 4 initial conditions for the two first-order differential equations (3.41) even though only 2 conditions are needed. In our notations, the two additional conditions (along with Eq. (3.42)) are

$$\left.\frac{\mathrm{d}S_i}{\mathrm{d}t}\right|_{t=0} = -D_s q^2 \rho_0 \,, \qquad \left.\frac{\mathrm{d}S_e}{\mathrm{d}t}\right|_{t=0} = -D_f q^2 (1-\rho_0) \,, \tag{3.45}$$

which are actually equivalent to each other and compatible with (3.37). Although one can interpret these redundant initial conditions as another way to state Eq. (3.37), it is more natural, from the mathematical point of view, to discard Eq. (3.45) and to keep the two initial conditions (3.42) and two physical relations (3.37). We emphasize that the effective "fast" diffusion coefficient D_f is used in the system (3.41) instead of the intrinsic diffusion coefficient D_e as a way to take into account hindrance of extracellular diffusion by cell boundaries.

Modified Kärger model

One obvious flaw of the Kärger model is that D_s, which was supposed to be a constant intrinsic diffusion coefficient, depends on the diffusion time (see Eq. (3.29)). Although it seems to be of no consequence in the final formula (3.43), it is a serious issue when one looks at the original equations (3.41). Should one treat D_s first as a constant and then add its time dependence in the final formula or on the contrary consider that it is time-dependent from the beginning? Another defect is that the Kärger model relies on the narrow pulse approximation that is not valid in the restricted diffusion regime $\xi \gtrsim 1$. In this case, the equation for the intracellular signal should be modified.

Actually, if one goes back to Eq. (3.28a), one can see that the time-dependence of D_s in Eq. (3.29) is simply another way to state that the intracellular signal does not depend on the diffusion time in the restricted diffusion regime. Thus one can modify the Kärger model in the following way, inspired by [196]:

$$\begin{cases} \dfrac{\mathrm{d}S_i}{\mathrm{d}t} = -S_i/\tau_{i\to e} + S_e/\tau_{e\to i} & \text{(3.46a)} \\[2ex] \dfrac{\mathrm{d}S_e}{\mathrm{d}t} = -D_f q^2 S_e - S_e/\tau_{e\to i} + S_i/\tau_{i\to e} & \text{(3.46b)} \end{cases}$$

with the initial conditions

$$S_i(t=0) = \alpha\rho_0 \qquad S_e(t=0) = 1-\rho_0 \,, \tag{3.47}$$

where $\alpha = \exp(-D_s b) < 1$ depends on q and δ but not on t_d. Compared to the Kärger model, the intracellular effective diffusion coefficient is set to zero but the

effect of D_s is incorporated via the initial condition for the intracellular signal. Here, α is the time-independent decrease of the intracellular signal computed by Neuman formulas (3.28a) and (3.28b). One can see that the system (3.46) provides the correct solution in the absence of exchange ($\tau_{i\to e}, \tau_{e\to i} \to \infty$).

The main physical motivation behind this model is that the intracellular magnetization reaches an equilibrium on a much shorter time-scale than the water exchange through the cell membranes ($R^2/D_i \ll \tau_K$). Because it does not evolve after this very short transient regime (in the absence of exchange), the corresponding effective diffusion coefficient is set to zero. The initial value $\alpha\rho_0$ that we set for the intracellular signal is precisely the value of the signal resulting from this transient regime.

Solving the system (3.46) yields

$$S = P'_1 \exp(-D'_1 q^2 t_d) + P'_2 \exp(-D'_2 q^2 t_d) \,, \tag{3.48}$$

where P'_1, P'_2, D'_1, D'_2 are functions of q given by

$$\begin{aligned}
D'_{1,2} &= \frac{1}{2}\left(X'_e + X'_i \mp \sqrt{(X'_e - X'_i)^2 + \frac{4}{q^4 \tau_{e\to i}\tau_{i\to e}}}\right) \,, \\
X'_e &= D_f + \frac{1}{q^2\tau_{e\to i}} \,, \qquad X'_i = \frac{1}{q^2\tau_{i\to e}} \,, \\
P'_1 &= \frac{D'_2(1-\rho_0(1-\alpha)) - (1-\rho_0)D_f}{D'_2 - D'_1} \,, \\
P'_2 &= \frac{(1-\rho_0)D_f - D'_1(1-\rho_0(1-\alpha))}{D'_2 - D'_1} \,.
\end{aligned}$$

One can see that the formulas for D'_1 and D'_2 are the same as the ones from the Kärger model with D_s set to zero. However, the formulas for P'_1 and P'_2 are different due to the change of initial conditions.

As in the previous section, we note that some authors [196, 200] wrote 4 initial conditions instead of 2 for Eqs. (3.46). Their two additional conditions read in our notations as

$$\left.\frac{\mathrm{d}S_i}{\mathrm{d}t}\right|_{t=0} = 0 \,, \qquad \left.\frac{\mathrm{d}S_e}{\mathrm{d}t}\right|_{t=0} = -D_f q^2 (1-\rho_0) \,, \tag{3.50}$$

which are equivalent to each other but *not* compatible with (3.37). Because these authors probably used the same initial conditions (3.47) as us for the derivations, their formulas are the same as ours. However, the additional conditions (3.50) implicitly discard (3.37), which expresses the conservation of mass and is thus a fundamental relationship between exchange times and water fractions. To avoid further confusion, the incompatible conditions (3.50) should be discarded.

Comparison of the models

We have presented three different macroscopic models for the exchange between the intracellular and the extracellular water in the restricted diffusion regime. The modified bi-exponential model is the most simple and intuitive one, the Kärger model is the canonical one, whereas the modified Kärger model is the most rigorous of the three in this situation. It is natural to ask whether these three models give similar or different results and under which conditions.

First, it follows from the mathematical definition of the modified Kärger model that it coincides with the Kärger model in the limit $D_s/D_f \to 0$. However, from a physical point of view, the modified Kärger model makes sense only if D_s is inversely proportional to t_d, which necessarily implies that $D_s \ll D_i$ (see Eq. (3.29)) and thus $D_s \ll D_f$. As a consequence, when the Kärger model and the modified Kärger model are applicable, they generally yield results that are close to each other.

As for the modified bi-exponential model with decreasing fraction ρ, one can expand the Kärger model at high gradients and long exchange time ($D_f q^2 \tau_K \gg 1$) to get:

$$D_1 \approx D_s + \frac{1}{q^2 \tau_{i\to e}}\,, \qquad D_2 \approx D_f\,, \tag{3.51a}$$

$$P_1 \approx \rho_0\,, \qquad P_2 \approx (1-\rho_0)\,, \tag{3.51b}$$

that shows that the modified bi-exponential model is close to the Kärger model in this regime. To see this, we treat separately the cases of short and long diffusion times. At short times ($D_f q^2 t_d \lesssim 1$), the extracellular signal is not completely attenuated, but one has $t_d \lesssim (D_f q^2)^{-1} \ll \tau_K$ so that exchange can be neglected. In other words, one can use $D_1 \approx D_s$ and $D_2 \approx D_f$, which yields the standard bi-exponential model. At long times ($D_f q^2 t_d \gg 1$), the extracellular signal is completely attenuated, and the total signal reduces to the intracellular part:

$$P_1 \exp(-D_1 q^2 t_d) \approx \rho_0 \exp(-D_s q^2 t_d) \exp(-t_d/\tau_{i\to e})\,, \tag{3.52}$$

which again coincides with the modified bi-exponential model. Discrepancies between the two models appear at low gradients ($D_f q^2 \tau_K \ll 1$), which is consistent with the condition (iv) discussed in 3.2.2.

In the next section we apply these three models to experimental data on yeast cells to compare their quality and range of applicability.

3.2.3 Material and Methods

Baker's yeast (Jästbolaget, Sweden) was purchased at a local supermarket, diluted with tap water in approximate volume ratio 1:2 (yeast:water), transferred

to a 5 mm NMR tube, stored in room temperature for four days, and finally centrifuged at 1500g for 2 min to form a packed cell sediment of 2 cm height. NMR experiments[4] were performed on a Bruker Avance-II spectrometer operating at 500.13 MHz ^{1}H resonance frequency. The magnet was fitted with a Bruker MIC-5 probe with 3 T/m maximum gradient at a current of 60 A. The ^{1}H signal of water was recorded with a pulsed gradient stimulated echo sequence [23] for an array of values of q, δ, and t_d [201–203]. More precisely, four values of δ were used: 3.0 ms, 5.6 ms, 10.6 ms, 20 ms, and six values for $t_d = \Delta - \delta/3$: 20.2 ms, 35.2 ms, 187.2 ms, 327.2 ms, 572.1 ms, 1000.2 ms, yielding 24 different curves. To avoid spurious effects of differences in T_2-relaxation between the intra- and extracellular components [204], the time duration for transverse relaxation was held constant at 44.8 ms for all measurements.

The variable $q = G\delta$ took 26 logarithmically spaced values from $5.3{\cdot}10^{-3}$ μm^{-1} to 1.4 μm^{-1} whatever δ and t_d. The parameter $b = q^2 t_d$ reached maximum values of approximately 40 ms/μm^2 for $t_d = 20.2$ ms and approximately 2000 ms/μm^2 for $t_d = 1000$ ms. The signal was systematically renormalized by the value S_0 at $b = 0$ obtained by fitting a single exponential function $S = S_0 \exp(-bD)$ to data points fulfilling $S/S_0 > 0.8$. Before performing any fit, we determined the noise level of the data to be about 0.25%. Because the signal never goes down below $3 \cdot 10^{-2}$ we conclude that the signal-to-noise ratio is always bigger than 10.

3.2.4 Results

The typical radius of the yeast cells is 2.5 μm (see top left panel of Fig. 2.4). The smallest encoding duration δ is 3 ms for which $(D_i\delta)^{1/2} \sim 2$ μm, implying the restricted diffusion regime ($\xi \approx 1$), but not the motional narrowing regime ($\xi \to \infty$). The advantage of being in this intermediate regime is that by fitting D_s with (3.29), one can estimate both physical quantities R and D_i, that is not possible in the motional narrowing regime (cf. (3.30)) [41].

Bi-exponential model with decaying ρ

We have applied the fit (3.33) to all the values of δ and t_d. The quality of the fit was assessed by the value of the residual error, which was very close to the estimated noise value, indicating a good fit. Moreover, the 95% confidence intervals on the fit parameters were each time about: $\rho \pm 1\%$, $D_f \pm 2\%$, $D_s \pm 4\%$.

The intracellular water fraction ρ does not depend on δ and decreases with t_d, from 0.42 at $t_d = 20.2$ ms to 0.23 at $t_d = 1000$ ms, and the exponential decay (3.36) fits well (Fig. 3.4), from which we estimate a typical leakage time $\tau_{i\to e}$ of

[4] Experiments were carried out by M. Nilsson and D. Topgaard from Lund University.

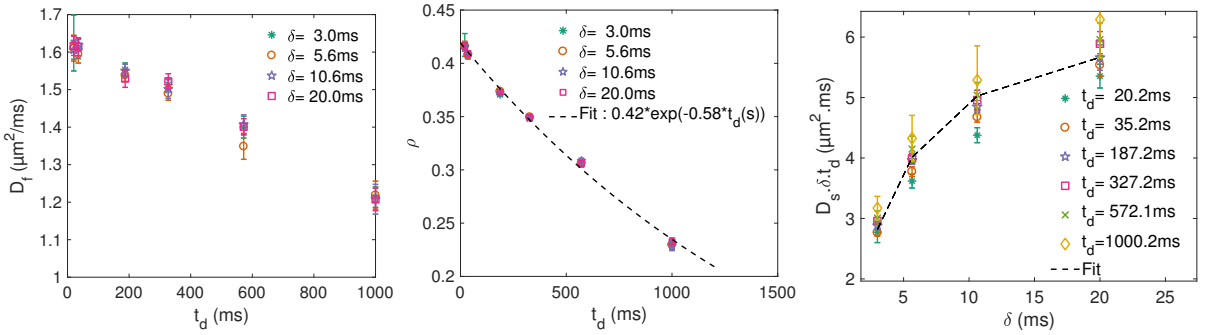

Figure 3.4: Parameters obtained from the bi-exponential fit (3.33). (left) The fast effective diffusion coefficient D_f, as a function of the diffusion time t_d; (center) The intracellular water fraction ρ as a function of t_d. Dashed line shows an exponential fit (3.36), with $\rho_0 = 0.42$ and $\tau = 1700$ ms; (right) The product $D_s \delta t_d$ as a function of δ. Dashed line shows a fit of the curves by Eq. (3.29).

about 1700 ± 100 ms. Moreover the intracellular water fraction ρ_0 is equal to 0.42 ± 0.01, that yields $\tau_K = \tau_{i\to e}/\rho_0 = 4000 \pm 300$ ms. Note that the hypothesis $\delta \ll \tau_{i\to e}$ is valid and that the value of ρ_0 is consistent with a packed sphere bed[5] [78].

The fast diffusion coefficient D_f does not depend on δ and slowly decreases with t_d, from 1.6 μm^2/ms at $t_d = 20.2$ ms to 1.2 μm^2/ms at $t_d = 1000$ ms (Fig. 3.4). As explained previously, one can interpret this decrease as the combined effect of hindered diffusion due to the high concentration of yeast cells and exchange with intracellular water. In [70] an asymptotic formula for the time dependent diffusion coefficient in a *dilute* suspension of spheres was derived. This formula indicates that the diffusion coefficient decreases towards a limit value as t_d^{-1} with a typical time scale given by R^2/D_e, which in our case is equal to about 5 ms. In a *crowded* suspension one expects this time scale to be linked to some correlation length of the distribution of the cells. For example, if the cells aggregate and form clusters of size $L \gg R$, D_f will decrease with a time scale $L^2/D_e \gg R^2/D_e$. Numerous works have also been devoted to the infinite time limit of the diffusion coefficient outside an isotropic random suspension of spheres [71–75], with a common agreement on the upper bound:

$$\frac{D(t=\infty)}{D_e} \leq \frac{1-\rho_0}{1+\rho_0/2}\,, \tag{3.53}$$

where the exact value of $D(t{=}\infty)/D_e$ depends on the distribution of spheres. In particular, this upper bound is reached in the case of a "well-separated" array

[5] The value of ρ_0 is the intracellular *water fraction*, that is smaller than the intracellular *volume fraction*.

of spheres, that is a suspension with no aggregates. In our case, $\rho_0 \approx 0.4$ so that (3.53) provides the upper bound $D(t = \infty)/D_e \leq 0.5$. The free diffusion coefficient of water at room temperature is around 2.3 μm^2/ms [42–44] thus the hindered diffusion coefficient should be lower than 1.2 μm^2/ms. However D_f is above 1.2 μm^2/ms even at t_d as high as 1000 ms. As a consequence, the exchange alone does not seem to explain the obtained values of D_f. Note that, in general, neglecting the effect of geometrical hindrance on the time variation of D_f leads to an underestimation of τ_K.

The product $D_s \delta t_d$ is not exactly constant but increases with δ (its value at $\delta = 20$ ms is approximately the double of its value at $\delta = 3$ ms) and slightly increases with t_d (a 20% increase from $t_d = 20$ ms to $t_d = 1000$ ms) (Fig. 3.4). The correction formula (3.29) accounts quite well for the variation with δ but is unable to reproduce the dependence on t_d because the correction term in Eq. (3.29) does not depend on t_d if $t_d \gg \delta$ (which is the case for almost all data points). We expect that the variation with t_d is caused by the exchange across the cell membranes. This dependence on t_d makes hard to give precise estimates of R and D_i. We get $R = 2.6 \pm 1$ μm and $D_i = 0.75 \pm 0.15$ μm^2/ms (95% confidence intervals), in agreement with the values found in the literature [41, 197].

Kärger model and modified Kärger model

On these experimental data, the Kärger model and the modified Kärger model yield very close values of the parameters, hence we only show in Fig. 3.5 a fit made with the modified Kärger model. In spite of small systematic deviations between the data and the model, the fit is good and yields (with 95% confidence intervals): $D_f = 1.73 \pm 0.03$ μm^2/ms, $D_i = 0.86 \pm 0.12$ μm^2/ms, $\rho_0 = 0.413 \pm 0.002$, $\tau_K = 3700 \pm 100$ ms and $R = 2.7 \pm 0.07$ μm. From Eqs. (3.35) and (3.37) one deduces the permeability $\kappa = (5.8 \pm 0.4)\, 10^{-4}$ μm/ms. These values are consistent with the literature [41, 197]. Fig. 3.5 illustrates also the property that the low-q decay of the signal is independent of δ whereas the high-q decay is independent of t_d (more precisely, varying t_d changes only the amplitude but not the shape of the curve).

Note however that the Kärger model is only suited to fit data with several values of t_d and δ at the same time. If one tries to fit only one curve $S(q)$ (that is, with one value of t_d and one value of δ), the fit is unstable. Indeed, we have already noted that the bi-exponential model fits the data well (no sign of a systematic deviation, RMSE close to the noise level estimation). As a consequence, the addition of another parameter τ_K does not significantly improves the quality of the fit. Moreover, the fit algorithm returns very high values of τ_K associated with very large error bars. In turn, these large error bars on τ_K affect the stability

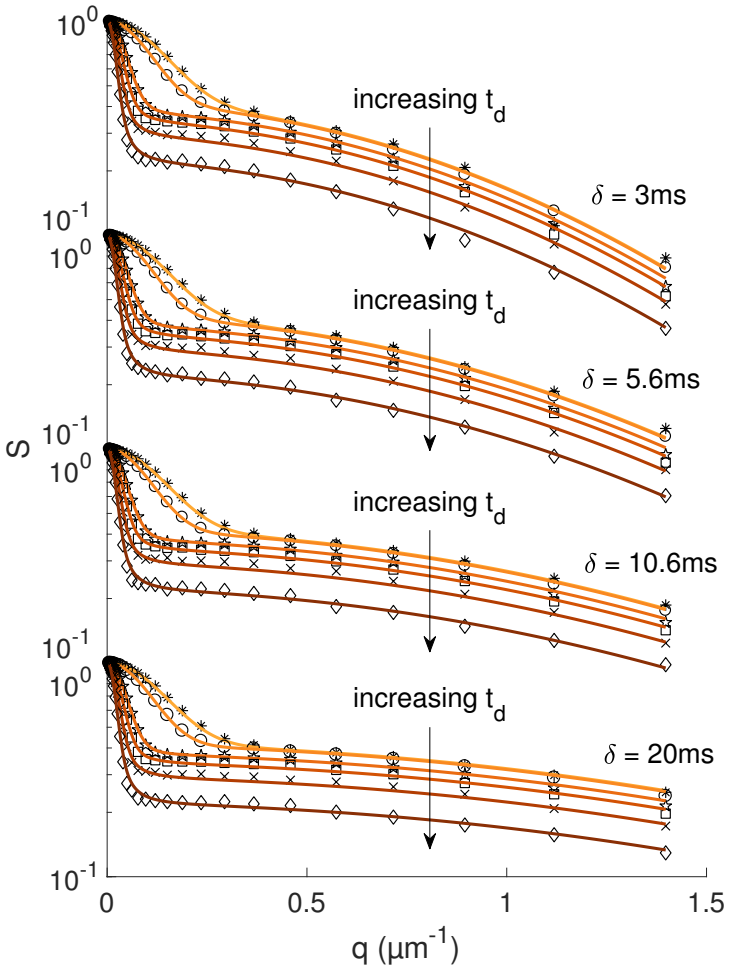

Figure 3.5: Fit of the data by the modified Kärger model. The signal is plotted against $q = G\delta$ for various values of δ and t_d (asterisk: 20.2 ms, circle: 35.2 ms, star: 187.2 ms, square: 327.2 ms, cross: 572.1 ms, diamond: 1000.2 ms). Note that the plots are vertically shifted with different δ for visibility.

of the whole fit because all the parameters are correlated (in particular ρ_0 and τ_K). This can be understood by looking at Fig. 3.6. The signal is sensitive to τ_K only when $\tau_K \sim t_d$. As $\tau_K/t_d \to 0$ the signal converges to the fast mono-exponential decay and as $\tau_K/t_d \to \infty$ the signal converges to the bi-exponential decay. As the bi-exponential fit is already good, the optimal value of τ_K is high compared to t_d and it is not well-determined. One also notices that the two curves with the highest τ_K (10^3 ms and 10^4 ms) have both the shape of a bi-exponential decay, the only difference being the apparent value of ρ_0 (the amplitude of the slow high-q decay).

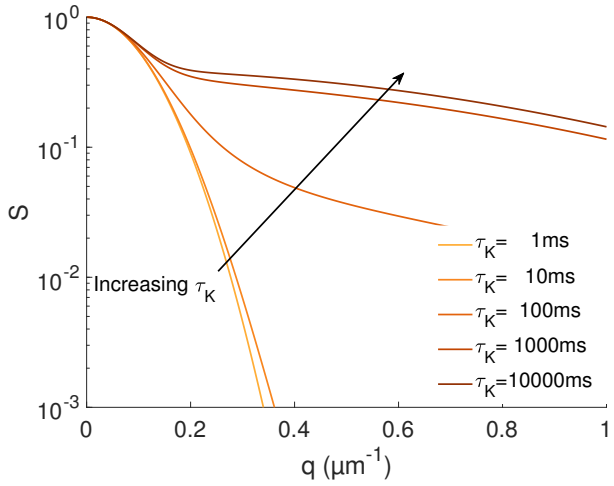

Figure 3.6: The Kärger signal for $t_d = 100$ ms and various values of τ_K. While the signal increases with τ_K, the dependence on τ_K is weak when $\tau_K \ll t_d$ or $\tau_K \gg t_d$.

3.2.5 Discussion

In summary, the bi-exponential model and both Kärger models yield rather close values of the parameters. In particular, the intracellular water fraction ρ_0 and the exchange time τ_K are very similar. The bi-exponential model shows its limitations when it comes to the analysis of the slow apparent diffusion coefficient D_s. Indeed $D_s t_d$ weakly depends on t_d whereas it should not, according to Eq. (3.29). This effect may be attributed to the exchange. In the same way, the slow dependence of D_f on t_d may be caused by the exchange as well as by the hindering by the cells. The errors bars on the parameters obtained from the bi-exponential model are also slightly larger than the ones obtained from the Kärger model.

The modified Kärger model is the most appropriate one from a theoretical point of view and can fit the whole data with one set of parameters. In some sense, this strength is also a weakness because the model is not applicable if one does not have full sets of data with variable q and t_d. Furthermore, this makes the model too "rigid"; for example, it is not clear how to take into account time-dependent diffusion coefficients.

On the other hand, the bi-exponential model with time-decaying ρ has a transparent physical interpretation and suggests the following experimental modality to quickly measure the exchange time: to choose a fixed value of q with fixed δ and to probe the signal as a function of diffusion time, for example with a multiple echo (CPMG) experiment (this is analogous to the Cg-simulations of Ref. [200]). At short times, the signal from the extracellular water is not completely destroyed, but at long times one only measures the intracellular signal, which decays as $\exp(-t/\tau_{i\to e})$, as shown above. Note that the same measurement with-

out any weighting gradient is also needed in order to estimate the T_2-relaxation beforehand. This modality bears similarities with the FEXSY and FEXI sequences [205, 206] (where an additional filtering sequence is used to destroy the extracellular signal). From a theoretical point of view, one should choose δ large enough in order to be in the restricted diffusion regime but small compared to $\tau_{i\to e}$. This is only possible if $\tau_{i\to e} \gtrsim 50$ ms. Another condition is that the echo time T should be chosen sufficiently long so that the extracellular magnetization is completely destroyed between two echoes ($D_e q^2 T \gg 1$) but still not too large compared to $\tau_{i\to e}$. On a conventional scanner with $g \leq 20$ mT/m these conditions require that $\tau_{i\to e} \gtrsim 250$ ms. With gradients higher than about 200 mT/m one can theoretically probe exchange time as short as 50 ms.

3.3 Quantitative estimation of mitochondrial content and permeability in muscles

3.3.1 Overview

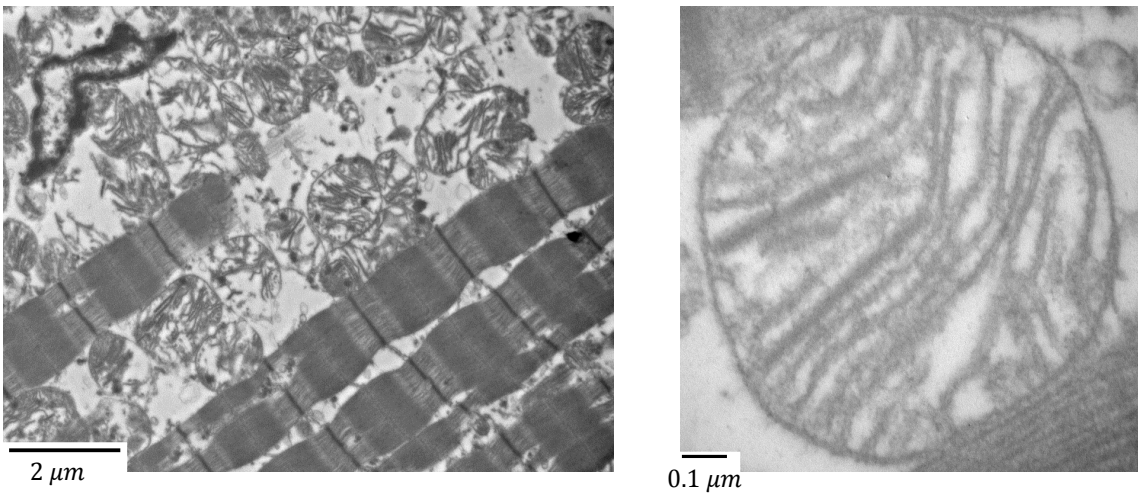

Figure 3.7: (left) The muscle structure at the sub-micron scale is essentially composed of aligned fibers (myofibrils) and micron-sized compartments (mitochondria). (right) magnified image of a single mitochondrion between two myofibrils. The seemingly round shape is a misleading artefact of slice direction. Most mitochondria have a prolate spheroid-like shape, as one may guess from the left panel image. These images were obtained with TEM microscopy by T. Astruc from QuaPa (UR370 Inra)

The previous section about experiments on a yeast cell suspension showed that it is possible to recover several interesting properties of the cells, such as volume fraction ρ, radius R, and permeability κ of cell membrane. We recall that the basic principle of the technique is to employ sufficiently strong diffusion weighting (i.e., large b-values) to create a contrast between intra- and extra-cellular magnetization. This opens interesting possibilities for dMRI in muscles, in particular to probe properties of mitochondria (see Fig. 3.7). Indeed, mitochondria bear similarities with yeast cells in terms of size (a few microns) and *possibly* membrane type (bi-lipidic plasma membrane). While mitochondria play a major biochemical role in cells and are related to several diseases, their current studies require invasive microscopy techniques such as TEM. Therefore, a non-invasive quantification of mitochondrial content, size, and permeability with diffusion MRI would be of great clinical interest. We present below preliminary results

in this direction[6]. A first set of experimental data allowed us to extract the mitochondrial content ρ and an estimation of the mitochondria diameter L. The study of permeation effects is still in progress at the moment.

Compared to the experiments on yeast cells presented above, several important differences should be noted.

Imaging

In this work, we aim to study the spatial dependence of tissue properties, i.e. to combine diffusion-weighted contrast and imaging. It is known that muscle fibers have different metabolic types and in turn different mitochondrial content. The baseline is that white fibers have fast contraction speed and anaerobic, glycolytic metabolism, with a low mitochondrial content; in contrast, red fibers have slow contraction speed and aerobic, oxidative metabolims, with high mitochondrial content. The full picture is more complicated and one can find a continuous transition from one type to the other [224]. Inside a muscle sample, several types of fiber often coexist, therefore the spatial repartition of fiber types could potentially be imaged through the measure of intra-mitochondrial signal. However, a fine spatial resolution would imply smaller voxels and lower signal-to-noise ratios, that limit the applicability of our method. Indeed, as we explained previously, the principle of the technique is to go to sufficiently high b-values so that signal from extra-mitochondrial water vanishes and one observes solely the signal from intra-mitochondrial water. This implies a significant signal decay that may become challenging because of noise issues. In other words, there is a need for a compromise between quality of diffusion-weighted signal and spatial resolution.

Anisotropy of the exterior medium

Figures 2.2 and 3.7 reveal a coherent orientation of muscle fibers. As we discussed in Sec. 2.1, diffusion in the exterior medium can be modeled as a diffusion tensor D_e, with faster diffusivity along the fibers than in the orthogonal plane [217]. The signal from exterior medium is then given by

$$S_e = (1-\rho)\exp\left(-\mathrm{Tr}(\mathrm{D}_e\mathrm{B})\right) \ . \tag{3.54}$$

As we explain in Sec. 2.2.1, at least 6 measurements with "independent" gradient direction are required to recover the diffusion tensor D_e.

[6] A manuscript is in preparation and our results were published in two conference proceedings [350, 351].

Other candidates for slow signal decay

The muscle structure is complex and it is not clear *a priori* that mitochondria are the only compartments that could contribute to the signal at high-b values. In particular, intra-myocellular lipid (IMCL) micron-sized droplets would be another natural candidate in terms of size and volume fraction [218]. Several studies demonstrated their role as energy fuel during exercise as well as energy storage for muscles [215]. Furthermore, it was suggested that the accumulation of IMCL due to excessive fat intake was one of the main mechanism of reduced insulin sensitivity in muscles [211, 212, 218].

Two main differences with mitochondria allow us to discard their influence on the signal. (i) Their chemical composition (lipid) allows one to distinguish them from water signals with magnetic resonance spectroscopy [211], or simply to destroy their signal selectively with fat suppression schemes [221]. We employed the latter method in the experiments described below. (ii) The slow diffusion coefficient of lipids, estimated to $D_{lip} \approx 6.6 \cdot 10^{-3}$ μm^2/ms implies that the IMCL signal is almost not attenuated even at $b = 10$ ms/μm^2, that was the typical order of magnitude of maximal b-values used in our experiments. In other words, IMCL would contribute as a constant "offset" of the signal, whereas mitochondrial water signal is expected to decay with increasing gradient strength, similarly to experiments with yeast cells described previously.

Shape and orientation

As one can see on the left panel of Fig. 3.7, mitochondria are non-spherical but typically prolate. Since the size of the compartments enter as L^4, one can see that the orientation between mitochondria and the gradient may have a strong effect. To estimate it, let us assume that mitochondria are circular cylinders with length L_1 and base diameter L_2, with $L_2 < L_1$. The cylindrical geometry is a crude assumption but allows us to perform analytical computations that help to capture the effect of orientation. Let us denote by $\mathbf{u}$ the direction of one cylinder, by $\mathbf{e}$ the direction of the gradient, and by θ the angle between the two vectors, i.e. $\cos\theta = (\mathbf{e} \cdot \mathbf{u})$. Diffusion along $\mathbf{u}$ and perpendicular to $\mathbf{u}$ are two independent motions, therefore one get the signal from water inside the cylinder in the motional narrowing regime ($D_i\delta \gg L_1^2$):

$$S \approx \exp\left(-\frac{1}{120}\frac{2G^2\delta L_1^4}{D_i}\cos^2\theta - \frac{7}{1536}\frac{2G^2\delta L_2^4}{D_i}\sin^2\theta\right) , \tag{3.55}$$

where we have used the known values of ζ_{-1} for a slab and a disk (see Secs. 1.2.2 and 4.3.1). Note that the factor 2 in front of $G^2\delta$ comes from two applied

gradient pulses. In the regime of weak attenuation of intra-mitochondrial signal, one can replace the exponential by its linearized expression. If we assume that mitochondria are uniformly oriented inside the voxel of interest, we obtain after averaging over θ:

$$S \approx \exp\left(-\frac{2G^2\delta}{D_i}\left[\frac{L_1^4}{360}+\frac{7L_2^4}{2304}\right]\right) . \tag{3.56}$$

Interestingly, the numerical coefficients $1/360$ and $7/2304$ are both close to the value of $\zeta_{-1} = 1/350$ for a sphere. If, as Fig. 3.7 seems to suggest, one has $L_1 \approx 2L_2$, then the term L_2^4 is a small correction to the term L_1^4. We conclude that one can replace the prolate mitochondria with diameter L_1 by spheres of diameter L_1 with a good approximation for the expression of the signal decay. In turn, if the orientation of mitochondria is coherent at the scale of the voxel, then one should observe a strong anisotropy of the signal as a function of the gradient because of the large difference between L_1^4 and L_2^4. From the biological viewpoint, mitochondria are found in two different places inside a muscle cell: either in the small space between two myofibrils (right panel of Fig. 3.7), or near the cell membrane (left panel of Fig. 3.7). While we expect the first situation to create an average orientation of mitochondria along myofibrils, mitochondria are generally more numerous in the second situation where there is no reason *a priori* to observe a preferred orientation [208]. The validation of this expectation is one of the aim of future experimental work.

Size distribution

The left panel of Fig. 3.7 suggests that the distribution of the diameter L may be very wide, with very small as well as very large mitochondria. This feature was reported in earlier microscopic observations of mitochondria [219]. The non-normalized signal from a single mitochondria scales as

$$s \sim L^3 \exp\left(-\zeta_{-1}\frac{2G^2\delta L^4}{D_i}\right) \approx L^3 - \zeta_{-1}\frac{2G^2\delta L^7}{D_i} , \tag{3.57}$$

therefore one can see that after averaging over all sizes, the intra-mitochondrial signal is equal to

$$S \approx \rho \exp\left(-\zeta_{-1}\frac{2G^2\delta}{D_i}\frac{\langle L^7\rangle}{\langle L^3\rangle}\right) , \tag{3.58}$$

where ρ is the intra-mitochondrial water fraction.

One can see that L^4 is replaced by $\langle L^7\rangle/\langle L^3\rangle$, that skews the estimated value of L towards high values. For example, if one assumes that the distribution of L

is log-normal with parameters μ and σ (i.e. $\log(L)$ is normally distributed with mean value μ and variance σ^2, a common model in biology), then

$$\langle L^n \rangle = e^{n\mu + n^2\sigma^2/2} , \qquad \left(\frac{\langle L^7 \rangle}{\langle L^3 \rangle} \right)^{1/4} = e^{\mu + 5\sigma^2} = e^{9\sigma^2/2} \langle L \rangle , \tag{3.59}$$

so that $(\langle L^7 \rangle / \langle L^3 \rangle)^{1/4}$ may be considerably larger than $\langle L \rangle$ if the distribution has a large coefficient σ, i.e. a large coefficient of variation[7]. This effect is illustrated on Fig. 3.8 for a moderate value $\sigma = 0.35$.

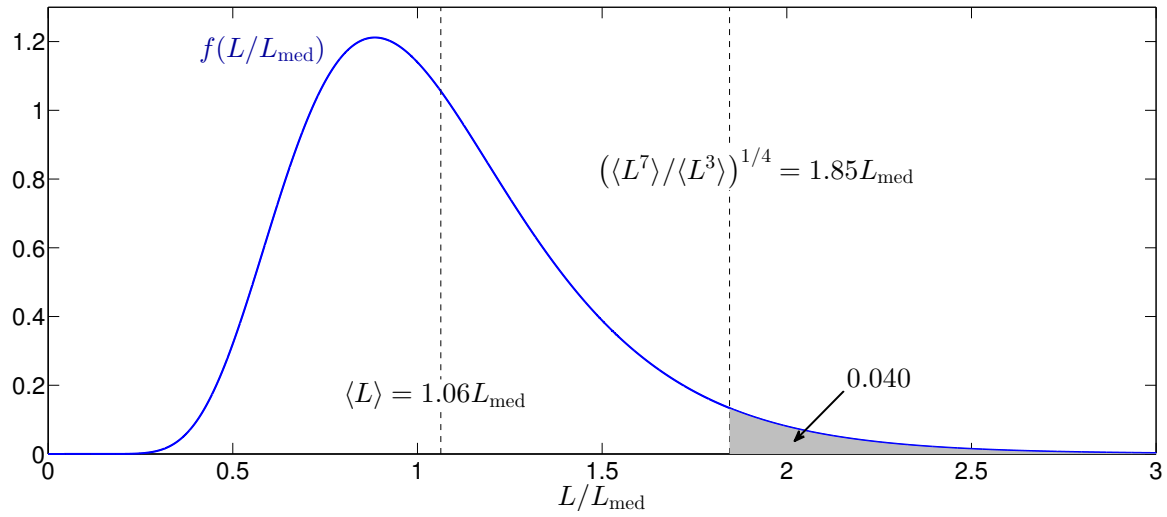

Figure 3.8: Example of log-normal distribution function f for $\mu = 0$ and $\sigma = 0.35$. The choice $\mu = 0$ is equivalent to rescaling the distribution by the median value L_{med}. One can see that $(\langle L^7 \rangle / \langle L^3 \rangle)^{1/4}$ is significantly larger than $\langle L \rangle$ and L_{med}. Moreover, it corresponds to the tail of the distribution, with only about 4% of realizations above this value.

Post-mortem degradation

If experiments are performed ex-vivo, there is a post-mortem degradation of muscle cells and possibly of mitochondria. It was shown that the inner structure of mitochondria disappears in a few days after animal death, while its outer membrane remains intact for at least a week [210, 225]. However, it is not clear how permeation is affected by cell death. On one hand, one would expect an increase of permeability with post-mortem time because of degradation of mitochondrial membranes. On the other hand, one could argue that water permeation

[7] The coefficient of variation of a log-normal distribution is equal to $(e^{\sigma^2} - 1)^{1/2}$, that is close to σ for $\sigma \lesssim 0.5$.

through the mitochondrial membrane is an active process performed by channel proteins and that cell death would lead to a decrease of permeability in the first hours after animal death. An experimental validation of either scenario will thus present an important physiological contribution.

3.3.2 Material and Methods

The experiments were performed by J.-M. Bonny, S. Clerjon, and G. Pagès at AgroResonance (QuaPA unit of INRA). A PGSE sequence with $\delta = 3.2$ ms, $\Delta = 10$ ms, and b-values up to 10 ms/μm^2 was applied in 6 gradient directions and for 32×32 $(0.3\text{ mm})^3$ voxels. The directions of the gradient that were used followed Eq. (2.18). As mentioned previously, a fat suppression scheme [221] was employed to reduce contributions from lipids. Two contrasted muscle samples were analyzed: Masseter (M1), an oxidative muscle with high mitochondrial content, and Longissimus Dorsi (LD2), a glycolytic muscle with low mitochondrial content. To avoid non-stationary effects caused by heating of the sample during acquisition, the temperature was regulated at 16°C. At this temperature, the diffusion coefficient of free water was measured [42]: $D_0 = 1.81$ μm^2/ms. The diffusion coefficient inside muscle tissues is expected to be smaller because of molecular crowding and hindered diffusion.

The aim of this protocol with constant Δ and δ was to identify the mitochondrial signal as well as to extract physical quantities such as volume fraction and typical size. For this purpose, the extra-mitochondrial medium is modeled by an effective diffusion tensor D_e and the intra-mitochondrial medium was assumed to be statistically isotropic with a diffusion coefficient D_i. The signal was then fitted by a tensorial bi-exponential model:

$$S = (1-\rho)\exp(-\mathrm{Tr}(\mathrm{BD}_e)) + \rho\exp(-bD_s)\ , \tag{3.60}$$

where D_s is the effective "slow" diffusion coefficient probed by dMRI in the restricted diffusion regime.

3.3.3 Results

The signal from a representative voxel of each sample is shown on Fig. 3.9, with the result of the fit (3.60). From the fit one can extract and analyze three model parameters: the restricted water fraction ρ, the effective "fast" diffusion tensor D_e, and the "slow" diffusion coefficient D_s. We emphasize that a good fit quality does not prove our hypotheses. In particular, there is no definite proof that the high-b signal comes from intra-mitochondrial water (our ongoing project, which

is not discussed in this manuscript, aims at validating these hypotheses). Bearing in mind this caveat, we discuss the following preliminary results.

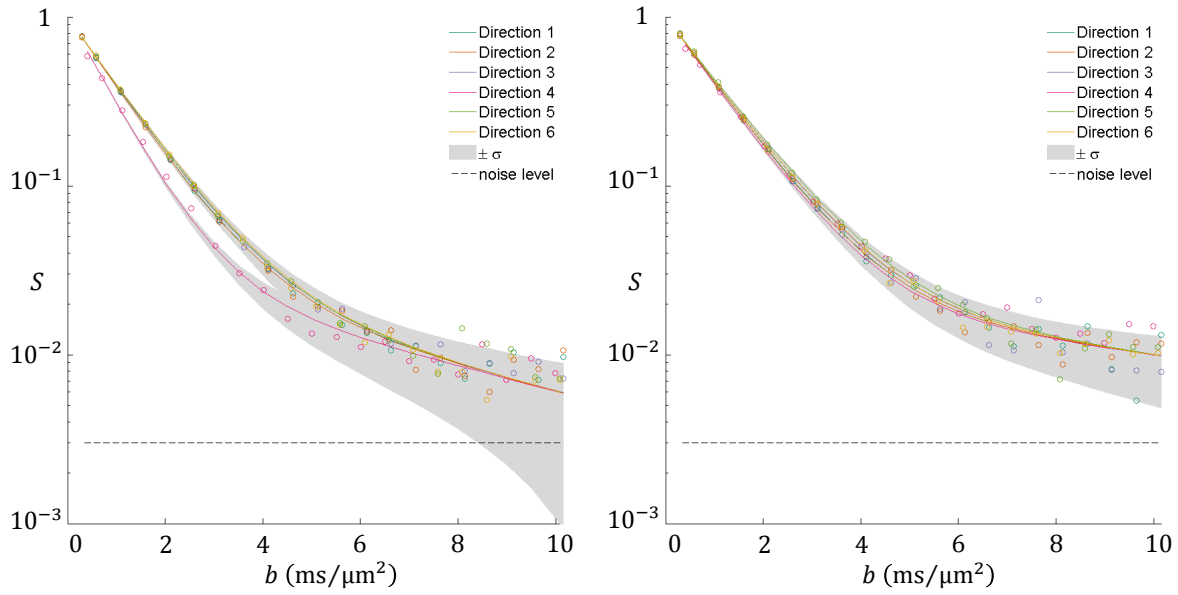

Figure 3.9: Signal measured for 6 gradient directions in a representative voxel of LD2 (left) and M1 (right), fitted by a bi-exponential tensorial model (3.60). The level of noise is about 0.3% of the reference signal. Gray shadowed region indicates the 67% confidence interval (fitted curves ± noise level). The fast decay of the signal at low b-values is attributed to the extra-mitochondrial water signal, whereas the slow decay at high b-values is attributed to the intra-mitochondrial water signal. The high-b signal is larger on the right panel, that is consistent with higher mitochondrial content in M1.

If the high-b measured signal is the intra-mitochondrial signal, then ρ represents the water fraction contained inside mitochondria, possibly reduced because of permeation to the exterior medium. As mitochondria are filled with around 64% of water [220, 222, 223], one can infer the mitochondrial volume fraction φ_{m} from ρ as

$$\varphi_{\mathrm{m}} = \frac{1}{0.64}\rho \approx 1.5\rho \ . \tag{3.61}$$

Maps of φ_{m} are presented for both muscle tissues on Fig. 3.10. Sample M1 displays two regions with respectively high ($\approx$ 15%) and low ($\approx$ 5%) values of φ_{m} whereas sample LD2 has a uniform low ($\approx$ 3%) value of φ_{m}. These results are in qualitative agreement with the muscle type as discussed above, and the values of φ_{m} are consistent with the literature [208, 209, 215]. Histological slices are planned in order to confirm and explain the existence of two different regions in sample M1. One can estimate that each voxel contains on the order of

10^6 mitochondria, therefore spatial variations cannot be attributed to statistical fluctuations.

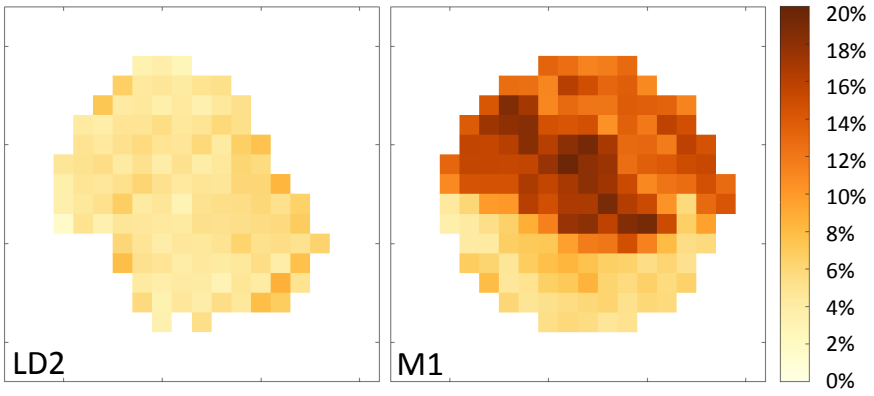

Figure 3.10: Map of the extracted mitochondrial volume fraction φ_{m} (see Eq. (3.61)) for both muscle samples. Each pixel corresponds to a $(0.3\ \mathrm{mm})^3$ region of the muscle sample.

The effective diffusion tensor D_e is shown in ellipsoid representation on Fig. 3.11. The idea of this representation is to diagonalize the tensor, to find its eigenvectors $\mathbf{u_1}, \mathbf{u_2}, \mathbf{u_3}$ and eigenvalues $\lambda_1, \lambda_2, \lambda_3$, then to draw an ellipsoid with semi-axes $\lambda_i \mathbf{u_i}$. In other words, the equation of the ellipsoid is $\mathbf{r} \cdot \mathrm{D}_e^{-2}\mathbf{r} = 1$. The left panel (LD2) reveals a very coherent orientation of diffusion tensors that was shown to be consistent with fiber orientations in the muscle. This can be related to the left panel of Fig. 3.9, where the signal corresponding to "Direction 4" decays faster than other curves at low b, that indicates faster diffusion along this direction. The largest eigenvalue of the diffusion tensor is on average equal to 1.25 $\mu\mathrm{m}^2/\mathrm{ms}$. This value is below the intrinsic diffusion coefficient of water, as expected. In contrast, the right panel (M1) exhibits more disorder, although there seems to be a global vertical orientation. The largest eigenvalue of the diffusion tensor is on average 1.05 $\mu\mathrm{m}^2/\mathrm{ms}$, which is again below the intrinsic diffusion coefficient of water.

Finally, the "slow" diffusion coefficient D_s was estimated around 0.07 $\mu\mathrm{m}^2/\mathrm{ms}$ for M1 and 0.20 $\mu\mathrm{m}^2/\mathrm{ms}$ for LD2. Low values of ρ imply a low residual signal at high b-values, and thus less reliable estimation of D_s due to noise. Therefore, the difference between its values for M1 and LD2, although significant compared to error bars, should be interpreted with caution. It was previously reported that white fibers may have very large inter-myofibrillar mitochondria [219]. This observation, combined with the low overall amount of mitochondria, may explain the larger value of D_s in LD2. Indeed, as we discussed above,

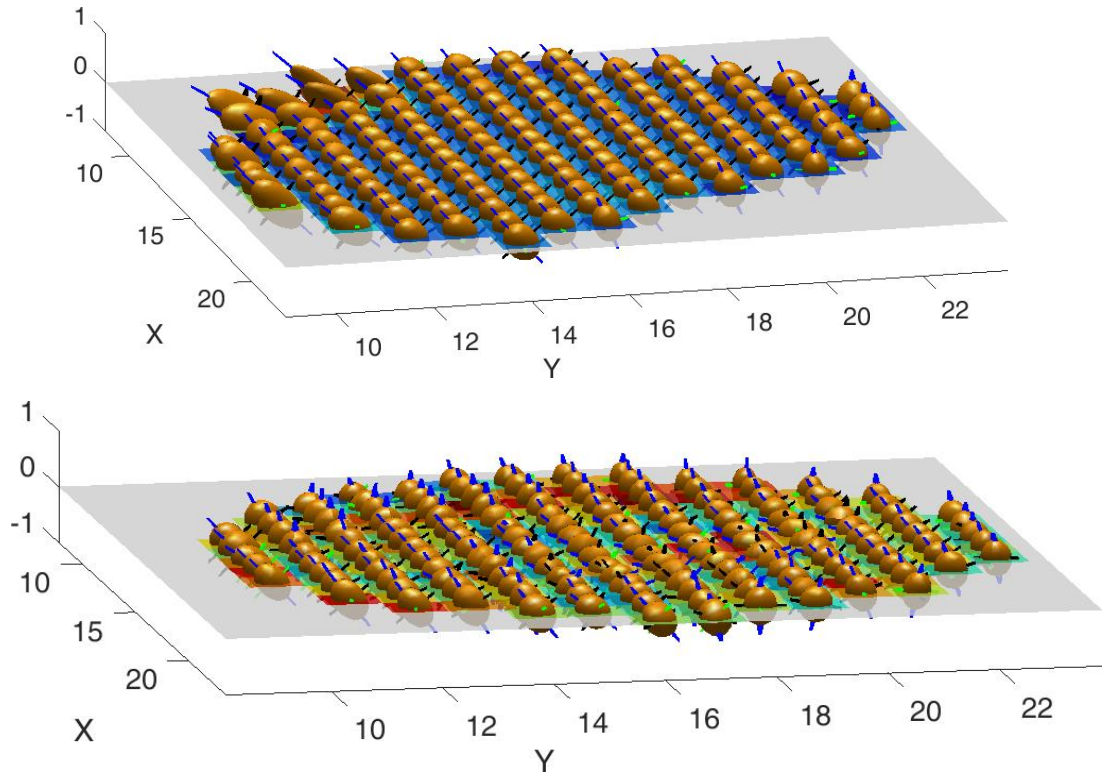

Figure 3.11: Ellipsoid representation of diffusion tensors D_e in each voxel of LD2 (left) and M1 (right). To facilitate interpretation, the eigenvector with the largest eigenvalue was drawn as a blue arrow.

the value of D_s is strongly biased towards very large mitochondria. From the value $D_s = 0.07\ \mu m^2/ms$ one can extract two informations. The first one is that this value is about ten times larger than the diffusion coefficient of lipids, and therefore cannot be attributed to IMCL. The second information is that Eq. (3.29) yields a diameter $L \approx 4-5\ \mu m$. Note that a more accurate estimation of L depends on the diffusion coefficient D_i of intra-mitochondrial water, that is unknown. As illustrated on the right panel of Fig. 3.7, mitochondria have a complex internal structure so that D_i might be significantly lower than the exterior diffusion coefficient that was measured as $1.25\ \mu m^2/ms$. However, the coefficient D_i enters with a power $1/4$ in the value of L, which makes the dependence on D_i rather weak. For instance, the value $4-5\ \mu m$ was obtained with $D_i/D_e = 0.5-1$.

The estimated value of L is much larger than the typical value $L \approx 2\ \mu m$ that is found in the literature. This may be partly explained by a bias towards large and exceptional values of L, as we discussed previously. Another contribution to this deviation would be the permeability of mitochondrial membrane that leads to faster signal attenuation than the pure motional narrowing regime.

3.4 Diffusion inside an array of permeable barriers

In the previous section, we have studied exchange between two pools of spins: small compartments and an infinite exterior medium. Now we turn to another situation where diffusion takes place in a medium segmented by numerous permeable barriers. At short times, the diffusive motion is almost not affected by the barriers, and one expects a behavior similar to the one studied in Sec. 2.3.1. In contrast, at long times, particles have diffused across multiple barriers and there should be a reduced diffusion coefficient D_∞ that describes the complex medium, coarse-grained by diffusion. As we shall see, the competition between permeability length ℓ_κ, typical inter-barrier spacing ℓ_s, and diffusion length ℓ_d yield different regimes for the diffusion propagator $\mathcal{G}(T, \mathbf{r_0}, \mathbf{r})$. From the diffusion propagator we will compute the dMRI signal in the narrow-gradient pulse regime, that introduces another length scale ℓ_q into the problem and a variety of regimes for the magnetization and the signal. Diffusion through multiple barriers is a broad topic with numerous applications and we begin this section with an overview of the literature. This allows us to better position our approach among previous works.

3.4.1 Introduction

One often characterizes diffusion processes by the diffusion propagator (or "heat kernel") $\mathcal{G}(T, \mathbf{r_0}, \mathbf{r})$. As we discussed in Sec. 1.1.2, when diffusion takes place in a homogeneous medium without boundaries, the propagator is a Gaussian distribution centered on $\mathbf{r_0}$ with variance $2D_0T = 2\ell_d^2$, where D_0 is the diffusion coefficient in the medium (see Eq. (1.7)). On the other hand, diffusion in complex systems such as biological cells or composite materials may exhibit non-Gaussian behavior due to confinement, hindrance by permeable barriers or heterogeneity of the diffusion coefficient.

Generally speaking, the diffusion propagator obeys the diffusion equation:

$$\partial_T \mathcal{G} = \nabla(D_0 \nabla \mathcal{G}) \,, \quad \mathcal{G}(T = 0, \mathbf{r_0}, \mathbf{r}) = \delta(\mathbf{r} - \mathbf{r_0}) \,, \tag{3.62}$$

where δ is the Dirac distribution, $\nabla = \partial_x$ in the one-dimensional case, and the diffusion coefficient D_0 can in general be space and time dependent to capture heterogeneities of the medium [12, 13]. Throughout this article, we refer to $\nabla(D_0\nabla)$ as the "diffusion operator". Note that if the diffusion coefficient is uniform, then the diffusion operator is simply proportional to the Laplace operator ∇^2. The complexity of the geometry is hidden in the boundary conditions imposed on

$\mathcal{G}$ at the outer boundaries and possible inner permeable barriers. Analytical solutions of Eq. (3.62) mainly rely on spectral decomposition over the diffusion operator eigenmodes which are explicitly known only for few geometries: slab, disk, sphere (and some simple extensions) [14]. The study of more complicated structures requires numerical simulations such as stochastic Monte-Carlo simulations [229, 230] or PDE solving with finite element or finite difference methods [231]. On top of being time-consuming these techniques give little theoretical insight into the dependence of the propagator on the physical parameters of the simulated medium. In this situation, one-dimensional models of heterogeneous systems partitioned by permeable barriers can help to uncover this dependence and to understand the role of diffusive exchange across the barriers. Note that three-dimensional diffusion in a stack of parallel planes with lateral invariance is naturally reduced to one-dimensional models. As a consequence, these models have a wide variety of applications, for example multilayer electrodes [232–234], coating of electronic components and improving the performance of semi-conductors [235–237], geophysics and thermal analyses of buildings [238–242], industrial processes [243–245], waste disposal and gas permeation in soils [246–249], drug delivery [250–252] and modeling tumor growth [253]. They can also be applied as approximation schemes for finding the spectrum of Sturm-Liouville problems where the coefficients of the differential operator are replaced by piecewise constant (or polynomial) functions (the so-called "Pruess method") [335–339]. Two applications of particular interest to us are diffusion magnetic resonance imaging (Sec. 3.4.5), and first-passage phenomena (Appendix B.2).

Because of this diversity of applications, many authors have more or less independently tackled such models of one-dimensional diffusion in heterogeneous structures, with various computational techniques: spectral decompositions, Green functions, Laplace transforms and others (see [15, 254] for a review of the subject). In this article we consider finite geometries, which are best treated by spectral decompositions (or "separation of variables"). To our knowledge, the most recent and complete work on this topic is the one by Hickson *et al* [231, 244, 245]. However it was mainly devoted to the case of heterogeneous structures with distinct diffusivities and without barriers. Moreover the spectrum was computed numerically and only few analytical results were obtained. On the other hand, some very general mathematical results were obtained by Gaveau *et al* for generic heterogeneous media without barriers [255]. Another technique was proposed in the recent work by Carr and Turner [256], in which the solution of Eq. (3.62) was decomposed on the Laplacian eigenmodes of each compartment separately, instead of the eigenmodes of the whole structure. This technique presents numerical advantages without providing analytical insights onto the spectrum of the diffusion operator.

In this section we present an efficient method to compute the eigenvalues and eigenfunctions of the diffusion operator in one-dimensional domains with multiple barriers. This method allows us to calculate the diffusion propagator and related quantities such as dMRI signal or first exit time distribution analytically for sufficiently regular geometries such as a finite periodic geometry or a microstructure inside a larger scale structure, and numerically for arbitrary structures.

This section is organized as follows. Section 3.4.2 is entirely devoted to analytics. We start with standard computations using transition matrices and obtain the equation of the spectrum as a transcendental equation $F(\lambda) = 0$ (Eq. (3.81)). Three following subsections are more technical; in particular, we express the normalization constant of the eigenmodes as a function of F (Eq. (3.94)), and we derive general consequences of the symmetry or the periodicity of the medium. Then we study in more detail the function F and obtain simple estimates of its roots with respect to the geometrical parameters of the medium, in particular the permeability of the barriers. This part is crucial for the numerical implementation of the method. This section is concluded with some extensions of our model. Section 3.4.3 illustrates our general approach on the example of a (finite) periodic structure with multiple identical barriers and compartments. The numerical implementation of the method is presented in Sec. 3.4.4. In particular, we discuss the major numerical challenges related to finding very close zeros of the eigenspectrum equation (3.81) and the proposed shortcuts based on the analytics from Sec. 3.4.2. Our computational technique is then applied to the computation of dMRI signal. We discuss thoroughly different regimes for the signal and with a focus on the effect of permeability of inner barriers. In Appendix B.2 the effect of permeable barriers on the diffusive motion is studied from another viewpoint, namely the first exit time distribution.

Some technical results are moved to Appendix B.3.1, which contains proofs of the existence of infinitely many eigenvalues, their non-degeneracy, their monotonic growth with respect to the barrier permeabilities, as well as a Courant nodal theorem for our particular model of diffusion with barriers.

3.4.2 Computation of the eigenmodes of the diffusion operator

General case

In this section we study the eigenmodes of the diffusion operator $\nabla(D_0\nabla)$ in a one-dimensional geometry (see Fig. 3.12). We reproduce the general computational scheme from Ref. [268] and propose improvements specific to the one-dimensional geometry. An interval $[0, L]$ is divided by barriers into m com-

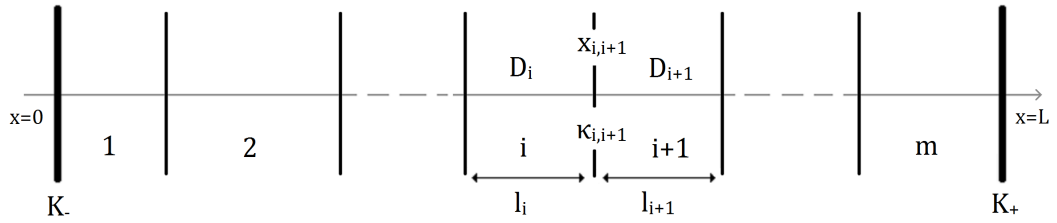

Figure 3.12: Illustration of the geometry. Arbitrarily spaced barriers split the interval $[0, L]$ into m compartments Ω_i of length l_i and diffusion coefficient D_i. The positions of the barriers are denoted by $x_{i,i+1}$ and their permeabilities by $\kappa_{i,i+1}$. One can also take into account relaxation or leakage at the two outer barriers by permeabilities K_-, K_+.

partments (or "cells") $\Omega_i = \left(x_{i-1,i}, x_{i,i+1}\right)$, $i = 1, \ldots, m$, where $x_{1,2}, \ldots, x_{m-1,m}$ are the positions of $m-1$ inner barriers, and $x_{0,1} = 0$ and $x_{m,m+1} = L$ correspond to the outer barriers. Each compartment is characterized by its length $l_i = x_{i,i+1} - x_{i-1,i} > 0$ and diffusion coefficient $D_i > 0$ and each barrier by its permeability $\kappa_{i,i+1} \geq 0$ or equivalently by its "resistance" to diffusive exchange: $r_{i,i+1} = 1/\kappa_{i,i+1}$. The endpoints 0 and L are characterized by non-negative permeabilities (or relaxaton coefficients) K_- and K_+, which can describe either impermeable inert boundaries (when $K_- = K_+ = 0$), or account for relaxation or leakage (when $K_-, K_+ > 0$). Note that the number of compartments, denoted m here, should not be confused with the magnetization.

The diffusion coefficient D_0 is thus a piecewise constant function:

$$D_0(x) = \sum_{i=1}^{m} D_i \mathbb{I}_{\Omega_i}(x), \tag{3.63}$$

where $\mathbb{I}_{\Omega_i}$ denotes the indicator function of Ω_i: $\mathbb{I}_{\Omega_i}(x) = 1$ if $x \in \Omega_i$ and 0 otherwise. This implies that the diffusion operator can be split into two terms:

$$\nabla(D_0\nabla) = D_0\nabla^2 + (\nabla D_0)\nabla = D_0\nabla^2 + \left(\sum_{i=1}^{m-1}(D_{i+1} - D_i)\delta(x - x_{i,i+1})\right)\nabla\ . \tag{3.64}$$

The second term vanishes at the interior points so that the diffusion operator is reduced to $D_0\nabla^2$. The same is true for the general class of diffusion operators $\nabla(D_0^\alpha \nabla(D_0^{1-\alpha}\,\cdot))$, where $0 \leq \alpha \leq 1$ is the Itô-Stratonovitch interpretation parameter (some authors use $1-\alpha$ instead of α) [309, 311]. Here we consider heterogeneous diffusion coefficients with discontinuities at the barriers, hence these operators coincide inside the compartments but yield different boundary conditions at the barriers. We discuss this technical point in Appendix D. Our choice

$\nabla(D_0\nabla)$ corresponds to the Hänggi-Klimontovich interpretation [312–316] with $\alpha = 1$, which is most often used in physical applications. The main reason is that it corresponds to the standard Fick law and that equilibrium solutions of the diffusion equation are constant, which is expected for, say, water diffusing in an isothermal medium. From a mathematical point of view, this choice ensures that the operator is self-adjoint, which allows us to use standard spectral methods.

The L^2-normalized eigenmodes u of the diffusion operator are then determined by the equation

$$D_0 u'' + \lambda u = 0 \,, \tag{3.65}$$

with the boundary conditions

$$D_i u'|_{\Omega_i} = D_{i+1} u'|_{\Omega_{i+1}} \qquad \text{at the barrier at } x_{i,i+1} \tag{3.66a}$$
$$D_i u'|_{\Omega_i} = \kappa_{i,i+1}(u|_{\Omega_{i+1}} - u|_{\Omega_i}) \qquad \text{at the barrier at } x_{i,i+1} \tag{3.66b}$$
$$D_1 u'(0) = K_- u(0) \tag{3.66c}$$
$$D_m u'(L) = -K_+ u(L) \,, \tag{3.66d}$$

and the normalization condition

$$\int_0^L u^2 = 1 \,, \tag{3.67}$$

where $u|_{\Omega_i}$ is the restriction of u to the cell Ω_i ($i = 1, \dots, m$) and prime denotes the derivative with respect to x.

If $\kappa_{i,i+1} = 0$ the compartments Ω_i and Ω_{i+1} do not communicate with each other: the flux is zero at the barrier and the discontinuity $(u|_{\Omega_{i+1}} - u|_{\Omega_i})(x_{i,i+1})$ is arbitrary. One can then study the two parts $[0, x_{i,i+1}]$ and $[x_{i,i+1}, L]$ separately. To avoid such trivial separations, we consider only non-zero permeabilities: $\kappa_{i,i+1} > 0$. Under this assumption we prove in Sec. B.3.1 that there are infinitely many eigenvalues λ_n, $n = 1, 2, \dots$, and all λ_n are simple. One can also easily prove that they are non-negative, and we sort them by ascending order: $0 \leq \lambda_1 < \lambda_2 < \dots$. Moreover, thanks to the self-adjointness of the diffusion operator $\nabla(D_0\nabla)$ we know that the eigenmodes u_n, $n = 1, 2, \dots$ form a complete orthonormal basis in the space $L^2(0, L)$ of square-integrable functions on $[0, L]$ [15, 254].

For simplicity we further assume that $K_- < \infty$, which allows us to write

$$u = \beta v \,, \quad v(0) = 1 \,, \tag{3.68}$$

with β being a normalization constant that ensures Eq. (3.67). The case of Dirichlet boundary conditions ($K_- = \infty$) requires another convention which is detailed in Sec. B.3.2. We study the (non-normalized) eigenmode v first and then we compute the normalization constant β.

Throughout this section we assume $\lambda \neq 0$. One can see that $\lambda = 0$ is only possible if the relaxation coefficients $K_\pm$ are equal to zero and in this case one gets a constant eigenmode $v = 1$ (and $\beta = 1/\sqrt{L}$).

Equation (3.65) has a general solution

$$v|_{\Omega_i}(x) = a_i^l \cos(\sqrt{\lambda/D_i}(x - x_{i-1,i})) + b_i^l \sin(\sqrt{\lambda/D_i}(x - x_{i-1,i})) \,, \tag{3.69}$$

or equivalently

$$v|_{\Omega_i}(x) = a_i^r \cos(\sqrt{\lambda/D_i}(x - x_{i,i+1})) + b_i^r \sin(\sqrt{\lambda/D_i}(x - x_{i,i+1})) \,, \tag{3.70}$$

where a_i^l, b_i^l and a_i^r, b_i^r are constants to be determined, related by

$$\begin{bmatrix} a_i^r \\ b_i^r \end{bmatrix} = \mathsf{R}_i \begin{bmatrix} a_i^l \\ b_i^l \end{bmatrix} \,, \qquad \mathsf{R}_i = \begin{bmatrix} \cos(\sqrt{\lambda/D_i} l_i) & \sin(\sqrt{\lambda/D_i} l_i) \\ -\sin(\sqrt{\lambda/D_i} l_i) & \cos(\sqrt{\lambda/D_i} l_i) \end{bmatrix} \,. \tag{3.71}$$

Note that

$$v|_{\Omega_i}(x_{i,i+1}) = a_i^r \,, \quad D_i v'|_{\Omega_i}(x_{i,i+1}) = \sqrt{\lambda D_i} b_i^r \,, \tag{3.72}$$

with similar formulas for a_i^l, b_i^l, so that one can write the boundary equations (3.66a) and (3.66b) as

$$\begin{bmatrix} a_{i+1}^l \\ b_{i+1}^l \end{bmatrix} = \mathsf{K}_{i,i+1} \begin{bmatrix} a_i^r \\ b_i^r \end{bmatrix} \,, \qquad \mathsf{K}_{i,i+1} = \begin{bmatrix} 1 & r_{i,i+1}\sqrt{\lambda D_i} \\ 0 & \sqrt{D_i/D_{i+1}} \end{bmatrix} \,. \tag{3.73}$$

The equations at the barriers can thus be restated in a matrix form:

$$\begin{bmatrix} a_{i+1}^l \\ b_{i+1}^l \end{bmatrix} = \mathsf{M}_{i,i+1} \begin{bmatrix} a_i^l \\ b_i^l \end{bmatrix} \,, \tag{3.74}$$

with the notation for the "transition matrix":

$$\mathsf{M}_{i,i+1} = \mathsf{K}_{i,i+1}\mathsf{R}_i \,, \tag{3.75}$$

with R_i and $\mathsf{K}_{i,i+1}$ defined by Eqs. (3.71), (3.73). In the same way, one can rewrite the endpoint conditions (3.66c), (3.66d):

$$\begin{bmatrix} -K_- & \sqrt{\lambda D_1} \end{bmatrix} \begin{bmatrix} a_1^l \\ b_1^l \end{bmatrix} = 0 \quad \text{and} \quad \begin{bmatrix} K_+ & \sqrt{\lambda D_m} \end{bmatrix} \begin{bmatrix} a_m^r \\ b_m^r \end{bmatrix} = 0 \,. \tag{3.76}$$

We have the additional condition $a_1^l = v(0) = 1$, therefore

$$\begin{bmatrix} a_1^l \\ b_1^l \end{bmatrix} = \begin{bmatrix} 1 \\ K_-/\sqrt{\lambda D_1} \end{bmatrix} \quad \text{and} \quad \begin{bmatrix} a_m^r \\ b_m^r \end{bmatrix} = \epsilon \begin{bmatrix} 1 \\ -K_+/\sqrt{\lambda D_m} \end{bmatrix} \,, \tag{3.77}$$

where ϵ is an unknown proportionality coefficient.

Equation (3.74), which relates the coefficients of one cell to those of the next cell, is compatible with Eq. (3.77), which prescribes the first and last cell coefficients (up to a proportionality factor), *only* if λ is an eigenvalue of the diffusion operator $\nabla(D_0\nabla)$. That is, by writing explicitly the condition that the product of all the transition matrices $\mathsf{M}_{i,i+1}$ should send the previously determined (a_1^l, b_1^l) onto the (a_m^l, b_m^l), we get the equation on the spectrum of the diffusion operator:

$$\mathsf{T}\begin{bmatrix} 1 \\ K_-/\sqrt{\lambda D_1} \end{bmatrix} = \epsilon \begin{bmatrix} 1 \\ -K_+/\sqrt{\lambda D_m} \end{bmatrix} , \tag{3.78}$$

with

$$\mathsf{T} = \mathsf{R}_m \mathsf{M}_{m-1,m} \dots \mathsf{M}_{1,2} . \tag{3.79}$$

Note that this condition is equivalent to

$$\begin{bmatrix} K_+/\sqrt{\lambda D_m} & 1 \end{bmatrix} \mathsf{T} = \eta \begin{bmatrix} -K_-/\sqrt{\lambda D_1} & 1 \end{bmatrix} , \tag{3.80}$$

and to

$$F(\lambda) := \begin{bmatrix} K_+/\sqrt{\lambda D_m} & 1 \end{bmatrix} \mathsf{T}(\lambda) \begin{bmatrix} 1 \\ K_-/\sqrt{\lambda D_1} \end{bmatrix} = 0 . \tag{3.81}$$

The proportionality coefficients ϵ and η are constrained by the relation: $\epsilon\eta = \det \mathsf{T} = \sqrt{\frac{D_1}{D_m}}$.

Computation of the norm

Now we compute the normalization constant β. Since the eigenmode v is a piecewise combination of sine and cosine functions, the constant β can be obtained by a direct integration (see Ref. [268]). This approach is convenient for numerical computations. Here we present another approach which is more suitable for analytical derivations. The starting point of the method is the spectral decomposition of the diffusion propagator:

$$\mathcal{G}(T, x_0, x) = \sum_{n=1}^{\infty} u_n(x_0) u_n(x) e^{-\lambda_n T} = \sum_{n=1}^{\infty} {\beta_n}^2 v_n(x_0) v_n(x) e^{-\lambda_n T} , \tag{3.82}$$

where $n = 1, 2, \dots$ spans the infinitely many eigenmodes of the diffusion operator. We now compute this propagator in a different way by solving explicitly Eq.

(3.62). Again, we use Eq. (3.64) to transform $\nabla(D_0\nabla)$ into $D_0\nabla^2$ at the interior points. Let $\hat{\mathcal{G}}(s, x_0, x)$ denote the Laplace transform of the propagator:

$$\hat{\mathcal{G}}(s, x_0, x) = \int_0^\infty e^{-st}\mathcal{G}(t, x_0, x)\,\mathrm{d}t \ . \tag{3.83}$$

Then $\hat{\mathcal{G}}$ obeys the equation

$$D_0(x)\hat{\mathcal{G}}''(s, x_0, x) = s\hat{\mathcal{G}}(s, x_0, x) - \delta(x - x_0) \ , \tag{3.84}$$

with the same boundary conditions (3.66a)-(3.66d) as for the propagator $\mathcal{G}$ in time domain. As in the previous section, prime denotes derivative with respect to x. We use the method from Sec. 3.4.2 to solve the homogeneous equation with the inner boundary conditions (3.66a), (3.66b) imposed at the barriers: if $s \neq 0$ we can build two solutions $\phi(s, x)$ and $\psi(s, x)$ such that:

- $\phi(s, x)$ is built from $\begin{bmatrix} a_1^l \\ b_1^l \end{bmatrix} = \begin{bmatrix} 1 \\ 0 \end{bmatrix}$: at the left endpoint its derivative with respect to x is zero and its value is one.
- $\psi(s, x)$ is built from $\begin{bmatrix} a_1^l \\ b_1^l \end{bmatrix} = \begin{bmatrix} 0 \\ 1 \end{bmatrix}$: at the left endpoint its derivative with respect to x is $\sqrt{s/D_1}$ and its value is zero.

It is then easy to obtain the complete solution because the Wronskian matrix

$$\mathrm{W} = \begin{bmatrix} \phi(s, x) & \psi(s, x) \\ \phi'(s, x) & \psi'(s, x) \end{bmatrix} \tag{3.85}$$

is quite simple. Indeed over any layer Ω_i the determinant of W is constant and equal to $\sqrt{sD_1}/D_i$. This is obtained from the differential equation obeyed by $\phi(s, x)$ and $\psi(s, x)$ and the boundary conditions at each barrier. The standard method for solving the second order differential equations then yields

$$\hat{\mathcal{G}} = \mu\phi + \nu\psi \ , \tag{3.86}$$

with the equation on μ, ν:

$$D_0(x)\begin{bmatrix} \mu'(s, x) \\ \nu'(s, x) \end{bmatrix} = \mathrm{W}^{-1}\begin{bmatrix} 0 \\ -\delta(x - x_0) \end{bmatrix} = -\frac{D_0(x)}{\sqrt{D_1 s}}\delta(x - x_0)\begin{bmatrix} -\psi(s, x) \\ \phi(s, x) \end{bmatrix} \ . \tag{3.87}$$

After a straightforward integration, we obtain

$$\hat{\mathcal{G}}(s,x_0,x) = \left(A + \frac{1}{\sqrt{D_1 s}}\psi(s,x_0)H(x-x_0)\right)\phi(s,x) + \left(B - \frac{1}{\sqrt{D_1 s}}\phi(s,x_0)H(x-x_0)\right)\psi(s,x)\ , \tag{3.88}$$

which is valid for any $x_0, x \in [0,L]$, and $s \neq 0$, where H is the Heaviside function and the constants A and B remain to be determined. We consider general relaxing conditions at the endpoints:

$$D\begin{cases} {}_1\partial_x\hat{\mathcal{G}}(x=0) = K_-\hat{\mathcal{G}}(x=0)\ , & \text{(3.89a)} \\ D_m\partial_x\hat{\mathcal{G}}(x=L) = -K_+\hat{\mathcal{G}}(x=L)\ , & \text{(3.89b)} \end{cases}$$

from which

$$A = \frac{\phi(s,x_0)(D_m\psi'(s,L)+K_+\psi(s,L)) - \psi(s,x_0)(D_m\phi'(s,L)+K_+\phi(s,L))}{D_mK_-\psi'(s,L)+K_+K_-\psi(s,L)+D_m\sqrt{D_1 s}\phi'(s,L)+K_+\sqrt{D_1 s}\phi(s,L)}\ , \tag{3.90a}$$

$$B = \frac{K_-A}{\sqrt{D_1 s}}\ . \tag{3.90b}$$

Now we simplify the above expressions. We anticipate that the non-normalized eigenmodes are $v_n(x) = v(\lambda_n,x)$, with

$$v(s,x) = \phi(s,x) + \frac{K_-}{\sqrt{D_1 s}}\psi(s,x)\ , \tag{3.91}$$

and we use Eq. (3.72) to get

$$A\phi(s,x) + B\psi(s,x) = \frac{v(s,x)\phi(s,x_0)}{K_-} - \frac{\sqrt{D_1 s}}{K_-}v(s,x)v(s,x_0)\frac{\begin{bmatrix} K_+ & \sqrt{D_m s}\end{bmatrix}\mathsf{T}(s)\begin{bmatrix}1\\0\end{bmatrix}}{F(s)}\ , \tag{3.92}$$

with T and F defined in Eqs. (3.79), (3.81), respectively, in which λ is replaced by s. To obtain the propagator in time domain, one needs to perform an inverse Laplace transform. This is done by looking for the poles $s = \lambda_n$ of $\hat{\mathcal{G}}$ and the above formula shows that they are given by the zeros of $F(s)$, as expected. We

prove in Sec. B.3.1 that these zeros are simple. At $s = \lambda_n$, one can use Eqs. (3.78) and (3.80) to compute the residue of $\hat{\mathcal{G}}$, which yields simply

$$\mathrm{Res}_{s=\lambda_n}(\hat{\mathcal{G}}) = \left.\frac{-\eta_n\sqrt{D_1 s}\, v(s,x)v(s,x_0)}{\frac{\mathrm{d}F}{\mathrm{d}s}}\right|_{s=\lambda_n} . \tag{3.93}$$

Note that this computation actually *proves* that the propagator $\mathcal{G}(t, x_0, x)$ can be written as the eigenmode decomposition (3.82), and one can identify the normalization coefficient:

$$\beta_n{}^{-2} = -\frac{1}{\eta_n\sqrt{D_1\lambda_n}}\frac{\mathrm{d}F}{\mathrm{d}\lambda}(\lambda_n) . \tag{3.94}$$

In general, one obtains η_n by computing the matrix product in Eq. (3.80). A great simplification occurs in the case of symmetric geometries, which is the topic of the next section.

Symmetry properties

For a geometry which is symmetric with respect to the middle of the interval $[0, L]$, some simplifications occur. In fact the symmetry of the geometry implies that the eigenmodes are either symmetric or anti-symmetric with respect to the middle of the interval, and as a consequence $\epsilon = \eta = +1$ or $\epsilon = \eta = -1$, respectively. These statements can be easily proved with the above matrix formalism. In fact, the symmetry of the geometry is equivalent to the two properties:

1. The endpoints vectors $\mathsf{V}_+ = \begin{bmatrix} 1 \\ -K_+/\sqrt{\lambda D_1} \end{bmatrix}$ and $\mathsf{V}_- = \begin{bmatrix} 1 \\ K_-/\sqrt{\lambda D_m} \end{bmatrix}$ have equal first components and opposite second components, which follows from the symmetry $K_- = K_+$, $D_1 = D_m$. With the notation $\mathsf{S} = \begin{bmatrix} 1 & 0 \\ 0 & -1 \end{bmatrix}$, this can be restated as $\mathsf{V}_\pm = \mathsf{S}\mathsf{V}_\mp$.
2. The inverse of the transition matrix T is obtained by replacing the off-diagonal terms by their opposite in its expression (note that this corresponds to the transformation $\sqrt{\lambda} \to -\sqrt{\lambda}$). In fact, this property is clearly true for the "elementary blocks" K and R and thus it is also the case for $\mathsf{R}_m\mathsf{K}_{m-1,m}\mathsf{R}_{m-1}\ldots\mathsf{K}_{1,2}\mathsf{R}_1$ because $\mathsf{R}_i = \mathsf{R}_{m+1-i}$ and $\mathsf{K}_{i,i+1} = \mathsf{K}_{m-i,m+1-i}$. In other words, $\mathsf{T}^{-1} = \mathsf{STS}$.

The consequence of these two properties is that Eq. (3.78) can be restated as: "V_- is an eigenvector of ST" and that this matrix is equal to its inverse:

$$(\mathsf{ST})^{-1} = \mathsf{T}^{-1}\mathsf{S}^{-1} = \mathsf{ST} . \tag{3.95}$$

This implies that the eigenvalues of this matrix, hence the proportionality coefficients ϵ, η in Eqs. (3.78) and (3.80), are equal to ± 1. We can also easily prove the symmetry or anti-symmetry of the eigenmodes. In fact, one has

$$\begin{bmatrix} a_i^l \\ b_i^l \end{bmatrix} = \mathsf{K}_{i-1,i}\mathsf{R}_{i-1}\dots\mathsf{R}_1\mathsf{V}_- \tag{3.96a}$$

$$\begin{bmatrix} a_{m+1-i}^r \\ b_{m+1-i}^r \end{bmatrix} = \mathsf{K}_{m+1-i,m+2-k}^{-1}\mathsf{R}_{m+2-k}^{-1}\dots\mathsf{R}_m^{-1}\epsilon\mathsf{V}_+ \tag{3.96b}$$

Hence

$$\begin{bmatrix} a_{m+1-i}^r \\ b_{m+1-i}^r \end{bmatrix} = \mathsf{S}\mathsf{K}_{i-1,i}\mathsf{S}\mathsf{S}\mathsf{R}_{i-1}\mathsf{S}\dots\mathsf{S}\mathsf{R}_1\mathsf{S}\epsilon\mathsf{V}_+ = \epsilon\mathsf{S}\begin{bmatrix} a_i^l \\ b_i^l \end{bmatrix} . \tag{3.97}$$

Let $x \in \Omega_i$, we write $x = x_{i-1,i} + \xi$, with $0 < \xi < l_i$, which implies by symmetry that $L - x = x_{m+1-i,m+2-i} - \xi$. According to Eqs. (3.69), (3.70), and (3.97), we have then

$$v(x) = \begin{bmatrix} a_i^l & b_i^l \end{bmatrix}\begin{bmatrix} \cos(\xi\sqrt{\lambda/D_i}) \\ \sin(\xi\sqrt{\lambda/D_i}) \end{bmatrix} \tag{3.98a}$$

$$= \epsilon\begin{bmatrix} a_{m+1-i}^r & b_{m+1-i}^r \end{bmatrix}\begin{bmatrix} \cos(-\xi\sqrt{\lambda/D_{m+1-i}}) \\ \sin(-\xi\sqrt{\lambda/D_{m+1-i}}) \end{bmatrix} = \epsilon v(L-x) , \tag{3.98b}$$

since $D_i = D_{m+1-i}$. Therefore the eigenmode is symmetric if $\epsilon = +1$ and anti-symmetric if $\epsilon = -1$. Moreover from Eq. (3.94) we deduce that the derivative $\frac{\mathrm{d}F}{\mathrm{d}\lambda}(\lambda_n)$ and η_n have opposite signs. Because the eigenvalues λ_n are the zeros of F, the derivative alternates between positive and negative sign, and so do η_n and ϵ_n. In particular, in the case of a symmetric geometry, the modes u_n are alternately symmetric and anti-symmetric. One can show that the first mode u_1 is always symmetric ($\epsilon_1 = \eta_1 = 1$), hence

$$\epsilon_n = \eta_n = (-1)^{n-1} . \tag{3.99}$$

Periodicity properties

A finite periodic geometry is an M-times repetition of an elementary block composed of N compartments: $(D_1; l_1)$, $(D_2; l_2)$, …, $(D_N; l_N)$. The transition matrix of the block is

$$\mathsf{M} = \mathsf{K}_{\text{inter}}\mathsf{R}_N\mathsf{K}_{N-1,N}\dots\mathsf{R}_1 , \tag{3.100}$$

where $\mathsf{K}_{\text{inter}}$ is the matrix corresponding to the inter-block barriers. Then the complete transition matrix T is equal to

$$\mathsf{T} = \mathsf{K}_{\text{inter}}^{-1}\mathsf{M}^M \ . \tag{3.101}$$

Because of the periodicity,

$$\det \mathsf{M} = \underbrace{\sqrt{\frac{D_N}{D_1}}}_{\det \mathsf{K}_{\text{inter}}} \sqrt{\frac{D_{N-1}}{D_N}} \cdots \sqrt{\frac{D_1}{D_2}} = 1 \ . \tag{3.102}$$

This property makes the computation of M^M easier, thanks to the formula

$$\mathsf{M}^M = \frac{\sin M\psi}{\sin \psi}\mathsf{M} - \frac{\sin(M-1)\psi}{\sin \psi}\mathsf{I}_2 \ , \tag{3.103}$$

where I_2 is the 2×2 identity matrix and ψ is implicitly defined by

$$\cos \psi = \frac{1}{2}\mathrm{Tr}\mathsf{M} \ . \tag{3.104}$$

Formula (3.103) implies that the inter-block variation of the coefficients a, b has the form:

$$a_{i_0+N(j-1)} = A\cos(j\psi) + B\sin(j\psi) \ , \qquad j = 1, \ldots, M \ , \tag{3.105}$$

with a similar formula for b, where A and B are coefficients which depend on the choice of the origin $i_0 \in \{1, \ldots, N-1\}$. Thus ψ governs the global behavior of the mode (when the number M of repeated blocks is sufficiently large).

Study of the spectrum

The main numerical difficulty of the above method is to solve Eq. (3.81) on the spectrum, that is to find the zeros of $F(\lambda)$. In fact, a standard method to find *all* the zeros of a function in a given interval is to compute the function on a fine set of points $(0, \epsilon, 2\epsilon, \ldots)$ and to look for the sign changes, that indicate the presence of at least one zero. By decreasing ϵ, one is assured at some point to find all the zeros of the function. However, in general one knows neither the number of zeros of the function in a given interval nor the minimal spacing between the zeros. In turn, missing some zeros would result in missed eigenmodes, and thus in inaccurate computation of the propagator and the related diffusion quantities. An example of $F(\lambda)$ shown in Fig. 3.13 illustrates that some roots may be very

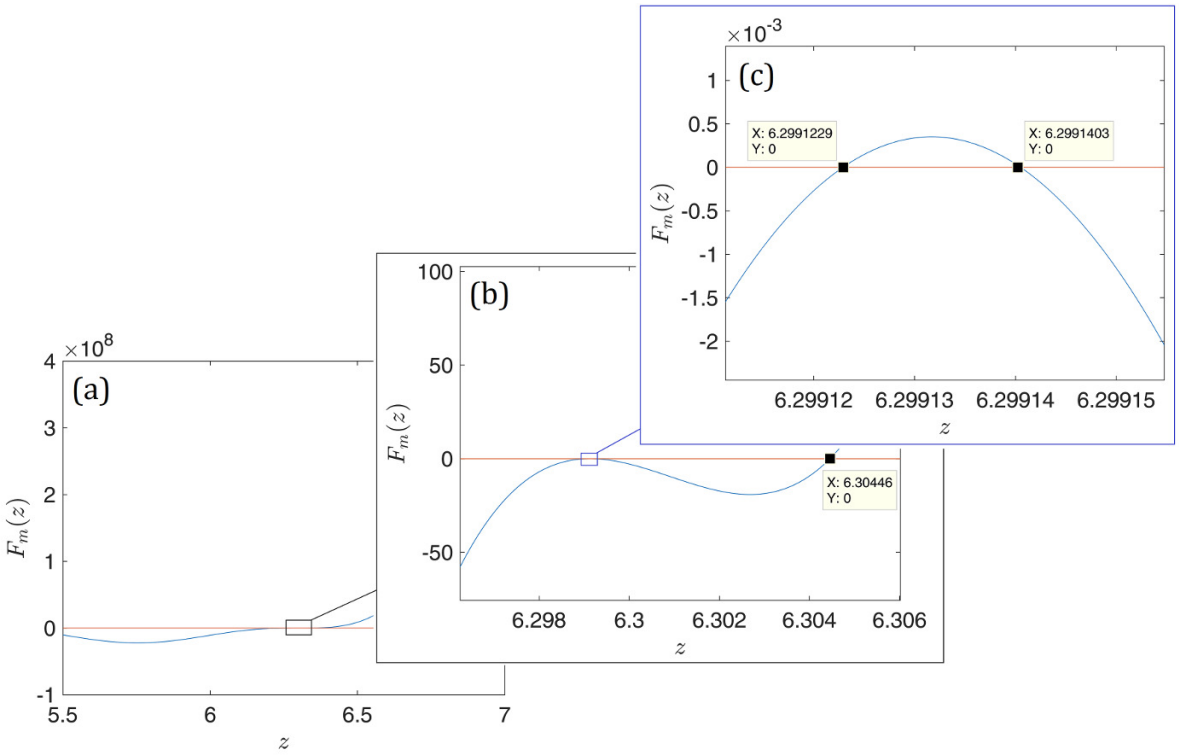

Figure 3.13: Example of roots which may prove challenging to find numerically with standard methods. We consider five compartments and $D_1 = \ldots = D_5 = 1$, $r_{1,2} = \ldots = r_{4,5} = 10$ and the lengths l_i of the five compartments are: 1; 1.2; 1.5; 1.2; 1, with reflecting boundary conditions at the endpoints: $K_\pm = 0$. The root $z = 6.30446$ (b) corresponds to $l_3 = 1.5$, with $n = 3$, $\zeta = 2$, whereas the two roots $z_\pm = 6.2991316 \pm 8.7 \cdot 10^{-6}$ (c) correspond to $l_1 = l_5 = 1$, with $n = 2$, $\zeta = 1$ (see explanations in the text). Notice the scale changes, horizontally and vertically, between (a), (b) and (c).

close to each other. We provide here a rough analysis of Eq. (3.81) in order to study this phenomenon.

We discard the elementary case of a single interval ($m = 1$) where the roots of F are explicitly known [12, 13]. Let us assume for simplicity that all the diffusion coefficients D_i and the barrier resistances $r_{i,i+1}$ are identical (denoted D_0 and r, respectively). Furthermore we set the relaxation coefficients $K_\pm$ to zero. We change the variable λ by $z = \sqrt{\lambda/D_0}$ and reveal an explicit dependence of F on the geometry (omitting D_0 and r for the sake of clarity):

$$F(\lambda) = F_m(z; l_1, \ldots, l_m) \ . \tag{3.106}$$

Regime $r \to 0$. This is the regime of almost fully-permeable barriers (i.e. "quasi-no-barrier" case). One has

$$\mathsf{K} = \mathsf{I}_2 + rD_0 z \mathsf{N} , \quad \mathsf{N} = \begin{bmatrix} 0 & 1 \\ 0 & 0 \end{bmatrix} , \tag{3.107}$$

from which we deduce the first-order expansion

$$F_m(z; l_1, \ldots, l_m) \approx -\sin(zL) + rD_0 z \sum_{i=1}^{m} \sin(z(l_1 + \cdots + l_i)) \sin(z(l_{i+1} + \cdots + l_m)) . \tag{3.108}$$

This formula implies that the roots are approximately equal to $z_0 = n\pi/L$, with an integer n. In fact, one can compute the first order correction to this formula, which yields

$$z \approx \frac{n\pi}{L} \left(1 - \frac{rD_0}{l_\mathrm{a}} \left[\frac{1}{m} \sum_{i=1}^{m} \sin^2 \left(n\pi \frac{l_1 + \cdots + l_i}{L} \right) \right] \right), \tag{3.109}$$

where $l_\mathrm{a} = L/m$ is the arithmetic mean of the l_i. The factor inside the brackets is always less than 1, hence the (first order) relative perturbation of the roots is at most rD_0/l_a. Therefore in the regime of almost fully-permeable inner barriers ($rD_0/l_\mathrm{a} \ll 1$) the roots are easy to find numerically because we have a good estimate of their position and a good lower bound of the distance between them. Note that $rD_0/l_\mathrm{a} \ll 1$ corresponds to diffusion control, where the time taken by a particle to reach a barrier is much larger than the time taken to cross it, as we discussed in Sec. 3.1.2.

Regime $r \to \infty$. Now we turn to the opposite regime of almost impermeable barriers, i.e. permeation control. In this case one writes

$$\mathsf{K} = rD_0 z \left(\mathsf{N} + \frac{1}{rD_0 z} \mathsf{I}_2 \right) . \tag{3.110}$$

For z large enough such that $rD_0 z \gg 1$, this yields

$$\begin{aligned} F_m(z; l_1, \ldots, l_m) \approx\ & (-rD_0 z)^{m-1} \sin(zl_1) \cdots \sin(zl_m) \\ & \times \left(1 - \frac{1}{rD_0 z} \sum_{i=1}^{m-1} \frac{\sin(z(l_i + l_{i+1}))}{\sin(zl_i) \sin(zl_{i+1})} + \ldots \right) . \end{aligned} \tag{3.111}$$

From this expression one gets the approximate roots $z_0 = n\pi/l_i$ with an integer n, as expected. The non-zero permeability of the barriers increases the values of the

roots by coupling the compartments to their nearest neighbors. The higher-order terms of the expansion (3.111) involve coupling between next-nearest neighbors, etc. From the above formula we expect the increase to be of order $(rD_0z_0)^{-1}$. The case $n = 0$ (that is, $z_0 = 0$) is special and we treat it later. Note that the above expansion is valid around $z_0 = n\pi/l_i$ (with $n > 0$) if $rD_0z_0 \gg 1$, that is $rD_0/l_i \gg 1$.

If we consider an *isolated* root $z_0 = n\pi/l_i$ (which means that all the other $n'\pi/l_{i'}$ are located at a relative distance much greater that $(rD_0z_0)^{-1}$), then we get

$$z \approx \frac{n\pi}{l_i} + \frac{\zeta_i}{n\pi r D_0}, \tag{3.112}$$

where ζ_i is the number of neighbors of the cell i ($\zeta_i = 2$ if $1 < i < m$, otherwise $\zeta_i = 1$).

The case of *non-isolated* roots is more complicated but also more interesting. In fact all the numerical difficulties come from this case. From the equation

$$\mathsf{R}_i \begin{bmatrix} 1 \\ 0 \end{bmatrix} \begin{bmatrix} 0 & 1 \end{bmatrix} \mathsf{R}_i - \begin{bmatrix} 1 \\ 0 \end{bmatrix} \begin{bmatrix} 0 & 1 \end{bmatrix} = -\sin(zl_i)\mathsf{R}_i \,, \tag{3.113}$$

we deduce the following general relation which is valid for any i from 1 to $m-1$:

$$F_m(z; l_1, \ldots, l_m) = \frac{\begin{bmatrix} F_i(z; l_1, \ldots, l_i)F_{m+1-i}(z; l_i, \ldots, l_m) \\ \quad - F_{i-1}(z; l_1, \ldots, l_{i-1})F_{m-i}(z; l_{i+1}, \ldots, l_m) \end{bmatrix}}{F_1(z; l_i)}. \tag{3.114}$$

Now we assume that there exist $i_1 < i_2$ such that

$$z_0 = \frac{n_1\pi}{l_{i_1}} = \frac{n_2\pi}{l_{i_2}} \,, \tag{3.115}$$

with n_1, n_2 integers. Note that $n_1/n_2 = l_{i_1}/l_{i_2}$. We look for an approximate root of the form $z = z_0(1+\eta)$, with $\eta \sim (rD_0z_0)^{-1}$ (where $\sim$ means "is of the same order of magnitude as").

First let us consider the case where two compartments i_1 and i_2 are not neighbors, that is $i_1 + 1 < i_2$. From Eq. (3.111) we infer

$$F_{i_1+1}(z; l_1, \ldots, l_{i_1+1}) \sim (rD_0z)^{i_1}\eta \sim (rD_0z)^{i_1-1} \,, \tag{3.116a}$$
$$F_{m-i_1}(z; l_{i_1+1}, \ldots, l_m) \sim (rD_0z)^{m-1-i_1}\eta \sim (rD_0z)^{m-2-i_1} \,, \tag{3.116b}$$
$$F_{i_1}(z; l_1, \ldots, l_{i_1}) \sim (rD_0z)^{i_1-1}\eta \sim (rD_0z)^{i_1-2} \,, \tag{3.116c}$$
$$F_{m-1-i_1}(z; l_{i_1+2}, \ldots, l_m) \sim (rD_0z)^{m-2-i_1}\eta \sim (rD_0z)^{m-3-i_1} \,, \tag{3.116d}$$

hence Eq. (3.114) becomes

$$F_m(z;l_1,\dots,l_m) = \frac{F_{i_1}(z;l_1,\dots,l_{i_1}) \times F_{m+1-i_1}(z;l_{i_1},\dots,l_m)}{F_1(z;l_{i_1})} \left(1+O((rD_0z)^{-2})\right). \tag{3.117}$$

We deduce that the roots of $F_m(z;l_1,\dots,l_m)$ are given by the roots of the functions $F_{i_1}(z;l_1,\dots,l_{i_1})$ and $F_{m+1-i_1}(z;l_{i_1},\dots,l_m)$, which are not coupled to the first order in $(rD_0z)^{-1}$:

$$z \approx z_0 + \frac{\zeta_{i_1}}{n_1\pi r D_0} \quad \text{and} \quad z \approx z_0 + \frac{\zeta_{i_2}}{n_2\pi r D_0}\,. \tag{3.118}$$

Note that the same is true for any number of "coinciding" roots as long as they correspond to non-adjacent compartments. The roots are at a relative distance of order $(rD_0z_0)^{-1}$ if $n_1/\zeta_{i_1} \neq n_2/\zeta_{i_2}$. If $n_1/\zeta_{i_1} = n_2/\zeta_{i_2}$ one has to compute the next-order corrections which involve the length of the other compartments, as explained previously. One can show that the term of order $(rD_0z_0)^{i_1-i_2}$ is always non-zero; for symmetric geometries $(rD_0z_0)^{i_1-i_2}$ may be the first non-zero term of the expansion of the relative difference of the roots.

Now we consider the case $i_2 = i_1 + 1$. We use Eq. (3.111) to get

$$F_m(z;l_1,\dots,l_m) \approx (-rD_0z)^{m-3} \left(\prod_{i\neq i_1,i_1+1} \sin(zl_i)\right) \times \left(n_1n_2X^2 - (\zeta_{i_1}n_1+\zeta_{i_2}n_2)X + (\zeta_{i_1}\zeta_{i_2}-1)\right)\,, \tag{3.119}$$

where $X = rD\pi\eta$. Thus we obtain two roots:

$$z_\pm = z_0 + \frac{X_\pm}{rD_0\pi}\,, \tag{3.120a}$$

$$X_\pm = \frac{\zeta_{i_1}n_1+\zeta_{i_2}n_2 \pm \sqrt{(\zeta_{i_1}n_1-\zeta_{i_2}n_2)^2+4n_1n_2}}{2n_1n_2}\,. \tag{3.120b}$$

Note that $z_+ - z_- \geq \frac{2}{\pi\sqrt{n_1n_2}rD_0}$. One can perform the same computations for a larger number of adjacent cells with "coinciding" roots: at the end one has to solve a polynomial equation in the variable X. The roots are always distinct and separated by a relative distance of order $(rD_0z_0)^{-1}$. Section 3.4.3 is devoted to the exact computation of the roots for an array of identical cells, which is a good example of such a situation.

In all the above computations we assumed $z_0 = n\pi/l_i$ with positive n. However there are also m roots located near zero. To find them we expand the sine and cosine functions in Eq. (3.111) and get to the first order in zl_h a polynomial

equation of degree m in the variable $Z = rD_0 l_\mathrm{h} z^2$, where $l_\mathrm{h} = m\left(\sum_{i=1}^m l_i^{-1}\right)^{-1}$ is the harmonic mean of the l_i. Hence we obtain m roots of the form:

$$z_n = \sqrt{\frac{Z_n}{rD_0 l_\mathrm{h}}}\,, \quad n = 1, \ldots, m \tag{3.121}$$

with Z_n spanning the solutions of the polynomial equation. Note that we assumed $rD_0/l_i \gg 1$ hence one has $zl_\mathrm{h} \ll 1$, which legitimates *a posteriori* the polynomial expansion. Furthermore, the first coefficients of the polynomial expansion are readily available from Eq. (3.111) and we get from them that:

$$\sum_{n=1}^{m} Z_n \approx 2m\,. \tag{3.122}$$

This formula is valid in the regime $rD_0/l_\mathrm{h} \gg 1$ and its simplicity comes from the particular choice of l_h we made (harmonic mean of the l_i). If one assumes that the roots Z_n are approximately equispaced at small n, then one obtains immediately that the first roots Z_n, and hence λ_n, follow a $1/m^2$ dependence on m.

From this analysis of the low permeability regime ($rD_0/l_i \gg 1$ for all i) we can draw several conclusions, partly illustrated in Fig. 3.13.

- the m first roots ($zl_\mathrm{h} \ll 1$) behave differently than the other ones. They typically spread over a distance $(rD_0 l_\mathrm{h})^{-1/2}$.

The following points only apply to the other roots ($zl_\mathrm{h} \gtrsim 1$).

- all the roots increase from their limits $z_0 = n\pi/l_i$ with the permeability of the inner barriers (a general mathematical proof of this statement is given in Sec. B.3.1). The relative increase is of the first order in $(rD_0 z_0)^{-1}$;

- very close roots associated to adjacent cells are coupled by the permeability of their barrier and separate from each other by a relative distance of order $(rD_0 z_0)^{-1}$;

- very close roots associated to non-adjacent cells are not coupled to the first order in $(rD_0 z)^{-1}$. The difficult case is when the two cells have the same length: then $n_1 = n_2$ and the relative distance between the two roots is in the best case of order $(rD_0 z_0)^{-2}$. In fact, it depends on the length of all other cells. For example, symmetric geometries typically lead to a relative distance between roots of order $(rDz_0)^{-|i_2 - i_1|}$.

All the previous computations are somewhat schematic because we made a particular choice of geometry (same diffusion coefficients, same permeability and

no relaxation at the outer boundaries) from the beginning. However, the above conclusions are globally still valid in the general case, with appropriate modifications. For example if one considers perfectly relaxing condition at the endpoints ($K_\pm = \infty$), then in the low-permeability limit the roots corresponding to the outer compartments are $z_0 = (n + 1/2)\pi/l_i$ ($i = 1$ or m), whereas the roots corresponding to the other compartments are $z_0 = n\pi/l_i$, $1 < i < m$ (with an integer n). Thus one has to consider separately the case of the outer compartments depending on the conditions at the outer boundaries. We come back to the relaxing case in Appendix B.2 and Appendix B.3.2. Moreover, the case of heterogeneous diffusion coefficients is treated analytically in the simplest case of a bi-periodic structure in Appendix B.3.3.

Extensions

The above analysis may be extended in many ways. First, one can consider more general boundary conditions. In particular, many experiments in heat conduction are done with one end of the system in contact with a heat source (acting as a constant heat flux or as a thermostat with a constant temperature). One should then replace our homogeneous outer boundary conditions (3.66c), (3.66d) by inhomogeneous boundary conditions. The only difference is in the steady-state solution ($\lambda = 0$) which is easy to obtain, whereas the transient solution remains the same (see also [244, 254]). One is then often interested in the "critical time", i.e. the typical time required to reach the steady-state solution. More precisely, one definition of the critical time is the time at which the average temperature over the sample is equal to some fraction $\alpha < 1$ of the average steady-state temperature over the sample. Other definitions and a thorough comparison of these definitions are detailed in [257, 258]. This time is essentially given by the study of the first non-zero eigenvalue of the diffusion operator, for which we are able to obtain estimates with respect to the geometrical parameters of the medium (such as Eq. (3.121), which yields $\lambda \sim (r l_\mathrm{h} m^2)^{-1}$, in the low-permeability regime). The situation is different when the boundaries are subject to modulated heating, which is the case in geophysics and building design [238–242], and in photothermal measurements [236, 237]. One can still transform the problem into an homogeneous boundary problem but it requires adding a suitable source term to the diffusion equation [254]. In some cases the main mechanism of heat relaxation at the outer boundaries is not conduction-convection but radiation, with a non-linear T^4 heat flux [261]. Finally, when considering diffusion of ions in multilayer chemical system such as electrodes, one writes chemical equilibrium condition at the interfaces: the ratio of concentrations on both sides of the interface is equal to the partition coefficient [232–234, 259, 260]. This is another type

of inner boundary condition, which leads to different K matrices, quite similar to the case of heterogeneous diffusion coefficients and no barriers.

Another possible generalization is the inclusion of bulk reaction rates inside the compartments. That is, to change Eq. (3.62) to a reaction-diffusion equation:

$$\partial_T \mathcal{G} = \nabla(D_0 \nabla \mathcal{G}) + \mu \mathcal{G} \,, \tag{3.123}$$

where μ may depend on space and $\mathcal{G}$ [257]. If μ is constant, then one gets the solution of Eq. (3.123) by multiplying the solution of Eq. (3.62) by $\exp(\mu t)$. The case of piecewise constant μ ($\mu = \mu_i$ on Ω_i) is slightly more complicated but may be easily incorporated into our computations. Such reaction-diffusion models may describe diffusion of molecules that can be trapped, killed, destroyed, or loose their activity [262, 263, 286–288] ($\mu < 0$) or, on the opposite, self-heating by temperature-induced oxidation [264] ($\mu > 0$). Other applications include ecology dynamics [265] and fabrication of multilayer foil materials [266, 267].

Last, one can consider other equations than the diffusion equation (3.62), for example:

- inhomogeneous Laplace (Poisson) equation: $\nabla(D_0 \nabla \Psi) = F$,
- inhomogeneous Helmholtz ($s > 0$) or modified Helmholtz ($s < 0$) equations: $(s + \nabla D_0 \nabla)\Psi = F$,
- inhomogeneous diffusion equation: $\partial_T \Psi - \nabla(D_0 \nabla \Psi) = F$, with initial condition $\Psi(x, T = 0) = U(x)$,
- inhomogeneous wave equation: $\partial_T^2 \Psi - \nabla(D_0 \nabla \Psi) = F$, with initial conditions $\Psi(x, T = 0) = U(x)$ and $\partial_T \Psi(x, T = 0) = V(x)$,

where F, U, V are given functions, and with the boundary conditions (3.66a), (3.66b), (3.66c), and (3.66d). Thanks to the knowledge of the eigenmodes basis of the diffusion operator $\nabla(D_0 \nabla)$, the above equations may be solved by decomposing u and F over this basis [12, 13].

The computational method that we presented is therefore relevant to many models and applications. Our main concern is application to dMRI, that is presented in detail in Sec. 3.4.5. We also discuss briefly first-exit time distribution in Appendix B.2.

3.4.3 Example: simple periodic geometry

In this section, we illustrate the application of our general method to the case of a (finite) periodic structure which is relevant for various applications. Throughout this section, we assume that all l_i, D_i, $\kappa_{i,i+1}$ are the same (denoted ℓ_s, D_0, κ

in the following). We apply the results of Sec. 3.4.2 and obtain the eigenmodes and eigenvalues u_n, λ_n. Similar computations for more complicated structures are presented in Sec. B.3.3 (bi-periodic geometry) and Sec. B.3.4 (two-scale geometry).

Eigenmodes

We assume reflecting boundary conditions at the endpoints ($K_\pm = 0$) and introduce the dimensionless parameters

$$\alpha = \ell_s\sqrt{\lambda/D_0} \qquad \text{and} \qquad \tilde{r} = 1/\tilde{\kappa} = rD_0/\ell_s = \ell_\kappa/\ell_s \ . \tag{3.124}$$

We recall that the parameter $\tilde{r}$ controls the transition between diffusion control ($\tilde{r} \ll 1$) and permeation control ($\tilde{r} \gg 1$), see Sec. 3.1.2. With these notations, the transition matrix of the elementary block is simply

$$\mathsf{M} = \mathsf{KR} = \begin{bmatrix} \cos\alpha - \tilde{r}\alpha\sin\alpha & \sin\alpha + \tilde{r}\alpha\cos\alpha \\ -\sin\alpha & \cos\alpha \end{bmatrix} , \tag{3.125}$$

and Eq. (3.78) on the spectrum becomes

$$\mathsf{K}^{-1}\mathsf{M}^m \begin{bmatrix} \alpha \\ 0 \end{bmatrix} = \epsilon \begin{bmatrix} \alpha \\ 0 \end{bmatrix} . \tag{3.126}$$

Since the geometry is symmetric, we already know that $\epsilon = \pm 1$. Furthermore we use the results of Sec. 3.4.2 to compute M^m: first we apply Eq. (3.104) to define ψ:

$$\cos\psi = \cos\alpha - \frac{\tilde{r}}{2}\alpha\sin\alpha \ , \tag{3.127}$$

then from Eq. (3.103), we get

$$\mathsf{M}^m = \begin{bmatrix} (\cos\alpha - \tilde{r}\alpha\sin\alpha)\frac{\sin m\psi}{\sin\psi} - \frac{\sin(m-1)\psi}{\sin\psi} & (\sin\alpha + \tilde{r}\alpha\cos\alpha)\frac{\sin m\psi}{\sin\psi} \\ -\sin\alpha\frac{\sin m\psi}{\sin\psi} & \cos\alpha\frac{\sin m\psi}{\sin\psi} - \frac{\sin(m-1)\psi}{\sin\psi} \end{bmatrix} . \tag{3.128}$$

Equation (3.126) can be further simplified by using the fact that $\mathsf{K}\begin{bmatrix} 1 \\ 0 \end{bmatrix} = \begin{bmatrix} 1 \\ 0 \end{bmatrix}$. We thus have the simple condition

$$\mathsf{M}^m \begin{bmatrix} 1 \\ 0 \end{bmatrix} = \epsilon \begin{bmatrix} 1 \\ 0 \end{bmatrix} , \tag{3.129}$$

which gives the equation on α (and thus on eigenvalues λ)

$$\sin\alpha \frac{\sin m\psi}{\sin\psi} = 0 \ . \tag{3.130}$$

This corresponds to two cases:

- $\sin\alpha = 0$, that is $\alpha = j\pi$, with $j = 0, 1, 2, \ldots$. We denote these solutions by $\alpha_{j,0}$ if j is even and $\alpha_{j,m}$ if j is odd. The vector $\begin{bmatrix} 1 \\ 0 \end{bmatrix}$ is an eigenvector of the matrix M with the eigenvalue $(-1)^j$, thus $\epsilon = (-1)^{jm}$.
- $\frac{\sin m\psi}{\sin\psi} = 0$, which gives $m\psi = p\pi$, where $p \in \{1, \ldots, m-1\}$, and can be restated according to Eq. (3.127) as:

$$\cos\alpha - \frac{\tilde{r}}{2}\alpha\sin\alpha = \cos p\pi/m \ , \quad p \in \{1, \ldots, m-1\} \ . \tag{3.131}$$

  For each value of p this yields an infinite array of solutions that we will denote as $\alpha_{j,p}$, where the j index means $j\pi \leq \alpha_{j,p} < (j+1)\pi$ $(j = 0, 1, \ldots)$. We have $\mathsf{M}^m = (-1)^p \mathsf{I}_2$, therefore $\epsilon = (-1)^p$.

Figure 3.14 illustrates the solutions $\alpha_{j,p}$ in the case $m = 4$ and $\tilde{r} = 0.4$. One can see that the solutions are grouped in branches of m values. Each branch begins at a multiple of π and ends below the next one. The branches of even j begin with $\psi = 0$ $(p = 0)$ and increase with increasing p, whereas the odd j branches begin with $\psi = \pi$ $(p = m)$ and increase with decreasing p. Note that we discard the branches with negative j because $\alpha \geq 0$ according to Eq. (3.124).

Note that α (or j) dictates the intra-compartment variation of the mode, whereas ψ (or p) is related to its inter-compartment variation (as we explained in Sec. 3.4.2). In fact, the index j is equal to the number of extrema of the mode in the first compartment (not counting the one at $x = 0$). If one is interested in the inter-compartment variation only, for example by looking at the value of the mode at the beginning of each compartment, then p represents the number of extrema of this variation over the whole interval. Moreover, the Courant nodal theorem (proved for our particular model in Sec. B.3.1) states that each eigenmode changes sign $p + jm$ times. Figure 3.15 shows the first modes of an array of $m = 4$ identical cells with impermeable outer barriers. The first two branches are represented. We have additionally plotted dots at the beginning of each compartment to make the inter-compartment variation more visible. This variation is even more apparent for a large number of cells. On Fig. 3.16 we show a plot of some modes for $m = 100$. We have chosen $p = 7$ and $j = 0, 1, 2$. One can see that

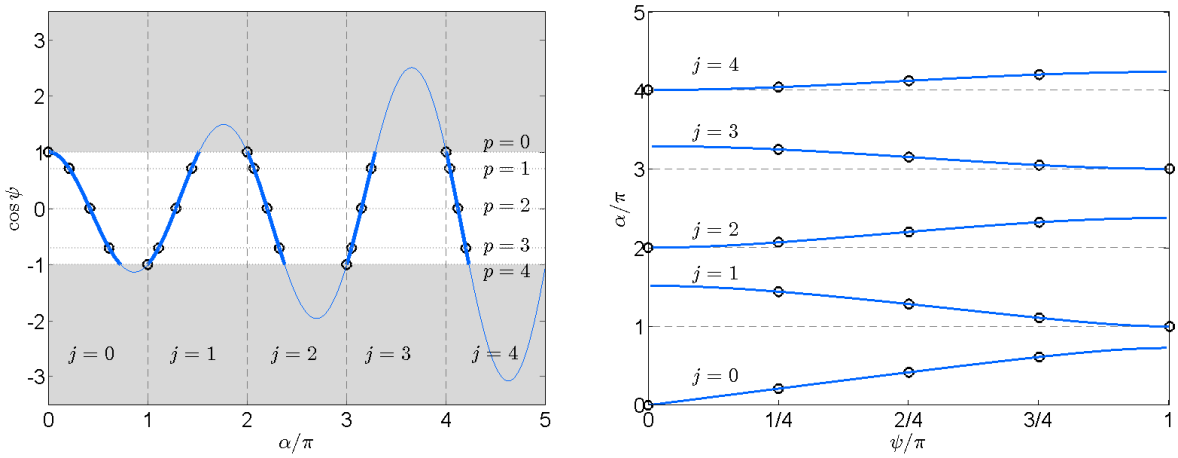

Figure 3.14: (left) Plot of $\cos\psi = \cos\alpha - \frac{\tilde{r}}{2}\alpha\sin\alpha$ with $\tilde{r} = 0.4$. Horizontal dotted lines indicate $\cos\psi = \cos p\pi/m$, $p = 0, \ldots, m$, with $m = 4$ and the circles represent the solutions $\alpha_{j,p}$. (right) An equivalent representation is the plot of $\alpha_{j,p}$ versus $\psi_p = p\pi/m$. One can see branches beginning at $j\pi$ and ending below $(j+1)\pi$. As α increases, the graph of $\cos\psi$ crosses the $[-1;1]$ interval with a steeper slope, which results in solutions closer to $j\pi$ as j increases.

although α is very different between the different modes, the overall behaviour of the modes is the same: the dots form a sine function with $p = 7$ extrema.

One can compare the results of this section with Bloch waves in solid state physics [325, 326]. Indeed the branches of solutions $\alpha_{j,p}$ are similar to energy bands, where j and p are analogous to the band index n and the wavenumber k, respectively. More precisely, α is equivalent to the square root of energy. This is no surprise because we are dealing with a (finite) periodic geometry. Although the periodicity is not expressed through an energy potential but boundary conditions, the mathematical framework is the same. This explains the striking similarity between Fig. 3.14 and energy band diagrams (where only the $k \geq 0$ half would be represented). This analogy will also be discussed in Sec. 4.4 about the spectrum of the BT operator in periodic domains.

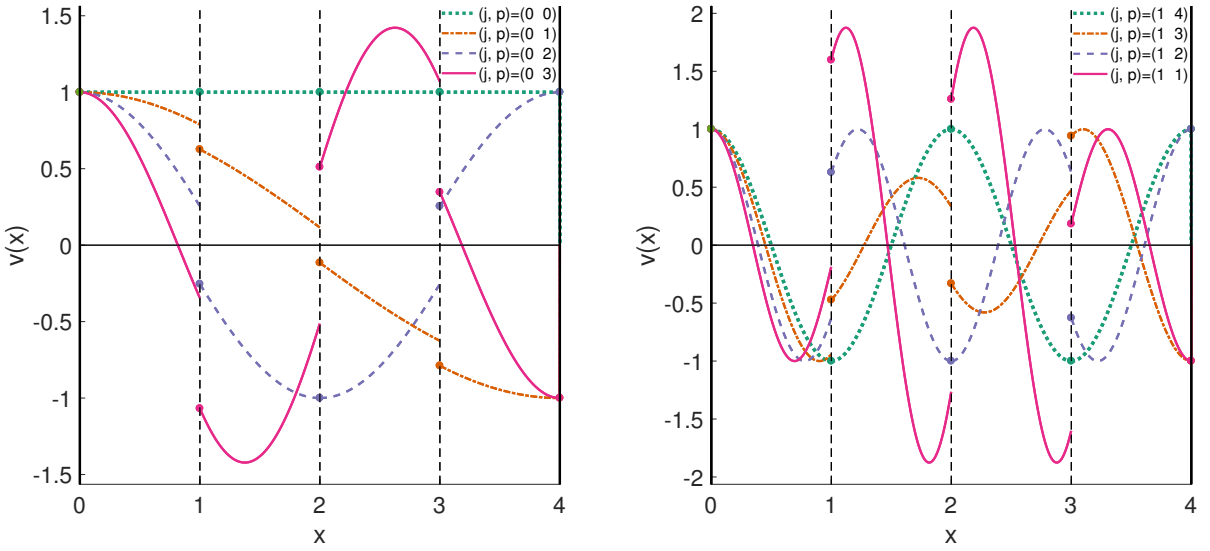

Figure 3.15: Plot of the diffusion operator eigenmodes for the array of $m = 4$ identical cells of length 1 with impermeable outer boundaries and $\tilde{r} = 0.4$. (left) $j = 0$, $p = 0, \ldots, m-1$; (right) $j = 1$, $p = m, \ldots, 1$. Note the discontinuities at the barriers which increase when $\alpha_{j,p}$ increases.

Computation of the norm

Because the geometry is symmetric and the relaxation coefficients $K_\pm$ are equal to zero, one can transform the formula (3.94) of the normalization constant into

$$\beta_{j,p}^{-2} = \frac{\ell_s}{2} \left| \begin{bmatrix} 0 & 1 \end{bmatrix} \frac{\mathrm{d}\mathsf{T}}{\mathrm{d}\alpha} \begin{bmatrix} 1 \\ 0 \end{bmatrix} \right|_{\alpha=\alpha_{j,p}} = \frac{\ell_s}{2} \left| \begin{bmatrix} 0 & 1 \end{bmatrix} \frac{\mathrm{d}\mathsf{M}^m}{\mathrm{d}\alpha} \begin{bmatrix} 1 \\ 0 \end{bmatrix} \right|_{\alpha=\alpha_{j,p}} \tag{3.132a}$$

$$= \frac{\ell_s}{2} \left| \frac{\mathrm{d}}{\mathrm{d}\alpha} \left(\sin\alpha \frac{\sin(m\psi)}{\sin\psi} \right) \right|_{\alpha=\alpha_{j,p}} . \tag{3.132b}$$

Now we use Eq. (3.130), which leads us to distinguish the two cases as above:

- $\sin\alpha = 0$: it corresponds to $\alpha = j\pi$, with a positive integer j (recall that we discard $\alpha = 0$). Then $\cos\psi = (-1)^j$ and $\frac{\sin m\psi}{\sin\psi} = m(-1)^{j(m-1)}$. We conclude that the normalization factor of the mode is:

$$\beta_{j,p}^2 = \frac{2}{m\ell_s} . \tag{3.133}$$

- $\frac{\sin m\psi}{\sin\psi} = 0$: it corresponds to $\alpha_{j,p}$ ($\psi = p\pi/m$), $p = 1, \ldots, m-1$ and $j = 0, 1, \ldots$. In this case, the derivative in Eq. (3.132b) is easily computed by

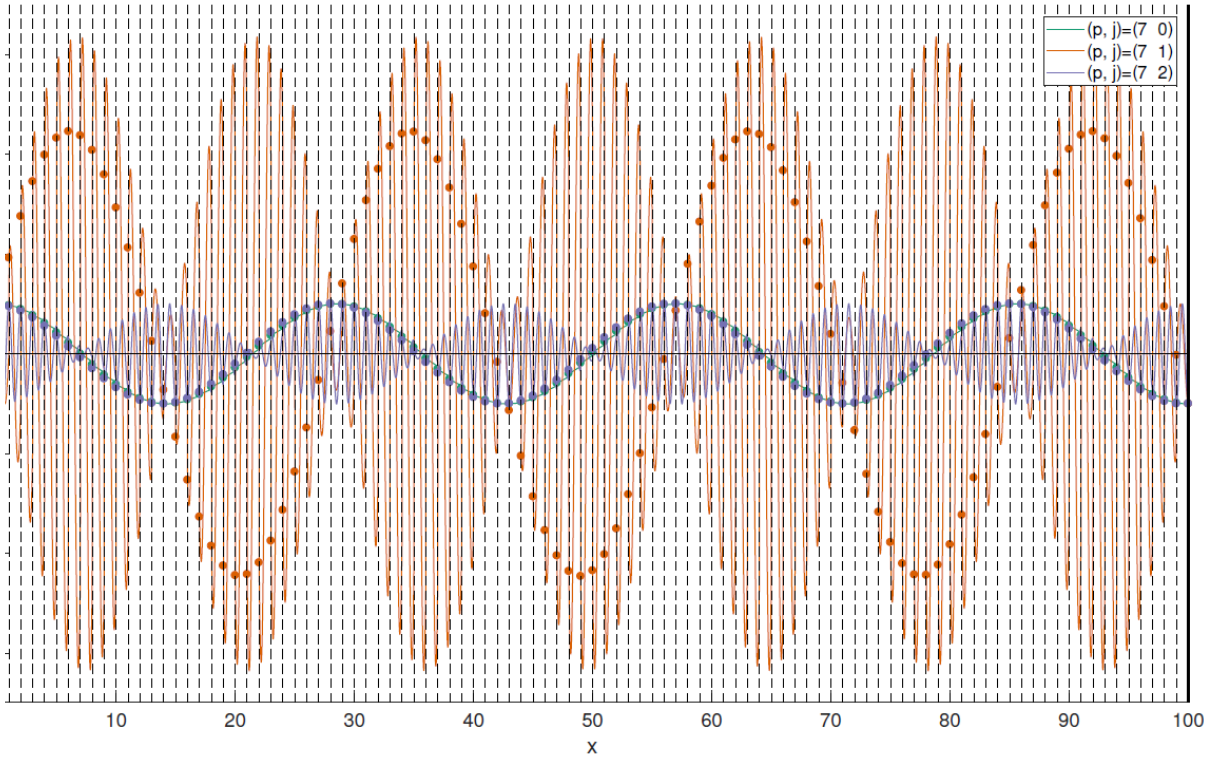

Figure 3.16: Plot of the modes for the simple periodic geometry with impermeable outer boundaries. The interval is composed of $m = 100$ cells and $\tilde{r} = 0.4$. The modes are taken from different branches ($j = 0, 1, 2$) but have all $p = 7$. The dots mark the value of the mode at the left point of each subinterval and help to visualize the inter-compartment behavior.

the chain rule:

$$\begin{aligned}\frac{\mathrm{d}}{\mathrm{d}\alpha}\left(\frac{\sin m\psi}{\sin\psi}\right) &= \frac{\mathrm{d}\cos\psi}{\mathrm{d}\alpha}\frac{\mathrm{d}\psi}{\mathrm{d}\cos\psi}\frac{\mathrm{d}}{\mathrm{d}\psi}\left(\frac{\sin m\psi}{\sin\psi}\right)\\ &= -\left(\sin\alpha\left(1+\frac{\tilde{r}}{2}\right)+\frac{\tilde{r}}{2}\alpha\cos\alpha\right)\left(\frac{-1}{\sin\psi}\right)\\ &\quad\times\frac{m\cos m\psi\sin\psi-\sin m\psi\cos\psi}{\sin^2\psi},\end{aligned}$$

which by evaluation at $\alpha_{j,p}$ yields:

$$\beta_{j,p}^2 = \frac{2}{m\ell_s}\frac{\sin^2 p\pi/m}{\sin\alpha_{j,p}\left(\sin\alpha_{j,p}\left(1+\frac{\tilde{r}}{2}\right)+\frac{\tilde{r}}{2}\alpha_{j,p}\cos\alpha_{j,p}\right)}. \tag{3.134}$$

3.4.4 Numerical Implementation

From a numerical point of view, the computational steps are the following: (i) to compute the transition matrix $M_{i,i+1}$ in Eq. (3.75) for each compartment; (ii) to apply Eq. (3.79) to get the complete transition matrix; (iii) to solve Eq. (3.81) to get the spectrum of the diffusion operator; each solution of Eq. (3.81) determines one eigenvalue whereas Eqs. (3.74) and (3.77) yield the coefficients a_i^l, b_i^l, $k = 1, \ldots, m$ for each (non-normalized) mode; (iv) to compute the normalization constant; combined with Eq. (3.69) it allows one to compute the eigenmode at any point of the interval.

Steps (i) and (ii) are easy and fast since we are dealing with 2×2 matrices. Step (iv) can be done either with Eq. (3.94), which involves a numerical derivative, or by a direct computation, using:

$$\int_0^l \left(a\cos(kx) + b\sin(kx)\right)^2 \, \mathrm{d}x = \frac{(a^2+b^2)l}{2} + \frac{(a^2-b^2)}{4k}\sin(2kl) + \frac{ab}{4k}(1-\cos(2kl)) \; . \tag{3.135}$$

The most complicated and time-consuming step is (iii). As we explained in Sec. 3.4.2, two or more solutions of Eq. (3.81) may be very close to each other in the case of low-permeability barriers (typically $\ell_s \ll \ell_\kappa$). The estimates we derived allow us to localize the roots that speeds up the computation. This is the crucial point and one of the major practical achievements of this work. This numerical improvement allows us to detect very close zeros (as those shown in Fig. 3.13) and to compute the eigenmodes of the diffusion operator in heterogeneous structures with hundreds of barriers. Moreover, Fig. 3.13 illustrates an interesting property of $F_m(z; l_1, \ldots, l_m)$ as a function of z: two local extrema are apparently always separated by a zero. Although we have no mathematical proof for this observation, it is very helpful because it allows us to detect pairs of close zeros by the change of sign of the derivative of the function, which may take place on a much larger scale than the change of sign of the function itself. One can also take advantage of the Courant nodal theorem (which is proven for our particular model in Sec. B.3.1): the n-th eigenmode has n nodal domains (connected components on which the eigenmode has a constant sign), or equivalently, the n-th eigenmode changes sign $n-1$ times (possibly at the barriers). This can be used as an efficient test to check *a posteriori* that no eigenvalue is missed.

In practice, the standard floating-point precision limits the relative accuracy of a numerical computation to about 10^{-15}. Let us assume that we are dealing with a geometry such that two eigenvalues λ_1 and λ_2 are much closer than this limit; for example they coincide up to 10^{-20}. With the above tricks we are still able

to detect those roots and even to compute accurately their position and spacing. However, the subsequent computations performed on λ_1 and λ_2 (for example, the computation of the eigenmodes or their norm) treat λ_1 and λ_2 as equal numbers. Even worse: the closeness of λ_1 and λ_2 is related to the very fast local variations of $F(\lambda)$ with λ, and as a consequence of the coefficients (a_i^l, b_i^l) and of the norm of the eigenmode. Therefore it is very difficult to compute accurately these quantities for two eigenmodes corresponding to very close eigenvalues. The estimates derived in Sec. 3.4.2 can be used to detect *a priori* such situations in which the spectral decomposition can numerically fail.

If one is interested in the diffusion propagator (3.82) or related quantities, the infinite collection of eigenmodes has to be truncated. This is done by sorting the eigenvalues λ_n in ascending order and then cutting off the ones such that $\lambda_n t \gg 1$, where t is the smallest diffusion time for which the computation is needed. The precise choice of the truncation threshold is a compromise between precision and speed of computation. Practically, one can check the validity of the truncation by re-doing the computation with a higher threshold and then comparing the two results.

3.4.5 Application to diffusion MRI

Overview

From the knowledge of the diffusion propagator one can access the dMRI signal in the narrow-gradient pulse regime (see Sec. 1.2.3), thus motivating numerous theoretical and experimental works on diffusion in complex geometries. As explained previously, restricted diffusion in simple domains such as slab, cylinder, sphere, can be treated analytically [22, 86–88]. In contrast, most works devoted to multi-layered systems with permeable barriers are numerical. Tanner took advantage of the simple expression of the Laplace eigenmodes in a slab geometry to study a finite periodic repetition of permeable barriers [269]. The same method was applied later by Kuchel and Durrant to unevenly spaced membranes [270]. These approaches were generalized by Grebenkov with a matrix formalism allowing efficient computation of the signal in general multi-layered planar, cylindrical or spherical structures, without the narrow-gradient pulse restriction [268]. Powles and co-workers proposed in [271] an opposite approach based on the (one-dimensional) analytical solution of the propagator $\mathcal{G}$ for one permeable barrier extended to several barriers by multiple reflections. Other numerical techniques such as a finite differences method were reported [272].

The first analytical expression of the dMRI signal in a one-dimensional geometry with periodic permeable barriers was provided by Sukstanskii *et al.* [273].

Relying on the periodicity of the system they computed directly the signal in Laplace domain without having to derive the diffusion propagator. Unevenly spaced membranes were treated in [102, 197] from the analytical solution for one membrane and under the assumption that the diffusing time is sufficiently short so that the layers are independent. Note that in contrast to almost all previously cited works the analysis performed in [102] does not confine to infinitely narrow pulses. Finally, Novikov *et al.* studied the effect of randomly placed permeable barriers on the diffusive motion [68, 69]. Using a renormalization group technique, they obtained structural universality classes characterized by the disorder introduced by the barriers, which in turn govern the long-time asymptotic behavior of the mean square displacement.

The method developed in Sec. 3.4.2 for computing the diffusion operator eigenmodes allows us to calculate the signal analytically for infinitely narrow gradient pulses, or numerically for arbitrary pulse sequences (see Sec. 1.1.5). In particular, this method generalizes earlier approaches [197, 269, 272, 273] and opens unprecedented opportunities for studying more sophisticated configurations of barriers such as microstructures inside larger scale structures. The computations are detailed in Sec. 3.4.5. We explain how one can obtain the dMRI signal from the Fourier transform of the eigenmodes u_n in the narrow pulse regime, then we derive the expression of the signal for the periodic geometry presented in Sec. 3.4.3. We discuss the effect of the permeability of the barriers on the dMRI signal in the regimes of short and long diffusion time. In particular, we obtain a scaling law of the form $\tilde{\kappa}t/(\tilde{\kappa}+1)$ involving t and $\tilde{\kappa} = \kappa\ell_s/D = \ell_s/\ell_\kappa$, which is valid in the long time regime ($\ell_d \gg \ell_s$). Computations for more sophisticated geometries are presented in Sec. B.3.2 (relaxation at the outer boundaries), B.3.3 (bi-periodic geometry), and B.3.4 (two-scale geometry).

Narrow-gradient regime for an array of identical cells and reflecting conditions at the outer boundaries

We consider now a gradient profile made of two pulses of duration $\delta \to 0$ and amplitude $G = Q/\delta \to \infty$ (see Sec. 1.2.3). The diffusion time between two pulses is denoted by Δ for consistency with literature. The signal is directly linked to the diffusion propagator $\mathcal{G}$ by Eq. (1.56b), that reads here:

$$S(\Delta) = \int_0^L \int_0^L \rho(x_0)\mathcal{G}(\Delta, x_0, x)e^{iQ(x-x_0)}\,\mathrm{d}x\,\mathrm{d}x_0\,, \tag{3.136}$$

where $\rho(x_0)$ is the initial spin density [2–4]. The spectral decomposition (3.82) yields

$$S(\Delta) = \sum_{n=1}^{\infty} e^{-\lambda_n \Delta} \int_0^L \int_0^L \rho(x_0) u_n(x_0) u_n(x) e^{iQ(x-x_0)} \, \mathrm{d}x \, \mathrm{d}x_0 \,, \tag{3.137}$$

If the initial density is uniform $\rho(x_0) = 1/L$, the symmetry between x and x_0 leads to the following simplification:

$$S(\Delta) = \frac{1}{L} \sum_{n=1}^{\infty} e^{-\lambda_n \Delta} \left| \int_0^L u_n(x) e^{iQx} \, \mathrm{d}x \right|^2 . \tag{3.138}$$

This formula was initially introduced in [22] to study the signal coming from a single isolated interval. Later the effect of permeable barriers was numerically studied in [269] for the most simple one-dimensional geometry where all l_i, D_i, $\kappa_{i,i+1}$ are the same (denoted ℓ_s, D_0, κ in the following).

In this section we apply the results of Sec. 3.4.3 and extend the results of Ref. [269]. In addition to Sec. 3.4.3 we compute the Fourier transform of the modes which gives us the signal S. In Sec. B.3.2 we extend this computation to relaxing conditions at the outer boundaries. A more complicated geometry consisting of a microstructure inside a larger scale structure is treated in Sec. B.3.4. For clarity, we recall the following definitions

$$\ell_{\mathrm{d}} = \sqrt{D_0 \Delta} \,, \qquad \ell_\kappa = \frac{D_0}{\kappa} \,, \qquad \ell_q = Q^{-1} \,. \tag{3.139}$$

We temporarily use the subscript k instead of i for the compartments in order to avoid any confusion with the imaginary unit $i = \sqrt{-1}$. As previously we use the position of the barrier to the left as the origin in the formula (3.69) of the eigenmodes. This means that we have to compute integrals of the form:

$$\int_0^{l_k} e^{iQx} \cos\left(x\sqrt{\lambda/D_k}\right) \mathrm{d}x = \frac{l_k}{2}\left(\frac{e^{i(Q+\sqrt{\lambda/D_k})l_k} - 1}{il_k(Q+\sqrt{\lambda/D_k})} + \frac{e^{i(Q-\sqrt{\lambda/D_k})l_k} - 1}{il_k(Q-\sqrt{\lambda/D_k})}\right),$$
$$\int_0^{l_k} e^{iQx} \sin\left(x\sqrt{\lambda/D_k}\right) \mathrm{d}x = \frac{l_k}{2i}\left(\frac{e^{i(Q+\sqrt{\lambda/D_k})l_k} - 1}{il_k(Q+\sqrt{\lambda/D_k})} - \frac{e^{i(Q-\sqrt{\lambda/D_k})l_k} - 1}{il_k(Q-\sqrt{\lambda/D_k})}\right).$$

We denote by L_k the row vector whose components are the above integrals. The Fourier transform of the eigenmode v is then simply

$$\int_0^L v(x) e^{iQx} \, \mathrm{d}x = \sum_{k=1}^{m} e^{iQx_{k-1,k}} \mathsf{L}_k \begin{bmatrix} a_k^l \\ b_k^l \end{bmatrix} . \tag{3.140}$$

Now we apply this general formula to our finite periodic geometry. The sum can be simplified because all L_k are the same:

$$\mathsf{L} = \frac{\ell_s}{2}\left[-i\left(\frac{e^{i(q-\alpha)}-1}{q-\alpha}+\frac{e^{i(q+\alpha)}-1}{q+\alpha}\right)\ \left(\frac{e^{i(q-\alpha)}-1}{q-\alpha}-\frac{e^{i(q+\alpha)}-1}{q+\alpha}\right)\right], \tag{3.141}$$

where $q = Q\ell_s$. Moreover $x_{k-1,k} = (k-1)\ell_s$ so we can rewrite the sum (3.140):

$$\begin{aligned}\int_0^L v(x)e^{iQx}\,\mathrm{d}x &= \sum_{k=1}^{m} e^{i(k-1)q}\mathsf{L}\begin{bmatrix}a_k^l\\ b_k^l\end{bmatrix} = \mathsf{L}\sum_{k=0}^{m-1} e^{ikq}\mathsf{M}^k\begin{bmatrix}1\\0\end{bmatrix}\\ &= \mathsf{L}(\mathsf{I}_2 - e^{iq}\mathsf{M})^{-1}(\mathsf{I}_2 - e^{imq}\mathsf{M}^m)\begin{bmatrix}1\\0\end{bmatrix}\\ &= (1-(-1)^p e^{imq})\mathsf{L}(\mathsf{I}_2 - e^{iq}\mathsf{M})^{-1}\begin{bmatrix}1\\0\end{bmatrix},\end{aligned} \tag{3.142}$$

where we have used Eq. (3.129) with $\epsilon = (-1)^p$. We can simplify the matrix product further with the remark that the comatrix operation is linear for 2×2 matrices, and that $\det \mathsf{M} = 1$, so that

$$\mathsf{L}(\mathsf{I}_2 - e^{iq}\mathsf{M})^{-1}\begin{bmatrix}1\\0\end{bmatrix} = \frac{\mathsf{L}(\mathsf{I}_2 - e^{iq}\mathsf{M}^{-1})}{\det(\mathsf{I}_2 - e^{iq}\mathsf{M})}\begin{bmatrix}1\\0\end{bmatrix} = \frac{\mathsf{L}(\mathsf{I}_2 - e^{iq}\mathsf{R}^{-1})}{\det(\mathsf{I}_2 - e^{iq}\mathsf{M})}\begin{bmatrix}1\\0\end{bmatrix}. \tag{3.143}$$

From the knowledge of the trace and determinant of the matrix M we compute

$$\det(\mathsf{I}_2 - e^{iq}\mathsf{M}) = -2e^{iq}(\cos\psi - \cos q)\,. \tag{3.144}$$

Furthermore,

$$\mathsf{L}(\mathsf{I}_2 - e^{iq}\mathsf{R}^{-1})\begin{bmatrix}1\\0\end{bmatrix} = -2ie^{iq}(\cos\alpha - \cos q)\frac{q\ell_s}{q^2-\alpha^2}\,. \tag{3.145}$$

Putting all the pieces together yields

$$\int_0^L v_{j,p}(x)e^{iqx}\,\mathrm{d}x = e^{imq/2}\frac{iq\ell_s(e^{-imq/2}-(-1)^p e^{imq/2})\frac{\cos q-\cos\alpha_{j,p}}{\cos q-\cos p\pi/m}}{q^2-{\alpha_{j,p}}^2}\,. \tag{3.146}$$

Note that the ratio is either real (p even) or imaginary (p odd) which is consistent with the symmetry or anti-symmetry of the mode (see Sec. 3.4.2).

Complete expression of the signal

Let us summarize our results. In the array of m identical cells one has $D_i = D_0$ and $l_i = \ell_s$, $i = 1, \ldots, m$. We thus introduce the dimensionless time $\tilde{t} = D_0\Delta/\ell_s^2 = \ell_d^2/\ell_s^2$, and $\tilde{q} = Q\ell_s = \ell_s/\ell_q$. The combination of the previous results yields the formula:

$$S = \frac{2(1-\cos m\tilde{q})}{(m\tilde{q})^2} + \sum_{j=1}^{\infty} \frac{4\tilde{q}^2(1-(-1)^{jm}\cos m\tilde{q})}{m^2\left(\tilde{q}^2-(j\pi)^2\right)^2} e^{-(j\pi)^2\tilde{t}} + \sum_{j=0}^{\infty}\sum_{p=1}^{m-1} \frac{2\tilde{q}^2}{m^2} \frac{1-(-1)^p\cos m\tilde{q}}{(\cos\tilde{q}-\cos p\pi/m)^2} \left(\frac{\cos\tilde{q}-\cos\alpha_{j,p}}{\tilde{q}^2-\alpha_{j,p}^2}\right)^2 (m\ell_s\beta_{j,p}^2) e^{-\alpha_{j,p}{}^2\tilde{t}} , \tag{3.147}$$

where $\beta_{j,p}^2$ is given by Eq. (3.134), and we made explicitly appear the size of the interval $L = m\ell_s$ to compensate the $1/L$ scaling of $\beta_{j,p}^2$.

If $m = 1$, there is no double sum on the second line of Eq. (3.147), and one retrieves the well-known result by Tanner [22]:

$$S_1(\tilde{q},\tilde{t}) = \frac{2(1-\cos\tilde{q})}{\tilde{q}^2} + \sum_{j=1}^{\infty} \frac{4\tilde{q}^2(1-(-1)^j\cos\tilde{q})}{\left(\tilde{q}^2-(j\pi)^2\right)^2} e^{-(j\pi)^2\tilde{t}} . \tag{3.148}$$

The opposite limit $m \to \infty$ was the motivation of the subsequent article by Tanner [269] and was derived analytically in [273]. When $m \to \infty$, each term of the sum in Eq. (3.147) vanishes except the ones for which $\cos p\pi/m$ is close to $\cos\tilde{q}$. Let us write

$$\tilde{q} = 2k\pi + p_0\pi/m + \epsilon/m , \quad p_0 \in \{0, \ldots, m-1\} , \quad 0 \le \epsilon < \pi . \tag{3.149}$$

Then we have:

$$\frac{1-(-1)^p\cos(m\tilde{q})}{m^2(\cos\tilde{q}-\cos p\pi/m)^2} \approx \frac{1-(-1)^{p_0-p}\cos\epsilon}{\pi^2\sin^2(\tilde{q})(p_0-p+\epsilon/\pi)^2} . \tag{3.150}$$

To get the signal in the $m \to \infty$ limit, we use the following identity:

$$\sum_{p=-\infty}^{\infty} \frac{1}{\pi^2} \frac{1-(-1)^p\cos\epsilon}{(p+\epsilon/\pi)^2} = 1. \tag{3.151}$$

The new equation on α is

$$\cos\psi = \cos\alpha - \frac{\tilde{r}}{2}\alpha\sin\alpha = \cos\tilde{q} , \tag{3.152}$$

and the expression of the signal becomes

$$S_\infty(\tilde{q},\tilde{t},\tilde{\kappa}) = \frac{2\tilde{q}^2}{\tilde{\kappa}} \sum_{n=1}^{\infty} \frac{{\alpha_n}^2 \sin\alpha_n e^{-{\alpha_n}^2\tilde{t}}}{({\alpha_n}^2-\tilde{q}^2)^2\left((2\tilde{\kappa}+1)\sin\alpha_n+\alpha_n\cos\alpha_n\right)} \,. \tag{3.153}$$

This is exactly the formula derived in [273] by the computation of the Laplace transform of $\int \mathcal{G}(T,x_0,x)e^{iQ(x-x_0)}\,\mathrm{d}x_0$ on an infinite periodic geometry. Note that although the geometry is infinite and thus the spectrum of the diffusion operator is continuous, the signal is expressed in terms of a discrete set of eigenvalues because of Eq. (3.152): the Fourier transform selects only the modes that globally oscillate at the wavenumber Q (recall that α only describes the intra-block oscillations, whereas the global behavior of the mode is dictated by ψ, according to Eq. (3.105)). A general explanation of this property will be given in the next chapter, where the behavior of the magnetization and signal in periodic structures is studied. As a consequence, one has to compute α_n, $n = 1, 2, \ldots$ for each value of $\tilde{q}$, in contrast to the finite geometry where the spectrum depends only on the geometry and needs to be calculated only once. This is an important numerical advantage of the finite geometry over the infinite one because the computation of the spectrum is one of the most time-consuming step (as explained in Sec. 3.4.2 and 3.4.4).

3.4.6 Dependence of the signal on the permeability

In this section we study the diffusion operator eigenvalues and the dMRI signal in various regimes in order to show the dependence of the signal on the dimensionless permeability of the inner barriers, $\tilde{\kappa}$, which characterizes the microstructure. We recall that $\tilde{\kappa} = \ell_s/\ell_\kappa$ controls the transition between diffusion control ($\tilde{\kappa} \gg 1$) and permeation control ($\tilde{\kappa} \ll 1$). In biological tissues, one has typically: $D_0 \sim 1\ \mu\mathrm{m}^2/\mathrm{ms}$, $\ell_s = 1-100\ \mu\mathrm{m}$, $\kappa \sim 10^{-3}-1\ \mu\mathrm{m/ms}$ (see Refs [170–183, 197]), and the experimental range of diffusion time is about $\Delta = 10-10^3$ ms. In Sec. 1.2.1, we showed that the minimal accessible values of ℓ_q was of the order of a few microns. Thus we have the following ranges of variation for our dimensionless parameters: $\tilde{\kappa} \sim 10^{-3}-10^2$, $\tilde{t} \sim 10^{-3}-10^3$, and $\tilde{q} \sim 0-10^2$.

In the limit $\tilde{\kappa} \to \infty$, one obviously recovers the signal associated to the whole interval of length $m\ell_s$ with no barriers, whereas in the opposite limit $\tilde{\kappa} \to 0$ one gets the signal (3.148) associated to one interval of length ℓ_s (we detail the mathematical proof in Sec. B.3.5). In other words

$$S(m,\tilde{q},\tilde{t},\tilde{\kappa}) \xrightarrow[\tilde{\kappa}\to\infty]{} S_1(m\tilde{q},\tilde{t}/m^2) \qquad \text{and} \qquad S(m,\tilde{q},\tilde{t},\tilde{\kappa}) \xrightarrow[\tilde{\kappa}\to 0]{} S_1(\tilde{q},\tilde{t}) \,. \tag{3.154}$$

We are interested in the transition from one limit to the other, that is the dependence of the signal on the permeability. Expansions of $\alpha_{j,p}$ at low and high permeability are derived in Sec. B.3.6. They show that the transition from $\tilde{\kappa} = 0$ to $\tilde{\kappa} = \infty$ does not occur at one fixed value of $\tilde{\kappa}$ but depends on the branch of eigenvalues that we consider. Typically for the branch j the transition occurs at $\tilde{\kappa} \sim j\pi/2$ if $j > 0$. As we have already seen, the $j = 0$ branch is particular and exhibits a $\tilde{\kappa}^{1/2}$ dependence at low $\tilde{\kappa}$ (see Eqs. (3.161) and (B.94)). In order to refine our analysis we distinguish short-time and long-time regimes.

Short-time regime

The short-time regime corresponds to $\tilde{t} \ll 1$ or equivalently, $\ell_d \ll \ell_s$. The physical interpretation is that almost no particles travel from one barrier to the other, therefore the barriers can be considered as independent. For this reason, the barrier spacing ℓ_s does not play any role in the behavior of the signal, except as a normalization factor.

From a mathematical point of view, several eigenvalues contribute to the sum (3.147). Since $j\pi < \alpha_{j,p} < (j+1)\pi$, one can see that all branches with $j \lesssim 1/\sqrt{\tilde{t}}$ have to be taken into account. As $\tilde{\kappa}$ increases the branches of solutions transform successively from the $\tilde{\kappa} = 0$ limit to the $\tilde{\kappa} = \infty$ limit. Beyond $\tilde{\kappa} \sim 1/\sqrt{\tilde{t}}$, the increase of $\tilde{\kappa}$ produces little change on the most contributing branches, hence on the signal. This behavior can be related to the discussion of Sec. 3.1.2, where we showed that, in the short-time regime, the fraction of particles that have crossed a barrier among the ones that have hit it grows as $F_c \sim \sqrt{\Delta/\tau_\kappa} = \tilde{\kappa}\sqrt{\tilde{t}}$. In other words, $\tilde{\kappa} \sim 1/\sqrt{\tilde{t}}$ is the value of the permeability from which almost every particle that has reached a barrier has crossed it.

To illustrate this effect, we consider the low-$\tilde{q}$ regime, $\tilde{q}^2\tilde{t} \ll 1$ or equivalently $\ell_d \ll \ell_q$. In this case, the signal is given by the Gaussian phase approximation (see Fig. 1.8 and Sec. 1.2.2):

$$S = \exp(-bD) = \exp(-(D/D_0)\tilde{q}^2\tilde{t}) \,, \tag{3.155}$$

with an effective diffusion coefficient D. In the previous chapter, we showed that in the short-time regime D follows Mitra formula (2.51):

$$\frac{D}{D_0} = 1 - \frac{4}{3\sqrt{\pi}}\sigma\ell_s\sqrt{\tilde{t}} + O(t) \,. \tag{3.156}$$

For a single interval of length ℓ_s the (dimensionless) surface-to-volume ratio is $\sigma\ell_s = 2$, and one should obtain therefore the same value for the whole interval with m compartments. However, this result is paradoxical because the effect of

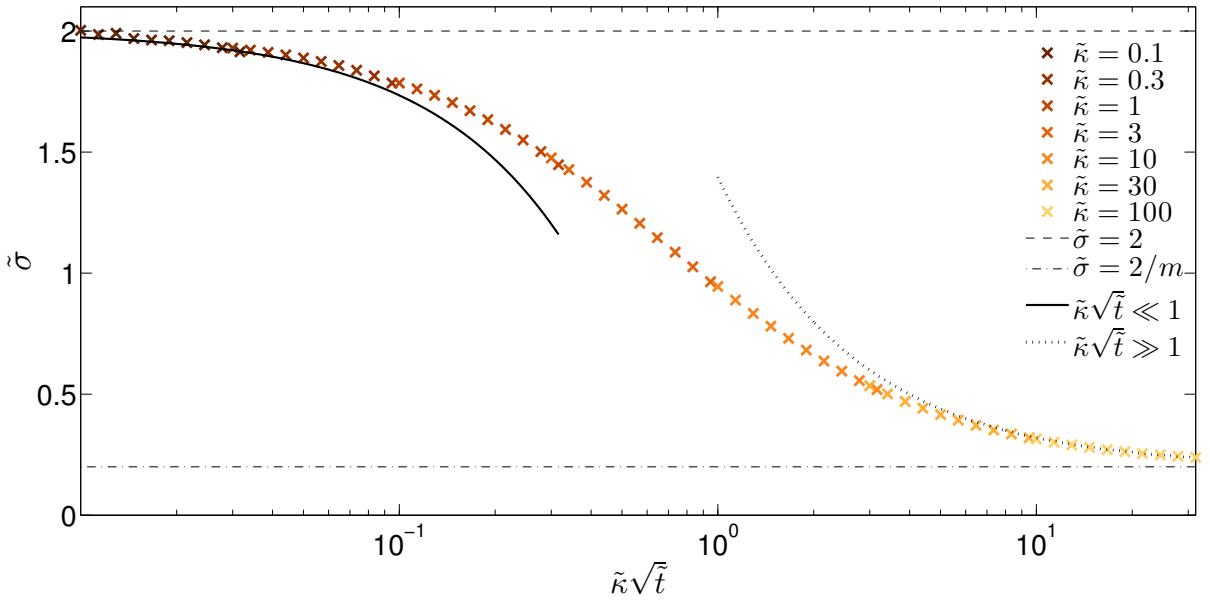

Figure 3.17: Effective surface-to-volume ratio $\tilde{\sigma}$ extracted from Mitra formula (2.51) as a function of $\tilde{\kappa}\sqrt{\tilde{t}}$ for various values of $\tilde{\kappa}$ and $\tilde{t}$, in the short-time regime $\tilde{t} \ll 1$. The formula without permeability correction yields a value of $\tilde{\sigma}$ that decreases from $\sigma = 2$ for a single interval to $\sigma = 2/m$ for the full interval without internal barriers (here $m = 10$). The scaling $\tilde{\kappa}\sqrt{\tilde{t}}$ makes all values fall on one master curve. The asymptotic formulas (3.158) and (3.159) are plotted by solid and dotted line, respectively.

internal barriers is expected to vanish in the limit $\tilde{\kappa} \to \infty$, in which case one would get $\sigma\ell_s = 2/m$. Therefore it seems that the "effective" surface-to-volume ratio extracted from Mitra formula

$$\tilde{\sigma} = (1 - D/D_0)\frac{3\sqrt{\pi}}{4\sqrt{\tilde{t}}} \tag{3.157}$$

depends on permeability and time. The solution to this paradox lies in the $O(t)$ correction term in the above formula. Indeed, at low permeability (i.e., permeation control), the next-order term would be $\sigma\ell_s\tilde{\kappa}\tilde{t}$ [53], so that

$$\tilde{\sigma} = 2\left(1 - \frac{3\sqrt{\pi}}{4}\tilde{\kappa}\sqrt{\tilde{t}}\right), \qquad (\tilde{\kappa}\sqrt{\tilde{t}} \ll 1), \tag{3.158}$$

This formula breaks down at high permeability, and one can compute

$$\tilde{\sigma} = \frac{2}{m} + \frac{2(m-1)}{m}\frac{3\sqrt{\pi}}{8}\frac{1}{\tilde{\kappa}\sqrt{\tilde{t}}}, \qquad (\tilde{\kappa}\sqrt{\tilde{t}} \gg 1). \tag{3.159}$$

Consistently with the discussion of the previous paragraph, one can see that $\tilde{\sigma}$ is controlled by a single parameter $\tilde{\kappa}\sqrt{\tilde{t}}$.

Numerical results are presented on Fig. 3.17. One can see that the scaling $\tilde{\kappa}\sqrt{\tilde{t}}$ makes all values fall on one master curve. At low $\tilde{\kappa}\sqrt{\tilde{t}} = \sqrt{\tilde{t}/\tau_\kappa}$, most particles that have hit an internal barrier have not crossed it, therefore one can treat internal barriers as almost impermeable, and $\tilde{\sigma} \approx 2$. In the opposite limit, almost all particles that have hit a barrier have crossed it, therefore one can treat internal barriers as fully permeable, so that $\tilde{\sigma} \approx 2/m$. There is a continuous transition from one regime to the other over a wide range of values of $\tilde{\kappa}\sqrt{\tilde{t}}$. Note that the asymptotic formulas (3.158) and (3.159) yield the correct behavior at respectively very small and very large $\tilde{\kappa}\sqrt{\tilde{t}}$ but fail to describe the intermediate regime.

Although we focused on the low-$\tilde{q}$ regime, the study of the Debye-Porod regime ($\ell_q \ll \ell_\mathrm{d}$) would lead to the same conclusion: the signal coming from the barriers is proportional to an effective surface-to-volume ratio $\tilde{\sigma}'$ that is a function of $\tilde{\kappa}\sqrt{\tilde{t}}$ and decreases from 2 to $2/m$ when $\tilde{\kappa}\sqrt{\tilde{t}}$ goes from 0 to ∞. Compared to the GPA regime where internal barriers are a weak correction to the bulk decay of the signal, in this regime the signal comes from barriers only, and the influence of permeability is high.

Long-time regime

Now we turn to the long-time regime $\tilde{t} \gtrsim 1$, or equivalently $\ell_\mathrm{d} \gtrsim \ell_\mathrm{s}$. In this regime, each particle explores at least one subinterval completely. Mathematically, the condition $\tilde{t} \gtrsim 1$ allows us to discard all branches with $j \geq 1$. Note that both affirmations are equivalent, as one can understand from Fig. 3.15 and the related discussion on the role of j, p on the behavior of eigenmodes. In particular, in the infinite time limit, all the modes with non-zero eigenvalues vanish and we are left with

$$S = \frac{2(1-\cos m\tilde{q})}{(m\tilde{q})^2} , \tag{3.160}$$

which is the well-known formula of the squared form factor of an interval of length $L = m\ell_\mathrm{s}$ (see Ref. [22] and Sec. 1.2.3). Note that relaxation at the outer boundaries would lead to zero signal in the long-time limit because $\lambda = 0$ would not be an eigenvalue of the diffusion operator anymore. As expected at long times the details of the geometry are averaged out and the signal depends only on the length of the whole interval, $L = m\ell_\mathrm{s}$. The next terms are given by the first solutions of the $j = 0$ branch. Let us study Eq. (3.131) at small α, ψ. Expanding the sine and cosine functions, one gets

$$\alpha = \psi\sqrt{\frac{\tilde{\kappa}}{\tilde{\kappa}+1}}\left(1 - \frac{\psi^2}{24(\tilde{\kappa}+1)^2}\right) + O(\psi^5) . \tag{3.161}$$

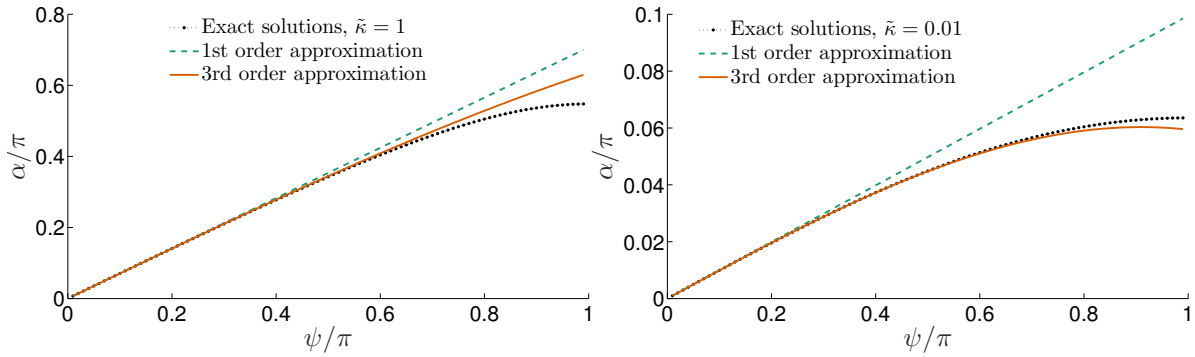

Figure 3.18: The $j = 0$ branch of solutions and its approximation by Eq. (3.161). (left) $\tilde{\kappa} = 1$; (right) $\tilde{\kappa} = 0.01$. One can see that the first order approximation formula is more accurate when $\tilde{\kappa}$ is higher which is consistent with Eq. (3.161).

Note that the third order correction is below 1% if $\psi/\pi < 0.15(\tilde{\kappa}+1)$ and approximately below 10% if $\psi/\pi < 0.5(\tilde{\kappa}+1)$. In particular the accuracy of the first-order approximation is always better than 10% for the first non-zero solution $\psi = \pi/m$ ($m > 1$). This is illustrated in Fig. 3.18 for two values of $\tilde{\kappa}$: 1 and 0.01. As expected, the approximation is more accurate for larger $\tilde{\kappa}$. Using this expansion we get the long-time asymptotic behavior

$$S \approx \frac{2(1-\cos m\tilde{q})}{(m\tilde{q})^2} + A_1(q)\exp\left(-\frac{\pi^2\tilde{\kappa}\tilde{t}}{m^2(\tilde{\kappa}+1)}\right), \tag{3.162}$$

where $A_1(\tilde{q})$ can be read on Eq. (3.147):

$$A_1(\tilde{q}) = \frac{2\tilde{q}^2}{m^2}\frac{1+\cos m\tilde{q}}{(\cos\tilde{q}-\cos\pi/m)^2}\left(\frac{\cos\tilde{q}-\cos\alpha_{0,1}}{\tilde{q}^2-\alpha_{0,1}^2}\right)^2 (m\ell_s\beta_{0,1}^2)\,. \tag{3.163}$$

Because $\alpha_{0,1}$ is small, we have approximately

$$A_1(\tilde{q}) \approx \frac{4(1+\cos m\tilde{q})(1-\cos\tilde{q})^2}{\tilde{q}^2m^2(\cos\tilde{q}-\cos\pi/m)^2}, \tag{3.164}$$

which does not depend on $\alpha_{0,1}$ anymore but only on $\psi_{0,1} = \pi/m$. In other words, $A_1(\tilde{q})$ weakly depends on $\tilde{\kappa}$. This approximation is especially accurate at high m (we checked numerically that the error is less than 3% for $m > 10$, for example). This is a consequence of the remark that the global behavior of the mode, hence its norm and Fourier transform, is dictated by ψ (see Eq. (3.105)).

From the expansion (3.162) we conclude that the parameter which controls the validity of the infinite-time limit is not t but rather $\tilde{\kappa}t/((\tilde{\kappa}+1)m^2)$. The m-dependence is obvious: m^2 is in fact the (dimensionless) time required to diffuse

through all the compartments if there are no barriers. One can then see that the effect of the barriers is to increase this diffusion time by a factor $(\tilde{\kappa}+1)/\tilde{\kappa}$.

More generally, we have:

$$S \approx \sum_{p=0}^{m-1} A_p(\tilde{q}) \exp\left(-\frac{p^2\pi^2\tilde{\kappa}t}{m^2(\tilde{\kappa}+1)}\right) , \tag{3.165}$$

where $A_p(\tilde{q})$ weakly depends on $\tilde{\kappa}$. Thus in the long-time regime, the signal depends on $\tilde{t}$ and $\tilde{\kappa}$ via the combination $\tilde{\kappa}\tilde{t}/(\tilde{\kappa}+1)$. In other words, the time-dependence of the signal yields an apparent diffusion coefficient

$$D_\infty = D_0\frac{\tilde{\kappa}}{\tilde{\kappa}+1} = \frac{1}{1/D_0 + 1/(\kappa\ell_s)} . \tag{3.166}$$

This formula is a well-known correction that can be derived by simple geometrical arguments [294]. When the permeability is high, the diffusion coefficient is slightly diminished. In the opposite limit $\tilde{\kappa} \ll 1$, i.e. permeation control, one gets an apparent diffusion coefficient: $D_\infty = D_0\tilde{\kappa} = \kappa\ell_s$, which does not depend on the "true" diffusion coefficient anymore. As we discussed in Sec. 3.1.2, the kinetics of diffusion are governed by the crossing of the barriers and not by the (much faster) intra-compartment diffusion.

As an application of the previous remark, let us consider the regime of permeation control $\tilde{\kappa} \ll 1$ at intermediate times: $1 \ll \tilde{t} \ll 1/\tilde{\kappa}$. Physically, this means that all particles have diffused multiple times inside at least one subinterval but that very few of them have crossed a barrier. Mathematically, the low-permeability expansion (B.94) of $\alpha_{0,p}$ shows that $\exp(-\alpha_{0,p}^2\tilde{t}) \approx 1$, so that $S \approx \sum_{p=0}^{m-1} A_p(\tilde{q})$ and from Sec. B.3.5 we get:

$$S \approx \frac{2(1-\cos\tilde{q})}{\tilde{q}^2} \qquad (1 \ll \tilde{t} \ll 1/\tilde{\kappa}) . \tag{3.167}$$

Thus, we recover the signal in the long-time limit for one compartment of length ℓ_s and not of length $L = m\ell_s$ (as in Eq. (3.160)), even though $\tilde{t} \gg 1$.

Figure 3.19 illustrates the long-time regime ($\tilde{t} > 1$) for an interval segmented into $m = 10$ compartments. On the top panel, the signal is plotted as a function of $\tilde{\kappa}\tilde{t}/(\tilde{\kappa}+1)$ at fixed $\tilde{q} = 0.5$ and different times. One can see that the scaling $\tilde{\kappa}\tilde{t}/(\tilde{\kappa}+1)$ makes all symbols fall onto one master curve. On the bottom panel, the signal is plotted as function of $\tilde{q}$ for three representative values of $\tilde{\kappa}\tilde{t}/(\tilde{\kappa}+1)$. At very low values of $\tilde{\kappa}\tilde{t}/(\tilde{\kappa}+1)$, almost no particle has crossed a barrier, and the signal is given by the squared form factor of a single interval (3.167). As a function of $\tilde{q}$, the signal exhibits a diffusion-diffraction pattern that reveals the

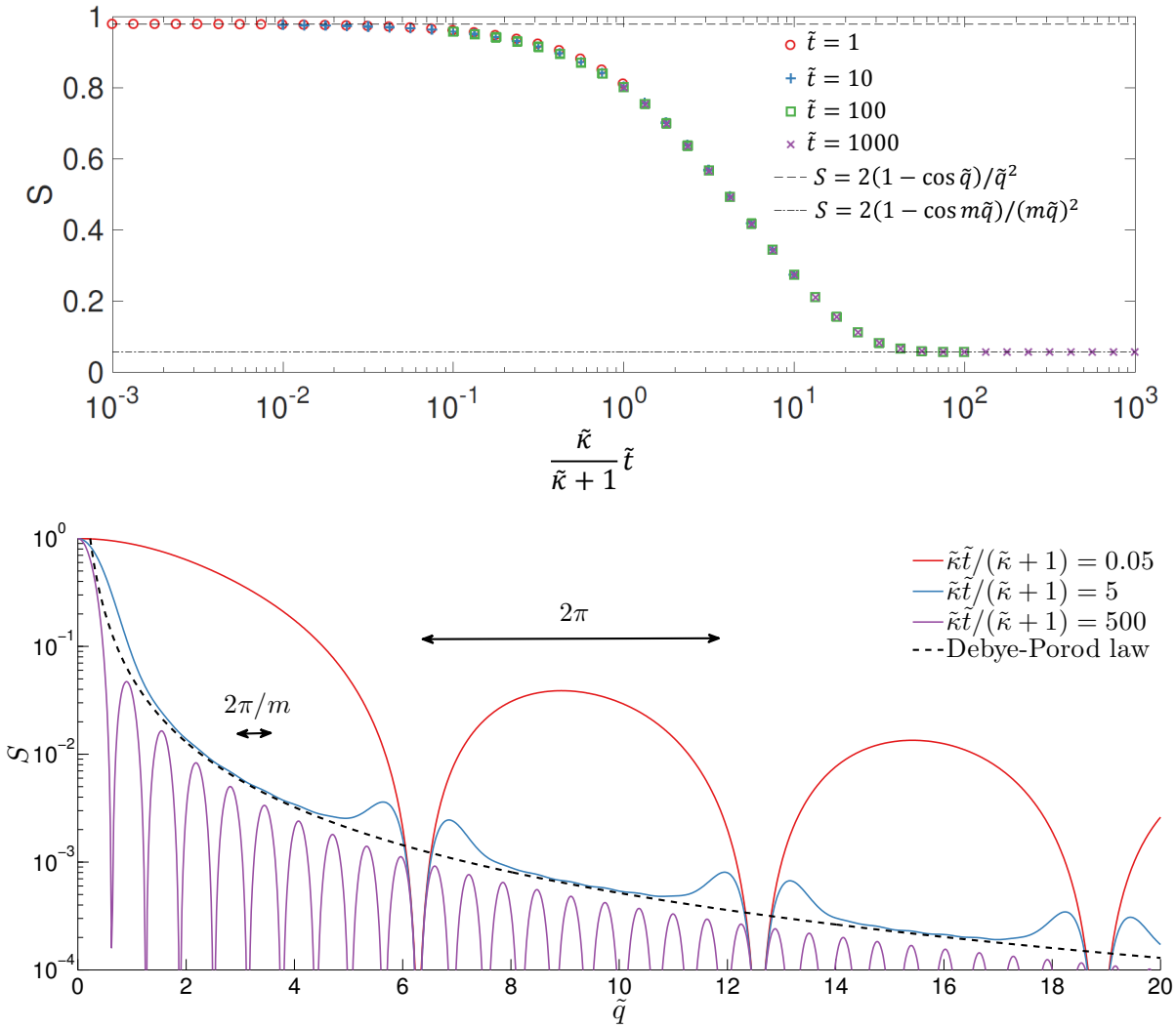

Figure 3.19: Signal at long diffusion times ($\tilde{t} > 1$) for $m = 10$ compartments. (top) The signal is plotted as a function of $\tilde{\kappa}\tilde{t}/(\tilde{\kappa}+1)$ for a fixed $\tilde{q} = 0.5$. One can see that the curves fall onto one master curve. The low- and high-permeability limits (Eqs. (3.167) and (3.160), respectively) are plotted by dashed and dash-dotted line, respectively. (bottom) The signal is plotted as a function of $\tilde{q}$ for three representative values of $\tilde{\kappa}\tilde{t}/(\tilde{\kappa}+1)$. The signal decreases with $\tilde{\kappa}\tilde{t}/(\tilde{\kappa}+1)$ and exhibits qualitatively different behaviors. The asymptotic Debye-Porod formula (1.62) ($S \sim 1/\tilde{q}^2$) is plotted by a dashed line for $\tilde{\kappa}\tilde{t}/(\tilde{\kappa}+1) = 5$.

size ℓ_s of the subintervals. As $\tilde{\kappa}\tilde{t}/(\tilde{\kappa}+1)$ increases, particles start to cross internal barriers and travel further. In this intermediate regime, diffusion in the bulk is effectively free with the reduced diffusion coefficient D_∞ and the signal mainly comes from contributions from the outer barriers, in the Debye-Porod regime (the corresponding asymptotic formula (1.62) is shown as dashed line

on the bottom panel). The diffusion-diffraction pattern is still present but much less pronounced. Finally, when $\tilde{\kappa}\tilde{t}/(\tilde{\kappa}+1)$ goes to infinity, particles travel multiple times through the whole interval and one recovers the limit (3.160), with a diffusion-diffraction behavior controlled by the total length $L = m\ell_s$: the signal as a function of $\tilde{q}$ exhibits peaks spaced by $2\pi/m$.

3.4.7 Summary

In this section, we presented an efficient method to compute the eigenmodes of the diffusion operator on a one-dimensional interval segmented by permeable barriers, which in turn give access to the diffusion propagator. One can then compute several diffusion-related quantities such as the dMRI signal for any pulse sequence or the first exit time distribution.

Although the general matrix formalism is applicable to other multi-layered structures such as concentric cylindrical or spherical shells [268], the main analytical simplifications follow from the translation invariance of the Laplacian eigenmodes which is specific to one-dimensional models. In particular we derived some estimates that help us to accurately compute the eigenvalues, even when they are extremely close to each other. This is the crucial numerical step that allowed us to deal with heterogeneous structures with hundreds of permeable barriers. This efficient method opens unprecedented opportunities to investigate the impact of microstructure onto diffusive motion.

Chapter 4

Localization

In the previous chapters we have encountered many different regimes for the magnetization (see Figs. 1.8 and 1.10). In Sec. 2.3 we have investigated the regime of short diffusion time $\ell_\mathrm{d} \ll \ell_\mathrm{s}$ and weak diffusion encoding $bD_0 \ll 1$ (i.e. $\ell_\mathrm{d} \ll \ell_g$ for extended-gradient and $\ell_\mathrm{d} \ll \ell_q$ for narrow-gradient). In Sec. 3.2, the study of small compartments led us to the motional narrowing regime $\ell_\mathrm{s} \ll \ell_\mathrm{d}$ and $\ell_\mathrm{s} \ll \ell_g$. Then in Sec. 3.4 we turned to narrow-gradient pulses and we studied the effect of exchange in the regimes of short-time, long-time, strong and weak position encoding.

The localization regime has not been discussed yet and is the object of this last chapter. It emerges in extended-gradient pulse experiments when the gradient length ℓ_g is smaller than any other relevant length scale, i.e. smaller than the diffusion length $\ell_g \ll \ell_\mathrm{d}$ and smaller than the structural scale $\ell_g \ll \ell_\mathrm{s}$. In the case of permeable boundaries, one would impose the additional condition $\ell_g \ll \ell_\kappa$, see Ref. [102]. This regime was first described theoretically by Stoller *et al.* in a profound yet technical paper devoted to the one-dimensional case (planar boundaries) [98]. Their results were qualitatively extended to higher dimensions (i.e., curved boundaries) and applied to explain the phenomenon of diffusive edge enhancement by de Swiet and Sen [99]. These theoretical findings were experimentally confirmed by Hürlimann *et al* in 1995 [100]. For about 20 years, the localization regime was almost completely ignored, probably because of (i) weak signals; (ii) mathematical technicity; and (iii) an overconfidence in the validity of low-b (perturbative) approaches such as Gaussian phase approximation. Recently, D. Grebenkov has asserted that the localization regime was accessible under moderate experimental conditions for almost any microstructure [101, 102]. Therefore, ignoring the localization regime could lead to misinterpretation of the measured signal.

We start this chapter with a qualitative description of the phenomenon of localization. Then follows a pedagogical presentation of the results of Stoller *et*

al., and their extension to curved boundaries. In Sec. 4.3, we turn to bounded domains and we investigate the peculiar phenomenon of spectral bifurcations and its consequence on the localization of the magnetization. The next section is devoted to periodic domains and contains results submitted in [348]. We show how one can solve numerically the Bloch-Torrey equation from computations on a single unit cell of the lattice, and we apply this technique to the investigation of various regimes of dMRI as well as spectral properties of the Bloch-Torrey operator. Finally, we present in Sec. 4.5 experimental validations in collaboration with K. Demberg and T. Kuder from German Cancer Research Center (DKFZ), Heidelberg, Germany, and these results were published in [347].

4.1 Qualitative description of the localization regime

Before going into the technical details of the localization regime, we ask a simple question: "why is the magnetization localized at high gradient strength?". We shall revise common misconceptions and provide a qualitative explanation for this behavior. Then we extend this qualitative description to emphasize the difference between the motional narrowing regime and the localization regime. As we described in the introduction, the main features of the localization regime are: (i) the magnetization is localized over the length $\ell_g = (G/D_0)^{-1/3}$ near points where the boundary is perpendicular to the gradient, and (ii) the signal decays as $-\log S \sim \ell_{\mathrm{d}}^2/\ell_g^2 = D_0^{1/3}G^{2/3}T$, in contrast to the free diffusion decay $-\log S \sim \ell_{\mathrm{d}}^6/\ell_g^6 = D_0G^2T^3$, and the motional narrowing decay $-\log S \sim \ell_{\mathrm{s}}^4\ell_{\mathrm{d}}^2/\ell_g^6 = G^2L^4T/D_0$ (see Table 1.1 for the definition of the length scales ℓ_{d}, ℓ_{s}, and ℓ_g). We emphasize that at large values of $bD_0 = D_0G^2T^3$, the signal in the localization regime is orders of magnitude above the signal in the free diffusion regime.

4.1.1 Reduced mean-squared displacement?

The main argument that is commonly put forward to rationalize localization of the magnetization is that the displacement of particles along the gradient direction is the most reduced at boundaries that are perpendicular to the gradient. Although this restriction is indeed present, we argue that its effect is far too weak to explain the drastic change in the signal decay in comparison to free diffusion. In Sec. 2.3.1, we obtained the formula for the mean-squared displacement for a particle near the boundary, illustrated on Fig. 2.6. The computation reveals that the mean-squared displacement is reduced at most by 40% of its nominal value. Although this is a strong effect in itself, it cannot explain that the decay of the

signal would not follow the $D_0 G^2 T^3$ law anymore. In fact, to be consistent one would model the signal as free diffusion with an effective diffusion coefficient D so that the signal would decay as DG^2T^3. Therefore, this explanation fails to reproduce the behavior of the localization regime.

From another viewpoint, the argument of "reduced displacement" implicitly assumes that the Gaussian phase approximation is valid so that the decay of the signal is directly related to the variance of the phase and in turn to the mean-square displacement of particles. However, the distribution of phases is not Gaussian anymore close to a boundary because of velocity correlations introduced by reflections on the boundary.

Another flaw in this reasoning is that it would yield a magnetization that is localized over ℓ_d and not over ℓ_g. Indeed as shown on Fig. 2.6, the mean-squared displacement is reduced inside a layer of thickness ℓ_d close to the boundary. Naturally, one would argue that in the regime of $\ell_\mathrm{d} \gg \ell_g$, particles that travel further than ℓ_g would yield a magnetization too small so that we discard them from the computation of the signal. This observation is the basis of the next argument.

4.1.2 Competition between confined trajectories and magnetization decay?

This qualitative argument was privately presented to me by V. Kiselev. Let us consider a single impermeable boundary at $x = 0$ and introduce a virtual boundary at $x = \ell$ that particles can freely cross. The number of particles $f(\ell)$ that remain confined between the two boundaries during the whole gradient sequence can be simply estimated[1] as

$$f(\ell) \sim \ell \exp\left(-\frac{\pi^2 \ell_\mathrm{d}^2}{4\ell^2}\right), \tag{4.1}$$

and the (non-normalized) signal coming from those particles follows from the motional narrowing regime in a slab of width ℓ under the hypothesis $\ell \ll \ell_\mathrm{d}$:

$$s(\ell) = f(\ell) \exp\left(-\frac{\ell^4 \ell_\mathrm{d}^2}{120 \ell_g^6}\right). \tag{4.2}$$

Then one studies the competition between motional narrowing decay and "leakage" of particles outside the virtual slab by maximizing the signal with respect

[1] This formula is obtained by solving the diffusion equation inside a slab with an absorbing boundary. Precisely, the long-time behavior $f(\ell) \sim (1|u_1)^2 e^{-\lambda_1 T}$ results from the computation of the first eigenmode, $u_1(x) = \sqrt{2/\ell}\cos(\pi x/2\ell)$, and the corresponding eigenvalue $\lambda_1 = D_0\pi^2/4\ell^2$.

to ℓ, that yields $\ell \approx 2.3\,\ell_g$ and the signal becomes

$$s(\ell) \sim \ell_g \exp\left(-0.70\,\ell_{\mathrm{d}}^2/\ell_g^2\right) . \tag{4.3}$$

Although the numerical coefficient is wrong that shows the limits of such a simple model, this reasoning provides the correct form of the signal. It shows that the signal is produced by exceptional trajectories of particles that stay close to the boundaries of the domain. Indeed, the strong diffusion encoding assumption $\ell_g \ll \ell_{\mathrm{d}}$ implies that $f(\ell)/\ell$ is very small for $\ell \sim \ell_g$.

This is an elegant idea that brings additional insight into the mechanisms behind the localization regime. However, there are several flaws in this argument. We discard technical details such as the use of the motional narrowing for non-impermeable boundaries.

The first one is to consider a virtual boundary that is perfectly absorbing and that prevents the entry of particles from the outside. In that regard, it is hard to give a physical meaning to $s(\ell)$, since the signal inside the slab should take into account neighboring particles that enter through the virtual boundary. One could argue that we discard particles from the outside because of their strongly decayed magnetization, however this argument fails for two reasons: (i) if $\ell \ll \ell_g$, particles that come from a distance $\sim \ell_g$ may enter the virtual slab without experiencing a strong decay, and therefore they cannot be neglected; (ii) if $\ell \gg \ell_g$, particles from the outside have weak magnetization, but so do particles inside, and it is not obvious whether the former can be neglected with respect to the latter.

The second difficulty is related: why should we maximize $s(\ell)$ with respect to ℓ? It would seem more consistent to take into account the signal from the whole medium by mean of integration over all values of ℓ or something similar.

The third issue is probably the most problematic one: the reasoning could be applied exactly the same way to any point of the medium, regardless of the presence of a boundary. Instead of considering a virtual boundary close to the impermeable boundary, one would consider two virtual boundaries and compute $s(\ell)$ for this "virtual slab". The only thing that would change is $f(\ell) \sim \exp\left(-\pi^2\ell_{\mathrm{d}}^2/\ell^2\right)$, and in turn the numerical coefficient inside the exponential. This observation emphasizes the aforementioned contradictions about the definition of $s(\ell)$.

Even though this reasoning yields the correct form of the signal, it does not explain why the magnetization is localized at the boundary. In the next paragraph, we suggest a new qualitative interpretation of the localization regime. We shall see at some point some similarities with the above idea, that might explain why it seems to work so well.

4.1.3 Symmetry breaking and local effective gradient

We turn to our own qualitative explanation of the localization regime. We shall see that the main effect of the boundary is not to reduce particles displacements but a symmetry breaking. This symmetry breaking yields an effective magnetic field that is not linear with position but has a V-shape. Then we show how localization occurs inside this effective magnetic field.

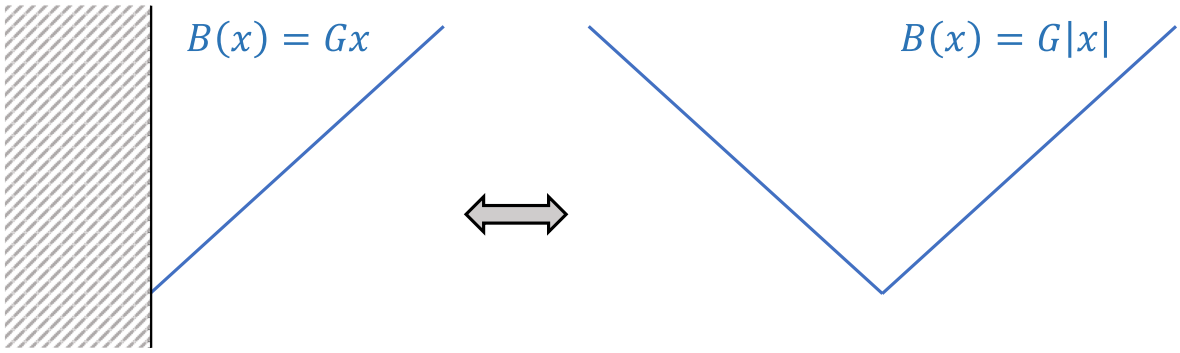

Figure 4.1: (left) Impermeable boundary and linear magnetic field. (right) No boundary and V-shaped magnetic field. Both situations are equivalent according to the method of images.

For simplicity, we consider a one-dimensional situation, with a barrier at $x = 0$ and particles diffusing inside the half-space $x \geq 0$. Using the method of images, one can remove the boundary provided that each particle on the right half-space is paired with a "mirror" particle on the left half-space. Therefore, the effect of the impermeable boundary can be taken into account by replacing the linear magnetic field $B(x) = Gx$ by a V-shape magnetic field $B(x) = G|x|$, as shown on Fig. 4.1. Note that in the Bloch-Torrey equation, the magnetic field plays the role of an *imaginary* potential, by analogy with the Schrödinger equation. Although it is tempting to make a parallel with localization inside a real potential, it is not evident that the same conclusion would hold for an imaginary potential.

In order to demonstrate the localization phenomenon, let us write the magnetization as an amplitude-phase representation, $m(t,x) = A(t,x)e^{i\varphi(t,x)}$, and write the Bloch-Torrey equation in terms of A, φ:

$$\partial_t A = D_0 A'' - D_0 A \varphi'^2 \,, \tag{4.4a}$$

$$\partial_t \varphi = D_0 \varphi'' + D_0 \frac{A'}{A} \varphi' + G|x| \,, \tag{4.4b}$$

where prime denotes derivative with respect to x. The initial condition is $A(t = 0, x) = 1$ and $\varphi(t = 0, x) = 0$. The first equation states that $A(t,x)$ obeys a

diffusion equation with a reaction rate $D_0\varphi'^2$. The second equation states that φ obeys a diffusion equation with a force term $-D_0A'/A$ and a source term $G|x|$. We emphasize that $\varphi(t,x)$ is a deterministic quantity that should not be confused with the random particle dephasing ϕ.

Short times

At short times, $A(t,x)$ is nearly constant and the evolution of the magnetization is dominated by the phase equation

$$\partial_t\varphi = D_0\varphi'' + G|x| \,, \tag{4.5}$$

whose solution is

$$\varphi(t,x) = G\int_0^t \left[x\,\mathrm{erf}\left(\frac{x}{\sqrt{4D_0t'}}\right) + \frac{\sqrt{4D_0t'}}{\sqrt{\pi}}\exp\left(-\frac{x^2}{4D_0t'}\right)\right]\mathrm{d}t' \tag{4.6a}$$

$$= G\left[tx\,\mathrm{erf}\left(\frac{x}{\sqrt{4D_0t}}\right) - \frac{2}{3}\frac{x^3}{4D_0}\left(1-\mathrm{erf}\left(\frac{x}{\sqrt{4D_0t}}\right)\right) + \frac{2}{3\sqrt{\pi}}\sqrt{4D_0t}\left(t+\frac{x^2}{4D_0}\right)\exp\left(-\frac{x^2}{4D_0t}\right)\right] \,, \tag{4.6b}$$

where erf is the Gauss error function

$$\mathrm{erf}(u) = \frac{2}{\sqrt{\pi}}\int_0^u e^{-v^2}\,\mathrm{d}v \,. \tag{4.7}$$

The formula for φ is rather involved but becomes much simpler after position and time derivation:

$$\partial_t\varphi(t,x) = Gx\,\mathrm{erf}\left(\frac{x}{\sqrt{4D_0t}}\right) + \frac{\sqrt{4D_0t}}{\sqrt{\pi}}\exp\left(-\frac{x^2}{4D_0t}\right) \,, \tag{4.8a}$$

$$\partial_t\varphi'(t,x) = G\,\mathrm{erf}\left(\frac{x}{\sqrt{4D_0t}}\right) \,. \tag{4.8b}$$

The rate of change of φ with time can be interpreted as an effective magnetic field averaged by diffusion, and the space derivative of this rate of change is an effective gradient averaged by diffusion. We have plotted these functions on Fig. 4.2. The main effect of diffusion is to "smooth" the V-potential over a length $\sim \ell_\mathrm{d}$ near $x = 0$, resulting in a local parabolic shape. In turn, the effective gradient takes smaller values in this region, that translates into smaller values of φ'^2. The results for free diffusion are recovered for $|x| \gg \ell_\mathrm{d}$, where one gets $\partial_t\varphi' = G$ and $[\varphi'(t,x)]^2 = (Gt)^2$. This limits the validity of the above equations to short

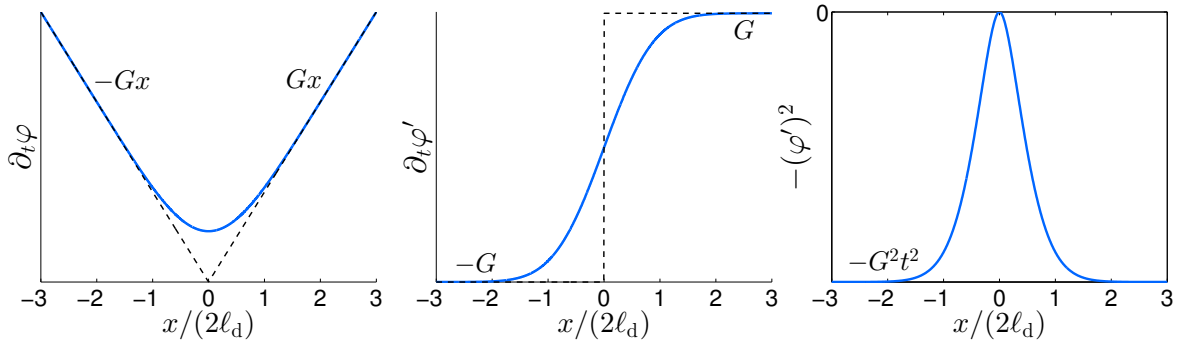

Figure 4.2: Plot of $\partial_t\varphi$ (left), $\partial_t\varphi'$ (middle), and $-\varphi'^2$ (right) at short times ($\ell_\mathrm{d} \ll \ell_g$).

times such that $D_0G^2t^3/3 \ll 1$, i.e. $\ell_\mathrm{d}^6/3\ell_g^6 \ll 1$. Indeed, these equations rely on the assumption that the amplitude of the magnetization remains approximately constant in space, i.e. that the free diffusion decay far from the boundary is not too large compared to the weak decay at $x = 0$. This corresponds to $\ell_\mathrm{d}/\ell_g = 1.0$–$1.25$ on Fig. 4.3: the amplitude is practically not affected and the phase profile exhibits the rounded V-shape profile that we just described.

Intermediate times

When the free diffusion decay cannot be neglected anymore, the evolution of the magnetization enters a second step that corresponds to intermediate times ($\ell_\mathrm{d}/\ell_g = 1.5$–$1.75$ on Fig. 4.3). The free diffusion decay term $D_0G^2t^3$ becomes rapidly very large and the amplitude A decays very fast except at the points where φ'^2 is significantly reduced, i.e. everywhere but in a thin layer of width $\sim \ell_\mathrm{d} \approx \ell_g$. In turn, the "force" $-D_0A'/A$ becomes a strong effect that broadens the phase profile. Intuitively, the amplitude of the magnetization becomes much stronger in the center than to the sides, therefore the diffusion process becomes dominated by the magnetization flux from the center to the sides. In competition with this broadening effect, the source term $G|x|$ tends to make the phase profile steeper. Since the force term enters through $D_0A'/A\varphi'$, one can see that there is a value of φ' at which both effects compensate each other. In parallel, the evolution of the amplitude A results from the competition of two effects that are diffusion and attenuation. The inhomogeneous attenuation of the amplitude enhances the effect of diffusion, and in turn diffusion tends to homogenize the amplitude profile. Therefore, a balance between these two effects is also reached after some time.

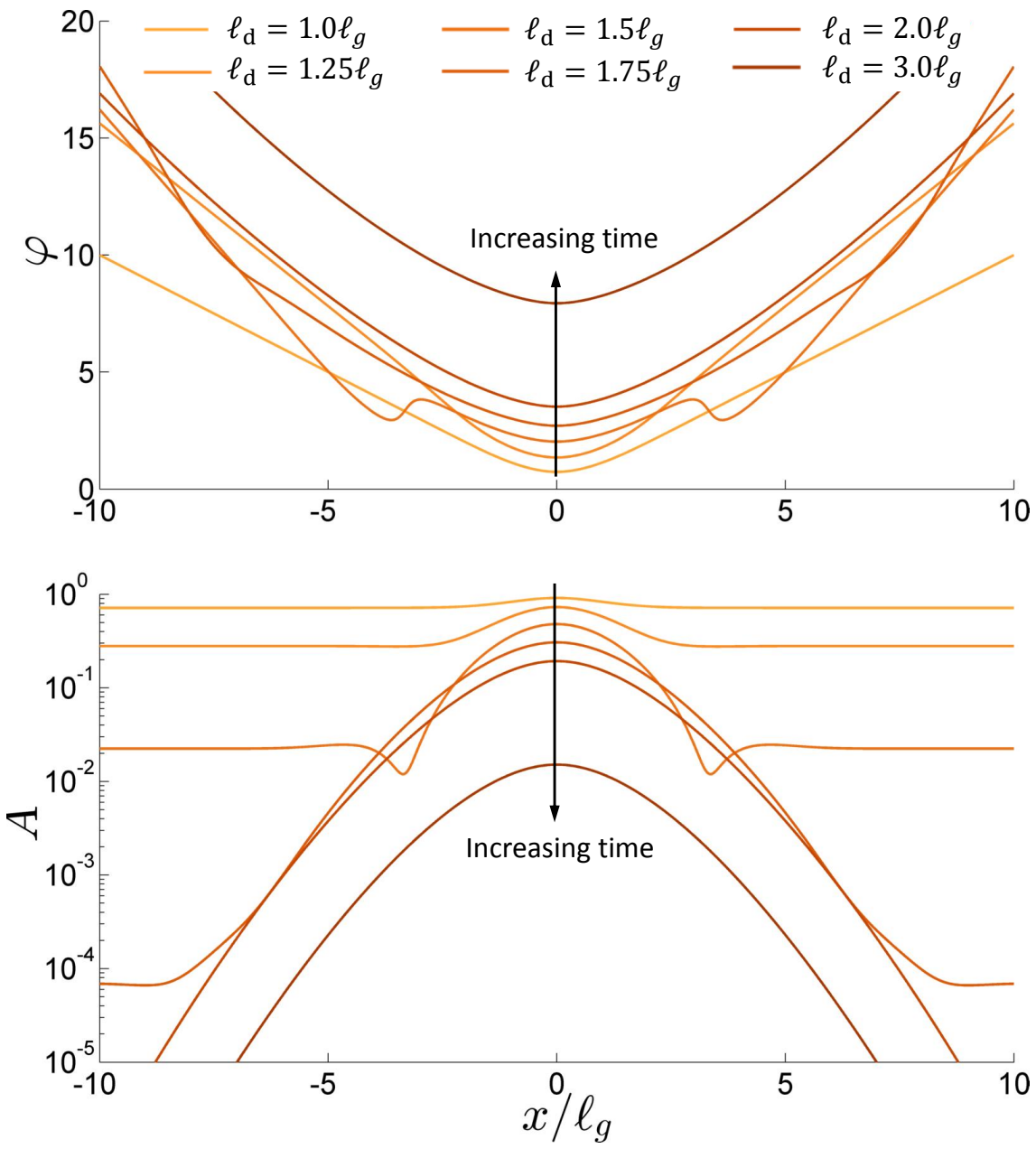

Figure 4.3: Time evolution of the magnetization profile in phase (top) and amplitude (bottom) representation, for a constant gradient. The barrier is located at $x = 0$ and the amplitude and phase profiles are reflected with respect to $x = 0$ according to the method of images. Refer to the text for description.

Long times

In this final step, a dynamic balance between competing effects is set (see Fig. 4.3 for $\ell_d/\ell_g = 2.0$–3.0). Diffusion tends to broaden the amplitude profile, but the strong decay $-\varphi'^2$ destroys the magnetization outside of $|x| \lesssim \ell_g$. Therefore, the

situation is analogous to that of a slab of width $\sim \ell_g$ with absorbing boundaries, hence the decay $-\log A \sim \ell_{\mathrm{d}}^2/\ell_g^2$. The source term $G|x|$ tends to make the phase profile steeper but the force term $-D_0 A'/A$ broadens it by "pushing" towards high $|x|$. In other words, particles at the center with a (relatively) strong magnetization diffuse away from the center and dominate particles at the sides that have a much weaker magnetization. Therefore, the source term $G|x|$ contributes only up to $|x| \approx \ell_g$, and the phase profile translates upwards as $\sim G\ell_g t = \ell_{\mathrm{d}}^2/\ell_g^2$. These conclusions reproduce exactly the behavior of the magnetization in the localization regime.

Note that similarly to the argument by V. Kiselev, we obtain that at long times the phenomenon is similar to diffusion inside a slab of width ℓ_g with absorbing boundaries. In other words, the signal in the localization regime is produced by rare trajectories that remain close to the boundary at all times. However, we do not rely on the motional narrowing regime formula and the effect of the boundary is explicitly taken into account as a symmetry breaking of the phase profile (more precisely, the phase profile becomes even instead of odd that leads to a region with reduced decay rate φ'^2). In particular, in the absence of a boundary, the magnetic field profile is linear and there is no region of space with a reduced effective gradient therefore there is no localization.

In the next paragraph, we further emphasize the mechanism of the localization regime by taking into account the size ℓ_{s} of the domain and by investigating qualitatively the transition between motional narrowing regime and localization regime.

4.1.4 Localization regime and motional narrowing regime

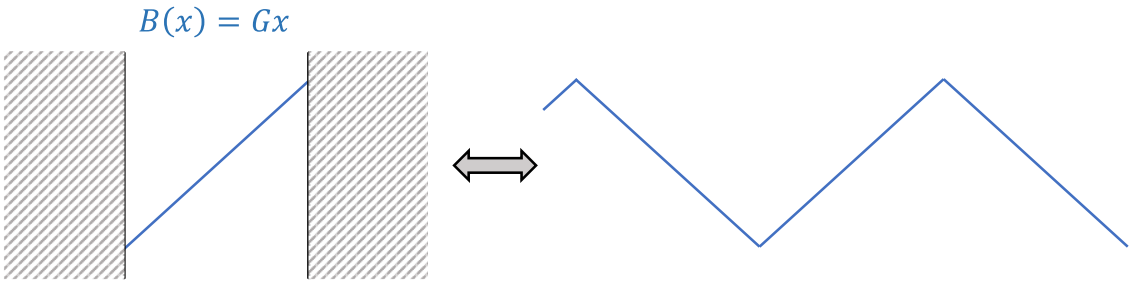

Figure 4.4: (left) Slab with impermeable boundaries and linear magnetic field. (right) No boundary and periodic triangular profile. Both situations are equivalent according to the method of images.

We employ the same qualitative description as above, but now we consider a finite slab of width ℓ_s. As illustrated on Fig. 4.4, the method of images yields a periodic triangular magnetic field, with period $2\ell_s$. To obtain the phase profile φ, the effective magnetic field $\partial_t\varphi$ and the effective gradient $\partial_t\varphi'$ averaged by diffusion at short times ($\ell_d \ll \ell_g$), we solve the diffusion equation for the phase profile without the term D_0A'/A and get

$$\varphi(t,x) = \frac{\ell_s^3}{\ell_g^3}\sum_{n=0}^{\infty}\frac{(-1)^n}{4\pi^4(n+1/2)^4}\sin\left((2n+1)\pi x/\ell_s\right)\left[1-e^{-(2n+1)^2\pi^2\ell_d^2/\ell_s^2}\right], \quad (4.9)$$

$$\partial_t\varphi(t,x) = G\ell_s\sum_{n=0}^{\infty}\frac{(-1)^n}{\pi^2(n+1/2)^2}\sin\left((2n+1)\pi x/\ell_s\right)e^{-(2n+1)^2\pi^2\ell_d^2/\ell_s^2}, \quad (4.10)$$

$$\partial_t\varphi'(t,x) = G\sum_{n=0}^{\infty}\frac{2(-1)^n}{\pi(n+1/2)}\cos\left((2n+1)\pi x/\ell_s\right)e^{-(2n+1)^2\pi^2\ell_d^2/\ell_s^2}. \quad (4.11)$$

The last two functions are plotted on Fig. 4.5. One can see that as time increases, the effective field and gradient become rounder and weaker because of compensation between positive and negative parts. Therefore, one is naturally led to distinguish between two regimes, depending on the range of validity of the above formulas, i.e. the time from which the amplitude decay plays a significant role.

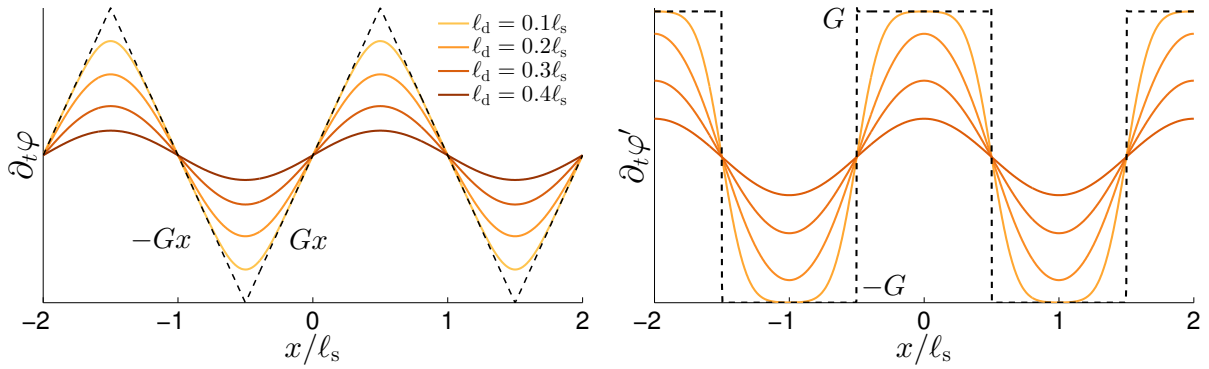

Figure 4.5: Effective magnetic field (left) and effective gradient (right) averaged by diffusion for $\ell_d \ll \ell_g$, at various ratios ℓ_d/ℓ_s. As time increases, both functions become rounder but also weaker because of compensation between positive and negative parts. Note that the slab corresponds to $-1/2 \leq x/\ell_s \leq 1/2$ and is repeated periodically according to the method of images.

Localization regime (large slab, strong gradient)

Let us first consider the case $\ell_g \ll \ell_s$ corresponding to the localization regime. For example, if $\ell_g = 0.1\ell_s$, the above formulas for φ, $\partial_t\varphi$ and $\partial_t\varphi'$ are valid until $\ell_d \approx$

$0.1\ell_s$, after which the amplitude decay becomes significant. This corresponds to the light yellow curves on Fig. 4.5. Since $\ell_d \ll \ell_s$, the effective magnetic field profile is close to triangular with a small parabolic part, similarly to the left panel of Fig. 4.2. The discussion of the above section applies without any modification to this regime, and the magnetization is localized at the boundaries.

Motional narrowing regime (small slab, weak gradient)

The opposite regime is $\ell_s \ll \ell_g$ and corresponds to the motional narrowing regime. In that case, the above formulas for $\partial_t\varphi$, $\partial_t\varphi'$ are valid over a very long time range (corresponding to the dark brown curves on Fig. 4.5). In particular, for $\ell_s \lesssim \ell_d \ll \ell_g$, Eq. (4.9) becomes

$$\varphi(t,x) \approx \frac{\ell_s^3}{\ell_g^3}\sum_{n=0}^{\infty}\frac{(-1)^n}{4\pi^4(n+1/2)^4}\sin\left((2n+1)\pi x/\ell_s\right) \tag{4.12a}$$

$$= \frac{\ell_s^3}{24\ell_g^3}\frac{x}{\ell_s}\left(3-4\frac{x^2}{\ell_s^2}\right), \qquad (-0.5 \le x/\ell_s \le 0.5), \tag{4.12b}$$

from which one obtains the decay rate

$$D_0\varphi'^2 \approx \frac{1}{64}\frac{D_0\ell_s^4}{\ell_g^6}\left[1-\left(\frac{2x}{\ell_s}\right)^2\right]^2, \qquad \frac{1}{\ell_s}\int_{-\ell_s/2}^{\ell_s/2} D_0\varphi'^2(t,x)\,\mathrm{d}x \approx \frac{D_0\ell_s^4}{120\ell_g^6}, \tag{4.13}$$

that yields an average signal decay $S \approx \exp(-(1/120)\ell_d^2\ell_s^4/\ell_g^6)$, which is the exact result for the motional narrowing, see Refs [3, 79, 81] and Sec. 1.2.2 and Sec. 4.3.1 below. At long times, the decay of the signal becomes significant, and one may wonder about the validity of the previous result. Actually, one can see that the decay of the signal occurs on a time scale $\ell_g^6/(D_0\ell_s^4)$ much larger than the diffusion time scale ℓ_s^2/D_0. As a consequence the diffusion term in the equation for the amplitude flattens any inhomogeneity in the amplitude profile. In turn, since the amplitude profile is nearly homogeneous at all times, the formula (4.12a) for φ, that relies on neglecting the force term D_0A'/A, is always valid at long times.

Breakdown of Gaussian phase approximation

As we discussed in Sec. 1.2.2, the motional narrowing regime may be obtained from the central limit theorem applied to successive explorations of a bounded domain [81]. The main hypothesis behind this reasoning is that any particle "loses memory" of its initial position after a time $\sim \ell_s^2/D_0$. This hypothesis allows

one to treat the acummulated phases over successive explorations of the domain as independent from each other, that is a crucial assumption for the central limit theorem to hold. This argument implies that the distribution of the random phase ϕ is Gaussian. In turn the signal is a Gaussian function of the gradient strength: $-\log S \sim G^2 L^4 T/D_0$. Since this reasoning relies on the central limit theorem, it seems very robust and it is *a priori* not clear why it would break down if the gradient length is much smaller than the pore diameter (i.e., $\ell_g \ll \ell_s$).

The above computation reveals that in the localization regime, a small fraction of particles, of order $\exp(-\ell_d^2/\ell_g^2)$, remains close to the boundary and dominates the signal due to the local symmetry breaking caused by the boundary. In terms of accumulated phase, this means that the velocity correlations introduced by the boundary make the phase distribution non-Gaussian for particles close to the boundary. At high gradient, these velocity correlations are strongly weighted by the gradient (see Eq. (1.27c)) and yield a significant contribution. Note, however, that the regime $\ell_g \ll \ell_s \ll \ell_d$ would yield a very weak signal, so that this discussion is of purely theoretical interest.

4.2 Localization at a single boundary

In this section we consider a porous medium with pores of diameter ℓ_s and we assume that the diffusion length ℓ_d and the gradient length ℓ_g are both much smaller than ℓ_s. By following the reasoning depicted on Fig. 2.5, we consider the effect of a single impermeable boundary on the magnetization. Contrary to Sec. 2.3.1 where the signal under weak diffusion encoding was governed by the variance of spin dephasing ϕ, we compute *non-perturbatively* the magnetization and signal and we study in particular the regime of strong diffusion encoding (i.e., $\ell_g \ll \ell_d$). We consider first the case of a planar boundary, then we take into account the effect of curvature [94, 95, 98, 99].

4.2.1 Planar boundary

Here, we revisit the seminal work by Stoller *et al* [98] and present results in a simpler form (see also [94] for a rigorous mathematical treatment). Let us assume that the boundary is the plane $x = 0$ and that diffusion occurs in the half-space $x \geq 0$. The initial magnetization is uniform and equal to 1. Note that the total signal is infinite because of unbounded geometry, however this is of no concern because we are interested in the magnetization at a given point $m(T, x, y, z)$, which is always finite.

In that case diffusion along x, y, and z are independent and the magnetization after a single gradient pulse of amplitude $\mathbf{G}$ and duration δ can be represented as

$$m(\delta, \mathbf{r}) = m_{1D}(\delta, x) \exp(iG_y\delta y - D_0 G_y^2 \delta^3/3) \exp(iG_z\delta z - D_0 G_z^2 \delta^3/3) \,, \quad (4.14)$$

where the contributions from G_y, G_z are given by the expressions for free diffusion. In the following, we compute m_{1D}, i.e. the magnetization profile along x. To simplify our notations, we assume that the gradient is along x, i.e. $G_x = G$ and $m_{1D} = m$. We first compute the effect of a single extended gradient pulse, then we obtain the expression of the magnetization after two opposite pulses.

One-dimensional Bloch-Torrey equation

To compute the magnetization profile m, we have to solve the one-dimensional Bloch-Torrey equation

$$\partial_t m = D_0 \partial_x^2 m + iGxm \,, \quad (4.15a)$$

$$\partial_x m|_{x=0} = 0 \,. \quad (4.15b)$$

In order to put this equation in a dimensionless form, we perform the scaling:

$$\tilde{x} = x/\ell_g \,, \qquad \tilde{t} = D_0 t/\ell_g^2 \,, \quad (4.16)$$

and we obtain the dimensionless BT equation:

$$\tilde{\partial}_t m = \tilde{\partial}_x^2 m + i\tilde{x} m \ . \tag{4.17a}$$

$$\tilde{\partial}_x m\big|_{\tilde{x}=0} = 0 \ . \tag{4.17b}$$

Eigenmode equation

To solve Eq. (4.17a), we look for eigenmodes $v_n(\tilde{x})$ of the one-dimensional dimensionless Bloch-Torrey operator

$$\tilde{\mathcal{B}} = -\tilde{\partial}_x^2 - i\tilde{x} \ , \tag{4.18}$$

in order to express $m(\tilde{t}, \tilde{x})$ as an eigenmode decomposition. We postpone until later the validity of this decomposition, i.e. the completeness of the eigenmode family, and we solve

$$-v'' - i\tilde{x}v = \tilde{\mu} v \ . \tag{4.19a}$$

$$v'|_{\tilde{x}=0} = 0 \ , \tag{4.19b}$$

for a complex coefficient $\tilde{\mu}$. Note that the minus sign in the definition of $\tilde{\mathcal{B}}$ is here to ensure a positive real part of $\tilde{\mu}$, as we have seen in Sec. 1.2.4. Now we make the abstract change of variables

$$\xi = i\tilde{x} + \tilde{\mu} \ . \tag{4.20}$$

The complex variable ξ runs along a vertical semi-axis in the complex plane when $\tilde{x}$ goes from 0 to ∞. With this change of variables, the eigenmode equation (4.19) becomes

$$\frac{\mathrm{d}^2 v}{\mathrm{d}\xi^2} - \xi v = 0 \tag{4.21a}$$

$$\left.\frac{\mathrm{d}v}{\mathrm{d}\xi}\right|_{\xi=-\tilde{\mu}} = 0 \ , \tag{4.21b}$$

that is the Airy equation.

Let us put aside the boundary condition (4.21b) for the moment and discuss the general solution of Eq. (4.21a). Since it is a second-order linear differential equation, any solution may be represented as a linear combination of two fundamental solutions. A particular solution is the Airy function that can be written as an improper integral for real argument:

$$\mathrm{Ai}(\xi) = \frac{1}{2\pi} \int_{-\infty}^{\infty} e^{i\xi u} e^{iu^3/3} \, \mathrm{d}u \ , \qquad (\xi \in \mathbb{R}) \ . \tag{4.22}$$

For a complex argument, the integral should be performed along a path in the complex plane that goes to infinity inside the sextants $0 < \arg(u) < \pi/3$ and $2\pi/3 < \arg(u) < \pi$, so that the factor $e^{iu^3/3}$ decays fast enough to compensate for the exponential growth of $e^{i\xi u}$. With this definition, the Airy function is real-valued for real arguments and is an entire function over the whole complex plane. Moreover, one can check that the Airy equation (4.21a) is invariant by $\xi \to e^{2i\pi/3}\xi$, so that one can form two new solutions $\mathrm{Ai}(e^{2i\pi/3}\xi)$ and $\mathrm{Ai}(e^{-2i\pi/3}\xi)$. Naturally, these three solutions are not independent and one has

$$\mathrm{Ai}(\xi) + e^{2i\pi/3}\mathrm{Ai}(e^{2i\pi/3}\xi) + e^{-2i\pi/3}\mathrm{Ai}(e^{-2i\pi/3}\xi) = 0 \,, \tag{4.23}$$

for any complex number ξ. Since ξ depends on the position x via $i\tilde{x}$, we shall see that it is more convenient to choose $\mathrm{Ai}(e^{\pm 2i\pi/3}\xi)$ as fundamental solutions and we define two functions

$$F_{\mathrm{r}}(z) = \mathrm{Ai}(ie^{-2i\pi/3}z) \,, \qquad F_{\mathrm{l}}(z) = \mathrm{Ai}(ie^{2i\pi/3}z) \,. \tag{4.24}$$

One can see that $F_{\mathrm{r}}(\tilde{x} - i\tilde{\mu})$ and $F_{\mathrm{l}}(\tilde{x} - i\tilde{\mu})$ are solutions of Eqs. (4.19a) without taking into account the boundary condition at $\tilde{x} = 0$. Moreover, they are symmetric of each other in the sense that

$$F_{\mathrm{l}}(z) = F_{\mathrm{r}}(-z^*)^* \,. \tag{4.25}$$

We show in Appendix C.2 that $F_{\mathrm{r}}(\tilde{x} - i\tilde{\mu})$ is (i) a fast decaying function for $\tilde{x} \to \infty$, with $-\log(|F_{\mathrm{r}}|) \sim \tilde{x}^{3/2}$, and (ii) a fast diverging function for $\tilde{x} \to -\infty$, with $\log(|F_{\mathrm{r}}|) \sim (-\tilde{x})^{3/2}$. According to the symmetry between F_{r} and F_{l} expressed by Eq. (4.25), the same conclusion holds for $F_{\mathrm{l}}(\tilde{x} - i\tilde{\mu})$ but with opposite $\tilde{x}$, i.e. it decays for $\tilde{x} \to -\infty$ and diverges for $\tilde{x} \to \infty$. One can see immediately that $F_{\mathrm{r}}(\tilde{x} - i\tilde{\mu})$ is the only solution of Eq. (4.19b) that is bounded at ∞ and that $F_{\mathrm{l}}(\tilde{x} - i\tilde{\mu})$ is the only solution that is bounded at $-\infty$. This is the reason for our choice of fundamental solutions (the subscript "r" stands for "right", and the subscript "l" stands for "left").

We recall that diffusion takes place in the "right" half-space $\tilde{x} \geq 0$. Since we are looking for an eigenmode that can be normalized, we conclude that

$$v = \beta F_{\mathrm{r}}(\tilde{x} - i\tilde{\mu}) \,, \tag{4.26}$$

with β a normalization coefficient that is explicited in the next paragraph. The eigenvalue $\tilde{\mu}$ is determined by the boundary condition (4.19b) $F_{\mathrm{r}}'(-i\tilde{\mu}) = 0$, yielding the solutions

$$\tilde{\mu}_n = e^{2i\pi/3}a_n \,, n = 1, 2, \dots \,, \tag{4.27}$$

where a_n are zeros of $\mathrm{Ai}'(z)$, $a_1 = -1.019$, $a_2 = -3.248$, $a_3 = -4.820$, $a_4 = -6.163$, $a_5 = -7.372$, etc. One can show that there are infinitely many zeros and that they are all real and negative. Note that the eigenvalues $\tilde{\mu}_n$ have all a positive real part, as we claimed above.

Properties of the eigenmodes

Let us summarize the results so far. We have looked for eigenmodes of the dimensionless BT equation (4.19a). If one goes back to the original BT equation, this is equivalent to solving

$$D_0 v_n'' + iGx v_n = -\mu_n v_n \,, \tag{4.28a}$$

$$v_n'(x=0) = 0 \,. \tag{4.28b}$$

We have obtained that there are infinitely many pairs (v_n, μ_n) that are solutions and they are given by

$$v_n = \beta_n F_\mathrm{r}\left(\frac{x}{\ell_g} - e^{i\pi/6}|a_n|\right) \,, \tag{4.29a}$$

$$\mu_n = \frac{D_0}{\ell_g^2} e^{-i\pi/3}|a_n| \,, \tag{4.29b}$$

where a_n are the zeros of the derivative of the Airy function [98, 99]. The fast decay of F_r for $x/\ell_g \gg 1$ confirms *a posteriori* the validity of the local computation (i.e., neglecting the influence of other boundary elements in the domain).

As we discussed in Sec. 1.2.4, the normalization condition of the eigenmodes is $\int v_n^2 = 1$. Although v_n is complex, the normalization does not involve the absolute value of v_n because of the non-Hermitianity of the BT operator. We show in Appendix C.1 that the normalization coefficient β_n is given by

$$\beta_n^{-2} = e^{i\pi/6}\ell_g |a_n| \mathrm{Ai}^2(a_n) \,. \tag{4.30}$$

Similarly to the computation of the normalization coefficient in the previous chapter (Sec. 3.4.2), the computation of β_n allows us to prove at the same time that the eigenmode family is complete. Therefore, the behavior of the magnetization results from the behavior of the eigenmodes v_n, and in turn of the function F_r.

On Fig. 4.6 we have plotted $F_\mathrm{r}(z)$ on the complex plane with separate plots for $\mathrm{Re}(F_\mathrm{r}(z))$, $\mathrm{Im}(F_\mathrm{r}(z))$, and $|F_\mathrm{r}(z)|$. These plots are consistent with the asymptotic behavior discussed previously: one can see that F_r is an oscillating function with an amplitude that decays to zero very fast if $-\pi/6 < \arg(z) < \pi/2$ and

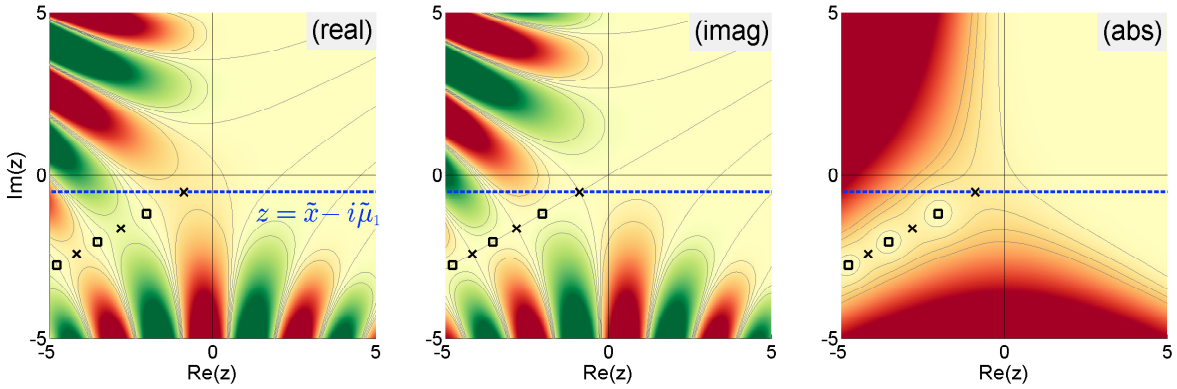

Figure 4.6: Real part, imaginary part, and absolute value of the fonction $F_r(z)$ in the complex plane. Positive values are displayed in red and negative values are displayed in green. A few contour lines in gray are plotted to guide the eye. Zeros of F_r are indicated by squares and zeros of its derivative are indicated by crosses. Eigenmodes of the BT equation (4.19a) are given by $F(\tilde{x} - i\tilde{\mu}_n)$ and we have represented the line $z = \tilde{x} - i\mu_1$ as a dashed blue line.

diverges very fast in the rest of the complex plane, with the exception of the line $\arg(z) = -5\pi/6$ where F_r is a slowly decaying real-valued oscillating function. Each eigenmode is given by the values of $F_r(z)$ on a horizontal line $z = \tilde{x} - i\tilde{\mu}_n$. The boundary condition (4.21b) is ensured if (i) this line goes through a zero of $F_r'(z)$ and if (ii) this zero corresponds to the position of the barrier $\tilde{x} = 0$ (the zeros of F_r' are indicated by crosses). Note that condition (i) imposes the real part of μ and condition (ii) imposes the imaginary part of μ. For example, if the barrier is moved to $x = x_0$ then all eigenvalues μ_n are shifted by $-iGx_0$ to satisfy condition (ii). As the order n of the eigenmode increases, the line $z = \tilde{x} - i\tilde{\mu}_n$ goes down in the complex plane, and the mode v_n displays increasingly large oscillations, with a maximum that gets further away from the boundary.

This behavior is illustrated on Fig. 4.7 where the first four modes are plotted separately. One can see that the modes are localized over a few ℓ_g at an increasing distance from the boundary at $\tilde{x} = 0$ and with larger and more numerous oscillations as n increases. Additionally, we have plotted the asymptotic formulas (C.18) and (C.19) as dashed and dotted lines. Surprisingly, Eq. (C.18) approaches the exact modes even at moderate values of $\tilde{x}$. For small values of $\tilde{x}$, the argument of $\tilde{x} - i\tilde{\mu}_n$ is close to $5\pi/6$ and Eq. (C.19) reproduces the modes very well, except for the first one (not shown). Note that for $n = 3$ and $n = 4$, both asymptotic formulas are visually undistinguishable, however deviations occur at low values of $\tilde{x}$. In Appendix C.2, we show that the eigenmodes obey approximately the

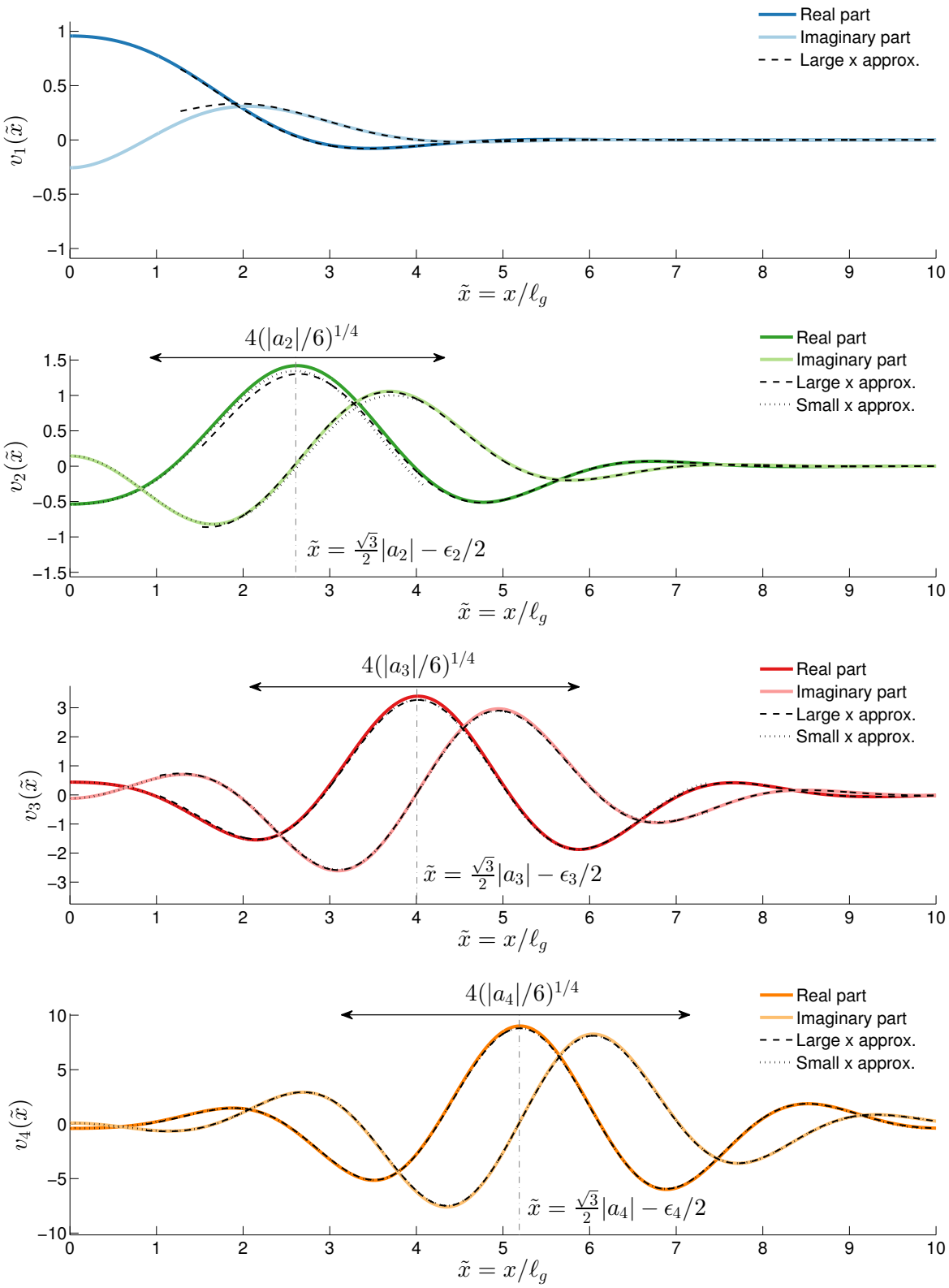

Figure 4.7: First eigenmodes of the one-dimensional BT operator. The vertical dash-dotted lines indicate the approximate center of symmetry of each mode, which is also the position of maximal amplitude, and the horizontal double arrows represent the typical width of each mode (see Eq. (4.31) and Appendix C.2). It is not shown for $n = 1$ since asymptotic formulas are grossly inaccurate in that case.

symmetry:

$$v_n\left((\sqrt{3}|a_n| - \epsilon_n)\ell_g - x\right) \approx v_n^*(x)\,, \qquad \epsilon_n = \frac{\pi}{6}\sqrt{\frac{2}{|a_n|}}\,. \tag{4.31}$$

The corresponding center of symmetry is represented as a vertical dashed-dotted line and it is visually consistent except for $n = 1$ (not shown). Finally, we compute in Appendix C.2 that the typical width of the eigenmode v_n is $4(|a_n|/6)^{1/4}$, and we have plotted is as a double arrow except for $n = 1$ for which the formula is inaccurate. Interestingly, the width of the eigenmode increases with n, however much slower than its average position x_n. We conclude that high-order eigenmodes are localized near the boundary but not at the boundary, as it is illustrated on Fig. 4.7.

Magnetization

In the previous paragraphs, we have solved the Bloch-Torrey equation for a constant gradient G. Now we consider the magnetization resulting from two gradient pulses $\pm G$ of duration δ without off-gradient diffusion time (i.e., the total duration is $T = 2\delta$). From the knowledge of the eigenmodes $v_n(x)$, one can compute the magnetization using Eq. (1.86d), reproduced here for convenience:

$$m(T = 2\delta, \mathbf{r}) = \sum_{n'}\sum_{n}(1|v_n^*)(v_n^*|v_{n'})v_{n'}(x)e^{-T(\mu_n^*+\mu_{n'})/2}\,, \tag{4.32}$$

where we recall that $(f|g)$ stands for the integral of fg over the whole domain (here the half-line $x \geq 0$). Even by replacing v_n with asymptotic formulas (see Appendix C.2), the prefactors $(1|v_n^*)(v_n^*|v_{n'})$ do not admit a closed expression, that prevents one from performing the summation. In other words, the above expression is not a convenient representation at short times when many terms contribute to the sum.

The spacing between the first two eigenvalues is given by:

$$\mathrm{Re}(\mu_2 T - \mu_1 T) = \frac{|a_2| - |a_1|}{2}\frac{\ell_\mathrm{d}^2}{\ell_g^2}\,, \tag{4.33}$$

therefore if $\ell_\mathrm{d} \gg \ell_g$ (i.e., long and strong gradient pulse) all terms with $n, n' > 1$ are negligible compared to the first term (with $n = n' = 1$):

$$m(T, x) = c_1 v_1(x)\exp\left(-\frac{|a_1|}{2}\frac{\ell_\mathrm{d}^2}{\ell_g^2}\right) + \dots\,, \tag{4.34}$$

where $c_1 = (1|v_1^*)(v_1^*|v_1)$. The above formula may seem paradoxical because it yields a finite signal. Far from the boundary (i.e., $x \gg \ell_\mathrm{d}$) the magnetization should be given by the free diffusion expression, i.e. $m \approx \exp(-\ell_\mathrm{d}^6/\ell_g^6)$. Although this quantity is extremely small because of $\ell_\mathrm{d} \gg \ell_g$, it is constant and its integral over the whole half-line is infinite. This mathematical paradox is discussed in Appendix C.2. Naturally, if one integrates the magnetization over a finite domain, the signal is at all times finite and the paradox disappears.

Hence, the above equation shows that in the regime $\ell_\mathrm{d} \gg \ell_g$, the signal is dominated by the contribution from the first eigenmode that is localized at the boundary and follows the asymptotic decay:

$$S = C_1 \ell_g \exp\left(-\frac{|a_1|}{2}\frac{\ell_\mathrm{d}^2}{\ell_g^2}\right) \tag{4.35a}$$

$$= C_1 \left(\frac{D_0}{G}\right)^{1/3} \exp\left(-|a_1| G^{2/3} D^{1/3} \delta\right) , \tag{4.35b}$$

where the second equality emphasizes the "uncommon" decay as $G^{2/3}$. The prefactor $C_1 \approx 5.888$ is obtained by numerical computation of the integrals $|(1|v_1)|^2(v_1|v_1^*)$ and we recall that $|a_1| \approx 1.0188$. This formula was first reported and experimentally confirmed in Ref. [100]. It gives the decay of the signal for the gradient perpendicular to the boundary. In the case of general gradient direction (4.14), the signal after two pulses is

$$S = C_1 \ell_g \exp\left(-|a_1| G_x^{2/3} D^{1/3} \delta\right) \exp\left(-\frac{2}{3} G_y^2 D \delta^3\right) \exp\left(-\frac{2}{3} G_z^2 D \delta^3\right) . \tag{4.36}$$

Since the decay caused by G_y and G_z is much faster than that caused by G_x, we conclude that the signal is the strongest for a gradient perpendicular to the boundary.

4.2.2 Curved boundary

The previous computation was done under the assumption that the diffusion length and the gradient length are both sufficiently short so that the curvature of the boundary can be neglected. However, it is not clear *a priori* if both conditions are required. Moreover, according to Eq. (4.36) we expect the magnetization to be the strongest near the point where the boundary is perpendicular to the gradient. Therefore, there are two localization length scales involved: (i) localization in the direction perpendicular to the boundary over the length ℓ_g, and (ii) localization in the direction parallel to the boundary over the length $\ell_{g,\|}$. The latter is the

object of this subsection. We shall derive results formerly obtained by de Swiet and Sen in [99] and extend their analysis to higher-order correction terms (see also Ref. [95] for rigorous results in two dimensions).

Bloch-Torrey equation near a curved boundary

As in the previous section, we assume that the gradient direction is along x and we denote its amplitude by G without subscript x to simplify the notations. We perform a local computation near a point where the gradient direction is perpendicular to the boundary. This point is now chosen as our origin and we denote by R_1 and R_2 the principal curvature radii of the surface at that point. We assume that R_1 and R_2 are finite but we make no hypothesis about their sign. Moreover, we choose the axes y_1, y_2 along the principal curvature directions (see Fig. 4.8). In all the computation that follows, we assume that x, y_1, y_2 are small in absolute value compared to $|R_1|$, $|R_2|$, and equality signs should be understood "up to a negligible higher-order term".

The boundary is locally described by the equation

$$x = -\frac{y_1^2}{2R_1} - \frac{y_2^2}{2R_2} \,. \tag{4.37}$$

Note that $x = 0$ along two lines if R_1 and R_2 have opposite signs, however the gradient is perpendicular to the boundary only at $y_1 = y_2 = 0$ since the component of the inward normal vector $\mathbf{n}$ are

$$n_1 = \frac{y_1}{R_1} \,, \qquad n_2 = \frac{y_2}{R_2} \,. \tag{4.38}$$

These equations imply a sign convention for x and R_1, R_2, depicted on Figs 4.8 and 4.9.

Now we perform a change of coordinates in which the boundary is flat, i.e. we choose a new coordinate r as the distance to the boundary

$$r = x + \frac{y_1^2}{2R_1} + \frac{y_2^2}{2R_2} \,. \tag{4.39}$$

To this coordinate is associated a unit vector $\mathbf{e_r}$ that coincides with the inward normal vector $\mathbf{n}$ on the boundary. Therefore, the Laplace operator in the coordinates r, y_1, y_2 is expressed as

$$\nabla^2 = \nabla \cdot (\mathbf{e_r}\, \partial_r + \mathbf{e_1}\, \partial_{y_1} + \mathbf{e_2}\, \partial_{y_2}) \tag{4.40a}$$

$$= \partial_r^2 + (\nabla \cdot \mathbf{e_r})\, \partial_r + \partial_{y_1}^2 + \partial_{y_2}^2 \tag{4.40b}$$

$$= \partial_r^2 + \left(\frac{1}{R_1} + \frac{1}{R_2}\right) \partial_r + \partial_{y_1}^2 + \partial_{y_2}^2 \,, \tag{4.40c}$$

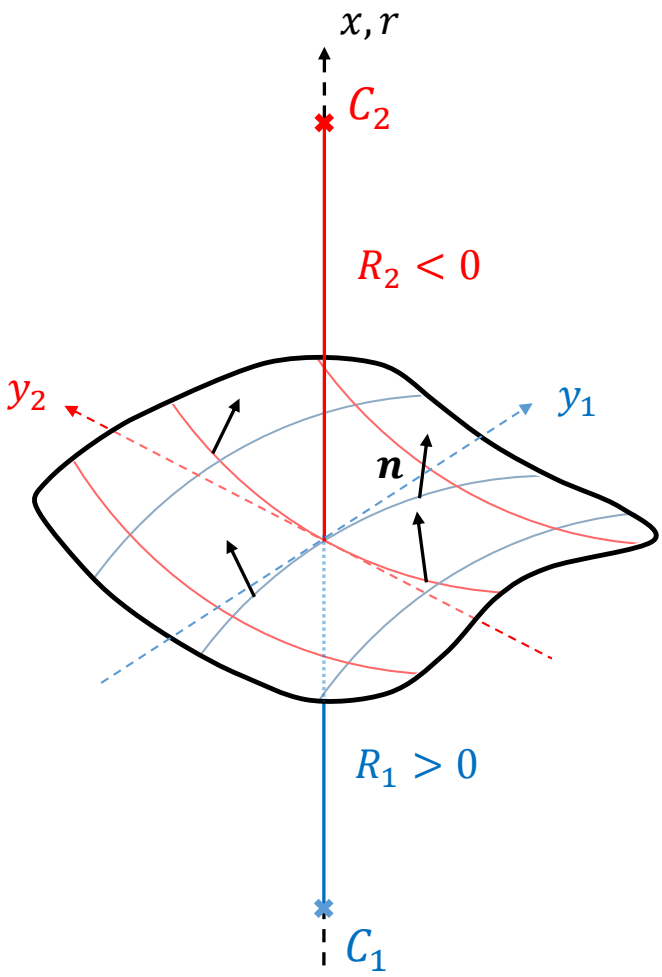

Figure 4.8: A curved boundary in three dimensions with the curvature centers C_1, C_2, the corresponding curvature radii R_1, R_2, with explicit sign convention, the coordinates y_1, y_2, and the inward normal vector $\mathbf{n}$ as an illustration of Eq. (4.38). Diffusion takes place in the half-space $r \geq 0$ (upper part of the figure).

where we used Eq. (4.38) to compute the divergence of $\mathbf{e_r}$ close to the boundary. The gradient term becomes

$$iGx = iGr - i\frac{G}{2R_1}y_1^2 - i\frac{G}{2R_2}y_2^2 \,. \tag{4.41}$$

To simplify our notations, we introduce

$$G_1 = \frac{G}{2R_1} \,, \qquad G_2 = \frac{G}{2R_2} \,, \qquad H = \frac{1}{2R_1} + \frac{1}{2R_2} \,. \tag{4.42}$$

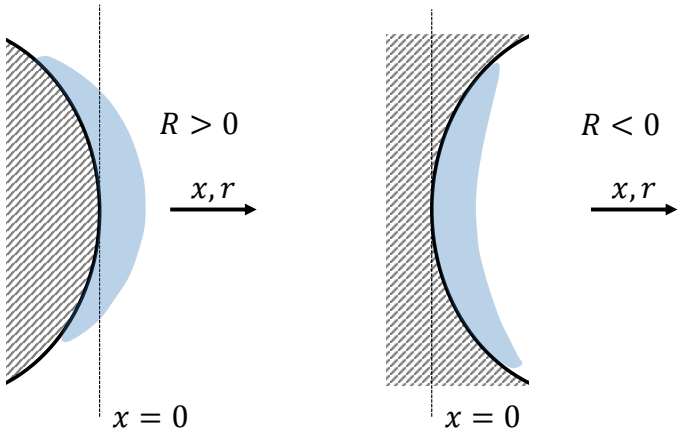

Figure 4.9: Sign convention for the curvature radius and the orientation of axes x and r. The shape of the eigenmode is schematically pictured as a blue shaded area. For $R < 0$, the eigenmode spreads more to the right (i.e., towards positive values of x, r) than for $R > 0$.

The Bloch-Torrey equation at a curved boundary becomes:

$$\partial_t m = \left[D_0(\partial_r^2 + 2H\partial_r) + iGr\right] m + \left[D_0\partial_{y_1}^2 - iG_1 y_1^2\right] m + \left[D_0\partial_{y_2}^2 - iG_2 y_2^2\right] m\,, \tag{4.43a}$$

$$\partial_r m|_{r=0} = 0\ . \tag{4.43b}$$

There are several advantages to this new formulation compared to the Bloch-Torrey equation in Cartesian coordinates. The curvature of the boundary enters explicitly as coefficients of the differential equation instead of implicitly through the boundary condition. Moreover, the differential equation and the boundary condition exhibits a separation of variables (emphasized by the brackets). Therefore, one can look for Bloch-Torrey eigenmodes and eigenvalues in the form

$$v_{n,l_1,l_2}(r, y_1, y_2) = f_n(r) g_{l_1}(y_1) h_{l_2}(y_2)\ , \qquad \mu_{n,l_1,l_2} = \zeta_n + \eta_{l_1} + \theta_{l_2}\ , \tag{4.44}$$

where n, l_1, l_2 are three indices and (f_n, ζ_n), (g_{l_1}, η_{l_1}), (h_{l_2}, θ_{l_2}) satisfy

$$-\left[D_0(\partial_r^2 + 2H\partial_r) + iGr\right] f_n = \zeta_n f_n\ , \qquad f_n'(0) = 0\ , \tag{4.45a}$$

$$-\left[D_0\partial_{y_1}^2 - iG_1 y_1^2\right] g_{l_1} = \eta_{l_1} g_{l_1}\ , \tag{4.45b}$$

$$-\left[D_0\partial_{y_2}^2 - iG_2 y_2^2\right] h_{l_2} = \theta_{l_1} h_{l_2}\ , \tag{4.45c}$$

with the additional condition that all functions are bounded at infinity. Moreover, if the initial condition $m(t = 0, r, y_1, y_2)$ can be written as a product of the same

form, then this remains true at all times, and one needs to solve three separate one-dimensional partial differential equations that simplifies the problem a lot. This is especially true for a uniform initial condition, that is the most common situation. In the following paragraph, we solve the eigenmode equations (4.45a) and (4.45b) and we discuss the corrections due to the curvature of the boundary.

Eigenmodes for a curved boundary

Let us start with the radial eigenmode equation (4.45a). One can see that it is nearly the same as the one-dimensional equation (4.28b) with an additional term $2D_0H\partial_r f_n$. In the previous subsection we obtained that the eigenmodes of the one-dimensional equation are localized over the length ℓ_g. Therefore a gross estimation of $2D_0H\partial_r f_n$ compared to $D_0\partial_r^2 f_n$ implies that is is a small correction if $H\ell_g \ll 1$. This condition is ensured if $\ell_g \ll |R_1|, |R_2|$, that we assume now. In that case one may look for an approximate eigenpair as a perturbation of Eqs. (4.29a) and (4.29b):

$$f_n(r) = \beta_n F_{\mathrm{r}}(r/\ell_g - e^{i\pi/6}|a_n|) + \delta f_n(r)\,, \qquad \zeta_n = \frac{D_0}{\ell_g^2} e^{-i\pi/3}|a_n| + \delta\zeta_n\,, \tag{4.46}$$

where δf_n and $\delta\zeta_n$ are small compared to f_n and ζ_n, respectively. Note that this notation should not be confused with the pulse duration δ. For brevity, we denote the eigenmode and eigenvalue without correction term by $f_n^{(0)}$ and $\zeta_n^{(0)}$. By injecting this form into the eigenmode equation (4.45a) and discarding second-order terms, we get the equation

$$-D_0\delta f_n'' - iGr\delta f_n - \zeta_n^{(0)}\delta f_n = \delta\zeta_n f_n^{(0)} + 2D_0H f_n^{(0)\prime}\,, \tag{4.47a}$$

$$\delta f_n'(0) = 0\,, \qquad \delta f_n \text{ bounded at } \infty\,. \tag{4.47b}$$

To solve the differential equation while taking into account the boundary condition, we project it onto the eigenbasis of the one-dimensional Bloch-Torrey equation. Thus, we write

$$\delta f_n = \sum_{n'} c_{n,n'} f_{n'}^{(0)} \tag{4.48}$$

and the equation on δf_n translates into the following equations on $c_{n,n'}$ and $\delta\zeta_n$:

$$(\zeta_{n'}^{(0)} - \zeta_n^{(0)})c_{n,n'} = 2D_0Hd_{n,n'} \qquad n \neq n' \tag{4.49a}$$

$$0 = \delta\zeta_n + 2D_0Hd_{n,n}\,, \tag{4.49b}$$

where

$$d_{n,n'} = \int_0^\infty f_n^{(0)\prime}(r) f_{n'}^{(0)}(r)\,\mathrm{d}r\,. \tag{4.50}$$

Equation (4.49b) yields the formula for $\delta\zeta_n$

$$\delta\zeta_n = -\frac{2D_0H}{\ell_g}\beta_n^2 \int_0^\infty F_{\mathrm{r}}'(r/\ell_g - e^{i\pi/6}|a_n|)F_{\mathrm{r}}(r/\ell_g - e^{i\pi/6}|a_n|)\,\mathrm{d}r \tag{4.51a}$$

$$= D_0H\beta_n^2 F_{\mathrm{r}}^2(-e^{i\pi/6|a_n|}) \tag{4.51b}$$

$$= e^{-i\pi/6}\frac{D_0H}{\ell_g|a_n|}\,. \tag{4.51c}$$

One can see that $\delta\zeta_n/\zeta_n \sim \ell_g H \ll 1$, that confirms *a posteriori* the validity of the above expansion. For conciseness, we present the computation of $d_{n,n'}$ for $n \neq n'$ in Appendix C.4. The result reads

$$d_{n,n'} = \frac{e^{-i\pi/6}}{\ell_g\sqrt{a_n a_{n'}}(a_{n'}/a_n - 1)}\,, \tag{4.52}$$

so that δf_n may be expressed as a series of Airy functions with explicit coefficients.

Now we turn to the equation for the lateral part (4.45b). To simplify our notations, we discard temporarily the subscript "1". Let us introduce the length scale

$$\ell_{g,\parallel} = \left(2|R|\ell_g^3\right)^{1/4}\,, \tag{4.53}$$

and perform the rescaling $\tilde{y} = y/\ell_{g,\parallel}$, $\tilde{\eta}_l = \eta_l\ell_{g,\parallel}^2/D_0$. The eigenmode equation takes the dimensionless form

$$-g_l'' \pm i\tilde{y}^2 g_l = \tilde{\eta}_l g_l\,, \tag{4.54}$$

that is the time-independent equation of a complex quantum harmonic oscillator and where the $\pm$ sign is the sign of R. The solutions of this equation are formally identical to the real quantum harmonic oscillator with the change $\tilde{y} \to e^{\mp i\pi/8}\tilde{y}$ and $\tilde{\eta}_l \to e^{\mp i\pi/4}\tilde{\eta}_l$, that yields

$$g_l(y) = K_l \exp\left(-e^{\pm i\pi/4}\tilde{y}^2/2\right) H_{l-1}\left(e^{\pm i\pi/8}\tilde{y}\right)\,, \tag{4.55a}$$

$$\tilde{\eta}_l = e^{\pm i\pi/4}(2l-1)\,, \tag{4.55b}$$

where H_l are Hermite polynomials (in particular, $H_0(z) = 1$) and K_l are normalization coefficients given by

$$K_l^{-2} = e^{\mp i\pi/8}\,2^{l-1}(l-1)!\sqrt{\pi}\,. \tag{4.56}$$

We have plotted the functions $g_l(\tilde{y})$ for $l = 1, 2, 3, 4$ on Fig. 4.10. These modes are qualitatively similar to the eigenmodes of the real quantum harmonic oscillator. As the index l increases, the number of oscillations and the lateral expansion of the modes increase.

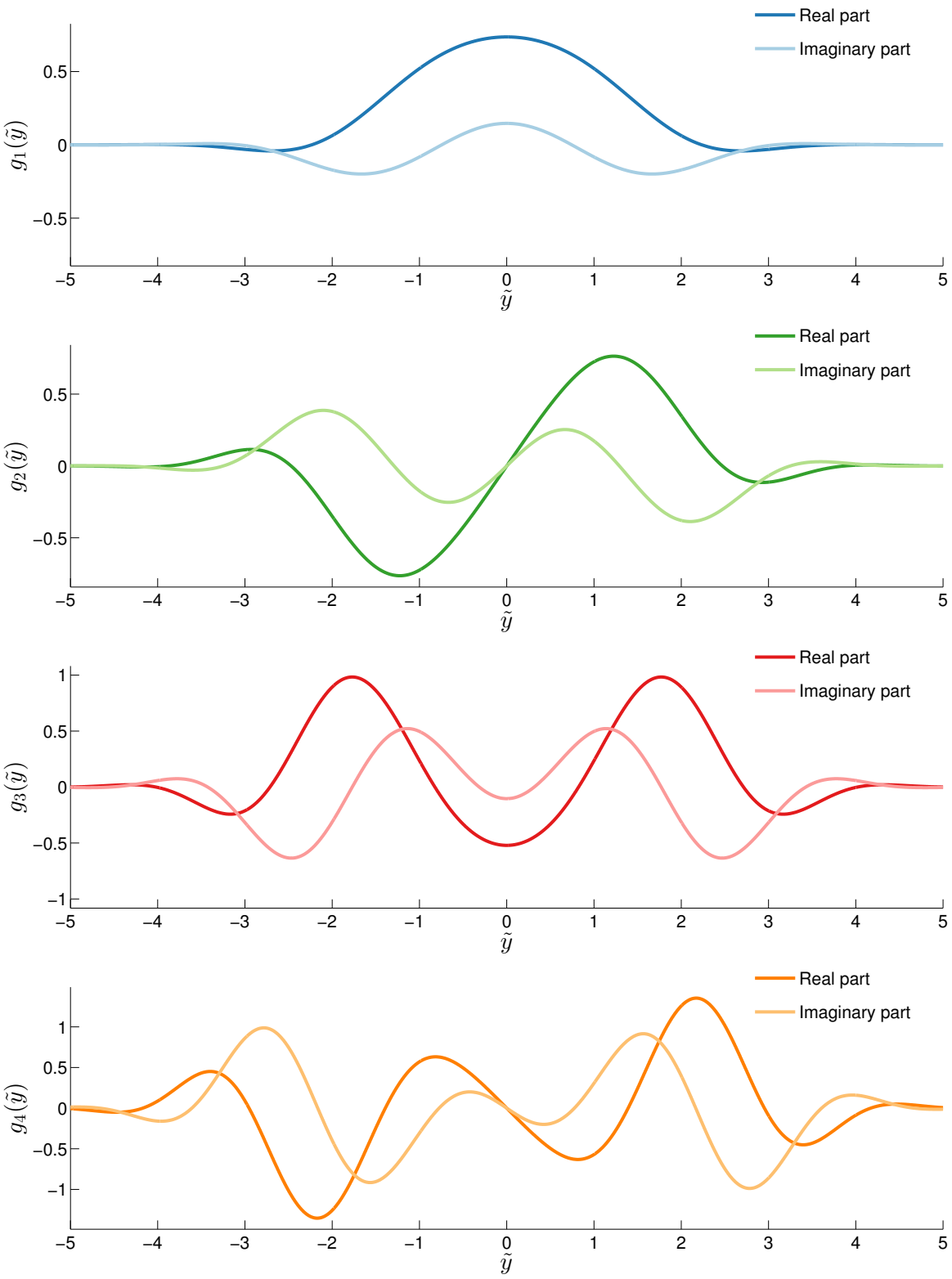

Figure 4.10: Lateral part of the first eigenmodes at a curved boundary (see description in the text).

Magnetization at a curved boundary

We obtained that the magnetization can still be represented as a spectral decomposition and that the eigenmodes are indexed by three integers n, l_1, l_2 that control the extension and oscillation of the eigenmode along r, y_1, y_2, respectively. The spectrum is given by

$$\begin{aligned}\mu_{n,l_1,l_2} &= e^{-i\pi/3}\frac{D_0}{\ell_g^2}|a_n| + e^{\pm i\pi/4}\frac{(2l_1-1)D_0}{\ell_{g,\parallel,1}^2} + e^{\pm i\pi/4}\frac{(2l_2-1)D_0}{\ell_{g,\parallel,2}^2} \\ &\quad + e^{-i\pi/6}\frac{D_0 H}{|a_n|\ell_g} \qquad (4.57)\\ &= e^{-i\pi/3}D_0^{1/3}G^{2/3}|a_n| + e^{\pm i\pi/4}\frac{(2l_1-1)D_0^{1/2}G^{1/2}}{(2|R_1|)^{1/2}} \\ &\quad + e^{\pm i\pi/4}\frac{(2l_2-1)D_0^{1/2}G^{1/2}}{(2|R_2|)^{1/2}} + e^{-i\pi/6}\frac{D_0^{2/3}G^{1/3}}{2|a_n|}\left(R_1^{-1}+R_2^{-1}\right)\ , \qquad (4.58)\end{aligned}$$

where the ± signs are the signs of the curvature radii R_1 and R_2 (see also Refs. [95, 99]). The interpretation of those signs follows from the interpretation of $-\mathrm{Im}(\mu_{n,l_1,l_2})/G$ as the average position of the eigenmode (see Sec. 1.2.4). The imaginary part of the correction terms has the same sign as R_1 and R_2, respectively. If R_1 is positive (convex boundary), the mode spreads more to the left (i.e., towards negative values of x) than in the opposite case of negative R_1 (concave boundary), as illustrated on Fig. 4.9.

A second point is that the real part of the eigenvalues is increased by the curvature of the boundary. This implies that the magnetization and the signal decay faster if the boundary is curved than if it is flat. We interpret this point by relating it to the remark that the decay of the signal for the planar boundary is faster if the gradient is not perpendicular to the boundary. Since a curved boundary is perpendicular to the gradient only at one point, it follows that the signal decays faster than for the planar boundary where the gradient is perpendicular at every point of the boundary.

The lateral part of the eigenmodes is localized over the length scale $\ell_{g,\parallel,1}$ along y_1 and over $\ell_{g,\parallel,2}$ along y_2. Therefore, as we claimed above, the curvature of the boundary introduces a new localization length that differs from the radial localization length ℓ_g. Note that these results were obtained under the condition that $\ell_g \ll |R_1|, |R_2|$. This condition implies in particular that $\ell_{g,\parallel}$ is larger than ℓ_g. However, the ratio $\ell_{g,\parallel}/\ell_g = (2|R|/\ell_g)^{1/4}$ increases slowly with $|R|/\ell_g$ because of the $1/4$ exponent.

Let us now investigate the role of ℓ_d. To simplify the discussion, we discard one of the curvature radii in the following. In other words, we consider a two-

dimensional situation which is equivalent to setting $R_2 = \infty$ (e.g., a cylinder). We shorten our notations again by dropping the subscript "1" in the formulas. The eigenvalues with the lowest real part are given by $\mu_{1,l}$, at least for the first values of l. In particular, the spacing between the first and the second eigenvalue is given by

$$\mathrm{Re}(\mu_{1,2}T - \mu_{1,1}T) = \sqrt{2}\frac{\ell_\mathrm{d}^2}{\ell_{g,\|}^2} \,. \tag{4.59}$$

This formula should be contrasted with that for a planar boundary (Eq. (4.33)) that involved $\ell_\mathrm{d}^2/\ell_g^2$. The interpretation of these two formulas is the following. The magnetization is initially uniform, hence delocalized. When time increases and reaches the value ℓ_g^2/D_0, the eigenmodes with $n > 1$ have significantly decayed and the magnetization profile does not evolve anymore in the radial direction. In other words, at that time the magnetization is fully localized in the direction perpendicular to the boundary. However, several eigenmodes with $n = 1$ and $l = 1, 2, \ldots$ may have a significant amplitude. Therefore the magnetization is delocalized in the direction parallel to the boundary. When the time is larger than $\ell_{g,\|}^2/D_0$, then all modes with $n > 1$ and $l > 1$ become negligible and the magnetization is also fully localized in the direction parallel to the boundary. At later times the magnetization profile does not evolve anymore and the signal decays exponentially with time with the rate $\mathrm{Re}(\mu_{1,1})$.

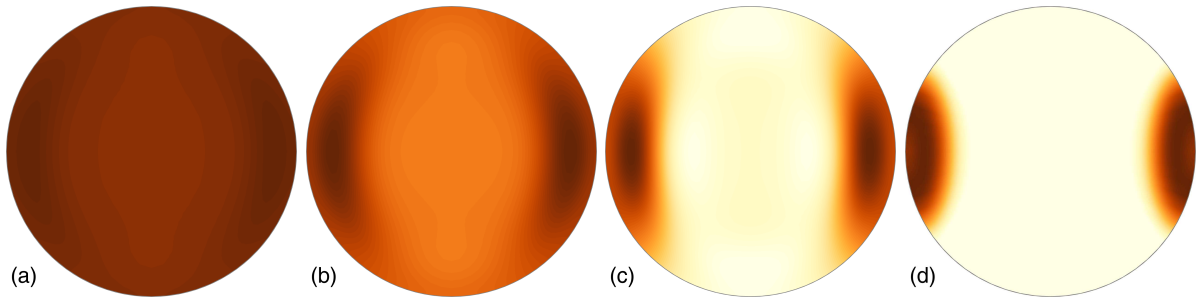

Figure 4.11: Absolute value of the transverse magnetization for increasing pulse duration and fixed gradient computed with a matrix formalism. (a) $\ell_\mathrm{d}/\ell_g = 0.84$: the magnetization is nearly uniform inside the disk; (b) $\ell_\mathrm{d}/\ell_g = 1.1$: the magnetization starts to localize along the gradient direction but remains nearly uniform along the boundary. (c) $\ell_\mathrm{d}/\ell_g = 1.3$: the magnetization is completely localized along the gradient direction and starts to shrink along the boundary; (d) $\ell_\mathrm{d}/\ell_g = 2.0$ (so that $\ell_\mathrm{d}/\ell_{g,\|} = 1.0$): the magnetization is localized both along the gradient (with size ℓ_g) and perpendicular to the gradient (with size $\ell_{g,\|}$).

We show on Fig. 4.11 the magnetization profile inside a disk for increasing pulse duration and fixed gradient strength. The radius of the disk is $R = 8\ell_g$ so that $\ell_{g,\|} = 2\ell_g$. One can see clearly the localization in two steps, first in the direction perpendicular to the boundary, then in the direction parallel to the boundary.

Therefore, one concludes that the localization regime emerges partially at time ℓ_g^2/D_0 and is fully established at time $\ell_{g,\parallel}^2/D_0$. However, this affirmation seems paradoxical because in the limit of infinite curvature radius R, the time $\ell_{g,\parallel}^2/D_0$ goes to infinity therefore the localization regime would never be established for a flat boundary. We investigate this (singular) limit in Appendix C.3. We show that one can sum the eigenmode expansion in the direction parallel to the boundary and recover the results of the previous subsection.

4.3 Bounded domain

Numerous theoretical, numerical, and experimental works have been devoted to studying the BT operator and the dMRI signal in bounded domains (intracellular space, isolated pores) [20, 22, 24, 79–81, 84, 87, 88, 99]. On theoretical side, the linear potential in the BT operator is a bounded perturbation of the (unbounded) Laplace operator, which has a discrete spectrum in bounded domains. As a consequence, the BT operator also has a discrete spectrum, and its spectral properties can be analyzed by rather standard mathematical tools [94, 95, 98–100, 102, 104]. At low gradient strength, perturbation methods are applicable and we shall discuss their limitation when presenting spectral bifurcations. On the numerical side, different computational techniques for dMRI have been developed (see Sec. 1.1.5), including finite difference/finite elements PDE solvers [30–32, 195, 272], Monte-Carlo simulations [34, 35, 58, 192], and spectral methods (matrix formalism) [3, 36, 37, 40]. However, all of these techniques are numerically challenging at high gradients because of the fine spatial scales involved in the signal formation, as well as the weak signal. This requires a fine mesh (for PDE solvers), a fine diffusion step and a large number of particles (for Monte Carlo algorithms), and a large number of Laplace eigenmodes (for spectral methods).

In the previous section we studied in detail the phenomenon of localization at a single boundary. The main hypothesis was that the structural length scale ℓ_s is much larger than ℓ_g and ℓ_d so that one can ignore the effect of other boundaries. We obtained that the n-th eigenmode is localized at a distance $\approx \sqrt{3}|a_n|\ell_g/2$ from the boundary (see Fig. 4.7 and Appendix C.2). Clearly one expects that this result breaks down for a finite pore when this distance becomes comparable to the pore diameter ℓ_s [98, 99].

We start by computing the Bloch-Torrey spectrum in the low-gradient regime, i.e. $\ell_s \ll \ell_g$, for which we recover the well-known motional narrowing regime [3, 79, 81]. We first present the simple case of a slab then we turn to a general bounded domain. Then we investigate the transition to the localization regime when ℓ_g becomes smaller than ℓ_s. In symmetric domains, this transition is abrupt and creates bifurcation points in the spectrum. We shall see that these bifurcation points are generic and subsist for non-symmetric domains if the gradient G is considered as a complex variable. Although a complex gradient strength has limited practical applications, the non-analyticity created by the bifurcation points imposes a finite convergence radius to any analytical expansion in powers of G. This is an intrinsic limitation to perturbative low-G approaches, independent of the symmetry of the domain.

4.3.1 Motional narrowing regime

In a slab

We consider here one-dimensional diffusion inside the interval $-\ell_s/2 \leq x \leq \ell_s/2$, under the gradient G and we are interested in the behavior of the eigenvalues μ_n of the BT operator in the limit $\ell_s \ll \ell_g$. Let us perform the rescaling

$$\tilde{x} = \frac{x}{\ell_s}\,, \qquad \tilde{\mu}_n = \frac{\ell_s^2}{D_0}\mu_n\,, \qquad \tilde{G} = G\ell_s^3/D_0 = \ell_s^3/\ell_g^3\,. \tag{4.60}$$

Note that here we rescale by the size of the interval ℓ_s and not by the gradient length ℓ_g as in the previous section. The hypothesis $\ell_s \ll \ell_g$ implies that $\tilde{G}$ is a small parameter.

With this rescaling, the eigenmodes of the Bloch-Torrey operator satisfy

$$-v_n'' - i\tilde{G}\tilde{x}v_n = \tilde{\mu}_n v_n\,, \tag{4.61}$$
$$v_n'(-1/2) = v_n'(1/2) = 0\,. \tag{4.62}$$

The gradient term is a weak perturbation of the Laplace operator and the eigenmodes and eigenvalues of the BT operator may be written as

$$v_n(\tilde{x}) = u_n(\tilde{x}) + i\tilde{G}u_n^{(1)}(\tilde{x}) + (i\tilde{G})^2u_n^{(2)}(\tilde{x}) + \dots\,, \tag{4.63}$$
$$\tilde{\mu}_n = \lambda_n + i\tilde{G}\lambda_n^{(1)} + (i\tilde{G})^2\lambda_n^{(2)} + \dots\,, \tag{4.64}$$

where $u_n(\tilde{x}), \lambda_n$ are the Laplacien eigenmodes and eigenvalues on the interval $[-1/2; 1/2]$ with Neumann boundary condition:

$$u_1(\tilde{x}) = 1\,, \tag{4.65}$$
$$u_n(\tilde{x}) = \sqrt{2}\cos((n-1)\pi\tilde{x} + (n-1)\pi/2)\,, \qquad n = 2, 3, \dots\,, \tag{4.66}$$
$$\lambda_n = (n-1)^2\pi^2\,. \tag{4.67}$$

The correction terms $i\tilde{G}$, $(i\tilde{G})^2$, ... are small relatively to λ_n for $n > 1$, however this is not the case for $n = 1$ since $\lambda_1 = 0$. Let us focus on this case and compute the first correction terms $\lambda_1^{(1)}$ and $\lambda_1^{(2)}$. By injecting the expansions (4.63) and (4.64) into the eigenmode equation (4.61) and by identifying terms of the same order in $i\tilde{G}$, one gets

$$-u_1^{(1)\prime\prime} = \tilde{x} + \lambda_1^{(1)}\,, \qquad u_1^{(1)\prime}(\pm 1/2) = 0\,, \tag{4.68}$$
$$-u_1^{(2)\prime\prime} = (\tilde{x} + \lambda_1^{(1)})u_n^{(1)} + \lambda_1^{(2)}\,, \qquad u_1^{(2)\prime}(\pm 1/2) = 0\,, \tag{4.69}$$

The integration of the first equation over $[-1/2; 1/2]$ yields $\lambda_1^{(1)} = 0$. Solving for $u_1^{(1)}$ gives then $u_1^{(1)} = \tilde{x}/8 - \tilde{x}^3/6$. Then the integration of the second equation over $[-1/2; 1/2]$ gives immediately $\lambda_1^{(2)} = -1/120$. Moreover, one can solve the differential equation and get $u_1^{(2)} = \tilde{x}^2/240 - \tilde{x}^4/96 + \tilde{x}^6/180$.

Therefore, the first eigenvalue of the BT operator on a slab of width ℓ_s is given in the low gradient regime by

$$\mu_1 = \frac{G^2 \ell_s^4}{120 D_0} , \tag{4.70}$$

that is the motional narrowing formula, as we explained in Sec. 1.2.4. Since one has

$$\mu_2 - \mu_1 \approx (\lambda_2 - \lambda_1)\frac{D_0}{\ell_s^2} = \pi^2 \frac{D_0}{\ell_s^2} , \tag{4.71}$$

the decay of the magnetization (and of the signal) follows $\exp(-\mu_1 T)$ in the regime of long diffusion time $\ell_d^2 \gg \ell_s^2$.

It is interesting to note that μ_1 is real to order $\tilde{G}^2$ because $\lambda_1^{(1)} = 0$. If one inspects the above computation, it simply follows from the fact that the integral of $\tilde{x}$ over the slab is zero. The interpretation is simply that the imaginary part of μ_1 is related to the average Larmor frequency of spins inside the domain. Since the eigenmode v_1 is nearly uniform, its time evolution reflects the average evolution of spins over the whole domain. If we wanted to compute the next order term, then we would get the equation

$$-u_1^{(3)\prime\prime} = \tilde{x} u_1^{(2)} + \lambda_1^{(2)} u_1^{(1)} + \lambda_1^{(3)} , \qquad u_1^{(3)\prime}(\pm 1/2) = 0 , \tag{4.72}$$

and integration over the whole interval yields again $\lambda_1^{(3)} = 0$. It is quite easy to prove that all odd orders are zero so that the expansion (4.64) contains only real terms. As we show in the next section, this peculiar property is related to the parity symmetry of the domain (see also Sec. 1.2.4).

Arbitrary bounded domain

Now we consider an arbitrary bounded domain Ω with diameter ℓ_s and we investigate again the limit $\ell_s \ll \ell_g$. After rescaling by ℓ_s, we obtain the dimensionless eigenmode equation (where quantities are denoted with a tilde after rescaling):

$$-\tilde{\nabla}^2 v_n - i\tilde{G}\tilde{x} v_n = \tilde{\mu}_n v_n , \tag{4.73}$$

$$\mathbf{n} \cdot \tilde{\nabla} v_n \Big|_{\partial\tilde{\Omega}} = 0 , \tag{4.74}$$

where $\mathbf{n}$ is the normal vector at the boundary. As above, $i\tilde{G}$ is a small parameter and we expand v_1 and $\tilde{\mu}_1$ in powers of $i\tilde{G}$, that yields the equations

$$-\tilde{\nabla}^2 u_1^{(1)} = (\tilde{x} + \lambda_1^{(1)})K \,, \qquad \mathbf{n}\cdot\tilde{\nabla}u_1^{(1)}\Big|_{\partial\tilde{\Omega}} = 0 \,, \tag{4.75}$$

$$-\tilde{\nabla}^2 u_1^{(2)} = (\tilde{x} + \lambda_1^{(1)})u_1^{(1)} + \lambda_1^{(2)}K \,, \qquad \mathbf{n}\cdot\tilde{\nabla}u_1^{(2)}\Big|_{\partial\tilde{\Omega}} = 0 \,, \tag{4.76}$$

where $K = \mathrm{vol}(\tilde{\Omega})^{-1/2}$ is the normalization factor of the constant eigenmode u_1. The integration of the first equation over the domain yields

$$\lambda_1^{(1)} = K^2 \int_{\tilde{\Omega}} \tilde{x}\, \mathrm{d}^3\tilde{\mathbf{r}} \,. \tag{4.77}$$

Note that the factor K^2 comes from integrating the constant $\lambda_1^{(1)}$ over the domain $\tilde{\Omega}$. As we discussed for the case of the interval, this term simply represents the average Larmor precession rate of spins in the domain. In the following we discard this effect by choosing the origin at the center of mass of the domain. To obtain the next-order correction term, we still need to obtain the expression of $u_1^{(1)}$. To this end we shall project it onto the basis of Laplacian eigenmodes. Let us write

$$K\tilde{x} = \sum_n B_n u_n(\tilde{x}) \,, \qquad B_n = K\int_{\tilde{\Omega}} \tilde{x}u_n(\tilde{x})\, \mathrm{d}^3\tilde{\mathbf{r}} \,. \tag{4.78}$$

In the notations of Sec. 1.1.5, one has $B_n = [B_x]_{1,n}$. Note that $B_1 = 0$ thus we sum over $n = 2, 3, \ldots$. Then one obtains simply

$$u_1^{(1)}(\tilde{x}) = \sum_{n\geq 2} \frac{B_n}{\lambda_n} u_n(\tilde{x}) \,. \tag{4.79}$$

Now by integrating the second equation, we get directly

$$\lambda_1^{(2)} = -K\int_{\tilde{\Omega}} \tilde{x}u_1^{(1)}\, \mathrm{d}^3\tilde{\mathbf{r}} \tag{4.80}$$

$$= -\sum_{n\geq 2} \frac{B_n^2}{\lambda_n} \,, \tag{4.81}$$

that is the general formula for the motional narrowing regime [3, 79, 81]. One can check that this formula gives the previous result $\lambda_1^{(2)} = 1/120$ for a slab, but also $7/1536$ for a cylinder and $1/350$ for a sphere[2].

[2]We recall that we have rescaled the domain by ℓ_s, which is the diameter of the pore (slab, cylinder, sphere). In contrast, the values provided in [3, 79, 81] correspond to a different choice (diameter of the slab, radius of the cylinder or sphere).

Symmetry properties

We recall that we call a domain symmetric under x-parity if it is invariant under an isometric transformation that reverses the x-axis (see Fig. 1.9 and related discussion). Let us assume that the domain is symmetric under x-parity and let us denote by $\mathcal{P}_x$ the associated transformation.

In that case, one can apply the parity transformation $\mathcal{P}_x$ to our equations and rewrite them in term of the functions $\mathcal{P}_x u_1^{(1,2)}$:

$$-\tilde{\nabla}^2(\mathcal{P}_x u_1^{(1)}) = (-\tilde{x} + \lambda_1^{(1)})K\,, \qquad \mathbf{n}\cdot\tilde{\nabla}(\mathcal{P}_x u_1^{(1)})\Big|_{\partial\tilde{\Omega}} = 0\,,$$
$$-\tilde{\nabla}^2(\mathcal{P}_x u_1^{(2)}) = (-\tilde{x} + \lambda_1^{(1)})(\mathcal{P}_x u_1^{(1)}) + \lambda_1^{(2)}K\,,$$
$$\mathbf{n}\cdot\tilde{\nabla}(\mathcal{P}_x u_1^{(2)})\Big|_{\partial\tilde{\Omega}} = 0\,.$$

Now we consider these equations in addition to the above ones. If one integrates the first equation, then $\lambda_1^{(1)}$ is equal to the average of $\tilde{x}$ and to its opposite therefore it is equal to zero, as expected. Additionally, $\mathcal{P}_x u_1^{(1)}$ and $u_1^{(1)}$ have opposite Laplacians and obey the same boundary condition, therefore they are opposite of each other. We conclude that $u_1^{(1)}$ is odd with respect to $\mathcal{P}_x$. The reasoning is similar to $u_1^{(2)}$: in that case we obtain that $\mathcal{P}_x u_1^{(2)}$ and $u_1^{(2)}$ have identical Laplacians and obey the same boundary condition therefore they are equal to each other. Thus $u_1^{(2)}$ is even with respect to $\mathcal{P}_x$. Recursively, one can easily prove that the k-th order correction term of the first eigenmode, $u_1^{(k)}$, has the same parity as k. Moreover, $\lambda_1^{(k)}$ is zero for odd k.

One can extend this result to any eigenmode and eigenvalue $v_n, \tilde{\mu}_n$. Since $\mathcal{P}_x$ and the Laplace operator commute, the Laplacian eigenmodes are either even or odd with respect to $\mathcal{P}_x$. By reproducing the same steps as above, one can prove that $u_n^{(k)}$ has the same parity as u_n if k is even and opposite parity if k is odd. This implies that the expansion

$$v_n(\tilde{x}) = u_n(\tilde{x}) + \sum_k (i\tilde{G})^k u_n^{(k)}(\tilde{x}) \tag{4.82}$$

has a real part of the same parity as u_n and an imaginary part of opposite parity. Moreover, one can prove that $\lambda_n^{(k)}$ is zero for odd k. Therefore the expansion

$$\tilde{\mu}_n = \lambda_n + \sum_k (i\tilde{G})^k \lambda_n^{(k)} \tag{4.83}$$

contains only real terms, and the spectrum of the BT operator is real to all orders in $\tilde{G}$. We shall see in the next subsection that this property cannot hold for any value of $\tilde{G}$ therefore the above asymptotic expansions fail for $\tilde{G}$ exceeding a finite convergence radius $\tilde{G}_c$.

4.3.2 Spectral bifurcations

Parity-symmetric domain

The conclusion of the above subsection calls for two remarks. The first one is that it is perfectly consistent with the discussion of Sec. 1.2.4 about symmetry properties of the BT operator. For convenience, we recall the main point of this discussion: for a parity symmetric domain, its eigenpairs μ_n, v_n fall into one of the two cases:
(i) the eigenvalue μ_n is real and $v_n = \pm\mathcal{P}_x v_n^*$ (delocalized eigenmode);
(ii) two eigenvalues μ_n and $\mu_{n'}$ form a complex conjugate pair, and $v_{n'} = \mathcal{P}_x v_n^*$ (pair of localized eigenmodes).

Thus, the conclusion of the previous subsection corresponds to case (i). However, this result seems to be in contradiction with Sec. 4.2 where we obtained a complex spectrum in the limit $\ell_g \ll \ell_s$, i.e. $\tilde{G} \gg 1$. The only solution to this paradox is that the expansions (4.82) and (4.83) are not valid for all values of $\tilde{G}$, i.e. they have a finite convergence radius $\tilde{G}_c$. For $\tilde{G} < \tilde{G}_c$, the expansion is valid but it breaks down for $\tilde{G} > \tilde{G}_c$.

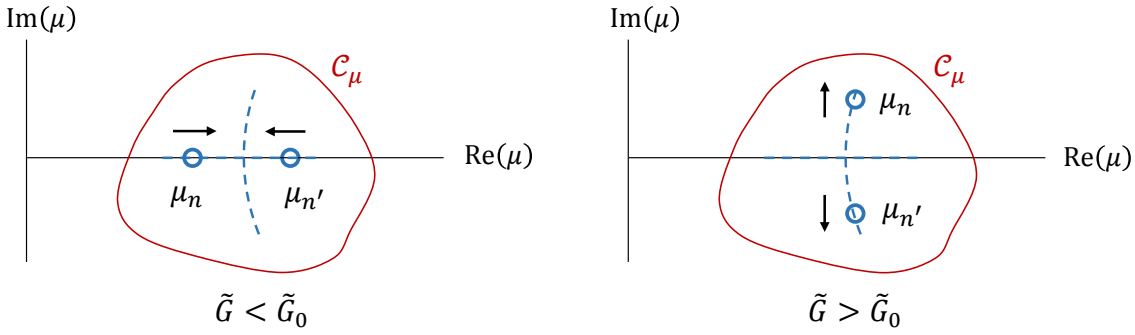

Figure 4.12: Illustration of the transition from two real eigenvalues to a complex conjugate pair. For $\tilde{G} = \tilde{G}_0$, μ_n and $\mu_{n'}$ bifurcate in the complex plane. By integrating the resolvent $(\mathcal{B}-\mu\mathcal{I})^{-1}$ over the contour C_μ, one obtains a two-dimensional projector $\Pi(\tilde{G})$ that is analytical in $\tilde{G}$ because the resolvent is analytical outside of poles (i.e., outside of eigenvalues of $\mathcal{B}$).

Note that the transition from case (i) to case (ii), i.e. from two real eigenvalues μ_n, $\mu_{n'}$ to a complex conjugate pair may occur only if μ_n and $\mu_{n'}$ coincide for some value $\tilde{G} = \tilde{G}_0$. As illustrated on Fig. 4.12, the coalescence of two eigenvalues creates a bifurcation point in the spectrum, i.e. a non-analyticity. This observation is consistent with the existence of a finite convergence radius $\tilde{G}_c$ for the expansions (4.82) and (4.83) (more precisely, one has $\tilde{G}_c \leq \tilde{G}_0$). These bi-

furcation points mark the transition from delocalized eigenmodes (i) to localized eigenmodes (ii), i.e. the emergence of the localization regime. This mathematical phenomenon was first shown by Stoller *et al.* for the BT operator in an interval with Neumann boundary condition [98].

Matrix model

We shall illustrate the mathematical phenomenon of spectral bifurcation on the simplest case of a 2×2 matrix. Although a differential operator acting on an infinite-dimensional functional space cannot be reduced to a matrix, the coalescence of two eigenmodes and eigenvalues is essentially captured by a computation on a vector space of dimension 2. To explain this point, we follow a suggestion by B. Helffer illustrated on Fig. 4.12. Let us choose an integration path C_μ in the complex μ-plane that circles around two eigenvalues μ_n and $\mu_{n'}$. We assume that these eigenvalues coalesce at $\tilde{G} = \tilde{G}_0$. Since the eigenvalues are discrete, it is possible to choose the path C_μ such that no other eigenvalue cross it over $\tilde{G}_0 - \epsilon < \tilde{G} < \tilde{G}_0 + \epsilon$ for a given $\epsilon > 0$. By integrating the resolvent $(\mathcal{B}(\tilde{G}) - \mu\mathcal{I})^{-1}$ of the BT operator over the path C_μ, one obtains a two-dimensional projector $\Pi(\tilde{G})$ over the space spanned by $v_n, v_{n'}$, at least for $\tilde{G} \neq \tilde{G}_0$. Note that $\Pi(\tilde{G})$ is a function of the variable $\tilde{G}$ with values in the infinite-dimensional space of continuous operators over the functional space $L^2(\Omega)$. For clarity, we emphasize the dependence of the BT operator $\mathcal{B}$ and the projector Π on $\tilde{G}$ by writing explicitly $\mathcal{B}(\tilde{G}), \Pi(\tilde{G})$.

Since the integration path C_μ does not cross any eigenvalue, the resolvent is an analytic function of μ and $\tilde{G}$ over C_μ, therefore $\Pi(\tilde{G})$ is an analytic function of $\tilde{G}$. In particular, the image of $\Pi(\tilde{G})$ is two-dimensional, even at the bifurcation point $\tilde{G} = \tilde{G}_0$. As we shall see, this does not imply that there are still two eigenmodes $v_n, v_{n'}$ at that point. The restriction of the BT operator $\mathcal{B}(\tilde{G})$ to the image of $\Pi(\tilde{G})$ yields a 2×2 matrix $\mathrm{A}(\tilde{G})$. If there are no other spectral bifurcations over the considered range of $\tilde{G}$, then the restriction of the BT operator to the kernel of $\Pi(\tilde{G})$ has an analytical spectrum, therefore the non-analyticity of the spectrum of $\mathcal{B}(\tilde{G})$ is fully captured by the matrix $\mathrm{A}(\tilde{G})$ as we claimed above. Note that a bifurcation involving a higher number of eigenvalues would yield a higher-dimensional matrix, however such bifurcations were not observed numerically. Moreover, a dimension counting argument[3] implies that such points

[3]The argument relies on the property that two varieties generically intersect if the sum of their dimension exceeds the dimension of the underlying space (i.e., the dimension of one variety exceeds the co-dimension of the other one). We apply this property to investigate the intersection between the two-dimensional variety spanned by the $n \times n$ matrices $\mathrm{M}(\tilde{G}, \lambda) = \mathrm{A}(\tilde{G}) - \lambda \mathrm{I}$ and the space N_r of $n \times n$ matrices with $n - r$ vanishing eigenvalues. The latter has co-dimension r.

should generically not exist.

We first consider the example of a Hermitian matrix, then we show how the general, non-Hermitian case, differs qualitatively. We consider a matrix of the general form

$$\mathsf{A}(\tilde{G}) = \begin{bmatrix} \lambda_0 + a & b \\ c & \lambda_0 - a \end{bmatrix} , \tag{4.84}$$

where λ_0, a, b, c are smooth functions of $\tilde{G}$ (the smoothness results from the analyticity of the projector $\Pi(\tilde{G})$). One can easily compute its eigenvalues $\lambda_\pm$ and eigenvectors $\mathsf{X}_\pm$:

$$\lambda_\pm = \lambda_0 \pm \sqrt{d} , \qquad \mathsf{X}_\pm = \begin{bmatrix} b \\ \pm\sqrt{d} - a \end{bmatrix} , \qquad d = bc + a^2 , \tag{4.85}$$

if $d \neq 0$. The eigenvalues coalesce at $\tilde{G} = \tilde{G}_0$ if $d(\tilde{G}_0) = 0$.

If $\mathsf{A}(\tilde{G})$ is Hermitian for all values of $\tilde{G}$, then $a \in \mathbb{R}$ and $c = b^*$, so that $d = |b|^2 + a^2$ is real and non-negative. Furthermore, $a(\tilde{G}_0) = b(\tilde{G}_0) = c(\tilde{G}_0) = 0$. In fact, this simply derives from the fact that a diagonalizable matrix with all eigenvalues equal to zero is the null matrix. This also implies that $d'(\tilde{G}_0) = 0$ and $d''(\tilde{G}_0) \neq 0$ in general, so that close to $\tilde{G}_0$ the eigenvalues are approximately equal to

$$\lambda_\pm = \lambda_0 \pm \sqrt{d''(\tilde{G}_0)/2}\, |\tilde{G} - \tilde{G}_0| . \tag{4.86}$$

Thus we can draw two main conclusions: (i) the spectrum does not present non-analytical bifurcation points, the eigenvalues merely cross each other at $\tilde{G} = \tilde{G}_0$; (ii) the dimension of the eigenspace $E_{\lambda=\lambda_0}$ at $\tilde{G} = \tilde{G}_0$ is 2.

Now we consider the general, non-Hermitian case. The function $d(\tilde{G})$ takes complex values and crosses 0 at $\tilde{G} = \tilde{G}_0$ with a non-zero derivative $d'(\tilde{G}_0)$. The phases of $\lambda_\pm - \lambda_0$ undergo a $\pi/2$ jump when $\tilde{G}$ passes through the critical value $\tilde{G}_0$ and the absolute values of $\lambda_\pm - \lambda_0$ have a typical $\sqrt{\left|d'(\tilde{G}_0)(\tilde{G} - \tilde{G}_0)\right|}$ shape for $\tilde{G}$ close to $\tilde{G}_0$. In particular, if $d(\tilde{G})$ is real, positive for $\tilde{G} < \tilde{G}_0$ and negative for

The intersection of $\mathsf{M}(\tilde{G}, \lambda)$ with N_1 is generically a variety of dimension 1 (i.e., a collection of curves) which corresponds to the spectrum $\lambda(\tilde{G})$ of $\mathsf{A}(\tilde{G})$. The intersection of $\mathsf{M}(\tilde{G}, \lambda)$ with N_2 is generically a variety of dimension 0 (i.e., isolated points) and corresponds to order-2 bifurcations in the spectrum of $\mathsf{A}(\tilde{G})$. Finally, higher-order bifurcations ($r \geq 3$) generically lead to an empty set.

$\tilde{G} > \tilde{G}_0$, and if $\lambda_0(\tilde{G})$ is real, one obtains close to the critical value $\tilde{G}_0$:

$$\tilde{G} < \tilde{G}_0 \qquad \begin{cases} \mathrm{Re}(\lambda_\pm) \approx \lambda_0(\tilde{G}) \pm \sqrt{d'(\tilde{G}_0)(\tilde{G}_0 - \tilde{G})} \\ \mathrm{Im}(\lambda_\pm) = 0 \end{cases} \tag{4.87a}$$

$$\tilde{G} > \tilde{G}_0 \qquad \begin{cases} \mathrm{Re}(\lambda_\pm) = \lambda_0(\tilde{G}) \\ \mathrm{Im}(\lambda_\pm) \approx \pm\sqrt{d'(\tilde{G}_0)(\tilde{G} - \tilde{G}_0)} \end{cases} \tag{4.87b}$$

At the critical value $\tilde{G} = \tilde{G}_0$, the matrix $\mathsf{A}(\tilde{G}_0)$ is in general not diagonalizable. Without loss of generality, let us assume that $b(\tilde{G}_0) \neq 0$. The matrix $\mathsf{A}(\tilde{G}_0)$ can then be reduced to a Jordan block with an eigenvector X_0 and a generalized eigenvector Y_0:

$$\mathsf{A}(\tilde{G}_0)\mathsf{X}_0 = 0\,, \qquad \mathsf{X}_0 = \begin{bmatrix} b(\tilde{G}_0) \\ -a(\tilde{G}_0) \end{bmatrix}\,, \tag{4.88a}$$

$$\mathsf{A}(\tilde{G}_0)\mathsf{Y}_0 = \mathsf{X}_0\,, \qquad \mathsf{Y}_0 = \begin{bmatrix} 0 \\ 1 \end{bmatrix}\,. \tag{4.88b}$$

Note that since the derivative of $\sqrt{d(\tilde{G})}$ is infinite at $\tilde{G} = \tilde{G}_0$, one has

$$\mathsf{Y}_0 = \left.\frac{d\mathsf{X}_\pm}{d\lambda_\pm}\right|_{\tilde{G}=\tilde{G}_0}\,, \tag{4.89}$$

where the derivative yields the same result for $(\mathsf{X}_+, \lambda_+)$ and $(\mathsf{X}_-, \lambda_-)$. Moreover, if $\mathsf{A}(\tilde{G})$ is a symmetric matrix (i.e. $b = c$), then $\mathsf{X}_0^T\mathsf{X}_0 = 0$, i.e., X_0 is "orthogonal" to itself for the real scalar product.

In comparison to the Hermitian case, our main conclusions are: (i) the spectrum is non-analytical at $\tilde{G} = \tilde{G}_0$; (ii) the eigenvectors $\mathsf{X}_\pm$ of A collapse onto one single eigenvector X_0, the matrix A can be reduced to a Jordan block with a generalized eigenvector Y_0 given by the rate of change of the eigenvectors $\mathsf{X}_\pm$ with their corresponding eigenvalues $\lambda_\pm$, evaluated at the critical point $\tilde{G} = \tilde{G}_0$.

We summarize the results for the Hermitian and non-Hermitian case graphically on Fig. 4.13. We emphasize that the dichotomy "Hermitian, no bifurcation" versus "non-Hermitian, bifurcation" is specific to two-dimensional matrices. In fact, if one considers a 4×4 matrix made of two 2×2 blocks where one is Hermitian and the other is non-Hermitian, then the eigenvalues of the Hermitian block will not display any bifurcation point when they cross even if the whole operator is not Hermitian. This somewhat artificial example shows that there

is no general relation between bifurcation points and non-Hermitianity except that the spectrum of an Hermitian operator never bifurcates. By reducing the full operator to a low-dimensionality matrix on the subspace associated to the coalescing point, one can make precise statements about bifurcation and Hermitianity, as we did in this two-dimensional case. The "translation" of the above conclusions to the case of the Bloch-Torrey operator and their consequences on spectral decompositions is detailed in Appendix C.5.

Arbitrary domain, complex bifurcations

For a parity-symmetric domain, the spectrum exhibits bifurcations for particular values of the dimensionless gradient $\tilde{G}$, where two real eigenvalues abruptly become a complex conjugate pair. In contrast, for a non parity-symmetric domain, all eigenvalues are generally complex for non-zero $\tilde{G}$ and there is no bifurcation point. However, this is true only for real values of $\tilde{G}$. By allowing $\tilde{G}$ to take complex values, one recovers bifurcation boints for any bounded domain. In other words, a slight asymmetry of the domain merely "moves" bifurcation points away from the real axis.

Generally speaking, by solving the eigenmode equation

$$-\tilde{\nabla}^2 v - i\tilde{G}\tilde{x} = \tilde{\mu} v \,, \tag{4.90}$$

$$\mathbf{n} \cdot \nabla v|_{\partial\tilde{\Omega}} = 0 \,, \tag{4.91}$$

one obtains a transcendental equation on $\tilde{\mu}$ of the generic form $F(\tilde{G}, \tilde{\mu}) = 0$, where F is an analytic function of $\tilde{G}$ and $\tilde{\mu}$. To show how bifurcations may result from this equation, let us consider a simple example:

$$F(z, w) = (w^2 - 1)^2 - z = 0 \,. \tag{4.92}$$

In this example, w stands for the eigenvalue and z for the gradient strength. This equation may be inverted to obtain w as a function of z but the inversion of the square function makes $w(z)$ a multivaluate function with four possible values in general (i.e., four "sheets" in the complex plane):

$$w(z) = \pm\sqrt{\pm\sqrt{z} + 1} \,. \tag{4.93}$$

or equivalently:

$$w_1(z) = \sqrt{\sqrt{z} + 1} \,, \qquad w_2(z) = \sqrt{-\sqrt{z} + 1} \,, \tag{4.94}$$

$$w_3(z) = -\sqrt{\sqrt{z} + 1} \,, \qquad w_4(z) = -\sqrt{-\sqrt{z} + 1} \,. \tag{4.95}$$

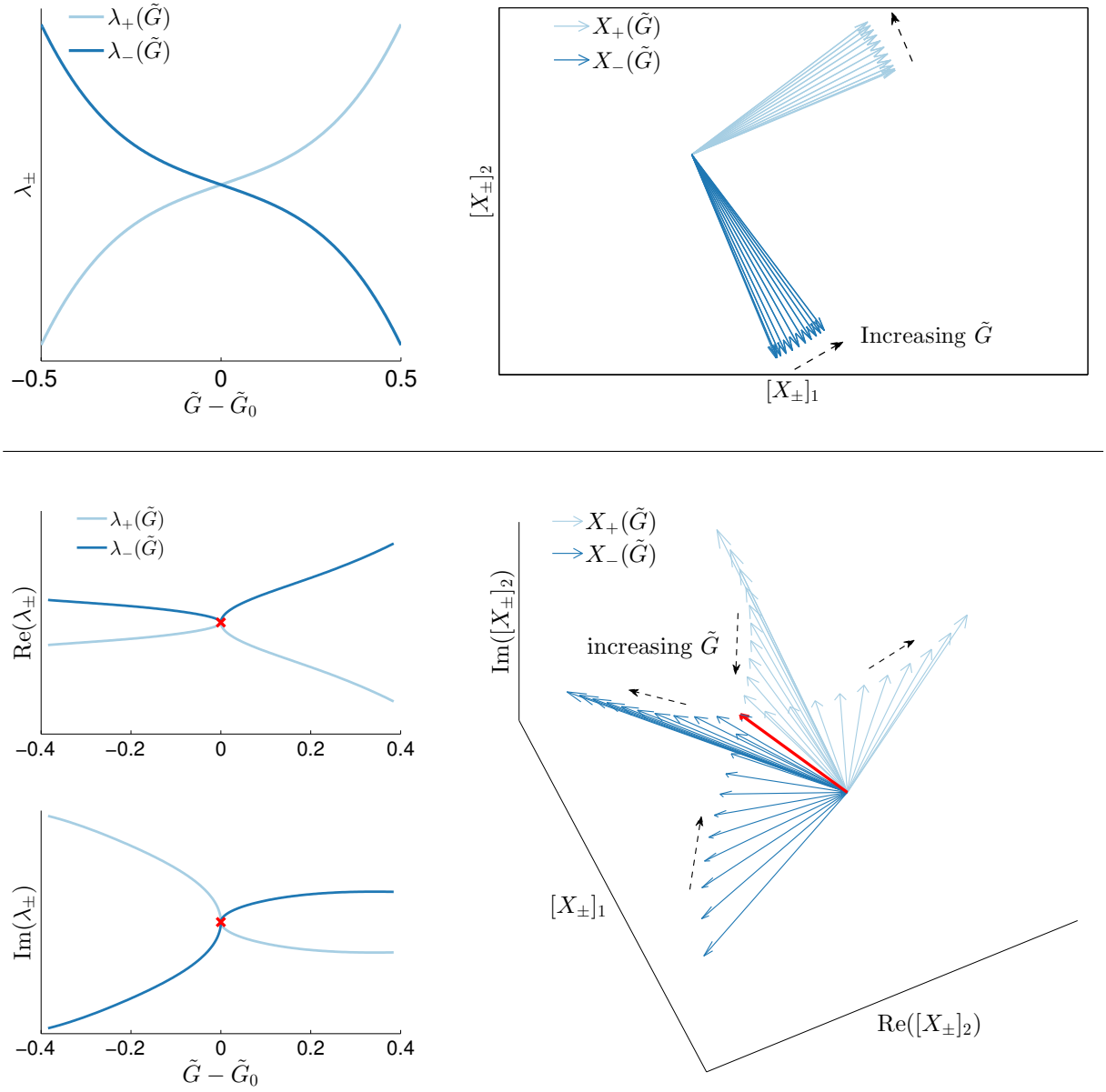

Figure 4.13: Eigenvalues and eigenvectors of a Hermitian and non Hermitian 2×2 matrix $\mathsf{A}(\tilde{G})$. (top) Hermitian case: the eigenvalues $\lambda_\pm(\tilde{G})$ cross each other at $\tilde{G} = \tilde{G}_0$, the eigenvectors $X_\pm(\tilde{G})$ are always orthogonal to each other and do not exhibit any particular behavior at $\tilde{G} = \tilde{G}_0$. (bottom) non-Hermitian case: the eigenvalues $\lambda_\pm(\tilde{G})$ exhibit a typical square-root behavior at $\tilde{G} = \tilde{G}_0$ ((indicated by a red cross), the eigenvectors $X_\pm(\tilde{G})$ collapse on a single vector at $\tilde{G} = \tilde{G}_0$, which creates an angular point (indicated by a red arrow). Note that $\tilde{G}$ was sampled with additional points near $\tilde{G}_0$ for better visualization of the bifurcation. The complex $X_\pm$ vectors were plotted with the convention that $\arg([X_\pm]_1) = 0$.

The multivaluation of $w(z)$ is closely related to the absence of unique determination of the argument of a complex number and the necessity of a "cut" in the complex plane. In what follows we consider the usual convention that the cut is along the negative real semi-axis. In other words, the square root is defined as follows:

$$\sqrt{\rho\, e^{i\theta}} = \sqrt{\rho}\, e^{i\theta/2}\,, \qquad \rho > 0\,,\ -\pi < \theta \leq \pi\,. \tag{4.96}$$

This choice makes the real part of $\sqrt{z}$ a continuous function when z crosses the cut (i.e., when θ jumps from π to $-\pi$). However, the imaginary part of $\sqrt{z}$ is not continuous and jumps from $i\sqrt{\rho}$ to $-i\sqrt{\rho}$.

The multivaluate function $w(z)$ exhibits three "branching" points where two sheets coincide: $w_1(0) = w_2(0) = 1$, $w_3(0) = w_4(0) = -1$, and $w_2(1) = w_4(1) = 0$. All these branching points have the same "structure", that is the one of $\pm\sqrt{z}$ at $z = 0$. We show on Fig. 4.14 the plot of the multivaluate function $w = \pm\sqrt{z}$. One can see two sheets that are individually discontinuous at the cut, and both sheets taken together form a continuous surface. By performing a 2π turn around $z = 0$, one goes from one sheet to the other, and a full 4π turn is required to go back to the initial point.

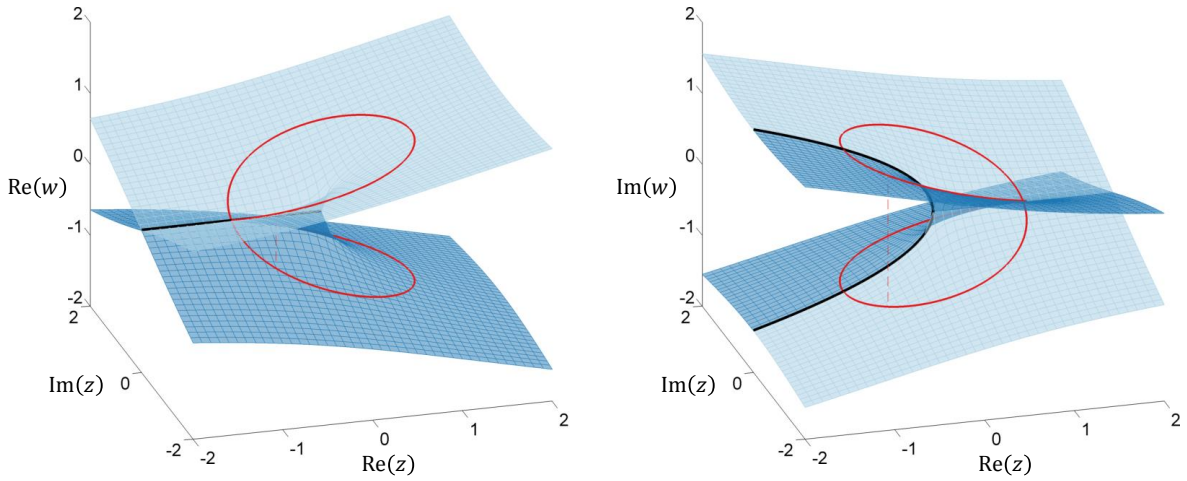

Figure 4.14: Plot of the real part (left) and imaginary part (right) of the bivaluate function $w(z) = \pm\sqrt{z}$ ("+" sheet in light blue and "−" sheet in dark blue). The cut along the real negative semi-axis is represented as a thick black line. Each sheet is discontinuous at the cut but both of them for a single continuous surface $w(z)$. The red contour depicts to a full 4π turn around $z = 0$ on the surface $w(z)$. After a 2π turn from the point (z_0, w_0), one reaches the point $(z_0, -w_0)$, as indicated by the red dashed line.

The plot of $w(z) = \pm\sqrt{\pm\sqrt{z}+1}$ is presented on Fig. 4.15. Although it is visually more complicated than the "simple" square root function, it is essentially the combination of three $\sqrt{z}$-branching points that connect 4 sheets together. By

circling around all branching points (shown in red), one goes through all sheets and reach the initial point after a 6π turn.

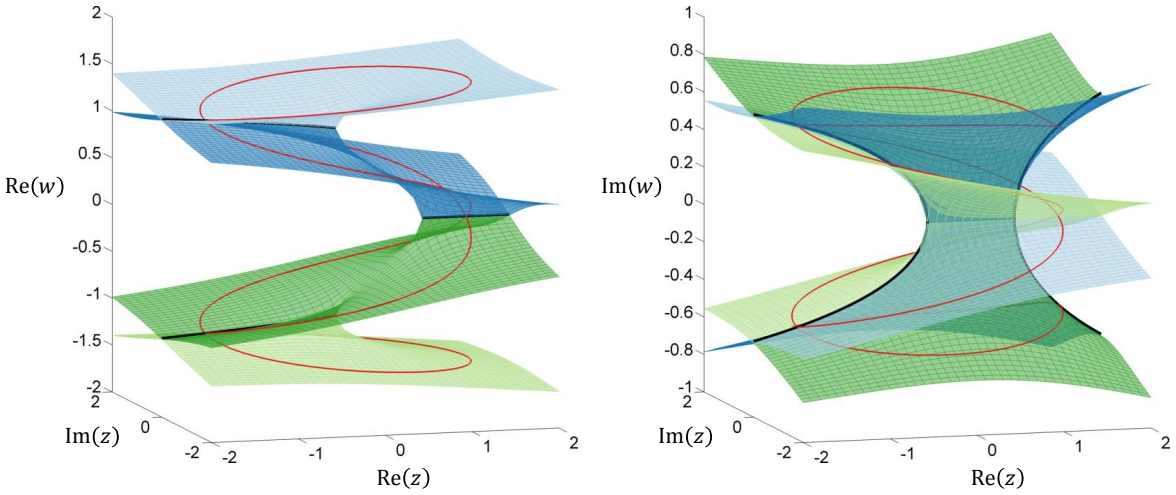

Figure 4.15: Plot of the real part (left) and imaginary part (right) of the multivaluate function $w(z) = \pm\sqrt{\pm\sqrt{z}+1}$. The color code is the following: ++ in light blue, +− in dark blue, −+ in light green and −− in dark green. The red contour depicts a full 6π turn around all branching points, and illustrates that all sheets are connected to each other and form a unique multivaluate surface.

The particular example that we chose is representative of bifurcations in the spectrum of the BT operator. Indeed, the computations of the previous paragraph on 2×2 matrices show that eigenvalues behave as $\sqrt{\tilde{G}-\tilde{G}_0}$ close to a bifurcation point. In other words, spectral bifurcations are related to branching points of a complex multivaluate function. From a mathematical point of view, the discrete spectrum $\tilde{\mu}_1(\tilde{G}), \tilde{\mu}_2(\tilde{G}), \ldots$ appears as different sheets of a unique multivaluate function $\tilde{\mu}(\tilde{G})$. This function $\tilde{\mu}(\tilde{G})$ simply results from the inversion of the transcendental eigenvalue equation $F(\tilde{G}, \tilde{\mu}) = 0$. This point of view reveals a way to find bifurcations in the complex plane. Let us consider a closed contour $C_{\tilde{G}}$ in the complex $\tilde{G}$-plane. If $C_{\tilde{G}}$ does not enclose any bifurcation point, then $\tilde{\mu}_n(\tilde{G})$ is analytical inside the the contour for any sheet $n = 1, 2, \ldots$, and one has

$$\oint_{C_{\tilde{G}}} \tilde{\mu}_n(\tilde{G})\, \mathrm{d}\tilde{G} = 0\ . \tag{4.97}$$

In contrast, if the path $C_{\tilde{G}}$ encloses bifurcation points, the path integral along $C_{\tilde{G}}$ is generally non zero anymore. Therefore, one can find bifurcation points by applying the following algorithm:

1. choose an initial closed path $C_{\tilde{G}}$ and compute $\oint_{C_{\tilde{G}}} \tilde{\mu}_n(\tilde{G})\, \mathrm{d}\tilde{G}$ for all sheets by following continuously the path $C_{\tilde{G}}$;

2. if the obtained value is non zero, split the path in smaller closed paths and perform the integral over each smaller path;

3. identify paths with non zero integral and repeat the previous step.

We show on Fig. 4.16 an example of such an algorithm. Numerically, one performs path integrals by discretizing the contour $C_{\tilde{G}}$, and a threshold should be found to decide between "zero" and "non-zero" integrals (indicated by red and black dots, respectively). A compromise should be found between fiability and speed. A too high threshold may result in missed bifurcation points. However, a too small threshold generally leads to a large number of path integrals. Since each integral requires the computation of the spectrum $\tilde{\mu}(\tilde{G})$ along the path $C_{\tilde{G}}$, a bad choice of the threshold may be very time-consuming. For the particular example shown on Fig. 4.16, one can see that the threshold was chosen somewhat too low because some red squares at the initial steps eventually disappear after a large number of iterations. In other words, a suspicion of bifurcation points was eventually dismissed, that resulted in too many computations.

The choice of the contour is also a matter of compromise. One one hand, one can choose a shape that tiles the plane, like a square. This allows one to have non-overlapping integration contours, which avoids counting one bifurcation point twice. On the other hand, one can choose a smooth contour, like a circle. This implies a better numerical accuracy for the integral computation and in turn a lower threshold may be chosen. However, this requires an additional criterion to discard "double" points that result from overlapping contours. Both cases are shown on Fig. 4.16.

The pattern of bifurcation points in the complex $\tilde{G}$ plane reveals a left-right symmetry. Let us consider the dimensionless Bloch-Torrey operator $\tilde{\mathcal{B}} = -\nabla^2 - i\tilde{G}x$ and perform a complex conjugation:

$$\tilde{\mathcal{B}}^* = -\nabla^2 + i\tilde{G}^* x = -\nabla^2 - i(-\tilde{G}^*)x \,, \tag{4.98}$$

therefore we immediately see that the bifurcation point pattern is always symmetric under the transformation $\tilde{G} \longrightarrow -\tilde{G}^*$, that explains the left-right symmetry of the pattern. Furthermore, the bifurcation pattern of x-parity-symmetric domains exhibits a top-bottom symmetry, according to

$$\mathcal{P}_x \tilde{\mathcal{B}}^* = -\nabla^2 - i\tilde{G}^* x \,, \tag{4.99}$$

where we used the parity symmetry to write $\mathcal{P}_x \nabla^2 = \nabla^2$. The above equation shows that for an x-parity symmetric domain, the bifurcation point pattern is symmetric under the transformation $\tilde{G} \longrightarrow \tilde{G}^*$, i.e. top-bottom symmetry. Note

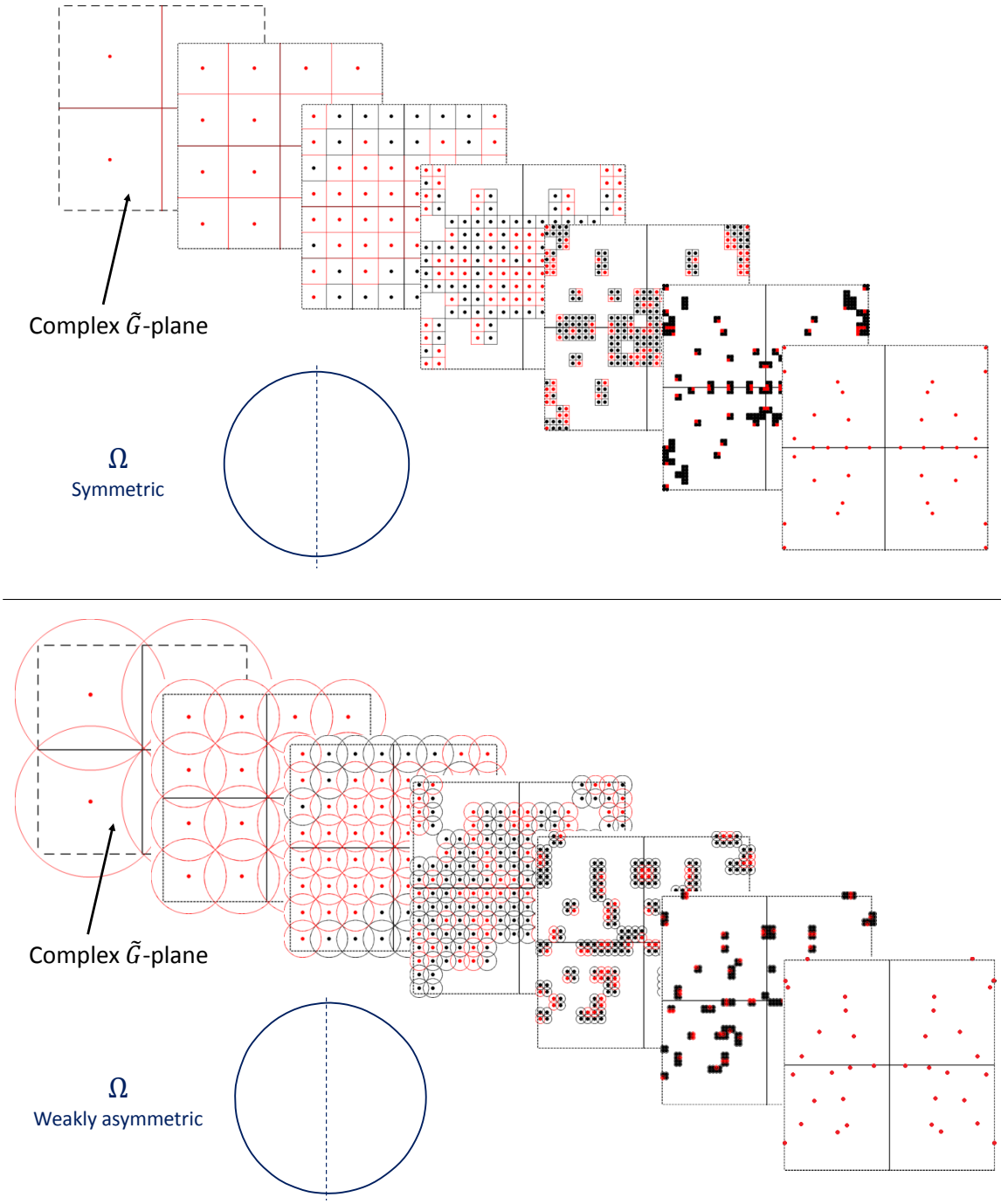

Figure 4.16: Several iterations of the algorithm to find spectral bifurcations in the complex $\tilde{G}$-plane. The red dots indicate contours that yield a non-zero contour integral. The range of $\tilde{G}$ is a square in the complex plane, from $-200(1+i)$ to $200(1+i)$. We emphasize that there are infinitely many bifurcation points in the complex plane but only a finite number appears because of the finite range of $\tilde{G}$. (Top) the domain Ω is a disk and we show the algorithm with square integration contours. (Bottom) the domain Ω is slightly asymmetric (a thin dashed line helps to visualize the asymmetry) and we show the algorithm with circular integration contours. Compared to the bifurcation pattern of a disk, the top-bottom symmetry is lost but bifurcation points still exist.

that the existence of bifurcation point on the real axis is consistent with the top-bottom symmetry of the bifurcation pattern. We show on Fig. 4.17 the multivaluate function $\tilde{\mu}(\tilde{G})$ (real part and imaginary part) for a disk. Although the figure is visually complicated by the superposition of numerous sheets, one recognizes the basic sqare root structure of bifurcation points, illustrated on Fig. 4.14.

The bifurcation point with the smallest absolute value defines a convergence radius outside of which low-gradients asymptotic expansions would fail because of the non-analyticity of the bifurcation. The finite radius of convergence of the cumulant expansion in terms of bD_0 was investigated in [84] for a one-dimensional model in the limit of narrow-gradient pulses. In that case, the gradient pulse effectively applies a e^{iqx} phase pattern across the domain and the decay of the magnetization is caused by the "blurring" of this pattern due to diffusion (see Sec. 1.2.3). In this regime, the signal is an analytic function of $bD_0 = q_x^2 D_0 \Delta$ because it is controlled by the spectrum of the Laplace operator that does not exhibit bifurcation points. As the authors explain, the finite convergence radius of the cumulant expansion is merely caused by the Taylor series of the logarithm function and related to the smallest (in absolute value) complex value of bD_0 for which the signal is zero. In contrast, we argue that the non-analyticity of the BT spectrum at finite gradient strength should intrinsically restrict the range of applicability of low-gradient expansions in all non-trivial domains.

4.3.3 Overlapping of eigenmodes

We have shown the transition between delocalized eigenmodes in the motional narrowing regime, and strongly localized eigenmodes in the localization regime. In this section, we investigate the crossover between these two extreme regimes. More precisely, we assume that the Bloch-Torrey eigenmodes are localized but not strongly enough so that eigenmodes on opposite sides of the domain overlap with each other.

We recall that the formulas for the magnetization and the signal after two opposite pulses of duration $\delta = T/2$ are

$$m(T = 2\delta, \mathbf{r}) = \sum_{n'} \sum_{n} (1|v_n^*)(v_n^*|v_{n'}) v_{n'}(x) e^{-T(\mu_n^* + \mu_{n'})/2}, \tag{4.100}$$

$$S = \frac{1}{\mathrm{vol}(\Omega)} \sum_{n'} \sum_{n} (1|v_n^*)(v_n^*|v_{n'})(v_{n'}|1) e^{-T(\mu_n^* + \mu_{n'})/2}, \tag{4.101}$$

The overlapping between the eigenmodes v_n and $v_{n'}$ is represented quantitatively by the factor $(v_n^*|v_{n'})$. If two modes on opposite sides of the domain overlap, it

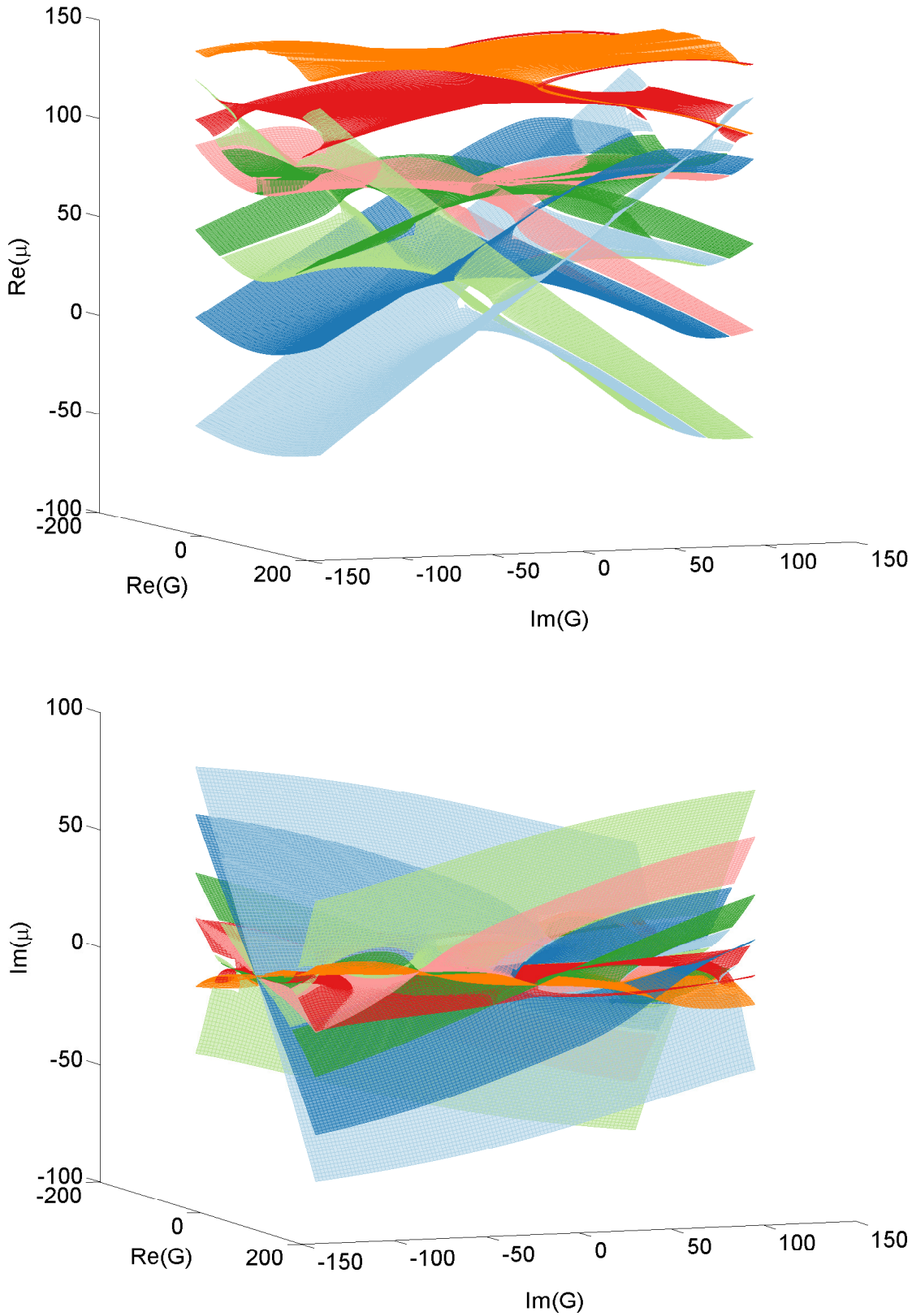

Figure 4.17: Real and imaginary part of the sheets $\tilde{\mu}(\tilde{G})$ of the BT spectrum in a disk (see also top panel of Fig. 4.16). The figure reveals a rich pattern of bifurcation points, with a similar structure as in Figs. 4.14 and 4.15.

yields a term in the signal with a complex exponential of time that may lead to oscillating patterns.

To illustrate this effect, let us consider a simple example of a slab of width L (with the gradient direction being orthogonal to the slab). In this setting, the eigenmodes of the Bloch-Torrey operator can be localized at either of two endpoints of the interval, but only if the gradient length ℓ_g is sufficiently small compared to L. To give a concrete numerical value, Stoller *et al* computed the value of the first bifurcation point (i.e., the first two eigenmodes start to localize at each side of the slab) and obtained $\ell_g/L = 0.38$. In the following, we assume that ℓ_g/L is smaller than this value so that the first two eigenmodes v_1 and v_2 are localized.

Due to the left-right symmetry ($x \longrightarrow -x$), the first two eigenmodes $v_1(x)$ and $v_2(x)$ satisfy the identity $v_2(x) = v_1^*(-x)$ and $\mu_2 = \mu_1^*$, and are localized at each endpoint of the interval. Thus the first two eigenvalues have the same real part and, in the limit of large T, the magnetization may be represented by a superposition of v_1 and v_2:

$$\begin{aligned} m(x,T) \approx &\left(c_{1,1} + c_{2,1}\, e^{-i\mathrm{Im}(\mu_1)T}\right) e^{-\mathrm{Re}(\mu_1)T} v_1(x) \\ &+ \left(c_{2,2} + c_{1,2}\, e^{i\mathrm{Im}(\mu_1)T}\right) e^{-\mathrm{Re}(\mu_1)T} v_2(x)\,, \end{aligned} \tag{4.102}$$

with $c_{n,n'} = (1|v_n^*)(v_n^*|v_{n'})$, and the signal is given by

$$S \approx C e^{-\mathrm{Re}(\mu_1)T}\,, \tag{4.103}$$

with

$$C = 2(C_{1,1} + \mathrm{Re}(C_{1,2}))\,, \tag{4.104}$$

where $C_{1,1}$ and $C_{1,2}$ are given by

$$C_{1,1} = |(1|v_1)|^2 (v_1^*|v_1)\,, \qquad C_{1,2} = (1|v_1^*)(v_1^*|v_2)(1|v_2) e^{i\mathrm{Im}(\mu_1)T}\,. \tag{4.105}$$

The factor 2 in (4.104) reflects the fact that two eigenmodes contribute to the signal. For a planar boundary located at $\pm L/2$, we obtained in Sec. 4.2.1 the following expression for the real and imaginary part of the first eigenvalue:

$$2\mathrm{Re}(\mu_1) = |a_1| \frac{D_0}{\ell_g^2}\,, \tag{4.106}$$

$$2\mathrm{Im}(\mu_1) = \pm \left(GL - \sqrt{3}|a_1| \frac{D_0}{\ell_g^2} \right)\,. \tag{4.107}$$

For a slab these expressions are modified because the boundaries may *a priori* not be treated independently. Here we assume that the overlapping between v_1

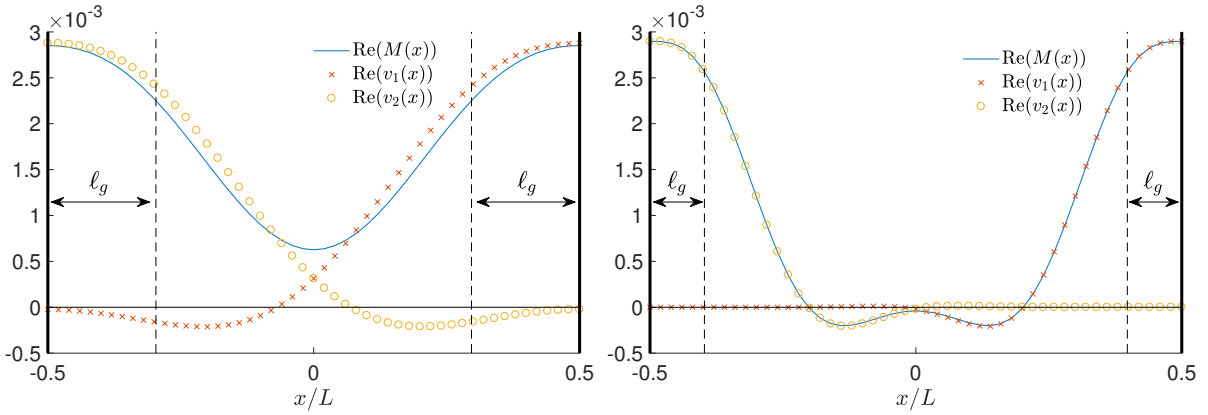

Figure 4.18: The real part of the transverse magnetization $m(T = 2\delta, x)$ in a slab for two different gradient strengths, in the long δ regime, as well as the real part of the first two eigenmodes $v_1(x)$ and $v_2(x)$ weighted by the coefficients of Eq. (4.102). We checked that the superposition of $v_1(x)$ and $v_2(x)$ reproduces perfectly the exact magnetization $m(T, x)$ in this regime. In both cases, one observes the localization of the magnetization near the endpoints of the interval. We chose a constant ratio $\ell_d/\ell_g = 2.5$ for both figures, so that the amplitude of the magnetization is approximately the same. (left) $\ell_g/L \approx 0.2$: one can see some overlapping between the two eigenmodes and $|(v_1^*|v_2)| = 0.23$. (right) $\ell_g/L \approx 0.1$: there is almost no overlapping of the eigenmodes and $|(v_1^*|v_2)| = 8.2 \cdot 10^{-4}$.

and v_2^* is sufficiently weak so that Eqs. (4.107) present a good approximation of the first eigenvalues μ_1, μ_2 for the slab.

Since at high gradients the imaginary part of μ_1 scales as G and its real part scales as $G^{2/3}$, the oscillations in the signal are somewhat faster than its global decay. In other words, the signal may exhibit several oscillations before reaching the noise floor. One may note that the dominant term, GL, of the imaginary part depends on the choice of origin $x = 0$. However, Eq. (4.105) was derived under the assumption of a symmetric slab, i.e. $x = 0$ at the middle of the slab. In the general case, the imaginary parts of the eigenvalues enter through their differences in the expression of the signal, thus the arbitrary choice of the origin $x = 0$ has no influence on the expression of the signal, as it should be for a refocused gradient sequence.

The conclusion of this computation is that the cross-term $C_{1,2}$ produces oscillations in the signal (by varying G or δ) on top of the asymptotic decay given by $\exp(-\mathrm{Re}(\mu_1)T)$. This cross-term is linked to the overlapping of the modes v_1 and v_2. In turn, this overlapping depends on the ratio between the width ℓ_g of the modes, and their spacing L: the smaller the ratio ℓ_g/L, the smaller the overlapping, and thus, the smaller the oscillating term. In the limit of well-separated modes, $(v_1^*|v_2) = 0$ and one has $C = 2C_{1,1}$, with no oscillation. The effect of overlapping of eigenmodes is illustrated in Fig. 4.18 where we plotted the transverse

magnetization in a slab for two different gradient strengths: at low gradients the localization pockets overlap and at high gradients they are well-separated. Note that we plotted only the real part of the magnetization; the imaginary part is non-zero but it does not contribute to the signal since its integral over the slab is zero. Although we illustrated this overlapping effect on the simple example of a slab, the conclusion (and the previous computations) may be generalized to any geometry, where L would denote the spacing between two localized eigenmodes.

The influence of $\Delta - \delta$

Until now we have considered a PGSE sequence with $\Delta = \delta$, i.e. without any gap between two gradient pulses. In this section we consider a more general PGSE sequence and investigate the influence of the diffusion step duration $\Delta - \delta$ on the transverse magnetization. Mathematically, the effect of this diffusion step is to multiply the transverse magnetization just after the first gradient pulse by the evolution operator $\mathcal{D} = \exp((\Delta - \delta)D_0\nabla^2)$. Then Eqs. (4.100), (4.101), and the consequent analysis remain applicable by replacing $(v_n^*|v_{n'})$ with the coefficient $\beta_{n,n'}$ defined by

$$\beta_{n,n'} = \int_\Omega (\mathcal{D}v_n^*)(\mathbf{r})v_{n'}(\mathbf{r})\,\mathrm{d}\mathbf{r}\,. \tag{4.108}$$

The dependence on $\Delta - \delta$ is now hidden in the coefficients $\beta_{n,n'}$. Note that if $\Delta = \delta$, then the operator $\mathcal{D}$ is the identity (since diffusion during zero time does not affect the magnetization) and we recover $\beta_{n,n'} = (v_n^*|v_{n'})$. If we consider the regime of long δ where only the first eigenmode contributes (without overlapping), the effect of the diffusion step results merely in a modification of the global amplitude of the magnetization through the new definition (4.108) of the coefficients $\beta_{1,1} = \beta_{2,2}$. In turn, the global amplitude of the signal is also affected by this coefficient and decreases with increasing $\Delta - \delta$.

The situation of two overlapping eigenmodes is more complex. The diffusion step also changes the values of the coefficients $\beta_{1,2}$, $\beta_{2,1}$, and hence the relative amplitude of the oscillating term $C_{1,2}$ (see Eqs. (4.104) and (4.105)). Diffusion is expected to increase the width of the localized eigenmodes, thus increasing the overlapping between them and enhancing the oscillations in the signal. This effect should be stronger for already overlapping modes than for well separated ones, in other words, when the ratio ℓ_g/L is not very small, where L denotes the distance between two localization pockets. The effect of the diffusion step on the localization regime in a one-dimensional setting was partly investigated in [102].

4.3.4 Summary

We summarize nearly all that we have presented so far on Fig. 4.19. This figure represents the eigenvalues and corresponding eigenmodes of the BT operator in a disk, as a function of the dimensionless gradient strength $\tilde{G}^{1/3} = \ell_s/\ell_g$. The power $1/3$ has no particular significance but was chosen to improve the clarity of the figure. At $\tilde{G} = 0$, the Bloch-Torrey operator is reduced to the Laplace operator, and one obtains the well-known Laplacian eigenmodes. Because of the rotational invariance of the disk, several eigenvalues are twice degenerate, because from one eigenmode one can *a priori* form another one by rotating it by an appropriate angle.

Another consequence of the symmetries of the disk is that eigenmodes exhibit various symmetries. On the figure, we have denoted by + a symmetric eigenmode and by − an antisymmetric eigenmode. The first sign refers to the symmetry along the x-axis and the second sign refers to symmetry along the y-axis. The symmetry of Laplacian eigenmodes is of considerable importance because the gradient term $i\tilde{G}x$ couples only modes with the same symmetry along y and with opposite symmetries along x. With signs, it means that the gradient couples $(+,+)$ to $(-,+)$ and $(-,-)$ to $(+,-)$. For example, the first bifurcation point (blue curves) involves the constant eigenmode with symmetry $(+,+)$, and the eigenmode with symmetry $(-,+)$ immediately above. A more complicated bifurcation pattern may be observed with the light orange curve which has a $(+,+)$ symmetry. One can see that it goes up and bifurcates with the dark orange curve that corresponds to the $(-,+)$ eigenmode at the top of the figure. However, a careful examination shows that this mode bifurcates first with the $(+,+)$ mode right below it, then they split again before bifurcating with the light orange curve.

At large gradient strength, nearly all plotted eigenvalues have bifurcated, and eigenmodes are localized on one side of the domain. Consistently with our results, eigenvalues with positive imaginary part correspond to eigenmodes localized on the left side of the disk. By applying the theory of localization at a curved boundary of Sec. 4.2.2, one can associate to each eigenmode two indices (n, l) that govern the behavior of the mode in the directions perpendicular and parallel to the boundary. As the order n increases, the extension of the modes along x increases until a point where they cannot be localized anymore. This explains why the bifurcation points associated to larger values of n occur at larger values of $\tilde{G}$, i.e., smaller values of ℓ_g/ℓ_s.

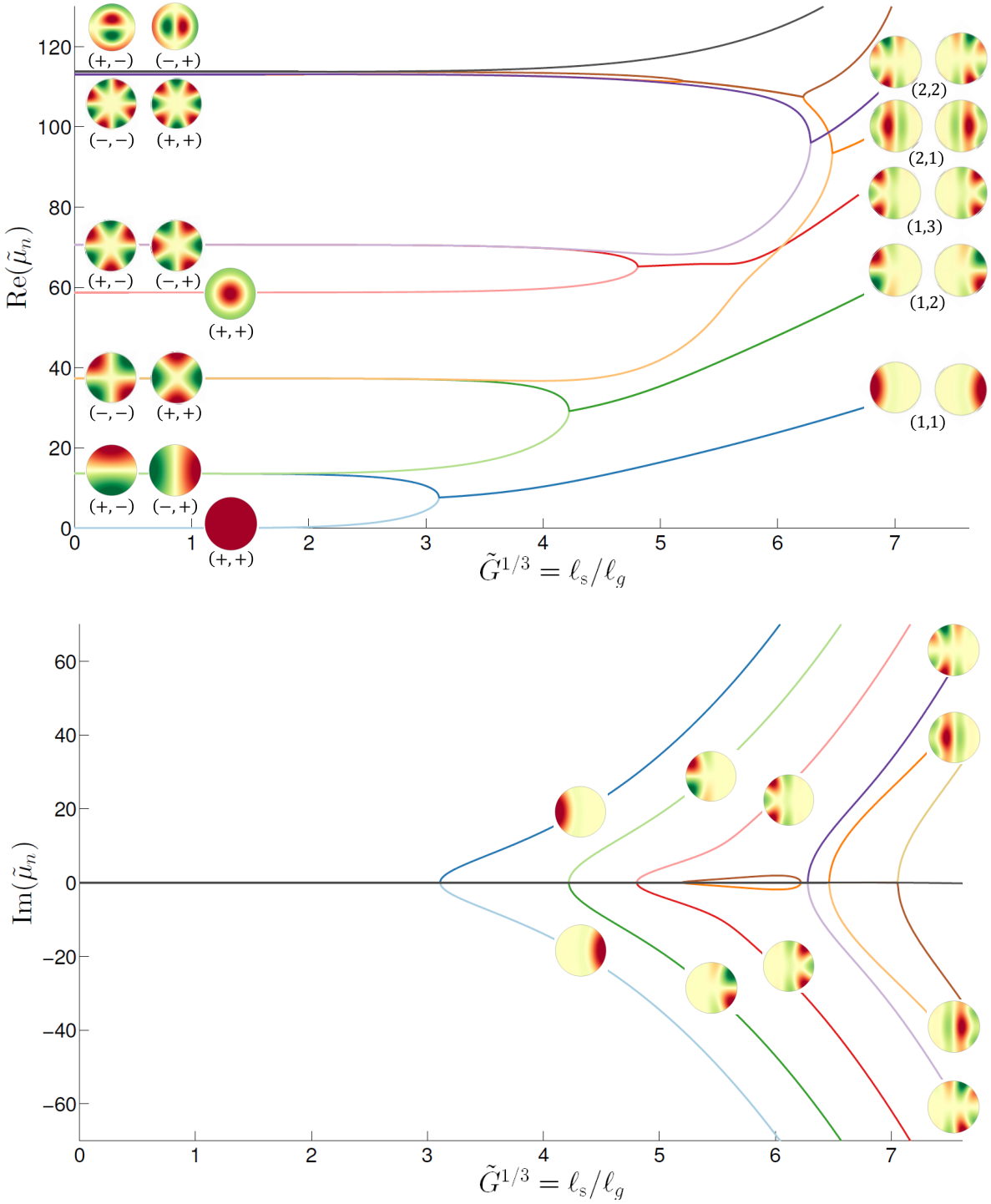

Figure 4.19: Graphical summary of the results for bounded domains (illustrated for the case of a disk). The spectrum of the BT operator inside a disk exhibits bifurcations for some particular values of ℓ_s/ℓ_g, that indicate the emergence of the localization regime. The profile of the eigenmodes is governed by two indices (n, l), that represent loosely the number of oscillations perpendicular and parallel to the boundary, respectively.

4.4 Periodic domain

4.4.1 Introduction

In the previous section, we studied the BT operator for bounded domains, in which the spectrum of this operator is discrete. Such domains however are not always suitable for modeling biological samples or mineral porous media which are interconnected and usually extended over a broad range of length scales. In this light, periodic domains may serve as more appropriate models and present a somewhat intermediate setting between bounded and unbounded domains, keeping the advantages of both: they can model macroscopic samples but computations can be performed in a single unit cell that dramatically reduces the size of the computational domain and the computation time. Evidently, complex biological or mineral samples, on which dMRI experiments are usually performed, are not simple periodic structures. In a living tissue, one would most likely find very diverse cell shapes, sizes, and arrangements, in a given voxel. However, the microstructure is probed at the scale of the diffusion length traveled by spin-bearing particles, that is much smaller than the voxel size. Although two "unit cells" of the real structure are always different, they are often statistically similar at this mesoscopic scale and may lead to almost identical behavior of the signal. In that regard, a periodic medium may be the best compromise between simplicity and relevance.

To our knowledge, the spectral properties of the BT operator have not been studied at all in periodic domains. One of the major challenges is that the gradient term in the BT operator is not periodic, so that standard methods of the quantum theory of solids [325, 326], in which potentials are typically periodic, are not applicable here. To overcome this problem, we will approximate the constant gradient in the BT operator or, more generally, the continuous-time gradient profile in the BT equation, by a sequence of infinitely narrow gradient pulses. In this approximation, the effects of the gradient term and of the Laplace operator are separated, and the problem can be reduced to that of the Laplace operator in a single unit cell with pseudo-periodic boundary conditions. This representation will allow us to develop efficient numerical computations and to investigate the spectral properties of the BT operator[4]. In particular, we will show how the localization of eigenmodes is related to bifurcation points in the spectrum in periodic domains. We will also discuss the validity of this approximation.

This section reproduces closely our publication [348] and is organized as fol-

[4]Note that it is *a priori* not clear whether eigenfunctions of the BT operator exist in the case of periodic domains because the gradient term is an unbounded perturbation of the Laplace operator.

lows. In Sec. 4.4.2, we present the theoretical basis of our numerical technique. We show that the BT equation cannot be straightforwardly reduced to a single unit cell and how to overcome this difficulty. The numerical implementation and results are described in Sec. 4.4.3. As the gradient strength increases, the magnetization localizes sharply around obstacles in the medium, at points where the boundary is orthogonal to the gradient direction. This behavior can be interpreted in terms of localized eigenmodes of the BT operator. We investigate these eigenmodes and the corresponding eigenvalues in Sec. 4.4.4. Finally, Sec. 4.4.5 summarizes our results.

4.4.2 Theoretical ground

For pedagogical reasons, the presentation of our technique is split into different steps of increasing generality. First we consider the case of a medium that is periodic along one axis (bounded along the other two). To be concise we call it a 1D-periodic medium, although the medium itself is not one-dimensional. The gradient is initially aligned with the periodicity axis, then we show how to take into account a general gradient direction. Finally the case of periodicity along several axes is discussed.

For convenience, we recall the Bloch-Torrey equation with the general Robin boundary condition at the boundary of the domain and a uniform initial magnetization:

$$\partial_t m = D_0 \nabla^2 m + i(G_x x + G_y y + G_z z) \qquad \text{in } \Omega\,, \tag{4.109a}$$

$$\mathbf{n} \cdot \nabla m - \kappa m|_{\partial\Omega} = 0\,, \tag{4.109b}$$

$$m(t = 0, \mathbf{r}) = 1\,, \tag{4.109c}$$

and the Bloch-Torrey operator is defined as

$$\mathcal{B} = -D_0 \nabla^2 - i(G_x x + G_y y + G_z z)\,. \tag{4.110}$$

Bloch-Torrey equation adapted to a 1D-periodic medium

Let us first consider a medium Ω which is periodic along a given direction, say x. In other words, the medium is invariant by the translation $x \longrightarrow x + a_x$, where a_x is the spatial period of the medium along x. A natural idea is to reduce the study of the whole medium to the study of a single unit cell, that is to a slab $\Omega_1 = \{(x, y, z) \mid -a_x/2 \leq x \leq a_x/2\}$, with appropriate boundary conditions, and then to expand the results to the whole medium. Note that this "slab" typically contains microstructural features, as illustrated on Fig. 4.20.

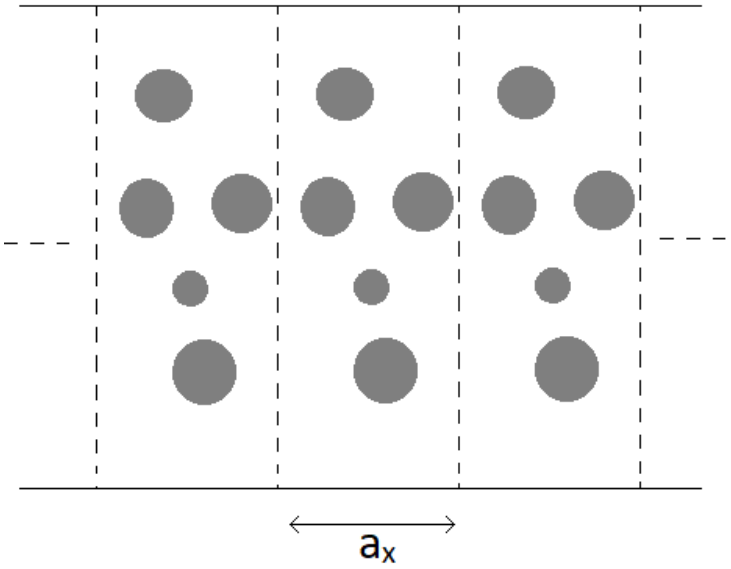

Figure 4.20: A schematic example of a 1D-periodic medium, where a_x is the spatial period. The dashed lines help to visualize a unit cell. The gray regions represent obstacles. Diffusion can occur either only in white region (so that boundaries of gray regions are impermeable), or in both gray and white regions (in which case boundaries of gray regions are permeable). In this thesis, we focus on the former setting but the method can be generalized to the latter one.

A simple case in which the reduction is straightforward is when the transverse magnetization $m(t, x, y, z)$ is at all times periodic along x; in that case, one can study the magnetization and related quantities on Ω_1 with periodic boundary conditions. However, although the initial condition (4.109c) is uniform (hence periodic), the BT equation (4.109a) that governs the time-evolution of the transverse magnetization is not periodic unless $G_x = 0$. Therefore, let us consider the case of $G_x \neq 0$ where one cannot directly reduce the BT equation to a single unit cell with periodic boundary conditions. For clarity we assume that the gradient is along x, in other words $G_y = G_z = 0$, and the general case will be presented later. We recall the definition

$$Q_x(t) = \int_0^t G_x(t')\,\mathrm{d}t' \ . \tag{4.111}$$

From Eq (4.109a), one can see that the magnetization at the position $x+a_x$ evolves in the same way as the magnetization at x, except for an accumulated phase:

$$m(t, x + a_x, y, z) = e^{iQ_x(t)a_x} m(t, x, y, z) \ . \tag{4.112}$$

Thus, in principle one can reduce the BT equation to a single unit cell, with the *time-dependent* boundary condition

$$m(t, a_x/2, y, z) = e^{iQ_x(t)a_x} m(t, -a_x/2, y, z) \ . \tag{4.113}$$

This time-dependent boundary condition makes the problem impractical from both theoretical and numerical points of view. An often-employed trick to discard the phase $e^{iQ_x(t)a_x}$ and reduce the problem to simple periodic boundary conditions is to introduce [31, 33]:

$$m_{\text{per}}(t,x,y,z) = e^{-iQ_x(t)x} m(t,x,y,z) \ , \tag{4.114}$$

so that Eq. (4.112) becomes

$$m_{\text{per}}(t,x+a_x,y,z) = m_{\text{per}}(t,x,y,z) \ . \tag{4.115}$$

Moreover, $Q_x(t) = 0$ at $t = 0$ and the refocusing condition (1.26) implies that $Q_x(t) = 0$ at the end of the gradient sequence, so that m and m_{per} coincide before and after the gradient sequence. The BT equation (4.109a) and boundary condition (4.109b) on m become new equations on m_{per} in the unit cell Ω_1:

$$\frac{\partial m_{\text{per}}}{\partial t} = D_0 \nabla^2 m_{\text{per}} + 2iD_0 Q_x(t) \frac{\partial m_{\text{per}}}{\partial x} - D_0 Q_x^2(t) m_{\text{per}} \tag{4.116a}$$

$$\mathbf{n} \cdot D_0 \nabla m_{\text{per}} + iD_0 Q_x(t) n_x m_{\text{per}} - \kappa m_{\text{per}}\big|_{\partial\Omega_1} = 0 \ , \tag{4.116b}$$

$$m_{\text{per}}(t, a_x/2, y, z) = m_{\text{per}}(t, -a_x/2, y, z) \ , \tag{4.116c}$$

with $m_{\text{per}}(t = 0, x, y, z) = 1$. As expected, the non-periodic $iG_x x$ term in Eq. (4.109a) has been replaced by new, periodic terms. Note that the boundary $\partial\Omega_1$ does not include frontiers between neighboring unit cells (here, the sections $x = -a_x/2$ and $x = a_x/2$), since these are taken into account by the periodic boundary condition.

The modified BT equation (4.116a) now has time-dependent coefficients and the new boundary condition (4.116b) is complex-valued and time-dependent. These features prevent the use of spectral methods that were very efficient to solve the BT equation in bounded domains. In the next section we show how one can reformulate the BT equation in a different way, in order to reduce the problem to a single unit cell while allowing the use of spectral methods.

Periodic boundary conditions

We still assume that the gradient is along the x-axis, in other words $G_y = G_z = 0$. The main idea of the method is to replace the continuous-time gradient profile by a series of infinitely narrow gradient pulses: computing the magnetization is then reduced to solving a series of diffusion problems with different (pseudo-)periodic boundary conditions. Note that the idea of replacing a gradient profile by multiple narrow pulses was introduced and exploited in [36, 38, 39] to compute

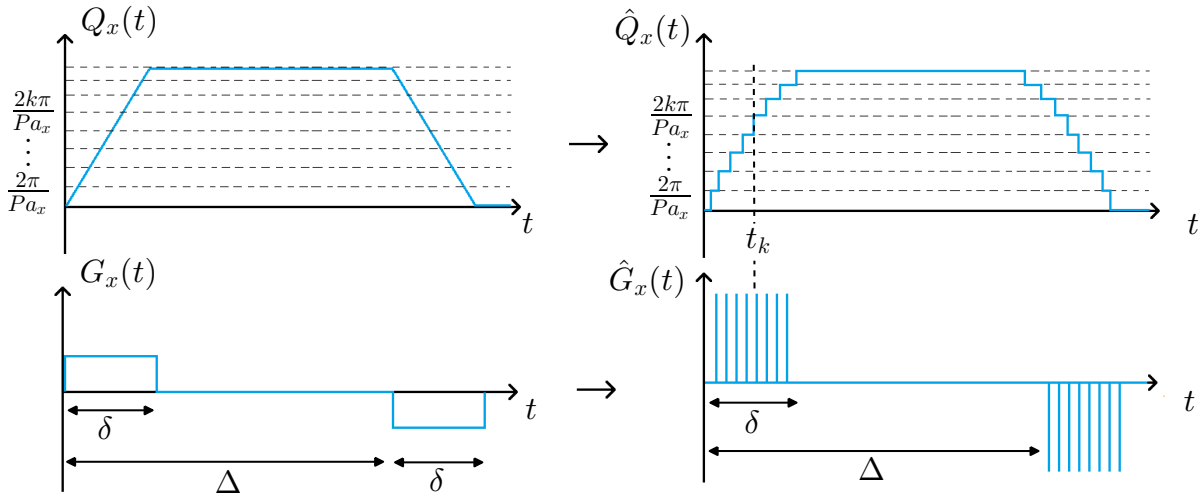

Figure 4.21: The $Q_x(t)$ function is sampled at multiples of $2\pi/(Pa_x)$, the gradient $G_x(t)$ becomes a series of Dirac peaks at times t_k, $k = 1, 2, \ldots$. Here, an example with two rectangular gradient pulses ("pulsed-gradient spin-echo sequence") is shown but the technique is applicable to any gradient profile.

the magnetization in bounded domains. One will see that the case of periodic domains is much more subtle.

For the sake of clarity, let us first present the simplest case that involves only periodic boundary conditions. If we sample the function $Q_x(t)$ at multiples of $2\pi/a_x$ and replace it by a step function $\hat{Q}_x(t)$, the gradient is then replaced by a series of Dirac peaks $\hat{G}_x(t)$ with weights $\pm 2\pi/a_x$ (see Fig. 4.21 with $P = 1$). In other words, a positive/negative gradient pulse effectively multiplies the magnetization by $\exp(\pm 2i\pi x/a_x)$.

If the initial magnetization is periodic along x, then it remains periodic at all times. Indeed, the gradient pulses and the diffusion steps both preserve the periodicity. Thus, one can project the magnetization on the eigenmodes of the Laplace operator on the slab Ω_1 with a periodic boundary condition along x coordinate:

$$-D_0\nabla^2 u_{0,n} = \lambda_{0,n} u_{0,n} \tag{4.117a}$$

$$u_{0,n}(x = a_x/2, y, z) = u_{0,n}(x = -a_x/2, y, z) \tag{4.117b}$$

$$\mathbf{n} \cdot D_0 \nabla u_{0,n} - \kappa u_{0,n}\big|_{\partial\Omega_1} = 0\,, \tag{4.117c}$$

where $n = 0, 1, \ldots$, and the eigenmodes $u_{0,n}$ are $L^2(\Omega_1)$-normalized. The reason

for the index "0" will be clarified when we move to the general (pseudo-periodic) case.

After projection on the eigenmode basis $u_{0,n}$, the magnetization is represented by a vector $\mathsf{m}(t)$:

$$m(t,x,y,z) = \sum_n m_n(t) u_{0,n}(x,y,z) \,, \tag{4.118a}$$

$$m_n(t) = \int_{\Omega_1} m(t,x,y,z) u^*_{0,n}(x,y,z)\, \mathrm{d}x\, \mathrm{d}y\, \mathrm{d}z \,. \tag{4.118b}$$

The computation of the magnetization is then reduced to matrix multiplications. A diffusion step of duration τ corresponds to left-multiplication by the matrix $\exp(-\tau\Lambda_0)$, where Λ_0 is a diagonal matrix with elements $\lambda_{0,n}, n \geq 0$. A positive gradient pulse corresponds to left-multiplication by the matrix Γ^x_0, whose elements are

$$\left[\Gamma^x_0\right]_{n,n'} = \int_{\Omega_1} u^*_{0,n} \exp(2i\pi x/a_x) u_{0,n'}\, \mathrm{d}x\, \mathrm{d}y\, \mathrm{d}z \,, \tag{4.119}$$

and a negative pulse corresponds to the matrix $(\Gamma^x_0)^\dagger$.

In summary, for a given periodic medium, one first computes a sufficient number of eigenmodes, constructs the matrix Γ^x_0, discretizes the gradient profile, and then computes the magnetization and/or the normalized signal via a matrix product of the form:

$$\mathsf{m} = \left(e^{-\tau_N \Lambda_0} \left(\Gamma^x_0\right)^\dagger \cdots \Gamma^x_0\, e^{-\tau_1 \Lambda_0}\, \Gamma^x_0 \right) \mathsf{m}_0 \,, \tag{4.120a}$$

$$S = \mathsf{m}_0^\dagger \mathsf{m} / (\mathsf{m}_0^\dagger \mathsf{m}_0) \,, \tag{4.120b}$$

where m_0 represents the initial condition (4.109c):

$$[\mathsf{m}_0]_n = \int_{\Omega_1} u^*_{0,n}\, \mathrm{d}x\, \mathrm{d}y\, \mathrm{d}z \,, \tag{4.121}$$

and the left multiplication by $\mathsf{m}_0^\dagger$ represents the integration over a unit cell. In Eq. (4.120a), N is the number of narrow pulses, $\tau_1, \tau_2, \ldots \tau_N$ are the time intervals between adjacent narrow pulses, and one has $\tau_1 + \tau_2 + \cdots + \tau_N = T$ the total duration of the gradient sequence (here we assume that the gradient sequence lasts up to the echo time T, at which the signal is measured). With the notations of Fig. 4.21, $\tau_k = t_{k+1} - t_k$ for $k = 1, \ldots, N$ with the convention $t_{N+1} = T$.

Pseudo-periodic boundary conditions

In general, it may be restrictive to sample $Q_x(t)$ at multiples of $2\pi/a_x$, especially at low gradient strength. The above method can be generalized to any sampling: for example one can sample $q_x(t)$ at every multiple of $2\pi/(Pa_x)$, with a given integer P (see again Fig. 4.21). In that case, each gradient pulse multiplies the magnetization by $\exp(\pm 2i\pi x/(Pa_x))$. Naturally, other sampling choices are possible. Because of the sampling, at all times the magnetization obeys:

$$m(t, a_x/2, y, z) = e^{ipa_x} m(t, -a_x/2, y, z) \ , \tag{4.122a}$$

$$p = \hat{Q}_x(t) \pmod{2\pi/a_x} \ . \tag{4.122b}$$

Throughout the text, we will call "p-pseudo-periodic" a function that obeys Eq. (4.122a), and p is the wavenumber that defines the pseudo-periodicity condition. Note that, as the function $\hat{Q}_x(t)$ is piecewise constant, there is a finite number of different values of p involved during the gradient sequence. For example, if one samples $Q_x(t)$ at multiples of $2\pi/(Pa_x)$ as in Fig. 4.21, there are only P different values of p.

Every p-pseudo-periodic function can be projected onto the p-pseudo-periodic eigenmode basis of the Laplace operator on Ω_1 [342]:

$$-D_0 \nabla^2 u_{p,n} = \lambda_{p,n} u_{p,n} \tag{4.123a}$$

$$u_{p,n}(x = a_x/2, y, z) = e^{ipa_x} u_{p,n}(x = -a_x/2, y, z) \tag{4.123b}$$

$$\mathbf{n} \cdot D_0 \nabla u_{p,n} - \kappa u_{p,n}\big|_{\partial\Omega_1} = 0 \ . \tag{4.123c}$$

The wavenumber $p = 0$ corresponds to periodic eigenmodes, which is consistent with our previous notations. A diffusive step of duration τ translates then into left-multiplication by the matrix $\exp(-\tau\Lambda_p)$, with Λ_p being a diagonal matrix with elements $\lambda_{p,n}, n \geq 0$. A narrow gradient pulse of weight q_0 corresponds to the left-multiplication by $\Gamma^x_{p\to p+q_0}$:

$$\left[\Gamma^x_{p\to p+q_0}\right]_{n,n'} = \int_{\Omega_1} u^*_{p+q_0,n} e^{iq_0 x} u_{p,n'} \, \mathrm{d}x \, \mathrm{d}y \, \mathrm{d}z \ , \tag{4.124}$$

that is the projection of the p-pseudo-periodic basis onto the $(p + q_0)$-pseudo-periodic basis after multiplication by $\exp(iq_0 x)$. Note that by performing several pulses in succession in order to cycle through a 2π phase difference between $x = -a_x/2$ and $x = a_x/2$, one gets the equivalent of one pulse of weight $2\pi/a_x$, in other words

$$\Gamma^x_0 = \Gamma^x_{p_{N-1}\to 2\pi/a_x} \Gamma^x_{p_{N-2}\to p_{N-1}} \cdots \Gamma^x_{p_1\to p_2} \Gamma^x_{0\to p_1} \ , \tag{4.125}$$

where $0 < p_1 < p_2 < \cdots < p_{N-1} < 2\pi/a_x$. This algebraic relation is a direct consequence of the completeness of the p-pseudo-periodic Laplacian eigenmode bases and shows how the $\Gamma^x_{p\to p+q_0}$ matrices generalize the Γ^x_0 matrix from the previous subsection.

Similarly to the periodic case presented above, one can compute the magnetization at all times by successively applying the matrix multiplications corresponding to the gradient sequence:

$$\mathsf{m} = \left(e^{-\tau_N \Lambda_0}\, \Gamma^x_{p_N\to 0} \cdots \Gamma^x_{p_1\to p_2}\, e^{-\tau_1 \Lambda_{p_1}}\, \Gamma^x_{0\to p_1}\right) \mathsf{m}_0 \,, \tag{4.126}$$

where N is the number of narrow pulses, $\tau_1, \tau_2, \ldots, \tau_N$ are the time intervals between adjacent narrow pulses and satisfy $\tau_1 + \tau_2 + \cdots + \tau_N = T$ the duration of the gradient sequence, and $p_1, p_2, \ldots, p_N$ are the sampled values of $Q_x(t)$ modulo $2\pi/a_x$. With the notations of Fig. 4.21, one has $p_k = \hat{Q}_x(t_k) \pmod{2\pi/ax}$ and $\tau_k = t_{k+1} - t_k$ for $k = 1, \ldots, N$ with the convention $t_{N+1} = T$. Due to the refocusing condition (1.26), the magnetization at the end of the gradient sequence is periodic again, so that the wavenumber p is equal to zero, hence the last gradient pulse matrix $\Gamma^x_{p_N\to 0}$ in Eq. (4.126). The initial condition m_0 is still given by Eq. (4.121), and the normalized signal can be computed with Eq. (4.120b).

Relation with Bloch bands, diffusion-diffraction, and diffusion pore imaging

The collection of all p-pseudo-periodic eigenvalues are exactly the Bloch bands of the periodic medium, a fundamental concept in condensed matter physics [325, 326]. The previous formulas potentially allow one to measure the Bloch bands of a periodic medium by performing a short-gradient pulses experiment and fitting the signal by a multi-exponential function of the diffusion time between two pulses (see Fig. 4.21, with the pulse duration $\delta \to 0$ and variable inter-pulse duration Δ). Indeed, a short gradient pulse of weight q_x allows one to select a given pseudo-periodicity wavenumber p, and the signal decays then according to the Laplacian eigenvalues corresponding to that wavenumber:

$$S = \sum_{n=0}^{\infty} \left|C_{p,n}(q_x)\right|^2 \exp(-\lambda_{p,n}\Delta) \,, \tag{4.127a}$$

$$C_{p,n}(q_x) = \frac{1}{\sqrt{\mathrm{vol}(\Omega_1)}} \int_{\Omega_1} e^{iq_x x} u^*_{p,n}(x,y,z)\, \mathrm{d}x\, \mathrm{d}y\, \mathrm{d}z \,, \tag{4.127b}$$

$$p = q_x \pmod{2\pi/a_x} \,. \tag{4.127c}$$

The notation for $C_{p,n}(q_x)$ is somewhat redundant because p is a function of q_x; its purpose is to present $C_{p,n}$ as a generalization of the form factor of bounded do-

mains that corresponds to $C_{0,0}$. As the eigenvalues $\lambda_{p,n}$ generally scale as D_0/a_x^2, the signal S typically exhibits a multi-exponential time-decay over the duration $\Delta \sim a_x^2/D_0$, and then becomes mono-exponential with Δ at longer times. In contrast with diffusion in the free space $\mathbb{R}^3$ where the signal decays as $\exp(-q_x^2 D_0 \Delta)$, the long-time decay of the signal in a periodic medium with microstructural features is controlled by $\lambda_{p,0}$ that is a bounded function of q_x. This observation generalizes our results on a periodic array of permeable barriers (see Sec. 3.4).

The above formula generalizes the expression used by Callaghan *et al.* in their seminal work [85]. In that work, a packing of monodisperse beads is treated as a collection of pores separated by a constant spacing along the gradient direction, i.e., a periodic lattice. As they were interested in the long-time limit when water molecules could diffuse through multiple pores, their main formula is exactly the first term ($n = 0$) of Eq. (4.127a). If one assumes zero surface relaxivity on the obstacles and pore boundaries, then $\lambda_{p,0} = 0$ for $p = 0$ and $\lambda_{p,0} > 0$ otherwise. Thus at long times, Eq. (4.127a) displays relatively sharp maxima at $q_x = 2k\pi/a_x$, $k = 0, 1, 2, \ldots$. This important feature, called "diffusion-diffraction pattern", allowed Callaghan *et al.* to recover the lattice step a_x (i.e., pore spacing). Moreover, the value of the squared generalized form factor $\left|C_{p,0}\right|^2$ allowed them to extract geometrical features of the pores, in particular their diameter (assuming a spherical shape), as we discussed in Sec. 1.2.3.

Note that one could improve this last step by getting access to the phase information of the form factor (lost because of the absolute value). This possibility was shown by Laun *et al.* in bounded domains by using asymmetric gradient sequences (short and long pulses, double diffusion encoding, and others), thus opening the field of diffusion pore imaging [90, 91]. However, it remains an open question in periodic domains. Plots of the magnetization and signal for a short-gradient pulses sequence are presented in Appendix C.9, and we focus on extended-gradient pulses sequence in the main text.

Sampling optimization

One can sample $Q_x(t)$ in different ways that lead to different step functions $\hat{Q}_x(t)$, which are more or less close to the original profile. In essence, this is similar to approximating integrals by Riemann sums or to rounding a decimal number. In fact, there are at least 4 natural approximation schemes: (i) "flooring" scheme where $\hat{Q}_x(t)$ is equal to the sampled value immediately below $Q_x(t)$; (ii) "ceiling" scheme would choose the value immediately above $Q_x(t)$; (iii) "rounding" scheme would choose the value which is the closest to $Q_x(t)$; (iv) "midpoint" scheme would be to place the gradient pulses (i.e. the jumps in $\hat{Q}_x(t)$) inbetween the pulses of the flooring scheme and those of the ceiling scheme (see Fig.

4.22). Although these 4 schemes are the most straigthforward ones, many others are possible. Note that the midpoint and rounding schemes give the same results if the gradient is constant. If one considers the free diffusion case as a benchmark, the criterion for the sampling scheme is to reproduce the b-value, $b = \int_0^T Q_x^2(t)\,\mathrm{d}t$, as accurately as possible. From the theory of Riemann sums, the most accurate sampling scheme among the four considered above would be the midpoint one, followed by the rounding one.

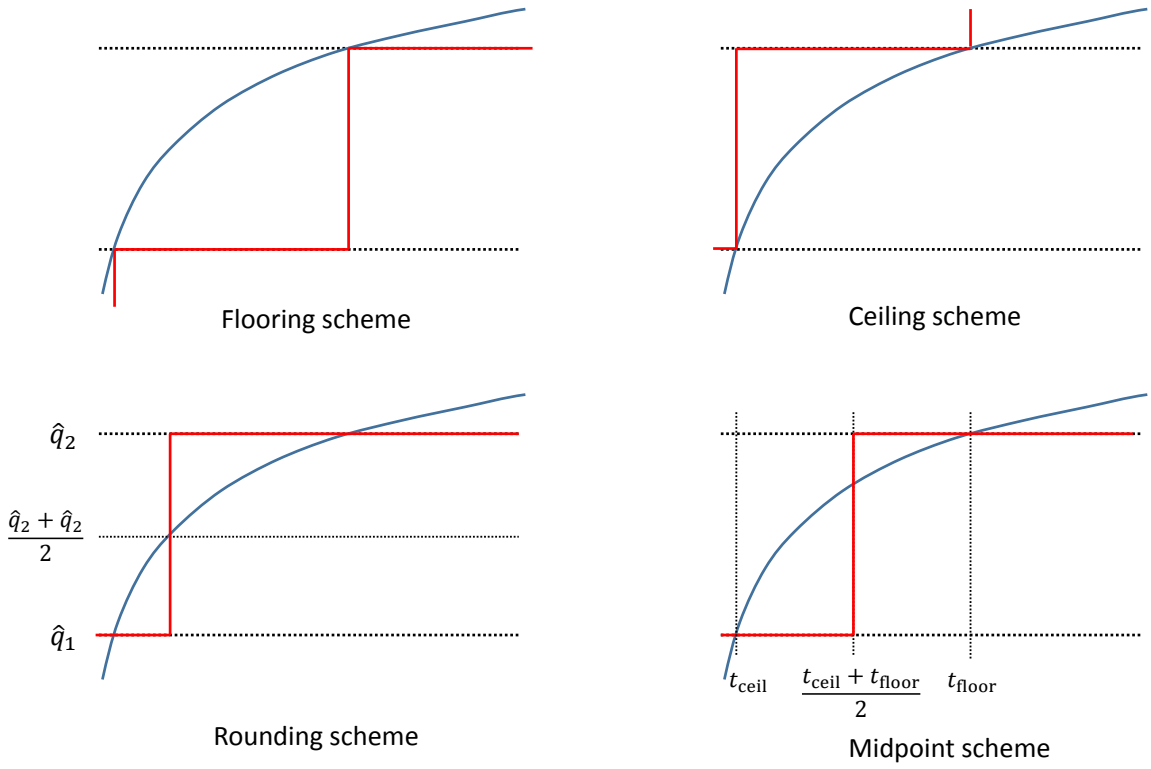

Figure 4.22: Illustration of four natural sampling schemes of a continuous function (blue) into a piecewise constant function (red).

The second point to optimize is the size of the steps of $\hat{Q}_x(t)$. For simplicity, we assume that Q_x is sampled at multiples of $2\pi/(Pa_x)$ as in Fig. 4.21. The larger we choose P, the finer the sampling and the better the approximation. To have a more quantitative view on this question, one can again consider free diffusion as a benchmark and compare the effect of a finite pulse of strength G and duration τ with a narrow pulse of weight $q_0 = G\tau$ such that $q_0 = 2\pi/(Pa_x)$. Following the conclusion of the previous subsection, the narrow pulse is applied at $t = \tau/2$.

Since the Q-value associated to both gradient pulses is the same, the only difference is the decay of the magnetization during the pulse itself. This decay is simply expressed as $\exp(-G^2\tau^3 D_0/3) = \exp(-q_0^2 D_0 \tau/3)$ for the continuous pulse,

and $\exp(-q_0^2 D_0 \tau/2)$ for the narrow pulse, resulting in a ratio of $\exp(-q_0^2 D_0 \tau/6)$. This additional decay accumulates over all pulses, so that if T is the total time during which the gradient is turned on, one gets that the multiple narrow pulses create an additional attenuation factor $\exp(-q_0^2 D_0 T/6)$ compared to the continuous gradient. One obtains the same formula by directly comparing the continuous-time value $bD_0 = D_0 \int_0^T q_x^2(t)\,\mathrm{d}t$ with its discrete version.

Now, according to the sampling scheme detailed previously, one should replace q_0 by $2\pi/(Pa_x)$ hence the relative error created by the sampling reads

$$\epsilon = 1 - \exp\left(-\frac{4\pi^2}{6P^2}\frac{D_0 T}{a_x^2}\right) \approx \frac{7}{P^2}\frac{D_0 T}{a_x^2}\,. \tag{4.128}$$

This estimation allows one to control the quality of the approximation as a function of P. Since any microstructure on a much finer scale than the diffusion length $\sqrt{D_0 T}$ would be modeled via reduced (effective) medium diffusivity, it is reasonable to assume that the diffusion length is at most of the order of magnitude of the lattice step: $\sqrt{D_0 T} \lesssim a_x$. Thus it is possible to choose a moderate value of P to ensure a good compromise between accuracy and computation time.

It should be noted that many gradient sequences, especially the pulsed-gradient spin-echo (PGSE) sequence [20, 22] (see Fig. 4.21), contain a free diffusion step during which the gradient is off. This means that $Q_x(t)$ (resp. $\hat{Q}_x(t)$) would take a constant value q_{off} (resp. $\hat{q}_{\mathrm{off}}$) over a duration t_{off}. In terms of b-value, the discrepancy between q_{off} and $\hat{q}_{\mathrm{off}}$ would accumulate over the whole duration t_{off} and yield a difference in b-values equal to $t_{\mathrm{off}}(q_{\mathrm{off}}^2 - \hat{q}_{\mathrm{off}}^2)$. Thus, if t_{off} is large, even a very fine sampling may lead to an important error. To prevent this, a simple solution is to add the constant value q_{off} explicitly in the sampling scheme.

Extension to higher dimensions

In the previous sections we dealt with a medium that is periodic along one direction, and the gradient was aligned with that direction. In this section, we show how to extend the results to an arbitrary gradient direction, as well as multi-dimensional periodic media.

First we assume that the medium is still periodic along x and bounded along y and z. The gradient direction is arbitrary and may change over time as well. Since the medium is bounded along y and z, the effect of G_y and G_z can be implemented using standard spectral methods [3, 36, 37, 40]. As we explained in Sec. 1.1.5, two main schemes were proposed in the literature, in which the gradient is either replaced by (i) a collection of narrow pulses [36, 38, 39] (similar to our method but without restrictions introduced by periodicity); or (ii) a stepwise function [3,

37, 40]. For clarity and consistency of notations we show here how to implement the narrow pulse approach, and the extension to the stepwise gradient approach is detailed in Appendix C.10.

Between two narrow G_x pulses, the magnetization is p-pseudo-periodic with a given wavenumber p and one can compute the effect of narrow gradient pulses of weight q_0 along y or z with the following matrices:

$$\left[\Gamma_p^y\right]_{n,n'} = \int_{\Omega_1} u_{p,n}^* e^{iq_0 y} u_{p,n'} \,\mathrm{d}x\,\mathrm{d}y\,\mathrm{d}z \tag{4.129a}$$

$$\left[\Gamma_p^z\right]_{n,n'} = \int_{\Omega_1} u_{p,n}^* e^{iq_0 z} u_{p,n'} \,\mathrm{d}x\,\mathrm{d}y\,\mathrm{d}z \ . \tag{4.129b}$$

There are two main differences between the Γ_p^y, Γ_p^z matrices and the $\Gamma^x_{p\to p+q_0}$ matrices presented above. First, since the y or z pulses do not interfere with the pseudo-periodic boundary condition along x, there is no restriction on the sampling of $Q_y(t)$ and $Q_z(t)$ as it is the case with $Q_x(t)$ where each new additional sampled value p requires the computation of a family of eigenmodes $u_{p,n}$. Moreover, since the boundary condition along y and z does not evolve with the G_y and G_z gradient pulses, one needs to compute only one Γ_p^y and Γ_p^z matrix for each value of p. The only requirement is that the value of q_0 in Eqs. (4.129a) and (4.129b) is sufficiently small to provide a correct sampling of $Q_y(t)$ and $Q_z(t)$.

If the medium is periodic along, say, x and y, then one has to sample both $Q_x(t)$ and $Q_y(t)$ in order to apply the same numerical technique. This leads to two pseudo-periodicity wavenumbers p_x and p_y, and two families of matrices $\Gamma^x_{p_x\to p_x+q_0,p_y}$, $\Gamma^y_{p_x,p_y\to p_y+q_0}$. If the medium is periodic along x, y and z, one has three indices and three families of $\Gamma^{\cdots}_{\cdots\to\cdots}$ matrices.

Particular orientations of the gradient may simplify the computations. The simplest example is when one of the component of the gradient is zero, in that case no sampling needs to be done and the magnetization is at all times periodic along that direction. Another example is the gradient which is perpendicular to a lattice vector. In that case, it might be interesting to re-define the unit cell to cancel all components of the gradient except one (see Fig. 4.23).

4.4.3 Numerical Implementation and Results

Numerical implementation

As discussed above, the computation of the magnetization and the normalized signal is reduced to matrix multiplications. However, all the matrices $\Gamma^x_{p\to p+q_0}$, Γ^y_p, Γ^z_p, Λ_p, depend on the Laplacian eigenfunctions with (pseudo-)periodic boundary

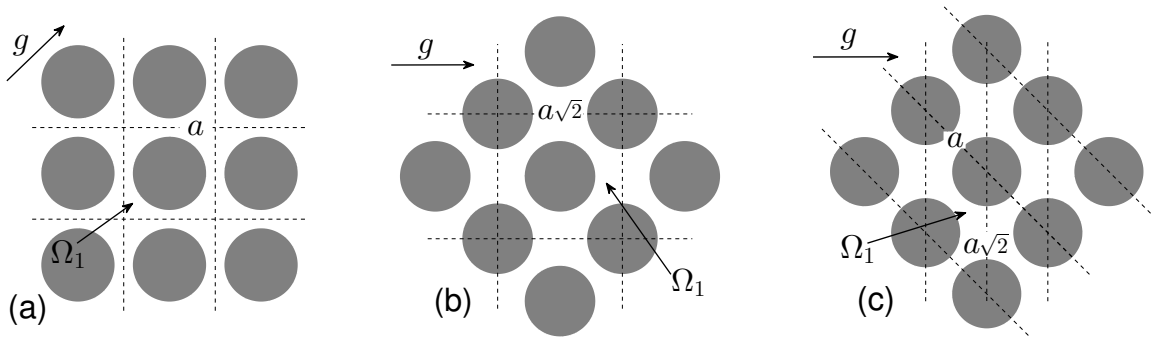

Figure 4.23: This figure shows that the choice of the unit cell (delimited by dashed lines) is arbitrary and can be tailored to the particular orientation of the gradient. The situation (a), (b) and (c) are geometrically equivalent but in (b), (c) the gradient is orthogonal to one of the lattice axes, that simplifies the computations. The unit cell in (b) has a convenient square shape but can be reduced further to (c), with a length along the gradient direction equal to $a/\sqrt{2}$.

conditions. Except for some trivial cases, these eigenfunctions are not known and need to be computed numerically. This computational step is usually the most time-consuming. However, once the eigenfunctions and the consequent matrices are computed for a given unit cell, one can apply them to various gradient sequences and strengths.

We implemented the algorithm in Matlab by using the finite element PDE toolbox, but other numerical solvers could be used to compute the Laplacian eigenfunctions. The practical difficulty was that periodic/pseudo-periodic boundary conditions are not available in the Matlab PDE solver. Thus we generated the mass and stiffness matrices by imposing Neumann boundary conditions on the outer boundaries of the unit cell and then modified those matrices in order to account for the periodic or pseudo-periodic boundary conditions[5]. The search for eigenmodes and eigenvalues has to be truncated at a given threshold. Typically, any eigenvalue much larger than $1/\tau$, where τ is the duration between two Dirac peaks, can be omitted because its contribution to the final result will be negligible. Indeed, the diffusion step between two peaks corresponds to the multiplication by the matrix $\exp(-\tau\Lambda_p)$. In practice, one can control the truncation error by increasing the truncation threshold and checking whether the variation of computed quantities is small. We also employed this check to control the number of mesh points in the domain.

In the following, we will present numerical results for the particular example of a 2D square lattice of circular impermeable obstacles with no surface relaxivity (i.e., $\kappa = 0$). For simplicity, we apply a PGSE sequence with rectangular gradient

[5]The code was written by A. Moutal.

pulses of duration δ and no diffusion time between two pulses (i.e., $\Delta = \delta$), so that the problem is fully determined by three length ratios: R/a, ℓ_g/a and ℓ_δ/a, where $a_x = a_y = a$ is the lattice step, R is the radius of obstacles and we recall that

$$\ell_g = (G/D_0)^{-1/3} \quad \text{and} \quad \ell_\delta = (D_0\delta)^{1/2} \tag{4.130}$$

are respectively the gradient and diffusion lengths. Note that here we write explicitly ℓ_δ instead of ℓ_d to avoid any confusion with the results of Appendix C.9 where we consider narrow-gradient sequences for which $\ell_d = \sqrt{D_0\Delta}$ shall be denoted by ℓ_Δ. The gradient length controls the competition between the Laplacian and gradient terms of the BT equation and can be interpreted as the typical length over which diffusing spins get uncorrelated phases. Results for very short gradient pulses and non-zero diffusion time between pulses are presented in Appendix C.9 and we show important and interesting qualitative differences in the transverse magnetization profile and the resulting signal. The initial transverse magnetization is uniform and equal to 1. We recall that the free-diffusion case (i.e., a periodic medium without any obstacle) would yield a uniform magnetization

$$m = \exp(-bD_0) = \exp\left(-\frac{2}{3}\left(\frac{\ell_\delta}{\ell_g}\right)^6\right) . \tag{4.131}$$

We chose to sample Q-values at multiples of $2\pi/(Pa)$ with a rounding sampling scheme (see Sec. 4.4.2). Thus we computed P families of eigenmodes for a given geometry. All computations were performed with $P = 120$, about 6000 mesh points in a single unit cell and 240 Laplacian eigenmodes for each pseudo-periodic boundary condition. The computation of all eigenmodes and eigenvalues took about 5 minutes on a standard desktop computer. Once this preliminary step has been performed, all computations of the magnetization took less than one second. For better visibility, we plot the magnetization inside one unit cell surrounded by its neighbors. We stress, however, that the computations were performed solely inside one unit cell and then the results were "copy-pasted" to other cells.

Results

Figure 4.24 shows the magnetization $m(T, x, y)$ after a PGSE sequence for a gradient in the left to right horizontal direction. This direction is expected to create the most important restriction to diffusion because of the proximity of neighboring obstacles along the gradient direction. Let us discuss first the top panel ($R/a = 0.4$, $\ell_\delta/a = 0.5$, $\ell_g/a = 0.25$). One can see that the magnetization has been strongly attenuated in regions where there is almost no geometrical restriction

by the obstacles. In contrast, one can interpret the areas with large magnetization (typically the red parts in the "abs" plot) as areas where the influence of the obstacles is strong. Because of the large diffusion length, this red area is very broad. When one decreases both the gradient length and diffusion length (middle then bottom panel), the effect of the obstacle is less spread by diffusion and the localization of the magnetization between the neighboring obstacles becomes sharper. In the bottom panel, the magnetization is actually localized on each obstacle, with a small overlap between two neighboring localization pockets.

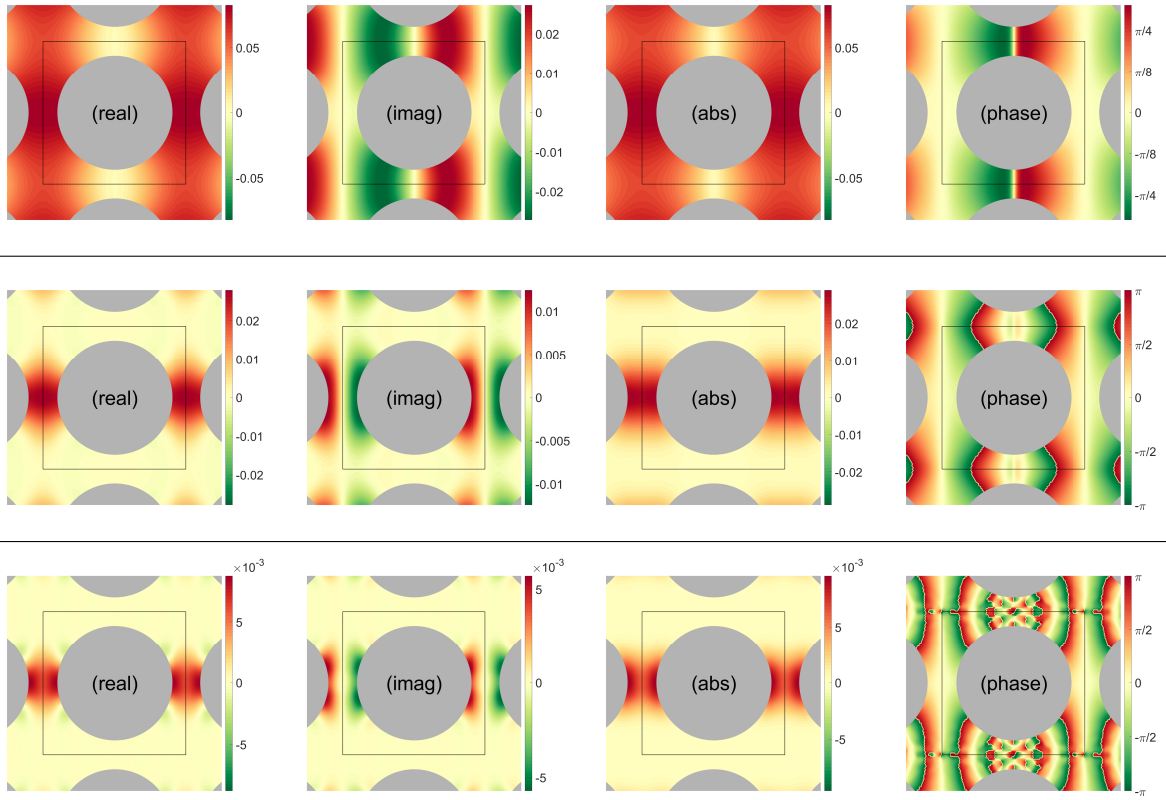

Figure 4.24: Plot of the magnetization (real and imaginary part, absolute value and phase) after a PGSE sequence. The gradient is in the left to right horizontal direction. The black square indicates the unit cell in which the computation was performed. For all figures, $R/a = 0.4$, and we kept a fixed ratio $\ell_\delta/\ell_g = 2$. The corresponding normalized signal is shown on the left panel of Fig. 4.26. (top) $\ell_g/a = 0.25$; (middle) $\ell_g/a = 0.1$; (bottom) $\ell_g/a = 0.05$.

Figure 4.25 shows the magnetization for the same set of parameters but with the gradient in the bottom-left to top-right diagonal direction. In that case, the geometrical restriction by the disks is much weaker (and thus the attenuation is stronger). This is especially visible on the top panel, where the magnetization is two orders of magnitude lower than that in the horizontal gradient case presented above. One still observes the same pattern as above on the top panel,

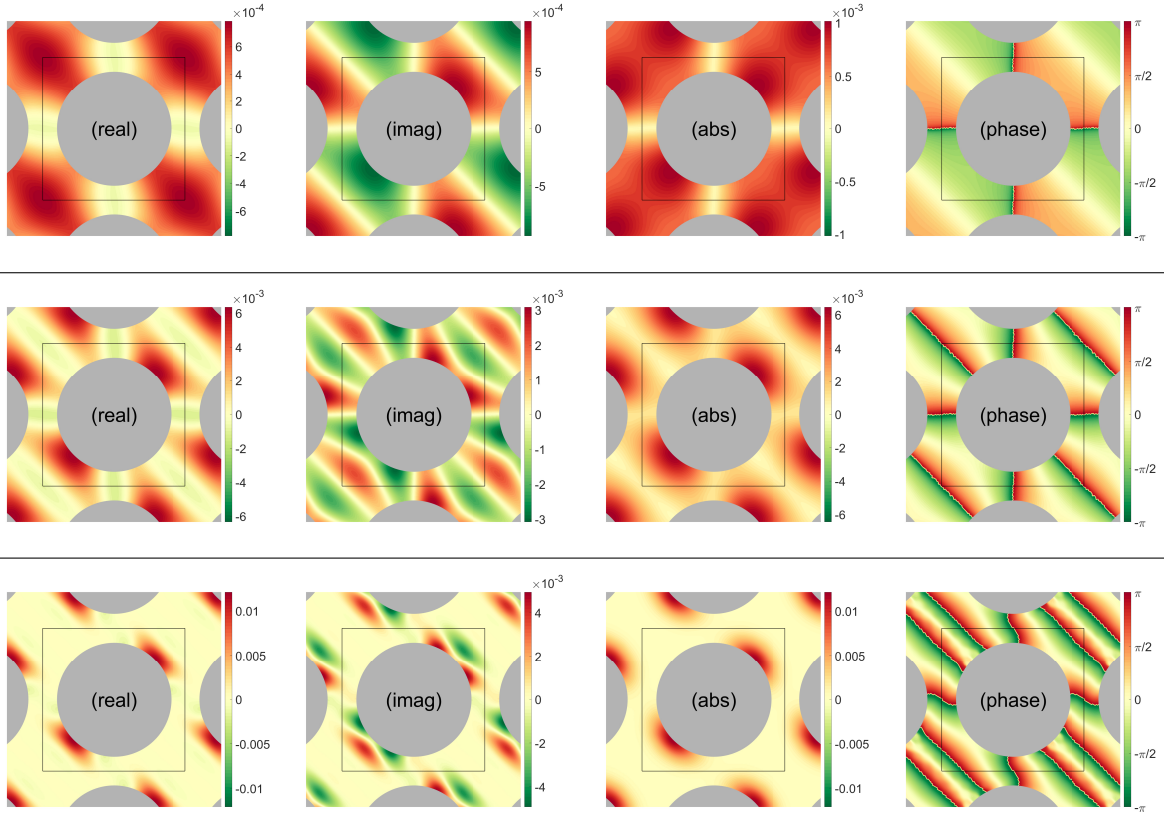

Figure 4.25: Plot of the magnetization (real and imaginary part, absolute value and phase) after a PGSE sequence. The gradient is in the bottom-left to top-right diagonal direction. The black square indicates the unit cell in which the computation was performed. For all figures, $R/a = 0.4$, and we kept a fixed ratio $\ell_\delta/\ell_g = 2$. The corresponding normalized signal is shown on the right panel of Fig. 4.26. (top) $\ell_g/a = 0.25$; (middle) $\ell_g/a = 0.1$; (bottom) $\ell_g/a = 0.05$.

with almost zero magnetization where there is no geometrical restriction along the gradient direction, and the largest magnetization inbetween two neighboring obstacles. As the gradient length and diffusion length decrease, the magnetization localizes more sharply near the obstacles. On the middle panel, one can already see magnetization pockets on each obstacle, with almost no overlap between neighboring obstacles.

In both cases (horizontal or diagonal gradient direction), at high gradient strength the localization along the gradient direction is much sharper than in the orthogonal direction (parallel to the boundary). As we showed in Sec. 4.2.2, the magnetization localizes on the scale ℓ_g along the gradient direction and on the scale

$$\ell_{g,\parallel} = (2\ell_g^3 R)^{1/4} \tag{4.132}$$

parallel to the boundary. In particular, the bottom panels of Figs. 4.24 and 4.25 correspond to a ratio $\ell_{g,\parallel}/\ell_g = 2$, which is visually consistent with the figures.

The (normalized) signal is presented in Fig. 4.26 as a function of $(\ell_\delta/\ell_g)^6$ for different fixed values of ℓ_δ/a and horizontal or diagonal gradient direction. At low values of ℓ_δ/ℓ_g the gradient encoding is weak so that the signal is well represented by an expression similar to the free diffusion decay (4.131):

$$\begin{aligned} S &\approx \exp(-bD(\ell_\delta/a)) \\ &\approx \exp\left(-\frac{2}{3}\frac{D(\ell_\delta/a)}{D_0}\left(\frac{\ell_\delta}{\ell_g}\right)^6\right), \end{aligned} \tag{4.133}$$

where $0 < D(\ell_\delta/a) < D_0$ is the effective diffusion coefficient that accounts for the restriction by obstacles in the domain. At infinitely short diffusion time, i.e. $\ell_\delta/a \to 0$, the effect of the obstacles becomes negligible so that $D(\ell_\delta/a) \to D_0$. This limit is plotted as a dotted line on Fig. 4.26. The short-time behavior of $D(\ell_\delta/a)$ was shown to be linear in $\ell_\delta\sigma$, where σ is the surface-to-volume ratio of the domain (see Sec. 2.3.1 and Refs [47, 48, 344]). For unbounded domains such as the one considered here, $D(\ell_\delta/a)$ has a positive limit at infinitely long times that can be interpreted as a measure of the tortuosity of the domain [76, 77]. Furthermore, the long-time asymptotic behavior of $D(\ell_\delta/a)$ is related to the structural disorder of the medium (see Secs. 1.2.2 and 1.2.3 and Ref. [69]). In that regard, periodic media present a special case of perfectly ordered media, however this is of little importance as long as the diffusion length is at most of the order of the lattice step (i.e. $\ell_\delta \lesssim a$). As we argued in the introduction and in Sec. 4.4.2, this is a natural assumption in the context of this paper as otherwise the effect of microstructure is averaged out by the diffusion, as it is discussed in [69].

At large values of ℓ_δ/ℓ_g, the decay of the signal is much slower than the free diffusion decay (4.131). As we plot the signal in terms of $(\ell_\delta/\ell_g)^6 = D_0G^2\delta^3$ for different fixed values of ℓ_δ, smaller values of δ (i.e., smaller ℓ_δ) correspond to a larger range of values of G (i.e., smaller values of ℓ_g are attained). Therefore, in this representation, a sharp localization phenomenon is obtained at large values of ℓ_δ/ℓ_g and small ℓ_δ. Bearing that in mind, we observe two distinct behaviors depending on the gradient direction.

(i) For the gradient in the horizontal direction (top panel of Fig. 4.26), the decay of the signal as a function of ℓ_δ/ℓ_g changes significantly when ℓ_δ decreases, and the signal displays oscillations at the lowest considered value of ℓ_δ. This behavior can be related to the previous observations about Fig. 4.24, that corresponds to $(\ell_\delta/\ell_g)^6 = 64$. At $\ell_\delta/a \geq 0.2$, the gradient length is too large compared to the inter-obstacle spacing so that the magnetization is not localized on each obstacle's boundary but rather inside the small slab-like space between two neighboring obstacles. As the diffusion length ℓ_δ is larger than the inter-obstacle

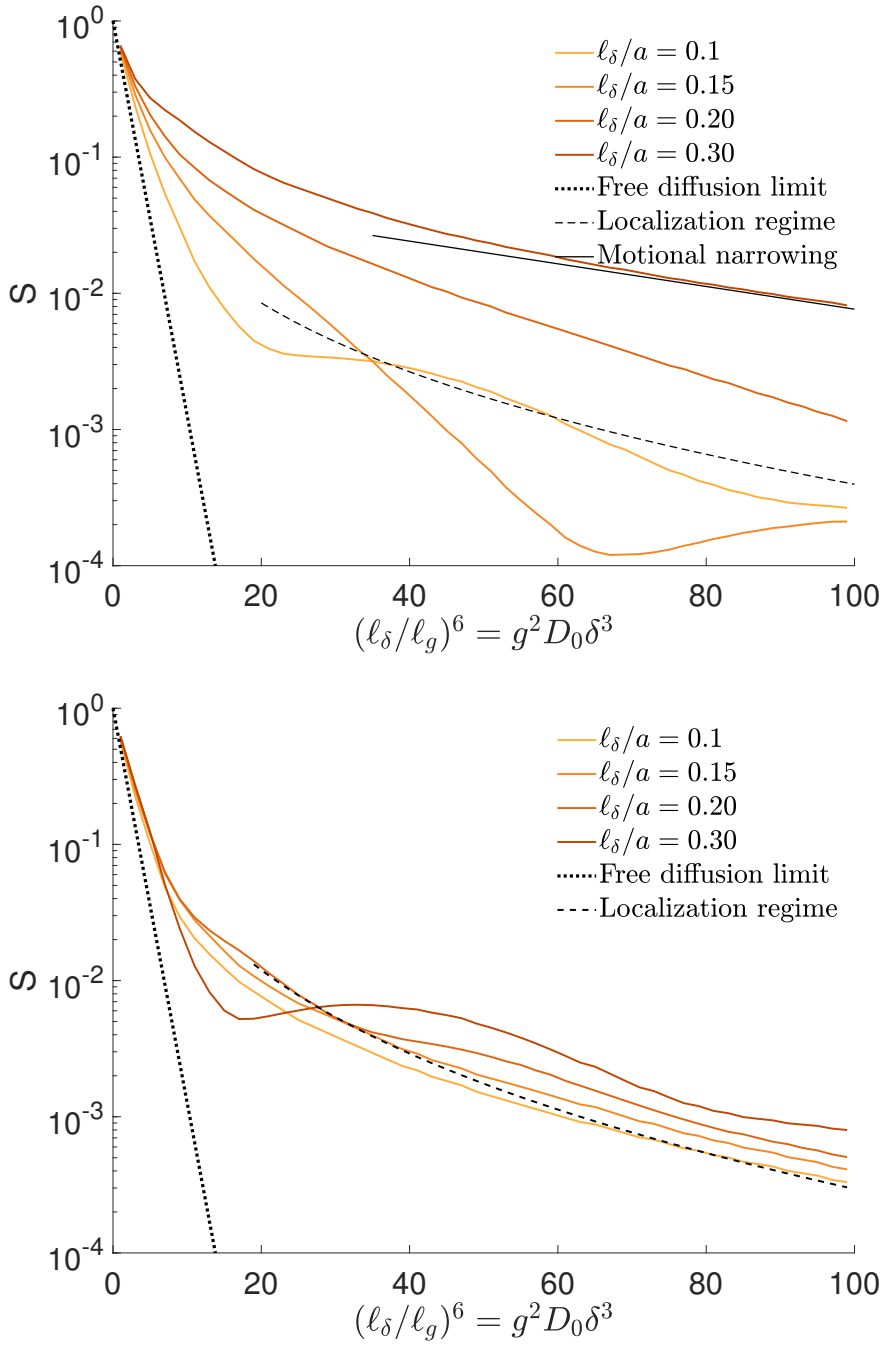

Figure 4.26: Signal as a function of $(\ell_\delta/\ell_g)^6 \propto bD_0$ for different values of ℓ_δ as well as asymptotic regimes (4.133) (in the limit $\ell_\delta/a \to 0$), (4.134) (for $\ell_\delta/a = 0.3$) and (4.135) (for $\ell_\delta/a = 0.1$). (top) The gradient is in the horizontal direction. (bottom) The gradient is in the diagonal direction. Refer to the text for discussion of the figure.

spacing, one can interpret this regime as a motional narrowing regime in an effective slab of width L:

$$S \approx C_{\rm mn} \exp\left(-\frac{1}{60}\frac{\ell_\delta^2 L^4}{\ell_g^6}\right)$$
$$\approx C_{\rm mn} \exp\left(-\frac{1}{60}\left(\frac{L}{\ell_\delta}\right)^4\left(\frac{\ell_\delta}{\ell_g}\right)^6\right), \tag{4.134}$$

where the above formula is valid in the regime $L/\ell_\delta \lesssim 1$ (see Secs. 1.2.2 and 4.3.1 and Refs [79–81]) and $C_{\rm mn}$ represents here the fraction of spins inside the small inter-obstacle space. A rough fitting of the signal at the longest diffusion length, i.e. $\ell_\delta/a = 0.3$, yields $L/a \approx 0.3$, that is larger than the inter-obstacle spacing $1 - 2R/a = 0.2$ as expected from the curvature of obstacles. This asymptotic regime is plotted as solid line on the top panel of Fig. 4.26 for $\ell_\delta/a = 0.3$.

In contrast, at smaller gradient length the localization regime emerges and the signal from localized magnetization pockets decays as

$$S \approx C_{\rm loc} \exp\left(-|a_1|\frac{\ell_\delta^2}{\ell_g^2} - \frac{\ell_\delta^2}{R^{1/2}\ell_g^{3/2}} - \frac{\sqrt{3}\ell_\delta^2}{2|a_1|R\ell_g}\right)$$
$$\approx C_{\rm loc} \exp\left(-\frac{\ell_\delta^2}{\ell_g^2}\left(|a_1| + \frac{\ell_g^{1/2}}{R^{1/2}} + \frac{\sqrt{3}}{2|a_1|}\frac{\ell_g}{R}\right)\right), \tag{4.135}$$

where $a_1 \approx -1.0188$ is the first zero of the derivative of the Airy function (see Sec. 4.2.2). The prefactor $C_{\rm loc}$ represents the fraction of spins in the localization pockets and one has $C_{\rm loc} \sim \ell_g \ell_{g,\parallel} \sim \ell_g^{7/4} R^{1/4}$. This asymptotic regime is plotted on Fig. 4.26 for $\ell_\delta/a = 0.1$. Moreover, the signal exhibits some oscillations that are related to overlapping of magnetization pockets, as we showed in Sec. 4.3.3. This is consistent with Fig. 4.24 where the magnetization pockets on two neighboring obstacles have some significant overlapping even at the highest gradient strength. Note that these oscillations may lead to a significant signal attenuation for some particular values of ℓ_δ and ℓ_g.

(ii) For the gradient in the diagonal direction (bottom panel of Fig. 4.26), the spacing between neighboring obstacles is much larger so that the localization regime emerges at larger gradient length. Correspondingly, all curves follow the asymptotic decay (4.135) and one observes some oscillations only for the largest diffusion length $\ell_\delta/a = 0.3$. This is consistent with Fig. 4.25 where the magnetization pockets on neighboring obstacles have almost no overlap even at the lowest gradient strength (top panel).

For completeness we have also performed some numerical simulations in a 3-dimensional cubic lattice with spherical impermeable obstacles (see Fig. 4.27). We used about 29000 mesh points, $P = 12$ and 350 Laplacian eigenmodes for each pseudo-periodicity condition. The physical parameters used were $R/a = 0.4$, $\ell_g/a = 0.15$, $\ell_\delta/a = 0.225$. The magnetization displays similar features compared to the 2D case. In particular it takes maximum values around "poles" of the spherical obstacles (i.e., points where the gradient is perpendicular to the boundary of obstacles). These magnetization pockets are well localized along the gradient direction on the scale ℓ_g but they are rather delocalized in the orthogonal plane (one can compute $\ell_{g,\parallel}/a = 0.23$). Thus they overlap on neighboring cells, that creates a pattern similar to the top panel of Fig. 4.25, with a rather intense magnetization in the "equatorial plane" of the obstacle, where one would expect a very weak magnetization if the obstacles were isolated or much further apart from each other. The right plot of Fig. 4.27 reveals this overlapping effect from neighboring cells.

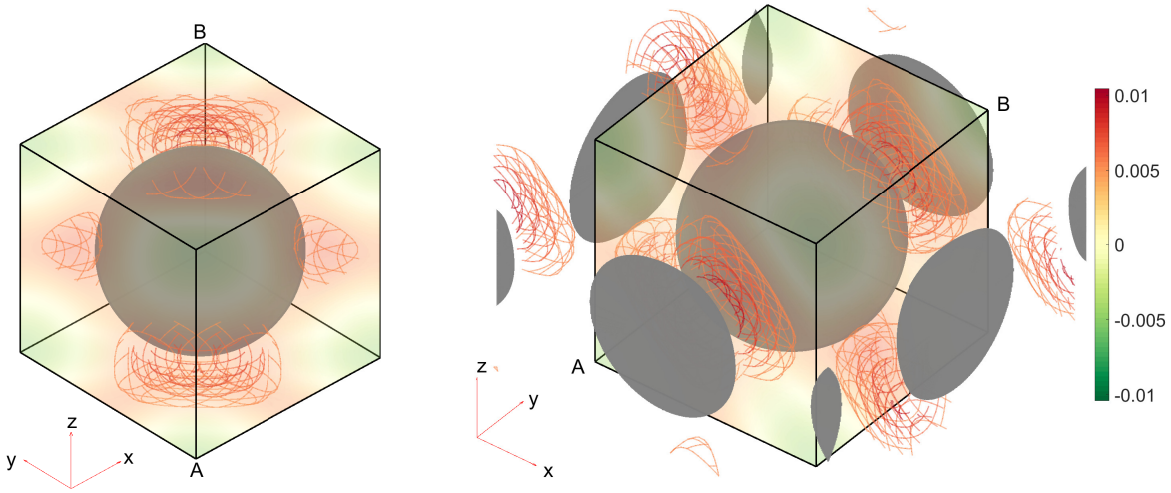

Figure 4.27: Real part of the magnetization $m(T, x, y, z)$ in a 3D cubic lattice of spherical obstacles after a PGSE sequence, plotted as a set of colored wired isosurfaces as well as volume colors (dark colors represent intense magnetization). The left plot represents a single unit cell and the right plot represents a different view with neighboring cells (the black cube helps to visualize a unit cell). The gradient is along $\mathbf{e_x} + \mathbf{e_y} + \mathbf{e_z}$ (the diagonal of the cube from A to B). The parameters are $R/a = 0.4$, $\ell_g/a = 0.15$, $\ell_\delta/a = 0.225$ and the normalized signal is $2.75 \cdot 10^{-3}$. One can see that the magnetization forms two localization pockets near the "poles" of the spheres, where the gradient is orthogonal to the boundary of obstacles. The magnetization is also high near the "equatorial plane" of the spheres; the right plot reveals that this is caused by the overlapping of neighboring localization pockets on the central unit cell.

4.4.4 Eigenmodes of the Bloch-Torrey operator in a periodic medium

In this section we study eigenmodes and eigenvalues of the BT operator $\mathcal{B}$ defined in Eq. (4.110):

$$\mathcal{B}v_n(x,y) = \mu_n v_n(x,y) \tag{4.136a}$$

$$\mathbf{n}\cdot D_0\nabla v_n - \kappa v_n|_{\partial\Omega} = 0\ . \tag{4.136b}$$

By convention, the eigenvalues are sorted by increasing real part. The existence and the properties of eigenmodes of the BT operator in a bounded domain have been studied in [94, 95, 98–100, 102, 104] (see also Sec. 4.3), whereas a class of unbounded domains (exterior of an obstacle) has been investigated in [94–97]. In contrast, no theoretical or numerical studies were devoted to the spectral properties of the BT equation in the periodic case.

For the sake of clarity, we restrict our discussion in this section to a 2D medium, periodic along x and y with periods a_x and a_y, and the gradient is aligned along x (i.e., $G_y = G_z = 0$). This particular case allows us to describe the effect of periodicity along the gradient and perpendicular to the gradient. Note that all of our discussions and results are actually valid for any 2D periodic medium with one periodicity axis orthogonal to the gradient and can be extended to any 3D medium with two periodicity axes orthogonal to the gradient. The general case of an arbitrary gradient direction is briefly discussed in Sec. 4.4.4. We emphasize that the results of this section require further mathematical analysis on the existence of the eigenmodes of the BT operator in periodic media. Throughout this section, we conjecture that these eigenmodes exist, and we shall provide strong numerical support to this conjecture.

Periodicity perpendicular to the gradient

Since the gradient is along x, the BT operator is invariant under any translation $y \longrightarrow y + a_y$. From the theory of Bloch bands in condensed matter physics [325, 326], we deduce that any eigenmode of $\mathcal{B}$ can be written in the form

$$v_{p_y,n}(x,y) = e^{ip_y y} w_{p_y,n}(x,y)\ , \tag{4.137}$$

where $w_{p_y,n}$ is periodic along y, $p_y \in [0, 2\pi/a_y)$ is the wavenumber associated to the eigenmode, and the index n is integer. As a consequence, the eigenmodes and eigenvalues of $\mathcal{B}$ would form continuous bands, each band being indexed by the integer n.

Note that if one considers a uniform initial magnetization, then only eigenmodes with $p_y = 0$ (i.e., periodic along y) will be populated. As such, eigenmodes

with $p_y \neq 0$ do not play any role in the signal formation. In the following, we discard the index p_y from notations for brevity and all our numerical results assume $p_y = 0$.

Periodicity along the gradient

The translation $x \longrightarrow x + a_x$ modifies the BT operator as $\mathcal{B} \longrightarrow \mathcal{B} - iG_x a_x$. Hence, we can conclude that any eigenmode $v_n(x, y)$ and eigenvalue μ_n of $\mathcal{B}$ would belong to a family of eigenmodes $v_n(x - ka_x, y)$ and eigenvalues $\mu_n - ikG_x a_x$, where $k \in \mathbb{Z}$. This is consistent with the idea that the BT eigenmode $v_n(x, y)$ is localized near an obstacle of the medium and that $v_n(x - ka_x, y)$ is localized on the same obstacle but in a different unit cell. Indeed, as we showed in Sec. 1.2.4, the imaginary part of μ_n can be interpreted as $-G_x$ times the position along x of the localized mode v_n. In the following, we discard the index k from notations for brevity.

Moreover, if the unit cell Ω_1 is not irreducible along the gradient direction, i.e. if there exists a lattice vector $\mathbf{e}$ such that $0 < e_x < a_x$, then all eigenmodes v_n can be translated by multiples of $\mathbf{e}$ which leads to a_x/e_x families of eigenvalues

$$\mu = \mu_n - ikG_x a_x - ik'G_x e_x \,, \quad k \in \mathbb{Z} \,, \quad k' = 0, \ldots, a_x/e_x - 1 \,, \tag{4.138}$$

where a_x/e_x is necessarily integer because of the hypothesis $G_y = 0$ and the properties of additive groups. To avoid this artificial splitting of one family of eigenvalues into a_x/e_x different families, we assume in the following that Ω_1 is irreducible along the gradient direction. In other words, for any given periodic medium, there are many choices of unit cells, and we always select an irreducible one[6]. An example of this situation is illustrated on Fig. 4.23 where the case (b) is reducible to (c).

General gradient direction

As we explained in Sec. 4.4.2, if the gradient is perpendicular to a generating vector of the lattice, one can redraw the unit cell and the previous discussion will be valid. Here we discuss the case of an arbitrary gradient direction and we assume that no lattice vector is perpendicular to the gradient. In that case, one cannot find any translation that leaves the BT operator invariant. However, the set $\{\mathbf{e} \cdot \mathbf{G}\}$, where the vector $\mathbf{e}$ spans all possible vectors of the lattice, is known to be a dense set in $\mathbb{R}$. Therefore to any eigenvalue μ_n is associated an infinite band $\mu_n + iv$, where v spans a dense set in $\mathbb{R}$. Although this case is formally the

[6]There are infinitely many choices of an irreducible unit cell.

most general one (in the sense that a randomly chosen gradient direction always falls into that situation), we discard it in our analysis for two reasons: (i) as this paper represents the first step in the study of the spectrum of the BT operator in periodic media, we focus on a simpler but physically relevant situation and postpone the general case for future research; (ii) slightly changing the gradient direction allows returning to the case discussed in this section where the gradient is orthogonal to all periodicity axes but one.

Numerical computation

One can use our numerical technique to investigate the properties of eigenmodes of the BT operator on a periodic medium. Let us stress again that since $\mathcal{B}$ does not respect the periodicity of the medium, it is impossible to study its eigenmodes and eigenvalues directly on a unit cell. However, the eigenmodes of the BT operator $\mathcal{B}$ are also the eigenmodes of its semi-group operator $\exp(-\tau\mathcal{B})$, whereas the eigenvalues μ_n are transformed into $\exp(-\tau\mu_n)$. Note that the minus sign comes from the definition (4.110) of $\mathcal{B}$ so that $\exp(-\tau\mathcal{B})$ represents the effect of a G_x gradient pulse of duration τ. If τ and G_x satisfy the condition

$$G_x \tau a = 2\pi \,, \tag{4.139}$$

then the semi-group operator respects the periodicity of the medium and one can study its eigenmodes and eigenvalues on a unit cell. Note that one can impose any p-pseudo-periodic boundary conditions on the unit cell, not only periodic ones. In other words, one can study the eigenmodes and eigenvalues of the semi-group operator $\exp(-\tau\mathcal{B})$ on the space of p-pseudo-periodic functions for any value of p. The application of a gradient pulse of a given duration is represented by the multiplication by a matrix (see Eq. (4.126)), hence the study of the eigenmodes and eigenvalues of the BT operator is reduced to the study of the eigenvectors and eigenvalues of a matrix. Performing this study for a given p-pseudo-periodic boundary condition, one obtains a family $(v'_{p,n}(x,y),\, \mu'_{p,n})$ of the p-pseudo-periodic eigenmodes and associated eigenvalues of the semi-group $\exp(-\tau\mathcal{B})$ on Ω_1:

$$\exp(-\tau\mathcal{B})v'_{p,n} = \mu'_{p,n} v'_{p,n} \,, \tag{4.140a}$$

$$\mathbf{n} \cdot D_0 \nabla v'_{p,n} - \kappa v'_{p,n}\Big|_{\partial\Omega_1} = 0 \,, \tag{4.140b}$$

$$v'_{p,n}(a_x/2, y) = e^{ipa_x} v'_{p,n}(-a_x/2, y) \,. \tag{4.140c}$$

In the following, we call them "numerical" eigenmodes and eigenvalues, to distinguish them from "true" eigenmodes and eigenvalues of the BT operator. It is

quite easy to see that $\mu'_{p,n}$ does not depend on p, hence we will denote it by μ'_n in the following.

The accuracy of the numerical computation can be assessed using Eq. (4.128) combined with Eq. (4.139), which yields a relative error:

$$\epsilon \approx \frac{1}{P^2}\frac{D_0}{G_x a^3} = \frac{1}{P^2}\left(\frac{\ell_g}{a}\right)^3 . \tag{4.141}$$

This formula implies that the numerical computation of eigenmodes and eigenvalues of the BT operator is more accurate at high gradients. In the following, we assume that the sampling of $Q_x(t)$ is fine enough (i.e., P is large enough) so that this error is negligible. Moreover, because of the condition (4.139), low gradients G_x require long pulse duration τ which increases the relative difference between the eigenvalues $\exp(-\tau\mu_n)$ of the semi-group operator $\exp(-\tau\mathcal{B})$. As eigenvalues are sorted by increasing real part, the accuracy in the numerical computation of μ_n is limited by the ratio $|\exp(-\mu_n\tau)/\exp(-\mu_0\tau)|$. If one denotes by h the relative precision of numerical computations (usually, $h = 2^{-52} \approx 2\cdot 10^{-16}$), then any eigenvalues μ_n such that

$$\mathrm{Re}(\mu_n - \mu_0) > -\frac{\log(h)}{\tau} \tag{4.142}$$

is "lost" because of the finite precision of numerical computations. The above equation, combined with Eq. (4.139), can be rewritten as

$$\mathrm{Re}(\mu_n - \mu_0) > -\frac{G_x a \log(h)}{2\pi} , \tag{4.143}$$

so that the limit between computable and non-computable eigenvalues is a line in a $\mu_n(G_x)$ plot (see Fig. 4.28 below).

The numerical eigenmodes $v'_{p,n}$ are pseudo-periodic, hence delocalized, that means that they are not eigenmodes of the BT operator. However, they are formed by a superposition of translated BT operator eigenmodes. In fact, let us assert the following formula

$$v'_{p,n}(x,y) \stackrel{?}{=} K_{p,n}\sum_{k\in\mathbb{Z}} e^{ipka_x} v_n(x - ka_x, y) , \tag{4.144}$$

with $K_{p,n}$ a normalization constant. First, one can note that the right-hand side of Eq. (4.144) is p-pseudo-periodic. Moreover, it is an eigenmode of $\exp(-\tau\mathcal{B})$ with the eigenvalue

$$\mu'_n = \exp\left(-\tau(\mu_n - ikG_x a_x)\right) , \quad k \in \mathbb{Z} . \tag{4.145}$$

Indeed, the right-hand side of Eq. (4.145) does not depend on k according to Eq. (4.139). This proves that Eq. (4.144) is correct.

From the "numerical" eigenvalues μ'_n, one can deduce the "true" eigenvalues μ_n of the BT operator according to

$$\begin{aligned}\mu_n &= -\log(\mu'_n)/\tau - 2ik\pi/\tau\,, \quad k \in \mathbb{Z} \\ &= -\frac{G_x a_x \log(\mu'_n)}{2\pi} - ikG_x a_x\,, \quad k \in \mathbb{Z}\,. \end{aligned} \tag{4.146}$$

As explained in Sec. 4.4.4, the above formula describes an infinite family of eigenvalues corresponding to eigenmodes localized on the same obstacle's boundary region but at different lattice sites. We applied the convention that the imaginary part of the complex logarithm belongs to $(-\pi, \pi]$ so that $k = 0$ corresponds to the smallest imaginary part in absolute value and to a mode centered on the unit cell Ω_1 ($-a_x/2 \le x \le a_x/2$). An example of spectrum obtained numerically is shown on Figs. 4.28 and 4.29 (discussed below).

Now we will show how one can recover the true eigenmodes v_n from the numerical ones $v'_{p,n}$. First, Eq. (4.144) implies that v_n can be computed as an infinite superposition of $v'_{p,n}$:

$$v_n(x,y) = \frac{a_x}{2\pi}\int_0^{2\pi/a_x} \frac{v'_{p,n}}{K_{p,n}}\,\mathrm{d}p\,. \tag{4.147}$$

However, this is clearly impractical from a numerical point of view because one would have to compute $v'_{p,n}$ for infinitely many values of p. Thus, let us consider the discrete version of the above formula, where $p = 2l\pi/(Pa_x)$, $l = 0, 1, \ldots, P-1$, and define

$$v'_n(x,y) = \frac{1}{P}\sum_{l=0}^{P-1} \frac{v'_{2l\pi/(Pa_x),n}(x,y)}{K_{2l\pi/(Pa_x),n}} \tag{4.148a}$$

$$= \sum_{k\in\mathbb{Z}} v_n(x - kPa_x, y)\,. \tag{4.148b}$$

Note that compared to Eq. (4.147) where integrating over all p leads to a perfect cancellation for all $k \neq 0$, the discrete sum in Eq. (4.148a) generates a Pa_x periodic pattern where the eigenmode $v_n(x,y)$ is repeated every P unit cell. Therefore, if P is large enough so that BT eigenmodes do not overlap over the distance Pa_x, the restriction of $v'_n(x,y)$ to $-Pa_x/2 \le x \le Pa_x/2$ gives the exact eigenmode $v_n(x,y)$.

The only difficulty in the above method is to find the values of the normalization constants $K_{p,n}$. We did not manage to find a normalization scheme that

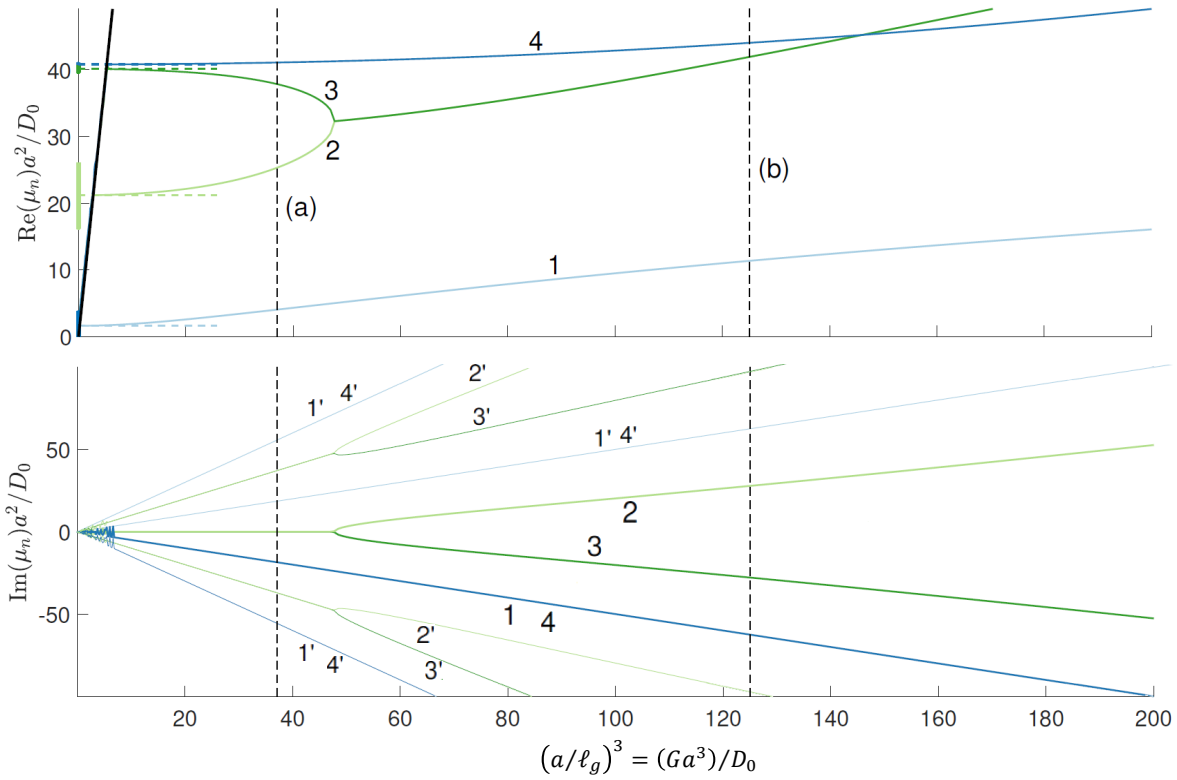

Figure 4.28: Several eigenvalues of the BT operator on a square lattice of circular impermeable obstacles with $R/a = 0.4$ and the gradient in the horizontal direction. The dimensionless eigenvalues $\mu_n a^2/D_0$ and dimensionless gradient $(a/\ell_g)^3$ ensure that the plot is independent of the actual value of a used in the computation. The numbers and colors help to associate the top plot to the bottom plot. (top) Real part of the spectrum. The numerical limit (4.143) is represented by a thick black line above which the computation of eigenvalues is limited by numerical accuracy. Moreover, dashed horizontal lines show the low gradient limit (4.150) and the bands $\lambda_{p,n}$ of the Laplace operator are plotted as vertical segments at $G = 0$. (bottom) Imaginary part of the spectrum. Equation (4.146) is plotted for $k = -1, 0, 1$ and branches of μ_n with $k \neq 0$ are denoted by "n'". Spurious fluctuations at small G are caused by difficulties in ordering complex eigenvalues with identical real parts. Vertical dashed lines indicate the values of the gradient used in Fig. 4.30: (a) $\ell_g/a = 0.3$; (b) $\ell_g/a = 0.2$.

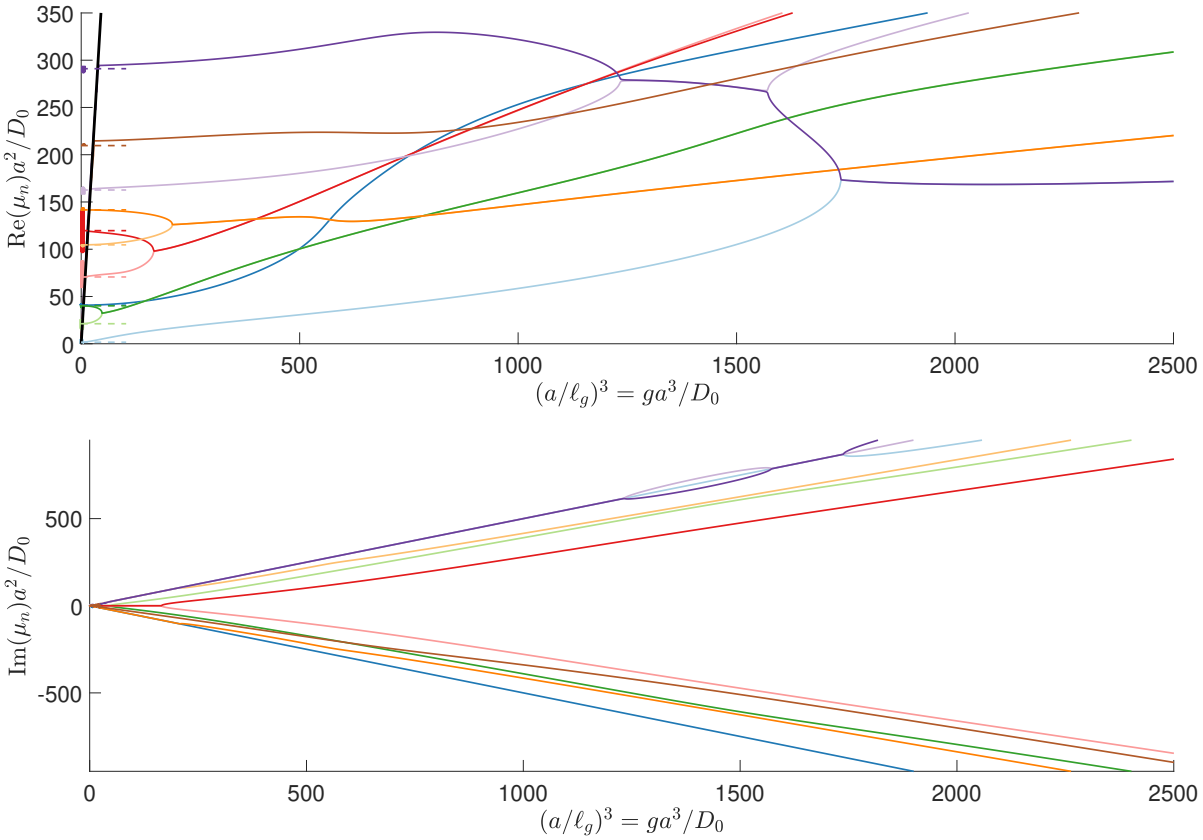

Figure 4.29: Same plot as in Fig. 4.28 but with a larger range of gradient values and additional branches of μ_n (some were omitted to improve visibility). The figure reveals a rich structure of bifurcation points.

would give access to them. However, one can easily find their values numerically by treating them as unknown quantities and solving Eq. (4.148a) as an optimization problem (typically, the optimization criterion is to cancel $v'_n(x, y)$ in as many unit cells as possible). This is how we obtained the eigenmodes presented in Fig. 4.30 (discussed below).

Asymptotic behavior at low and large gradient

At large gradient strength, the gradient length ℓ_g becomes much smaller than any other geometrical length in the medium. Therefore, there is no difference between a bounded and a periodic domain because in both cases the eigenmode is localized over the length ℓ_g and its properties depend only on the local properties of the obstacle's boundaries such as curvature, as we showed in Sec. 4.2.2 (see also Refs. [95–97, 347]).

At low gradient strength, the diffusion effect becomes predominant over the gradient effect so that the p-pseudo-periodic numerical eigenmodes $v'_{p,n}$ are close

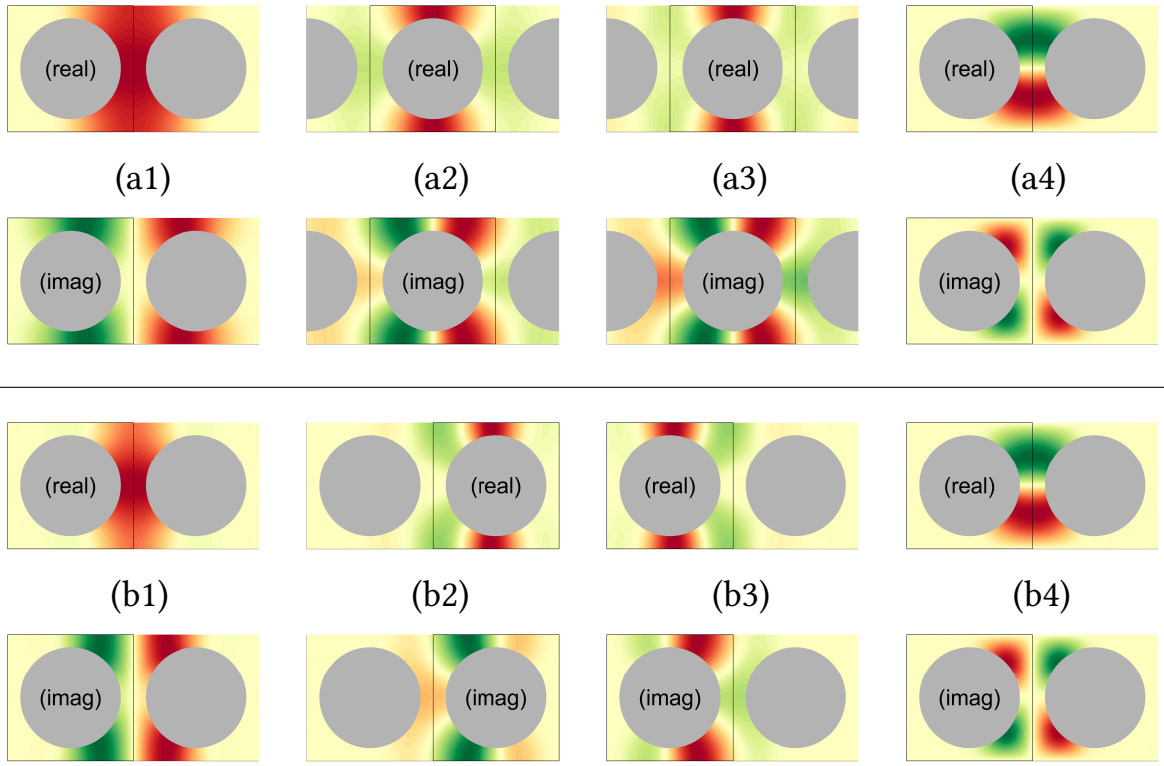

Figure 4.30: Real and imaginary part of the first four eigenmodes of the BT operator on a square lattice of circular impermeable obstacles with the gradient in the horizontal direction, for two different gradient strengths: (a) $\ell_g/a = 0.3$; (b) $\ell_g/a = 0.2$. Refer to Fig. 4.28 for the corresponding eigenvalues. Whereas modes 1 and 4 show little variation from (a) to (b), the pair 2, 3 undergoes a bifurcation that dramatically affects its symmetry properties. The black square helps to visualize the unit cell Ω_1 and to interpret the imaginary part of μ_n on Fig. 4.28. The color scale is the same as on Figs. 4.24 and 4.25: green for negative, red for positive, intense colors correspond to large absolute value.

to the p-pseudo-periodic Laplacian eigenmodes $u_{p,n}$. In the matrix product (4.126) that would represent $\exp(-\tau\mathcal{B})$, the main effect of the matrices $\Gamma_{p\to p+q_0}$ is to "move" along the Bloch bands of the medium by projecting $u_{p,n}$ onto $u_{p+q_0,n}$, whereas the decay of the eigenmode is mainly caused by the diffusion matrices $\exp(-\tau_j\Lambda_{p_j})$. Thus, as the gradient becomes infinitely small and for an infinitely fine sampling of $Q_x(t)$, the numerical eigenvalues of $\exp(-\tau\mathcal{B})$ tend to (we keep the notations of Eq. (4.126)):

$$\exp(-\tau\mu_n') \underset{G_x\to 0}{\approx} \exp(-\tau_N\lambda_{0,n})\ldots\exp(-\tau_2\lambda_{p_2,n})\exp(-\tau_1\lambda_{p_1,n}) \tag{4.149a}$$

$$\underset{\text{fine sampling}}{\to} \exp\left(-\int_0^\tau \lambda_{p(t)}\,\mathrm{d}t\right) = \exp\left(\frac{-\tau a_x}{2\pi}\int_0^{2\pi/a_x}\lambda_{p,n}\,\mathrm{d}p\right), \tag{4.149b}$$

so that the true eigenvalues of the BT operator are given by (see Eq. (4.146)):

$$\mu_n(G_x = 0^+) = \langle \lambda_{p,n} \rangle \,, \tag{4.150}$$

where $\langle \lambda_{p,n} \rangle$ is the average value of $\lambda_{p,n}$ over p:

$$\langle \lambda_{p,n} \rangle = \frac{a_x}{2\pi} \int_0^{2\pi/a_x} \lambda_{p,n} \, \mathrm{d}p \,. \tag{4.151}$$

Therefore the continuous bands $\lambda_{p,n}$ of the Laplace operator (i.e., BT operator with $G_x = 0$) are collapsed into their average values $\langle \lambda_{p,n} \rangle$, $n = 0, 1, \ldots$ when G_x is very small but non zero. Thus, the gradient term of the BT operator cannot be treated as a small perturbation of the Laplace operator because the limit $G_x \to 0$ is singular. This peculiar behavior is shown in Figs. 4.28 and 4.29 where the bands of the Laplace operator are drawn as vertical segments at $G_x = 0$ and the asymptotic formula (4.150) is plotted as horizontal dashed lines. One can see that these dashed lines naturally extend the solid curves beyond our computational limit shown by thick black line (see Sec. 4.4.4). This effect is similar to Wannier-Stark localization for electrons in a crystal under a weak electric field [328, 329]. In that case the linear potential term is real so that the spectrum is real. Energy states have the general form $\mu_{n,k} = \langle \lambda_{p,n} \rangle + kGa$ and form a quasi-continuum. In contrast, the imaginary potential that we study here produces a spectrum of the form $\mu_{n,k} = \langle \lambda_{p,n} \rangle + ikGa$ which is discrete.

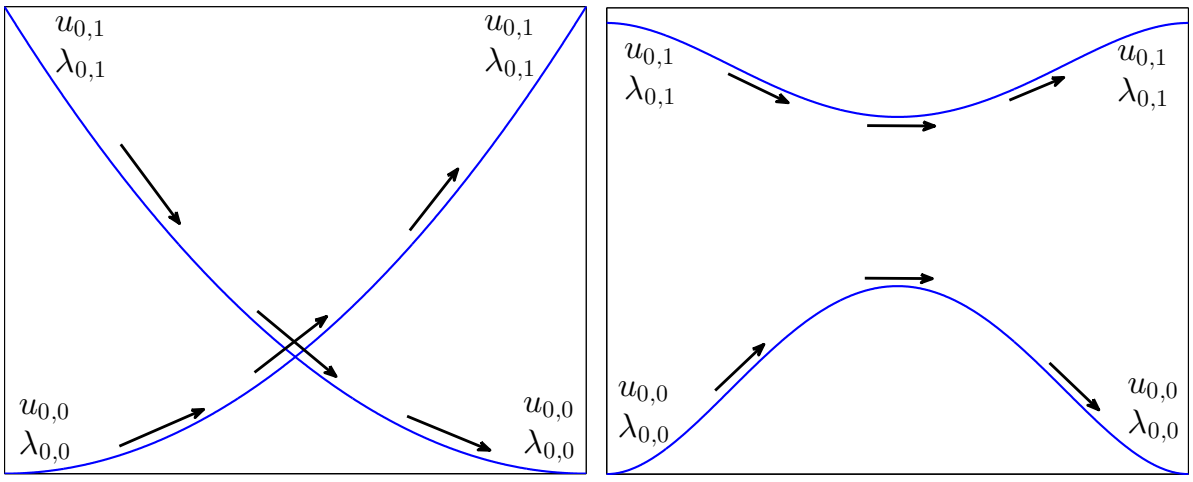

Figure 4.31: The first two Laplacian bands for: (left) free space, where the bands cross each other; (right) a domain with obstacles such as the one considered throughout the text, with no crossing between bands. The arrows help to visualize the "motion" along bands created by small pulses e^{iq_0x} and show that $u_{p,n}$ cannot be a quasi-eigenmode of $\exp(-\tau\mathcal{B})$ for $G_x \to 0$ if bands n and $n+1$ cross each other.

The above reasoning implicitly assumes that the Bloch bands of the medium are isolated, i.e. that by continuously increasing the wavenumber p, each band

$u_{p,n}, \lambda_{p,n}$ continuously evolves without crossing any other bands and that the limit $p \longrightarrow 2\pi/a_x$ yields the "initial point" $u_{0,n}, \lambda_{0,n}$. The isolated versus non-isolated bands situations is illustrated on Fig. 4.31. One can see that Eq. (4.150) is not applicable to the case where bands cross each other because the eigenmode $u_{0,0}$ is continuously transformed into $u_{0,1}$ by the successive narrow pulses. As a consequence of the "avoided crossing" theorem of von Neumann and Wigner [327], the Bloch bands cannot cross if the unit cell Ω_1 is irreducible along x. In contrast, there does not exist any irreducible unit cell for free space so that the formula (4.150) is not applicable, which is consistent with emptiness of the spectrum of the BT operator [94].

Spectral bifurcations in a periodic domain

The plot of the eigenvalues μ_n as functions of the gradient reveals some bifurcation (or "branching") points, where two eigenvalues with the same imaginary part and different real parts branch into two eigenvalues with the same real part and different imaginary parts. As we have discussed in Sec. 4.3, the bifurcation points are related to the emergence of the localization regime and to the parity-symmetry of the domain. In a periodic domain, the situation is more complicated because the medium is symmetric with respect to an infinite number of axes. However, the essence of the phenomenon remains the same.

If the unit cell Ω_1 is symmetric under the parity transformation $x \longrightarrow -x$, then the BT operator is invariant under parity and conjugation:

$$\left(-D_0\nabla^2 - iG(-x)\right)^* = -D_0\nabla^2 - iGx \ . \tag{4.152}$$

Therefore, if $v_n(x,y,z)$ is an eigenmode of $\mathcal{B}$ with eigenvalue μ_n, then the function $v_n^*(-x,y,z)$ is an eigenmode of $\mathcal{B}$ with eigenvalue μ_n^*. This leads to two different situations.

(i) When $\mathrm{Im}(\mu_n) = kG_x a_x/2$ for a given integer k, then $\mu_n^* = \mu_n - ikg_x a_x$ so that it is actually the same eigenvalue but translated to another unit cell (see Eq. (4.146)). In general the eigenvalue μ_n is simple so that $v_n^*(-x,-y,-z) = v_n(x - ka_x, y, z)$, which means that the eigenmode v_n has a symmetric shape (its real part is symmetric and imaginary part antisymmetric), and is centered at the middle of a unit cell (if k is even) or on the boundary between two unit cells (if k is odd). From the spectrum and the corresponding eigenmodes shown in Figs. 4.28 and 4.30, one can see that this corresponds to (a1), (b1), (a4), (b4) where k is odd (the eigenmodes are centered on the spacing between two obstacles at $x = a_x/2$) and to (a2), (a3) where k is even (the eigenmodes are centered on the obstacle at $x = 0$).

(ii) When $\mathrm{Im}(\mu_n) \neq kG_x a_x/2$, then μ_n^* does not belong to the same family of eigenvalues as μ_n, i.e., there is an integer $n' \neq n$ such that $\mu_{n'} = \mu_n^*$. Then one has $v_{n'}(x, y, z) = v_n^*(-x, -y, -z)$: the shape of the eigenmode $v_{n'}$ is the same as that of the eigenmode v_n after parity transformation. One can see that this situation corresponds to eigenmodes (b2) and (b3) on Fig. 4.30, where μ_2 and μ_3 form a complex conjugate pair and the eigenmodes v_2 and v_3 are localized on the left and right sides of the obstacle, respectively.

The transition between these two situations creates a branching point where two eigenvalues coalesce to form a complex conjugate pair. Note that, in contrast with Hermitian operators, the corresponding eigenmodes also coalesce at the branching point. This is supported by the fact that the eigenmodes (a2) and (a3) are very close to each other in Fig. 4.30, as they were plotted not far from their branching point (see vertical dashed lines on Fig. 4.28).

If the domain is not invariant under parity symmetry, then the eigenmodes still localize at large gradients but there is no longer a sharp transition between "delocalized" and "localized" states. Note, however, that there are still branching points in the spectrum if one considers complex values of the gradient, as we discussed in Sec. 4.3.

4.4.5 Summary

The aims of this section were twofold. One one hand, we have developed a numerical method to solve efficiently the BT equation in periodic media. By replacing the continuous integrated gradient profile $(Q_x(t), Q_y(t), Q_z(t))$ by a step function, this equation can be solved in a single unit cell by spectral methods, allowing for very fast and accurate computations, especially at high gradients. This is of significant practical importance for numerical simulations in dMRI as periodic media can describe a wide range of unbounded media if the spin-bearing particles visit at most a few unit cells in the course of the gradient sequence. Numerical simulations in a simple model (array of circular obstacles) reveal diverse regimes (effective free diffusion, motional narrowing, localization, diffusion-diffraction) for the transverse magnetization and the signal. The spacing between obstacles along the gradient direction was shown to be a crucial parameter by comparing results for the gradient in the horizontal direction and in the diagonal direction. In particular, the competition between this spacing and the gradient length controls the emergence of the localization regime at high gradient strength.

On the other hand, this numerical method allowed us for the first time to compute the eigenmodes and eigenvalues of the BT operator in periodic media. The non-Hermitian character of the BT operator led to several interesting phe-

nomena. The most spectacular one is that its spectrum is discrete even though periodic domains are infinite. More precisely, even a very small gradient term causes the continuous Bloch bands of the Laplace operator to collapse on their average values. One sees therefore that the low gradient limit is singular in periodic domains that urges for re-thinking conventional perturbative results that are still dominant in the field of dMRI (see the review [3]). As the gradient increases, the BT eigenmodes start to localize near the obstacles of the domain and we have shown that this localization is associated to bifurcation points in the spectrum. Moreover, the emergence of this localization regime corresponds to a strong deviation in the measured signal compared to the freely diffusing case and related perturbation formulas. Mathematically, the bifurcation points create non-analyticity of the spectrum that prevents the use of low-gradient asymptotic expansions beyond some critical value of the gradient, hence the sharp difference in signal decay between low gradients and high gradients. Several mathematical questions remain open, among which the existence of the eigenmodes of the BT operator in general (non trivial) domains and their completeness outside of the set of bifurcation points are probably the most important.

4.5 Experimental validation

4.5.1 Introduction

As we explained at the beginning of Chapter 4, the work by Hürlimann *et al* [100] on diffusion in a slab is the only undeniable experimental evidence of the localization regime. While deviations from the Gaussian phase approximation were abundantly observed in biological tissues and mineral samples [5, 67, 85, 93, 116–120, 137], it is usually difficult to identify unambiguously the origin of these deviations. In other words, the observed deviations may be related to the localization regime, but may also originate from co-existing populations of water with different effective diffusion coefficients, mixture of restricted and hindered diffusion, etc. The existence of the localization regime in more general domains and, in particular, in unbounded domains (e.g., the extracellular space) has not yet been addressed experimentally. In this section, we present experimental data showing the emergence of the localization regime in two complementary geometries: diffusion inside cylinders and diffusion outside an array of rods. We also treat a slab geometry as a reference case.

The section is organized as follows. Section 4.5.2 describes the experimental setup and the numerical simulations. In Sec. 4.5.3, we show that our theoretical analysis and numerical computations are in excellent agreement with the experimental data. The characteristic stretched-exponential decay of the signal in the localization regime is observed at moderately high gradients and in various geometries, including unbounded diffusion outside obstacles. Finally, we discuss the implications of these results in Sec. 4.5.7.

4.5.2 Material and Methods

Experiments[7] were performed using hyperpolarized xenon-129 gas ($\gamma \approx 74 \cdot 10^6$ $s^{-1}T^{-1}$) continuously flowing through phantoms containing different diffusion barrier geometries. Utilizing gas diffusion compared to water diffusion entails a several orders of magnitude larger diffusion coefficient which allows probing structures on the millimeter scale, which can easily be constructed with 3D-printers. Due to the weak signal of thermally polarized gas, hyperpolarized xenon gas with a considerably higher NMR signal was employed. Hyperpolarization was achieved by Rb/Xe-129 spin-exchange optical pumping (SEOP) [133–135]. For technical reasons [133], a gas mixture (Air Liquide Deutschland GmbH, Düsseldorf, Germany) composed of xenon (0.95 Vol %), nitrogen (8.75 Vol%) and

[7]The experiments were performed by K. Demberg and T. Kuder from German Cancer Research Center (DKFZ), Heidelberg, Germany. The presented results were published in [347].

#	Geometry	Dimensions
1	slab	$L = 3$ mm
2	cylinders	$2R = 3.8$ mm
3	cylinders	$2R = 2$ mm
4	array of rods	17×10 rods
		$2R = 3.2$ mm; $L = 4$ mm
		$L_V = 1.48$ mm; $L_H = 1.35$ mm
5	array of rods	20×10 rods
		$2R = 3.2$ mm; $L = 3.4$ mm
		$L_V = 0.78$ mm; $L_H = 1.08$ mm

Table 4.1: Characteristics of the phantoms (see Fig. 4.32).

helium-4 (rest) was used. The free diffusion coefficient of xenon in this gas mixture was measured to be $D_0 = (3.7 \pm 0.2) \cdot 10^{-5}$ m^{2}s^{-1} [92], which is one order of magnitude larger than for pure xenon gas [136]. The gas was transferred at a small constant flow (approximately 150 mL/min) to the phantom positioned in an in-house built xenon coil in the isocenter of the magnet of a 1.5 T clinical MR scanner (Magnetom Symphony, A Tim System, Siemens Healthcare, Erlangen, Germany) with a maximal employed gradient amplitude of 32 mT/m. The experimental set-up and hyperpolarization process are detailed in [91, 92].

The phantoms used are illustrated in Fig. 4.32 and described in Table 4.1. Phantom 1 contains parallel plates separated by a distance of $L = 3$ mm, built by the in-house workshop from PMMA. For the phantoms 2 and 3, two blocks containing cylindrical tubes (with two different diameters $2R$) in a hexagonal arrangement were 3D-printed. Here, the gas diffuses inside the cylinders. Since all cylinders are identical and isolated from each other, this setting is equivalent to a single cylinder of diameter $2R$. Phantoms 4 and 5 consist of cylindrical solid rods on a square grid attached to a base plate and a roof plate with holes for gas in and out flow, so that the gas diffuses outside the cylinders. The geometry is defined by the diameter of the rods ($2R$) and by the rod center-to-center distance (L).

Phantoms 2-5 were printed with the PolyJet technology (Objet30 Pro, VeroClear as printing material, Stratasys, Ltd., Eden Prairie, MN, USA) and then inserted in a casing with a base area of 70.1 mm $\times$ 42.3 mm. Consequently, for

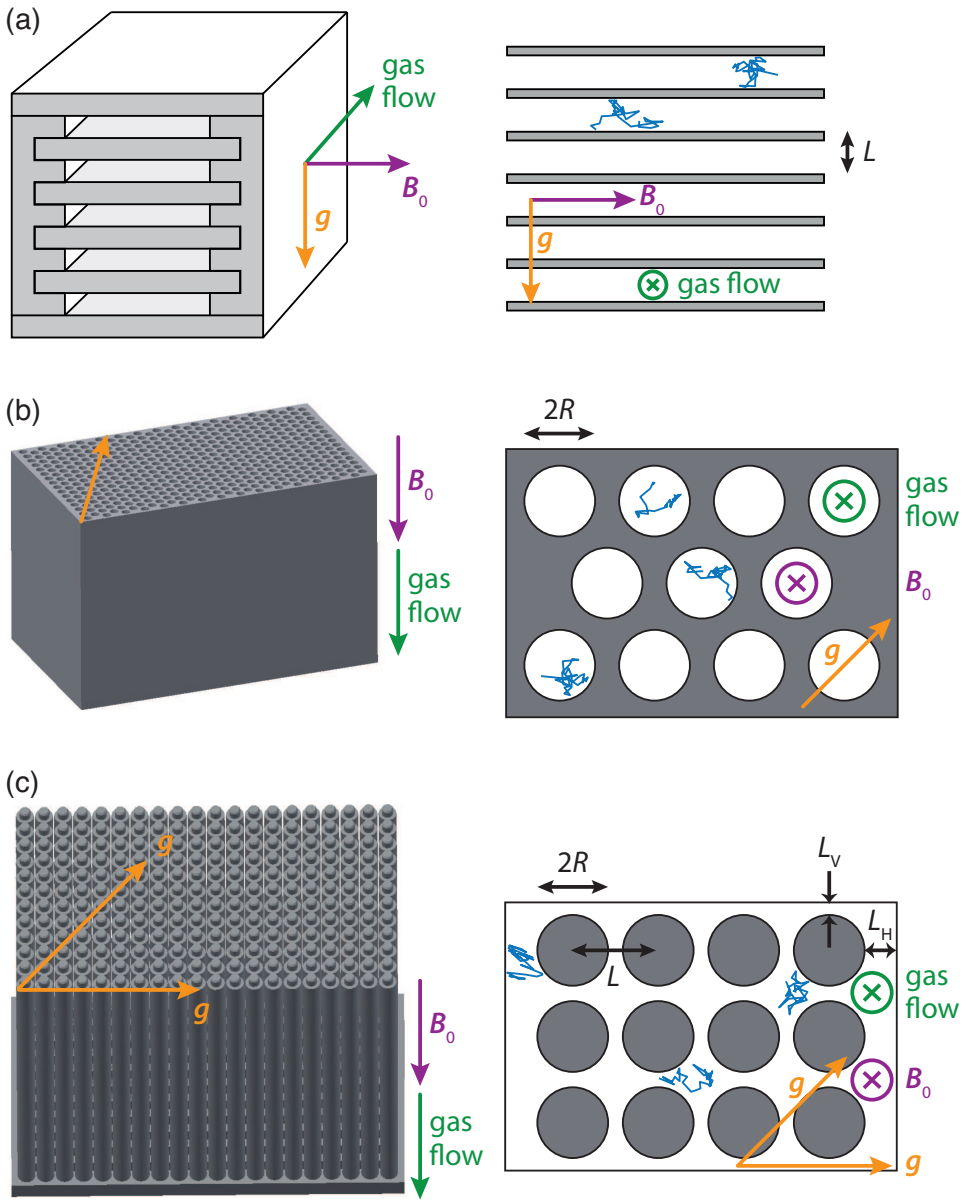

Figure 4.32: Phantoms with corresponding magnified schematic depiction showing relevant length scales. (a) Phantom 1: Parallel plates. (b) Phantoms 2 and 3: Cylindrical tubes. (c) Phantoms 4 and 5: Cylindrical rods on a square grid.

phantoms 4 and 5, there are border regions between the array of rods and the enclosing walls in which diffusion also takes place. For all phantoms, surface relaxivity and permeation can be ignored for high-gradient experiments.

Phantom 1 was positioned with the gas flow directed in the horizontal direction perpendicular to the main magnetic field and the gradient vector was pointing in the vertical direction in a sagittal slice of 50 mm thickness orthogonal to the plates and to the gas flow direction, see Fig. 4.32. Phantoms 2-5 were positioned with the gas flow directed parallel to the main magnetic field and the

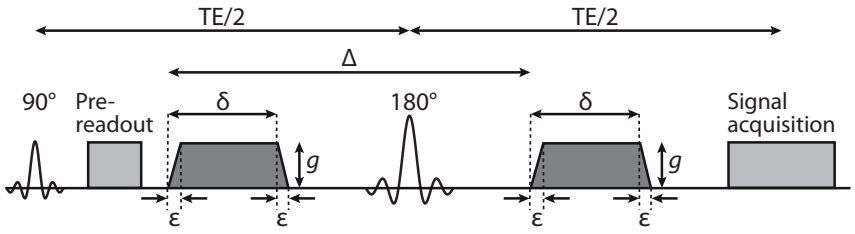

Figure 4.33: PGSE sequence. The spin echo forms at time $T = \mathrm{TE}$.

gradients were applied in the transversal plane of the scanner orthogonal to the gas flow direction (slice thickness 45 mm). For phantoms 4 and 5, measurements were taken with the gradient vector pointing along the left-right direction or the diagonal direction. In all cases, the gas flow did not influence the diffusion-weighted NMR signal.

A pulsed-gradient spin-echo (PGSE) sequence was applied as depicted in Fig. 4.33. The durations δ of the trapezoidal gradient pulses were set to 6 ms and include flat top time plus the ramp-up time of $\varepsilon = 0.32$ ms. The gradient separation time was $\Delta = 9.34$ ms. The diffusion-weighted signal was sampled by gradually increasing the gradient amplitude in 32 steps from 0 to $g_{\max} = 32$ mT/m, recording the spin echo signal and acquiring up to 15 averages. The time between two consecutive 90° excitation pulses, i.e. the time between two measurements, was set to 18 s to restore the polarization in the phantom via gas flow. To account for fluctuations in the polarization level the recorded spin echo was averaged and normalized to an additional signal pre-readout directly after the 90° excitation pulse. To obtain the diffusion-induced signal attenuation, all points were normalized to the point acquired without diffusion weighting (i.e., at $g = 0$). The SNR at low gradient strength was in the order of 1000.

The numerical computation of the signal in a slab and in a cylinder is effectively reduced to that in an interval and a disk, respectively. For these simple shapes, the most efficient and accurate computation of the signal is realized with the matrix formalism, in which the Bloch-Torrey equation is projected onto the basis of explicitly known Laplacian eigenmodes to represent the signal via matrix products and exponentials (see Sec. 1.1.5 and Refs. [3, 36–38, 40, 268]). The matrix formalism was also used to compute the transverse magnetization in these two domains (see similar computations in [102]). In turn, the numerical computation of the signals for phantoms 4 and 5 (arrays of rods) was performed differently. While the matrix formalism could in principle be applied, the need for a numerical computation of Laplacian eigenmodes in such structures makes this approach less efficient. Thus, we performed Monte Carlo simulations including the borders around the rod arrays with $2.5 \cdot 10^7$ random walkers and $1.6 \cdot 10^5$

steps per random walk trajectory. In order to compute the eigenmodes of the Bloch-Torrey operator in the rods geometry, we used the PDE solver from Matlab (The MathWorks, Natick, MA USA) in a square array of 3×3 rods with Dirichlet boundary conditions on the outer boundary and we kept only the eigenmodes that were localized on the central rod. Since the distance from the central rod to the outer boundary is about L, which was much larger than ℓ_g and ℓ_δ in our simulations, the effect of the outer boundary is negligible, so that the computed eigenmodes are very close to the ones for the infinitely periodic array of rods[8].

4.5.3 Results

We present the experimental and numerical results for diffusion in three different geometries: inside slabs, inside cylinders, and outside arrays of rods. The localization regime in the slab geometry was already investigated experimentally by Hürlimann *et al* [100], whereas only a few theoretical studies were devoted to the cylinder geometry [95, 99, 101]. The signal for an array of rods was previously computed numerically in [101] using a finite-element method [31].

We shall present the experimental results in terms of the typical lengths

$$\ell_g = (D_0/G)^{1/3} = (D_0/\gamma g)^{1/3} , \qquad \ell_\delta = \sqrt{D_0 \delta} . \tag{4.153}$$

Similarly to the previous section, we do not use ℓ_d here to avoid any confusion, since the experiments were performed with $\Delta - \delta > 0$. For our particular gradient sequence and the parameters of the xenon gas mixture, one can compute $\ell_\delta = 0.5$ mm and ℓ_g decreases from 0.8 mm to 0.25 mm for g ranging from 1 mT/m to 32 mT/m. So, by increasing the gradient, ℓ_g crosses ℓ_δ and the localization regime emerges.

4.5.4 Slab geometry

We choose the axes such that the slab is orthogonal to the x-axis. Note that this convention is different from the one that we adopted in Sec. 1.2, where the gradient was directed along the x-axis. One can then decompose the diffusive motion independently along the three axes x, y, z and get

$$S = \exp(-bD_0 \sin^2\theta)\, S_{1\mathrm{D}}(L, G\cos\theta) , \tag{4.154}$$

[8] As this work was performed before that on periodic domains (Sec. 4.4), we did not use our numerical technique for periodic media to compute the magnetization and signal. The practical limitations of this analysis actually stimulated the development of the advanced numerical technique.

where θ is the angle between the gradient and the x-axis and $S_{1D}(L, G)$ is the signal from an interval of length L. Here, the first factor is the signal attenuation due to diffusion in the lateral plane yz, which is almost free as outer boundaries are separated by distances that greatly exceed both ℓ_g and ℓ_δ (about 40 mm). One gets the slowest decay by ensuring that the gradient is orthogonal to the slab, i.e. $\theta = 0$, which was chosen in the experiments and numerical simulations. This is expected since in this situation the boundary restricts diffusion along the gradient direction the most.

The signals are presented in Fig. 4.34. At low gradients, the Gaussian phase approximation is valid with an effective diffusion coefficient D. Note, however, the deviation from the free diffusion signal $S = e^{-bD_0}$ due to restriction by the slab. A short-time analysis (see Sec. 2.3 and Refs. [47, 48, 99, 346]) yields an apparent diffusion coefficient

$$D \approx D_0 \left(1 - \eta \frac{4}{3\sqrt{\pi}} \sigma \sqrt{D_0 T}\right) , \tag{4.155}$$

where σ is the surface-to-volume ratio of the confining domain ($\sigma = 2/L$ for a slab), $\eta \approx 0.9$ is a numerical prefactor that depends on the sequence (Eq. (2.63)), and $T = \Delta + \delta$ is the duration of the gradient sequence. This is a short-time approximation in the sense that $\eta\sqrt{D_0 T}/L$ should be small enough. In addition, this formula relies on the Gaussian phase approximation which requires small b-values. For our parameters, we get $D \approx 0.66 D_0$ and the agreement between e^{-bD} and the signal at low gradients is good.

Additionally, we computed the kurtosis correction term from the cumulant expansion. Two different methods were used: (i) we evaluated the second derivative of the logarithm of the computed signal with respect to b by fitting the low-b part ($bD_0 < 1$) of $\log(S)$ by a quadratic polynomial; (ii) we searched for a value of the kurtosis that would fit best the computed signal over the largest range of b-values. The second method yielded a value of the kurtosis twice as large compared to the first method and a much better visual agreement with the theoretical and experimental curves. In Fig. 4.34, we show the result of the second method. One can see that the signal is well fitted up to $bD_0 \approx 6 - 7$, then the localization regime emerges and the cumulant expansion diverges very fast from the theoretical and experimental curves. The deviation of the cumulant expansion from the signal occurs at smaller b-values when we use the kurtosis computed from the first method (not shown). For clarity of the figures, we do not show the kurtosis correction for the other geometries. Note that in the narrow-pulse, short diffusion time limit, the kurtosis may be computed exactly as a function of the surface-to-volume ratio of the geometry [207].

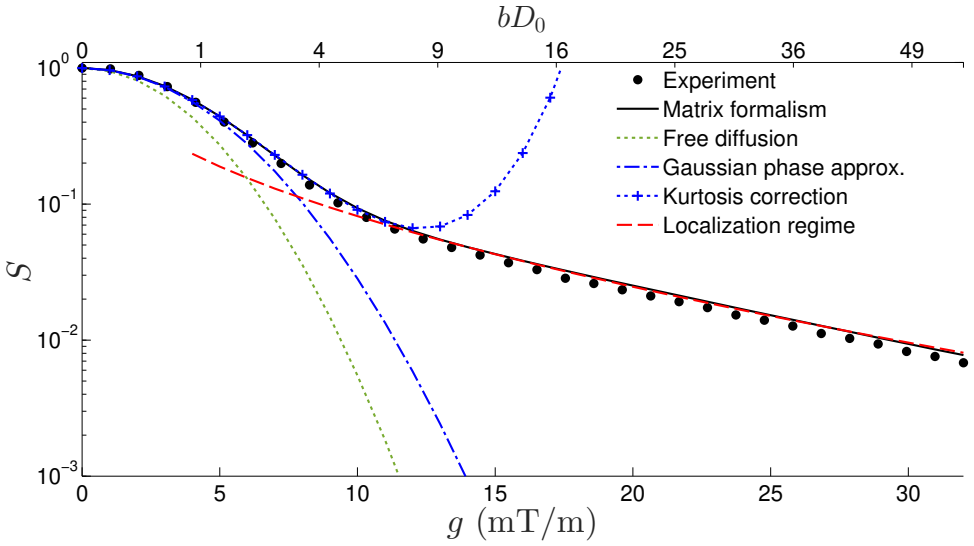

Figure 4.34: Signal attenuation for phantom 1 (a slab of width 3 mm). Experimental results are shown by full circles and matrix formalism computation by a solid line. The signal for free diffusion e^{-bD_0} is indicated by a dotted line, whereas the low-b, short-time approximation e^{-bD}, where D is given by Eq. (4.155), is plotted as a dashed-dotted line. We also plot the cumulant expansion with kurtosis correction as dotted line with pluses. The high-gradient asymptotic formula (4.156) of the localization regime appears as a dashed line.

At higher gradients, the signal follows the asymptotic decay (see Eq. (4.35b) and Refs. [3, 98–101])

$$S_{\text{slab}} \approx 2C_{1,1} \exp(-|a_1|\ell_\delta^2/\ell_g^2) \,, \tag{4.156}$$

where the prefactor $C_{1,1}$ can be computed exactly and scales as ℓ_g/L, and we recall that $a_1 \approx -1.0188$ is the first zero of the derivative of Airy function. One can interpret this prefactor as the fraction of spins inside the two boundary layers of thickness $\sim \ell_g$ where the signal is localized. As we discussed in Sec. 4.3.3, $C_{1,1}$ decreases with increasing diffusion step duration $\Delta-\delta$. Note that the localization regime emerges at gradients as small as 10 mT/m, for which $\ell_\delta/\ell_g \approx 1.3$ and $bD_0 \approx 5$ (we recall that $bD_0 = (\Delta/\delta - 1/3)(\ell_\delta/\ell_g)^6$). Since the width of the slab is much greater than ℓ_g, one can treat the localization layers on both sides of the slab as independent from each other (see Fig. 4.18 and the discussion in Sec. 4.3.3).

We observe a remarkable agreement between the experimental data, exact solution via the matrix formalism, and the asymptotic relation (4.156). Note that the latter contains no fitting parameter (the prefactor $C_{1,1}$ was found by computing the eigenmodes numerically). Systematic minor deviations of the experimental points may be caused by weak misalignment of the gradient direction

(i.e. θ slightly different from 0 in Eq. (4.154)) or weak surface relaxivity. Note that we performed all computations with a rectangular gradient profile instead of a trapezoidal one (in other words, with $\varepsilon = 0$, see Fig. 1.6) and we checked that not accounting for the trapezoidal profile had a negligible influence on the computed signal due to the very short ramp-up time ($\varepsilon = 0.34$ ms).

4.5.5 Diffusion inside a cylinder

If the diameter of the cylinder is much larger than the gradient length ℓ_g and the diffusion length ℓ_δ, then the cylinder geometry may be reduced to two curved boundary elements near the points where the gradient is perpendicular to the boundary. The transverse magnetization inside a cylinder, obtained with a matrix formalism computation, supports this argument (Fig. 4.35). In fact, as the gradient increases, the magnetization gradually transforms from a flat uniform profile to the one that is localized around two opposite points on the boundary of the cylinder and displays two independent pockets at sufficiently high gradients.

In Fig. 4.36 we show the signal for diffusion inside a cylinder of diameter 3.8 mm. Although the signal decays faster than in the slab, one observes a similar stretched-exponential behavior. Using Eqs. (4.58) and (4.103), one gets the asymptotic decay for the cylinder:

$$S_{\rm cyl} \approx C \exp\left(-|a_1|\frac{\ell_\delta^2}{\ell_g^2} - \frac{\ell_\delta^2}{R^{1/2}\ell_g^{3/2}} + \frac{\sqrt{3}\ell_\delta^2}{2|a_1|R\ell_g}\right), \tag{4.157}$$

where C is given by Eq. (4.104). Here, R is large enough so that there is no overlapping between the first two eigenmodes, and $C = 2C_{1,1}$. The prefactor $C_{1,1}$ can be computed numerically from the eigenmodes and scales approximately as $\ell_g\ell_{g,\parallel}/R^2 \sim (\ell_g/R)^{7/4}$ (see 4.2.2). One observes the perfect agreement between experiment, matrix formalism computation, and asymptotic formula at high gradients (without any fitting parameter). Note also that Eq. (4.156) with only the leading term is not accurate (not shown) so that the correction terms in the exponential are indeed important.

For a cylinder of a smaller diameter ($2R = 2$ mm, see Fig. 4.37), the signal shows some oscillations that are usually reminiscent of diffusion-diffraction patterns for infinitely narrow gradients. (see Sec. 1.2.3 and Refs. [36, 85, 86, 88, 89]). Here, this is the consequence of the overlap of two localization pockets because $\ell_g/(2R)$ is not small enough, as discussed in Sec. 4.3.3. The signal is still given by Eq. (4.157) but one cannot neglect the cross-term $C_{1,2}$ in the expression (4.104) of C. The oscillations are then described by $C_{1,2}$ and appear on top of the asymptotic stretched-exponential decay. These oscillations shown in Fig. 4.37 are very

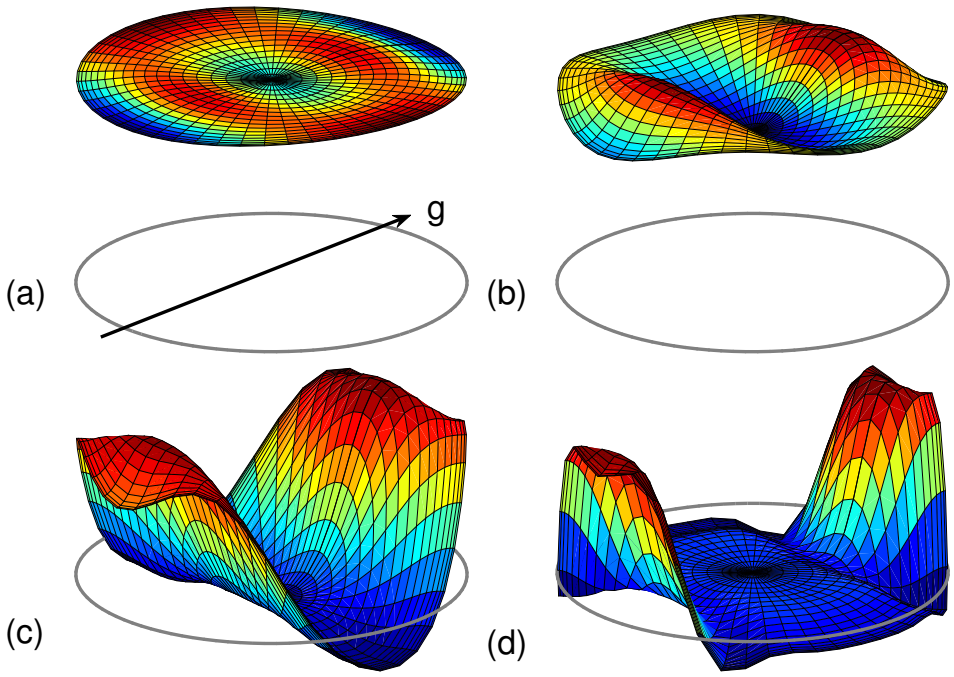

Figure 4.35: Transverse magnetization computed by matrix formalism inside phantom 2 (a cylinder of diameter 3.8 mm) for four values of the gradient g: (a) 2 mT/m, (b) 5 mT/m, (c) 10 mT/m and (d) 32 mT/m. The direction of the gradient is indicated by an arrow.

well reproduced by the asymptotic formulas (4.105) and (4.107) with $L = 2R$, where the coefficients $(1|v_1)$, $(1|v_2)$, and $\beta_{1,2}$ were computed numerically from the eigenmodes. These coefficients generally depend on the gradient strength G and $\beta_{1,2}$ additionally depends on the diffusion step duration $\Delta - \delta$ (see Sec. 4.3.3). This overlapping phenomenon is supported by Fig. 4.38 which illustrates that the magnetization inside the cylinder is not well localized even at the highest gradient available.

4.5.6 Diffusion outside an array of rods

The geometry of phantoms 4 and 5 is defined by L, the center-to-center spacing between rods, and $2R$, the diameter of the rods. We consider three different cases: (a) phantom 4 ($L = 4$ mm and $2R = 3.2$ mm) with the gradient vector in the diagonal direction; (b) phantom 5 ($L = 3.4$ mm and $2R = 3.2$ mm) and gradient vector in the diagonal direction; (c) phantom 5 and gradient vector in the horizontal direction.

The main difference between these three cases is the spacing e_p between two neighboring rods along the gradient direction, i.e. the spacing between two neighboring localization pockets (see Fig. 4.39): $e_p = e_d = \sqrt{2}L - 2R = 2.5$ mm in (a); $e_p = e_d = 1.6$ mm in (b); and $e_p = e_h = 0.2$ mm in (c). Figure 4.40 shows the

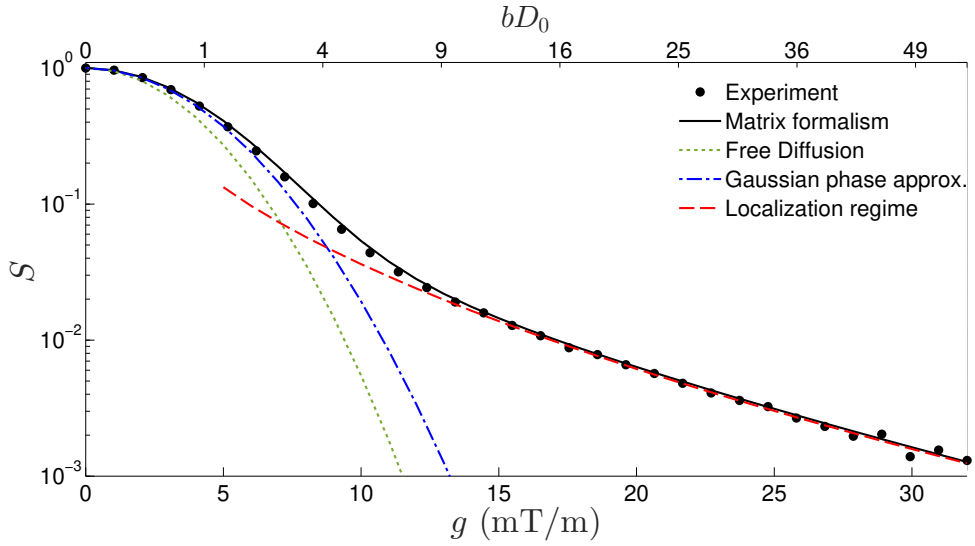

Figure 4.36: Signal attenuation for diffusion inside phantom 2 (a cylinder of diameter 3.8 mm). Experimental results are shown by full circles and matrix formalism computation by a solid line. The signal for free diffusion is indicated by a dotted line, whereas the short-time approximation e^{-bD}, where D is given by Eq. (4.155), is plotted as a dashed-dotted line. The high-gradient asymptotic formula (4.157) of the localization regime appears as a dashed line.

signal for these three cases, ordered by descending e_p. Note that here the signal is formed by the magnetization localized near the rods and by the magnetization localized near the borders of the casing in which the phantom is enclosed. We did not plot the low-b, short time approximation $E = e^{-bD}$ here because the surface-to-volume ratio of the structure is too large so that the approximate formula (4.155) for D is not valid.

First of all, one can note an excellent agreement between experimental data and Monte Carlo simulations. The high-G asymptotic behavior of the eigenvalues and the signal in a rods geometry is similar to the one for cylinders in Eq. (4.157) except for a sign change due to the opposite curvature (see Eq. (4.58))

$$S_{\text{rods}} \approx C \exp\left(-|a_1|\frac{\ell_\delta^2}{\ell_g^2} - \frac{\ell_\delta^2}{R^{1/2}\ell_g^{3/2}} - \frac{\sqrt{3}\ell_\delta^2}{2|a_1|R\ell_g}\right), \tag{4.158}$$

where C is given by Eq. (4.104) and may be computed numerically from the eigenmodes. This formula matches very well the signal at high gradients in case (a) (see Fig. 4.40 (a)).

In the previous subsection, we already saw the signal without oscillations (Fig. 4.36) due to well-localized states, as well as the signal with oscillations (Fig. 4.37) due to a partial overlap of two localization pockets when the size of the

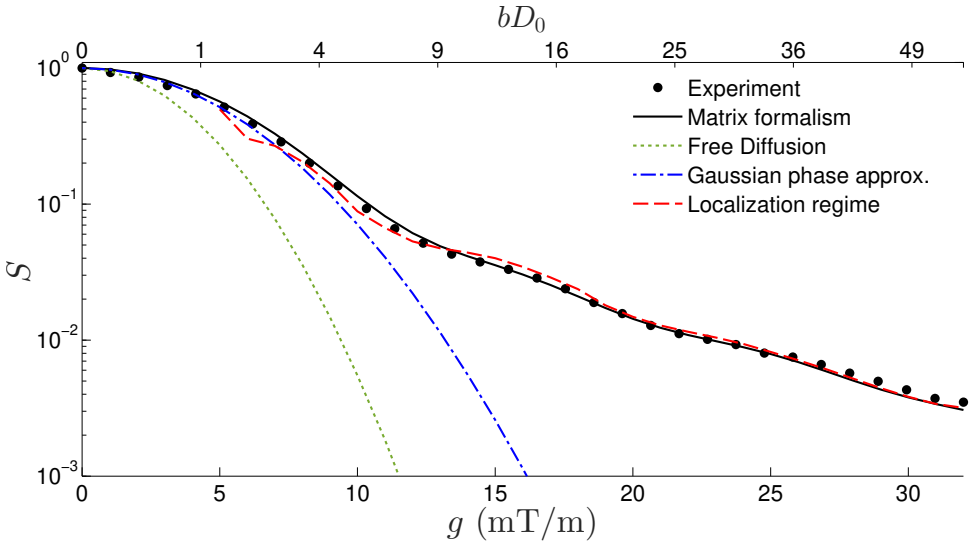

Figure 4.37: Signal attenuation for diffusion inside phantom 3 (a cylinder of diameter 2 mm). Experimental results are shown by full circles and matrix formalism computation by a solid line. The signal for free diffusion is indicated by a dotted line, whereas the short-time approximation e^{-bD}, where D is given by Eq. (4.155), is plotted as a dashed-dotted line. The high-gradient asymptotic formula (4.157) of the localization regime appears as a dashed line.

confining domain is not very large compared to ℓ_δ and ℓ_g. Here the same phenomenon occurs. With e_p much larger than ℓ_g (case (a)), there is little overlapping between the localization pockets of neighboring rods. This ensures the localization of the eigenmodes and the small amplitude of the oscillations in the signal (see Sec. 4.3.3), i.e. the validity of $C = 2C_{1,1}$. In the case where the ratio between e_p and ℓ_g is smaller, i.e. localization pockets overlap more (case (b)), more pronounced oscillations on top of the overall decay (4.158) arise (see Fig. 4.40 (b)). The signal is still described by Eq. (4.158), and the oscillations are contained in the cross-term $C_{1,2}$ from the expression (4.104) of C and may be computed from Eqs. (4.105) and (4.107) (with $L = e_p$). Systematic deviations between the exact signal and the asymptotic formulas may be attributed to the truncation of Eq. (4.58), neglecting higher-order modes in the expression of the signal, and not accounting for the borders in the experimental setup.

In turn, in case (c) e_p is smaller than ℓ_g even at the highest gradient available. If one could approximate the small space between two neighboring rods as a slab, then the ratio ℓ_g/e_p would be too large for localization to be relevant (see Sec. 4.3.3). Our conjecture is that the residual signal at high gradients may be interpreted as a kind of motional narrowing regime (see [3, 79]) inside the small gaps of width e_p between the rods.

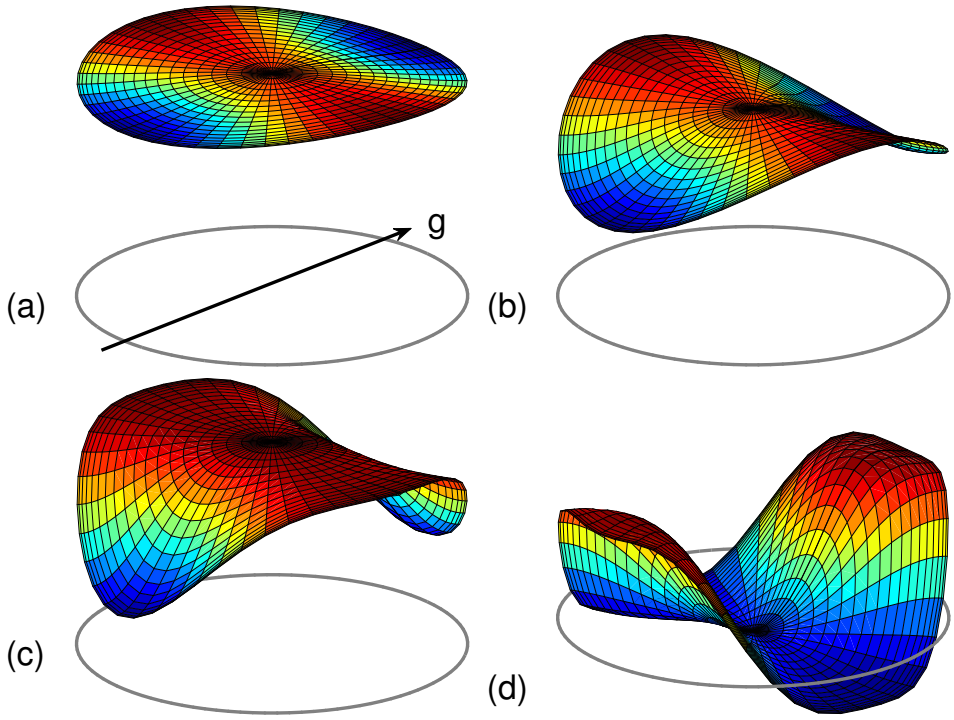

Figure 4.38: Transverse magnetization computed by matrix formalism inside phantom 3 (a cylinder of diameter 2 mm) for four values of the gradient g: (a) 2 mT/m, (b) 5 mT/m, (c) 10 mT/m and (d) 32 mT/m. The direction of the gradient is indicated by an arrow.

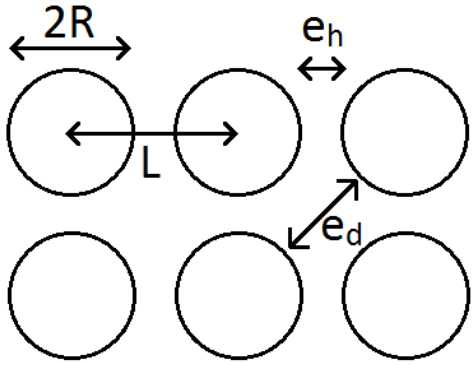

Figure 4.39: Schematic representation of the rods showing the lengths e_d and e_h. The spacing e_p between two localized pockets is equal to e_d if the gradient is in the diagonal direction and to e_h if the gradient is in the horizontal or vertical direction.

4.5.7 Discussion and Conclusion

We have observed and described the localization regime in three geometries: slab, cylinder, and array of circular obstacles (rods). The localization regime appears whenever the gradient length $\ell_g = (D_0/G)^{1/3}$ is much smaller than the diffusion length $\ell_\delta = (D_0\delta)^{1/2}$ and any relevant geometrical length scale ℓ_s of the medium

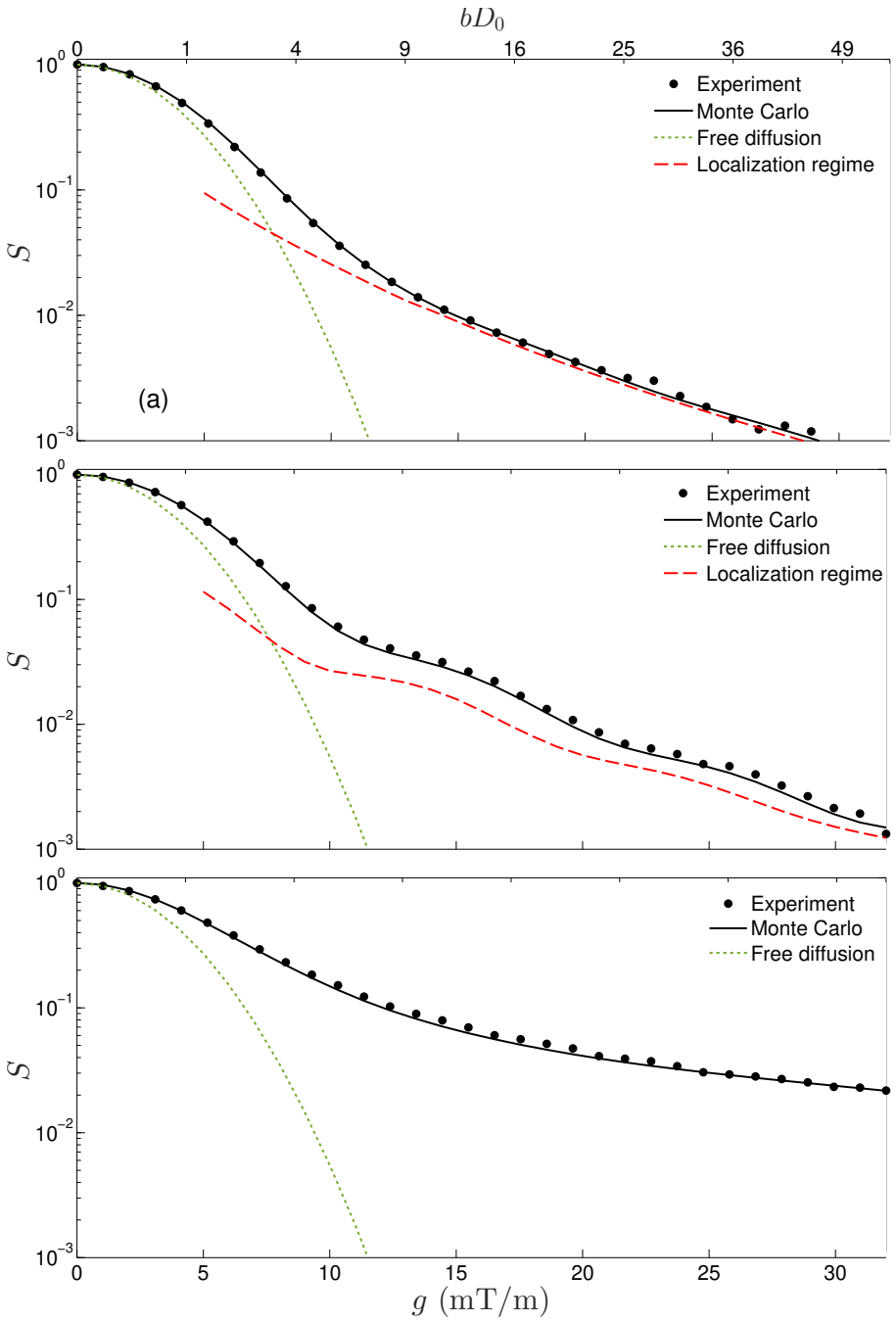

Figure 4.40: Signal attenuation for diffusion in phantoms 4 and 5 (array of rods of diameter 3.2 mm and center-to-center spacing 4 mm and 3.4 mm, respectively). (a) phantom 4 with the gradient in the diagonal direction, spacing $e_p = 2.5$ mm; (b) phantom 5 and diagonal gradient direction, spacing $e_p = 1.6$ mm; (c) phantom 5 and horizontal gradient direction, spacing $e_p = 0.2$ mm. Experimental results are shown by full circles and Monte Carlo simulations by a solid line. The signal for free diffusion is indicated by a dotted line. The high-gradient asymptotic formula (4.158) of the localization regime appears as a dashed line. The latter is not shown for (c) as this regime is not applicable here, see the text.

along the gradient direction. Thus, it is universal at high gradients and non-narrow pulses. In this regime, the transverse magnetization is localized near the obstacles, boundaries, or membranes of the sample. For this reason, the signal is particularly sensitive to the microstructure of the medium. In particular, possible oscillations of the signal are caused by a partial overlap between localized magnetization pockets and thus contain information about mutual arrangements of obstacles.

Let us clarify the role of the conditions (i) $\ell_g \ll \ell_\delta$ and (ii) $\ell_g \ll \ell_s$. Condition (i) ensures that the eigenmode decomposition of the transverse magnetization may be truncated to its first terms. In turn, the signal decays exponentially with δ and its dependence on G is essentially determined by the first eigenvalue of the Bloch-Torrey operator. Furthermore, condition (ii) is necessary for the localization of the eigenmodes of the Bloch-Torrey operator and the validity of the high-G expansion of its eigenvalues. Thus, both conditions are required for the localization of the transverse magnetization and the stretched-exponential decay of the signal with G.

An extreme case where condition (i) is not satisfied would be the narrow pulses limit ($G \to \infty$ and $\delta \to 0$). Although these experiments require high gradients, they do not achieve the localization regime. In fact, whereas the localization regime emerges when $G^2\delta^3 D_0 \gg 1$, narrow-pulse experiments correspond to $G \to \infty$ and $\delta \to 0$ such that $G\delta = q$ is a finite value. This leads to $G^2\delta^3 D_0 \to 0$. In other words, the signal attenuation is not produced by the encoding step but by the subsequent diffusion step with $g = 0$. This is evident from the fact that the signal is left unchanged if one sets $\Delta = 0$, i.e. no diffusion time between two short gradient pulses. On the other hand, condition (ii) is typically not satisfied in the motional narrowing regime ($G \to 0$ and $\delta \to \infty$). Here, the eigenmodes of the Bloch-Torrey operator are close to the eigenmodes of the Laplace operator. In particular, the first Laplacian eigenmode is constant if one assumes impermeable, non-relaxing boundaries. Therefore, the transverse magnetization at long times is uniform inside the sample (see Sec. 4.3.1).

Slab and cylinder are confined geometries that may model an intracellular space. It is well-known that such domains produce non-Gaussian signals, for example in the limit of narrow pulses (e.g. diffusion-diffraction patterns, see [36, 85, 86, 88, 89]). However, in most former studies the signal from the extracellular space was assumed to be Gaussian, and non-Gaussian effects were attributed to multiple contributing pools. In other words, one assumes either that the b-values are sufficiently small so that the Gaussian phase approximation is applicable or that the obstacles may be treated as an effective medium with an effective diffusivity D such that the diffusion process is Gaussian. The latter assumption is in principle valid only in the very long time limit, as it has been

discussed for weak diffusion weighting, e.g. in Refs [68, 69]. Our measurements reveal the non-Gaussianity of the extracellular signal at high gradients and we have shown that it simply results from the localization of the magnetization at the outer boundaries of the obstacles. Ignoring this effect may lead to false interpretations created by commonly used fitting models.

We stress that the localization regime in our setting starts to emerge with moderate gradients of about 10 mT/m, or at bD_0 about 5. These conditions are easily achieved in most clinical scanners. Note that the localization regime emerges under the condition $\ell_\delta/\ell_g \gg 1$ which can be restated as $bD_0 \propto D_0\gamma^2 g^2\delta^3 \gg 1$. In order to rescale the experimental conditions from xenon gas to water, we compute the ratio $(\gamma^2 D_0)_{\text{xenon}}/(\gamma^2 D_0)_{\text{water}} \approx 10^3$. This means that in order to have the same value of $\gamma^2 D_0 g^2\delta^3$, one has to increase g and δ such that $g^2\delta^3$ is 10^3 times larger with water than with xenon. For example, the experiments by Hürlimann *et al* were performed with $\delta = 60$ ms which is approximately 10 times longer than in our experiments, and gradients of comparable magnitude as ours (around 20 mT/m).

Conclusion

We have investigated three theoretical aspects of diffusion magnetic resonance imaging: anisotropy of the microstructure, permeability of boundaries, and localization of the magnetization at high gradient. We shall present a summary of results and perspectives related to these three aspects.

Although it was recognized very early that dMRI is a technique that is sensitive to anisotropic diffusion effects, the possibility of disentangling microscopic anisotropy from macroscopic anisotropy was recently demonstrated and renewed interest in the study and measurement of anisotropic effects. However, the case of mesoscopic anisotropy had not been systematically studied yet. We obtained a generalization of Mitra formula and revealed a correction term that results from the coupling between the anisotropy of the confining domain and the gradient sequence. Ignoring this correction may lead to a gross error on the estimated surface-to-volume ratio, even for linear encoding sequences. Furthermore, we demonstrated that it is possible to average mesoscopic anistropy provided that the gradient sequence satisfies a new isotropy criterion. We developed a simple and fast algorithm for generating such gradient sequences that can also incorporate various practical constraints such as flow compensation, heat limitation, and gradient cancellation. These findings are expected to improve the accuracy of surface-to-volume estimation but also to lead to new metrics and potential biomarkers based on mesoscopic anisotropy.

In biological samples, microstructural elements at the micrometric scale are typically cells, which have permeable membranes. Therefore the "common" assumption of impermeable boundaries, which simplifies the theoretical analysis, might not be valid for biomedical applications. We have studied the effect of permeability from two somewhat opposite viewpoints. First, we considered a collection of small compartments with weak permeation exchange with the exterior medium. We revisited three common theoretical models and applied them to a "model" experimental system with yeast cells. The membrane permeability, radius, and volume fraction of the cells were recovered accurately. Then we aimed at applying the same protocol to muscle tissues in order to recover the mi-

tochondrial content and possibly to measure the mitochondrial membrane permeability. This work is still in progress and can open valuable medical and food science applications. In a second part, we studied the effect of stacked permeable barriers on the diffusive motion and we obtained scaling laws in the short and long-time regime. These results emphasize that the permeability of a membrane, although constant, has an increasing effect as time increases not only because of a larger number of particles that reach the membrane, but also because of the increasing probability to actually cross the membrane. Moreover we developed a flexible numerical technique that allowed us to investigate diffusion through several hundreds of barriers in one dimension, which may have interesting applications to the study of diffusion inside disordered media.

Theoretical aspects of diffusion NMR have been broadly explored at weak gradients by means of perturbation theory. In biomedical applications, the apparent diffusion coefficient and kurtosis are employed as biomarkers to detect stroke, tumors, lesions, partial tissue destruction, etc. In spite of its considerable progress in medicine and material sciences, the comprehensive theory of diffusion NMR remains to be elaborated. The "localization" regime of long and strong gradient pulses is still largely unexplored and we aimed at filling that gap. We asserted that no satisfying qualitative explanation of the localization mechanism had yet been proposed. It seems to us that this is symptomatic of the relative lack of knowledge, and perhaps lack of interest, related to this regime. Ignoring the localization regime may lead to a wrong interpretation of experimental results, by e.g. invoking a compartmentalization of magnetization in order to explain a deviation from the classical mono-exponential decay. We have shown by means of theoretical developments, numerical computations and — last but not least — experimental validation, that the localization regime is a generic feature of strong diffusion weighting experiments, in any non-trivial domain. In particular, the localization of the magnetization in unbounded domains dismisses the common assumption of Gaussian diffusion in extracellular space. Although exploiting the potential advantages of the localization regime is still challenging in experiments (partly due to strongly attenuated signals), the high sensitivity of the signal to the microstructure at strong gradients is a promising avenue for creating new experimental protocols. If former theoretical efforts were essentially focused on eliminating the dephasing effects and reducing the mathematical problem to the computation of the diffusion propagator and related quantities, future developments have to aim at exploiting the advantages of high gradients.

Appendix A

Supplementary material to Chapter 2

This appendix contains technical developments related to Sec. 2.3. In Sec. A.1 we show a general framework to obtain the Mitra formula to any order in $(D_0 T)^{1/2}$. Section A.2 contains computations of the structural $\mathsf{S}^{(3)}$-tensor for sphere-like shapes. Then in Sec. A.3 we investigate the maximal value of the coefficient $\tau^{(3)}$. Finally, we show in Sec. A.4 that one cannot design a gradient sequence that is "universally" isotropic in the sense that all tensors $\mathsf{T}^{(m)}$ would be isotropic.

A.1 Systematic computation of generalized Mitra formula to any order

The signal is proportional to the expectation of the transverse magnetization which has a form of the characteristic function of the random dephasing ϕ acquired by diffusing spin-carrying molecules:

$$S = \mathbb{E}[e^{i\phi}], \quad \phi = \gamma \int_0^T B(\mathbf{r}(t), t)\, \mathrm{d}t\ , \tag{A.1}$$

where T is the echo time, $\mathbf{r}(t)$ is the random trajectory of the nucleus, γ is the gyromagnetic ratio, and $\gamma B(\mathbf{r}, t)$ is the Larmor frequency corresponding to the magnetic field. In this work, we consider the most general form of the linear gradient $\mathbf{G}(t)$:

$$\gamma B(\mathbf{r}, t) = \mathbf{G}(t) \cdot \mathbf{r} = G_x(t)x + G_y(t)y + G_z(t)z. \tag{A.2}$$

In particular, the dephasing can be decomposed as

$$\phi = \phi_x + \phi_y + \phi_z, \quad \phi_i = \int_0^T dt\, G_i(t)(\mathbf{e_i} \cdot \mathbf{r}(t)) \quad (i = x, y, z), \tag{A.3}$$

where $\mathbf{e_x}$, $\mathbf{e_y}$ and $\mathbf{e_z}$ are the units vectors in three directions, and $(\mathbf{e_i} \cdot \mathbf{r}(t))$ is the projection of the molecule position at time t onto the direction $\mathbf{e_i}$.

The effective diffusion coefficient is related to the second moment of the dephasing, i.e., we need to evaluate

$$\mathbb{E}[\phi^2] = \sum_{i,j=x,y,z} \mathbb{E}[\phi_i \phi_j]. \tag{A.4}$$

We emphasize that the three components ϕ_x, ϕ_y and ϕ_z are independent only for free diffusion, whereas confinement would typically make them correlated. In other words, one cannot *a priori* ignore the cross terms such as $\mathbb{E}[\phi_x\phi_y]$.

In order to compute these terms, we use the following representation [3]:

$$\begin{aligned}\mathbb{E}[\phi_i\phi_j] = &\int_0^T \mathrm{d}t_1 \int_{t_1}^T \mathrm{d}t_2 \int_\Omega \mathrm{d}\mathbf{r_0} \int_\Omega \mathrm{d}\mathbf{r_1} \int_\Omega \mathrm{d}\mathbf{r_2} \int_\Omega \mathrm{d}\mathbf{r_3} \\ &\times \rho(\mathbf{r_0}) P_{t_1}(\mathbf{r_0}, \mathbf{r_1}) P_{t_2-t_1}(\mathbf{r_1}, \mathbf{r_2}) P_{T-t_2}(\mathbf{r_2}, \mathbf{r_3}) \\ &\times \left[B_i(\mathbf{r_1}, t_1) B_j(\mathbf{r_2}, t_2) + B_j(\mathbf{r_1}, t_1) B_i(\mathbf{r_2}, t_2)\right] \,, \end{aligned} \tag{A.5}$$

where $P_t(\mathbf{r}, \mathbf{r}')$ is the propagator in the domain Ω, and $\rho(\mathbf{r_0})$ is the initial density of particles (the initial magnetization after the 90° rf pulse). If the boundary is fully reflecting and $\rho(\mathbf{r_0})$ is uniform, then the integrals over $\mathbf{r_0}$ and $\mathbf{r_3}$ yield 1, so that

$$\begin{aligned}\mathbb{E}[\phi_i\phi_j] = &\frac{1}{\mathrm{vol}(\Omega)} \int_0^T \mathrm{d}t_1 \int_{t_1}^T \mathrm{d}t_2 \int_\Omega \mathrm{d}\mathbf{r_1} \int_\Omega \mathrm{d}\mathbf{r_2} P_{t_2-t_1}(\mathbf{r_1}, \mathbf{r_2}) \\ &\times \left[B_i(\mathbf{r_1}, t_1) B_j(\mathbf{r_2}, t_2) + B_j(\mathbf{r_1}, t_1) B_i(\mathbf{r_2}, t_2)\right] \,. \end{aligned} \tag{A.6}$$

We get thus

$$\begin{aligned}\mathbb{E}[\phi_i\phi_j] = &\int_0^T \mathrm{d}t_1 \, G_i(t_1) \int_{t_1}^T \mathrm{d}t_2 \, G_j(t_2) K_{ij}(t_2 - t_1) \\ &+ \int_0^T \mathrm{d}t_1 \, G_j(t_1) \int_{t_1}^T \mathrm{d}t_2 \, G_i(t_2) K_{ji}(t_2 - t_1), \end{aligned} \tag{A.7}$$

where

$$K_{ij}(t) = \frac{1}{\mathrm{vol}(\Omega)} \int_\Omega \int_\Omega p_i(\mathbf{r_1}) P_t(\mathbf{r_1}, \mathbf{r_2}) p_j(\mathbf{r_2}) \, \mathrm{d}\mathbf{r_1} \, \mathrm{d}\mathbf{r_2}, \tag{A.8}$$

with $p_i(\mathbf{r}) = (\mathbf{e_i} \cdot \mathbf{r})$. Since $K_{ij}(t) = K_{ji}(t)$ due to the symmetry of the propagator, we can rewrite the moment as

$$\mathbb{E}[\phi_i\phi_j] = \int_0^T g_i(t_1) \int_0^T g_j(t_2) K_{ij}(|t_2 - t_1|) \, \mathrm{d}t_1 \, \mathrm{d}t_2. \tag{A.9}$$

We rely on the general short-time expansion for the heat kernels (see [332–334] and references therein)

$$K_{ij}(t) = \sum_{m \geq 0} c_m(p_i, p_j) \, (D_0 t)^{m/2}, \tag{A.10}$$

with

$$c_0(f, h) = \frac{1}{\mathrm{vol}(\Omega)} \int_\Omega f(\mathbf{r}) h(\mathbf{r}) \, \mathrm{d}\mathbf{r} \,, \tag{A.11a}$$

$$c_1(f, h) = 0 \,, \tag{A.11b}$$

$$c_2(f, h) = -\frac{1}{\mathrm{vol}(\Omega)} \int_\Omega \nabla f(\mathbf{r}) \cdot \nabla h(\mathbf{r}) \, \mathrm{d}\mathbf{r} \,, \tag{A.11c}$$

$$c_3(f, h) = \frac{4}{3\sqrt{\pi}} \frac{1}{\mathrm{vol}(\Omega)} \int_{\partial\Omega} \frac{\partial f(\mathbf{r})}{\partial n} \frac{\partial h(\mathbf{r})}{\partial n} \, \mathrm{d}S \,, \tag{A.11d}$$

where $\partial/\partial n = (\mathbf{n}\cdot\nabla)$ is the normal derivative at the boundary, and $\mathbf{n}$ is the unit inward normal vector at the boundary. We note that the expansion (A.10) is an asymptotic series which has to be truncated. In our case, we get

$$c_0(p_i,p_j) = \frac{1}{\mathrm{vol}(\Omega)}\int_\Omega (\mathbf{e_i}\cdot\mathbf{r})(\mathbf{e_j}\cdot\mathbf{r})\,\mathrm{d}\mathbf{r}\,, \tag{A.12a}$$

$$c_1(p_i,p_j) = 0\,, \tag{A.12b}$$

$$c_2(p_i,p_j) = -\delta_{ij}\,, \tag{A.12c}$$

$$c_3(p_i,p_j) = \frac{4}{3\sqrt{\pi}}\frac{1}{\mathrm{vol}(\Omega)}\int_{\partial\Omega}(\mathbf{e_i}\cdot\mathbf{n})(\mathbf{e_j}\cdot\mathbf{n})\,\mathrm{d}s \tag{A.12d}$$

(in the last integral, the normal vector $\mathbf{n}$ depends on the boundary point). Combining these results, we get

$$\begin{aligned}\mathbb{E}[\phi_i\phi_j] = &\int_0^T \mathrm{d}t_1\, G_i(t_1)\int_0^T \mathrm{d}t_2\, G_j(t_2)\\ &\times\left(-\delta_{ij}D_0|t_2-t_1| + \frac{4}{3\sqrt{\pi}}\sigma \mathsf{S}^{(3)}_{ij}(D_0|t_2-t_1|)^{3/2}+\cdots\right),\end{aligned} \tag{A.13}$$

where σ is the surface-to-volume ratio and the "structural" matrix $\mathsf{S}^{(3)}$ is defined by

$$\mathsf{S}^{(3)} = \frac{1}{\mathrm{surf}(\partial\Omega)}\int_{\partial\Omega}\mathbf{n}\otimes\mathbf{n}\,\mathrm{d}^2s\,, \tag{A.14}$$

and the zeroth order term (with c_0) vanished due to the rephasing condition

$$\int_0^T G_i(t)\,\mathrm{d}t = 0 \qquad (i=x,y,z). \tag{A.15}$$

We can write this result more compactly as

$$\mathbb{E}[\phi_i\phi_j/2] = bD_0\left(\delta_{ij}\mathsf{T}^{(2)}_{ij} - \frac{4\ell_\mathrm{d}}{3\sqrt{\pi}}\sigma\mathsf{S}^{(3)}_{ij}\mathsf{T}^{(3)}_{ij}+\cdots\right), \tag{A.16}$$

where we introduced the "temporal" matrices

$$\mathsf{T}^{(m)} = -\frac{T}{2b}\int_0^T\int_0^T \mathbf{G}(t)\otimes\mathbf{G}(t')\left|\frac{t-t'}{T}\right|^{m/2}\mathrm{d}t\,\mathrm{d}t'\,, \tag{A.17}$$

and we recall the definition of the diffusion length $\ell_\mathrm{d} = \sqrt{D_0T}$. As a consequence, we compute the second moment as

$$\frac{\mathbb{V}[\phi]}{2bD_0} = \mathrm{Tr}(\mathsf{T}^{(2)}) - \frac{4}{3\sqrt{\pi}}\sigma\ell_\mathrm{d}\,\mathrm{Tr}(\mathsf{S}^{(3)}\mathsf{T}^{(3)})+\cdots\,. \tag{A.18}$$

Note that this formula can also be obtained from the results of Frølich *et al* [61]. They compute the effective diffusion coefficient from the velocity auto-correlation function that is then expressed in terms of a double-surface integral of the diffusion propagator. By performing two integration by parts, this integral is essentially identical to our Eq. (A.8).

Let us introduce the auxiliary function

$$\mathbf{h}(t) = \int_0^T \mathbf{G}(t')|t - t'|\,\mathrm{d}t' \,. \tag{A.19}$$

We split the above integral and perform an integration by parts

$$\mathbf{h}(t) = \int_0^t \mathbf{Q}(t')\,\mathrm{d}t' - \int_t^T \mathbf{Q}(t')\,\mathrm{d}t' \,, \tag{A.20}$$

where we used the conditions $\mathbf{Q}(0) = \mathbf{0}$ and $\mathbf{Q}(T) = \mathbf{0}$. Now we note that

$$\int_0^T \mathrm{d}t \int_0^t \mathbf{G}(t) \otimes \mathbf{Q}(t')\,\mathrm{d}t' = \int_0^T \mathrm{d}t' \int_{t'}^T \mathbf{G}(t) \otimes \mathbf{Q}(t')\,\mathrm{d}t \tag{A.21a}$$

$$= -\int_0^T \mathbf{Q}(t') \otimes \mathbf{Q}(t')\,\mathrm{d}t' \,, \tag{A.21b}$$

where we used again $\mathbf{Q}(T) = \mathbf{0}$. In the same way one gets

$$\int_0^T \mathrm{d}t \int_t^T \mathbf{G}(t) \otimes \mathbf{Q}(t')\,\mathrm{d}t' = \int_0^T \mathbf{Q}(t') \otimes \mathbf{Q}(t')\,\mathrm{d}t' \,. \tag{A.22}$$

Putting all the pieces together, one finally obtains

$$\mathsf{T}^{(2)} = \frac{1}{b}\int_0^T \mathbf{Q}(t) \otimes \mathbf{Q}(t)\,\mathrm{d}t \,, \tag{A.23}$$

so that $\mathsf{T}^{(2)}$ is actually the b-matrix renormalized by the b-value [141–143]. Since

$$\mathrm{Tr}(\mathsf{T}^{(2)}) = \frac{1}{b}\int_0^T |\mathbf{Q}(t)|^2\,\mathrm{d}t = 1 \,, \tag{A.24}$$

we recover the signal attenuation for free diffusion $S = e^{-\mathbb{V}[\phi]/2} = e^{-bD_0}$ in the absence of confinement. In turn, the effective diffusion coefficient, which is experimentally determined from the dependence of $-\ln S$ on b at small b-value, is expressed through the second moment as

$$D(T) = \lim_{b\to 0} \frac{-\ln S}{b} = \lim_{b\to 0} \frac{\mathbb{V}[\phi]/2}{b} \,, \tag{A.25}$$

from which, using (A.18) we obtain Eq. (2.51).

A.2 Structural matrix of sphere-like shapes.

In this appendix we show an approximate computation of the surface area $\mathrm{surf}(\partial\Omega)$ and the $\mathrm{S}^{(3)}$ matrix of a domain that is a small perturbation of a sphere. Then we provide an exact computation for a spheroid (i.e., an ellipsoid of revolution).

A.2.1 Approximate computation

Let us write the equation of the surface of the domain Ω in spherical coordinates: $r(\theta, \phi)$, where r is the radius, θ is the colatitude and ϕ the longitude along the surface. We recall that with these conventions, we have an orthogonal basis $(\mathbf{e_r}, \mathbf{e}_\theta, \mathbf{e}_\phi)$, where $\mathbf{e_r}$ is the outward unit radial vector, $\mathbf{e}_\theta$ is directed South along the meridian, and $\mathbf{e}_\phi$ is directed East, perpendicular to $\mathbf{e_r}$ and $\mathbf{e}_\theta$. We also introduce the spherical gradient:

$$\nabla_{\mathrm{s}} f = \frac{1}{r}\frac{\partial f}{\partial \theta}\mathbf{e}_\theta + \frac{1}{r\sin\theta}\frac{\partial f}{\partial \phi}\mathbf{e}_\phi \,, \tag{A.26}$$

for a function $f(\theta, \phi)$.

We now write $r(\theta, \phi) = R(1 + \varepsilon(\theta, \phi))$, where $\varepsilon(\theta, \phi)$ is a small perturbation. The surface element can then be expressed as

$$\begin{aligned} \mathrm{d}s &= r^2(1 + \|\nabla_{\mathrm{s}} r\|^2)^{1/2} \sin\theta \,\mathrm{d}\theta \,\mathrm{d}\phi \\ &= R^2(1 + 2\varepsilon(\theta, \phi)) \sin\theta \,\mathrm{d}\theta \,\mathrm{d}\phi + O(\varepsilon^2) \,. \end{aligned} \tag{A.27}$$

In the same way, one computes the inward normal vector as

$$\begin{aligned} \mathbf{n} &= -(1 + \|\nabla_{\mathrm{s}} r\|^2)^{-1/2} \,(\mathbf{e_r} - \nabla_{\mathrm{s}} r) \\ &= -\mathbf{e_r} + \nabla_{\mathrm{s}} r + O(\varepsilon^2) \,. \end{aligned} \tag{A.28}$$

Then the surface area of the domain Ω can be approximated as

$$\mathrm{surf}(\partial\Omega) \approx 4\pi R^2 \left(1 + \frac{1}{2\pi}\int_0^\pi \mathrm{d}\theta \int_0^{2\pi} \mathrm{d}\phi \,\varepsilon(\theta, \phi) \sin\theta\right) \,. \tag{A.29}$$

In the special case of a domain with a symmetry of revolution, we choose the axis of revolution as the polar axis of the spherical coordinates and get the simpler formula

$$\mathrm{surf}(\partial\Omega) \approx 4\pi R^2 \left(1 + \int_0^\pi \varepsilon(\theta) \sin\theta \,\mathrm{d}\theta\right) \,. \tag{A.30}$$

Now we turn to the $\mathrm{S}^{(3)}$ matrix. As we already obtained $\mathrm{surf}(\partial\Omega)$, what remains to compute is the following matrix

$$\widetilde{\mathrm{S}^{(3)}} = \int_{\partial\Omega} \mathbf{n} \otimes \mathbf{n} \,\mathrm{d}s \,, \tag{A.31}$$

and then $\mathrm{S}^{(3)} = \widetilde{\mathrm{S}^{(3)}}/\mathrm{surf}(\partial\Omega)$. In order to compute the $\widetilde{\mathrm{S}^{(3)}}$ matrix, we choose a fixed basis $(\mathbf{e_x}, \mathbf{e_y}, \mathbf{e_z})$, where $\mathbf{e_z}$ is directed along the polar axis, $\mathbf{e_x}$ corresponds to the direction $\phi = 0$ and $\mathbf{e_y}$ to the direction $\phi = \pi/2$. We also introduce the vector $\mathbf{e}_\rho$, which is the normalized

projection of $\mathbf{e_r}$ on the equatorial plane. In other words, $\mathbf{e}_\rho = \cos(\phi)\mathbf{e_x}+\sin(\phi)\mathbf{e_y}$. Furthermore, we assume that Ω has a symmetry of revolution around $\mathbf{e_z}$. Thus ε only depends on θ and we denote derivative by a prime: $\varepsilon'(\theta) = \frac{\partial \varepsilon}{\partial \theta}$. First we compute the following integral over ϕ:

$$I(\theta) = \frac{1}{2\pi}\int_0^{2\pi} (\mathbf{e_r} - \varepsilon'(\theta)\mathbf{e}_\theta) \otimes (\mathbf{e_r} - \varepsilon'(\theta)\mathbf{e}_\theta)\ \mathrm{d}\phi\ . \tag{A.32}$$

Writing

$$\mathbf{e_r} = \cos(\theta)\mathbf{e_z} + \sin(\theta)\mathbf{e}_\rho\ , \tag{A.33a}$$

$$\mathbf{e}_\theta = \cos(\theta)\mathbf{e}_\rho - \sin(\theta)\mathbf{e_z}\ , \tag{A.33b}$$

we compute:

$$\frac{1}{2\pi}\int_0^{2\pi} \mathbf{e}_\rho\ \mathrm{d}\phi = \mathbf{0}\ , \tag{A.34a}$$

$$\frac{1}{2\pi}\int_0^{2\pi} \mathbf{e}_\rho \otimes \mathbf{e}_\rho\ \mathrm{d}\phi = \frac{1}{2}(\mathbf{e_x}\otimes\mathbf{e_x} + \mathbf{e_y}\otimes\mathbf{e_y})\ . \tag{A.34b}$$

From the above relations we get

$$\begin{aligned} I(\theta) \approx\ & \left(\cos^2\theta + \sin(2\theta)\varepsilon'(\theta)\right)\mathbf{e_z}\otimes\mathbf{e_z} \\ & + \frac{1}{2}\left(\sin^2\theta - \sin(2\theta)\varepsilon'(\theta)\right)(\mathbf{e_x}\otimes\mathbf{e_x} + \mathbf{e_y}\otimes\mathbf{e_y})\ . \end{aligned} \tag{A.35}$$

The $\widetilde{\mathrm{S}^{(3)}}$ matrix is then computed from

$$\widetilde{\mathrm{S}^{(3)}} = 2\pi\int_0^{\pi} r^2(\theta) I(\theta)\sin\theta\ \mathrm{d}\theta\ , \tag{A.36}$$

which yields (up to $O(\varepsilon^2)$)

$$\frac{\widetilde{\mathrm{S}^{(3)}}_{xx}}{4\pi R^2} = \frac{1}{3} + \frac{1}{2}\int_0^{\pi} (\varepsilon\sin^3\theta - \varepsilon'(\theta)\sin^2\theta\cos\theta)\ \mathrm{d}\theta\ , \tag{A.37a}$$

$$\widetilde{\mathrm{S}^{(3)}}_{yy} = \widetilde{\mathrm{S}^{(3)}}_{xx}\ , \tag{A.37b}$$

$$\frac{\widetilde{\mathrm{S}^{(3)}}_{zz}}{4\pi R^2} = \frac{1}{3} + \int_0^{\pi} (\varepsilon\cos^2\theta\sin\theta + \varepsilon'(\theta)\sin^2\theta\cos\theta)\ \mathrm{d}\theta\ , \tag{A.37c}$$

and the off-diagonal terms are null. Integrating the second terms by part and using (A.30), we finally get:

$$\mathrm{S}^{(3)}_{xx} = \frac{1}{3} + \int_0^{\pi} \varepsilon(\theta)\left(\cos^2\theta - 1/3\right)\sin\theta\ \mathrm{d}\theta + O(\varepsilon^2)\ , \tag{A.38a}$$

$$\mathrm{S}^{(3)}_{yy} = \mathrm{S}^{(3)}_{xx}\ , \tag{A.38b}$$

$$\mathrm{S}^{(3)}_{zz} = 1 - 2\mathrm{S}^{(3)}_{xx}\ . \tag{A.38c}$$

In the case of linear gradient encoding with the gradient oriented either along $\mathbf{e_x}$ or along $\mathbf{e_z}$, the relative variation of η is given by (see Eq. (2.63))

$$\frac{\mathrm{S}^{(3)}_{xx} - \mathrm{S}^{(3)}_{zz}}{\mathrm{S}^{(3)}_{zz}} \approx 9\int_0^{\pi} \varepsilon(\theta)\left(\cos^2\theta - 1/3\right)\sin\theta\ \mathrm{d}\theta\ . \tag{A.39}$$

A.2.2 Exact computation for a spheroid

Let us consider a spheroid (ellipsoid with a symmetry of revolution) with axis $\mathbf{e_z}$. Here we do not consider a small perturbation from a sphere anymore, so that we switch to cylindrical coordinates (ρ, ϕ, z) that are more convenient for this computation. Let us recall that ρ is the distance to the revolution axis. The vectors of the basis $(\mathbf{e}_\rho, \mathbf{e}_\phi, \mathbf{e_z})$ have all been defined in the previous section. We denote by a the equatorial radius of the spheroid and by c the distance from the center to the poles (see Fig. A.1). In other words, a and c are the two semi-axes of the spheroid. Two cases will be treated separately: the prolate spheroid ($a \leq c$) and the oblate spheroid ($c \leq a$). More precisely, we detail the computations for the prolate case and only give the results for the oblate case, as the computations are very similar.

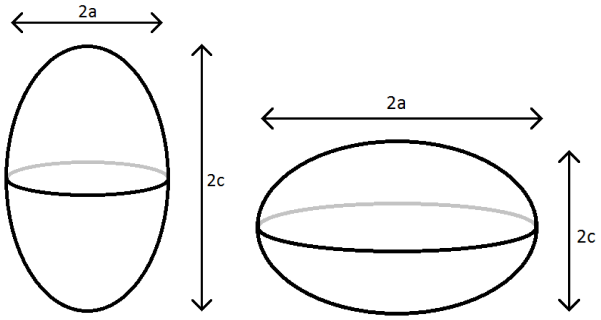

Figure A.1: A spheroid (ellipsoid of revolution) is defined by two semi-axes: its equatorial radius a and the distance from the center to the poles c. Two situations can occur: (left) the prolate spheroid, with $a \leq c$; (right) the oblate spheroid, with $c \leq a$.

For the prolate spheroid, we introduce the eccentricity e as $e = \sqrt{1-(a/c)^2}$. Note that $e = 0$ corresponds to a sphere of radius $a = c$ and $e = 1$ to a stick of length $2c$, oriented along $\mathbf{e_z}$. We have

$$\rho(z) = a\sqrt{1-(z/c)^2}\,, \tag{A.40}$$

and the surface area of the spheroid is readily computed from

$$\begin{aligned} S^{\text{prol}} &= 2\pi \int_{-c}^{c} \rho(z)\sqrt{1+[\rho'(z)]^2}\,\mathrm{d}z \\ &= 2\pi ac \int_{-1}^{1} \sqrt{1-e^2x^2}\,\mathrm{d}x\,, \end{aligned} \tag{A.41}$$

which yields

$$S^{\text{prol}} = 2\pi ac\left(\frac{\arcsin(e)}{e} + \sqrt{1-e^2}\right)\,. \tag{A.42}$$

For an oblate spheroid, the eccentricity is defined as $e = \sqrt{1-(c/a)^2}$ and the formula for the surface area becomes

$$S^{\text{obl}} = 2\pi\left(a^2 + c^2\frac{\operatorname{artanh}(e)}{e}\right)\,. \tag{A.43}$$

Now we turn to the computation of $\widetilde{\mathrm{S}^{(3)}}$. The inward normal vector is given by

$$-\left(1+[\rho'(z)]^2\right)^{-1/2}(\mathbf{e}_\rho + \rho'(z)\mathbf{e_z})\,. \tag{A.44}$$

First we compute the integral over ϕ:

$$\begin{aligned} I(z) &= \frac{1}{2\pi}\int_0^{2\pi} (\mathbf{e}_\rho + \rho'(z)\mathbf{e}_z) \otimes (\mathbf{e}_\rho + \rho'(z)\mathbf{e}_z)\, \mathrm{d}\phi \\ &= \frac{1}{2}\mathbf{e}_x \otimes \mathbf{e}_x + \frac{1}{2}\mathbf{e}_y \otimes \mathbf{e}_y + [\rho'(z)]^2\, \mathbf{e}_z \otimes \mathbf{e}_z \,. \end{aligned} \tag{A.45}$$

The $\widetilde{\mathrm{S}^{(3)}}$ matrix is then given by

$$\widetilde{\mathrm{S}^{(3)}} = 2\pi \int_{-c}^{c} \rho(z)(1+\rho'(z)^2)^{-1/2} I(z)\, \mathrm{d}z \,. \tag{A.46}$$

The following computations assume the prolate case. Thanks to the relations

$$\widetilde{\mathrm{S}^{(3)}}^{\mathrm{prol}}_{xx} = \widetilde{\mathrm{S}^{(3)}}^{\mathrm{prol}}_{yy} = (S^{\mathrm{prol}} - \widetilde{\mathrm{S}^{(3)}}^{\mathrm{prol}}_{zz})/2 \,, \tag{A.47}$$

we only have to compute $\widetilde{\mathrm{S}^{(3)}}^{\mathrm{prol}}_{xx}$ in order to have the full $\widetilde{\mathrm{S}^{(3)}}^{\mathrm{prol}}$ matrix. We have

$$\begin{aligned} \widetilde{\mathrm{S}^{(3)}}^{\mathrm{prol}}_{xx} &= \pi ac \int_{-1}^{1} \frac{1-x^2}{\sqrt{1-e^2x^2}}\, \mathrm{d}x \\ &= 2\pi ac \left(\frac{\arcsin e}{e} - \frac{1}{2e^2}\left(\frac{\arcsin e}{e} - \sqrt{1-e^2} \right) \right) \,, \end{aligned} \tag{A.48}$$

and then deduce

$$\widetilde{\mathrm{S}^{(3)}}^{\mathrm{prol}}_{zz} = 2\pi ac \left(\frac{\arcsin e}{e} - \sqrt{1-e^2} \right) \frac{1-e^2}{e^2} \,. \tag{A.49}$$

Using (A.42), we come to the matrix $\mathrm{S}^{(3)}$ for the prolate spheroid.

In the oblate case, one gets

$$\widetilde{\mathrm{S}^{(3)}}^{\mathrm{obl}}_{xx} = \pi c^2 \left(\frac{\operatorname{artanh} e}{e} + \frac{1}{e^2}\left(\frac{\operatorname{artanh} e}{e} - 1 \right) \right) \,, \tag{A.50a}$$

$$\widetilde{\mathrm{S}^{(3)}}^{\mathrm{obl}}_{zz} = 2\pi \left(a^2 - \frac{c^2}{e^2}\left(\frac{\operatorname{artanh} e}{e} - 1 \right) \right) \,, \tag{A.50b}$$

from which the matrix $\mathrm{S}^{(3)}$ is deduced using (A.43).

A.3 Maximal value of $\tau^{(3)}$

In the case of linear gradient encoding in a spherical domain, we obtained that Mitra's formula is corrected by a factor $\tau^{(3)}$ which is computed from the gradient profile according to Eq. (2.62). In this section, we investigate the maximum and the minimum values of $\tau^{(3)}$. We have

$$\tau^{(3)} = \frac{3}{8bT} \int_0^T \int_0^T Q(t)Q(t') \left| \frac{t-t'}{T} \right|^{-1/2} \mathrm{d}t \, \mathrm{d}t' \,. \tag{A.51}$$

Note that despite its singularity at 0, the function $1/\sqrt{|t|}$ is integrable, hence the above integral is well-defined. Next, we apply a change of variables from $t \in [0, T]$ to $t/T \in [0, 1]$ and $Q(t)$ to $q(t/T)$, which gives

$$\tau^{(3)} = \frac{3}{8\|q\|^2} \int_0^1 \int_0^1 q(t)q(t')|t-t'|^{-1/2} \, \mathrm{d}t \, \mathrm{d}t' \,, \tag{A.52}$$

with the usual L_2 norm. One can understand the above expression as a scalar product

$$\tau^{(3)} = \frac{3}{8} \frac{\langle q, \mathcal{K}q \rangle}{\langle q, q \rangle} \,, \tag{A.53}$$

with an integral operator $\mathcal{K}$ with the kernel $|t-t'|^{-1/2}$

$$(\mathcal{K}q)(t) = \int_0^1 q(t')|t-t'|^{-1/2} \, \mathrm{d}t' \,. \tag{A.54}$$

One can see that $\mathcal{K}$ is a weakly singular convolution operator because the kernel can be expressed as $K(t-t')$ (with $K(t) = 1/\sqrt{|t|}$). Denoting by $\hat{q}(\omega)$ the Fourier transform of $q(t)$ and by $\hat{K}(\omega)$ the Fourier transform of $K(t)$, one gets

$$\langle q, \mathcal{K}q \rangle = \frac{1}{2\pi} \int_{-\infty}^{\infty} |\hat{q}(\omega)|^2 \hat{K}(\omega) \, \mathrm{d}\omega \,, \tag{A.55}$$

with $\hat{K}(\omega) = \sqrt{2\pi/|\omega|}$. This shows that $\tau^{(3)}$ is always positive (in other words, the operator $\mathcal{K}$ is positive-definite). This result is expected from a physical point of view: if $\tau^{(3)}$ were negative, then the effective diffusion coefficient would increase with time that is nonphysical. The minimum value 0 can be asymptotically obtained, for example, with very fast oscillating gradients. It is, indeed, clear from Eq. (A.55) that if $g(t)$ is a cosine function with angular frequency ω_0 such that the number of periods $N_0 = \omega_0 T/(2\pi) \gg 1$, then $|\hat{q}(\omega)|^2$ is concentrated around $\pm\omega_0$, and we obtain $\tau^{(3)} \approx 3/(8\sqrt{N_0}) \sim \omega_0^{-1/2}$, a result that was obtained as well in [59] (see also Fig. 2.7).

Now we turn to the maximum value of $\tau^{(3)}$. The condition that $Q(t)$ is null outside of $[0, 1]$ is difficult to take into account in Fourier space and we could not extract further information from Eq. (A.55). In order to bound the maximum value of $\tau^{(3)}$, one can use the Cauchy inequality:

$$\begin{aligned} |(\mathcal{K}q)(t)| &= \left| \int_0^1 \sqrt{K(t-t')} q(t') \sqrt{K(t-t')} \, \mathrm{d}t' \right| \\ &\leq \left(\int_0^1 K(t-t') \, \mathrm{d}t' \right)^{\frac{1}{2}} \left(\int_0^1 q^2(t') K(t-t') \, \mathrm{d}t' \right)^{\frac{1}{2}} \,. \end{aligned}$$

One can easily compute the function

$$\int_0^1 K(t-t')\,\mathrm{d}t' = 2\sqrt{t} + 2\sqrt{1-t}\,, \tag{A.56}$$

whose maximum is $2\sqrt{2}$. Thus, one gets

$$|(\mathcal{K}q)(t)| \leq \left(2\sqrt{2}\int_0^1 q^2(t')K(t-t')\,\mathrm{d}t'\right)^{\frac{1}{2}}\,. \tag{A.57}$$

Using again the Cauchy inequality, one obtains

$$\langle q, \mathcal{K}q\rangle \leq 2^{3/4}\|q\|\left(\int_0^1\int_0^1 q^2(t')K(t-t')\,\mathrm{d}t'\,\mathrm{d}t\right)^{\frac{1}{2}}\,.$$

The same reasoning about the maximum value of the integral of K yields

$$\langle q, \mathcal{K}q\rangle \leq 2^{3/2}\|q\|^2\,, \tag{A.58}$$

and finally

$$\tau^{(3)} \leq \frac{3\sqrt{2}}{4} \approx 1.06\,. \tag{A.59}$$

We also know from the examples in Fig. 2.7 that $\tau^{(3)} = 1$ can be achieved for $q \equiv 1$, which implies that the maximum value of $\tau^{(3)}$ is in the interval $[1, 1.06]$.

The problem can be considered from another point of view. Due to the symmetry of the operator $\mathcal{K}$, it is well-known that the function q maximizing $\langle q, \mathcal{K}q\rangle/\|q\|^2$ is the eigenfunction of $\mathcal{K}$ with the highest eigenvalue. As a consequence, if one searches for a good estimation of the maximum $\tau^{(3)}$ as well as the corresponding "optimal" gradient profile, then one can use the following procedure: (i) to choose an initial profile q_0 which is sufficiently general or sufficiently close to a guessed optimal profile; (ii) to apply iteratively the operator $\mathcal{K}$ and to renormalize the result; (iii) to stop when the sequence has converged.

For example, the initial profile $q_0(t/T) = 1$, which corresponds to two infinitely narrow gradient pulses at time 0 and T, yields $\tau^{(3)} = 1$, which is close to the optimal value. Thus, it is a good initial condition for the iterative process. The result of such a procedure is shown in Fig. A.2. This yields an optimum value of $\tau^{(3)}$ of about 1.006, thus very close to 1. It is worth to note, however, that the optimal profile $q(t/T)$ differs clearly from $q_0(t/T) = 1$ (note also that q_0 is not an eigenfunction of $\mathcal{K}$).

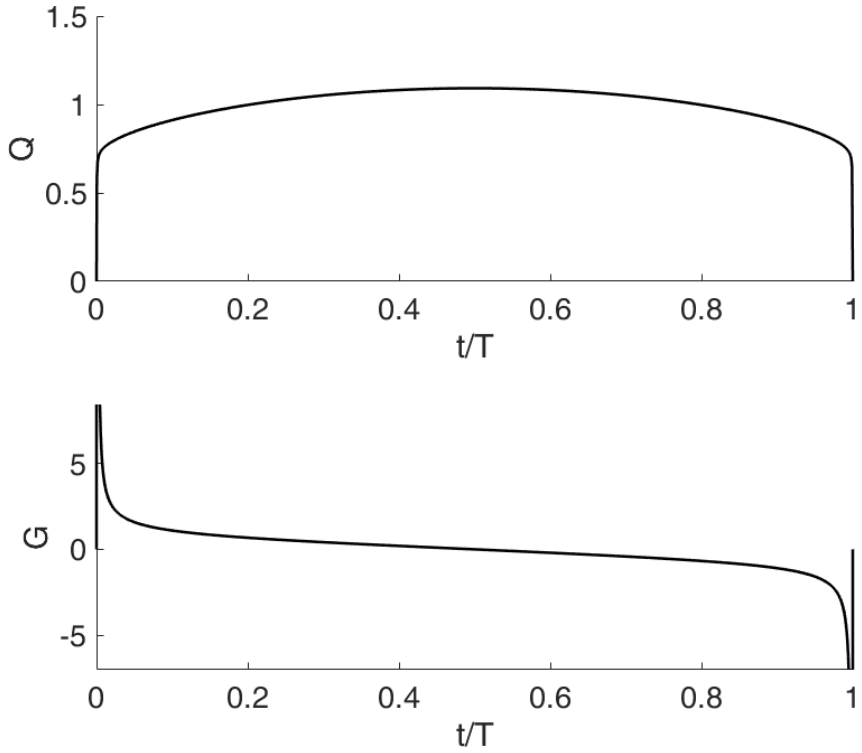

Figure A.2: The result of the iterative procedure in order to obtain the optimal profile that maximizes the value of $\tau^{(3)}$.

A.4 Fully isotropic sequence

The conventional condition $\mathsf{T}^{(2)} \propto \mathsf{I}$ removes the microscopic anisotropy in the diffusion tensor, whereas the new isotropy condition $\mathsf{T}^{(3)} \propto \mathsf{I}$ eliminates the mesoscopic anisotropy in the leading order of the short-time expansion. One can thus naturally ask whether it is possible to design a "fully isotropic" sequence that removes anisotropy in all order of $(D_0T)^{1/2}$? In this appendix we show that it is impossible to find a gradient sequence such that $\mathsf{T}^{(m)}$ is isotropic for all integer values $m = 2, 3, 4, \ldots$. In other words, one cannot find a sequence which produces an isotropic time-dependence of $D(T)$ to every order in $(D_0T)^{1/2}$. To show this we restrict ourselves to the values of m that are multiple of 4, $m = 4l$, with $l = 1, 2, \ldots$.

$$\begin{aligned} \mathsf{T}_{ij}^{(4l)} &= -\frac{T^{1-2l}}{2b} \int_0^T \int_0^T G_i(t_1) G_j(t_2) (t_2 - t_1)^{2l} \, \mathrm{d}t_1 \mathrm{d}t_2 \\ &= -\frac{T^{1-2l}}{2b} \sum_{k=0}^{2l} (-1)^k \binom{2l}{k} \alpha_i^{(k)} \alpha_j^{(2l-k)} \, , \end{aligned} \tag{A.60}$$

where

$$\alpha_i^{(k)} = \int_0^T G_i(t) t^k \, \mathrm{d}t \, . \tag{A.61}$$

We will now prove that the isotropy of $\mathsf{T}^{(4l)}$ for any integer l implies that $\alpha_i^{(k)} = 0$ for all $i = x, y, z$ and all integer k. Note that the property for $k = 0$ corresponds to the refocusing condition (1.26) that we assumed throughout the paper. We prove our statement by recurrence on l and k. First, let us consider $l = 1$ and prove the $k = 1$ case. One has

$$\mathsf{T}_{ij}^{(4)} = -\frac{T^{-1}}{2b} \left(-2\alpha_i^{(1)} \alpha_j^{(1)} \right) \, . \tag{A.62}$$

If $i \neq j$, then $\mathsf{T}_{ii}^{(4)} = \mathsf{T}_{jj}^{(4)}$ and $\mathsf{T}_{ij}^{(4)} = 0$ so that $\alpha_i^{(1)} = \alpha_j^{(1)} = 0$.

Now we assume that $\alpha_i^{(k)} = 0$ for all $i = x, y, z$ and for all $k < k'$ up to a given rank k'. Then almost all the terms in the expression of $\mathsf{T}_{ij}^{(4k')}$ vanish and we are left with

$$\mathsf{T}_{ij}^{(4k')} = -\frac{T^{1-2k'}}{2b} \left((-1)^{k'} \binom{2k'}{k'} \alpha_i^{(k')} \alpha_j^{(k')} \right) \, , \tag{A.63}$$

and with the same reasoning as in the previous case, we deduce that $\alpha_i^{(k')} = 0$ for any i. By recurrence, we have proven that $\alpha_i^{(k)} = 0$ for all i and k.

What remains to prove is that the only continuous function $f(t)$ that satisfies the conditions $\int_0^T f(t) t^k \, \mathrm{d}t = 0$ for all integer values of k is the null function $f = 0$. Let us assume that f is nonzero, i.e., there exists an interval (a, b) with $a < b$ such that $f(t) \neq 0$ for any $t \in (a, b)$ (e.g., $f(t) > 0$ on this interval). Since polynomials form a dense subset of continuous functions on $[0, T]$, one can build a sequence of polynomials that converges to a continuous function that would be zero outside (a, b) and positive inside (a, b). Thus there would exist a polynomial $P(t)$ such that $\int_0^T f(t) P(t) \, \mathrm{d}t > 0$, which is incompatible with the statement: for all $k = 0, 1, 2, \ldots$ $\int_0^T f(t) t^k \, \mathrm{d}t = 0$. Note that this argument can be easily extended to functions with a finite number of jumps.

Appendix B

Supplementary material to Chapter 3

In Appendix B.1, we study the permeation process for a random walk near a planar boundary. We compute the distribution of crossing times and show that the scaling (3.11) creates a compensation between a vanishingly small crossing probability and an infinitely large number of reflections on the boundary, in the continuous limit. This computation reveals that the barrier crossing is a non self-averaging process and we provide some basic results about such processes. In Appendix B.1, we present computations of the first exit time distribution outside an array of permeable barriers. Although not directly related to dMRI, we obtain interesting results that provide new insight into diffusion through multiple barriers and inside disordered media. Finally, the last part of this appendix contains extended technical developments related to Sec. 3.4.

B.1 Random walk model of permeability

B.1.1 Distribution of crossing times

In this appendix, we compute the distribution of times at which the particle crosses a barrier from simple random walk computations. Our formulas reproduce exactly the ones obtained by considering directly a partially reflected Brownian motion, and the reader may argue that our lengthy derivation is much less efficient than the powerful formalism of stochastic processes [274]. While this argument is perfectly valid, we also feel that it is interesting to present a rather elementary computation that requires only little knowledge of random walks. The computation is presented for a planar boundary, and would become rather involved for an arbitrary geometry. In the somewhat extreme (but physically relevant) example of fractal boundary, the absence of lower bound on geometrical length scales *a priori* prevents one from considering discrete random walks and taking the continuous limit, as we do here. In that case, the partially reflected Brownian motion becomes the natural tool to study permeation effects.

We consider a one-dimensional random walk on a half-space $x \geq 0$, where the plane $x = 0$ is the barrier. The lattice step is denoted by a, the time step is τ, and the barrier crossing probability is (see Eq. (3.11) and related discussion)

$$\epsilon = \frac{\kappa a}{D_0 + 2\kappa a} \underset{a\to 0}{\approx} \kappa a/D_0 \,. \tag{B.1}$$

We consider a particle starting at the origin and we compute the probability that it crosses the barrier after n time steps. To cross the barrier, the particle has to reach the barrier a sufficient number of times to compensate for the small crossing probability ϵ. Therefore, there is a coupling between the random walk and the random crossing controlled by ϵ.

The probability that the particle crosses the barrier after exactly r attempts is given by

$$P_{\mathrm{b}}(r) = \epsilon(1-\epsilon)^{r-1} \,. \tag{B.2}$$

Moreover, by classic considerations about random walk, one can compute the probability that the particle meets the barrier for the r-th time after exactly n time steps:

$$P_{\mathrm{m}}(r,n) = 2^{r-n}\frac{r}{n-r}\binom{n-r}{n/2} \,. \tag{B.3}$$

The factor $n/2$ appears because the particle can go back to the origin only after an even number of steps. The following computations are done under the assumption that n is even. Therefore the probability that the particle crosses the barrier after exactly n time steps is

$$P_{\mathrm{c}}(n) = \sum_{r=1}^{n/2} P_{\mathrm{b}}(r)P_{\mathrm{m}}(r,n) \tag{B.4}$$

$$= \sum_{r=1}^{n/2} \epsilon(1-\epsilon)^{r-1}2^{r-n}\frac{r}{n-r}\binom{n-r}{n/2} \,. \tag{B.5}$$

The above sum may be expressed in terms of the hypergeometric function, however a simpler expression is obtained in the continuous limit, when $a, \tau, \epsilon \to 0$. One can see that at fixed n, $P_{\mathrm{c}}(n) \underset{\epsilon\to 0}{\to} 0$ therefore we will evaluate the sum (B.5) with $n, r \to \infty$. To this end, we write $r = nx/2$ so that the sum becomes an integral over $0 \le x \le 1$. With this notation, one gets the approximate formula

$$P_{\mathrm{c}}(n) \approx \frac{1}{\sqrt{2\pi n}}\int_0^1 \frac{nx\epsilon}{2\sqrt{(1-x)(1-x/2)}}\exp\left(-\frac{nx^2}{8}-\frac{nx\epsilon}{2}\right)\mathrm{d}x \tag{B.6}$$

$$\approx 2\frac{\epsilon}{\sqrt{2\pi n}}\left[1-\sqrt{\pi\epsilon^2 n/2}\,\mathrm{erfcx}\left(\sqrt{\epsilon^2 n/2}\right)\right] \,, \tag{B.7}$$

with the scaled complementary error function

$$\mathrm{erfcx}(u) = \frac{2}{\sqrt{\pi}}\int_u^\infty e^{u^2-x^2}\,\mathrm{d}x \,. \tag{B.8}$$

One can see that

$$P_{\mathrm{c}}(n) \underset{n\to\infty}{\approx} 2\sqrt{\frac{1}{2\pi}}\frac{1}{\epsilon n^{3/2}} \,, \tag{B.9}$$

so that the mean value of n is infinite. This can be seen as a consequence of a well-known property of the one-dimensional random walk where the probability to return to the origin is 1 but the mean return time is infinite. If the mean return time was a finite value $\langle n_{\mathrm{return}}\rangle$, then the mean crossing time would be related to the mean number of attempts to cross the barrier times $\langle n_{\mathrm{return}}\rangle$, i.e., $\langle n\rangle \sim \epsilon^{-1}\langle n_{\mathrm{return}}\rangle$. The above formula (B.7) reveals the scaling $\epsilon^2 n$, that

contradicts this naive reasoning. This peculiar behavior is studied in a more general setting in Appendix B.1.2.

In the continuous limit, one can rewrite the above distribution (B.7) in two different ways. First, one can write it as a distribution for the time $t = n\tau$. Since the probability is zero for odd values of n, one has to divide the right hand side of (B.7) by 2, as a mean value between odd and even values of n. One can also rewrite the distribution in terms of $y = a\sqrt{n} = \sqrt{D_0 t}$, that can be interpreted as the typical diffusion length parallel to the barrier during time t. This yields the following formulas:

$$P_c(t) = \frac{1}{\sqrt{\pi\tau_\kappa t}}\left[1 - \sqrt{\pi t/\tau_\kappa}\,\mathrm{erfcx}\left(\sqrt{t/\tau_\kappa}\right)\right] , \tag{B.10}$$

$$P_c(y) = \frac{1}{\ell_\kappa\sqrt{\pi}}\left[1 - \sqrt{\pi}\,y/\ell_\kappa\,\mathrm{erfcx}\left(y/\ell_\kappa\right)\right] , \tag{B.11}$$

with the natural scales

$$\tau_\kappa = D_0/\kappa^2 , \qquad \ell_\kappa = D_0/\kappa . \tag{B.12}$$

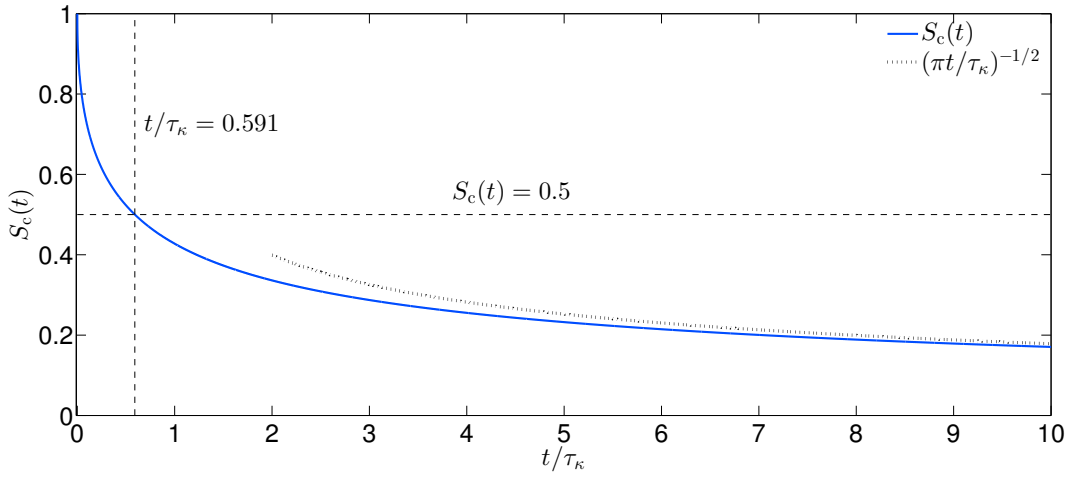

Figure B.1: The survival probability (B.13) for a particle starting at the barrier as a function of time. The scale τ_κ may be interpreted as a typical barrier crossing time since half of the particles have crossed the barrier after $t = 0.591\tau_\kappa$. However, the survival probability decays very slowly (as $(\pi t/\tau_\kappa)^{-1/2}$) so that the average crossing time is infinite. This infinite average crossing time corresponds to particles making very long excursions before coming back to the barrier and is typical of random walks in unbounded domains.

These formulas yield a natural interpretation of τ_κ as the typical time taken by an individual particle to cross the barrier. In turn, ℓ_κ is the typical length explored by a particle along the barrier before crossing it. The fact that one obtains finite scales in the continuous limit indicates that the scaling $\epsilon = \kappa a/D_0$ is correct. In other words, there is a compensation between an infinitely small crossing probability and an infinitely large number of hits per unit of time. One can compute the survival probability of the particle as a function of time (the same formula holds for y after a simple change of variable):

$$S_c(t) = \int_t^\infty P_c(t')\,\mathrm{d}t' = \mathrm{erfcx}(\sqrt{t/\tau_\kappa}) . \tag{B.13}$$

This function is plotted on Fig. B.1. One can see that the survival probability decays very fast at short times, so that half of the particles initially at the barrier have crossed it after $t = 0.591\tau_K$. However, the very slow decay of $S_c(t)$ at long times indicates that a significant fraction of particles diffuse away from the barrier and come back to it after very long excursions, thus yielding an infinite average crossing time.

B.1.2 Non self-averaging

In this appendix we discuss *qualitatively* the phenomenon of non self-averaging, that can be loosely thought as the opposite of the law of large numbers. This phenomenon describes random variables that have infinite mean values and leads to counter-intuitive behaviors, as we shall explain. Let us consider a positive random variable X with infinite mean value. We denote by $P(x)$ its tail distribution function, i.e.

$$P(x) = \mathbb{P}(X \geq x) \ . \tag{B.14}$$

One has $P(0) = 1$, $F(\infty) = 0$, and $\langle X \rangle = \infty$ is equivalent to

$$\int_0^\infty P(x)\, \mathrm{d}x = \infty \ . \tag{B.15}$$

In particular we consider the common situation of a power-law tail

$$P(x) \underset{x\to\infty}{=} \frac{C}{x^p} \ , \qquad 0 < p < 1 \ . \tag{B.16}$$

Now we perform the following experiment. We draw N independent values of X and we study the maximum value obtained. We denote this new random variable by M_N and its repartition function by P_N. One has

$$P_N(x) = \mathbb{P}(M_N \geq x) = 1 - (1 - F(x))^N \underset{x\to\infty}{=} \frac{NC}{x^p} \ . \tag{B.17}$$

The value of M_N that occurs with maximum probability is found as the zero of the double derivative of P_N, that yields at large values of N:

$$P_N''(x_m) = 0 \ , \qquad x_m = \left(\frac{NCp}{1+p}\right)^{1/p} \ . \tag{B.18}$$

As one can see, x_m grows with N as $N^{1/p}$, i.e. faster than N.

Now let us turn to the sum $S_N = X_1 + \cdots + X_N$, with repartition function $\hat{P}_N$. First, one can compute the repartition function of S_2 as a convolution

$$\hat{P}_2(x) = \mathbb{P}(X_1 + X_2 \geq x) = P(x) - \int_0^x P'(y)P(x-y)\, \mathrm{d}y \ . \tag{B.19}$$

In the limit of infinitely large x, the second term in the right-hand side can be simply estimated using (B.16), that yields

$$\hat{P}_2(x) \underset{x\to\infty}{=} \frac{2C}{x^p} \ . \tag{B.20}$$

By recurrence, one obtains then

$$\hat{P}_N(x) \underset{x\to\infty}{=} \frac{NC}{x^p} \,. \tag{B.21}$$

Therefore, the tail of P_N and the tail of $\hat{P}_N$ coincide, in other words the probability law that governs large values of S_N is identical to the probability law that governs large values of M_N. Intuitively, if one sorts $X_1, \ldots, X_N$ in descending order, the first value(s) tend to be much larger than the rest, so that the value of the sum S_N is dominated by the value of the maximum M_N. In turn, one deduces that S_N grows as $N^{1/p}$. The terminology "non self-averaging" becomes clear. If one performs the arithmetic average of N copies of X, i.e. S_N/N, the result is a random variable that does not converge with increasing N. On the contrary, S_N/N tends to take larger and larger values as N increases. Our analysis reveals that large values of S_N/N are dominated by individual extreme events. Therefore the behavior of the arithmetic average S_N/N cannot be understood as an "average behavior" of X. This behavior is to be contrasted with the law of large numbers that applies if $p > 1$. In that case, X has finite mean value $\langle X \rangle$ and self-averages in the sense that the sum of N independent copies of X grows as $\langle X \rangle N$. In that case the arithmetic average S_N/N converges (almost surely) to the value $\langle X \rangle$ when N tends to infinity.

In the example of permeation through a barrier (Appendix B.1.1), a particle performs several excursions away from the barrier before crossing it. The probability of crossing is denoted by ϵ, and the typical number of excursions is thus $N \sim \epsilon^{-1}$ The variable X represents the duration of one excursion, i.e. the first return time to the origin. It is a classic result in probability theory (see, e.g., the book [275]) that its repartition function scales at large times as a power law with exponent $p = 1/2$. Therefore the total time before the barrier is crossed scales as $N^{1/p} = \epsilon^{-2}$, as we obtained by direct computation (see Eq. (B.7)).

B.2 First exit time distribution out of an array of permeable barriers

Another application of the diffusion operator eigenmodes is the computation of the first exit time distribution. First exit times are a particular case of first passage phenomena, which find many applications in physics, chemistry, biology, or economics. In particular, one-dimensional models are relevant to a wide variety of phenomena in which an event is triggered when a fluctuating variable reaches a given threshold (examples include avalanches, neuron firing, or sell/buy orders) as well as diffusion controlled reactions such as fluorescence quenching or predation [289, 290]. In general planar domains, exit times were thoroughly investigated in the so-called "narrow-escape limit" [291] and few results are available for arbitrary escape areas [292, 293].

In order to compute the first exist time distribution out of an array of permeable barriers, let us consider *perfectly relaxing* conditions at the outer boundaries of the interval $[0, L]$: $K_\pm = \infty$. Then the quantity

$$\int_0^L \mathcal{G}(t, x, x')\, \mathrm{d}x'$$

represents the probability of not reaching the outer boundaries for a particle starting at x, up to the time t. In other words, if one denotes by T_x the random variable equal to the first exit time of a particle starting at x, then the tail distribution and the probability density of T_x are respectively given by:

$$P_{T_x}(t) = \mathbb{P}(T_x > t) = \sum_{n=1}^{\infty} e^{-\lambda_n t} u_n(x) \left(\int_0^L u_n(x')\, \mathrm{d}x' \right), \tag{B.22}$$

$$\rho_{T_x}(t) = \frac{\mathbb{P}(t < T_x < t + \mathrm{d}t)}{\mathrm{d}t} = \sum_{n=1}^{\infty} \lambda_n e^{-\lambda_n t} u_n(x) \left(\int_0^L u_n(x')\, \mathrm{d}x' \right). \tag{B.23}$$

We briefly present the case of a regular geometry, based on the computation of the eigenmodes with perfectly relaxing outer boundaries performed in Sec. B.3.2. We obtain the first exit time distribution and we study the limit of a large number of barriers (where the size L of the large interval remains constant). Similarly to the computation of the dMRI signal, we obtain a scaling law of the form $\tilde{\kappa}\tilde{t}/(\tilde{\kappa}+1)$. However, here the limit $m \to \infty$ ensures that the scaling law is valid *for any time* $\tilde{t}$. Then we turn to irregular geometries where l_i and $\kappa_{i,i+1}$ are randomly distributed and we observe the same scaling law, with a new definition for $\tilde{\kappa}$ which depends on permeabilities and positions of the barriers. Numerical computations show a very good agreement even for a moderate number of barriers ($m \approx 10$). Moreover, we analyze the regime of very low permeability, where the diffusive motion can be replaced by a discrete hopping model, and exhibit a perfect agreement with previously obtained results. Finally, we briefly discuss some implications for diffusion inside disordered media.

B.2.1 Regular geometry

Let us study the first exit time distribution (B.23) for a geometry similar to the example of Sec. 3.4.3 and 3.4.5: it consists of an array of m identical cells of length L/m, where L is independent of m, with *perfectly relaxing* conditions at the outer boundaries ($K_\pm = \infty$). The computations

are detailed in Sec. B.3.2. Since $u_n(0) = 0$, one cannot use the normalization $v(0) = 1$ from Sec. 3.4.2, so we write $u = \beta w$ with another normalization, $w'(0) = \sqrt{\lambda/D}$, which corresponds to $\begin{bmatrix} a_1^l \\ b_1^l \end{bmatrix} = \begin{bmatrix} 0 \\ 1 \end{bmatrix}$. Because the geometry is symmetric the eigenmodes of the diffusion operator u_n, $n = 1, 2, \ldots$ are alternately symmetric or anti-symmetric (see Sec. 3.4.2); the latter give a zero contribution in the sum in Eqs. (B.22) and (B.23). As for the symmetric eigenmodes, one obtains:

$$\int_0^L w(x)\,\mathrm{d}x = \frac{2\ell_s}{\alpha}\,, \tag{B.24}$$

$$\beta^{-2} = \frac{-m\ell_s}{2}\frac{\sin\alpha\left(1+\frac{\tilde{r}}{2}\right)+\frac{\tilde{r}}{2}\alpha\cos\alpha}{\sin^2\psi}\left(\sin\alpha\cos m\psi + \frac{\tilde{r}\alpha(m-1)}{m}\cos((m-1)\psi)\right) + \frac{m\ell_s}{2}\left(\frac{\sin\alpha}{\alpha}-\cos\alpha\right)\frac{\sin m\psi}{m\sin\psi}\,, \tag{B.25}$$

where α is a solution of the equation

$$\sin\alpha\frac{\sin m\psi}{\sin\psi} + \tilde{r}\alpha\frac{\sin((m-1)\psi)}{\sin\psi} = 0\,. \tag{B.26}$$

We recall that

$$\lambda = D_0\alpha^2/\ell_s^2 = D\alpha^2 m^2/L^2\,, \tag{B.27}$$

and we introduce the dimensionless time:

$$\tilde{t} = D_0 t/L^2\,. \tag{B.28}$$

Note that the solutions α depend only on m and $\tilde{\kappa}$, hence the tail distribution is a function of $\tilde{t}$, m, $\tilde{\kappa}$, and the starting point x:

$$\mathbb{P}(T_x > t) = P_x(\tilde{t}, m, \tilde{\kappa})\,,$$
$$\rho_{T_x}(t) = -\partial_t P_x = -\frac{L^2}{D_0}\partial_{\tilde{t}} P_x = \frac{L^2}{D_0}\tilde{\rho}_x(\tilde{t}, m, \tilde{\kappa})\,,$$

$\tilde{\rho}_x(\tilde{t}, m, \tilde{\kappa})$ being the probability density function of the dimensionless random variable DT_x/L^2.

We consider now the limit $m \to \infty$. We recall that $\tilde{\kappa} = \kappa\ell_s/D = \kappa L/(mD_0)$ is the dimensionless parameter that governs the transition from diffusion control ($\tilde{\kappa} \gg 1$) to permeation control ($\tilde{\kappa} \ll 1$). Here, $\tilde{\kappa}$ depends on m if κ, D_0, L are fixed. However in what follows we consider $\tilde{\kappa}$ and m as independent parameters. From Eq. (B.27) we get that only the smallest solutions α contribute to the sum in Eqs. (B.22) and (B.23), hence we use Eq. (B.60) which immediately implies that in the $m \to \infty$ limit all the curves fall on a unique master curve of the variable $\tilde{\kappa}\tilde{t}/(\tilde{\kappa}+1)$:

$$P_x(\tilde{t}, m, \tilde{\kappa}) \approx P_x^*\left(\frac{\tilde{\kappa}\tilde{t}}{\tilde{\kappa}+1}\right)\,, \tag{B.29}$$

$$\tilde{\rho}_x(\tilde{t}, m, \tilde{\kappa}) \approx \frac{\tilde{\kappa}}{\tilde{\kappa}+1}\rho_x^*\left(\frac{\tilde{\kappa}\tilde{t}}{\tilde{\kappa}+1}\right)\,. \tag{B.30}$$

This master curve (P_x^*, ρ_x^*) is precisely the one corresponding to an interval without any barriers ($\tilde{\kappa} \to \infty$). The interpretation is that a very large number of barriers can be modeled as an effective medium with the diffusion coefficient $D_\infty = D_0\tilde{\kappa}/(\tilde{\kappa}+1)$. In particular, one obtains the formula for the mean first exit time:

$$\mathbb{E}[T_x] = \frac{x(L-x)}{2D_\infty} = \frac{x(L-x)}{2D_0}\frac{\tilde{\kappa}+1}{\tilde{\kappa}} \,. \tag{B.31}$$

Note that from the second equality in Eq. (B.60) we get that one should replace $\tilde{\kappa}$ by $\tilde{\kappa}\left(1+\frac{2}{m}\right)$ in order to obtain the scaling laws (B.29) and (B.30), and thus Eq. (B.31), to the first order in $1/m$.

B.2.2 Irregular geometry

Now we turn to an irregular geometry: the lengths of the intervals and the permeabilities of the inner barriers are randomly distributed. We still impose that the whole interval has a constant length L. If the number of compartments m is sufficiently large, we expect that the effective medium description still holds, with an effective value of $\tilde{\kappa}$. The formula for $\tilde{\kappa}$ should involve all the lengths l_i and permeabilities $\kappa_{i,i+1}$. Moreover in the case of a regular geometry, $l_i = \ell_s$ and $\kappa_{i,i+1} = \kappa$, and one should retrieve $\tilde{\kappa} = \kappa\ell_s/D_0$. If l_i and $\kappa_{i,i+1}$ are independent, we find numerically that the formula

$$\tilde{\kappa} = \frac{\langle l\rangle}{\langle r\rangle D_0} \,, \tag{B.32}$$

where $\langle\cdot\rangle$ denotes arithmetic mean, works well for large values of m (typically, $m \gtrsim 100$). As a consequence, an irregular geometry does not differ from a regular geometry provided that the number of compartments is sufficiently large, when one replaces ℓ_s by $\langle l\rangle$ and r by $\langle r\rangle$.

However, this formula fails at small values of m. The following reasoning suggests indeed that the formula of $\tilde{\kappa}$ should involve a correlation between the position of the barriers and their resistances. Let us assume for simplicity that the lengths of the compartments are randomly generated in such a way that the geometry is symmetric with respect to the middle of the interval (and that m is odd). One can then see the structure as $(m-1)/2$ nested subintervals $I_1 \subset I_2 \subset \cdots \subset [0,L]$ of sizes $L_1 < L_2 < \cdots < L$ and enclosed by barriers of resistances $R_1, R_2, \ldots, R_{(m-1)/2}$ (see Fig. B.2). We let a large number of particles diffuse from $x = L/2$. First they diffuse inside the first subinterval I_1, so that they "feel" $\tilde{r}_1 = D_0R_1/L_1$. Let us assume that the barriers are quasi-impermeable, that is $\tilde{r}_1 \gg 1$. According to Eq. (B.31), after a time $T_1 \sim L_1^2\tilde{r}_1(8/D_0) \sim L_1R_1$ they have crossed the first barriers. The particle density is then quite homogeneous inside the second subinterval I_2 and so the particles feel $\tilde{r}_2 = D_0R_2/L_2$. After a time $T_2 \sim L_2R_2$ they cross the second barriers, they homogenize inside the third subinterval, and so on. The mean exit time is thus proportional to $\sum_{i=1}^{(m-1)/2} R_iL_i$. According to Eq. (B.31) and to the condition that we recover $\tilde{r} = rD_0/\ell_s$ for a regular geometry in the $m = \infty$ limit, one can guess:

$$\tilde{\kappa} = \tilde{r}^{-1} = \frac{L^2}{4D_0}\left(\sum_{i=1}^{(m-1)/2} R_iL_i\right)^{-1} = \frac{L^2}{4D_0}\left(\sum_{i=1}^{m-1} r_{i,i+1}\left|x_{i,i+1} - L/2\right|\right)^{-1} \,. \tag{B.33}$$

Interestingly, the correction $\tilde{\kappa} \to \tilde{\kappa}\left(1+\frac{2}{m}\right)$ is contained in this formula in case of a regular geometry (see Sec. B.2.1). This formula was obtained for a symmetric geometry and it has to

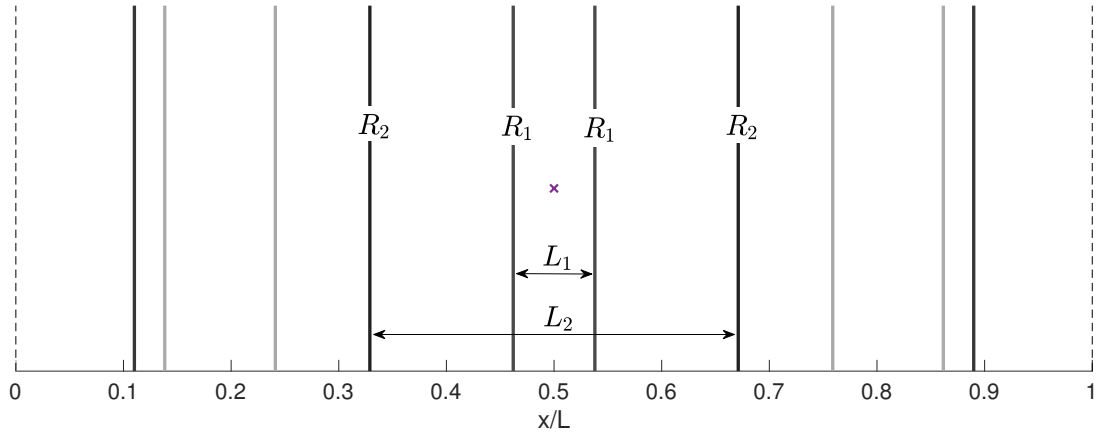

Figure B.2: An example of a random symmetric structure (with $m = 11$ compartments). The solid vertical lines picture the barriers (the darker the line, the higher the resistance of the barrier). One can see this structure as nested subintervals of lengths $L_1 < L_2 < \dots$ enclosed by barriers of resistances $R_1, R_2, \dots$. The cross indicates the starting position of the particles, $x = L/2$.

be refined for asymmetric geometries. In particular, it is not clear how it should be changed if the starting point x is not at the middle of the interval anymore. The same reasoning suggests a formula such as:

$$\tilde{\kappa} = \frac{x^2}{4D_0}\left(\sum_{i=1}^{i_0-1} r_{i,i+1}(x - x_{i,i+1})\right)^{-1} + \frac{(L-x)^2}{4D_0}\left(\sum_{i=i_0}^{m-1} r_{i,i+1}(x_{i,i+1} - x)\right)^{-1}, \tag{B.34}$$

if $x \in \Omega_{i_0}$. However the numerical agreement is not as good as with a symmetric geometry and $x = L/2$. Therefore we focus on Eq. (B.33) in the following. Note that Eq. (B.33) gives different weights to the barriers depending on their position with respect to the middle of the interval, which is rather intuitive. Indeed one expects a barrier located exactly at the middle of the interval to have no effect at all (given the symmetry of the geometry) whereas barriers located near the exit points should have the greatest effect.

If the permeabilities of the barriers and the lengths of the compartments are independent random variables and are distributed in a way that $\langle r \rangle$ is finite, then Eqs. (B.32) and (B.33) are identical in the limit $m \to \infty$. Furthermore, according to the central limit theorem we expect their deviation to be of order $m^{-1/2}$. Figure B.3 shows a comparison of the two formulas. We have plotted the first exit time distribution for random structures such as the one shown in Fig. B.2, with $m = 11$ compartments. The lengths of the compartments and the barrier resistances follow an exponential distribution. We choose various mean values of the barrier resistances and we compute $\tilde{\kappa}$ according to Eq. (B.32) or Eq. (B.33). Then we apply the scaling $t \to \tilde{\kappa}t/(\tilde{\kappa} + 1)$. One can see that with Eq. (B.33) all the curves fall onto one master curve, whereas Eq. (B.32) leads to significant deviations. Even though Eq. (B.32) is less accurate than Eq. (B.33), the latter involves the correlation between the position of the barriers and their permeabilities, which may be unknown in actual experiments. In this case one should use Eq. (B.32), which is more "universal".

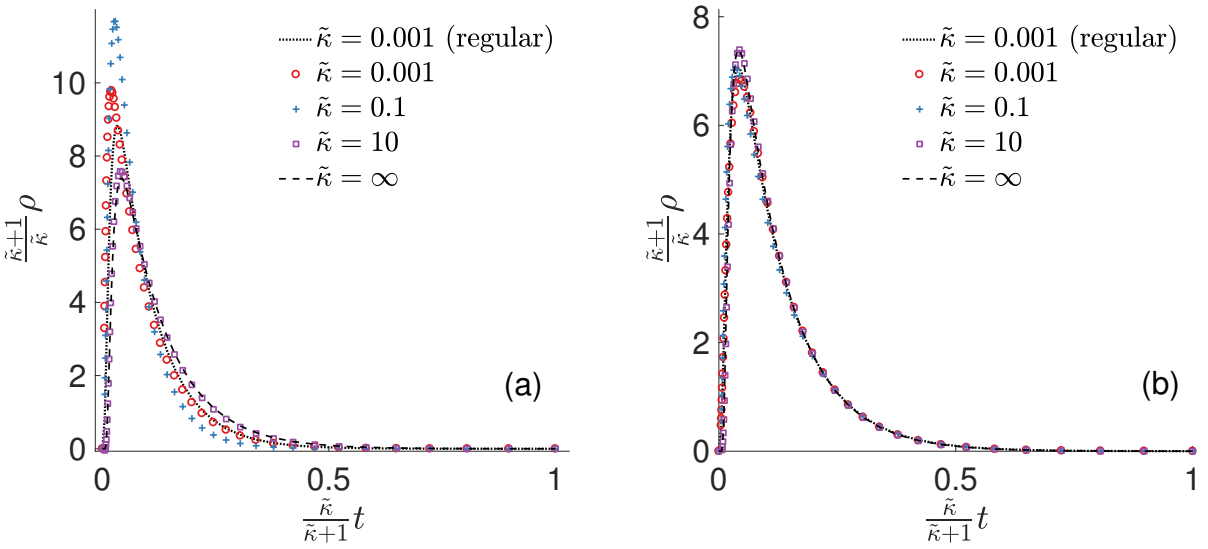

Figure B.3: The probability density of the first exit time from an interval segmented into $m = 11$ compartments by random barriers of variable mean resistance (such as in Fig. B.2). We apply the scale change: $t \to \tilde{\kappa}t/(\tilde{\kappa}+1)$, where $\tilde{\kappa}$ is computed either with Eq. (B.32) or Eq. (B.33). The dotted and dashed lines correspond to a regular geometry with quasi-impermeable and permeable barriers, respectively. (a) $\tilde{\kappa}$ is computed with Eq. (B.32). One can see that the curves corresponding to the regular geometry do not coincide very well, while the curves corresponding to the random structures exhibit large deviations between each other. (b) $\tilde{\kappa}$ is computed with Eq. (B.33). Visually, all the curves fall onto one master curve.

B.2.3 Relation to random hopping models

The above results allow us to investigate the particular case $\tilde{\kappa} \ll 1$. As discussed previously, in this regime the intra-compartment diffusion is much faster than the inter-compartment exchange, hence our diffusion model becomes equivalent to a random walk process on a discrete one-dimensional lattice of size m. The hopping rate from site i to site $i+1$ and from site i to site $i-1$ are respectively given by:

$$W_{i\to i+1} = \frac{\kappa_{i,i+1}}{l_i}, \quad \text{and} \quad W_{i\to i-1} = \frac{\kappa_{i-1,i}}{l_i}. \tag{B.35}$$

Such models of discrete random walks with random hopping rates have been considered by many authors [295–299], and in particular from the perspective of first exit times [300–305]. In particular, Murthy and Kehr discuss in [302] various cases for the distribution of the hopping rates $W_{i\to i+1}$. They consider discrete random walks starting from the left endpoint (site 0, reflecting condition) of the lattice and analyze the first exit time through the right endpoint (site N, absorbing condition). By reflecting the whole lattice with respect to the left endpoint, it is equivalent to a symmetric geometry with a starting point at the middle of the interval (and $m = 2N+2$). In two particular cases they obtain exact formulas for the mean first exit time:

- "Symmetric case", with $W_{i\to i+1} = W_{i+1\to i}$, which in our case corresponds to $l_i = l_{i+1} = l$.

The mean exit time is then given by

$$\mathbb{E}[T] \overset{MK89}{=} \sum_{i=1}^{N} \frac{i}{W_{m/2+i\to m/2+i+1}} = \frac{1}{2}\sum_{i=1}^{m-1} |i - m/2| l r_{i,i+1}$$
$$= \frac{1}{2}\sum_{i=1}^{m-1} |x_{i,i+1} - L/2| r_{i,i+1} = \frac{L^2}{8D\tilde{\kappa}} .$$

The first equality is from [302] (with suitable changes of notations). Using Eq. (B.35), we obtain at the end the same formula as Eq. (B.31) (recall that $\tilde{\kappa} \ll 1$ and $x = L/2$), where $\tilde{\kappa}$ is given by Eq. (B.33).

- "Random sojourn probabilities", with $W_{i\to i+1} = W_{i\to i-1}$, which translates into $r_{i,i+1} = r_{i-1,i} = r$. The mean exit time is given by

$$\mathbb{E}[T] \overset{MK89}{=} \sum_{i=1}^{N} \frac{i}{W_{m-i\to m-i+1}} = \sum_{i=1}^{N}\sum_{k=1}^{i} l_{m-i} r = \sum_{k=1}^{N}\left(\sum_{i=1}^{k} l_{m/2+i}\right) r$$
$$= \frac{1}{2}\sum_{k=1}^{m-1} |x_{k,k+1} - L/2| r = \frac{L^2}{8D\tilde{\kappa}} .$$

Again, the first equality is from [302]. By rearranging the sum, it transforms exactly into Eq. (B.31).

We conclude that our formula Eq. (B.33) introduces an effective permeability $\tilde{\kappa}$ which is consistent with the predictions of the random hopping rate models and accurately describes the first exit time distribution even for moderate number of barriers.

B.2.4 Diffusion inside disordered media

Diffusion in disordered media may be modeled by two classes of disorder (see Ref. [306] and references therein). In the first class, called "annealed disorder", the local environment in which particles diffuse changes over time scales comparable to the diffusion time scale and one is naturally led to model the diffusion coefficient D_0 as a stochastic process that evolves independently from the particle position. In contrast, when the disordered medium is static, the diffusion coefficient is a static function of position. Therefore the diffusivity felt by a particle is directly correlated with its position. This second situation is called "quenched disorder".

We consider here quenched disorder in the one-dimensional case from the point of view of first-passage time. Although unrelated in apparence, we discuss briefly how the study of diffusion through multiple membranes brings some insight into the problem of diffusion inside a random field of diffusivity $D_0(x)$. To this effect, we model a 1D disordered medium by an interval of fixed length L made of a very large number of subintervals with random lengths l_i and diffusion coefficients D_i. For simplicity we assume that l_i and D_i are independent random variables, except that we impose a symmetric geometry with respect to $x = L/2$. This geometry represents the discretized version of a continuous random diffusivity field $D_0(x)$, where the typical length of subintervals is the correlation length of $D_0(x)$. We emphasize that there are no barriers in this discrete geometry. However, we showed in Sec. 3.1.1 that a thin layer of size e and diffusivity D_e is equivalent to a permeable barrier with permeability $\kappa = D_e/e$. Therefore the results of the previous section lead us to distinguish two situations.

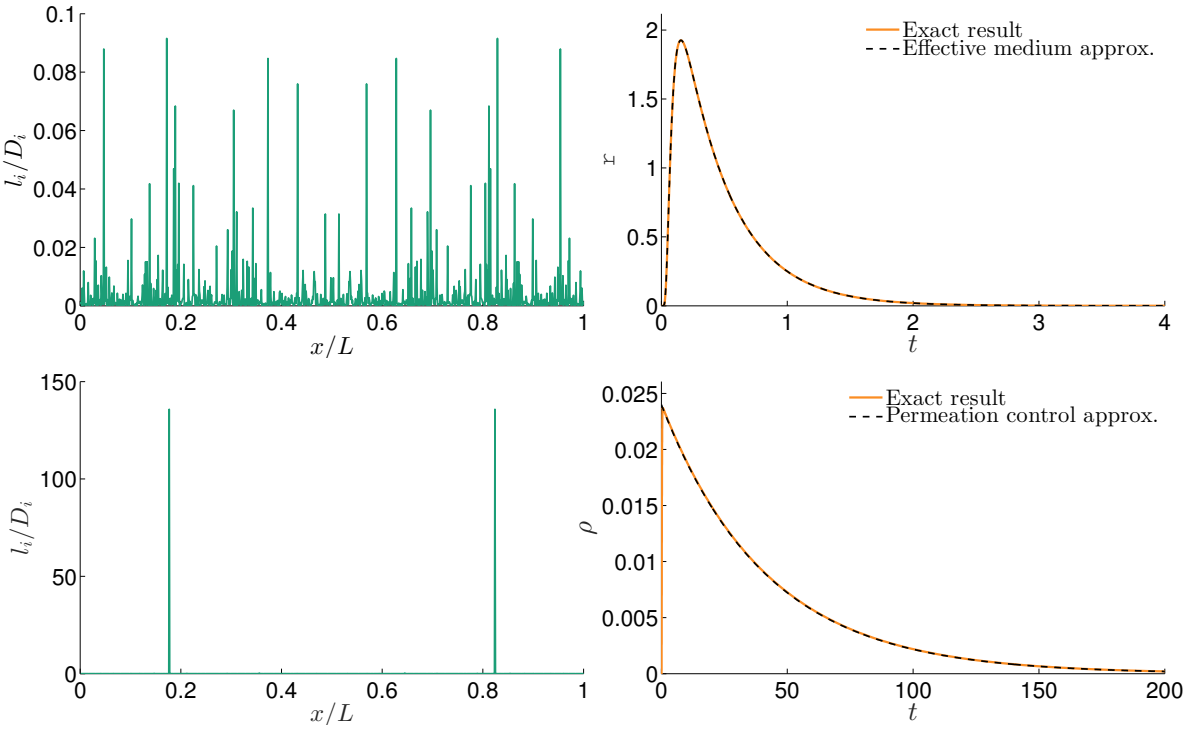

Figure B.4: We have plotted the distribution of effective barrier resistances $r_i = l_i/D_i$ for two different random media with $m = 1000$ compartments (left) and the corresponding first-exit time distribution computed for the same random media (right). In the self-averaging case (top), the quantity r_i is drawn from a distribution with finite average value, and the first exit-time distribution is equal to that of a homogeneous medium with diffusion coefficient $D_{\text{eff}} = \langle 1/D_i \rangle^{-1}$. In contrast, the non self-averaging case (bottom) generally yields few exceptional values of r_i that dominate the whole distribution. In that case the first-exit time distribution is controlled by permeation through this effective barrier and yields a mono-exponential decay of ρ after a very short transient regime.

Self-averaging situation

This corresponds to the case where $r_i = l_i/D_i$ has a finite average value, i.e. $1/D_i$ has a finite average value. This situation is illustrated on the top panel of Fig. B.4. The distribution of r_i over the whole interval exhibits several maxima therefore the disordered medium may be replaced by an interval with homogeneous diffusion coefficient and several barriers of resistances r_i. Since the number of barriers is very large, the reduced permeability can be computed from Eq. (B.32), that yields a diffusion coefficient $D_\infty = \langle 1/D_i \rangle^{-1}$.

Non self-averaging situation

This is the opposite situation where $\langle 1/D \rangle$ has an infinite average value. As we discuss in Appendix B.1.2, a random realization of r_i typically yields a few values that are much higher than the rest. This is illustrated on the bottom panel of Fig. B.4. Therefore, the medium may be replaced by an interval with homogeneous diffusion coefficient and few barriers of very high resistances. In the situation of Fig. B.4 where only one pair of barriers should be considered, the exit time is under permeation control, i.e. the kinetically limiting process is the barrier

crossing and not diffusion to the end of the interval. Therefore, the distribution of first exit times is mono-exponential after a very short transient time, and Eq. (B.59) yields the rate of the exponential decay:

$$\lambda = \frac{2}{r_{\max} L_{\max}} , \tag{B.36}$$

where $r_{\max}$ is the maximum value of r_i and $L_{\max}$ is the spacing between the corresponding barriers. Note that λ is exactly the inverse of the global exchange time of the effective interval of length $L_{\max}$, as expected (see Sec. 3.1.2).

B.3 Computation for the 1D case

This section contains technical developments related to Sec. 3.4. Sec. B.3.1 contains proofs of the existence of infinitely many eigenvalues, their non-degeneracy, their monotonic growth with respect to the barrier permeabilities, as well as a Courant nodal theorem for our particular model of diffusion with barriers. Then we present general computations for a finite periodic geometry with relaxation conditions at the outer boundaries in Sec. B.3.2. The case of infinite relaxation is of particular interest for the first-exit time distribution. The computations are also presented for more sophisticated structures such as bi-periodic (Sec. B.3.3) and two-scale geometry (Sec. B.3.4). The two final sections are devoted to technical results for the finite periodic geometry with impermeable endpoints. Sec. B.3.5 presents the limit of the signal in the zero- and infinite-permeability limit, and Sec. B.3.6 contains asymptotic expansions of the eigenvalues that are crucial for the discussion of the behavior of the dMRI signal.

B.3.1 Mathematical proofs

In this section we prove the non-degeneracy of the eigenvalues of the diffusion operator under the assumption that all inner membranes are permeable $\kappa_{i,i+1} > 0, i = 1, \dots, m-1$. In fact this statement involves two facts: (i) the eigenvalues λ_n of the diffusion operator are distinct; (ii) the zeros of F are simple, that is $F'(\lambda_n) \neq 0, n = 1, 2, \dots$ (in this section, prime denotes derivative with respect to λ). Furthermore we shall obtain as a corollary that there are infinitely many eigenvalues λ_n, that they grow monotonically with the inner and outer barrier permeabilities $\kappa_{i,i+1}$ and $K_\pm$, as well as a Courant nodal theorem for the eigenmodes.

The assumption of non-zero permeability is crucial. Indeed it is clear that any inner impermeable barrier would split the structure into two non-communicating parts. The eigenmodes for the whole structure would then be given by the eigenmodes for one part and the other separately. If the two parts are identical, each eigenvalue is twice degenerate. We make no other assumption about the geometry and we consider general relaxing outer boundary conditions.

Uniqueness of the eigenmodes

Let us assume that there exist two eigenmodes u and $\tilde{u}$ satisfying Eqs. (3.65)-(3.67), with the same eigenvalue λ. We shall prove that u is proportional to $\tilde{u}$. Because u and $\tilde{u}$ both satisfy Eq. (3.66c), one has $\frac{u'(0)}{u(0)} = \frac{\tilde{u}'(0)}{\tilde{u}(0)}$ hence there exists a constant A such that

$$u(0) - A\tilde{u}(0) = 0 \qquad \text{and} \qquad u'(0) - A\tilde{u}'(0) = 0 \,.$$

Let us denote $u - A\tilde{u}$ by w. This function satisfies Eqs. (3.65)-(3.67) because all these equations are linear. What remains to show is that w is equal to 0 over the whole interval $[0, L]$. We prove it by induction on the index of the compartment i. The main mathematical argument is Cauchy-Lipschitz uniqueness theorem for second order linear differential equations (U): "if f satisfies a second order linear differential equation over an interval Ω and $f(c) = f'(c) = 0$, with $c \in \Omega$, then $f(x) = 0$ for every $x \in \Omega$".

- We apply (U) to $w|_{\Omega_1}$: $w|_{\Omega_1}(0) = w'|_{\Omega_1}(0) = 0$ and $D_1 w''|_{\Omega_1} + \lambda w|_{\Omega_1} = 0$, hence $w|_{\Omega_1} = 0$.

- Let us assume that $w|_{\Omega_i} = 0$, with $0 < i < m-1$. Then, because $\kappa_{i,i+1} \neq 0$, the inner boundary conditions in Eqs. (3.66a) and (3.66b) imply that $w|_{\Omega_{i+1}}(x_{i,i+1}) = w'|_{\Omega_{i+1}}(x_{i,i+1}) = 0$. Because $w|_{\Omega_{i+1}}$ obeys the equation $D_{i+1}w''|_{\Omega_{i+1}} + \lambda w|_{\Omega_{i+1}} = 0$, one can apply again (U), which implies $w|_{\Omega_{i+1}} = 0$.

Simplicity of the zeros of F

Now we prove that $F'(\lambda_n) \neq 0$ for any eigenvalue λ_n. In order to simplify the notations we consider the case where $K_\pm$ are finite. However the proof follows the same steps in the case of infinite $K_\pm$. Throughout the proof we implicitly discard the case $\lambda = 0$. Let us recall that if we consider the function $v(\lambda, x)$ which satisfies Eqs. (3.65)-(3.66c) as well as the condition $v(0) = 1$ (we have proven above that this function is unique), then

$$F(\lambda) = \frac{K_+}{D_m} v(\lambda, L) + \frac{\partial v}{\partial x}(\lambda, L) \ . \tag{B.37}$$

Instead of writing v as a sum of sine and cosine functions (see Eq. (3.69)), we introduce an amplitude and phase representation:

$$v|_{\Omega_i}(x) = A_i(\lambda)\cos(\sqrt{\lambda/D_i}x + \phi_i(\lambda)) = A_i(\lambda)\cos(\Phi_i(\lambda, x)) \ , \tag{B.38}$$

with $A_i \geq 0$. It is clear from Eq. (3.69) that A_i and ϕ_i do not depend on x. Moreover we have proven in the above paragraph that $A_i(\lambda)$ is non-zero for all i and λ. We now translate the boundary conditions (3.66a)-(3.66d) in terms of Φ_i. Equation (3.66c) yields: $K_- A_i \cos\phi_1 + \sqrt{\lambda D_1}\sin\phi_1 = 0$, hence

$$\tan\phi_1 = -\frac{K_-}{\sqrt{\lambda D_1}} \qquad (-\pi/2 \leq \phi_1 \leq 0) \ . \tag{B.39}$$

Equtaions (3.66a) and (3.66b) can be restated as

$$-A_i\sqrt{\lambda D_i}\sin(\Phi_i) = -A_{i+1}\sqrt{\lambda D_{i+1}}\sin(\Phi_{i+1}) = \kappa_{i,i+1}(A_{i+1}\cos(\Phi_{i+1}) - A_i\cos(\Phi_i))$$

at $x = x_{i,i+1}$, hence by eliminating A_i and A_{i+1}, we get

$$\frac{\cot\Phi_i(\lambda, x_{i,i+1})}{\sqrt{D_i}} - \frac{\cot\Phi_{i+1}(\lambda, x_{i,i+1})}{\sqrt{D_{i+1}}} = r_{i,i+1}\sqrt{\lambda} \ , \tag{B.40}$$

with $0 \leq \Phi_{i+1}(\lambda, x_{i,i+1}) - \Phi_i(\lambda, x_{i,i+1}) < \pi$. Finally, one can rewrite Eq. (B.37) as

$$\begin{aligned} F(\lambda) &= A_m(\lambda)\left(\frac{K_+}{D_m}\cos\Phi_m(\lambda, L) - \sqrt{\lambda/D_m}\sin\Phi_m(\lambda, L)\right) \\ &= A_{m+1}(\lambda)\cos(\Phi_m(\lambda, L) + \phi_{m+1}(\lambda)) \ , \end{aligned} \tag{B.41}$$

with:

$$A_{m+1}(\lambda) = A_m(\lambda)\sqrt{\left(\frac{K_+}{D_m}\right)^2 + \frac{\lambda}{D_m}} \ , \qquad \cot\phi_{m+1}(\lambda) = \frac{K_+}{\sqrt{\lambda D_m}} \tag{B.42}$$

and $0 \leq \phi_{m+1} \leq \pi/2$. We have $A_{m+1}(\lambda) \neq 0$ for any λ and $-\pi/2 < \Phi_m(0,L) + \phi_{m+1}(0) \leq \pi/2$, hence Eq. (3.81) is equivalent to $\Phi_m(\lambda_n, L) + \phi_{m+1}(\lambda_n) = (2n-1)\pi/2$. The derivative of F at $\lambda = \lambda_n$ is then given by

$$F'(\lambda_n) = (-1)^n A_{m+1}(\lambda_n) \left(\Phi'_m(\lambda_n, L) + \phi'_{m+1}(\lambda_n)\right) . \tag{B.43}$$

It is clear from Eq. (B.42) that $\phi'_{m+1}(\lambda) \geq 0$ for any λ. In order to prove that $F'(\lambda_n) \neq 0$, it is then sufficient to show that $\Phi'_m(\lambda, L) > 0$. We prove by induction on the index of the compartment i that $\Phi'_i(\lambda, x)$ is positive for any λ and any $x \in \Omega_i$:

- From Eq. (B.39) we get that ϕ_1 is an increasing function of λ. As $\Phi_1(\lambda, x) = \sqrt{\lambda/D_1}x + \phi_1(\lambda)$, we immediately get that $\Phi'_1(\lambda, x) > 0$ for any $x \in \Omega_1$.
- Let us assume that $\Phi_i(\lambda, x_{i,i+1})$ is an increasing function of λ. According to Eq. (B.40), let us introduce the function:

$$f(\lambda, y) = \cot^{-1}\left(\sqrt{\frac{D_{i+1}}{D_i}}\cot y - r_{i,i+1}\sqrt{\lambda D_{i+1}}\right) . \tag{B.44}$$

  Because cot is a decreasing function, f is an increasing function of y and a non-decreasing function of λ, which implies that $\Phi_{i+1}(\lambda, x_{i,i+1}) = f(\lambda, \Phi_i(\lambda, x_{i,i+1}))$ is an increasing function of λ. It is then clear that $\Phi_{i+1}(\lambda, x) = \Phi_{i+1}(\lambda, x_{i,i+1}) + \sqrt{\lambda/D_{i+1}}(x - x_{i,i+1})$ is an increasing function of λ for any $x \in \Omega_{i+1}$.

This proves the simplicity of the zeros of F. Moreover, we also obtain that $\Phi_m(\lambda, L)$ grows indefinitely with λ. According to Eq. (B.41), this implies that there are infinitely many values of λ such that $F(\lambda) = 0$. In other words, there are infinitely many eigenvalues λ_n.

Monotonicity of the eigenvalues with respect to the permeabilities

The previous computations enable us to show that the eigenvalues grow monotonically with the inner and outer permeabilities $\kappa_{i,i+1}$ and $K_\pm$. In fact, because $\Phi_m(\lambda, L) + \phi_{m+1}(\lambda)$ is an increasing function of λ, we just have to prove that $\Phi_m(\lambda, L) + \phi_{m+1}(\lambda)$ is a non-increasing function of $\kappa_{i,i+1}$ and $K_\pm$, which follows immediately from Eqs. (B.39), (B.44) and (B.42).

Courant nodal theorem

Let us define the nodal domains of an eigenmode u_n as connected components on which u_n does not change sign. We prove here that u_n has exactly n nodal domains, which means that it changes sign $n-1$ times (recall that we numbered the modes $n = 1, 2, \ldots$). Note that these sign changes can occur at discontinuity points of u_n. The proof relies on the amplitude and phase representation detailed above. Let us then write

$$u_n(x) = A(\lambda_n, x)\cos(\Phi(\lambda_n, x)) , \tag{B.45}$$

where A and Φ are piecewise continuous functions of x defined by $A|_{\Omega_i} = A_i$ and $\Phi|_{\Omega_i} = \Phi_i$. The changes of sign of the eigenmode occur when the phase Φ crosses an odd multiple of $\pi/2$. Indeed, $A(\lambda_n, x)$ has a constant sign, and from Eq. (B.40) we get that the jumps of Φ at the

barriers are always less than π (which means that Φ cannot cross two odd multiples of $\pi/2$ at the same time).

Moreover, we know the phase at the left endpoint: $\Phi(\lambda_n, 0) = \phi_1(\lambda_n) \in [-\pi/2; 0]$ and the phase at the right endpoint: $\Phi(\lambda_n, L) = (2n-1)\pi/2 - \phi_{m+1}(\lambda_n) \in [(n-1)\pi; (n-1)\pi + \pi/2]$. We conclude that the interval $(\Phi(\lambda_n, 0); \Phi(\lambda_n, L))$ contains exactly $n-1$ odd multiple of $\pi/2$, thus the eigenmode has n nodal domains.

B.3.2 Computations for an array of identical cells with symmetric relaxation conditions at the outer boundaries

In this section we extend the computation presented in Sec. 3.4.3 by allowing relaxation or leakage at the endpoints of the interval. In other words, we relax the reflecting boundary conditions $K_\pm = 0$ at the outer membranes. In particular we will also study the limit $K_\pm \to \infty$ which is the perfectly relaxing case that we use in Appendix B.2. The cells are the same: $l_i = \ell_s, D_i = D_0, \kappa_{i,i+1} = \kappa$, and the relaxation coefficients are identical: $K_+ = K_- = K$. In addition to the notations (3.124), we introduce: $\tilde{K} = Kl/D$.

Eigenmodes

Because the geometry is symmetric we know that $\epsilon = \pm 1$. In this case we need to solve the general equation (3.126)

$$\mathsf{K}^{-1}\mathsf{M}^m \begin{bmatrix} \alpha \\ \tilde{K} \end{bmatrix} = \epsilon \begin{bmatrix} \alpha \\ -\tilde{K} \end{bmatrix} . \tag{B.46}$$

With the help of Eq. (3.128) we can compute the matrix $\mathsf{K}^{-1}\mathsf{M}^m$:

$$\mathsf{K}^{-1}\mathsf{M}^m = \begin{bmatrix} \cos\alpha \frac{\sin m\psi}{\sin\psi} - \frac{\sin(m-1)\psi}{\sin\psi} & \sin\alpha \frac{\sin m\psi}{\sin\psi} + \tilde{r}\alpha \frac{\sin(m-1)\psi}{\sin\psi} \\ -\sin\alpha \frac{\sin m\psi}{\sin\psi} & \cos\alpha \frac{\sin m\psi}{\sin\psi} - \frac{\sin(m-1)\psi}{\sin\psi} \end{bmatrix} . \tag{B.47}$$

Thus Eq. (B.46) yields the system

$$\begin{cases} \left(\cos\alpha + \tilde{K}\frac{\sin\alpha}{\alpha}\right)\frac{\sin m\psi}{\sin\psi} - \left(1 - \tilde{r}\tilde{K}\right)\frac{\sin(m-1)\psi}{\sin\psi} = \pm 1 \\ \left(\cos\alpha - \frac{1}{\tilde{K}}\alpha\sin\alpha\right)\frac{\sin m\psi}{\sin\psi} - \frac{\sin(m-1)\psi}{\sin\psi} = \mp 1 \end{cases} , \tag{B.48}$$

which is equivalent to the equation

$$\left(\cos\alpha + \frac{1}{2}\left(\frac{\tilde{K}}{\alpha} - \frac{\alpha}{\tilde{K}}\right)\sin\alpha\right)\frac{\sin m\psi}{\sin\psi} - \left(1 - \frac{\tilde{r}\tilde{K}}{2}\right)\frac{\sin(m-1)\psi}{\sin\psi} = 0 . \tag{B.49}$$

Combined with Eq. (3.127) it forms a system whose solutions α_n determine the eigenvalues λ_n. Compared to the $K = 0$ case from Sec. 3.4.3, the solutions α_n are modified and in general increase with $\tilde{K}$.

In the particular case $\tilde{K} = 2\tilde{\kappa}$, Eq. (B.49) simplifies into

$$\frac{\sin m\psi}{\sin\psi} = 0 \quad \text{or} \quad \cos\alpha + \frac{1}{2}\left(\frac{\tilde{K}}{\alpha} - \frac{\alpha}{\tilde{K}}\right)\sin\alpha = 0 . \tag{B.50}$$

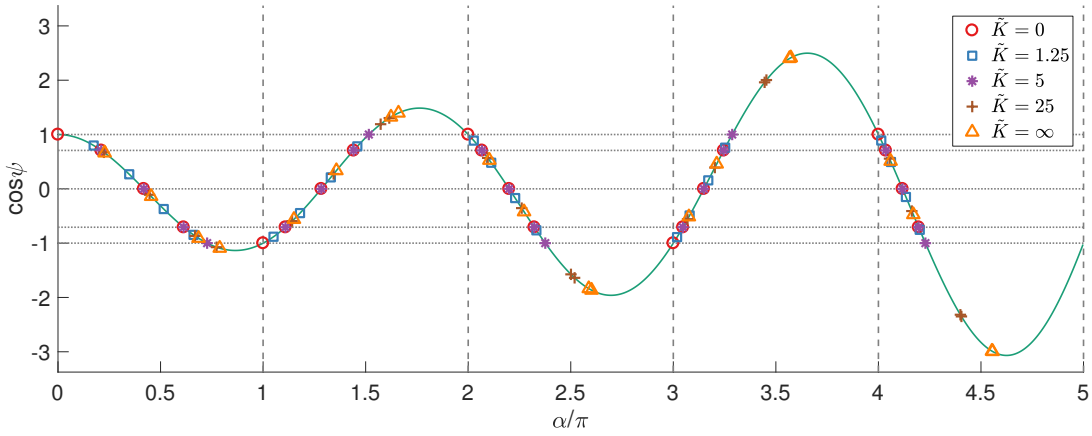

Figure B.5: Spectrum of the finite periodic geometry with $m = 4$ compartments and $\tilde{r} = 0.4$, for $\tilde{K} = 0$ (circles), $\tilde{K} = \tilde{\kappa}/2 = 1.25$ (squares), $\tilde{K} = 2\tilde{\kappa} = 5$ (asterisks), $\tilde{K} = 10\tilde{\kappa} = 25$ (pluses) and $\tilde{K} = \infty$ (triangles). The values of α increase with $\tilde{K}$. Notice how the spectra for $\tilde{K} = 0$ and $\tilde{K} = 2\tilde{\kappa}$ coincide except at the beginning and the end of the branches.

The first equation gives the $\alpha_{j,p}$ ($p = 1, \ldots, m-1$) from the earlier considered $K = 0$ case. The second equation gives the solutions of $\cos\psi = \pm 1$ that are not multiple of π (that we denote as $\alpha_{j,m}$ if j is even and $\alpha_{j,0}$ if j is odd, to be consistent with our previous notations). The condition $\tilde{K} = 2\tilde{\kappa}$ can be interpreted as "one inner barrier is equivalent to two stacked outer barriers" or equivalently "the crossing of one inner barrier transforms $\begin{bmatrix} -1 \\ \frac{\tilde{K}}{\alpha} \end{bmatrix}$ into $\begin{bmatrix} 1 \\ \frac{\tilde{K}}{\alpha} \end{bmatrix}$". In this way the reason why the $\alpha_{j,p}$ are solutions becomes clear: the matrix $\mathsf{K}\left(\mathsf{K}^{-1}\mathsf{M}^m\right) = \mathsf{M}^m$ should send $\begin{bmatrix} 1 \\ \frac{\tilde{K}}{\alpha} \end{bmatrix}$ onto plus or minus itself. The $\alpha_{j,p}$ (with $1 < p < m$) are solutions of $\mathsf{M}^m = \pm \mathsf{I}_2$ and the $\alpha_{j,0}$ and $\alpha_{j,m}$ are such that $\begin{bmatrix} 1 \\ \frac{\tilde{K}}{\alpha} \end{bmatrix}$ is an eigenvector of M.

As a consequence, the spectrum for the case $\tilde{K} = 2\tilde{\kappa}$ differs little from the spectrum for the impermeable outer boundary condition. The only difference lies in the beginning and the end of the branches (see Fig. B.5). This is nevertheless not a small difference because the eigenvalue $\lambda = 0$ (which is absent of the spectrum if $\tilde{K} > 0$) plays an important role in the long-time limit of the diffusion propagator as we have discussed in Sec. 3.4.6.

Beyond this special value of $\tilde{K}$, the solutions α_n continue to increase so that some values of ψ_n become complex (because $|\cos\psi| > 1$, which is apparent in Fig. B.5). More precisely they have the general form $\psi = ix$ or $\psi = \pi + ix$, with $x \in \mathbb{R}$. These values correspond to eigenmodes strongly localized inside the outer compartments. Indeed, Eq. (3.105) implies that the coefficients a and b vary like linear combinations of cosh and sinh functions of the compartment index i. The physical interpretation is simple: when $\tilde{K} \gg \tilde{\kappa}$ we are indeed in a regime where the leakage through the outer membranes is much faster than the exchange through the inner barriers. As a consequence the outer compartments evolve separately from the inner compartments, which corresponds mathematically to the existence of localized eigenmodes. On the other hand, when $\tilde{K} \ll \tilde{\kappa}$, the outer leakage is much slower than the inner exchange,

thus all compartments are coupled. We treat the limit $\tilde{K} \to \infty$ below in Sec. B.3.2.

Computation of the norm

The general formula (3.94) reads

$$\beta^{-2} = \frac{\ell_s}{2} \left| \frac{\mathrm{d}}{\mathrm{d}\alpha} \left(\begin{bmatrix} \frac{\tilde{K}}{\alpha} & 1 \end{bmatrix} \mathsf{T}(\alpha) \begin{bmatrix} 1 \\ \frac{\tilde{K}}{\alpha} \end{bmatrix} \right) \right|_{\alpha=\alpha_n} . \tag{B.51}$$

After lengthy computations, one gets

$$\begin{aligned} \beta^{-2} = {} & \frac{\epsilon \ell_s}{2} \frac{\sin\alpha \left(1 + \frac{\tilde{r}}{2}\right) + \frac{\tilde{r}}{2}\alpha\cos\alpha}{\sin^2\psi} \left(\left(\frac{\tilde{K}}{\alpha}\right)^2 \sin\alpha + 2\frac{\tilde{K}}{\alpha}\cos\alpha - \sin\alpha \right) \left(\frac{(m-1)\sin\psi}{\sin(m-1)\psi} - \cos m\psi \right) \\ & + \frac{\epsilon l}{2} \frac{\sin m\psi}{\sin\psi} \left(\frac{\sin\alpha}{\alpha} \left(1 + 2\tilde{K} + \left(\frac{\tilde{K}}{\alpha}\right)^2 \right) + \left(1 - \left(\frac{\tilde{K}}{\alpha}\right)^2 \right) \cos\alpha \right) . \end{aligned} \tag{B.52}$$

Note that when $\tilde{K} = 2\tilde{\kappa}$ we have to compute separately the cases $\psi = 0$ and $\psi = \pi$. We get

$$\beta^{-2} = \frac{m\ell_s}{2} \left(-\cos\alpha - 2\frac{\tilde{K}}{\alpha}\sin\alpha + \left(\frac{\tilde{K}}{\alpha}\right)^2 \left(\cos\alpha + \frac{m-1}{m\tilde{\kappa}} \right) + 2\frac{\tilde{K}}{m\alpha^2} \right) \qquad \text{if } \psi = 0,$$

$$\beta^{-2} = \frac{m\ell_s}{2} \left(\cos\alpha + 2\frac{\tilde{K}}{\alpha}\sin\alpha - \left(\frac{\tilde{K}}{\alpha}\right)^2 \left(\cos\alpha - \frac{m-1}{m\tilde{\kappa}} \right) + 2\frac{\tilde{K}}{m\alpha^2} \right) \qquad \text{if } \psi = \pi.$$

Fourier transform

Except for the conditions at the outer boundaries, the geometry is the same as in Sec. 3.4.5. Hence the computation follows the same steps. Using the condition (B.46), we are led to compute the product

$$\mathsf{L} \left(\mathsf{I}_2 - e^{i\tilde{q}} \mathsf{R}^{-1} \mathsf{K}^{-1} \right) \left(\mathsf{I}_2 - \epsilon e^{im\tilde{q}} \mathsf{K} \mathsf{S} \right) \begin{bmatrix} \alpha \\ \tilde{K} \end{bmatrix} .$$

Skipping the technical computations, one gets depending on $\epsilon = \pm 1$

$$\int_0^L v(x) e^{i\tilde{q}x} \, \mathrm{d}x = \frac{e^{im\tilde{q}/2} 2\ell_s}{(\tilde{q}^2 - \alpha)^2 (\cos\tilde{q} - \cos\psi)} (A\cos(m\tilde{q}/2) + B\sin(m\tilde{q}/2)) \qquad \text{if } \epsilon = +1, \tag{B.53}$$

$$\int_0^L v(x) e^{i\tilde{q}x} \, \mathrm{d}x = \frac{-ie^{im\tilde{q}/2} 2\ell_s}{(\tilde{q}^2 - \alpha)^2 (\cos\tilde{q} - \cos\psi)} (A\sin(m\tilde{q}/2) - B\cos(m\tilde{q}/2)) \qquad \text{if } \epsilon = -1, \tag{B.54}$$

where

$$A = \tilde{K} \left((\cos\alpha - \cos\tilde{q}) + \frac{\tilde{r}}{2} (\tilde{q}\sin\tilde{q} - \alpha\sin\alpha) \right) , \quad B = \tilde{q}(\cos\tilde{q} - \cos\alpha) \left(1 - \frac{\tilde{r}\tilde{K}}{2} \right) . \tag{B.55}$$

Complete expression of the dMRI signal

According to Eq. (3.138), the signal is expressed as a sum over all eigenmodes u_n. We recall that the eigenmodes are alternately symmetric (odd n) and anti-symmetric (even n). Combining the above results (B.52)-(B.55), one gets

$$S = \sum_{n=1}^{\infty} \frac{\left(A_n^2 + B_n^2 + (-1)^{n-1}(A_n^2 - B_n^2)\cos m\tilde{q} + (-1)^{n-1} 2A_n B_n \sin m\tilde{q}\right) 4\beta_n^2 e^{-\alpha_n^2 \tilde{t}}}{(\tilde{q}^2 - {\alpha_n}^2)^2(\cos\tilde{q} - \cos\psi_n)^2}\,, \tag{B.56}$$

where β_n is given by Eq. (B.52), A_n and B_n by Eq. (B.55), ψ_n by Eq. (3.127) and α_n are solutions of Eq. (B.49). For $m = 1$, we recover the signal derived by Coy and Callaghan [87].

Perfectly relaxing outer boundaries

Note that the limit $\tilde{K} \to \infty$ is singular because of the chosen normalization (3.68). This is particularly clear in Eq. (3.77) where $b_1^l \to \infty$. In fact, $\tilde{K} = \infty$ represents Dirichlet conditions at the outer boundaries: $u(0) = u(L) = 0$. To avoid the singularity we use another normalization:

$$u = \beta w\,, \quad w'(0) = \sqrt{\lambda/D}\,, \tag{B.57}$$

which corresponds to the coefficients (for w)

$$\begin{bmatrix} a_1^l \\ b_1^l \end{bmatrix} = \begin{bmatrix} \frac{\sqrt{\lambda D_1}}{K_-} \\ 1 \end{bmatrix}\,.$$

When $\tilde{K} \to \infty$, Eq. (B.49) simplifies into

$$\sin\alpha \frac{\sin m\psi}{\sin\psi} + \tilde{r}\alpha \frac{\sin(m-1)\psi}{\sin\psi} = 0\,. \tag{B.58}$$

We now study the solutions of this equation in three different regimes: high-permeability, low-permeability, and very large number of compartments. We rely on the discussion developed in Sec. 3.4.2, which leads us to the following conclusions.

High-permeability regime In the high-permeability regime ($\tilde{r} \ll 1$), the solutions are located near the limits $\alpha_0 = n\pi/m$, which correspond also to $\psi_0 = n\pi/m$ ($n = 1, 2, \ldots$). More precisely one can compute the first-order expansion:

$$\begin{cases} \alpha_n \approx \dfrac{n\pi}{m}\left(1 - \dfrac{\tilde{r}(m-2)}{2m}\right) & \text{if } n \text{ is not a multiple of } m, \\ \alpha_n \approx \dfrac{n\pi}{m}\left(1 - \dfrac{\tilde{r}(m-1)}{m}\right) & \text{otherwise.} \end{cases}$$

As already noted this case presents no difficulty from the numerical point of view.

Low-permeability regime In the low-permeability regime ($\tilde{\kappa} \ll 1$), the solutions are divided into two categories.

• First, the solutions corresponding to the "inner" compartments: $1 < k < m$. These solutions form groups located around $\alpha_0 = j\pi$ (j being an integer). In fact they correspond to $\psi \in \mathbb{R}$, at which $\sin(m\psi)$ and $\sin((m-1)\psi)$ are of the same order. This implies that Eq. (B.26) becomes in the low-permeability limit

$$\frac{\sin((m-1)\psi)}{\sin\psi} = 0 \,,$$

which is (almost) the equation of the spectrum of $m-1$ identical cells with impermeable outer boundaries (3.130). One gets simply the solutions $\psi_0 = p\pi/(m-1)$, $p = 1, \ldots, m-2$, thus the solutions in the first category are approximately determined by

$$\cos\alpha - \frac{\tilde{r}}{2}\alpha\sin\alpha = \cos(p\pi/(m-1)), \quad p = 1, \ldots, m-2 \,.$$

We study this equation in details in Sec. B.3.6. In particular, applying Eq. (B.94) one gets for the $m-2$ first solutions:

$$\alpha_n \approx 2\sqrt{\tilde{\kappa}}\sin\left(\frac{n\pi}{2(m-1)}\right) \,, \quad n = 1, \ldots, m-2 \,. \tag{B.59}$$

• Second, the solutions corresponding to the outer compartments $k = 1, m$. These solutions form pairs $\alpha_\pm$ such that

$$\left(n+\frac{1}{2}\right)\pi - \alpha_+ \approx \left(n+\frac{1}{2}\right)\pi - \alpha_- \sim \frac{\tilde{\kappa}}{(n+1/2)\pi} \,,$$
$$\alpha_+ - \alpha_- \sim \left(\frac{\tilde{\kappa}}{(n+1/2)\pi}\right)^{m-1} \,,$$

with $n = 1, 2, \ldots$. Therefore in the low-permeability limit ($\tilde{\kappa} \to 0$) these pairs are very difficult to detect, especially when one is dealing with a large number of compartments m. As explained in Sec. 3.4.4, even if one finds the roots, the subsequent computation of the eigenmodes and their norm may be inaccurate. However in this regime these solutions are much larger than the smallest one from the first category which goes to zero according to Eq. (B.59). Hence they have little influence on the first exit time distribution (B.23) because of the very fast exponential decay compared to the first terms of the sum.

Limit $m \to \infty$ From the above discussion we get that the $m-2$ first solutions of Eq. (B.26), $\alpha_1, \ldots, \alpha_{m-2}$, satisfy

$$n\pi/m < \psi_n < n\pi/(m-1) \,, \quad n = 1, \ldots, m-2 \,.$$

Thus one may write $\psi_n = \frac{n\pi}{m-x}$, with $0 < x < 1$. Let us rewrite Eq. (B.26) as

$$\sin\alpha_n \sin(m\psi_n) + \tilde{r}\alpha_n \sin((m-1)\psi_n) = (-1)^n \left[\sin\alpha_n \sin\left(\frac{xn\pi}{m-x}\right) - \tilde{r}\alpha_n \sin\left(\frac{(1-x)n\pi}{m-x}\right)\right]$$
$$= 0 \,.$$

Now we study the limit $m \to \infty$ with fixed n. Then $\psi_n, \alpha_n \ll 1$ and the above equation transforms into

$$\frac{(-1)^n \alpha_n n\pi}{m-x}(x - \tilde{r}(1-x)) = 0\,,$$

from which we get $x = \tilde{r}/(1+\tilde{r}) = 1/(1+\tilde{\kappa})$. Let us use the expansion (3.161):

$$\alpha_n \approx \sqrt{\frac{\tilde{\kappa}}{\tilde{\kappa}+1}}\frac{n\pi}{m-\frac{1}{\tilde{\kappa}+1}} \approx \sqrt{\frac{\tilde{\kappa}\left(1+\frac{2}{m}\right)}{\tilde{\kappa}\left(1+\frac{2}{m}\right)+1}}\frac{n\pi}{m}\,, \quad n = 1, \dots, m-2\,. \tag{B.60}$$

Computation of the norm

The formula (3.94) for the norm becomes

$$\beta^{-2} = \int_0^L w^2 = \frac{-\sqrt{D_1}}{2\eta}\frac{\mathrm{d}}{\mathrm{d}\sqrt{s}}\left(\begin{bmatrix}\frac{K_+}{K_-} & \frac{\sqrt{D_m s}}{K_-}\end{bmatrix}\mathsf{T}(s)\begin{bmatrix}\frac{\sqrt{D_1 s}}{K_-}\\ 1\end{bmatrix}\right)\Bigg|_{s=\lambda}\,.$$

In the particular geometry we are dealing with and in the case $\tilde{K} = \infty$, this gives

$$\beta^{-2} = \frac{-\epsilon\ell_s}{2}\left|\begin{bmatrix}1 & 0\end{bmatrix}\frac{\mathrm{d}\mathsf{T}}{\mathrm{d}\alpha}\begin{bmatrix}0\\1\end{bmatrix}\right| \tag{B.61}$$

$$= \frac{-\epsilon m\ell_s}{2}\frac{\sin\alpha\left(1+\frac{\tilde{r}}{2}\right)+\frac{\tilde{r}}{2}\alpha\cos\alpha}{\sin^2\psi}\left[\sin\alpha\cos m\psi + \frac{\tilde{r}\alpha(m-1)}{m}\cos((m-1)\psi)\right]$$
$$+ \frac{\epsilon m\ell_s}{2}\left(\frac{\sin\alpha}{\alpha}-\cos\alpha\right)\frac{\sin m\psi}{m\sin\psi}\,. \tag{B.62}$$

Computation of the Fourier transform

In the same way, the computation of the Fourier transform of w simplifies into

$$\frac{e^{im\tilde{q}/2}2\ell_s\alpha}{(\tilde{q}^2-\alpha)^2(\cos\tilde{q}-\cos\psi)} \times \begin{cases} A\cos(m\tilde{q}/2) + B\sin(m\tilde{q}/2) & \text{if } \epsilon = +1 \\ -i(A\sin(m\tilde{q}/2) - B\cos(m\tilde{q}/2)) & \text{if } \epsilon = -1 \end{cases}\,, \tag{B.63}$$

with

$$A = \left[(\cos\alpha - \cos\tilde{q}) + \frac{\tilde{r}}{2}(\tilde{q}\sin\tilde{q} - \alpha\sin\alpha)\right]\,, \quad B = \frac{\tilde{r}}{2}\tilde{q}(\cos\alpha - \cos\tilde{q})\,. \tag{B.64}$$

B.3.3 Bi-periodic geometry

In this section, we briefly apply our method to the computation of the spectrum of the diffusion operator on a finite periodic geometry where the elementary block is made of two different compartments (repeated M times). Such a system may model laminated steel coils in industrial processes [243, 244] or intra- and extra-cellular spaces in biology [192, 270, 272]. This is also a good example of the numerical simplifications that our method enables. The lengths of the compartments are denoted by l_e and l_i, their diffusion coefficients by D_e and D_i and the barrier between the two compartments has a permeability κ (or equivalently a resistance $r = 1/\kappa$). For

simplicity we assume reflecting boundary conditions at the outer boundaries. Let us introduce the notations

$$\tau_i = l_i^2/D_i \qquad \text{and} \qquad \tau_e = l_e^2/D_e \ . \tag{B.65}$$

In that case, the equation (3.78) on the spectrum is $\mathsf{M}^M \begin{bmatrix} 1 \\ 0 \end{bmatrix} = \epsilon \begin{bmatrix} 1 \\ 0 \end{bmatrix}$, with

$$\mathsf{M} = \begin{bmatrix} 1 & r\sqrt{\lambda D_i} \\ 0 & \sqrt{D_i/D_e} \end{bmatrix} \begin{bmatrix} \cos(\sqrt{\lambda\tau_i}) & \sin(\sqrt{\lambda\tau_i}) \\ -\sin(\sqrt{\lambda\tau_i}) & \cos(\sqrt{\lambda\tau_i}) \end{bmatrix} \begin{bmatrix} 1 & r\sqrt{\lambda D_e} \\ 0 & \sqrt{D_e/D_i} \end{bmatrix} \begin{bmatrix} \cos(\sqrt{\lambda\tau_e}) & \sin(\sqrt{\lambda\tau_e}) \\ -\sin(\sqrt{\lambda\tau_e}) & \cos(\sqrt{\lambda\tau_e}) \end{bmatrix} . \tag{B.66}$$

Because the geometry is *not* symmetric, ϵ is not necessary equal to ± 1. Moreover we have $\epsilon\eta = \sqrt{D_e/D_i}$. Following the same reasoning as in Sec. 3.4.3, we obtain that the solutions of Eq. (3.78) can be decomposed into two types:

- the ones such that $\begin{bmatrix} 1 \\ 0 \end{bmatrix}$ is an eigenvector of the transition matrix of one block, M, from Eq. (B.66). This gives the condition:

$$r\sqrt{\lambda D_i D_e} = \sqrt{D_i}\cot(\sqrt{\lambda\tau_e})\sin(\sqrt{\lambda\tau_i}) + \sqrt{D_e}\sin(\sqrt{\lambda\tau_e})\cot(\sqrt{\lambda\tau_i}) \ . \tag{B.67}$$

  Moreover, one has

$$\epsilon = \left(\cos(\sqrt{\lambda\tau_e})\cos(\sqrt{\lambda\tau_i}) - \sqrt{\frac{D_i}{D_e}}\sin(\sqrt{\lambda\tau_e})\sin(\sqrt{\lambda\tau_i}) - r\sqrt{\lambda D_i}\cos(\sqrt{\lambda\tau_e})\sin(\sqrt{\lambda\tau_i})\right)^{-M} ; \tag{B.68}$$

- the ones such that $\mathrm{Tr}(\mathsf{M}) = 2\cos p\pi/M$, with $p = 1, \dots, M-1$, which corresponds to $\mathsf{M}^M = (-1)^p \mathsf{I}_2$ and thus to $\epsilon = (-1)^p$. This gives the equation

$$\begin{aligned} 2\cos p\pi/M = 2\cos(\sqrt{\lambda\tau_e})\cos(\sqrt{\lambda\tau_i}) &- \left(\sqrt{\frac{D_i}{D_e}} + \sqrt{\frac{D_e}{D_i}}\right)\sin\left(\sqrt{\lambda\tau_e}\right)\sin\left(\sqrt{\lambda\tau_i}\right) \\ &- 2r\sqrt{\lambda}\left(\sqrt{D_e}\sin\left(\sqrt{\lambda\tau_e}\right)\cos\left(\sqrt{\lambda\tau_i}\right) + \sqrt{D_i}\cos\left(\sqrt{\lambda\tau_e}\right)\sin\left(\sqrt{\lambda\tau_i}\right)\right) \\ &+ r^2\lambda\sqrt{D_i D_e}\sin\left(\sqrt{\lambda\tau_e}\right)\sin\left(\sqrt{\lambda\tau_i}\right) \ , \qquad p = 1, \dots, M-1 \ . \end{aligned} \tag{B.69}$$

It is interesting to compare the above equations with the analysis conducted in Sec. 3.4.2. Indeed, one can see that in the limit of quasi-impermeable barriers ($r \to \infty$), Eq. (B.67) yields approximately

$$\sqrt{\lambda/D_e} \approx \frac{n\pi}{l_e} + \frac{1}{n\pi r D_e} \qquad \text{and} \qquad \sqrt{\lambda/D_i} \approx \frac{n\pi}{l_i} + \frac{1}{n\pi r D_i} \ , \quad n = 1, 2, \dots , \tag{B.70}$$

which is exactly Eq. (3.112) with $\zeta = 1$, that is for the outer compartments. In the same way, Eq. (B.69) yields approximately

$$\begin{aligned} \sqrt{\lambda/D_e} &\approx \frac{n\pi}{l_e} + \frac{2}{n\pi r D_e} + \frac{l_e\sqrt{D_e/D_i}X_p}{(n\pi r D_e)^2} \ , \\ \sqrt{\lambda/D_i} &\approx \frac{n\pi}{l_i} + \frac{2}{n\pi r D_i} + \frac{l_i\sqrt{D_i/D_e}Y_p}{(n\pi r D_i)^2} \ , \end{aligned} \tag{B.71}$$

where $n = 1, 2, \ldots$, and X_p, Y_p are dimensionless coefficients which depend on the value of $\cos p\pi/M$, with $p = 1, \ldots, M-1$. One recognizes the first order correction from Eq. (3.112) for inner compartments. The second order correction is also discussed in Eq. (3.4.2) and arises from the next-nearest neighbor coupling between the compartments of the same type. Therefore, in the low-permeability limit, the spectrum is made of groups of M closely packed eigenvalues located around $\lambda = D_e(n\pi/l_e)^2$ or $\lambda = D_i(n\pi/l_i)^2$: one eigenvalue is given by Eq. (B.67) then the following $M-1$ eigenvalues are given by Eq. (B.69). These groups correspond to eigenmodes localized inside all compartments of type "e" or "i", respectively. More precisely, the first eigenvalue of each group corresponds to an eigenmode localized inside an outer compartment and the $M-1$ following eigenvalues correspond to eigenmodes localized inside all inner compartments.

Equations (B.67) and (B.69) "disentangle" these groups of eigenvalues, that allows one to compute very fast the spectrum of the diffusion operator for any number of repetitions M and any barrier permeability. This is a major simplification of the numerical problem of the determination of the spectrum (see Sec. 3.4.2 and 3.4.4). The same remark applies to any finite periodic geometry, provided that the repeated elementary block is not too long.

B.3.4 Two-scale geometry

Eigenmodes

We consider again the repetition of an elementary block but without restricting ourselves to a small block. Indeed the structure is the repetition of M arrays of N identical cells, each array being separated from others by a "large barrier" (see Fig. B.6). For simplicity we assume reflecting boundary conditions at the endpoints. The cells are of length l, the barriers are of permeability κ, the diffusion coefficient is D, and the "larger barriers" are of permeability κ_L. In addition to the notations (3.124), we introduce:

$$\tilde{r}_L = 1/\tilde{\kappa}_L = D/(\kappa_L l) \quad \text{and} \quad \tilde{\rho} = \tilde{r}_L - \tilde{r}\ . \tag{B.72}$$

Strictly speaking, $\tilde{\rho}$ may be negative, however we have in mind the opposite case where the "larger barriers" are less permeable than the inner barriers.

We have two different matrices to consider:

- the matrix associated to the microstructure is $\mathsf{M}_1 = \begin{bmatrix} 1 & \tilde{r}\alpha \\ 0 & 1 \end{bmatrix} \begin{bmatrix} \cos\alpha & \sin\alpha \\ -\sin\alpha & \cos\alpha \end{bmatrix}$.
- the matrix associated to the macrostructure is $\mathsf{M}_2 = \begin{bmatrix} 1 & \tilde{\rho}\alpha \\ 0 & 1 \end{bmatrix} {\mathsf{M}_1}^N$.

Thanks to the formula (3.128), we can compute the matrix M_2:

$$\mathsf{M}_2 = \frac{1}{\sin\psi} \begin{bmatrix} \sin(N+1)\psi & (\sin\alpha + \tilde{R}\alpha\cos\alpha)\sin N\psi \\ -(\cos\alpha + \tilde{\rho}\alpha\sin\alpha)\sin N\psi & -\tilde{\rho}\alpha\sin(N-1)\psi \\ -\sin\alpha\sin N\psi & \cos\alpha\sin N\psi - \sin(N-1)\psi \end{bmatrix}. \tag{B.73}$$

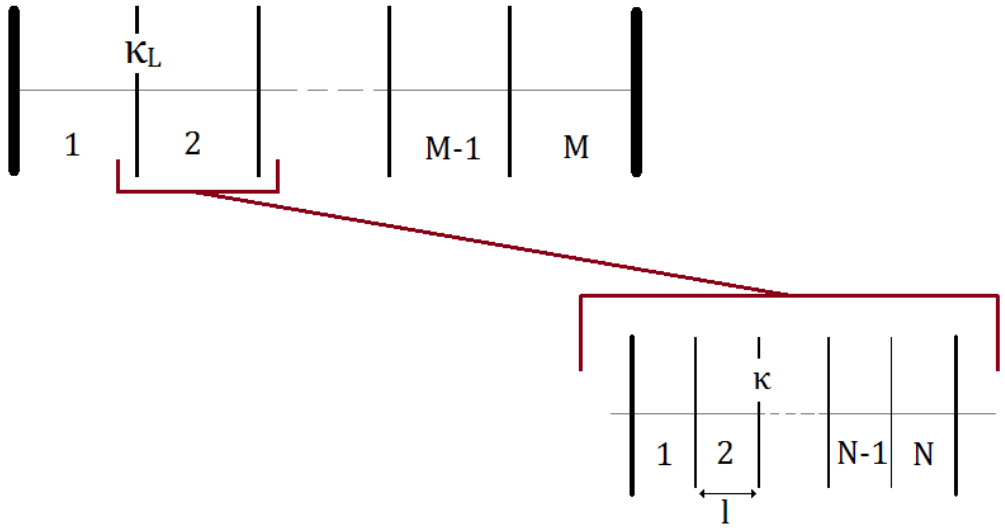

Figure B.6: Illustration of the two-scale geometry, which is a repetition of M blocks of N cells. All the cells have the same length l and diffusion coefficient D and are separated by barriers of permeability κ. The blocks are separated by barriers of permeability κ_L.

Since the geometry is symmetric, Eq. (3.78) of the spectrum is

$$\mathsf{M}_2{}^M \begin{bmatrix} 1 \\ 0 \end{bmatrix} = \epsilon \begin{bmatrix} 1 \\ 0 \end{bmatrix} , \tag{B.74}$$

with $\epsilon = \pm 1$, and by analogy with the finite periodic geometry from Sec. 3.4.3 we have two cases:

- $\sin\alpha \frac{\sin N\psi}{\sin\psi} = 0$: the vector $\begin{bmatrix} 1 \\ 0 \end{bmatrix}$ is an eigenvector of the matrix M_2. This condition gives exactly the solutions $\alpha_{j,p}$, $j = 0, 1, \ldots$ and $p = 0, \ldots, N$ (Sec. 3.4.3). One has $\epsilon = (-1)^{pM}$.
- The trace of the matrix M_2 is $2\cos P\pi/M$, for $P \in \{1, \ldots, M-1\}$: $\mathsf{M}_2{}^M$ is plus or minus the identity matrix I_2, which gives the condition:

$$\cos N\psi - \frac{\tilde{r}}{2}\alpha \sin\alpha \frac{\sin N\psi}{\sin\psi} = \cos P\pi/M , \quad P = 1, \ldots, M-1 . \tag{B.75}$$

  In this case $\epsilon = (-1)^P$. Again, we use a special notation for the solutions: $\alpha_{j,p,P}$, where the index j means $j\pi \leq \alpha_{j,p,P} < (j+1)\pi$ and the index p means $p\pi/N \leq \psi_{j,p,P} < (p+1)\pi/N$. The $P = 0$ (resp., $P = M$) case corresponds then to the solutions for the finite periodic case $\alpha_{j,p}$ if p is even (resp. if p is odd).

The interpretation of the indices j, p, P follows the same line of reasoning as with the simple periodic geometry: they give the intra-compartment, inter-compartment (or intra-block) and inter-block variation of the mode, respectively..

Computation of the norm:

We use again Eq. (3.103):

$$\begin{bmatrix}0 & 1\end{bmatrix}\mathsf{T}\begin{bmatrix}1\\0\end{bmatrix} = \begin{bmatrix}0 & 1\end{bmatrix}(\mathsf{K}_2\mathsf{M}^N)^M\begin{bmatrix}1\\0\end{bmatrix} = \frac{\sin M\phi}{\sin\phi}\begin{bmatrix}0 & 1\end{bmatrix}\mathsf{K}_2\mathsf{M}^N\begin{bmatrix}1\\0\end{bmatrix}$$
$$= \frac{\sin M\phi}{\sin\phi}\frac{\sin N\psi}{\sin\psi}\begin{bmatrix}0 & 1\end{bmatrix}\mathsf{M}\begin{bmatrix}1\\0\end{bmatrix} = -\frac{\sin M\phi}{\sin\phi}\frac{\sin N\psi}{\sin\psi}\sin\alpha\,, \tag{B.76}$$

where we have introduced ϕ defined by

$$\cos\phi = \frac{1}{2}\mathrm{Tr}(\mathsf{K}_2\mathsf{M}^m) = \cos N\psi - \frac{\tilde{r}}{2}\alpha\sin\alpha\frac{\sin N\psi}{\sin\psi}\,. \tag{B.77}$$

Now we have three cases:

1. $\sin\alpha = 0$, which corresponds to $\alpha_{j,0}$ and $\alpha_{j,N}$. One gets
$$\beta^2 = \frac{2}{MNl}\,.$$

2. $\frac{\sin N\psi}{\sin\psi} = 0$, which corresponds to $\alpha_{j,p}, p = 1,\ldots,N-1$. In this case we get
$$\beta^2_{j,p} = \frac{2}{ml}\frac{\sin^2 p\pi/N}{\sin\alpha_{j,p}\left(\sin\alpha_{j,p}\left(1+\frac{\tilde{r}}{2}\right)+\frac{\tilde{r}}{2}\alpha_{j,p}\cos\alpha_{j,p}\right)}\,.$$

3. $\frac{\sin M\phi}{\sin\phi} = 0$, which corresponds to the general case. We use the chain rule again to compute the derivative with respect to α:
$$\frac{\mathrm{d}}{\mathrm{d}\alpha}\left(\frac{\sin M\phi}{\sin\phi}\right) = \frac{\mathrm{d}\cos\phi}{\mathrm{d}\alpha}\frac{\mathrm{d}\phi}{\mathrm{d}\cos\phi}\frac{\mathrm{d}}{\mathrm{d}\phi}\left(\frac{\sin M\phi}{\sin\phi}\right)\,,$$
$$\frac{\mathrm{d}\cos\phi}{\mathrm{d}\alpha} = -N\frac{1-\cos N\psi\cos P\pi/M}{\sin N\psi\sin\psi}\left[\left(1+\frac{\tilde{r}}{2}\right)\sin\alpha+\frac{\tilde{r}}{2}\alpha\cos\alpha\right]$$
$$+\frac{\cos N\psi-\cos P\pi/M}{\sin^2\psi}\left[\frac{\sin^2\alpha}{\alpha}+\frac{\tilde{r}}{2}(\alpha+\sin\alpha\cos\alpha)\right]\,,$$
$$\frac{\mathrm{d}\phi}{\mathrm{d}\cos\phi}\frac{\mathrm{d}}{\mathrm{d}\phi}\left(\frac{\sin M\phi}{\sin\phi}\right) = \left(\frac{-1}{\sin P\pi/M}\right)\left(\frac{(-1)^P}{\sin P\pi/M}\right)\,.$$

Hence we get the normalization constant:

$$\beta^2_{j,p,P} = \left.\frac{\frac{2\sin^2(P\pi/M)\sin\psi}{ml\sin\alpha\sin N\psi}}{\left[\begin{array}{l}\frac{1-\cos N\psi\cos P\pi/M}{\sin N\psi\sin\psi}\left(\left(1+\frac{\tilde{r}}{2}\right)\sin\alpha+\frac{\tilde{r}}{2}\alpha\cos\alpha\right)\\ \quad+\frac{\cos N\psi-\cos P\pi/M}{N\sin^2\psi}\left(\frac{\sin^2\alpha}{\alpha}+\frac{\tilde{r}}{2}(\alpha+\sin\alpha\cos\alpha)\right)\end{array}\right]}\right|_{\alpha=\alpha_{j,p,P}}\,. \tag{B.78}$$

Fourier transform

In the same way as for the finite periodic geometry, we have only one L to consider, so we need to compute

$$\begin{aligned}\sum_i e^{ik\tilde{q}}\mathsf{L}_i \begin{bmatrix} a_i^l \\ b_i^l \end{bmatrix} &= \mathsf{L}\sum_{i=0}^{M-1}\sum_{i=0}^{N-1} e^{i\tilde{q}(KN+k)}{\mathsf{M}_1}^k{\mathsf{M}_2}^K \begin{bmatrix} 1 \\ 0 \end{bmatrix} \\ &= \mathsf{L}(\mathsf{I}_2 - e^{i\tilde{q}}\mathsf{M}_1)^{-1}(\mathsf{I}_2 - e^{iN\tilde{q}}{\mathsf{M}_1}^N)(\mathsf{I}_2 - e^{i\tilde{q}N}\mathsf{M}_2)^{-1}(\mathsf{I}_2 - e^{iNM\tilde{q}}{\mathsf{M}_2}^M)\begin{bmatrix} 1 \\ 0 \end{bmatrix}. \end{aligned} \tag{B.79}$$

Using Eq. (B.74) on the spectrum and the linearity of the comatrix operation, we get to simplify a lot the above expression:

$$\sum_i e^{ik\tilde{q}}\mathsf{L}_i \begin{bmatrix} a_i^l \\ b_i^l \end{bmatrix} = (1-(-1)^P e^{iNM\tilde{q}})\frac{\det(\mathsf{I}_2 - e^{iN\tilde{q}}{\mathsf{M}_1}^N)}{\det(\mathsf{I}_2 - e^{iN\tilde{q}}\mathsf{M}_2)}\mathsf{L}(\mathsf{I}_2 - e^{i\tilde{q}}\mathsf{M}_1)^{-1}\begin{bmatrix} 1 \\ 0 \end{bmatrix}. \tag{B.80}$$

And finally

$$\int_0^L v(x)e^{iQx}\,\mathrm{d}x = \frac{i\tilde{q}l\left(1-(-1)^P e^{iNM\tilde{q}}\right)\frac{\cos N\psi_{j,p,P}-\cos N\tilde{q}}{\cos P\pi/M-\cos N\tilde{q}}\frac{\cos\alpha_{j,p,P}-\cos\tilde{q}}{\cos\psi_{j,p,P}-\cos\tilde{q}}}{\tilde{q}^2-{\alpha_{j,p,P}}^2}. \tag{B.81}$$

Complete expression of the dMRI signal

We gather the above expressions to obtain the signal as a function of $\tilde{q} = Ql$ and $t = D\Delta/l^2$:

$$\begin{aligned} S = {} & \frac{2(1-\cos m\tilde{q})}{(m\tilde{q})^2} + \sum_{j=1}^{\infty}\frac{4\tilde{q}^2(1-(-1)^{jm}\cos m\tilde{q})}{m^2\left(\tilde{q}^2-(j\pi)^2\right)^2}e^{-(j\pi)^2\tilde{t}} \\ & + \sum_{j=0}^{\infty}\sum_{p=1}^{N-1}\frac{2l\tilde{q}^2}{m}\frac{1-(-1)^{pM}\cos m\tilde{q}}{(\cos\tilde{q}-\cos p\pi/N)^2}\left(\frac{\cos\tilde{q}-\cos\alpha_{j,p}}{\tilde{q}^2-\alpha_{j,p}^2}\right)^2\beta_{j,p}^2 e^{-{\alpha_{j,p}}^2\tilde{t}} \\ & + \sum_{j=1}^{\infty}\sum_{p=0}^{N}\sum_{P=1}^{M-1}\frac{2ml\tilde{q}^2(1-(-1)^P\cos m\tilde{q})}{M^2(\cos N\tilde{q}-\cos P\pi/M)^2}\left(\frac{\cos\tilde{q}-\cos\alpha_{j,p,P}}{\tilde{q}^2-{\alpha_{j,p,P}}^2}\right)^2\left(\frac{\cos N\tilde{q}-\cos N\psi_{j,p,P}}{N(\cos\tilde{q}-\cos\psi_{j,p,P})}\right)^2 \\ & \qquad \times\beta_{j,p,P}^2 e^{-{\alpha_{j,p,P}}^2\tilde{t}}, \end{aligned} \tag{B.82}$$

where $\beta_{j,p}^2$ and $\beta_{j,p,P}^2$ are given by Eqs. (3.132b) and (B.78), respectively.

B.3.5 Limit of the dMRI signal for the periodic geometry as $\tilde{\kappa} \to 0$ and $\tilde{\kappa} \to \infty$

High-permeability limit: $\tilde{\kappa} \to \infty$

In this limit, one has:

$$\begin{cases} \alpha_{j,p} = j\pi + p\pi/m & \text{if } j \text{ is even,} \\ \alpha_{j,p} = j\pi + (m-p)\pi/m & \text{if } j \text{ is odd.} \end{cases} \tag{B.83}$$

In particular, $\cos\alpha_{j,p} = \cos\psi_{j,p}$, so the expression of the signal simplifies into

$$S = \frac{2(1-\cos mq)}{(mq)^2} + \sum_{j=1}^{\infty} \frac{4q^2(1-(-1)^{jm}\cos mq)}{m^2\left(q^2-(j\pi)^2\right)^2} e^{-(j\pi)^2 t} + \sum_{j=0}^{\infty}\sum_{p=1}^{m-1} \frac{2\ell_s q^2}{m} \frac{1-(-1)^p\cos mq}{(q^2-\alpha_{j,p}^2)^2} \beta_{j,p}^2 e^{-{\alpha_{j,p}}^2 t} ,$$

with $\beta_{j,p}^2 = 2/(m\ell_s)$. Hence:

$$S = \frac{2(1-\cos m\tilde{q})}{(m\tilde{q})^2} + \sum_{n=1}^{\infty} \frac{4\tilde{q}^2(1-(-1)^n\cos m\tilde{q})}{\left((m\tilde{q})^2-(n\pi)^2\right)^2} e^{-(n\pi)^2\tilde{t}/m^2} , \tag{B.84}$$

which is the formula of the signal for one interval of length $L = ml$, as expected.

Low-permeability limit: $\tilde{\kappa} \to 0$

Although the result is intuitively expected, the computation is more complicated. The mathematical reason is that in the limit $\tilde{\kappa} \to 0$, $\alpha_{j,p} = j\pi$ so that the eigenmodes of the branch j are degenerate. Using Eq. (3.131), one gets the expression of the signal:

$$S = \frac{2(1-\cos m\tilde{q})}{(m\tilde{q})^2} + \sum_{j=1}^{\infty} \frac{4\tilde{q}^2(1-(-1)^{jm}\cos m\tilde{q})}{m^2\left(\tilde{q}^2-(j\pi)^2\right)^2} e^{-(j\pi)^2\tilde{t}} + \sum_{j=0}^{\infty}\sum_{p=1}^{m-1} \frac{2\ell_s\tilde{q}^2}{m} \frac{1-(-1)^p\cos m\tilde{q}}{(\cos\tilde{q}-\cos p\pi/m)^2} \left(\frac{\cos\tilde{q}-(-1)^j}{\tilde{q}^2-(j\pi)^2}\right)^2 \beta_{j,p}^2 e^{-(j\pi)^2 t} ,$$

with

$$\begin{cases} \beta_{j,p}^2 = \frac{2}{m\ell_s}(1+(-1)^j\cos p\pi/m) & \text{if } j>0, \\ \beta_{0,p}^2 = \frac{1}{m\ell_s}(1+(-1)^j\cos p\pi/m) \ . \end{cases}$$

Gathering all the terms, we obtain

$$S = S_0(\tilde{q})\frac{2(1-\cos\tilde{q})^2}{m^2\tilde{q}^2} + \frac{4\tilde{q}^2}{m^2}\sum_{j=1}^{\infty} S_j(\tilde{q}) \frac{(1-(-1)^j\cos\tilde{q})^2}{(\tilde{q}^2-(j\pi)^2)^2} e^{-(j\pi)^2\tilde{t}} , \tag{B.85}$$

with

$$S_j(\tilde{q}) = \sum_{p=0}^{m} \frac{(1-(-1)^p\cos m\tilde{q})(1+(-1)^j\cos p\pi/m)}{(\cos\tilde{q}-\cos p\pi/m)^2(1+\theta_p)} , \quad j=0,1,\dots , \tag{B.86}$$

where $\theta_p = 1$ if $p = 0$ or m, and $\theta_p = 0$ otherwise. To compute $S_j(\tilde{q})$, we introduce the following polynomial:

$$P(X) = \prod_{p=0}^{m} (X - \cos p\pi/m) \ . \tag{B.87}$$

The analysis of its roots and degree leads to the following formula:

$$P(\cos\tilde{q}) = N\sin(m\tilde{q})\sin\tilde{q} , \tag{B.88}$$

where N is an unknown proportionality coefficient whose value is not needed in the following. This allows us to compute

$$P'(\cos\tilde{q}) = \left(\frac{-1}{\sin\tilde{q}}\right) N\left(m\cos(m\tilde{q})\sin\tilde{q} + \sin(m\tilde{q})\cos\tilde{q}\right) , \tag{B.89}$$

$$P'(\cos p\pi/m) = Nm(-1)^{p+1}(1+\theta_p) . \tag{B.90}$$

Now we use the standard partial fraction expansion formula, for any polynomial Q such that $\deg Q \leq \deg P$:

$$\frac{Q(X)}{P(X)} = C + \sum_{p=0}^{m} \frac{Q(\cos p\pi/m)}{P'(\cos p\pi/m)(X - \cos p\pi/m)} , \tag{B.91}$$

where prime denotes the derivative with respect to X and C is a constant. With the polynomial $R(\cos q) = \cos mq$, we get according to Eq. (B.91)

$$\begin{aligned} S_j(\tilde{q}) &= Nm\left[\left(\frac{R(X)(1+(-1)^j X)}{P(X)}\right)' - R(X)\left(\frac{1+(-1)^j X}{P(X)}\right)'\right]_{X=\cos\tilde{q}} \\ &= NmR'(\cos\tilde{q})\frac{1+(-1)^j\cos\tilde{q}}{P(\cos\tilde{q})} . \end{aligned}$$

Computing the derivative of R and using Eq. (B.88), one finally gets

$$S_j(\tilde{q}) = \frac{m^2}{1-(-1)^j\cos\tilde{q}} . \tag{B.92}$$

Now we come back to Eq. (B.85), which yields

$$S = \frac{2(1-\cos\tilde{q})}{\tilde{q}^2} + \sum_{j=1}^{\infty} \frac{4\tilde{q}^2(1-(-1)^j\cos\tilde{q})}{(\tilde{q}^2-(j\pi)^2)^2} e^{-(j\pi)^2\tilde{t}} , \tag{B.93}$$

which is the expected formula of the signal for one interval of length l.

B.3.6 Expansions for $\alpha_{j,p}$ for the periodic geometry

Low-permeability limit: $\tilde{\kappa} \to 0$ In this case we rewrite Eq. (3.127) as $\alpha\sin\alpha = 2\tilde{\kappa}(\cos\alpha - \cos\psi)$. We start with the branch $j = 0$. Let us write $\alpha = u\sqrt{2\tilde{\kappa}(1-\cos\psi)}$. Then

$$\begin{aligned} \alpha\sin\alpha &= 2\tilde{\kappa}(1-\cos\psi)u^2\left(1 - \frac{1}{3}\tilde{\kappa}(1-\cos\psi)u^2\right) + O(\tilde{\kappa}^3) , \\ (\cos\alpha - \cos\psi) &= (1-\cos\psi) - \tilde{\kappa}(1-\cos\psi)u^2 + O(\tilde{\kappa}^2) , \end{aligned}$$

from which we derive

$$\alpha_{0,p} = 2\tilde{\kappa}^{1/2}\sin(p\pi/2m) - \tilde{\kappa}^{3/2}\left(\sin(p\pi/2m) - \frac{2}{3}\sin^2(p\pi/2m)\right) + O(\tilde{\kappa}^{5/2}) . \tag{B.94}$$

Now, if $\alpha = j\pi + \epsilon$, one has

$$\alpha\sin\alpha = (-1)^j(j\pi\epsilon + \epsilon^2 + O(\epsilon^3)) , \qquad (\cos\alpha - \cos\psi) = (-1)^j(1-(-1)^j\cos\psi + O(\epsilon^2)) ,$$

which gives

$$\alpha_{j,p} = \begin{cases} j\pi + \dfrac{4\tilde{\kappa}}{j\pi}\sin^2(p\pi/2m) - \dfrac{(4\tilde{\kappa})^2}{(j\pi)^3}\sin^4(p\pi/2m) + O(\tilde{\kappa}^3) & \text{if } j \text{ is even,} \\ j\pi + \frac{4\tilde{\kappa}}{j\pi}\sin^2((m-p)\pi/2m) - \frac{(4\tilde{\kappa})^2}{(j\pi)^3}\sin^4((m-p)\pi/2m) + O(\tilde{\kappa}^3) & \text{if } j \text{ is odd.} \end{cases} \tag{B.95}$$

This is consistent with the idea that at very low permeability the compartments become independent so that $\alpha_{j,p}$ (with $p = 1, \ldots, m-1$) are identical and equal to $j\pi$. One notices that the deviation from this limit decreases with j which is consistent with previous observations (Fig. 3.14).

High permeability limit: $\tilde{r} \to 0$ Again, we start with the $j = 0$ branch. Let us write $\alpha = \psi - u$. Then we have the equations:

$$\begin{aligned} \cos\alpha &= \cos\psi\left(1 - \frac{u^2}{2} + O(u^4)\right) + \sin\psi(u + O(u^3)) \,, \\ \alpha\sin\alpha &= \psi\sin\psi + u\sin\psi + u\psi\cos\psi + O(u^3) \,, \end{aligned}$$

which yield

$$\alpha_{0,p} = \frac{p\pi}{m}\left(1 - \frac{\tilde{r}}{2} + \frac{\tilde{r}^2}{4}\left[1 + \frac{p\pi/m}{2\tan(p\pi/m)}\right] + O\left(\tilde{r}^3\right)\right) \,. \tag{B.96}$$

For the other branches, the computations are similar:

$$\alpha_{j,p} = \begin{cases} (j\pi + p\pi/m)\left(1 - \dfrac{\tilde{r}}{2} + \dfrac{\tilde{r}^2}{4}\left[1 + \dfrac{j\pi + p\pi/m}{2\tan(p\pi/m)}\right]\right) + O\left(\tilde{r}^3\right) & j \text{ even,} \\ (j\pi + (m-p)\pi/m)\left(1 - \frac{\tilde{r}}{2} + \frac{\tilde{r}^2}{4}\left[1 + \frac{j\pi + (m-p)\pi/m}{2\tan((m-p)\pi/m)}\right]\right) + O\left(\tilde{r}^3\right) & j \text{ odd.} \end{cases} \tag{B.97}$$

Again, the interpretation is quite clear. When the permeability is very high, $\tilde{r} \to 0$ and the $\alpha_{j,p}$ approach the solutions for one interval of length ml, for which $\alpha_n = n\pi/m$ ($n = 0, 1, \ldots$). Consistently with the above low-permeability regime, the deviation from the limit $\tilde{\kappa} = \infty$ increases with j.

Appendix C

Supplementary material to Chapter 4

This Appendix contains several developments regarding the eigenmodes of the Bloch-Torrey operator and the localization regime. In Appendix C.1, we compute the normalization factor of one-dimensional Bloch-Torrey eigenmodes on the half-line and we prove at the same time that these eigenmodes form a complete basis, which ensures the validity of spectral decompositions. Then we provide asymptotic formulas for them in Appendix C.2. From these asymptotic formulas we obtain an interesting symmetry property as well as a qualitative consistency check with the formula for free diffusion decay far from the boundary. In Appendix C.3, we investigate the singular limit of a curved boundary with infinite curvature radius. We show that the spectrum of the Bloch-Torrey becomes dense in this limit, and that one recovers the result for the flat boundary by summing lateral eigenmodes. Then we turn to the question of the validity of spectral decompositions near a spectral bifurcation. We show that such decompositions remain valid as long as one includes a "generalized eigenmode" into the series. In Appendix C.6, we study the magnetization inside a slab with slightly curved boundaries and we show in some cases a coexistence of localization and motional narrowing regime. The next appendix is a supplement to Sec. 4.4, where we compute numerically the transverse magnetization and signal in a periodic medium for short-gradient pulse sequences. The comparison with extended-gradient sequences reveals interesting qualitative differences. Finally, we discuss in Appendix C.11 the definition of the spectrum of a differential operator. Although the rigorous mathematical definition differs from the qualitative one commonly used by physicists, we show that they are consistent with each other. Moreover, we show how non-Hermitian operators may have an *empty* spectrum.

C.1 Completeness and normalization of 1D BT eigenmodes

In Sec. 4.2.1, we presented the computation of the eigenmodes of the BT operator on the half-line $x \geq 0$ with an impermeable boundary at $x = 0$. We recall that the eigenmode equation yields two solutions $F_{\mathrm{r}}(\tilde{x} - i\tilde{\mu})$ and $F_{\mathrm{l}}(\tilde{x} - i\tilde{\mu})$ and we keep only F_{r} because it is the only one to be bounded for $\tilde{x} \to \infty$. In this section, we follow the same procedure as in Sec. 3.4.2 in order to (i) compute the normalization factors of the Bloch-Torrey eigenmodes; (ii) prove their completeness, i.e. the validity of spectral decompositions. This computation relies on standard methods from the theory of differential equations. We emphasize that these results

were first derived by Stoller *et al* [98] then extended in [94, 102]. We present them here for self-consistency.

To this end, we solve for the Green function $\mathcal{F}(t, \tilde{x}_0, \tilde{x})$ of the dimensionless Bloch-Torrey equation

$$\partial_t \mathcal{F} = \mathcal{F}'' + i\tilde{x}\mathcal{F} \,, \tag{C.1a}$$
$$\mathcal{F}(t=0, \tilde{x}_0, \tilde{x}) = \delta(\tilde{x} - \tilde{x}_0) \,, \tag{C.1b}$$
$$\mathcal{F}'(t, \tilde{x}_0, 0) = 0 \,, \qquad \mathcal{F}(t, \tilde{x}_0, \infty) = 0 \,, \tag{C.1c}$$

where $'$ denotes derivative with respect to $\tilde{x}$ and $\delta(\cdot)$ is the Dirac distribution. We perform a Laplace transform $\mathcal{F}(t, \tilde{x}_0, \tilde{x}) \to \hat{\mathcal{F}}(s, \tilde{x}_0\tilde{x})$, and the equations become

$$s\hat{\mathcal{F}} - \delta(\tilde{x} - \tilde{x}_0) = \hat{\mathcal{F}}'' + i\tilde{x}\hat{\mathcal{F}} \,, \tag{C.2a}$$
$$\hat{\mathcal{F}}'(s, \tilde{x}_0, 0) = 0 \,, \qquad \hat{\mathcal{F}}(s, \tilde{x}_0, \infty) = 0 \,, \tag{C.2b}$$

According to the computations of Sec. 4.2.1 that we recalled briefly above, we can solve the second order differential equation (without boundary condition yet) with the general decomposition

$$\hat{\mathcal{F}}(s, \tilde{x}, \tilde{x}_0) = \phi(s, \tilde{x}_0, \tilde{x}) F_\mathrm{r}(\tilde{x} + is) + \psi(s, \tilde{x}_0, \tilde{x}) F_\mathrm{r}(\tilde{x} + is) \,, \tag{C.3}$$

with yet unknown functions ϕ and ψ. Let us introduce the Wronskian matrix

$$\mathrm{W} = \begin{bmatrix} F_\mathrm{r}(\tilde{x} + is) & F_\mathrm{l}(\tilde{x} + is) \\ F_\mathrm{r}'(\tilde{x} + is) & F_\mathrm{l}'(\tilde{x} + is) \end{bmatrix} . \tag{C.4}$$

Note that its determinant obeys $\det(\mathrm{W})' = 0$. To compute it, we evaluate it at $\tilde{x} = -is$, which yields

$$\det(\mathrm{W}) = ie^{2i\pi/3}\mathrm{Ai}(0)\mathrm{Ai}'(0) - ie^{-2i\pi/3}\mathrm{Ai}(0)\mathrm{Ai}'(0) \tag{C.5a}$$
$$= -\frac{1}{2\pi} \,. \tag{C.5b}$$

By injecting Eq. (C.3) into Eq. (C.2a), one gets a system for ϕ, ψ:

$$\begin{bmatrix} \phi' \\ \psi' \end{bmatrix} = \mathrm{W}^{-1} \begin{bmatrix} 0 \\ -\delta(\tilde{x} - \tilde{x}_0) \end{bmatrix} = 2\pi\delta(\tilde{x} - \tilde{x}_0) \begin{bmatrix} -F_\mathrm{l}(\tilde{x} + is) \\ F_\mathrm{r}(\tilde{x} + is) \end{bmatrix} . \tag{C.6}$$

After integration, we obtain the Green function in Laplace domain

$$\begin{aligned} \hat{\mathcal{F}}(x, \tilde{x}_0, \tilde{x}) = &\left(A - 2\pi F_\mathrm{l}(\tilde{x}_0 + is) H(\tilde{x} - \tilde{x}_0)\right) F_\mathrm{r}(\tilde{x} + is) \\ &+ \left(B + 2\pi F_\mathrm{r}(\tilde{x}_0 + is) H(\tilde{x} - \tilde{x}_0)\right) F_\mathrm{l}(\tilde{x} + is) \,, \end{aligned} \tag{C.7}$$

where H is the Heaviside function ($H(x) = 0$ for $x < 0$ and $H(x) = 1$ for $x \geq 0$).

The constants A and B remain to be determined by the boundary condition (C.2b):

$$AF_\mathrm{r}'(is) + BF_\mathrm{l}'(is) = 0 \,, \qquad B + 2\pi F_\mathrm{r}(\tilde{x}_0 + is) = 0 \,, \tag{C.8}$$

from which we get

$$A = 2\pi \frac{F_\mathrm{l}'(is) F_\mathrm{r}(\tilde{x}_0 + is)}{F_\mathrm{r}'(is)} \,, \qquad B = -2\pi F_\mathrm{r}(\tilde{x}_0 + is) \,. \tag{C.9}$$

By putting all the pieces together, we obtain the formula of the Green function in Laplace domain

$$\begin{aligned}\hat{\mathcal{F}}(s,\tilde{x}_0\tilde{x}) = 2\pi\frac{F_{\rm l}'(is)F_{\rm r}(\tilde{x}_0+is)F_{\rm r}(\tilde{x}+is)}{F_{\rm r}'(is)}\\ - 2\pi F_{\rm l}(\tilde{x}_0+is)H(\tilde{x}-\tilde{x}_0)F_{\rm r}(\tilde{x}+is)\\ + 2\pi F_{\rm r}(\tilde{x}_0+is)H(\tilde{x}_0-\tilde{x})F_{\rm l}(\tilde{x}+is)\ .\end{aligned} \tag{C.10}$$

To obtain the Green function in time domain, we invert the Laplace transform by looking for the poles of $\hat{\mathcal{F}}$. Since the functions $F_{\rm r}$ and $F_{\rm l}$ are analytic, there is no contribution from the second and third term in Eq. (C.10). Therefore the poles s_n of $\hat{\mathcal{F}}$ are the solutions of $F_{\rm r}'(is)=0$, which gives $s_n = -\tilde{\mu}_n = e^{-i\pi/3}|a_n|$, as expected. The residues of the poles are simply

$$\mathrm{Res}_{s=-\tilde{\mu}_n}(\hat{\mathcal{F}}) = \frac{e^{-i\pi/6}\tilde{v}_n(\tilde{x}_0)\tilde{v}_n(\tilde{x})}{\beta_n^2|a_n|\mathrm{Ai}^2(a_n)}\ . \tag{C.11}$$

In this formula, we have introduced the expression for the dimensionless eigenmodes $\tilde{v}_n(\tilde{x}) = \tilde{\beta}_n F_{\rm r}(\tilde{x}-i\tilde{\mu}_n)$. Furthermore, we have used the Wronskian and the differential equation on $F_{\rm r}$ to simplify the expression. We conclude that the Green fonction can be represented as a spectral decomposition

$$\mathcal{F}(t,\tilde{x}_0,\tilde{x}) = \sum_n \frac{e^{-i\pi/6}}{\tilde{\beta}_n^2|a_n|\mathrm{Ai}^2(a_n)}\tilde{v}_n(\tilde{x}_0)\tilde{v}_n(\tilde{x})e^{-\tilde{\mu}_n t}\ . \tag{C.12}$$

By evaluating this expression at $t=0$, one obtains that the Dirac distribution can be represented as a spectral decomposition:

$$\delta(\tilde{x}-\tilde{x}_0) = \sum_n \frac{e^{-i\pi/6}}{\tilde{\beta}_n^2|a_n|\mathrm{Ai}^2(a_n)}\tilde{v}_n(\tilde{x}_0)\tilde{v}_n(\tilde{x})\ . \tag{C.13}$$

This proves that the eigenmode family is complete. Moreover, after integration against $\tilde{v}_n(\tilde{x})$, one gets

$$\tilde{v}_n(\tilde{x}_0) = \int_0^\infty \tilde{v}_n(\tilde{x})\delta(\tilde{x}-\tilde{x}_0)\,\mathrm{d}\tilde{x} \tag{C.14a}$$

$$= \sum_{n'} \frac{e^{-i\pi/6}}{\tilde{\beta}_{n'}^2|a_{n'}|\mathrm{Ai}^2(a_{n'})}\tilde{v}_{n'}(\tilde{x}_0)\int \tilde{v}_n\tilde{v}_{n'} \tag{C.14b}$$

$$= \frac{e^{-i\pi/6}}{\tilde{\beta}_n^2|a_n|\mathrm{Ai}^2(a_n)}\tilde{v}_n(\tilde{x}_0)\ , \tag{C.14c}$$

which yields the formula for the normalization factor

$$\tilde{\beta}_n^{-2} = e^{i\pi/6}|a_n|\mathrm{Ai}^2(a_n)\ . \tag{C.15}$$

This is the normalization factor of the dimensionless eigenmodes $\tilde{v}_n(\tilde{x})$. To go back to the eigenmodes $v_n(x)$, one simply performs a change of variable $x=\ell_g\tilde{x}$ in the normalization condition:

$$1 = \int_0^\infty \tilde{v}_n^2(\tilde{x})\,\mathrm{d}\tilde{x} = \frac{1}{\ell_g}\int_0^\infty \tilde{v}_n^2(x/\ell_g)\,\mathrm{d}x = \int_0^\infty v_n^2(x)\,\mathrm{d}x\ . \tag{C.16}$$

From this formula, we deduce that the normalization factor β_n of the eigenmode v_n is

$$\beta_n^{-2} = \ell_g\tilde{\beta}_n^{-2} = \ell_g e^{i\pi/6}|a_n|\mathrm{Ai}^2(a_n)\ . \tag{C.17}$$

C.2 Asymptotic behavior of the 1D BT eigenmodes

In this appendix we provide asymptotic formulas for the function F_{r} and thus for one-dimensional BT eigenmodes $v_n(x) = \beta_n F_{\mathrm{r}}(x/\ell_g - e^{i\pi/6}|a_n|)$. On Fig. 4.7, we have plotted the eigenmodes along with these asymptotic expressions, and we observe a very good agreement between the exact and asymptotic expressions. Therefore, we shall use these asymptotic expressions to obtain simpler expressions of the modes v_n. From these expressions, we deduce (i) a symmetry property of the eigenmodes; (ii) a qualitative agreement with the free diffusion decay and the transition to localization regime.

C.2.1 Asymptotic expression

Standard mathematical techniques [343] allow one to prove the following asymptotic behavior for F_{r}:

$$F_{\mathrm{r}}(\tilde{x} - i\tilde{\mu}) \underset{\tilde{x}\to\pm\infty}{\approx} \frac{\exp\left(-\frac{2}{3}\left[e^{-i\pi/6}(\tilde{x} - i\tilde{\mu})\right]^{3/2}\right)}{2\sqrt{\pi}\left[e^{-i\pi/6}(\tilde{x} - i\tilde{\mu})\right]^{1/4}}, \tag{C.18}$$

in other words, $F_{\mathrm{r}}(\tilde{x} - i\tilde{\mu})$ is well approximated by the product of an oscillating function and: (i) a fast decaying function for $\tilde{x} \to \infty$, with $-\log(|F_{\mathrm{r}}|) \sim \tilde{x}^{3/2}$, or (ii) a fast diverging function for $\tilde{x} \to -\infty$, with $\log(|F_{\mathrm{r}}|) \sim (-\tilde{x})^{3/2}$. On Fig. C.1, we show graphically this asymptotic behavior. Note that the term $\left[e^{-i\pi/6}(\tilde{x} - i\tilde{\mu})\right]^{3/2}$ has a discontinuity when $\tilde{x} - i\tilde{\mu}$ crosses the line of argument $5\pi/6$ in the complex plane. This line corresponds to the points where the approximate formula (C.18) is the least accurate, and around those points it should be replaced by

$$F_{\mathrm{r}}(z) \underset{\arg(z)\approx 5\pi/6}{\approx} \sin\left(\frac{2}{3}\left[-e^{-i\pi/6}z\right]^{3/2} + \frac{\pi}{4}\right) \frac{1}{\sqrt{\pi}\left[-e^{-i\pi/6}z\right]^{1/4}}, \tag{C.19}$$

that becomes increasingly accurate as $|z|$ increases. As we show on Fig. 4.7, this asymptotic formula represents well the behavior of the eigenmodes close to the boundary, whereas Eq. (C.18) is more accurate far from the boundary.

Moreover, one can use the asymptotic formula (C.19) to get an approximate expansion for the zeros of the derivative of the Airy function [343]:

$$a_n \underset{n\to\infty}{\approx} -\left(\frac{3}{2}\pi(n - 3/4)\right)^{2/3}, \qquad n = 1, 2, \ldots \tag{C.20}$$

We show the first values obtained from this formula[1] and the comparison with the tabulated values in the table below. Except for the first value which is off by about 10%, the next values are very close to the exact a_n.

We consider an eigenmode of relatively large order n, and we first look for the maximum of its amplitude. We use Eq. (C.18), that yields

$$F_{\mathrm{r}}(x/\ell_g - e^{i\pi/6}|a_n|) \approx \frac{\exp\left(-\frac{2}{3}\left[e^{-i\pi/6}x/\ell_g - |a_n|\right]^{3/2}\right)}{2\sqrt{\pi}\left[e^{-i\pi/6}x/\ell_g - |a_n|\right]^{1/4}}. \tag{C.21}$$

[1] Higher-order terms are given in [343]. For instance, the next term is $\frac{7}{48}\left(\frac{3}{2}\pi(n - 3/4)\right)^{-4/3}$, which is a very small relative correction for $n \geq 2$ (a 0.4% relative correction for $n = 2$).

tabulated values	−1.0188	−3.2482	−4.8201	−6.1633	−7.3722
approximate values	−1.1155	−3.2616	−4.8263	−6.1671	−7.3749

Table C.1: Tabulated values for a_n, $n = 1, \ldots, 5$, and approximate values (C.20).

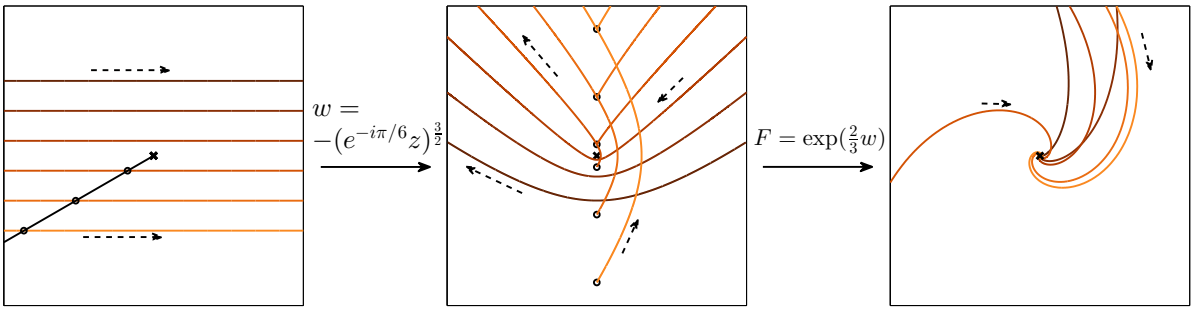

Figure C.1: Complex representation of the asymptotic formula (C.18). (left) We have plotted $z = \tilde{x} - i\tilde{\mu}$ for several values of $\tilde{\mu}$ as colored lines, and the dashed arrows indicate the direction of increasing $\tilde{x}$. (middle) Complex map of the quantity $w = -(e^{-i\pi/6}z)^{3/2}$. The circles indicate discontinuities at the branching points that are caused by the non-integer exponent of z. The corresponding cut in the z-plane is indicated by thick black line in the left panel. When $\tilde{x}$ goes to ∞ or $-\infty$, w goes to ∞ with argument $3\pi/4$ or $\pi/4$, respectively. (right) Complex map of the asymptotic formula $F = \exp(2w/3)$. The spiraling pattern indicates an oscillating and decaying behavior.

At large values of x/ℓ_g and $|a_n|$, we may assume that the denominator varies much slower than the numerator and therefore we discard it temporarily. Thus we have reduced the problem to the study of the exponential factor and more precisely of

$$w = -\left[e^{-i\pi/6}x/\ell_g - |a_n|\right]^{3/2} . \tag{C.22}$$

One can see on the middle panel of Fig. C.1 that between $x = 0$ and $x = \infty$ (i.e. from a small circle and following the dashed arrows), the real part of w increases then decreases. The maximum of $\mathrm{Re}(w)$ corresponds to the maximum of the amplitude of v_n. The plot suggests that this maximum is attained when w goes through the real axis, i.e. for

$$x_n = \frac{\sqrt{3}}{2}|a_n|\ell_g . \tag{C.23}$$

One can rewrite w as a function of $\xi = x - x_n$, that yields

$$w = \frac{1}{\ell_g^{3/2}}\left[\frac{x_n}{\sqrt{3}} + i\xi\right]^{3/2} \underset{\xi \ll x_n}{\approx} \left(\frac{x_n}{\ell_g\sqrt{3}}\right)^{3/2} + i\frac{3^{3/4}}{2}\frac{x_n^{1/2}\xi}{\ell_g^{3/2}} - \frac{3^{5/4}}{8}\frac{\xi^2}{x_n^{1/2}\ell_g^{3/2}} , \tag{C.24}$$

that proves *a posteriori* that the maximum of $\mathrm{Re}(w)$ is reached at $x = x_n$.

Moreover, close to $x = x_n$, the denominator that we discarded earlier is approximately equal to

$$2\sqrt{\pi}\left[e^{-i\pi/6}x/\ell_g - |a_n|\right]^{1/4} \approx 2e^{-i\pi/6}\pi^{1/2}3^{-1/8}x_n^{1/4}\ell_g^{-1/4} . \tag{C.25}$$

Finally, we compute the normalization factor β_n with Eqs. (C.19) and (4.30), that yield

$$\beta_n \approx e^{-i\pi/12}\pi^{1/2}2^{-1/4}3^{1/8}x_n^{-1/4}\ell_g^{-1/4} \,. \tag{C.26}$$

Putting everything together, we obtain the approximate formula for v_n close to its maximum:

$$v_n(x) \underset{\xi \ll x_n}{\approx} \frac{3^{1/4}}{2^{5/4}x_n^{1/2}} \exp\left(\frac{2x_n^{3/2}}{3^{7/4}\ell_g^{3/2}} + i\frac{x_n^{1/2}\xi}{3^{1/4}\ell_g^{3/2}} - \frac{3^{3/4}\xi^2}{4x_n^{1/2}\ell_g^{3/2}} + i\frac{\pi}{12}\right) \,. \tag{C.27}$$

Moreover, one can use Eq. (C.20) to get an approximate expression for x_n

$$x_n \underset{n \gg 1}{\approx} \frac{3^{7/6}\pi^{2/3}}{2^{5/3}}\left(n + \frac{1}{4}\right)^{2/3} \,. \tag{C.28}$$

Equation (C.27) reveals that the eigenmode v_n is the product of an oscillating function with period $\ell_g(2/|a_n|)^{1/2}$ and an envelope with half-width $(8|a_n|/3)^{1/4}\ell_g$. Interestingly, at large n the oscillating behavior is much faster than the decaying behavior, which is consistent with the observation that

$$\mathrm{Re}(\mu_n) = \frac{|a_n|}{2}\frac{D_0}{\ell_g^2} \tag{C.29}$$

is equal to D_0 times the inverse square of the oscillation period (see also discussion in Sec. 1.2.4).

C.2.2 Eigenmode symmetry

From the approximate expression of w, one would conclude that the eigenmode is symmetric with respect to x_n. However, this is not exactly true because of the additional phase $\pi/12$ that comes from the normalization factor and from the denominator. One way to compensate this phase is to introduce $\eta = \xi + \ell_g\epsilon_n/2$ such that

$$i\frac{x_n^{1/2}\xi}{3^{1/4}\ell_g^{3/2}} + i\frac{\pi}{12} = i\frac{x_n^{1/2}\eta}{3^{1/4}\ell_g^{3/2}} \,, \tag{C.30}$$

that yields

$$\epsilon_n = \frac{3^{1/4}\pi\ell_g^{1/2}}{6x_n^{1/2}} = \frac{\pi}{6}\sqrt{\frac{2}{|a_n|}} \,. \tag{C.31}$$

In principle, one can compute next-order corrections by taking into account the quadratic term in the exponential (but also the variation of the denominator with ξ). If we discard these corrections, we obtain the approximate symmetry

$$v_n(2x_n + \epsilon_n\ell_g - x) \approx v_n(x)^* \,. \tag{C.32}$$

Figure 4.7 shows graphically that this relation is valid close to the maximum $x = x_n$ of the eigenmode.

C.2.3 Qualitative transition between localization and free diffusion

We emphasize that the spectral decompositions such as Eqs. (1.86d), (1.86e), (C.12) cannot be computed exactly, even with the somewhat simpler asymptotic formulas derived above. Here we propose a qualitative analysis that shows the consistency between the localized eigenmodes v_n and the free diffusion decay far from the boundary.

The above asymptotic formula for v_n shows that its amplitude is maximal at $x = x_n$ and that it is approximately given by

$$|v_n(x_n)| \sim \exp\left(\frac{2x_n^{3/2}}{3^{7/4}\ell_g^{3/2}}\right) . \tag{C.33}$$

In contrast, the first eigenmode decays approximately as

$$|v_1(x_n)| \sim \exp\left(-\frac{\sqrt{2}x_n^{3/2}}{3\ell_g^{3/2}}\right) . \tag{C.34}$$

One can see that the n-th eigenmode is significantly larger than the first eigenmode at $x = x_n$. Therefore, there is a competition between the very large ratio between v_n and v_1, and their decay rate with time. More precisely, the decay of the n-th eigenmode with time follows

$$|\exp(-\mu_n T)| \approx \exp\left(-\frac{\ell_{\mathrm{d}}^2 x_n}{\sqrt{3}\ell_g^3}\right) . \tag{C.35}$$

We conclude from the above equations that the n-th eigenmode becomes negligible compared to v_1 if (here we discard the time decay of v_1 because it is much slower than that of v_n)

$$|v_n(x_n)||\exp(-\mu_n T)| \ll |v_1(x_n)| \Leftrightarrow \frac{\ell_{\mathrm{d}}^2 x_n}{\sqrt{3}\ell_g^3} - \frac{2x_n^{3/2}}{3^{7/4}\ell_g^{3/2}} \gg \frac{\sqrt{2}x_n^{3/2}}{3\ell_g^{3/2}} \tag{C.36}$$

$$\Leftrightarrow \ell_{\mathrm{d}}^4 \gg x_n \ell_g^3 . \tag{C.37}$$

At the time when $|v_n(x_n)||\exp(-\mu_n T)|$ becomes comparable with $|v_1(x_n)|$, i.e. $\ell_{\mathrm{d}}^4 \approx x_n \ell_g^3$, one can compute the amplitude:

$$-\log|v_1(x_n)| \sim \frac{x_n^{3/2}}{\ell_g^{3/2}} \approx \frac{\ell_{\mathrm{d}}^6}{\ell_g^6} . \tag{C.38}$$

Quite counter-intuitively, the superposition of very large eigenmodes with a very strong time decay produces a constant magnetization far from the boundary. When time increases, the high-order eigenmodes decay much faster than the first eigenmodes localized at the boundary. The crossover occurs when $\ell_{\mathrm{d}}^4 \approx x\ell_g^3$, and our approximate computation shows that the amplitude of the first eigenmode at that point is given by the free diffusion formula. Thus, *qualitatively*, the expression of the eigenmodes is consistent with the free diffusion decay far from the boundary (see Fig. C.2).

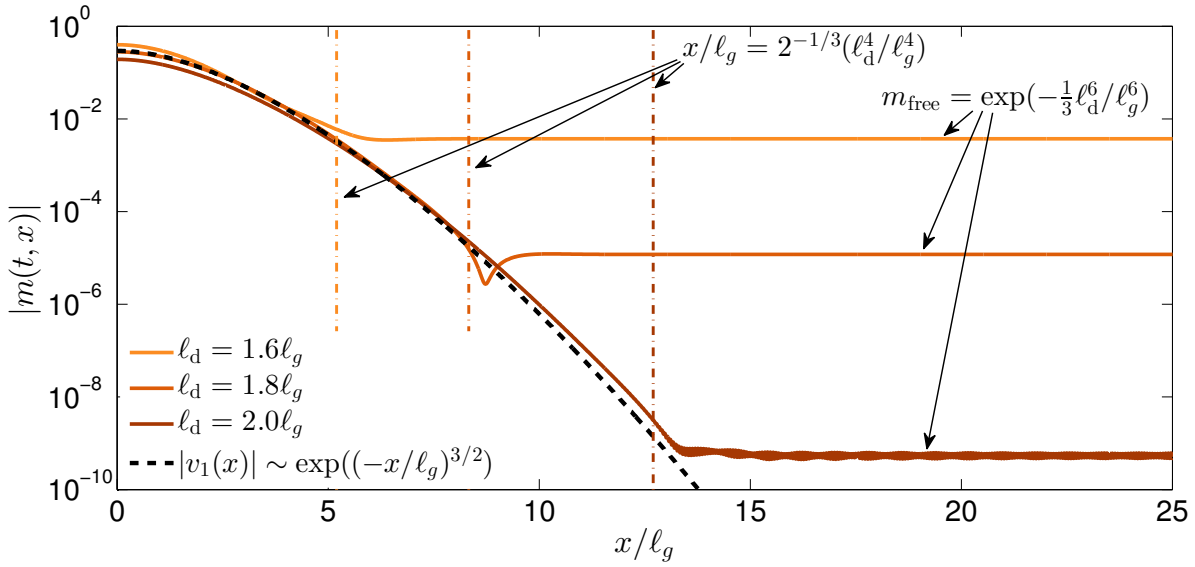

Figure C.2: Absolute value of the magnetization computed numerically for the half-line with an impermeable boundary at $x = 0$, for three different values of the ratio ℓ_d/ℓ_g. One can see a transition between the profile given by the first eigenmode, and a constant magnetization that is given by the free diffusion expression. The transition occurs at $x \approx 2^{-1/3}\ell_d^4/\ell_g^3$. Spurious fluctuations for $\ell_d = 2\ell_g$ are caused by numerical roundoff errors.

C.3 Spectrum in the limit of infinite curvature radius

We consider a two-dimensional medium and we study localization near a curved boundary in the limit of infinite curvature radius R (see Sec. 4.2.2 for the general case). As illustrated on Fig. C.3 the spectrum of the Bloch-Torrey operator becomes continuous. Therefore, the limit $R \to \infty$ is singular because the spectrum differs significantly between the case of very large R and the case of strictly infinite R. This can be qualitatively understood from the observation that a flat boundary is invariant by translation parallel to itself whereas a curved boundary is not. Therefore, a very large but finite R produces a symmetry breaking compared to the case of infinite R.

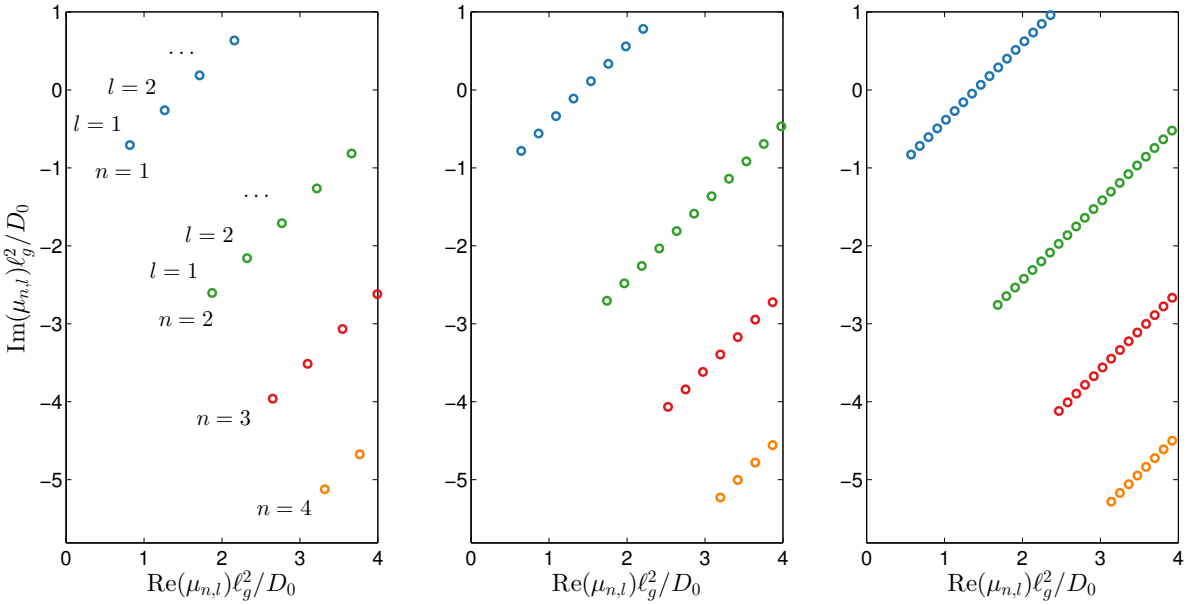

Figure C.3: Complex representation of the spectrum of the BT operator for a curved boundary. Different colors correspond to different values of n, and eigenvalues of the same color differ by the index l. The curvature radius R increases from left to right: (left) $R = 5\ell_g$; (middle) $R = 20\ell_g$; (right) $R = 80\ell_g$. As R increases, the spectrum becomes denser and is continuous in the limit $R \to \infty$.

Let us write the expression of the magnetization after a single gradient pulse of duration δ:

$$m(\delta, x, y) = m_\perp(\delta, x) m_\parallel(\delta, y) \ , \tag{C.39}$$

where $m_\perp(\delta, x)$ is the profile of the magnetization perpendicular to the boundary and $m_\parallel(\delta, y)$ is the profile parallel to the boundary. We recall that this factorization is approximate follows from the variable separation in the Bloch-Torrey operator (4.43a) at a slightly curved boundary.

In the limit of $R \gg \ell_g$, the profile $m_\perp(\delta, x)$ becomes very close to the magnetization profile for a planar boundary

$$m_\perp(\delta, x) = \sum_n \alpha_n \beta_n F_{\mathrm{r}}(x/\ell_g - e^{i\pi/6}|a_n|) \exp(-e^{-i\pi/3}|a_n|\ell_{\mathrm{d}}^2/\ell_g^2) + O(\ell_g/R) \ , \tag{C.40a}$$

$$\alpha_n = \beta_n \int_0^\infty F_{\mathrm{r}}(x/\ell_g - e^{i\pi/6}|a_n|) \, \mathrm{d}x \ . \tag{C.40b}$$

As we mentioned previously, to our knowledge this series cannot be summed therefore there is no closed form of $m_\perp(\delta, x)$. In contrast, the magnetization profile parallel to the boundary can be computed by summing the whole eigenmode series

$$m_\parallel(\delta, y) = \sum_l \left(\int_{-\infty}^{\infty} g_l(y')\, \mathrm{d}y' \right) g_l(y) \exp(-\eta_l \delta) \tag{C.41a}$$

$$= \exp\left[-e^{\pm i\pi/4} \tanh\left(e^{\pm i\pi/4} \frac{2D_0\delta}{\ell_{g,\parallel}^2} \right) \frac{y^2}{2\ell_{g,\parallel}^2} \right] \cosh\left(e^{\pm i\pi/4} \frac{2D_0\delta}{\ell_{g,\parallel}^2} \right)^{-1/2} . \tag{C.41b}$$

In this formula, g_l, η_l are the eigenmodes and eigenvalues of the lateral part of the Bloch-Torrey operator (see Eq. (4.55)). At long times, $D_0\delta \gg \ell_{g,\parallel}^2$, the above formula is reduced to the first eigenmode, as expected. In the opposite regime of short diffusion times or large curvature radius, $D_0\delta \ll \ell_{g,\parallel}^2$, one gets to the first order in time:

$$m_\parallel(\delta, y) \underset{D_0\delta \ll \ell_{g,\parallel}^2}{\approx} \exp\left(-i \frac{G y^2}{2R} \right) , \tag{C.42}$$

that is simply the dephasing due to the local field along the boundary. If one goes to the next order in time, the decay due to diffusion appears

$$m_\parallel(\delta, y) \underset{D_0\delta \ll \ell_{g,\parallel}^2}{\approx} \exp\left(-i \frac{G y^2}{2R} \right) \exp\left(-\frac{1}{3} \left(\frac{Gy}{R} \right)^2 D_0 \delta^3 \right) . \tag{C.43}$$

Note that the additional exponential term is very close to 1 in the limit $D_0\delta \ll \ell_{g,\parallel}^2$. If one applies a second pulse of duration δ immediately after the first one but with opposite amplitude, the refocusing condition makes the phase term disappear and one obtains

$$m_\parallel(T, y) \underset{D_0\delta \ll \ell_{g,\parallel}^2}{\approx} \exp\left(-\frac{1}{12} \left(\frac{Gy}{R} \right)^2 D_0 T^3 \right) . \tag{C.44}$$

To summarize, as R increases, the spectrum of the BT operator is getting denser. However, the summation of the eigenmodes at fixed n yields in this limit the magnetization profile (C.43) that is the formula for free diffusion inside the magnetic field $-iGy^2/(2R)$ and is very close to 1. Therefore one can identify two situations and associated regimes.

(i) $\ell_{g,\parallel}^2 \gg \ell_g^2$: there is a large time separation between localization in the direction perpendicular to the boundary and localization in the direction parallel to the boundary. In that case there is a large range of times where the magnetization along the boundary is practically uniform and the signal decays according to the formula for the one-dimensional localization regime. This situation corresponds to a boundary with very large curvature radius.

(ii) $\ell_{g,\parallel}^2 \gtrsim \ell_g^2$: localization in the direction parallel to the boundary occurs on the same time scale than localization in the direction perpendicular to the boundary. Therefore the signal exhibits a complex behavior for $\ell_g^2 \lesssim T \lesssim \ell_{g,\parallel}^2$ with a transition to the localization decay controlled by $\mu_{1,1}$.

C.4 Computation of the matrix elements $d_{n,n'}$

In this appendix we present a detailed computation of the coefficients

$$d_{n,n'} = \int_0^\infty v_n'(x) v_{n'}(x)\, \mathrm{d}x \tag{C.45}$$

where $v_n(x)$ denote the one-dimensional BT eigenmodes on the half-line $x \geq 0$ with Neumann boundary condition at $x = 0$. These coefficients enter in the computation of the radial correction of BT eigenmodes at a curved boundary (see Sec. 4.2.2). The case $n = n'$ is straigthforward:

$$d_{n,n} = -\frac{1}{2} v_n^2(0) = \frac{e^{-i\pi/6}}{\ell_g |a_n|} \,. \tag{C.46}$$

In the following, we assume $n \neq n'$.

To compute the integral, we shall make appear explicitly the Bloch-Torrey operator $\mathcal{B} = -D_0\nabla^2 - iGx$ by relying on the property $\mathcal{B}v_n = \mu_n v_n$:

$$\mu_{n'} d_{n,n'} = \int_0^\infty v_n'(x)(\mathcal{B}v_{n'})(x)\, \mathrm{d}x \tag{C.47a}$$

$$= -D_0 \int_0^\infty v_n'(x) v_{n'}''(x)\, \mathrm{d}x - iG \int_0^\infty x v_n'(x) v_{n'}(x)\, \mathrm{d}x \,. \tag{C.47b}$$

We now integrate by parts twice the first term and we get

$$\int_0^\infty v_n'(x) v_{n'}''(x)\, \mathrm{d}x = v_n''(0) v_{n'}(0) + \int_0^\infty v_n'''(x) v_{n'}(x)\, \mathrm{d}x \,. \tag{C.48}$$

By putting all terms together, we can make appear again the BT operator

$$\mu_{n'} d_{n,n'} = \int_0^\infty (\mathcal{B}v_n')(x) v_{n'}(x)\, \mathrm{d}x - D_0 v_n''(0) v_{n'}(0) \,. \tag{C.49}$$

Note that the function $v_n', v_{n'}$ do not satisfy the symmetry property of the BT operator, i.e. one has $(v_n'|\mathcal{B}v_{n'}) \neq (\mathcal{B}v_n'|v_{n'})$ (see Sec. 1.2.4). One can see that the correction term is non zero because v_n' does not satisfy the Neumann boundary condition at $x = 0$. Mathematically, v_n' does not belong to the domain of the BT operator therefore the symmetry property is not applicable to this function.

Now we use the formulas

$$\mathcal{B}v_n' = (\mathcal{B}v_n)' + iGv_n = \mu_n v_n' + iGv_n \,, \qquad D_0 v_n''(0) = -\mu_n v_n(0) \tag{C.50}$$

to finally get the expression of $d_{n,n'}$

$$\mu_{n'} d_{n,n'} = \mu_n d_{n,n'} + \mu_n v_n(0) v_{n'}(0) \quad \Rightarrow \quad d_{n,n'} = \frac{\mu_n}{\mu_{n'} - \mu_n} v_n(0) v_{n'}(0) \,. \tag{C.51}$$

This formula can be simplified further by using the formula (4.29) for v_n and μ_n, which gives

$$d_{n,n'} = \frac{e^{-i\pi/6}}{\ell_g \sqrt{a_n a_{n'}}\,(a_{n'}/a_n - 1)} \,. \tag{C.52}$$

C.5 Spectral decomposition at a bifurcation point

In this appendix, we "translate" the general results of Sec. 4.3.2 on order-2 bifurcations analyzed with a matrix model in the language of eigenmodes of the Bloch-Torrey operator. In particular, we investigate the validity of the spectral decomposition (1.80), that we reproduce here for convenience

$$f(\mathbf{r}) \stackrel{?}{=} \sum_n (f|v_n) v_n(\mathbf{r}) \,, \tag{C.53}$$

where

$$(f|g) = \int_\Omega f(\mathbf{r}) g(\mathbf{r}) \, \mathrm{d}^3\mathbf{r} \,, \tag{C.54}$$

and the eigenmodes v_n are normalized by the condition $(v_n|v_n) = 1$. We recall that there is no complex conjugate in the definition of $(\cdot|\cdot)$ because of the non-Hermitianity of the BT operator. We emphasize that the validity of this formula is the cornerstone of the study of the eigenmodes and eigenvalues of the Bloch-Torrey operator.

C.5.1 Behavior of the eigenmodes at the bifurcation

Let us consider two eigenpairs (v_1, μ_1) and (v_2, μ_2) that undergo a bifurcation at $\tilde{G} = \tilde{G}_0$. The matrix model of Sec. 4.3.2 shows that v_1 and v_2 collapse onto a single eigenmode v_0 at the bifurcation. Moreover, since v_1 and v_2 are "orthogonal" with respect the bilinear form $(\cdot|\cdot)$ if $\tilde{G} \neq \tilde{G}_0$, we conclude by continuity that v_0 is self-orthogonal[2], i.e. $(v_0|v_0) = 0$.

The computations in Sec. 4.3.2 imply that close to the bifurcation point one can write

$$v_1(\mathbf{r}) \approx \beta_1(\tilde{G}) \left[v_0(\mathbf{r}) + (\tilde{G} - \tilde{G}_0)^{1/2} \varepsilon_0(\mathbf{r}) \right] \,, \tag{C.55}$$

$$v_2(\mathbf{r}) \approx \beta_2(\tilde{G}) \left[v_0(\mathbf{r}) - (\tilde{G} - \tilde{G}_0)^{1/2} \varepsilon_0(\mathbf{r}) \right] \,, \tag{C.56}$$

where the function $\varepsilon_0(\mathbf{r})$ is *a priori* unknown and depends on the details of the bifurcation point under study, and where $\beta_1(\tilde{G})$ and $\beta_2(\tilde{G})$ are normalization coefficients. To the first order in $(\tilde{G} - \tilde{G}_0)^{1/2}$, v_1 and v_2 are orthogonal to each other and the normalization condition is

$$2\beta_1^2(\tilde{G})(\tilde{G} - \tilde{G}_0)^{1/2}(v_0|\varepsilon_0) = -2\beta_2^2(\tilde{G})(\tilde{G} - \tilde{G}_0)^{1/2}(v_0|\varepsilon_0) = 1 \,, \tag{C.57}$$

therefore

$$v_1(\mathbf{r}) \approx k(\tilde{G} - \tilde{G}_0)^{-1/4} v_0(\mathbf{r}) + k(\tilde{G} - \tilde{G}_0)^{1/4} \varepsilon_0(\mathbf{r}) \,, \tag{C.58}$$

$$v_2(\mathbf{r}) \approx ik(\tilde{G} - \tilde{G}_0)^{-1/4} v_0(\mathbf{r}) - ik(\tilde{G} - \tilde{G}_0)^{1/4} \varepsilon_0(\mathbf{r}) \,, \tag{C.59}$$

with the constant $k = (2(v_0|\varepsilon_0))^{-1/2}$. We recall that the eigenvalues μ_1, μ_2 behave as

$$\mu_1 \approx \mu_0 + (\tilde{G} - \tilde{G}_0)^{1/2} \eta_0 \,, \qquad \mu_1 \approx \mu_0 - (\tilde{G} - \tilde{G}_0)^{1/2} \eta_0 \,, \tag{C.60}$$

with an unknown coefficient η_0. By writing the dimensionless Bloch-Torrey operator as

$$\tilde{\mathcal{B}} = -\nabla^2 - i\tilde{G}_0 x - i(\tilde{G} - \tilde{G}_0)x = \tilde{\mathcal{B}}_0 - i(\tilde{G} - \tilde{G}_0)x \,, \tag{C.61}$$

[2] Since v_0 is complex and $(\cdot|\cdot)$ does not contain complex conjugate, the condition $(v_0|v_0) = 0$ may be achieved for a non zero function v_0.

one can expand the eigenmode equation in powers of $(\tilde{G}-\tilde{G}_0)$ and keep the lowest-order term

$$\tilde{\mathcal{B}} v_1 = \mu_1 v_1 \,, \qquad \tilde{\mathcal{B}} v_2 = \mu_2 v_2 \tag{C.62}$$

$$\Leftrightarrow \tilde{\mathcal{B}}_0 \varepsilon_0 = \mu_0 \varepsilon_0 + \eta_0 v_0 \,. \tag{C.63}$$

One recognizes in the last equation the typical Jordan block associated to a bifurcation point (see Sec. 4.3.2).

C.5.2 Regularity of the spectral decomposition at a bifurcation point

The above equations (C.58) and (C.59) reveal that the eigenmodes v_1 and v_2 diverge as $(\tilde{G}-\tilde{G}_0)^{-1/4}$ at the boundary. This behavior is intuitively expected because they tend to the self-orthogonal eigenmode v_0, therefore the normalization coefficients β_1, β_2 diverge as $\tilde{G} \to \tilde{G}_0$. One may wonder whether this divergence produces specific effects in the spectral decomposition (C.53) such as a resonance effects where two eigenmodes near a bifurcation point would dominate the series. We show here that this is not the case and that, in some sense, two infinitely large values cancel each other that yields a continuous behavior in the limit $\tilde{G} \to \tilde{G}_0$. Note that this regularization follows from the general argument that the projector $\Pi(\tilde{G})$ over the space spanned by v_1, v_2 is an analytic function of $\tilde{G}$ at the bifurcation point (see Sec. 4.3.2).

Let us isolate the terms with v_1 and v_2 in the sum (C.53) and define:

$$f_{1,2}(\mathbf{r}) = (f|v_1)v_1(\mathbf{r}) + (f|v_2)v_2(\mathbf{r}) \,. \tag{C.64}$$

Now we use the previous expansions (C.58) and (C.59) and we obtain, close to the bifurcation point:

$$\begin{aligned} f_{1,2}(\mathbf{r}) \approx k^2 \Big((\tilde{G}-\tilde{G}_0)^{-1/4}(f|v_0) + (\tilde{G}-\tilde{G}_0)^{1/4}(f|\varepsilon_0) \Big) \\ \times \Big((\tilde{G}-\tilde{G}_0)^{-1/4} v_0(\mathbf{r}) + (\tilde{G}-\tilde{G}_0)^{1/4} \varepsilon_0(\mathbf{r}) \Big) \\ - k^2 \Big((\tilde{G}-\tilde{G}_0)^{-1/4}(f|v_0) - (\tilde{G}-\tilde{G}_0)^{1/4}(f|\varepsilon_0) \Big) \\ \times \Big((\tilde{G}-\tilde{G}_0)^{-1/4} v_0(\mathbf{r}) - (\tilde{G}-\tilde{G}_0)^{1/4} \varepsilon_0(\mathbf{r}) \Big) , \end{aligned} \tag{C.65}$$

which simplifies into

$$f_{1,2}(\mathbf{r}) \approx \frac{(f|\varepsilon_0)}{(v_0|\varepsilon_0)} v_0(\mathbf{r}) + \frac{(f|v_0)}{(v_0|\varepsilon_0)} \varepsilon_0(\mathbf{r}) \,, \tag{C.66}$$

where we recall that we have neglected higher order terms that would yield a contribution in $O((\tilde{G}-\tilde{G}_0)^{1/2})$.

Two important observations can be made: (i) the diverging terms in $(\tilde{G}-\tilde{G}_0)^{-1/4}$ have canceled each other and $f_{1,2}(\mathbf{r})$ has a finite value in the limit $\tilde{G} \to \tilde{G}_0$; (ii) at the bifurcation point, $f_{1,2}(\mathbf{r})$ is expressed as a linear combination of the eigenmode $v_0(\mathbf{r})$ and the additional function $\varepsilon_0(\mathbf{r})$. This shows that the spectral decomposition is still valid if the eigenmode family is supplemented with a "generalized eigenmode" $\varepsilon_0(\mathbf{r})$. Note that the function $\varepsilon_0(\mathbf{r})$ is the analogous of the vector Y_0 for the matrix model considered in Sec. 4.3.2.

If the function f represents the magnetization, then one can compute its time-evolution by exponentiating the Bloch-Torrey operator over the basis $(v_0, \varepsilon_0, v_3, v_4, \ldots)$. The only difference

with the general case lies in the 2×2 Jordan block associated to v_0, ε_0 (see Eq. (C.63)), that yields

$$\exp\left(-T\begin{bmatrix}\mu_0 & \eta_0\\ 0 & \mu_0\end{bmatrix}\right) = \exp(-\mu_0 T)\,[\mathsf{I} - \eta_0 T \mathsf{N}]\ , \tag{C.67}$$

where I is the 2×2 identity matrix and N is a 2×2 matrix with zeros everywhere except $\mathsf{N}_{1,2} = 1$. One may recognize the typical te^{-t} evolution of a critically damped harmonic oscillator, which also originates from the exponential of a Jordan block. Therefore, the evolution of the magnetization during an extended gradient pulse is given by

$$m(T,\mathbf{r}) = \frac{(1|\varepsilon_0) - \eta_0 T (1|v_0)}{(v_0|\varepsilon_0)} v_0(\mathbf{r}) e^{-\mu_0 T} + \frac{(1|v_0)}{(v_0|\varepsilon_0)} \varepsilon_0(\mathbf{r}) e^{-\mu_0 T} + \sum_{n\geq 3} (1|v_n) v_n(\mathbf{r}) e^{-\mu_n T}\ . \tag{C.68}$$

C.6 Slab with curved boundaries

In this appendix, we study the magnetization inside a slab with slightly curved boundaries. For simplicity, we assume that the domain is two-dimensional, and we shall consider three cases: biconcave slab (interior of an ellipse), convex-concave slab (annulus space), and biconvex slab (space between neighboring disks). The first case yields a universal correction factor to the motional narrowing formula for a slab with planar boundaries. In contrast, the second and third cases reveal a superposition of motional narrowing and localization behavior.

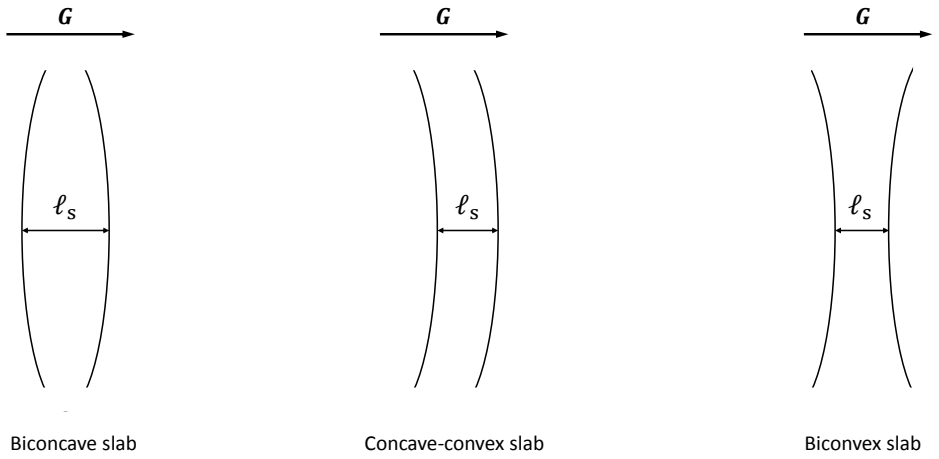

Figure C.4: Schematic description of three cases of "curved slab" considered in this appendix.

C.6.1 Biconcave slab

We treat the biconcave slab by performing the computations for the interior of an ellipse. The minor axis of the ellipse is the width of the slab ℓ_s, and we denote the major axis by $2c$. As illustrated on Fig. C.4, the gradient is directed along the minor axis of the ellipse. In the regime of large gradient, $\ell_g \ll \ell_s$, the magnetization localizes on each side of the slab, and the analysis of Sec. 4.2.2 is valid. Let us focus on the opposite regime $\ell_g \gg \ell_s$, that is the motional narrowing regime. We assume that the curvature radius $R = c^2/\ell_s$ is much larger in absolute value than ℓ_s. In that case one can model a curved slab as a superposition of small slabs with variable lengths (see Fig. C.5)

$$L(y) = \ell_s \sqrt{1 - y^2/c^2} \, . \tag{C.69}$$

Now we consider the application of a constant gradient pulse with amplitude G and duration T such that $\ell_d \gg \ell_s$ and $\ell_d \ll |R|$. The first assumption implies that the motional narrowing regime is set, while the second assumption allows us to treat the small slab elements as independent from each other, therefore the non-normalized signal results from the superposition of the signals produced by each slab:

$$s = \int_{-c}^{c} L(y) \exp\left(-\frac{G^2 T L(y)^4}{120 D_0}\right) \mathrm{d}y \, . \tag{C.70}$$

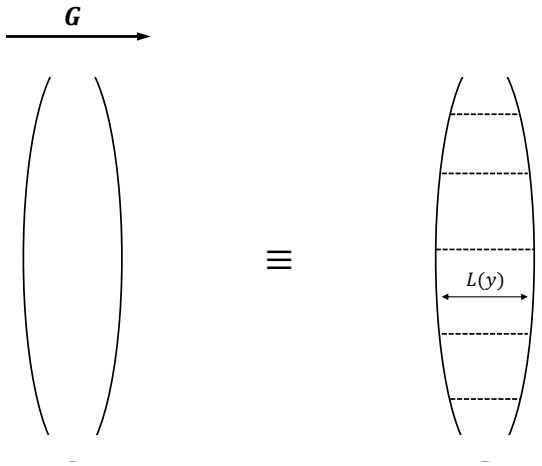

Figure C.5: In the limit of very large curvature radius, a curved slab may be approximated as a superposition of small slab elements with variable length $L(y)$.

Let us assume that the decay of the signal is weak so that the exponential can be linearized:

$$s \approx \int_{-c}^{c} L(y) \left[1 - \frac{G^2 T L(y)^4}{120 D_0}\right] \mathrm{d}y \,, \tag{C.71}$$

therefore the normalized signal is given by

$$S \approx \exp\left(-\frac{I_5}{I_1}\frac{G^2 T \ell_s^4}{120 D_0}\right) \,, \tag{C.72}$$

with the following integral

$$I_n = \int_{-1}^{1} (1-u^2)^{n/2} \,\mathrm{d}u \,. \tag{C.73}$$

With the change of variables $u = \cos\theta$, one can easily compute $I_5/I_1 = 5/8$, so that the motional narrowing for a long ellipse is given by

$$S \approx \exp\left(-\frac{1}{192}\frac{G^2 T \ell_s^4}{D_0}\right) \,. \tag{C.74}$$

The decay of the signal at long times is governed by the real part of the first eigenvalue μ_1 of the Bloch-Torrey operator according to $S \sim \exp(-\mathrm{Re}(\mu_1)T)$. Furthermore, the analysis of Sec. 4.3.1 shows that the spectrum is real at low gradients for parity-symmetric domains such as an ellipse. Therefore we conclude

$$\mu_1 \approx \frac{1}{192}\frac{G^2 \ell_s^4}{D_0} \,. \tag{C.75}$$

We have checked numerically this formula by computing the Bloch-Torrey spectrum at low gradient for ellipses with aspect ratios $c/\ell_s = 2$, 4, and 6. The numerical computations were performed with a matrix formalism as described in Sec. 1.1.5. The results are shown on Fig. C.6. We have plotted the first (rescaled) eigenvalue $\tilde{\mu}_1 = \mu_1 \ell_s^2 / D_0$ as a function of the rescaled gradient squared $\tilde{G}^2 = G^2 \ell_s^6 / D_0^2$. At low gradient strength, all ellipses yield the same linear behavior with a slope $1/192$, in accordance with Eq. (C.75).

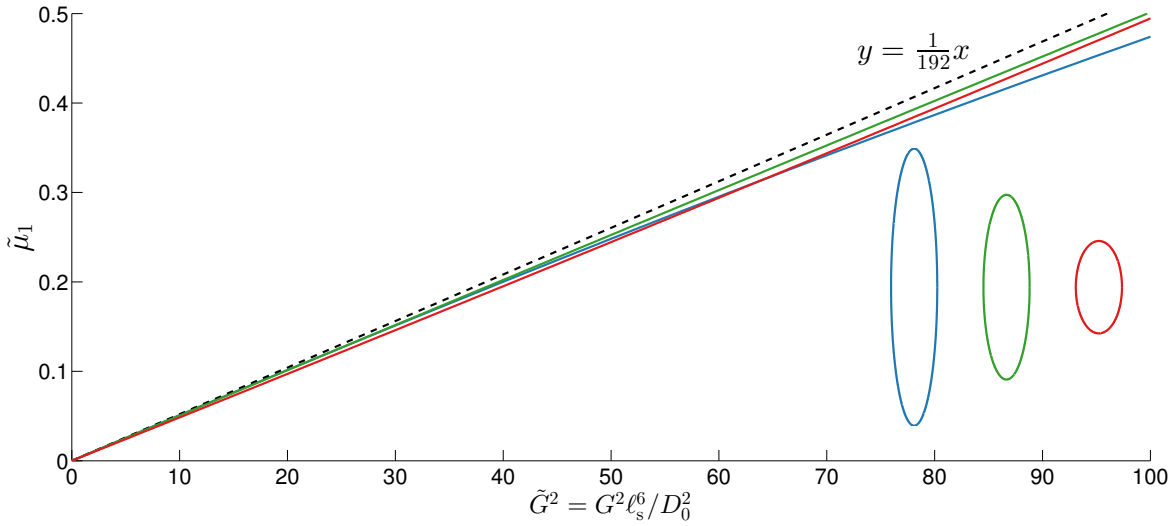

Figure C.6: First eigenvalue of the Bloch-Torrey operator in an ellipse with aspect ratios c/ℓ_s equal to 2 (red), 4 (green), and 6 (blue). At low gradients, all curves coincide with the motional narrowing formula with coefficient $1/192$.

C.6.2 Convex-concave slab

Now we turn to the behavior of the magnetization in an annulus space, with width ℓ_s and curvature radius R. We assume that R is much larger than any other relevant length scale so that this annulus space can be seen locally as a "slab" with curved boundaries. As illustrated on Fig. C.4, we restrict our analysis around a point where the gradient is perpendicular to the boundary. As above, if $\ell_g \ll \ell_s$, the magnetization is localized on each side of the slab, which corresponds to the analysis carried out in Sec. 4.2.2. We are interested in the opposite regime $\ell_s \ll \ell_g$.

Similarly to Sec. 4.2.2, one can perform a coordinate change and rewrite the Bloch-Torrey operator in terms of the radial distance r and the lateral coordinate y:

$$\mathcal{B} \approx -D_0\partial_r^2 - \frac{D_0}{R}\partial_r - iGr - D_0\partial_y^2 + iG\frac{y^2}{R} \,. \tag{C.76}$$

Let us assume that the radial distance r is counted from the center of the slab. In that case, the boundaries of the curved slab correspond to $r = -\ell_s/2$ and $r = \ell_s/2$. Thus, this coordinate change replaces a slab with curved boundaries by a slab with planar boundaries. Since the curvature radius R is assumed to be much larger than the slab width ℓ_s, the term $D_0\partial_r/R$ may be neglected and the Bloch-Torrey operator is then the sum of the operator for a slab with flat boundary plus the operator for a parabolic magnetic field. By applying the same analysis as in Secs. 4.2.2 and 4.3.1, one immediately obtains that the first eigenpair of the Bloch-Torrey operator may be written as

$$v_1(r,y) = f_1(r)g_1(y) \,, \qquad \mu_1 = \frac{1}{120}\frac{G^2\ell_s^4}{D_0} + e^{i\pi/4}\frac{D_0^{1/2}G^{1/2}}{(2R)^{1/2}} \,. \tag{C.77}$$

The function $f_1(r)$ is given a perturbative expansion (4.63) and is approximately constant over the slab width. In turn, the eigenvalue associated to $f_1(r)$ yields the first term in the expression

of μ_1. The function $g_1(y)$ is given by Eq. (4.55) and the corresponding eigenvalue yields the second term in the expression of μ_1. Thus, the behavior of the magnetization is that of motional narrowing along r and localization along y. This peculiar phenomenon is illustrated on Fig. C.7. We have plotted the first eigenpair (v_1, μ_1) of the BT operator for increasing gradient strength. One can see the localized state of the magnetization along y, with a localization length that decreases with increasing gradient. In contrast, the magnetization remains nearly uniform in the radial direction. The agreement between the approximate expression for μ_1 and the numerical results is very good.

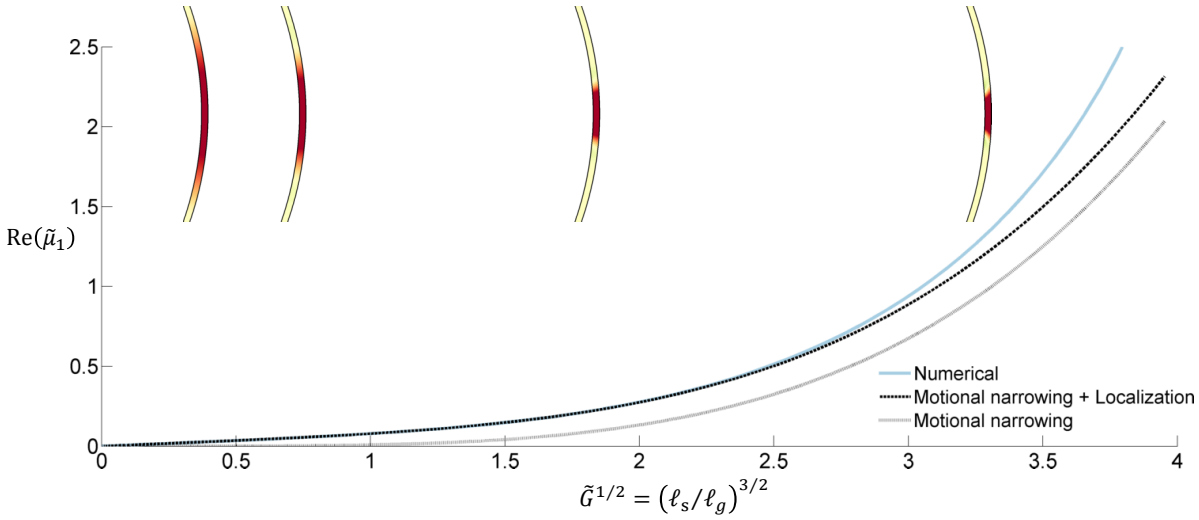

Figure C.7: First eigenvalue of the Bloch-Torrey operator in an annulus space as a function of $(\ell_s/\ell_g)^{3/2}$. The corresponding eigenmode is represented for several values of the gradient. The asymptotic formula (C.77) for the first eigenvalue is plotted by a black dashed line, whereas its first term (motional narrowing) is plotted as a gray line to emphasize the effect of the second term. One observes a localization behavior in the direction parallel to the boundary and a delocalized behavior in the direction perpendicular to the boundary.

One can clearly see the localization parallel to the boundary, while the magnetization profile in the radial direction is nearly constant. At large gradient, deviations with Eq. (C.77) occur. At even larger gradient, the eigenvalue eventually bifurcates and the eigenmode splits into two localized eigenmodes (not shown).

C.6.3 Biconvex slab

Finally, we consider a biconvex slab that is the space between two circles of radius R, separated by a distance ℓ_s. Similarly to the previous situation, we consider the regime $\ell_s \ll \ell_g$ where the magnetization along the gradient is expected to be delocalized. We were not able to address this problem analytically. Numerical simulations reveal a striking similarity between this case and the annulus space considered previously (see Figs. C.7 and C.8).

Therefore we conjecture that the magnetization for the biconvex slab is essentially similar to the magnetization for the annulus space. Because of the left-right symmetry of the biconvex slab, the eigenvalue of a delocalized mode is necessarily real, therefore we are led to the

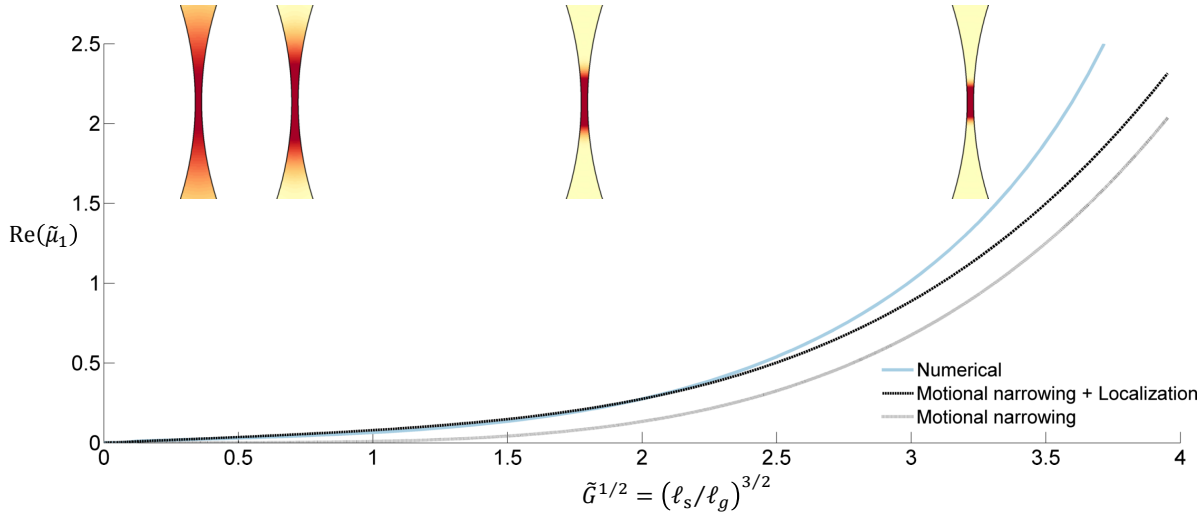

Figure C.8: First eigenvalue of the Bloch-Torrey operator in an annulus space as a function of $(\ell_s/\ell_g)^{3/2}$. The corresponding eigenmode is represented for several values of the gradient. The conjectured asymptotic formula (C.78) for the first eigenvalue is plotted by a black dashed line, whereas its first term (motional narrowing) is plotted as a gray line to emphasize the effect of the second term. One observes a localization behavior in the direction parallel to the boundary and a delocalized behavior in the direction perpendicular to the boundary.

conjectured formula

$$\mu_1 = \frac{1}{120}\frac{G^2\ell_s^4}{D_0} + \frac{1}{\sqrt{2}}\frac{D_0^{1/2}G^{1/2}}{(2R)^{1/2}}\,, \tag{C.78}$$

which is visually accurate at low gradient (see Fig. C.8).

C.7 From Localization to narrow-gradients

We show in this appendix that the formalism of spectral decomposition over the Bloch-Torrey eigenmodes allows one to recover the formula of the magnetization for a short-gradient pulse sequence. Since such sequences employ very strong gradients, one can use the results derived for the localization regime. Note however that the phenomena associated to narrow-gradients are different from that of the localization regime because the pulses are very short and create a position-encoding and not a diffusion-encoding mechanism.

We recall the spectral decomposition of the magnetization after a PGSE sequence (see Sec. 4.3.3):

$$m(\Delta+\delta,\mathbf{r}) = \sum_{n,m\geq 1} \alpha_n^* \beta_{n,m} v_m(\mathbf{r}) e^{-(\mu_n^*+\mu_m)\delta} , \tag{C.79}$$

with the following definitions for α_n and $\beta_{n,m}$:

$$\alpha_n = \int_\Omega v_n(\mathbf{r})\, \mathrm{d}^3\mathbf{r} , \tag{C.80}$$

$$\beta_{n,m} = \int_\Omega (\mathcal{D} v_n^*)(\mathbf{r}) v_m(\mathbf{r})\, \mathrm{d}^3\mathbf{r} , \tag{C.81}$$

where we have introduced the diffusion operator:

$$\mathcal{D} = \exp((\Delta-\delta)\nabla^2) . \tag{C.82}$$

At high gradients, we have shown in Sec. 4.2.1 that the eigenmodes v_n are localized at the boundary of the domain and the eigenvalues μ_n follow the asymptotic expansion:

$$\mu_n\delta \approx -iqx_n + e^{\mp i\pi/3}|a_n| q\ell_g , \tag{C.83}$$

with $q = G\delta$, $\ell_g = (G/D_0)^{-1/3}$, and x_n is the x-coordinate of the localization point of v_n. The $\mp$ sign depends whether localization happens to the left or to the right of the boundary point.

In the limit of narrow pulses, $\delta \to 0$, $G \to \infty$ and q remains constant and finite. The consequences are twofold: (i) since the gradient G is very large, the eigenmodes v_n of the Bloch-Torrey operator are strongly localized; (ii) $\ell_g \to 0$ so that Eq. (C.83) is reduced to:

$$\mu_n\delta \approx -iqx_n . \tag{C.84}$$

As a consequence, one can write

$$v_n(\mathbf{r}) e^{-\mu_n\delta} \approx v_n(\mathbf{r}) e^{iqx} , \tag{C.85}$$

$$\alpha_n e^{-\mu_n\delta} \approx \int_\Omega v_n e^{iqx}\, \mathrm{d}^3\mathbf{r} , \tag{C.86}$$

and Eq. (C.79) becomes

$$m(\Delta+\delta,\mathbf{r}) = \sum_{n,m} \left(\int_\Omega v_n e^{iqx}\, \mathrm{d}^3\mathbf{r}\right)^* \left(\int_\Omega (\mathcal{D}v_n)^*(\mathbf{r}) v_m\, \mathrm{d}^3\mathbf{r}\right) v_m(\mathbf{r}) e^{iqx} \tag{C.87}$$

$$= (\mathcal{D} e^{-iqx}) e^{iqx} , \tag{C.88}$$

which is exactly the formula for the magnetization under the NPA that can be obtained by considering the diffusion propagator on the domain Ω.

C.8 Localization for a radial gradient

Let us consider a rotationnally invariant domain with dimensionality d (e.g. disk, sphere). We denote the radial coordinate by r and we consider the time-independent Bloch-Torrey equation with a *radial* gradient on this domain:

$$D_0\nabla^2 v + iGrv + \mu v = 0\,, \tag{C.89}$$

We split the Laplace operator in radial and spherical part:

$$\nabla^2 v = \partial_r^2 v + \frac{d-1}{r}\partial_r v + \frac{1}{r^2}\nabla_s^2 v\,. \tag{C.90}$$

In the following we consider solutions of Eq. (C.89) that depend only on r, i.e. we set $\nabla_s^2 m = 0$. Note that for $d = 3$ the expression of the Laplace operator simplifies into

$$\nabla^2 m = \frac{1}{r}\partial_r^2(rm)\,. \qquad (d=3) \tag{C.91}$$

We now consider only the case $d = 3$. Using Eq. (C.91), we get the following equation on $f(r) = rv$

$$D_0 f'' + (\mu + iGr)f = 0\,, \tag{C.92}$$

that is the one-dimensional Bloch-Torrey equation, with a general solution

$$f(r) = AF_{\mathrm{r}}\left(\frac{x}{\ell_g} - i\frac{\ell_g^2\mu}{D_0}\right) + BF_{\mathrm{l}}\left(\frac{x}{\ell_g} - i\frac{\ell_g^2\mu}{D_0}\right)\,, \tag{C.93}$$

where the eigenvalue μ and the numerical coefficients A and B depend on the boundary condition, i.e. on the studied geometry. In the following, we consider the exterior and the interior of a sphere.

Exterior of a sphere

Let us denote the radius of the sphere by R. The boundary conditions are

$$\begin{cases} \partial_r v(r=R) = 0 \\ v(r\to\infty) \to 0 \end{cases} \Leftrightarrow \begin{cases} Rf'(\xi_R) - f(\xi_R) = 0 \\ B = 0 \end{cases}\,, \tag{C.94}$$

where $\xi_R = R/\ell_g - i\ell_g^2\mu/D_0$. Therefore, we have to compute the solution of

$$\frac{F_{\mathrm{r}}'}{F_{\mathrm{r}}}(\xi_R) = \frac{\ell_g}{R}\,. \tag{C.95}$$

Now let us assume that the radius of the sphere is much greater than the gradient length. Then the solutions are approximately given by the zeros of the derivative of F_{r}, i.e. $\xi_R \approx e^{i\pi/6}a_n$. One can obtain a better approximation by considering the derivative of the function $F_{\mathrm{r}}'/F_{\mathrm{r}}$ at $e^{i\pi/6}a_n$:

$$\left(\frac{F_{\mathrm{r}}'}{F_{\mathrm{r}}}\right)'(e^{i\pi/6}a_n) = e^{2i\pi/3}|a_n|\,, \tag{C.96}$$

which yields the approximate solution $\xi_R \approx -e^{i\pi/6}|a_n| + e^{-2i\pi/3}\frac{\ell_g}{R|a_n|}$. Note that one can compute higher order corrections in a similar way. From this solution we deduce the eigenvalues

$$\mu_n = -iGR + e^{-i\pi/3}|a_n|\frac{D_0}{\ell_g^2} + e^{-i\pi/6}\frac{D_0}{\ell_g R|a_n|} + O(D_0/R^2)\,, \tag{C.97}$$

and the eigenfunctions

$$v_n(r) = \frac{1}{r}F_{\mathrm{r}}\left(\frac{r-R}{\ell_g} - e^{i\pi/6}|a_n| - \frac{e^{i\pi/3}}{|a_n|}\frac{\ell_g}{R} + O((\ell_g/R)^2)\right)\,. \tag{C.98}$$

Note that for the gradient in a constant direction (i.e., not radial), the existence of eigenmodes has not been rigorously established yet [95].

Interior of a sphere

The boundary conditions are

$$\begin{cases} \partial_r v(r=R) = 0 \\ (rv)(r=0) = 0 \end{cases} \Leftrightarrow \begin{cases} Rf'(\xi_R) - f(\xi_R) = 0 \\ f(\xi_0) = 0 \end{cases}\,, \tag{C.99}$$

where $\xi_0 = -i\ell_g^2\mu/D_0$. Since all gradient vectors diverge from (or converge at) the center of the sphere, it is not surprising that the magnetization may localize at the point $r = 0$; however this is more a mathematical artifact that originates from our choice of a radial gradient than a physical effect, therefore we discard it. Let us assume once again that $\ell_g \ll R$, then we expect the magnetization to be localized near the boundary of the sphere and we write

$$\xi_0 = -i\ell_g^2\mu/D_0 = R/\ell_g + \eta\,, \tag{C.100}$$

with $\eta = O(1)$. Then the condition $f(\xi_0) = 0$ becomes

$$f(\eta + R/\ell_g) \to 0 \quad (R/\ell_g \to \infty)\,, \tag{C.101}$$

which implies that $A = 0$, and we are left with the equation

$$\frac{F_1'}{F_1}(\eta) = \frac{\ell_g}{R}\,. \tag{C.102}$$

Using the same technique as above, we find

$$\mu_n = -iGR + e^{i\pi/3}|a_n|\frac{D_0}{\ell_g^2} - e^{i\pi/6}\frac{D_0}{\ell_g R|a_n|} + O(D_0/R^2)\,, \tag{C.103}$$

and

$$v_n(r) = \frac{1}{r}F_1\left(\frac{r-R}{\ell_g} + e^{-i\pi/6}|a_n| - \frac{e^{-i\pi/3}}{|a_n|}\frac{\ell_g}{R} + O((\ell_g/R)^2)\right)\,. \tag{C.104}$$

Comparison with general asymptotic formulas

Let us compare the above formulas for μ_n with the asymptotic one (4.58) derived in Sec. 4.2.2. In our formulas, there is no $\ell_g^{-3/2}$ term, because our potential iGr is constant along the boundary. If we take into account that the mean curvature of a sphere is $H = 1/R$, we find that our formulas for μ_n coincide with Eq. (4.58).

C.9 Short-gradient sequence in a periodic medium

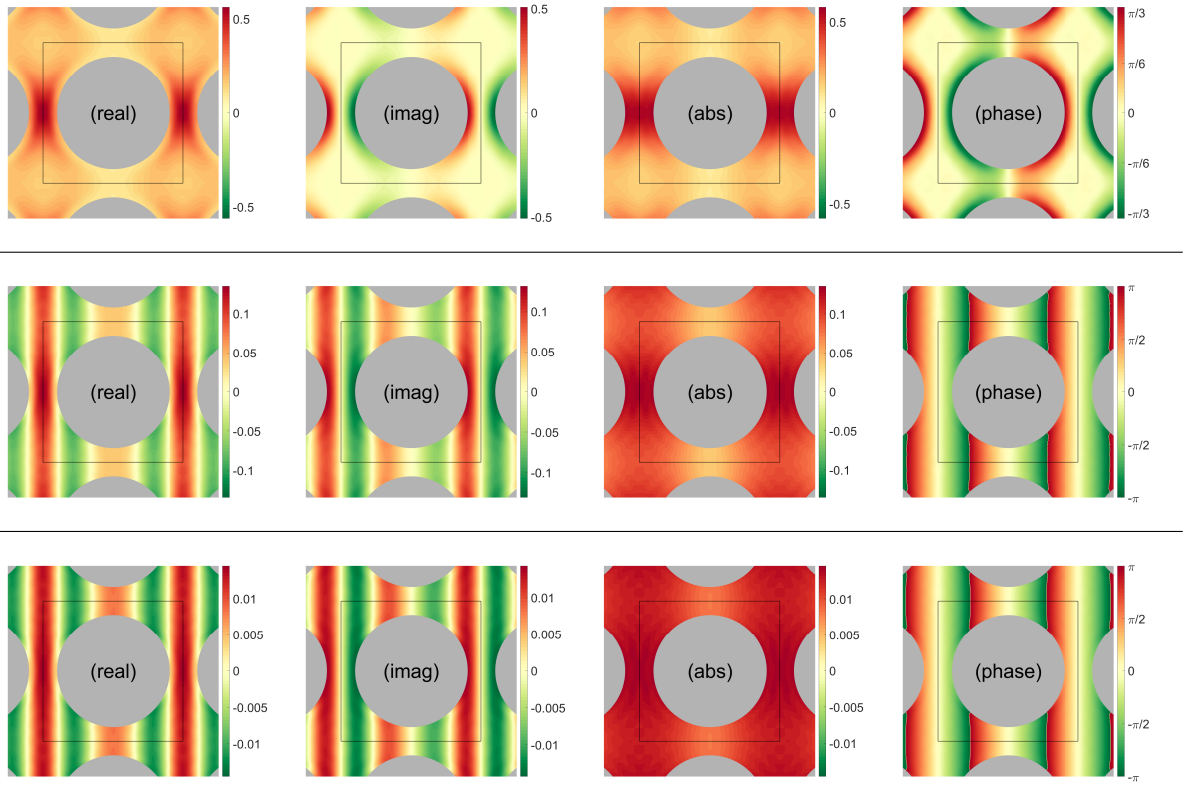

Figure C.9: Plot of the magnetization (real and imaginary part, absolute value and phase) after a narrow-pulse sequence. The gradient is in the left to right horizontal direction. The black square indicates the unit cell in which the computation was performed. For all figures, $R/a = 0.4$, and we kept a fixed value $qa = 14\pi/3$. The corresponding normalized signal is shown on the top panel of Fig. C.11. (top) $\ell_\Delta/a = 0.1$; (middle) $\ell_\Delta = 0.3$; (bottom) $\ell_\Delta/a = 1.0$.

In this appendix, we present and discuss the behavior of the magnetization and the signal for a short gradient pulse sequence (see Fig. 4.21 with $\delta \to 0$). As in the main text, we consider a 2D square lattice of impermeable circular obstacles with radius R and lattice step a. In that case, there are three relevant dimensionless quantities: R/a, qa, and ℓ_Δ/a, where q is the weight of the narrow gradient pulses and $\ell_\Delta = \sqrt{D\Delta}$ is the diffusion length traveled by spin-bearing particles during the time Δ between two pulses. Note that we write explicitly ℓ_Δ instead of ℓ_d to avoid any confusion with the extended-gradient pulse case. Diffusion in free space would yield a uniform magnetization

$$m = \exp(-bD_0) = \exp\left(-q^2\ell_\Delta^2\right) \ . \tag{C.105}$$

Note that the short-gradient pulse limit corresponds to $D_0G^2\delta^3 \to 0$ so that the mechanism behind the attenuation of the signal is different from the extended-gradient pulse situation presented in the main text. Correspondingly, the magnetization and the signal exhibit new behaviors as we shall now explain. Let us first assume that the gradient is along x, i.e. in the horizontal direction. The first gradient pulse multiplies the magnetization in the medium by e^{iqx}, then diffusion "blurs" this pattern and the second pulse multiplies the magnetization by

e^{-iqx}. As a consequence, the magnetization shows two very different patterns depending on the duration of the diffusion step.

(i) If the diffusion step duration is short so that $q\ell_\Delta \lesssim 1$, there is little "blurring" of the phase pattern by diffusion. Just before the second pulse, the magnetization is close to e^{iqx} but with a lower amplitude, because spins with different phases are mixed by diffusion: the average phase at a given position remains the same but dephasing of spins causes attenuation of magnetization. Close to obstacles, the phase pattern e^{iqx} is modified because it is "cut" by the boundaries. For this reason, the attenuation of the magnetization is less pronounced and the resulting phase of spins is modified as well. Thus, right after the second pulse, the magnetization is nearly uniform except for boundary regions where the magnetization is more intense (so-called "edge enhancement", see [105]) and has a significative imaginary part (after integration, this imaginary part cancels so that the signal is real).

(ii) if the diffusion step duration is long so that $q\ell_\Delta \gg 1$, the phase pattern is completely blurred by diffusion. However, the magnetization is not uniform because of the p-pseudo-periodicity created by the gradient pulse, where $p = q \pmod{2\pi/a}$. In terms of Laplacian eigenmodes, all $u_{n,p}$ with $n > 1$ relax and the magnetization is close to $u_{0,p}$ (with attenuation) after the diffusion step (and before the second pulse). Therefore, after the second pulse, the magnetization is close to $u_{0,p}e^{-iqx}$, that is somewhat similar to $e^{-i\tilde{q}x}$, where $\tilde{q}$ denotes here the multiple of $2\pi/a$ that is the closest to q.

These two regimes are shown on Fig. C.9 for the gradient in the horizontal direction and $qa = 14\pi/3$, where the top panel corresponds to $\ell_\Delta/a = 0.1$, i.e. $q\ell_\Delta = 1.5$ (case (i)), and the bottom panel corresponds to $\ell_\Delta/a = 1.0$, i.e. $q\ell_\Delta = 15$ (case (ii)). The middle panel corresponds to $\ell_\Delta/a = 0.3$, i.e. $q\ell_\Delta = 4.4$, that is an intermediate case between (i) and (ii).

The case of the gradient in the diagonal direction is very similar except that the length of the unit cell along the gradient direction is different. As it is shown in Fig. 4.23, although the diagonal of the unit cell is equal to $a\sqrt{2}$, one can reduce it further so that the actual period along the gradient direction is $a/\sqrt{2}$. Another way to see this is that the set $\{\mathbf{g}\cdot\mathbf{e}\}$, where $\mathbf{e}$ spans all vectors of the lattice, is equal to $(ga/\sqrt{2})\,\mathbb{Z}$. Thus, the same discussion as that for the horizontal case holds if one replaces a by $a/\sqrt{2}$. Following this conclusion, Fig. C.10 was obtained with $qa/\sqrt{2} = 14\pi/3$ and the gradient in the diagonal direction.

The normalized signal is plotted on Fig. C.11 as a function of $qa/(2\pi)$ for the gradient in the horizontal direction and as a function of $qa/(2\sqrt{2}\pi)$ for the gradient in the diagonal direction. In the weak blurring regime (i.e., $q\ell_\Delta \lesssim 1$), the signal decays according to an expression similar to Eq. (4.133):

$$S \approx \exp(-bD(\ell_\Delta/a)) = \exp\left(-\frac{D(\ell_\Delta/a)}{D_0}q^2\ell_\Delta^2\right), \tag{C.106}$$

where $0 < D(\ell_\Delta/a) < D_0$ is the effective diffusion coefficient that accounts for the restriction by obstacles in the domain. Because the gradient sequence considered here is not the same as the one for which Eq. (4.133) was written, the coefficient D is not the same but shares some common features [344]: $D(0) = D_0$, D is a linear function of $\sigma\ell_\Delta$ close to 0 and $D(\infty)$ yields the universal tortuosity limit of the medium. We have plotted Eq. (C.106) on Fig. C.11 for different values of ℓ_Δ/a (the parameter $D(\ell_\Delta/a)$ was obtained by fitting the low-q part of each curve). In the strong blurring regime (i.e., $q\ell_\Delta \gg 1$), the signal exhibits different behaviors depending on the diffusion length, that can be interpreted with the help of Eq. (4.127a) and related to the above discussion of the magnetization profile.

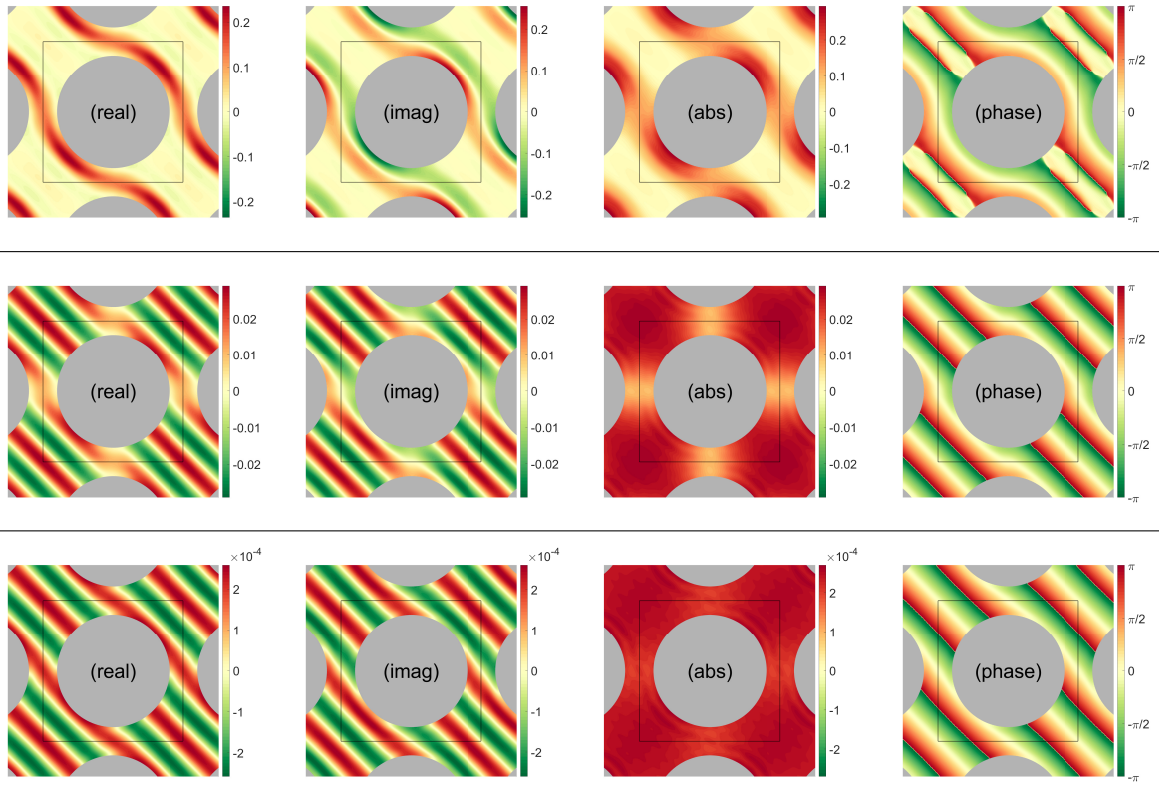

Figure C.10: Plot of the magnetization (real and imaginary part, absolute value and phase) after a narrow-pulse sequence. The gradient is in the bottom-left to top-right diagonal direction. The black square indicates the unit cell in which the computation was performed. For all figures, $R/a = 0.4$, and we kept a fixed value $qa/\sqrt{2} = 14\pi/3$. The corresponding normalized signal is shown on the bottom panel of Fig. C.11. (top) $\ell_\Delta/a = 0.1$; (middle) $\ell_\Delta = 0.3$; (bottom) $\ell_\Delta/a = 1.0$.

At short diffusion time (e.g. $\ell_\Delta/a \approx 0.1$), nearly all eigenmodes contribute to the signal in (4.127a) so that this expansion is not the best tool to understand the behavior of the signal. Because of the short diffusion time, one can treat the effect of the obstacle's boundary as a sum of independent contributions from small boundary regions (as in [84] where the signal in an interval is split into a sum "left boundary + bulk + right boundary"). As we show in Sec. 1.2.3, the strong blurring regime yields the following expression for the signal in a two-dimensional macroscopically isotropic domain:

$$S \approx \frac{\sigma \ell_\Delta}{\pi (bD_0)^{3/2}} = \frac{\sigma}{\pi q^3 \ell_\Delta^2}\,, \tag{C.107}$$

where $\sigma = 2\pi R/(a^2 - \pi R^2)$ is the surface-to-volume ratio of the domain. This is the two-dimensional Debye-Porod law where the signal is dominated by contributions from the boundaries in the medium.

At slightly longer diffusion time (e.g., $\ell_\Delta/a \approx 0.3$), high-order eigenmodes are almost fully attenuated and the signal is nearly equal to the first form factor $C_{p,0}(q_x)$ that depends on the structure of the unit cell. For example, the drop in signal at $qa/(2\pi) \approx 4$ for the gradient in the horizontal direction is characteristic of the particular value $R/a = 0.4$ for which the computation was performed. At even longer diffusion time, the exponential decay of the first eigenmode emerges and the signal is close to $C_{p,0}(q)\exp(-\lambda_{p,0}D_0\Delta)$. As we explained in Sec.

4.4.2, $\lambda_{p,0} = 0$ for $p = 0$ so that the signal exhibits "diffusion-diffraction" peaks that reveal the periodicity of the medium. The signal for the gradient in the diagonal direction shows peaks at integer values of $qa/(2\sqrt{2}\pi)$, that confirms the value of the period $a/\sqrt{2}$. Moreover, for $\ell_\Delta/a \gtrsim 1$, the decay of the signal at small values of qa is mainly dictated by $\exp(-\lambda_{0,p} D_0 \Delta)$ and not by the form factor $C_{p,0}(q_x)$ that has a slower decay with q. Combined with Eq. (C.106), this observation yields the following low-p asymptotic behavior:

$$\lambda_{0,p} \approx \beta(\infty) p^2 \,, \tag{C.108}$$

i.e., the behavior of the first Laplacian band at low wavenumber is directly related to the tortuosity limit of the medium. This observation generalizes our results in a periodic array of permeable barriers (see Sec. 3.4).

The comparison of Figs. C.9, C.10 and C.11 with Figs. 4.24, 4.25 and 4.26 reveals important qualitative differences. First, one can note a visual similarity between the localized magnetization in the bottom panels of Figs. 4.24, 4.25 and the edge enhancement effect that can be observed on the top panels of Figs. C.9 and C.10. However, we argue that these two regimes are vastly different. In fact, the localization regime arises when the motion encoding by the gradient is strong (i.e., $bD_0 \gg 1$) so that the transverse magnetization is strongly attenuated everywhere but in a small layer of thickness ℓ_g close to the obstacles, resulting in a weak signal. In contrast, the edge enhancement effect shown here appears even at weak gradient encoding (i.e., $bD_0 \lesssim 1$) so that the transverse magnetization is rather intense everywhere in the medium but enhanced near obstacles, resulting in a strong signal. Furthermore, a short-gradient pulse sequence with strong encoding (i.e., $bD_0 \gg 1$) gives rise to a peculiar striped pattern as shown on the bottom panels of Figs. C.9 and C.10. This delocalized pattern is in some sense the "opposite" of the localizated magnetization pockets shown on Figs. 4.24 and 4.25. This is especially apparent in the resulting signal: whereas the short-gradient pulse experiment probes the global structure of the domain that is revealed through the diffusion-diffraction pattern, the extended-gradient pulse experiment probes the local properties of obstacle's boundaries around localization points. Intuitively, the reason behind these differences is that the limit $\delta \to 0$, $g \to \infty$ with constant $G\delta = q$ yields $G^2\delta^3 = 0$. In other words, there is no motion encoding during the narrow gradient pulse, and the attenuation of the transverse magnetization is caused by the subsequent diffusion step. This is in sharp contrast with extended-gradient pulses that continuously encode the random motion of spin-bearing particles.

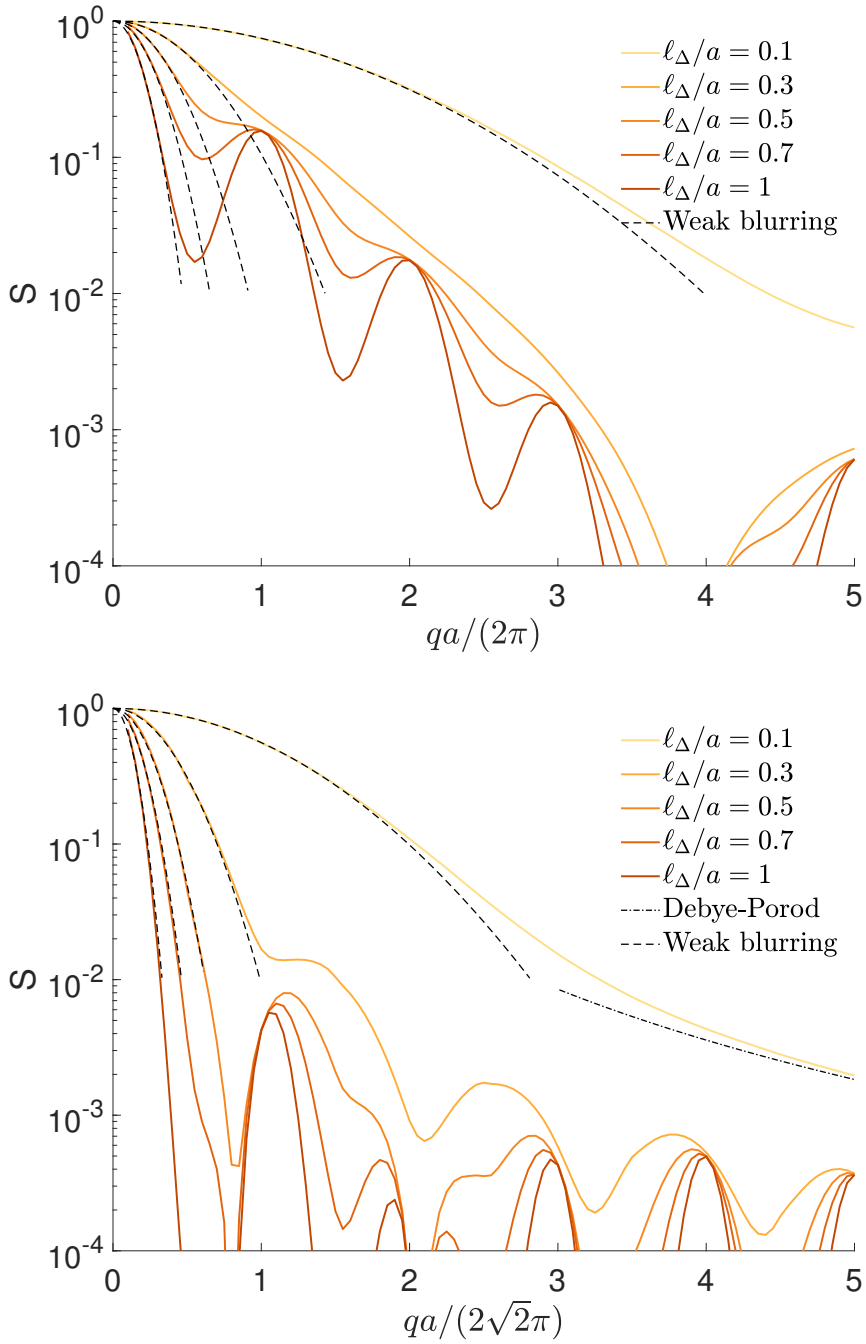

Figure C.11: Signal after a narrow-pulse sequence for different values of ℓ_Δ/a and asymptotic formulas (C.106) and (C.107) for the shortest diffusion time considered here, $\ell_\Delta/a = 0.1$. (top) The gradient is in the horizontal direction. (bottom) The gradient is in the diagonal direction. Refer to the text for discussion of the figure.

C.10 Another spectral method in 1D-periodic medium

In this appendix, we consider a 1D-periodic medium and show how to implement the effect of G_y and G_z gradients with an alternative spectral method to the one presented in Sec. 4.4.2. Instead of replacing G_y and G_z by a collection of narrow pulses, one can replace them by stepwise functions (see also Sec. 1.1.5). In fact, in bounded domains the effect of a constant gradient can be computed exactly with matrix multiplications.

Between two narrow G_x pulses, the magnetization is p-pseudo-periodic with a given wavenumber p and one can compute two matrices B_y and B_z:

$$\left[\mathsf{B}_{y,p}\right]_{n,n'} = \int_{\Omega_1} y\, u^*_{p,n} u_{p,n'}\, \mathrm{d}x\, \mathrm{d}y\, \mathrm{d}z \tag{C.109}$$

$$\left[\mathsf{B}_{z,p}\right]_{n,n'} = \int_{\Omega_1} z\, u^*_{p,n} u_{p,n'}\, \mathrm{d}x\, \mathrm{d}y\, \mathrm{d}z\ . \tag{C.110}$$

These two matrices encode the y and z terms of BT equation. Therefore, a constant G_y, G_z gradient pulse of duration τ is represented by the left-multiplication by the matrix $\exp(-D_0\tau\Lambda_p + iG_y\mathsf{B}_{y,p} + iG_z\mathsf{B}_{z,p})$. Note that one has to compute as many different $\mathsf{B}_{y,p}$ and $\mathsf{B}_{z,p}$ matrices as there are different values of p involved in the sampling.

C.11 Clarifications on the spectrum of a differential operator

Physicists and mathematicians employ the word "spectrum" with different meanings, which may lead to some confusion. In this Appendix, we illustrate by examples the mathematical definition of the spectrum and its distinction from a physical one. We shall see that in the end it is mostly consistent with the physicits' point of view and that according to this definition, the spectrum of the Bloch-Torrey operator is *empty* in free space. As this is a didactic discussion of terminology, we do not claim for mathematical rigor here.

Let us consider a differential operator $\mathcal{A}$. This operator is defined on the space of functions with some prescribed properties (smoothness, boundary conditions, etc.). Moreover, for technical reasons, one often restricts the operator to square-integrable functions $u \in L_2$. All these conditions define the domain $\mathcal{D}_\mathcal{A}$ of the operator.

An eigenmode (also called eigenfunction, or eigenvector, or eigenstate) of $\mathcal{A}$ is a function $u_\lambda \in \mathcal{D}_\mathcal{A}$ such that $\mathcal{A}u_\lambda = \lambda u_\lambda$, where $\lambda \in \mathbb{C}$ is the corresponding eigenvalue. Mathematically, the spectrum of $\mathcal{A}$, denoted $\sigma(\mathcal{A})$ is not the set of eigenvalues of $\mathcal{A}$ but a larger set: it is the set of all $\lambda \in \mathbb{C}$ such that $\mathcal{A} - \lambda$ is not invertible [340]. The eigenvalues present a particular case in which $\mathcal{A} - \lambda$ is not injective and thus form a subset of the spectrum; both definitions are not equivalent in (infinite-dimensional) functional spaces. In particular, as we shall discuss below, the set of eigenvalues may be empty even though the spectrum is not.

As an example, let us consider the Laplace operator on $\mathbb{R}$, $\mathcal{A} = -\mathrm{d}^2/\mathrm{d}x^2$, whose spectrum is $[0, \infty)$ from the physicists' point of view. We shall see that it is also the case according to the mathematical definition of $\sigma(\mathcal{A})$. Solving the equation $\mathcal{A}u = \lambda u$ with $\lambda \in \mathbb{R}$ yields

$$u_\lambda(x) = \exp(\pm i\lambda^{1/2}x) \qquad \text{if} \quad \lambda \geq 0\,, \tag{C.111}$$

$$u_\lambda(x) = \exp(\pm|\lambda|^{1/2}x) \qquad \text{if} \quad \lambda \leq 0\,. \tag{C.112}$$

None of these solutions is square-integrable, hence they do not belong to $\mathcal{D}_\mathcal{A}$ and they are not eigenmodes of $\mathcal{A}$ in the mathematical sense. If $\lambda < 0$, then $u_\lambda(x)$ diverges exponentially at ∞ or $-\infty$. If $\lambda \geq 0$, $u_\lambda(x)$ does not diverge at $\pm\infty$ and is in fact a tempered distribution. One can then see $u_\lambda(x)$ as a linear form on $\mathcal{D}_\mathcal{A}$ that satisfies an eigenmode equation. Therefore, u_λ with $\lambda \geq 0$ is a "generalized eigenmode" in the sense that

$$\forall v \in \mathcal{D}_\mathcal{A}, \quad \langle u_\lambda, (\mathcal{A} - \lambda)v\rangle = \langle(\mathcal{A} - \lambda)u_\lambda, v\rangle = 0\,, \tag{C.113}$$

so that the range of $\mathcal{A} - \lambda$ is included in the orthogonal space of u_λ, thus $\mathcal{A} - \lambda$ is not surjective and $\lambda \in \sigma(\mathcal{A})$. Another way to prove this result is to construct an approximate eigenmode by multiplying $u_\lambda(x)$ by a sequence of finitely supported functions with increasing support. The fact that $u_\lambda(x)$ does not diverge at $\pm\infty$ allows one to control the above approximation and prove that $\lambda \in \sigma(\mathcal{A})$. Note that we did not consider the case where λ is not real since $\mathcal{A}$ is Hermitian (or self-adjoint). It is easy to see from the general form of $u_\lambda(x)$

$$u_\lambda(x) = \exp(\pm i\lambda^{1/2}x)\,, \qquad \lambda \in \mathbb{C} \tag{C.114}$$

that $u_\lambda(x)$ diverges at ∞ or $-\infty$ whenever $\mathrm{Im}(\lambda) \neq 0$. One concludes here that the operator $\mathcal{A} = -\mathrm{d}^2/\mathrm{d}x^2$ has a continuous spectrum and no eigenvalues.

Now we discuss the case of the one-dimensional Bloch-Torrey operator on $\mathbb{R}$: $\mathcal{A} = \mathrm{d}^2/\mathrm{d}x^2 - ix$. As we shall see, this operator exhibits an empty spectrum (note that the spectrum of an

Hermitian operator is never empty). We apply the same procedure as in the previous example and look for solutions of the equation $\mathcal{A}u_\lambda = \lambda u_\lambda$:

$$u_\lambda(x) = F_{\mathrm{r}}(x - i\lambda) \quad \text{or} \tag{C.115}$$

$$u_\lambda(x) = F_{\mathrm{l}}(x - i\lambda)\ , \tag{C.116}$$

where F_{r} and F_{l} are defined in Eq. (4.24). Both these functions, for any $\lambda \in \mathbb{C}$, exhibit a fast divergence (as an exponential of $|x|^{3/2}$) at $-\infty$ hence they cannot be generalized eigenmodes. From another point of view, the divergence of $u_\lambda(x)$ at $-\infty$ prohibits the construction of a sequence of approximate eigenmodes. The spectrum of $\mathcal{A}$ is then empty.

One may argue that this is merely a matter of convention and that the spectrum of the Bloch-Torrey operator may be seen to be continuous (and in fact, equal to $\mathbb{C}$) if the rapidly diverging functions $u_\lambda(x)$ from Eqs. (C.115) and (C.116) are allowed. However, to be consistent with this convention, one would also have to consider $u_\lambda(x)$ from Eq. (C.114), for any $\lambda \in \mathbb{C}$, as an eigenmode of the Laplace operator and the spectrum of the Laplace operator on $\mathbb{R}$ would be $\mathbb{C}$. Therefore, to be consistent with the general convention that the spectrum of the Laplace operator on $\mathbb{R}$ is $[0, \infty)$, one must conclude that the spectrum of the Bloch-Torrey operator on $\mathbb{R}$ is empty. Note that this discussion extends to other domains in higher dimension.

Appendix D

Langevin equation and its interpretation

In this Appendix, we investigate diffusion in a spatially heterogeneous medium (i.e., with a position-dependent diffusion coefficient). It is quite well-known (see e.g. book [324]) that in this setting the diffusion equation is not uniquely determined and that a free parameter "α" enters in the diffusion equation. We first recall this peculiar mathematical phenomenon by showing how a seemingly well-defined Langevin equation yields infinitely many possible Fokker-Planck equations. Then we proceed to show that the indetermination of α results from coarse-graining of microscopic mechanisms and that there is no "true" value of α, from both mathematical and physical points of view. Then we discuss the behavior of an intensive quantity at an interface and we focus on the particular case of a thin, weakly diffusive membrane (see also Sec. 3.1.1). Depending on the value of α, a variety of phenomena is obtained. Finally, we perform the limit from a regularized Langevin equation (inertia, colored noise) to the singular Langevin equation (no inertia, white noise) and we obtain different values of α depending on the way that the limit is performed.

D.1 Introduction and notations

D.1.1 Langevin equation

The Langevin equation typically describes the one-dimensional motion of a massive particle inside a viscous fluid when subjected to a deterministic force and a random force:

$$m\ddot{x} = -\zeta\dot{x} - \partial_x U + \zeta\sqrt{2D_0}N(t)\ , \tag{D.1}$$

where U is a potential (typically depending on x) and m, ζ, D_0 are coefficients that play the role of the mass of the particle, the damping coefficient of the fluid, and the diffusivity of the particle in the fluid. The force (or "noise") $N(t)$ is a random (typically Gaussian) variable for any time t. In the following we further assume that $N(t)$ is a stationary process (no ageing) with zero mean. The noise is called "white" if $N(t)$ and $N(t')$ are independent whenever $t \neq t'$. Conversely it is "colored" if there are some time correlations, in which case one can write

$$\langle N(t)N(t')\rangle = \frac{\sigma_\mathrm{n}^2}{\tau_\mathrm{n}} C\left(\frac{t-t'}{\tau_\mathrm{n}}\right)\ , \tag{D.2}$$

where C is the two-point correlation function, which is normalized such that $C(0) = 1$ and $\int_{-\infty}^{\infty} C = 1$. Typically, C is an even fuction monotonically decaying at infinity, for example

$C(u) = e^{-2|u|}$. One can see that σ_n and τ_n play the roles of standard deviation and relaxation time of the noise, respectively. If $\tau_n \to 0$, the noise becomes gradually uncorrelated and one recovers the white noise, for which

$$\langle N(t)N(t')\rangle = \sigma_n^2 \delta(t-t') \ . \tag{D.3}$$

In this case, $N(t)$ is ill-defined as a random Gaussian variable and one circumvents this difficulty by considering it as a distribution and stating that $\int_a^b N(t)\mathrm{d}t$ is a Gaussian variable with zero mean and variance $(b-a)\sigma_n^2$, for any $a < b$.

This equation is often used to model the motion of a micron-sized particle interacting with a surrounding fluid by: (i) very frequent collisions with the fluid molecules with no bias; (ii) a macroscopic viscous drag. In other words, the total force exerted by the molecules on the particle can be split in a random part (collisions with no bias) and a mean part (viscous drag), because of the huge size ratio between the particle and the molecules. In usual fluids, a quick computation leads to a rate of collisions of about 10^{21} per second. If one assumes the collisions to be nearly independent, this leads to a correlation time $\tau_n \sim 10^{-21}s$. Because this time is much shorter than the temporal resolution of any experiment, the noise is modeled as a white noise.

Let us now consider another timescale of interest: the "inertial" relaxation time of the particle

$$\tau_i = \frac{m}{\zeta} \ . \tag{D.4}$$

This time embodies the ratio between inertia effects and viscous damping effects. One can understand it as the time taken by the viscous drag to "stop" the particle. If the particle and the fluid have the same densities (which is usually the case in experiments in order to eliminate gravity effects), then one can estimate this time as $\tau_i = \frac{2}{9}R^2/\nu$, where R is the radius of the particle and ν is the cinematic viscosity of the fluid. For example, if one chooses $R \sim 1\mu m$ and $\nu \sim 10^{-6}m^2/s$ (order of magnitude of the water viscosity), then $\tau_i \sim 1\mu s$. Increasing the viscosity of the fluid shortens this time even more. In the limit of infinitely short τ_i, one is led to discard inertia effects.

Both assumptions (infinitely short τ_n and infinitely short τ_i) yield together the well-known overdamped version of the Langevin equation

$$\dot{x} = -\frac{1}{\zeta}\partial_x U + \sqrt{2D_0}N(t) \ , \tag{D.5}$$

with a Gaussian white noise $N(t)$.

D.1.2 Simplified Langevin equation, Fokker-Planck equation

One interesting feature of Eq. (D.5) is that it leads to a Fokker-Planck equation on the particle density $f(x,t)$

$$\partial_t f = \partial_x\left(\frac{f}{\zeta}\partial_x U\right) + D_0\partial_x^2 f \ , \tag{D.6}$$

in which one recognizes a diffusion equation with a deterministic drift. Its stationary solution coincides with the Boltzman distribution

$$f_\infty(x) = A\exp(-U(x)/(k_B T)) \ , \tag{D.7}$$

where D_0, T, ζ satisfy the Stokes-Einstein relation

$$D_0 = \frac{k_B T}{\zeta} \ . \tag{D.8}$$

Note that keeping the inertia term $m\ddot{x}$ in the Langevin equation would have led to a coupled Fokker-Planck equation for x and $\dot{x}$, whereas time correlations in the noise would have prevented us from getting a *differential* Fokker-Planck equation at all because of memory effects.

Many physical phenomena may be modeled by a Langevin equation because, ultimately, the phenomenon is well-described by the resulting Fokker-Planck equation. In other words, any phenomenon that obeys the diffusion equation (D.6) can be modeled by the corresponding Langevin equation (D.5), even though the microscopic mechanism may differ greatly. The Langevin equation should then be understood as a coarse-grained description of the system, with the coarse-grained coefficients ζ, D and the coarse-grained potential $U(x)$. However, the process of coarse-graining may lead to some surprises.

A typical example is given by particles diffusing with "microscopic" diffusivity D_m inside a "microscopic" potential $U_m(x)$ with multiple wells. If we assume the Langevin equation to be a valid description of the microscopic system, then its equilibrium distribution is given by Boltzmann formula

$$f_{\infty,m}(x) = A_m \exp(-U_m(x)/(k_B T)) \ . \tag{D.9}$$

When coarse-grained, the system yields Gaussian diffusion again, however with a different diffusion coefficient D_0 that depends on the structure of the potential $U_m(x)$, such as the depth and width of the wells. The coarse-grained potential $U(x)$ is obtained through a local space averaging that we denote by $U(x) = \overline{U_m(x)}$. As a consequence, the resulting Boltzman distribution (D.7) may not coincide with $\overline{f_m}$, the locally averaged microscopic equilibrium distribution because in general

$$\overline{\exp\left(-\frac{U_m(x)}{k_B T}\right)} \neq \exp\left(-\frac{\overline{U_m(x)}}{k_B T}\right) \ . \tag{D.10}$$

For instance, let us consider that the bottom and the width of the potential wells are all identical but the tops are slowly modulated [309]. At low temperature, this slow modulation does not affect f_m, and thus $\overline{f_m}$ is independent of x. However, the averaged potential $U(x)$ now depends on x, that contradicts Eq. (D.7). At the same time, one can see that the diffusion coefficient D_0 depends on x, which *a priori* violates the validity of the Fokker-Planck equation (D.6).

D.2 Langevin equation with space-dependent coefficients

Suprisingly, the term $\sqrt{2D_0}N(t)$ becomes mathematically ambiguous if D_0 depends on x. The intuitive reason is that, in the absence of inertia or noise correlations, $x(t)$ may perform relatively large "jumps" that make $\sqrt{2D_0(x(t))}N(t)$ take different values depending on whether one evaluates $D_0(x(t))$ at "$t - 0$" (just before the jump), or at "$t + 0$" (just after the jump), or a mixture of both. We emphasize that this ambiguity is only caused by spatial heterogeneity and not by possible time dependence of the parameters of Langevin equation.

To make this statement more precise, we consider the simplest Langevin equation

$$\dot{x} = \sqrt{2D_0(x(t))}N(t) \tag{D.11}$$

and we integrate it over a short time interval:

$$\Delta x = \int_0^{\Delta t} \sqrt{2D_0(x(t))}N(t)\mathrm{d}t \ . \tag{D.12}$$

Now let us imagine that we want to evaluate $D(x)$ after the jump, that is

$$\Delta x_+ = \sqrt{2D_0(x(0)+\Delta x)} \int_0^{\Delta t} N(t)\mathrm{d}t \ . \tag{D.13}$$

The definition of Gaussian white noise implies that

$$\int_0^{\Delta t} N(t)\mathrm{d}t = \xi\sqrt{\Delta t} \ , \tag{D.14}$$

where ξ is Gaussian variable with zero mean and unit variance. Then, to the first order in $\sqrt{\Delta t}$, one can insert the expression of Δx_+ inside the right-hand side of the equation:

$$\Delta x_+ = \left(\sqrt{2D_0(x(0))} + \partial_x D_0 \xi\sqrt{\Delta t} + O(\Delta t)\right)\xi\sqrt{\Delta t} \tag{D.15}$$

$$= \sqrt{2D_0(x(0))}\xi\sqrt{\Delta t} + \partial_x D_0 \xi^2 \Delta t + O(\Delta t^{3/2}) \ . \tag{D.16}$$

In the above expression, the derivative of $D_0(x)$ can be taken either at $x(0)$ or $x(\Delta t)$ without changing the result up to order Δt. The first two terms on the right-hand side of the equation contribute equally in the limit $\Delta t \to 0$ because $\langle\xi\rangle = 0$ and $\langle\xi^2\rangle = 1$. By summing a large number of small increments Δx_+, the fluctuations of ξ^2 vanish and one can replace ξ^2 by its mean value, 1. More precisely, the law of large numbers implies that fluctuations of ξ^2 have a negligible effect to order Δt. The first term is Δx_- and one can see that it differs from Δx_+ by a drift term corresponding to a velocity

$$V = \partial_x D_0 \ . \tag{D.17}$$

In the previous computations, we discarded the potential $U(x)$ for the sake of clarity, but one can easily show that the same results hold if the potential is present in the Langevin equation.

To summarize, when evaluating the diffusion coefficient $D_0(x)$ after the jump, one adds a drift towards the higher values of D_0, compared to when it is evaluated before the jump. This is not surprising because if one evaluates the value of $D_0(x)$ after the jump, then a jump towards higher values of D_0 will be increased, whereas a jump towards lower values of D_0 will be decreased. What is surprising is that the jumps are sufficiently large to make this effect survive in the limit $\Delta t \to 0$.

Hence there is no unique definition of the Fokker-Planck equation associated to a Langevin equation with space-dependent diffusivity. In fact, there are as many possibilities as the ways to evaluate $D_0(x)$ during the jump. For instance, if one decides to evaluate $D_0(x)$ at the time $\alpha\Delta t$, with $0 \le \alpha \le 1$, then one gets a drift term equal to αV. The Fokker-Planck equation is then

$$\partial_t f = \partial_x\left(\frac{f}{\zeta}\partial_x U\right) + \partial_x^2(D_0 f) - \alpha\partial_x\left(f\partial_x D_0\right) \ , \tag{D.18}$$

from which we get the expression of the diffusive flux

$$J_\alpha = -\partial_x(D_0 f) + \alpha f \partial_x D_0 = -D_0^\alpha \partial_x (D_0^{1-\alpha} f) \ . \tag{D.19}$$

One can also derive the equilibrium distribution:

$$f_{\infty,\alpha} = \frac{A}{D_0^{1-\alpha}} \exp\left(- \int \frac{\partial_x U}{k_B T} \right) , \tag{D.20}$$

which simplifies in the case of constant T:

$$f_{\infty,\alpha} = \frac{A}{D_0^{1-\alpha}} \exp\left(- \frac{U(x)}{k_B T} \right) \ . \tag{D.21}$$

Three cases have been given special names

- $\alpha = 0$ is called "Itô";
- $\alpha = 1/2$ is called "Stratonovich";
- $\alpha = 1$ is called "isothermal", or "Hänggi-Klimontovich".

These cases exhibit different mathematical properties. The Itô operator $\partial_x^2(D_0 f)$ is a Laplacian-type operator, which makes it a preferred choice for many mathematical studies. Moreover, because the diffusion coefficient is evaluated before the jump in the Langevin equation, the position $x(t)$ and the noise $N(t)$ are independent random variables. The Stratonovich choice arises naturally as a limit of the Langevin equation when the noise $N(t)$ is colored and the noise correlation time τ_n goes to zero [317] (as we shall see in Sec. D.5). As a consequence, classical differential calculus (such as a change of variables) is applicable in the Langevin equation under this interpretation. The isothermal diffusion operator $\partial_x(D_0 \partial_x f)$ is self-adjoint and leads to homogeneous stationary solution in the absence of potential.

From a physical point of view, there are *a priori* no reasons to prefer one choice over the others. Although the Hänggi-Klimontovich choice ($\alpha = 1$) is the only one that yields the Boltzmann distribution in the case of constant T (Eq. (D.21)), we have seen in the previous section that for a coarse-grained system the equilibrium distribution may differ from the Boltzmann distribution. Moreover, one may simply consider the additional term $\alpha \partial_x(f \partial_x D_0)$ as a new potential term. This point of view allows to switch from one interpretation to the other simply by changing the potential $U(x)$. In other words, although the choice of α leads to infinitely many possible Fokker-Planck equation, all those equations have the same form of a diffusion term plus a force term. In particular, if there is no *a priori* reason that the force term takes a particular value, then the "paradox" of the choice of α disappears.

In order to illustrate the physical relevance of any value of α, let us consider a medium which is split in two parts of equal volume, the first part having a small diffusion coefficient D_1 and the second part having a large diffusion coefficient D_2. There is no external potential in the system. We let a particle diffuse in the medium and ask about the proportion of time spent in each part in the limit of long times. By ergodicity of the system, these proportions are given by the equilibrium distribution of the system. Hence, applying the Boltzmann distribution, one obtains that the time spent in each part is asymptotically the same, because the two parts have equal volume. This is in favour of the Hänggi-Klimontovich interpretation. However, another

line of reasoning gives an opposite result. One may argue that the diffusion coefficients do not affect the trajectory of the particle but only the "speed" at which the particle travels along it. As a consequence, the particle will go faster when experiencing the larger diffusion coefficient D_2 than when experiencing the smaller diffusion coefficient D_1. One concludes that the particle will spend more time in the first region. One can compute that the proportion of time spent in region i is ${D_i}^{-1}/({D_1}^{-1}+{D_2}^{-1})$, in which one recognizes the result given by the Itô interpretation (see Eq. (D.21)).

The so-called "Ito-Stratonovich" dilemma simply reveals that a heterogeneous system is not fully described by the diffusion coefficient $D_0(x)$. In the coarse-graining process, the diffusion coefficient emerges as an aggregate of several microscopical properties of the medium. Although this approach is perfectly valid for a homogeneous system, it remains ambiguous for a heterogeneous one where more informations on the microscopical mechanism behind the space variation of D_0 is required to write the Fokker-Planck equation.

D.3 Examples

Some authors proposed simple examples of systems that, after coarse-graining, can be described by diffusion with a space-dependent diffusion coefficient. Depending on the microscopic parameters of the systems, one obtains different interpretations (i.e., different values of α). We present two examples: the Lorentz gas and diffusion inside slowly modulated periodic potential. Both these examples show in different ways that the value of α has nothing to do with *a priori* considerations about the "correct" sampling point in the integral (D.12) but simply reflects the indetermination of the Fokker-Planck equation without knowledge of the microscopical mechanisms at play.

D.3.1 Lorentz gas

A particularly illuminating example is the random Lorentz gas system [310]: a particle moves ballistically and reflects on the boundary of randomly distributed disks. Following [310] we consider a two-dimensional Lorentz gas. There are three parameters in this system: the velocity v of the particle, the radius r of the disks, and the free volume fraction φ. As the disks cannot overlap, φ cannot take values below the compact packing limit $\varphi_{\min} = 1 - \pi/\sqrt{12} \approx 0.093$. When coarse-graining, the motion of the particle becomes diffusive. One can show by scaling arguments that the diffusion coefficient D_0 has the form

$$D_0 = vrF(\varphi) \,, \tag{D.22}$$

and the function $F(\varphi)$ is monotonically increasing from 0 at $\varphi = \varphi_{\min}$ to ∞ at $\varphi = 1$. Let us impose that the velocity of the particles is fixed. Then one can tune the diffusion coefficient by changing either r or φ. In particular one can reproduce the thought experiment of the previous section with two pairs (r_1, φ_1), and (r_2, φ_2) that produce two different diffusion coefficients D_1 and D_2.

Because the microscopic system is ergodic, the proportion of time spent by the particle in each part is simply proportional to their free volume fraction φ_1 and φ_2. If $\varphi_1 = \varphi_2$, the diffusion coefficients may be different because of different r_1 and r_2, however, the particle will

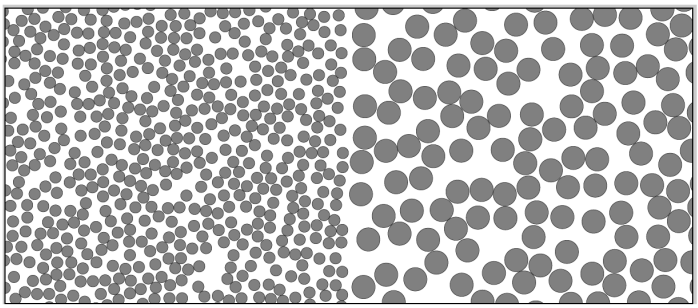

$\varphi_1 = 0.5; r_1 = 0.3; D_1 = 0.09$ $\varphi_2 = 0.5; r_2 = 0.6; D_2 = 0.18$

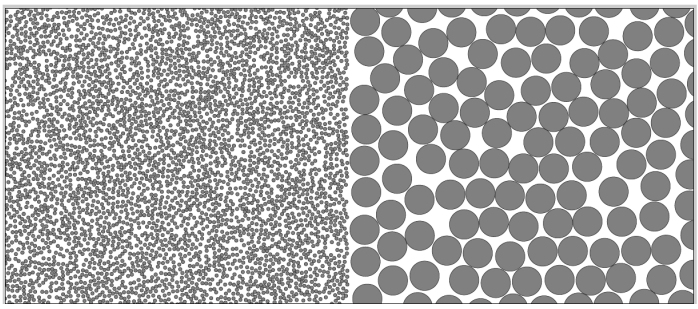

$\varphi_1 = 0.6;\ r_1 = 0.09; D_1 = 0.047$ $\varphi_2 = 0.3;\ r_2 = 0.75; D_2 = 0.094$

Figure D.1: Two examples of a Lorentz gas system split in two halves with different properties. One can see that in each case the free volume φ and the disk radius r are tuned to produce a diffusion coefficient twice larger in the right half than in the left half, i.e. $D_2 = 2D_1$. (top) $\varphi_1 = \varphi_2$ therefore the particles spend as much time in the left part than in the right part, in favor of Hänggi-Klimontovich interpretation. (bottom) $\varphi_1 = 2\varphi_2$ so that particles spend twice much time in the left part than in the right part, in favor of Itô interpretation. Figure adapted from Ref. [310].

spend an equal amount of time in each part. This corresponds to the Hänggi-Klimontovich interpretation. However, if one chooses $\varphi_1 \neq \varphi_2$, then the conclusion is different. By tuning φ and r, one can in fact produce any value of α. We will show in Sec. D.5 that this result may also be obtained by performing the coarse-graining explicitly.

D.3.2 Diffusion inside a slowly modulated periodic potential

In [309], Sokolov studied diffusion inside a slowly modulated periodic potential $U_m(x)$ such as the ones on Fig. D.2. We reproduce here his results and discussion in a simplified setting. After coarse-graining over a scale much larger than the period of the potential, the behavior of particles becomes diffusive with a coarse-grained diffusion D_0 that is controlled by the properties of the microscopic potential U_m, as we show below. For clarity we denote the microscopic position by x and the coarse-grained position by X.

We denote the slowly varying period of the potential by λ, its minima and maxima by $U_{\min}$ and $U_{\max}$, and we assume that these quantities are slowly position-dependent (i.e. they vary with X). Moreover, we assume that the temperature is constant and that $k_B T \ll U_{\max} - U_{\max}$. The coarse-grained potential $\overline{U_m}(X)$ is given by

$$\overline{U_m}(X) \approx \frac{U_{\max} + U_{\max}}{2} \,. \tag{D.23}$$

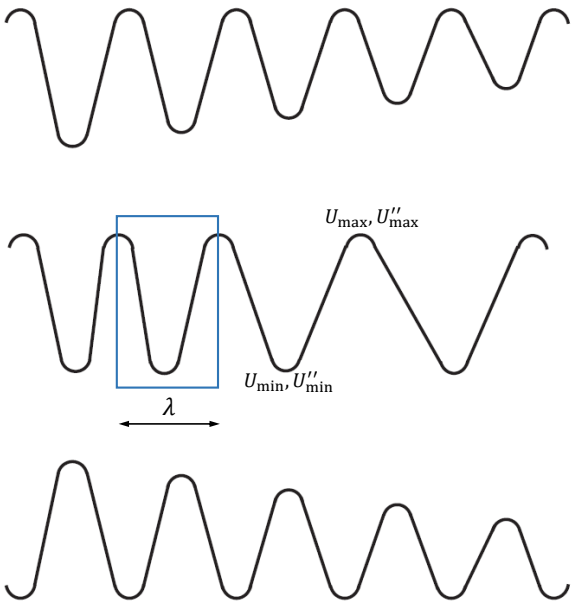

Figure D.2: Three examples of slowly modulated potential that yield an increasing coarse-grained diffusivity from left to right. The blue rectangle indicates one period over which averages are performed. (top) Trap model, where minima of the potential slowly increase; (middle) accordion model, where the period of the potential slowly increases; (bottom) barrier model, where the maxima of the potential slowly decrease. (Figure adapted from Ref. [309])

This simple formula is valid only if the potential has a symmetric profile in the integration range. In particular, correction terms would involve the difference in width of the wells, i.e.

$$\overline{U_m}(X) - \frac{U_{\max} + U_{\max}}{2} \sim (U_{\max} - U_{\max}) \left(\frac{1}{\sqrt{U''_{\max}}} - \frac{1}{\sqrt{U''_{\max}}} \right) , \tag{D.24}$$

where U'' denotes the second derivative of U_m, which is evaluated here at the minima and maxima of U_m. In the following, we set this correction term to 0 by imposing that $U''_{\max} = U''_{\max}$, therefore we use Eq. (D.23). Note that if a position-dependent λ is achieved by dilatation of the potential along x, then $U'' \sim 1/\lambda^2$. In that case $U''_{\max}$ and $U''_{\max}$ have the same spatial variations.

The coarse-grained diffusion coefficient is simply obtained from $D_0 = \lambda^2/(2\tau_{\text{jump}})$, where τ_{jump} is the typical time between two jumps above the barriers of potential. In the low-temperature limit, τ_{jump} is given by Arrhenius law, so that

$$D_0(X) = R(X)\lambda^2 \exp\left(-\frac{U_{\max} - U_{\max}}{k_B T} \right) , \tag{D.25}$$

where $R(X)$ is a rate that results from the geometric average of the rates at which the particle crosses the potential minima and maxima, i.e. $R(X) \sim D_m k_B T/\sqrt{U''_{\max} U''_{\max}}$ (one can show that the numerical prefactor is π, see Ref. [309]). On Fig. D.2, the potentials are drawn with constant $U''_{\max}$ and $U''_{\max}$, however in principle they can be position-dependent too. Finally, the coarse-grained equilibrium distribution is given by

$$\overline{f_m}(X) = \frac{A(X)}{\lambda} \exp\left(-\frac{U_{\max}}{k_B T} \right) , \tag{D.26}$$

where $A(X) \sim \sqrt{U''_{\max}/k_BT}$ is related to the width of the potential well. Note that with our hypothesis $U''_{\max} = U''_{\max}$, one has $A(X) = C/\sqrt{R(X)}$, where C is a constant. The coarse-grained equilibrium distribution $\overline{f_m}$ differs from the classical Boltzmann distribution (D.7) by a prefactor $\chi(X)$:

$$\overline{f_m}(X) = \chi(X) \exp\left(-\frac{\overline{U_m}}{k_BT}\right), \qquad \chi(X) = \frac{A(X)}{\lambda} \exp\left(\frac{U_{\max} - U_{\max}}{2k_BT}\right) = C D_0^{-1/2}(X) . \quad \text{(D.27)}$$

Sokolov concludes, by identification between Eqs. (D.21), (D.25) and (D.26), that each case presented on Fig. D.2 corresponds to a different interpretation. (i) The trap model corresponds to varying $U_{\max}$, and one can see that $\overline{f_m} \sim D_0^{-1}$, i.e. $\alpha = 0$ (Itô interpretation). (ii) The accordion model corresponds to varying λ, therefore $\overline{f_m} \sim D_0^{-1/2}$, i.e. $\alpha = 1/2$ (Stratonovich interpretation). (iii) The barrier model corresponds to varying $U_{\max}$, in that case $\overline{f_m}$ is constant through the medium and independent of D_0, i.e. $\alpha = 1$ (Hänggi-Klimontovich interpretation). Naturally, when all parameters vary at the same time, any value of α may be obtained in principle and α is generally position-dependent as well.

D.4 Continuity at an interface

In this section, we discuss the implication of the generalized expression (D.19) of the flux on a discontinuous interface between two regions with different diffusion coefficients. Then we turn to the case of a thin membrane with reduced diffusivity, which can model a permeable barrier (see Sec. 3.1.1). We assume that the medium is well described by an inhomogeneous diffusion coefficient D_0 with no external potential and a constant interpretation parameter α.

D.4.1 Continuity equations

Let us consider two half spaces $x < 0$ and $x > 0$, with diffusion coefficients $D_0 = D_-$ and $D_0 = D_+$, respectively. We shall denote by f a generic quantity "carried" by diffusing particles (such as magnetization, density, temperature). The local conservation of particles implies that the flux is continuous at the interface:

$$D_0^\alpha \partial_x (D_0^{1-\alpha} f)\big|_{x=0} = D_- \partial_x f|_{x=0^-} = D_+ \partial_x f|_{x=0^+} . \quad \text{(D.28)}$$

If one pictures a discontinuous interface as a very thin layer where the diffusion coefficient D_0 changes continuously from D_- to D_+, then the continuity of the flux yields two conditions: (i) $D_0^{1-\alpha} f$ is continuous at the interface; (ii) the fluxes on both sides of the interface are equal, i.e. $D_- \partial_x f|_{x=0^-} = D_+ \partial_x f|_{x=0^+}$.

Note that condition (i) implies that f is discontinuous at the interface if $\alpha \neq 1$ and that $f(0^+)/f(0^-) = (D_-/D_+)^{1-\alpha}$. Interestingly, such a condition is reminiscent of chemical systems in which the ratio of concentrations on both sides of the interface is equal to the partition coefficient [232–234, 259, 260].

D.4.2 Thin membrane

Now we consider a thin layer $-e/2 \leq x \leq e/2$ of width e and with diffusivity D_e inside such as on Fig. 3.2. Let us introduce the fluxes in each region:

$$J_- = -D_- \partial_x f|_{x=-e/2} , \qquad J_e = -D_e \partial_x f|_{x=0} , \qquad J_+ = -D_+ \partial_x f|_{x=e/2} . \tag{D.29}$$

We assume that the layer thickness is negligible compared to the scale of variation of the flux, therefore we have $J_- = J_e = J_+$ and we shall denote this constant flux by J in the following. This yields a first condition

$$D_- \partial_x f|_{x=-e/2} = D_+ \partial_x f|_{x=e/2} . \tag{D.30}$$

Now let us write the discontinuity equations at each interface. For clarity we denote by f_e the values of f inside the membrane, to distinguish them from the values outside.

$$f_e(-e/2) = \left(\frac{D_-}{D_e}\right)^{1-\alpha} f(-e/2) , \qquad f_e(e/2) = \left(\frac{D_+}{D_e}\right)^{1-\alpha} f(e/2) . \tag{D.31}$$

Furthermore, the variation of f_e inside the membrane can be computed from

$$f_e(e/2) - f_e(-e/2) \approx e \partial_x f|_{x=0} = \frac{eJ}{D_e} . \tag{D.32}$$

By combining these equations, we can relate $f(e/2)$ to $f(-e/2)$ by

$$f(e/2) = \left(\frac{D_e}{D_+}\right)^{1-\alpha} \left[\left(\frac{D_-}{D_e}\right)^{1-\alpha} f(-e/2) + \frac{Je}{D_e} \right] , \tag{D.33}$$

that we can simplify into

$$D_+^{1-\alpha} f(e/2) = D_-^{1-\alpha} f(-e/2) - J \frac{e}{D_e^\alpha} . \tag{D.34}$$

By analogy with Sec. 3.1.1, one recognize the permeability κ_α of the membrane on the right-hand side:

$$\kappa_\alpha = \frac{D_e^\alpha}{e} . \tag{D.35}$$

Moreover, one can compute the number n_e of particles trapped inside the membrane as

$$n_e \approx f_e(0) e \approx \frac{D_-^{1-\alpha} f(-e/2) + D_+^{1-\alpha} f(e/2)}{2} \frac{e}{D_e^{1-\alpha}} . \tag{D.36}$$

Therefore, one obtains a permeable barrier in the limit $e \to 0$ if two conditions are satisfied:

1. κ_α has a finite limit, that yields $D_e \sim e^{1/\alpha}$;
2. n_e goes to zero, i.e. $D_e^{1-\alpha} \gg e$.

By combining both conditions, one obtains $e^{(1-\alpha)/\alpha} \gg e$, that is verified in the limit $e \to 0$ only if $\alpha > 1/2$.

D.4.3 Summary

To summarize, there are generally three situations at an interface depending on the value of α. The first one occurs when $\alpha = 1$. In that case, f is continuous at any interface and one can model a permeable barrier by a thin membrane with $D_e/e = \kappa$. This yields the usual boundary equation at a permeable barrier, and the discontinuity of f is proportional to the flux J. This is the case considered in Chapter 3.

A somewhat opposite situation is obtained for $\alpha \leq 1/2$. In that case, f is always discontinuous at an interface, and f^+/f^- is related to the ratio of diffusivities on both sides of the interface. However, it is not possible to model a permeable barrier by a thin membrane. In fact, the discontinuity J/κ_α tends to zero when $e \to 0$ otherwise the number of particles inside the membrane goes to infinity, which is not physical. Note that the value $\alpha = 1/2$ is special and corresponds to $\kappa_{1/2} = \sqrt{D_e}/e$, i.e. a finite permeability corresponds to a finite crossing time e^2/D_e of the membrane. In that case the number of particles inside the membrane is finite and given by $n_e \sim 1/\kappa_\alpha$. Such a situation could model a trap with a finite escape time.

The intermediate situation $1/2 < \alpha < 1$ is a mixture of both cases. The function f is discontinuous at interfaces, with a ratio f^+/f^- that depends on the ratio of diffusivities on both sides. In addition, a thin membrane may model a permeable barrier, with an additional discontinuity that is proportional to the flux.

D.5 Singular limit

We have explained previously that the existence of the interpretation parameter α is a consequence of the "singularity" of the Langevin equation, in which the absence of inertia and/or the absence of correlations in the noise allow relatively large "jumps". In turn, if one goes back to the general Langevin equation (D.5) with $m \neq 0$ (i.e. $\tau_\mathrm{i} > 0$) and a colored noise with $\tau_\mathrm{n} > 0$, then the ambiguity of interpretation disappears. Therefore it is natural to ask what happens in the limit $\tau_\mathrm{i} \to 0$, $\tau_\mathrm{n} \to 0$. This question (or a similar one) has been considered by several authors [318–323] in various contexts (e.g. constant temperature, or constant damping, or absence of inertia, and so on) and we take this opportunity to present quite general results in a unified way, without claiming for mathematical rigor.

For convenience, we summarize our results here. There are two main situations depending on the ratio between τ_i and τ_n:

1. if $\tau_\mathrm{i} \ll \tau_\mathrm{n}$, i.e. if inertia can be neglected compared to correlations in the noise, then the limit yields the Stratonovich interpretation $\alpha = 1/2$;

2. if $\tau_\mathrm{n} \ll \tau_\mathrm{i}$, i.e. if the correlations in the noise can be neglected compared to inertia, then there is no unique answer. If the temperature T is constant, then one obtains the Hänggi-Klimontovich interpretation $\alpha = 1$. If, on the contrary, the damping coefficient ζ is constant, one obtains the Itô interpretation $\alpha = 0$. In general, one obtains any (and possibly position-dependent) value of α.

We start with the first case, then we show how the second case may obtained from the first one. We shall denote a small time step by Δt and compute the variation of quantities from $t = 0$ to $t = \Delta t$. Therefore, we shall discard all higher-order terms (such as $\Delta t^{3/2}$, Δt^2, etc.)

in the following computations, without always expliciting them. In the same way, we shall discard all terms that go to zero as either τ_n or τ_i goes to zero.

D.5.1 No inertia, colored noise

We consider the stochastic equation

$$\dot{x} = \sqrt{2D_0(x)}N(t) \,, \tag{D.37}$$

where N is a colored noise with correlation time τ_n. We do not consider any external potential to simplify the formulas but it can be included in a straightforward way. If $\Delta t \ll \tau_n$, the integral of $N(t)$ over the time Δt is a quantity of order Δt; in contrast if $\Delta t \gg \tau_n$, then the integral of $N(t)$ over the time Δt is of order $\sqrt{\Delta t}$ (as it is the case for white noise). This is the crucial point on which the following computation relies.

We consider a time step $\Delta t \ll \tau_n$ and we compute the variation of x over Δt:

$$\Delta x = \int_0^{\Delta t} \sqrt{2D_0(x(t))}N(t)\,\mathrm{d}t = O(\Delta t) \,. \tag{D.38}$$

Therefore, one has approximately

$$\Delta x = \int_0^{\Delta t} \sqrt{2D_0(x(0))}N(t)\,\mathrm{d}t + O(\Delta t^2) \,. \tag{D.39}$$

One can see that because of the "small" jump of size $\Delta x = O(\Delta t)$, there is no interpretation parameter α, since one would get a correction term of order Δt^2 by evaluating $D_0(x(t))$ at $t = \Delta t$ instead of $t = 0$.

Now, in order to obtain the associated Fokker-Planck equation, we consider a test function $\varphi(x)$ and we compute its variation over the time Δt:

$$\varphi(x(\Delta t)) - \varphi(x(0)) = \varphi(x(0) + \Delta x) - \varphi(x(0)) = \int_0^{\Delta t} \varphi'(x(t))\sqrt{2D_0(x(t))}N(t)\,\mathrm{d}t \,. \tag{D.40}$$

This term is of order Δt and its value depends on the correlation between $x(t)$ and $N(t)$. More precisely, we have to compute a quantity of the general form $\langle B(t)\psi(x(t))\rangle$. To perform this computation, let us choose a large integer k and write this quantity as a time integral

$$N(t)\psi(x(t)) = N(t)\psi(x(t - k\tau_n) + \int_{t-k\tau_n}^{t} \psi'(x(s))\sqrt{2D_0(x(s))}N(s)N(t)\,\mathrm{d}s \,, \tag{D.41}$$

where we have inserted the evolution equation (D.37) of x inside the integral. Now we use the assumption of large k to deduce $\langle N(t)\psi(x(t - k\tau_n)\rangle = 0$, and we use the definition (D.2) of the noise correlator to perform the average:

$$\langle N(t)\psi(x(t))\rangle = \int_{t-k\tau_n}^{t} \left\langle \psi'(x(s))\sqrt{2D_0(x(s))}\right\rangle \frac{\sigma_n^2}{\tau_n} C\left(\frac{t-s}{\tau_n}\right) \mathrm{d}s \tag{D.42}$$

$$\underset{\tau_n \to 0}{\to} \frac{1}{2}\left\langle \psi'(x(t))\sqrt{2D_0(x(t))}\right\rangle \,. \tag{D.43}$$

This result allows us to conlude the computation of the variation of φ:

$$\langle \varphi(x(\Delta t)) - \varphi(x(0)) \rangle = \int_0^{\Delta t} \frac{1}{2} \left\langle \left(\varphi' \sqrt{2D_0} \right)' (x(t)) \sqrt{2D_0(x(t))} \right\rangle \mathrm{d}t \tag{D.44}$$

$$\approx \frac{\Delta t}{2} \left\langle \left(\varphi' \sqrt{2D_0} \right)' (x(t)) \sqrt{2D_0(x(t))} \right\rangle \ . \tag{D.45}$$

If we denote by $P(t,x)$ the probability density of x at time t, then we have shown that

$$\int \varphi(x) \partial_t P(t,x) \, \mathrm{d}x = \left\langle \frac{\mathrm{d}}{\mathrm{d}t} \left(\varphi(x(t)) \right) \right\rangle \tag{D.46}$$

$$= \frac{1}{2} \left\langle \left(\varphi' \sqrt{2D_0} \right)' (x(t)) \sqrt{2D_0(x(t))} \right\rangle \tag{D.47}$$

$$= \int \frac{1}{2} \sqrt{2D_0(x)} \left(\varphi' \sqrt{2D_0} \right)' (x) P(t,x) \, \mathrm{d}x \tag{D.48}$$

$$= \int \frac{1}{2} \varphi(x) \left(\sqrt{2D_0} \left(\sqrt{2D_0} P \right)' \right)' \, \mathrm{d}x \ . \tag{D.49}$$

The above formula is valid for any test function $\varphi(x)$, therefore the probability distribution $P(t,x)$ obeys the following Fokker-Planck equation

$$\partial_t P = \partial_x \left(\sqrt{D_0} \partial_x \left(\sqrt{D_0} P \right) \right) \ , \tag{D.50}$$

that corresponds to Stratonovich interpretation $\alpha = 1/2$. This result is somewhat expected because a colored noise may be seen as a regular function that approximates a white noise as $\tau_\mathrm{n} \to 0$, and a theorem [317] shows that such a limit always yields Stratonovich interpretation.

D.5.2 White noise and inertia

Now we consider the opposite situation where $N(t)$ is a white noise and the particle obeys

$$\ddot{x} = -\xi(x)\dot{x} + \sqrt{2D_0(x)} \xi(x) N(t) \ , \tag{D.51}$$

where $\xi(x) = \zeta(x)/m$ is the inverse of the inertial relaxation time τ_i. Let us introduce the function

$$\Xi(t,t') = \int_t^{t'} \xi(x(s)) \, \mathrm{d}s \ . \tag{D.52}$$

Then one can integrate the time evolution equation as

$$\dot{x}(t) - \dot{x}(0) = \int_0^t \exp\left(-\Xi(s,t)\right) \sqrt{2D_0(x(s))} \xi(x(s)) N(s) \, \mathrm{d}s \ . \tag{D.53}$$

Loosely speaking, this equation looks like a Langevin equation without inertia and with a colored noise. We shall follow this intuition and transform the right-hand side to make appear an effective colored noise $\hat{N}(t)$. This requires to get rid of all factors that depend on $x(t)$.

Note that the exponential factor effectively limits the integration range to $\sim \tau_{\mathrm{i}}$, therefore the right-hand side is of order $\sqrt{\tau_{\mathrm{i}}}$. This allows us to write Ξ as

$$\Xi(t,t') \approx \int_t^{t'} \left(\xi(x(t)) + \xi'(x(t)) \int_t^s \dot{x}(r)\,\mathrm{d}r\right) \mathrm{d}s \tag{D.54}$$

$$\approx (t'-t)\xi(x(t)) + O(\tau_{\mathrm{i}}^{3/2}) \,. \tag{D.55}$$

Now we have to simplify the factor $\xi(x)\sqrt{2D_0(x)}$, that we denote by $\eta(x)$. One has

$$\eta(x(s)) \approx \eta(x(t)) - \eta'(t) \int_s^t \dot{x}(r)\,\mathrm{d}r \tag{D.56}$$

and we inject the integrated evolution equation of $\dot{x}$ into this formula, that yields approximately

$$\eta(x(s)) \approx \eta(x(t)) - \eta(x(t))\eta'(x(t)) \int_s^t \int_0^r e^{-(r-u)\xi(x(t))} N(u)\,\mathrm{d}u\,\mathrm{d}r - \eta'(x(t))(t-s)\dot{x}(0) \,. \tag{D.57}$$

Let us introduce the colored noise

$$\hat{N}(t) = \xi(x(t)) \int_0^t e^{-\xi(x(t))(t-s)} N(s)\,\mathrm{d}s \,. \tag{D.58}$$

One can see that it has a correlation time $\sim \tau_{\mathrm{i}}$. By combining the above equations, one can rewrite the evolution equation on x as

$$\begin{aligned}\dot{x}(t) - \dot{x}(0) &= \eta(x(t))\hat{N}(t) \\ &\quad - \eta(x(t))\eta'(x(t)) \int_0^t \int_s^t \int_0^r e^{-(t-s)\xi(x(t))} e^{-(r-u)\xi(x(t))} N(s)N(u)\,\mathrm{d}u\,\mathrm{d}r\,\mathrm{d}s \,.\end{aligned} \tag{D.59}$$

The last term is random but may be reduced to its average value (the argument is similar to the one that allowed us to simplify Eq. (D.16)):

$$\begin{aligned}&\left\langle \int_0^t \int_s^t \int_0^r e^{-(t-s)\xi(x(t))} e^{-(r-u)\xi(x(t))} N(s)N(u)\,\mathrm{d}u\,\mathrm{d}r\,\mathrm{d}s \right\rangle \\ &\qquad = \int_0^t \int_s^t e^{-(t-s)\xi(x(t))} e^{-\xi(x(t))(r-s)}\,\mathrm{d}r\,\mathrm{d}s \approx \frac{1}{2\xi(x(t))^2}\end{aligned} \tag{D.60}$$

Therefore, we obtain that the Langevin equation with inertia becomes a Langevin equation without inertia but with a colored noise and a drift term:

$$\dot{x} = \sqrt{2D_0(x)}\hat{N}(t) - \frac{\eta\eta'}{2\xi^2}(x) \,. \tag{D.61}$$

From the previous subsection we know that the resulting Fokker-Planck equation yields the Stratonovich interpretation in the $\tau_{\mathrm{i}} \to 0$ limit:

$$\begin{aligned}\partial_t P &= \partial_x \left(\sqrt{D_0}\partial_x \left(\sqrt{D_0}P\right)\right) + \partial_x \left(\frac{\eta\eta'}{2\xi^2}P\right) \\ &= \partial_x \left(D_0 \partial_x P\right) + \partial_x \left(D_0 \frac{T'}{T} P\right) \,,\end{aligned} \tag{D.62}$$

where we have written that equation in order to make explicitly appear the Hänggi-Klimontovich interpretation $\alpha = 1$. Indeed, one can see that if T is constant, then the second term in the right-hand side vanishes. In turn, the situation where ζ is constant yields $D_0 T'/T = D_0'$, therefore the Fokker-Planck equation yields the Itô interpretation $\alpha = 0$. Naturally, any value of α is obtained if both T and ζ are position-dependent:

$$1 - \alpha = \frac{T'/T}{T'/T - \zeta'/\zeta} \,. \tag{D.63}$$

Note that $T'/T - \zeta'/\zeta = D_0'/D_0$ so that it vanishes for a constant diffusivity D_0, in which case the interpretation, i.e. the value of α, does not matter.

D.5.3 The Lorentz gas revisited

One can check the consistency of the above computations on the particular example of the Lorentz gas. Indeed, the motion of a particle that bounces on hard disks is *a priori* well described by a Langevin equation with inertia and a white noise. The temperature is a measure of the kinetic energy density inside the medium that yields

$$k_B T = v^2 \varphi^{-1} \,, \tag{D.64}$$

where φ is the free volume fraction in the medium. Now we assume a constant value of α and we use the above equation (D.63), that gives

$$(1 - \alpha) \frac{D_0'}{D_0} = -\frac{\varphi'}{\varphi} \,. \tag{D.65}$$

By integrating the above equation, we immediately get

$$\frac{1}{D_0^{1-\alpha}} \sim \varphi \,, \tag{D.66}$$

that is fully consistent with Eq. (D.21) and the discussion of Appendix D.3.1.

This page is unintentionally left not blank.

Bibliography

General references

[1] A. Abragam, *The Principles of Nuclear Magnetic Resonance*. Oxford University Press, 1961.

[2] P. T. Callaghan, *Principles of Nuclear Magnetic Resonance Microscopy*. Clarendon Press, 1st ed., 1991.

[3] D. S. Grebenkov, "NMR survey of reflected Brownian motion," *Rev. Mod. Phys.*, vol. 79, pp. 1077–1137, 2007.

[4] W. Price, *NMR studies of translational motion: Principles and applications*. Cambridge Molecular Science, 2009.

[5] V. G. Kiselev, "Fundamentals of diffusion MRI physics," *NMR Biomed.*, vol. 30, no. 3, p. e3602, 2017.

[6] V. G. Kiselev, D. S. Novikov, "Transverse NMR relaxation in biological tissues," *NeuroImage*, 2018.

[7] D. K. Jones, *Diffusion MRI: Theory, Methods, and Applications*, Oxford University Press, New York, USA, 2011.

[8] D. E. Sadava, D. M. Hillis, H. C. Heller, and M. R. Berenbaum, *Life, The Science of Biology*, W. H. Freeman, Tenth Edition, 2012.

[9] D. S. Grebenkov, "From the microstructure to diffusion NMR, and back," in *Diffusion NMR of Confined Systems : Fluid Transport in Porous Solids and Heterogeneous Materials*, Ed. R. Valiullin, The Royal Society of Chemistry, pp. 52–110, 2016.

[10] D. S. Novikov, E. Fieremans, S. N. Jespersen, and V. G. Kiselev, "Quantifying brain microstructure with diffusion MRI: Theory and parameter estimation," *NMR Biomed.*, vol. 32:e3998

[11] D. S. Novikov, V. G. Kiselev, and S. N. Jespersen, "On modeling," *Magn. Reson. Med.*, vol. 79, pp. 3172–3193, 2018.

[12] H. S. Carslaw and J. C. Jaeger, *Conduction of Heat in Solids*, Clarendon Press, 1959.

[13] J. Crank, *The Mathematics of Diffusion*, Clarendon Press, 1975.

[14] D. S. Grebenkov and B.-T. Nguyen, "Geometrical structure of Laplacian eigenfunctions," *SIAM Rev.*, vol. 55, pp. 601–667, 2013.

[15] M. D. Mikhailov and M. N. Ozisik, *Unified Analysis and Solutions of Heat and Mass Diffusion*, John Wiley & Sons, 1984.

Fundamental articles in NMR and dMRI

[16] N. Bloembergen, E. M. Purcell, and R. V. Pound, "Relaxation Effects in Nuclear Magnetic Resonance Absorption," *Phys. Rev.*, vol. 73, p. 679, 1948.

[17] E. L. Hahn, "Spin Echoes," *Phys. Rev.*, vol. 80, pp. 580–594, 1950.

[18] H. Y. Carr and E. M. Purcell, "Effects of diffusion on free precession in nuclear magnetic resonance experiments," *Phys. Rev.*, vol. 94, p. 630, 1954.

[19] H. C. Torrey, "Bloch equations with diffusion terms," *Phys Rev.*, vol. 104, pp. 563–565, 1956.

[20] E. O. Stejskal and J. E. Tanner, "Spin diffusion measurements: Spin echoes in the presence of a time dependent field gradient," *J. Chem. Phys.*, vol. 42, p. 288, 1965.

[21] E. O. Stejskal, "Use of spin echoes in a pulsed magnetic-field gradient to study anisotropic, restricted diffusion and flow," *J. Chem. Phys.*, vol. 43, p. 3597, 1965.

[22] J. E. Tanner and E. O. Stejskal, "Restricted self-diffusion of protons in colloidal systems by the pulsed-gradient, spin-echo method," *J. Chem. Phys.*, vol. 49, pp. 1768–1777, 1968.

[23] J. E. Tanner, "Use of the stimulated echo in NMR diffusion studies," *J. Chem. Phys.*, vol. 52, pp. 2523–2526, 1970.

[24] K. R. Brownstein and C. E. Tarr, "Importance of classical diffusion in NMR studies of water in biological cells," *Phys. Rev. A*, vol. 19, pp. 2446–2553, 1979.

[25] D. Le Bihan and E. Breton, "Imagerie de diffusion in vivo par résonance magnétique nucléaire," *C. R. Acad. Sc. Paris*, vol. 301, p. 1109, 1985.

Diffusion MR Imaging

[26] D. Le Bihan, E. Breton, D. Lallemand, P. Grenier, E. Cabanis, and M. Jeantet Laval, "MR Imaging of intravoxel incoherent motions: application to diffusion and perfusion in neurologic disorders," *Radiology*, vol. 161, pp. 401—407, 1986.

[27] K.-D. Merboldt, W. Hänicke, and J. Frahm, "Self-diffusion NMR imaging using stimulated echoes," *J. Magn. Reson.*, vol. 64, pp. 479–486, 1985.

[28] D. G. Taylor and M. C. Bushell, "The spatial mapping of translational diffusion coefficients by the NMR imaging technique," *Phys. Med. Biol.*, vol. 30, pp. 345–349, 1985.

[29] P. M. Pattany, J. J. Phillips, L. C. Chiu, J. D. Lipcamon, J. L. Duerk, J. M. McNally, and S. N. Mohapatra, "Motion artifact suppresion technique (MAST) for MR imaging," *J. Comput. Assisted Tomogr.*, vol. 11, pp. 369–377, 1987.

Finite difference/elements for dMRI

[30] S. N. Hwang, C.-L. Chin, F. W. Wehrli, and D. B. Hackney, "An image-based finite difference model for simulating restricted diffusion," *Magn. Reson. Med.*, vol. 50, pp. 373–382, 2003.

[31] D. V. Nguyen, J.-R. Li, D. Grebenkov, and D. Le Bihan, "A finite element method to solve the Bloch-Torrey equation applied to diffusion magnetic resonance imaging," *J. Comput. Phys.*, vol. 263, pp. 283–302, 2014.

[32] C. H. Ziener, T. Kampf, H.-P. Schlemmer, and L. R. Buschle, "Spin echoes: full numerical solution and breakdown of approximative solutions," *Journal of Physics: Condensed Matter*, vol. 31, p. 155101, 2019.

[33] J. Xu, M. D. Does, and J. C. Gore, "Numerical study of water diffusion in biological tissues using an improved finite difference method", *Phys. Med. Biol.*, vol. 52, pp. N111–N126, 2007.

Monte-Carlo for dMRI

[34] D. S. Grebenkov, "A fast random walk algorithm for computing the pulsed-gradient spin-echo signal in multiscale porous media," *J. Magn. Reson.*, vol. 208, pp. 243–255, 2011.

[35] L. M. Burcaw, E. Fieremans and D. S. Novikov, "Mesoscopic structure of neuronal tracts from time-dependent diffusion," *Neuroimage*, vol. 114, pp. 18–37, 2015.

Spectral methods for dMRI

[36] P. T. Callaghan, "A simple matrix formalism for spin echo analysis of restricted diffusion under generalized gradient waveforms," *J. Magn. Reson.*, vol. 129, pp. 74–84, 1997.

[37] A. V. Barzykin, "Exact solution of the Torrey-Bloch equation for a spin echo in restricted geometries," *Phys. Rev. B.*, vol. 58, pp. 14171–14174, 1998.

[38] A. Caprihan, L. Z. Wang, and E. Fukushima, "A multiple-narrow-pulse approximation for restricted diffusion in a time-varying field gradient," *J. Magn. Res. A*, vol. 118, pp. 94–102, 1996.

[39] A. L. Sukstanskii and D. A. Yablonskiy, "Effects of Restricted Diffusion on MR Signal Formation," *J. Magn. Reson.*, vol. 157, pp. 92–105, 2002.

[40] D. S. Grebenkov, "Laplacian eigenfunctions in NMR. I. A numerical tool," *Conc. Magn. Reson. A*, vol. 32A, pp. 277–301, 2008.

Measurement of diffusion coefficients

[41] I. Åslund, D. Topgaard, "Determination of the self-diffusion coefficient of intracellular water using PGSE NMR with variable gradient pulse length," *J. Magn. Reson.*, vol. 201, pp. 250 – 254, 2009.

[42] P. Tofts, D. Lloyd, C. Clark, G. Barker, G. Parker, P. McConville, C. Baldock, J. Pope, "Test liquids for quantitative MRI measurements of self-diffusion coefficient in vivo," *Magn. Reson. Med.*, vol. 43, pp. 368–374, 2000.

[43] R. Mills, "Self-diffusion in normal and heavy water in the range $1 - 45°$," *J. Phys. Chem.*, vol. 77, pp. 685–688, 1973.

[44] J. H. Wang, "Self-diffusion coefficients of water," *J. Phys. Chem.*, vol. 69, pp. 4412–4412, 1965.

[45] D. C. Douglass and D. W. McCall, "Diffusion in Paraffin Hydrocarbons," *J. Phys. Chem.*, vol. 62, pp. 1102–1107, 1958.

[46] D. E. Woessner, "Self-diffusion measurements in liquids by the spin-echo technique," *Rev. Sci. Instr.*, vol. 31, p. 1146, 1960.

Time-dependent diffusion coefficient in a porous medium

[47] P. P. Mitra, P. N. Sen, L. M. Schwartz, and P. Le Doussal, "Diffusion propagator as a probe of the structure of porous media," *Phys. Rev. Lett.*, vol. 68, pp. 3555–3558, 1992.

[48] P. P. Mitra, P. N. Sen, and L. M. Schwartz, "Short-time behavior of the diffusion coefficient as a geometrical probe of porous media," *Phys. Rev. B*, vol. 47, pp. 8565–8574, 1993.

[49] L. L. Latour, P. P. Mitra, R. L. Kleinberg, and C. H. Sotak, "Time-dependent diffusion coefficient of fluids in porous media as a probe of surface-to-volume ratio," *J. Magn. Res. A*, vol. 101, no. 3, pp. 342 – 346, 1993.

[50] P. P. Mitra and P. N. Sen, "Effects of microgeometry and surface relaxation on NMR pulsed-field-gradient experiments: Simple pore geometries," *Phys. Rev. B*, vol. 45, pp. 143–156, 1992.

[51] K. G. Helmer, B. J. Dardzinski, and C. H. Sotak, "The application of porous-media theory to the investigation of time-dependent diffusion in in vivo systems," *NMR Biomed.*, vol. 8, no. 7, pp. 297–306, 1995.

[52] K. G. Helmer, M. D. Hürlimann, T. M. de Swiet, P. N. Sen, and C. H. Sotak, "Determination of ratio of surface area to pore volume from restricted diffusion in a constant field gradient," *J. Magn. Res. A*, vol. 115, no. 2, pp. 257–259, 1995.

[53] P. N. Sen, "Time-dependent diffusion coefficient as a probe of geometry," *Conc. Magn. Res. A*, vol. 23A, no. 1, pp. 1–21, 2004.

[54] E. J. Fordham, S. J. Gibbs, and L. D. Hall, "Partially restricted diffusion in a permeable sandstone: Observations by stimulated echo PFG NMR," *Magn. Reson. Imaging*, vol. 12, no. 2, pp. 279–284, 1994. Proceedings of the Second International Meeting on Recent Advances in MR Applications to Porous Media.

[55] M. D. Hürlimann, K. G. Helmer, L. L. Latour, and C. H. Sotak, "Restricted diffusion in sedimentary rocks. Determination of surface-area-to-volume ratio and surface relaxivity," *J. Magn. Res. A*, vol. 111, no. 2, pp. 169–178, 1994.

[56] L. L. Latour, K. Svoboda, P. P. Mitra, and C. H. Sotak, "Time-dependent diffusion of water in a biological model system.," *PNAS*, vol. 91, no. 4, pp. 1229–1233, 1994.

[57] R. W. Mair, G. P. Wong, D. Hoffmann, M. D. Hürlimann, S. Patz, L. M. Schwartz, and R. L. Walsworth, "Probing porous media with gas diffusion NMR," *Phys. Rev. Lett.*, vol. 83, pp. 3324–3327, 1999.

[58] M. Carl, G. W. Miller, J. P. Mugler, S. Rohrbaugh, W. A. Tobias, and G. D. Cates, "Measurement of hyperpolarized gas diffusion at very short time scales," *J. Magn. Reson.*, vol. 189, no. 2, pp. 228 – 240, 2007.

[59] D. S. Novikov and V. G. Kiselev, "Surface-to-volume ratio with oscillating gradients," *J. Magn. Reson.*, vol. 210, no. 1, pp. 141 – 145, 2011.

[60] G. Lemberskiy, S. H. Baete, M. A. Cloos, D. S. Novikov, and E. Fieremans, "Validation of surface-to-volume ratio measurements derived from oscillating gradient spin echo on a clinical scanner using anisotropic fiber phantoms," *NMR Biomed.*, vol. 30, no. 5, p. e3708, 2017.

[61] A. F. Frølich, S. N. Jespersen, L. Østergaard, and V. G. Kiselev, "The effect of impermeable boundaries of arbitrary geometry on the apparent diffusion coefficient," *J. Magn. Reson.*, vol. 194, pp. 128–135, 2008.

[62] F. B. Laun, T. A. Kuder, F. Zong, S. Hertel, and P. Galvosas, "Symmetry of the gradient profile as second experimental dimension in the short-time expansion of the apparent diffusion coefficient as measured with NMR diffusometry," *J. Magn. Reson.*, vol. 259, pp. 10 – 19, 2015.

[63] F. B. Laun, K. Demberg, A. M. Nagel, M. Uder, and T. Kuder, "On the Vanishing of the t-term in the Short-Time Expansion of the Diffusion Coefficient for Oscillating Gradients in Diffusion NMR," *Front. Phys.*, vol. 5, pp. 56, 2017.

[64] G. Lemberskiy, A. B. Rosenkrantz, J. Veraart, S. S. Taneja, D. S. Novikov, E. Fieremans, "Time-dependent diffusion in prostate cancer," *Invest. Radiol.*, vol. 52, pp. 405-411, 2017.

[65] O. Reynaud, "Time-Dependent Diffusion MRI in Cancer: Tissue Modeling and Applications," *Front. Phys.*, vol. 5, p. 58, 2017.

[66] J. Xu, M. D. Does, and J. C. Gore, "Dependence of temporal diffusion spectra on microstructural properties of biological tissues," *Magn. Reson. Imag.*, vol. 29, pp. 380-–390, 2011.

Disordered media in the long-time limit

[67] D. S. Novikov, V. G. Kiselev, "Effective medium theory of a diffusion-weighted signal," *NMR Biomed.*, vol. 23, pp. 682–697, 2010.

[68] D. S. Novikov, E. Fieremans, J. H. Jensen, and J. A. Helpern, "Random walks with barriers," *Nat. Phys.*, vol. 7, pp. 508–514, 2011.

[69] D. S. Novikov, J. H. Jensen, J. A. Helpern, and E. Fieremans, "Revealing mesoscopic structural universality with diffusion," *PNAS*, vol. 111, pp. 5088–5093, 2014.

[70] T. M. de Swiet, P. N. Sen, "Time dependent diffusion coefficient in a disordered medium," *J. Chem. Phys.*, vol. 104, pp. 206–209, 1996.

Diffusion coefficient in the tortuosity regime

[71] J. C. Maxwell, *A treaty on eletricity and magnetism*, vol. 1, 2nd ed., Clarendon Press, 1873.

[72] Z. Hashin, S. Shtrikman, "A variational approach to the theory of the effective magnetic permeability of multiphase materials," *J. Appl. Phys.*, vol. 33, pp. 3125–3131, 1962.

[73] H. L. Weissberg, "Effective diffusion coefficient in porous media," *J. Appl. Phys.*, vol. 34, pp. 2636–2639, 1963.

[74] D. J. Jeffrey, "Conduction through a random suspension of spheres," *Proc. Roy. Soc. Lond. A*, vol. 335, pp. 355–367, 1973.

[75] J. van Brakel, P. Heertjes, "Analysis of diffusion in macroporous media in terms of a porosity, a tortuosity and a constrictivity factor," *Int. J. Heat Mass Transfer*, vol. 17, pp. 1093–1103, 1974.

[76] L. L. Latour, R. L. Kleinberg, P. P. Mitra, and C. H. Sotak, "Pore-size distributions and tortuosity in heterogeneous porous media," *J. Magn. Reson. A*, vol. 112, PP. 83–91, 1995.

[77] J. W. Haus and K. W. Kehr, "Diffusion in regular and disordered lattices," *Phys. Rep.*, vol. 150, pp. 263–406, 1987.

[78] D. P. Haughey and G. S. G. Beveridge, "Structural properties of packed beds – A review," *Can. J. Chem. Engng.*, vol. 47, pp. 130–140, 1969.

Motional narrowing regime

[79] B. Robertson, "Spin-echo decay of spins diffusing in a bounded region,", *Phys. Rev.*, vol. 151, pp. 273–277, 1966.

[80] R. C. Wayne and R. M. Cotts, "Nuclear-magnetic-resonance study of self-diffusion in a bounded medium," *Phys. Rev.*, vol. 151, pp. 264–272, 1966.

[81] C. H. Neuman, "Spin echo of spins diffusing in a bounded medium," *J. Chem. Phys.*, vol. 60, pp. 4508–4511, 1974.

Debye-Porod law

[82] P. Debye, H. R. Anderson, and H. Brumberger, "Scattering by an Inhomogeneous Solid. II. The correlation function and its application," *J. Appl. Phys.*, vol. 28, pp. 679, 1957

[83] P. N. Sen, M. D. Hürlimann, and T. M. de Swiet, "Debye-Porod law of diffraction for diffusion in porous media," *Phys. Rev. B*, vol. 51, pp. 601–604, 1995.

[84] A. F. Frøhlich, L. Ostergaard, and V. G. Kiselev, "Effect of impermeable boundaries on diffusion-attenuated MR signal," *J. Magn. Reson.*, vol. 179, pp. 223–233, 2006.

Diffusion-diffraction pattern

[85] P. T. Callaghan, A. Coy, D. MacGowan, K. J. Packer, and F. O. Zelaya, "Diffraction-like Effects in NMR Diffusion Studies of Fluids in Porous Solids," *Nature*, vol. 351, pp. 467–469, 1991.

[86] P. T. Callaghan, A. Coy, T. P. J. Halpin, D. MacGowan, K. J. Packer, abd F. O. Zelaya, "Diffusion in porous systems and the influence of pore morphology in pulsed gradient spin-echo nuclear magnetic resonance studies," *J. Chem. Phys.*, vol. 97, pp. 651–662, 1992.

[87] A. Coy and P. T. Callaghan, "Pulsed gradient spin echo nuclear magnetic resonance for molecules diffusing between partially reflecting rectangular barriers," *J. Chem. Phys.*, vol. 101, pp. 4599–4609, 1994.

[88] P. T. Callaghan, "Pulsed-gradient spin-echo NMR for planar, cylindrical, and spherical pores under conditions of wall relaxation," *J. Magn. Reson. A*, vol. 113, pp. 53–59, 1995.

[89] P. Linse and O. Söderman, "The validity of the short-gradient-pulse approximation in NMR studies of restricted diffusion. Simulations of molecules diffusing between planes, in cylinders, and spheres," *J. Magn. Reson. A*, vol. 116, pp. 77–86, 1995.

Diffusion Pore Imaging

[90] F. B. Laun, T. A. Kuder, A. Wetscherek, B. Stieltjes, and W. Semmler, "NMR-based diffusion pore imaging," *Phys. Rev. E*, vol. 86, p. 021906, 2012.

[91] K. Demberg, F. B. Laun, J. Windschuh, R. Umathum, P. Bachert, and T. A. Kuder, "Nuclear magnetic resonance diffusion pore imaging: Experimental phase detection by double diffusion encoding," *Phys. Rev. E.*, vol. 95, p. 022404, 2017.

[92] T. A. Kuder, P. Bachert, J. Windschuh, and F. B. Laun, "Diffusion pore imaging by hyperpolarized Xenon-129 nuclear magnetic resonance," *Phys. Rev. Lett.*, vol. 111, p. 028101, 2013.

[93] F. B. Laun, T. A. Kuder, W. Semmler, and B. Stieltjes, "Determination of the defining boundary in nuclear magnetic resonance diffusion experiments," *Phys. Rev. Lett.*, vol. 107, p. 048102, 2011.

Localization regime and its application to diffusive edge enhancement

[94] D. S. Grebenkov, B. Helffer, and R. Henry, "The complex Airy operator on the line with a semipermeable barrier," *SIAM J. Math. Anal.*, vol. 49, pp. 1844–1894, 2017.

[95] D. S. Grebenkov and B. Helffer, "On spectral properties of the Bloch-Torrey operator in two dimensions," *SIAM J. Math. Anal.*, vol. 50, pp. 622–676, 2018.

[96] Y. Almog, D. S. Grebenkov, and B. Helffer, "Spectral semi-classical analysis of a complex Schrödinger operator in exterior domains," *J. Math. Phys.*, vol. 59, p. 041501, 2018.

[97] Y. Almog, D. S. Grebenkov, and B. Helffer, "On a Schrödinger operator with a purely imaginary potential in the semiclassical limit," *Commun. Part. Diff. Eq.*, vol. 44, pp. 1542–1604, 2019.

[98] S. D. Stoller, W. Happer, and F. J. Dyson, "Transverse spin relaxation in inhomogeneous magnetic fields," *Phys. Rev. A*, vol. 44, pp. 7459–7477, 1991.

[99] T. M. de Swiet and P. N. Sen, "Decay of nuclear magnetization by bounded diffusion in a constant field gradient," *J. Chem. Phys.*, vol. 100, no. 8, pp. 5597–5604, 1994.

[100] M. D. Hürlimann, K. G. Helmer, T. M. de Swiet, and P. N. Sen, "Spin echoes in a constant gradient and in the presence of simple restriction," *J. Magn. Reson. A*, vol. 113, pp. 260–264, 1995.

[101] D. S. Grebenkov, "Diffusion MRI/NMR at high gradients: Challenges and perspectives," *Microporous Mesoporous Mater.*, vol. 269, pp. 79–82, 2018.

[102] D. S. Grebenkov, "Exploring diffusion across permeable barriers at high gradients. II. Localization regime," *J. Magn. Reson.*, vol. 248, pp. 164–176, 2014.

[103] P. Le Doussal and P. N. Sen, "Decay of nuclear magnetization by diffusion in a parabolic magnetic field: An exactly solvable model," *Phys. Rev. B*, vol. 46, pp. 3465–3485, 1992.

[104] M. Herberthson, E. Özarslan, H. Knutsson, and C.-F. Westin, "Dynamics of local magnetization in the eigenbasis of the Bloch-Torrey operator," *J. Chem. Phys.*, vol. 146, p. 124201, 2017.

[105] T. M. de. Swiet, "Diffusive Edge Enhancement in Imaging," *J. Magn. Reson. B*, vol. 109, pp. 12–18, 1995.

Application of dMRI to brain structure and function

[106] M. E. Moseley, Y. Cohen, and J. Mintorovitch, "Early detection of regional cerebral ischemia in cats: Comparison of diffusion- and T2-weighted MRI and spectroscopy," *Magn. Reson. Med.*, vol. 14, pp. 330–346, 1990.

[107] M. Tariq, T. Schneider, D. C. Alexander, C. A. G. Wheeler-Kingshott, and H. Zhang, "Bingham–NODDI: Mapping anisotropic orientation dispersion of neurites using diffusion MRI," *NeuroImage*, vol. 133, pp. 207–223, 2016.

[108] H. Zhang, P. L. Hubbard, G. J. M. Parker, and D. C. Alexander, "Axon diameter mapping in the presence of orientation dispersion with diffusion MRI," *NeuroImage*, vol. 56, pp.8 1301–1315, 2011.

[109] D. S. Tuch, T. G. Reese, M. R. Wiegell, V. J. Wedeen, "Diffusion MRI of complex neural architecture,"

[110] J. Frahm, P. Dechent, J. Baudewig, K. Merboldt, "Advances in functional MRI of the human brain," *Prog. Nucl. Magn. Reson. Spectrosc.*, vol. 44, pp. 1 – 32, 2004.

[111] D. L. Bihan, H. Johansen-Berg, "Diffusion MRI at 25: Exploring brain tissue structure and function," *Neuroimage*, vol. 61, pp. 324 – 341, 2012.

[112] D. Le Bihan, "Molecular diffusion, tissue microdynamics and microstructure," *NMR Biomed.*, vol. 8, pp. 375–386, 1995.

[113] D. Le Bihan, "The 'wet mind': water and functional neuroimaging," *Phys. Med. Biol.*, vol. 52, pp. R57–R90, 2007.

[114] D. Le Bihan, "Looking into the functional architecture of the brain with diffusion MRI," *Nat. Rev. Neurosci.*, vol. 4, pp. 469–480, 2003.

[115] D. Le Bihan, C. Poupon, A. Amadon, and F. Lethimonnier, "Artifacts and Pitfalls in Diffusion MRI," *J. Magn. Reson. Imaging*, vol. 24, pp. 478–488, 2006.

[116] D. S. Novikov, S. N. Jespersen, V. G. Kiselev, and E. Fieremans, "Quantifying brain microstructure with diffusion MRI: Theory and parameter estimation," *NMR Biomed.*, vol. 32, p. e3998, 2018.

[117] F. Grinberg, E. Farrher, L. Ciobanu, F. Geffroy, D. Le Bihan, and N. J. Shah, "Non-Gaussian diffusion imaging for enhanced contrast of brain tissue affected by ischemic stroke," *PLOS One*, vol. 9, c89225, 2014.

[118] D. A. Yablonskiy, J. L. Bretthorst, and J. J. H. Ackerman, "Statistical model for diffusion attenuated MR signal," *Magn. Reson. Med.*, vol. 50, pp. 664–669, 2003.

[119] J. H. Jensen, J. A. Helpern, A. Ramani, H. Lu, and K. Kaczynski, "Diffusion kurtosis imaging: the quantification of non-Gaussian water diffusion by means of magnetic resonance imaging," *Magn. Reson. Med.*, vol. 53, pp. 1432–1440, 2005.

Bi-exponential model in biomedical applications

[120] T. Niendorf, R. M. Dijkhuizen, D. G. Norris, M. van Lookeren Campagne, K. Nicolay, "Biexponential diffusion attenuation in various states of brain tissue: Implications for diffusion-weighted imaging," *Magn. Reson. Med.*, vol. 36, pp. 847–857, 1996.

[121] R. V. Mulkern, H. Gudbjartsson, C.-F. Westin, H. P. Zengingonul, W. Gartner, C. R. G. Guttmann, R. L. Robertson, W. Kyriakos, R. Schwartz, D. Holtzman, F. A. Jolesz, S. E. Maier, "Multi-component apparent diffusion coefficients in human brain," *NMR Biomed.*, vol. 12, pp. 51–62, 1999.

[122] C. A. Clark, D. Le Bihan, "Water diffusion compartmentation and anisotropy at high b values in the human brain," *Magn. Reson. Med.*, vol. 44, pp. 852–859, 2000.

[123] C.-L. Chin, F. W. Wehrli, S. N. Hwang, M. Takahashi, D. B. Hackney, "Biexponential diffusion attenuation in the rat spinal cord: Computer simulations based on anatomic images of axonal architecture," *Magn. Reson. Med.*, vol. 47, pp. 455–460, 2002.

[124] J. V. Sehy, J. J. Ackerman, J. J. Neil, "Evidence that both fast and slow water ADC components arise from intracellular space," *Magn. Reson. Med.*, vol. 48, pp. 765–770, 2002.

[125] Z. Ababneh, H. Beloeil, C. B. Berde, G. Gambarota, S. E. Maier, R. V. Mulkern, "Biexponential parameterization of diffusion and T2 relaxation decay curves in a rat muscle edema model: Decay curve components and water compartments," *Magn. Reson. Med.*, vol. 54, pp. 524–531, 2005.

[126] D. S. Grebenkov, "Use, misuse, and abuse of apparent diffusion coefficients," *Conc. Magn. Res. A*, vol. 36A, pp. 24–35, 2010.

[127] A. Schwarcz, P. Bogner, P. Meric, J.-L. Correze, Z. Berente, J. Pál, F. Gallyas, T. Doczi, B. Gillet, J.-C. Beloeil, "The existence of biexponential signal decay in magnetic resonance diffusion-weighted imaging appears to be independent of compartmentalization," *Magn. Reson. Med.*, vol. 51, pp. 278–285, 2004

[128] V. G. Kiselev, K. A. Il'yasov, "Is the "biexponential diffusion" biexponential?," *Magn. Reson. Med.*, vol. 57, pp. 464–469, 2007.

[129] J. Pfeuffer, S. W. Provencher, R. Gruetter, "Water diffusion in rat brain in vivo as detected at very large b values is multicompartmental," *MAGMA*, vol. 8, pp. 98–108, 1999.

[130] Y. Assaf and Y. Cohen, "Non-mono-exponential attenuation of water and N-acetyl aspartate signals due to diffusion in brain tissue," *J. Magn. Reson.*, vol. 131, pp. 69–85, 1998.

[131] D. Le Bihan, S.-i. Urayama, T. Aso, T. Hanakawa, and H. Fukuyama, "Direct and fast detection of neuronal activation in the human brain with diffusion MRI," *PNAS*, vol. 103, pp. 8263–8268, 2006.

[132] G. J. Stanisz, A. Szafer, G. A. Wright, and R. M. Henkelman, "An analytical model of restricted diffusion in bovine optic nerve," *Magn. Reson. Med.*, vol. 37, pp. 103–111, 1997.

Hyperpolarization and application to lung imaging

[133] T. G. Walker and W. Happer, "Spin-exchange optical pumping of noble-gas nuclei," *Rev. Mod. Phys.*, vol. 69, p. 629, 1997.

[134] N. J. Shah, T. Ünlü, H.-P. Wegener, H. Halling, K. Zilles, and S. Appelt, "Measurement of rubidium and xenon absolute polarization at high temperatures as a means of improved production of hyperpolarized ^{129}Xe," *NMR Biomed.*, vol. 13, no. 4, pp. 214–219, 2000.

[135] A.-M. Oros and N. J. Shah, "Hyperpolarized xenon in NMR and MRI," *Phys. Med. Biol.*, vol. 49, R105, 2004.

[136] R. H. Acosta, L. Agulles-Pedrós, S. Komin, D. Sebastiani, H. W. Spiess, and P. Blümler, "Diffusion in binary gas mixtures studied by NMR of hyperpolarized gases and molecular dynamics simulations," *Phys. Chem. Chem. Phys.*, vol. 8, pp. 4182–4188, 2006.

[137] R. E. Jacob, G. Laicher, and K. R. Minard, "3D MRI of non-Gaussian ^{3}He gas diffusion in the rat lung," *J. Magn. Reson.*, vol. 188, pp. 357–366, 2007.

[138] B. T. Saam, D. A. Yablonskiy, V. D. Kodibagkar, J. C. Leawoods, D. S. Gierada, J. D. Cooper, S. S. Lefrak, and M. S. Conradi "MR imaging of diffusion of 3He gas in healthy and diseased lungs," *Magn. Reson. Med.*, vol. 44, pp. 174–179, 2000.

[139] S. B. Fain, S. R. Panth, M. D. Evans, A. L. Wentland, J. H. Holmes, F. R. Korosec, M. J. O'Brien, H. Fountaine, and T. M. Grist, "Early emphysematous changes in asymptomatic smokers: Detection with 3He MR imaging," *Radiology*, vol. 239, pp. 875–883, 2006.

Anisotropy, diffusion tensor imaging and tractography

[140] V. J. Wedeen, D. L. Rosene, R. Wang, G. Dai, F. Mortazavi, P. Hagmann, J. H. Kaas, and W.-Y. I. Tseng, "The geometric structure of the brain fiber pathways," *Science*, vol. 335, p. 1628, 2012.

[141] P. J. Basser, J. Mattiello, and D. Le Bihan, "Estimation of the effective self-diffusion tensor from the NMR spin echo," *J. Magn. Res. B*, vol. 103, no. 3, pp. 247–254, 1994.

[142] J. Mattiello, P. J. Basser, and D. Le Bihan, "Analytical expressions for the b Matrix in NMR diffusion imaging and spectroscopy," *J. Magn. Res. A*, vol. 108, no. 2, pp. 131–141, 1994.

[143] P. J. Basser, J. Mattiello, and D. Le Bihan, "MR diffusion tensor spectroscopy and imaging," *Biophys. J.*, vol. 66, no. 1, pp. 259 – 267, 1994.

[144] P. J. Basser and D. K. Jones, "Diffusion-tensor MRI: theory, experimental design and data analysis: a technical review," *NMR Biomed.*, vol. 15, no. 7-8, pp. 456–467, 2002.

[145] J. R. Hansen, "Pulsed NMR study of water mobility in muscle and brain tissue," *Biochim. Biophys. Acta*, vol. 230, pp. 482–486, 1971.

[146] T. L. Chenevert, J. A. Brunberg, and J. G. Pipe, "Anisotropic diffusion in human white matter: demonstration with MR techniques in vivo," *Radiology*, vol. 177, pp. 401–405, 1990.

[147] M. Moseley, "Diffusion tensor imaging and aging – a review," *NMR Biomed.*, vol. 15, pp. 553–560, 2002.

[148] D. Le Bihan, J.-F. Mangin, C. Poupon, C. A. Clark, S. Pappata, N. Molko, and H. Chabriat, "Diffusion tensor imaging: Concepts and applications," *J. Magn. Reson. Imaging*, vol. 13, pp. 534–546, 2001.

[149] D. K. Jones, M. A. Horsefield, and A. Simmons, "Optimal strategies for measuring diffusion in anisotropic systems by magnetic resonance imaging," *Magn. Reson. Med.*, vol. 42, pp. 515–525, 1999.

[150] P. L. Hubbard, K. M. McGrath, and P. T. Callaghan, "Evolution of a lamellar domain structure for an equilibrating lyotropic liquid crystal," *J. Phys. Chem. B*, vol. 110, pp. 20781–20788, 2006.

[151] D. A. Yablonskiy, A. L. Sukstanskii, J. C. Leawoods, D. S. Gierada, G. L. Bretthorst, S. S. Lefrak, J. D. Cooper, and M. S. Conradi, "Quantitative in vivo Assessment of Lung Microstructure at the Alveolar Level with Hyperpolarized ^{3}He Diffusion MRI," *PNAS*, vol. 99, p. 3111, 2002.

[152] P. J. Basser, "Inferring microstructural features and the physiological state of tissues from diffusion-weighted images," *NMR BioMed.*, vol. 8, no. 7, pp. 333–344, 1995.

Spherical encoding and micro-anisotropy quantification

[153] S. Eriksson, S. Lasic, and D. Topgaard, "Isotropic diffusion weighting in PGSE NMR by magic-angle spinning of the q-vector," *J. Magn. Reson.*, vol. 226, pp. 13–18, 2013.

[154] S. Lasič, F. Szczepankiewicz, S. Eriksson, M. Nilsson, and D. Topgaard, "Microanisotropy imaging: quantification of microscopic diffusion anisotropy and orientational order parameter by diffusion MRI with magic-angle spinning of the q-vector," *Front. Phys.*, vol. 2, p. 11, 2014.

[155] F. Szczepankiewicz, S. Lasič, D. van Westen, P. C. Sundgren, E. Englund, C.-F. Westin, F. Ståhlberg, J. Lätt, D. Topgaard, and M. Nilsson, "Quantification of microscopic diffusion anisotropy disentangles effects of orientation dispersion from microstructure: Applications in healthy volunteers and in brain tumors," *Neuroimage*, vol. 104, pp. 241 – 252, 2015.

[156] C.-F. Westin, H. Knutsson, O. Pasternak, F. Szczepankiewicz, E. Özarslan, D. van Westen, C. Mattisson, M. Bogren, L. J. O'Donnell, M. Kubicki, D. Topgaard, and M. Nilsson, "Q-space trajectory imaging for multidimensional diffusion MRI of the human brain," *Neuroimage*, vol. 135, pp. 345 – 362, 2016.

[157] S. N. Jespersen, J. L. Olesen, A. Ianuş, and N. Shemesh, "Effects of nongaussian diffusion on "isotropic diffusion" measurements: An ex-vivo microimaging and simulation study," *J. Magn. Reson.*, vol. 300, pp. 84–94, 2019.

[158] E. C. Wong, R. W. Cox, and A. W. Song, "Optimized isotropic diffusion weighting," *Magn. Res. Med.*, vol. 34, no. 2, pp. 139–143, 1995.

[159] R. A. de Graaf, K. P. J. Braun, and K. Nicolay, "Single-shot diffusion trace ^{1}H NMR spectroscopy," *Magn. Res. Med.*, vol. 45, no. 5, pp. 741–748, 2001.

[160] J. Valette, C. Giraudeau, C. Marchadour, B. Djemai, F. Geffroy, M. A. Ghaly, D. Le Bihan, P. Hantraye, V. Lebon, and F. Lethimonnier, "A new sequence for single-shot diffusion-weighted NMR spectroscopy by the trace of the diffusion tensor," *Magn. Res. Med.*, vol. 68, no. 6, pp. 1705–1712, 2012.

[161] D. Topgaard, "Isotropic diffusion weighting in PGSE NMR: Numerical optimization of the q-MAS PGSE sequence," *Microporous Mesoporous Mater.*, vol. 178, pp. 60 – 63, 2013. Proceedings of the 11th Internatioanl Bologna Conference on Magnetic Resonance in Porous Media (MRPM11).

[162] D. Topgaard "Multidimensional diffusion MRI," *J. Magn. Reson.*, vol. 275, pp. 98–113, 2017.

[163] J. P. de Almeida Martins and D. Topgaard, "Two-dimensional correlation of isotropic and directional diffusion using NMR," *Phys. Rev. Lett.*, vol. 116, p. 087601, 2016.

[164] S. Vellmer, R. Stirnberg, D. Edelhoff, D. Suter, T. Stöcker, and I. I. Maximov, "Comparative analysis of isotropic diffusion weighted imaging sequences," *J. Magn. Reson.*, vol. 275, pp. 137 – 147, 2017.

Multiple diffusion encoding

[165] Y. Cheng, and D. G. Cory, "Multiple scattering by NMR" *J. Am. Chem. Soc.*, vol. 121, no. 34, pp. 7935–7936, 1999.

[166] P. P. Mitra, "Multiple wave-vector extensions of the NMR pulsed-field-gradient spin-echo diffusion measurement," *Phys. Rev. B*, vol. 51, pp. 15074–15078, 1995.

[167] N. Shemesh, S. N. Jespersen, D. C. Alexander, Y. Cohen, I. Drobnjak, T. B. Dyrby, J. Finsterbusch, M. A. Koch, T. Kuder, F. Laun, M. Lawrenz, H. Lundell, P. P. Mitra, M. Nilsson, E. Özarslan, D. Topgaard, C.-F. Westin, "Conventions and nomenclature for double diffusion encoding NMR and MRI" *Magn. Res. Med.*, vol. 75, pp. 82–87, 2015.

[168] S. Mori and P. C. M. Van Zijl, "Diffusion weighting by the trace of the diffusion tensor within a single scan," *Magn. Reson. Med.*, vol. 33, no. 1, pp. 41–52, 1995.

[169] S. N. Jespersen, H. Lundell, C. K. Sønderby, and T. B. Dyrby, "Orientationally invariant metrics of apparent compartment eccentricity from double pulsed field gradient diffusion experiments," *NMR Biomed.*, vol. 26, pp. 1647–1662, 2013.

Measurement of permeability of biological membranes

[170] D. A. T. Dick, "The permeability coefficient of water in the cell membrane and the diffusion coefficient in the cell interior," *J. Theor. Biol.*, vol. 7, pp. 504–531, 1964.

[171] J. D. Quirk, G. L. Bretthorst, T. Q. Duong, A. Z. Snyder, C. S. Srpinger, J. J. H. Ackerman, and J. J. Neil, "Equilibrium water exchange between the intra- and extracellular spaces of mammalian brain," *Magn. Reson. Med.*, vol. 50, pp. 493–499, 2003.

[172] H. Van As, "Intact plant MRI for the study of cell water relations, membrane permeability, cell-to-cell and long-distance water transport," *J. Exper. Botany*, vol. 58, pp. 743–756, 2007.

[173] C. R. House, *Water Transport in Cells and Tissues*, Edward Arnold, Ltd., London, UK, p. 156, 1974.

[174] A. Finkelstein, *Water Movement Through Lipid Bilayers, Pores, and Plasma Membranes: Theory and Reality*, John Wiley and Sons, New York, p. 155, 1987.

[175] C. Labadie, J.-H. Lee, G. Vétek, and C. S. Springer, "Relaxographic imaging," *J. Magn. Reson. B*, vol. 105, pp. 99–112, 1994.

[176] J. V. Sehy, A. A. Banks, J. J. H. Ackerman, and J. J. Neil, "Importance of intracellular water apparent diffusion to the measurement of membrane permeability," *Biophys. J.*, vol. 83, pp. 2856–2863, 2002.

[177] T. H. Haines and L. S. Liebovitch, "A molecular mechanism for the transport of water across phospholipid bilayers," in *Permeability and Stability of Lipid Bilayers*, Eds E. A. Disalvo and S. A. Simon, CRC Press, pp. 123–136, 1995.

[178] S. A. Gradilone, J. E. Ochoa, F. Garcia, M. C. Larocca, J. M. Pellegrino, and R. A. Marinelli, "Hepatocyte membrane water permeability measured by silicone layer filtering centrifugation," *Anal. Biochem.*, vol. 302, pp. 104–107, 2002.

[179] D. G. Stout, P. L. Steponkus, L. D. Bustard, and R. M. Cotts, "Water permeability of chlorella cell membranes by nuclear magnetic resonance: measured diffusion coefficients and relaxation times," *Plant Physiol.*, vol. 62, pp. 146–151, 1978.

[180] M. C. Steward, Y. Seo, J. M. Rawlings, and R. M. Case, "Water permeability of acinar cell membranes in the isolated perfused rabbit mandibular salivary gland," *J. Physiol.*, vol. 431, pp. 571–583, 1990.

[181] T. Imae, H. Shinohara, M. Sekino, S. Ueno, H. Ohsaki, K Mima, and K. Ootomo, "Estimation of cell membrane permeability of the rat brain using diffusion magnetic resonance imaging," *J. Appl. Phys.*, vol. 103, p. 07A311, 2008.

[182] R. A. Garrick and F. P. Chinard, "Membrane permeability of isolated lung cells to nonelectrolytes at different temperatures," *Am. J. Physiol.*, vol. 243, pp. C285–C292, 1982.

[183] M. D. Herbst and J. H. Goldstein, "A review of water diffusion measurement by NMR in human red blood cells," *Am. J. Physiol.*, vol. 256, pp. C1097–1104, 1989.

Exchange in dMRI and Kärger model

[184] G. J. Stanisz, "Diffusion MR in biological systems: Tissue compartments and exchange," *Isr. J. Chem.*, vol. 43, pp. 33–44, 2003.

[185] J.-H. Lee, C. S. Springer, "Effects of equilibrium exchange on diffusion-weighted NMR signals: The diffusigraphic "shutter-speed"," *Magn. Reson. Med.*, vol. 49, pp. 450–458, 2003.

[186] J. Kärger, "Zur Bestimmung der Diffusion in einem Zweibereichsystem mit Hilfe von gepulsten Feldgradienten," *Ann. Phys.*, vol. 479, pp. 1–4, 1969.

[187] J. Kärger, "Der Einfluß der Zweibereichdiffusion auf die Spinechodämpfung unter Berücksichtigung der Relaxation bei Messungen mit der Methode der gepulsten Feldgradienten," *Ann. Phys.*, vol. 482, pp. 107–109, 1971.

[188] J. Kärger, "NMR self-diffusion studies in heterogeneous systems," *Adv. Colloid Interface Sci.*, vol. 23, pp. 129 – 148, 1985.

[189] J. Kärger, H. Pfeifer, W. Heink, "Principles and application of self-diffusion measurements by nuclear magnetic resonance," vol. 12 of *Advances in Magnetic and Optical Resonance*, Academic Press, pp. 1 – 89, 1988.

[190] J.-P. Melchior, G. Majer, K.-D. Kreuer, "Why do proton conducting polybenzimidazole phosphoric acid membranes perform well in high-temperature PEM fuel cells?," *Physical Chemistry Chemical Physics*, vol. 19, pp. 601–612, 2017.

[191] A. Lauerer, R. Kurzhals, H. Toufar, D. Freude, J. Kärger, "Tracing compartment exchange by NMR diffusometry: Water in lithium-exchanged low-silica X zeolites," *Journal of Magnetic Resonance*, vol. 289, pp. 1 – 11, 2018.

[192] E. Fieremans, D. S. Novikov, J. H. Jensen, J. A. Helpern, "Monte Carlo study of a two-compartment exchange model of diffusion," *NMR Biomed.*, vol. 23, pp. 711–724, 2010.

[193] M. Nilsson, D. van Westen, F. Ståhlberg, P. C. Sundgren, J. Lätt, "The role of tissue microstructure and water exchange in biophysical modelling of diffusion in white matter," *Magnetic Resonance Materials in Physics, Biology and Medicine*, vol. 26, pp. 345–370, 2013.

[194] J. Coatléven, H. Haddar, J.-R. Li, "A macroscopic model including membrane exchange for diffusion MRI," *SIAM J. Appl. Math.*, vol. 74, pp. 516–546, 2014.

[195] J.-R. Li, H. T. Nguyen, D. V. Nguyen, H. Haddar, J. Coatléven, D. L. Bihan, "Numerical study of a macroscopic finite pulse model of the diffusion MRI signal," *J. Magn. Reson.*, vol. 248, pp. 54 – 65, 2014.

[196] W. S. Price, A. V. Barzykin, K. Hayamizu, M. Tachiya, "A model for diffusive transport through a spherical interface probed by pulsed-field gradient NMR," *Biophys. J.*, vol. 74, pp. 2259 – 2271, 1998.

[197] D. S. Grebenkov, D. V. Nguyen, J.-R. Li, "Exploring diffusion across permeable barriers at high gradients. I. Narrow pulse approximation," *J. Magn. Reson.*, vol. 248, pp. 153–163, 2014.

[198] H. T. Nguyen, D. S. Grebenkov, D. V. Nguyen, C. Poupon, D. L. Bihan, J.-R. Li, "Parameter estimation using macroscopic diffusion MRI signal models," *Physics in Medicine & Biology*, vol. 60, p. 3389, 2015.

[199] L. Ning, M. Nilsson, S. Lasič, C.-F. Westin, Y. Rathi, "Cumulant expansions for measuring water exchange using diffusion MRI," *J. Chem. Phys.*, vol. 148, p. 074109, 2018.

[200] C. Meier, W. Dreher, D. Leibfritz, "Diffusion in compartmental systems. I. A comparison of an analytical model with simulations," *Magn. Reson. Med.*, vol. 50, pp. 500–509, 2003.

[201] I. Åslund, C. Cabaleiro-Lago, O. Söderman, D. Topgaard, "Diffusion NMR for determining the homogeneous length-scale in lamellar phases," *J. Phys. Chem. B*, vol. 112, pp. 2782–2794, 2008.

[202] I. Åslund, B. Medronho, D. Topgaard, O. Söderman, C. Schmidt, "Homogeneous length scale of shear-induced multilamellar vesicles studied by diffusion NMR," *J. Magn. Reson.*, vol. 209, pp. 291 – 299, 2011.

[203] S. Lasič, I. Åslund, C. Oppel, D. Topgaard, O. Söderman, M. Gradzielski, "Investigations of vesicle gels by pulsed and modulated gradient NMR diffusion techniques," *Soft Matter*, vol. 7, pp. 3947–3955, 2011.

[204] S. Eriksson, K. Elbing, O. Söderman, K. Lindkvist-Petersson, D. Topgaard, S. Lasič, "NMR quantification of diffusional exchange in cell suspensions with relaxation rate differences between intra and extracellular compartments," *PLoS One*, vol. 12, pp. 1–18, 2017.

[205] I. Åslund, A. Nowacka, M. Nilsson, D. Topgaard, "Filter-exchange PGSE NMR determination of cell membrane permeability," *J. Magn. Reson.*, vol. 200, pp. 291 – 295, 2009.

[206] S. Lasič, M. Nilsson, J. Lätt, F. Ståhlberg, D. Topgaard, "Apparent exchange rate mapping with diffusion MRI," *Magn. Reson. Med.*, vol. 66, pp. 356–365, 2011.

[207] D. S. Novikov, J. H. Jensen, and J. A. Helpern, "Permeability and surface area of cell membranes from the DWI signal," *Proc. Intl. Soc. Mag. Reson. Med.*, vol. 17, p. 450, 2009.

Muscles: fiber types, biological processes, mitochondria, lipid droplets

[208] B. Pathi, S. T. Kinsey, M. E. Howdeshell, C. Priester, R. S. McNeill, and B. R. Locke, "The formation and functional consequences of heterogeneous mitochondrial distribution in skeletal muscle," *J. Exp. Biol.*, vol. 215, pp. 1871–1883, 2012.

[209] S. Kuzmiak, B. Glancy, K. L. Sweazea, and W. T. Willis, "Mitochondrial function in sparrow pectoralis muscle," *J. Exp. Biol.*, vol. 215, pp. 2039–2050, 2012.

[210] A. Ouali, M. Gagaoua, Y. Boudida, S. Becila, A. Boudjellal, C. H. Herrera-Mendez, and M. A. Sentandreu, "Biomarkers of meat tenderness: Present knowledge and perspectives in regards to our current understanding of the mechanisms involved," *Meat Science*, vol. 95, pp. 854–870, 2013.

[211] P. Cao, S.-J. Fan, A. M. Wang, V. B. Xie, Z. Qiao, G. M. Brittenham, and Ed. X. Wu, "Diffusion magnetic resonance monitors intramyocellular lipid droplet size in vivo," *Magn. Res. Med.*, vol. 73, pp. 59–69, 2015.

[212] S. Golla, J. Ren, C. R. Malloy, and J. M. Pascual, "Intromyocellular lipid excess in the mitochondrial disorder MELAS," *Neurol. Genet.*, vol. 3, p. e160, 2017.

[213] M. B. Bischoff, W. R. Richter, and R. J. Stein, "Ultrastructural changes in pig hepatocytes during the transitional period from late foetal to early neonatal life," *J. Cell. Sci.*, vol. 4, pp. 381–395, 1969.

[214] H. J. Mersmann, J. Goodman, J. M. Houk, and S. Anderson, "Studies on the biochemistry of mitochondria and cell morphology in the neonatal swine hepatocyte," *J. Cell. Biol.*, vol. 53, pp. 335–347, 1972.

[215] H.-C. E. Koh, J. Nielsen, B. Saltin, H.-C. Holmberg, and N. Ørtenblad, "Pronounced limb and fibre type differences in subcellular lipid droplet content and distribution in elite skiers before and after exhaustive exercise," *J. Physiol.*, vol. 595, pp. 5781–5795, 2017.

[216] H. Hoppeler and M. Flück, "Plasticity of skeletal muscle mitochondria: Structure and function," *Med. Sci. Sports Exerc.*, vol. 35, pp. 95–104, 2003.

[217] S. T. Kinsey, B. R. Locke, B. Penke, and T. S. Moerland, "Diffusional anisotropy is induced by subcellular barriers in skeletal muscle," *NMR Biomed.*, vol. 12, pp. 1–7, 1999.

[218] V. B. Schrauwen-Hinderling, M. K. C. Hesselink, P. Schrauwen, and M. E. Kooi, "Intramyocellular lipid content in human skeletal muscle," *Obesity*, vol. 14, pp. 357–367, 2006.

[219] T. Ogata and Y. Yamasaki, "Ultra-high resolution scanning electron microscopy of mitochondria and sarcoplasmic reticulum arrangement in human red, white, and intermediate muscle fibers," *Anat. Rec.*, vol. 248, pp. 214–223, 1997.

[220] J. Berthet and P. Baudhuin, "A remark about the determination of the water content of mitochondria," *J. Cell Biol.*, vol. 34, pp. 701–702, 1967.

[221] J. M. Gomori, G. A. Holland, R. I. Grossman, W. B. Gefter, and R. E. Lenkinski, "Fat suppression by section-select gradient reversal on spin-echo MR imaging," *Radiol.*, vol. 168, pp. 493–495, 1988.

[222] M. L. Williams, "Water content and metabolic activity of mitochondria from fetal rat liver," *Biochim. Biophys. Acta*, vol. 188, pp. 221–229, 1966.

[223] A. P. Somlyo, M. Bond, and A. V. Somlyo, "Calcium content of mitochondria and endoplasmic reticulum in liver frozen rapidly *in vivo*," *Nature*, vol. 314, PP. 622–625, 1985.

[224] A. Listrat, B. Lebret, I. Louveau, T. Astruc, M. Bonnet, L. Lefaucheur, B. Picard, and J. Bugeon, "How muscle structure and composition influence meat and flesh quality," *ScientificWorldJournal*, vol. 2016, p. 3182746, 2016.

[225] M. T. Abbott, A. M. Pearson, J. F. Price, and G. R. Hooper, "Ultrastructural changes during autolysis of red and white porcine muscle," *J. Food. Sci.*, vol. 42, pp. 1185–1188.

[226] G. G. Cleveland, D. C. Chang, C. F. Hazelwood, and H. E. Rorschach, "Nuclear magnetic resonance measurement of skeletal muscle: Anisotropy of the diffusion coefficient of the intracellular water," *Biophys. J.*, vol. 16, pp. 1043–1053, 1976.

[227] P. van Gelderen, D. Despres, P. C. M. Vanzijl, and C. T. W. Moonen, "Evaluation of restricted diffusion in cylinders. Phosphocreatine in rabbit leg muscle," *J. Magn. Res. B*, vol. 103, pp. 255–260, 1994.

[228] J. Oudeman, A. J. Neverdeen, G. J. Strijkers, M. Maas, P. R. Luijten, and M. Froeling, "Techniques and applications of skeletal muscle diffusion tensor imaging: A review," *J. Magn. Reson. Imaging*, vol. 43, pp. 773–788, 2016.

Diffusion in multilayered structures

[229] A. Lejay and G. Pichot, "Simulating diffusion processes in discontinuous media: A numerical scheme with constant time steps," *J. Comput. Phys.*, vol. 231, pp. 7299–7314, 2012.

[230] A. Lejay, "Estimation of the mean residence time in cells surrounded by semi-permeable membranes by a Monte Carlo method," Research Report RR-8709, Inria Nancy - Grand Est (Villers-lès-Nancy, France) ; INRIA, 2015. URL:`https://hal.inria.fr/hal-01140960`

[231] R. I. Hickson, S. I. Barry, G. N. Mercer, and H. S. Sidhu, "Finite difference schemes for multilayer diffusion," *Math. Comput. Modell.*, vol. 54, pp. 210–220, 2011.

[232] J.-P. Diard, N. Glandut, C. Montella, and J.-Y. Sanchez, "One layer, two layers, etc. An introduction to the EIS study of multilayer electrodes. Part 1: Theory," *J. Electroanal. Chem.*, vol. 578, pp. 247–257, 2005.

[233] V. Freger, "Diffusion impedance and equivalent circuit of a multilayer film," *Electrochem. Commun.*, vol. 9, pp. 957–961, 2005.

[234] R. Ngameni and P. Millet, "Derivation of the diffusion impedance of multi-layer cylinders. Application to the electrochemical permeation of hydrogen through Pd and PdAg hollow cylinders," *Electrochim. Acta*, vol. 131, pp. 52–59, 2014.

[235] G. L. Graff, R. E. Williford and P. E. Burrows, "Mechanisms of vapor permeation through multilayer barrier films: Lag time versus equilibrium permeation," *J. Appl. Phys.*, vol. 96, pp. 1840–1849, 2004.

[236] Y. G. Gurevich, I. Lashkevich and G. Gonzalez de la Cruz, "Effective thermal parameters of layered films: An application to pulsed photothermal techniques," *Int. J. Heat Mass Transfer*, vol. 52, pp. 4302–4307, 2009.

[237] N. Muñoz Aguirre, G. González de la Cruz, Y. G. Gurevich, G. N. Logvinov, and M. N. Kasyanchuk, "Heat Diffusion in Two-Layer Structures: Photoacoustic Experiments," *physica status solidi (b)*, vol. 220, pp. 781–787, 2000.

[238] P. Grossel and F. Depasse, "Alternating heat diffusion in thermophysical depth profiles: multilayer and continuous descriptions," *J. Phys. D: Appl. Phys.*, vol. 31, p. 216, 1998.

[239] X. Lu and P. Tervola, "Transient heat conduction in the composite slab-analytical method," *J. Phys. A: Math. Gen.*, vol. 38, p. 81, 2005.

[240] X. Lu, P. Tervola and M. Viljanen, "Transient analytical solution to heat conduction in composite circular cylinder," *Int. J. Heat Mass Transfer*, vol. 49, pp. 341–348, 2006.

[241] F. de Monte, "Transient heat conduction in one-dimensional composite slab. A 'natural' analytic approach," *Int. J. Heat Mass Transfer*, vol. 43, pp. 3607–3619, 2000.

[242] S. Barbaro, C. Giaconia and A. Orioli, "A Computer Oriented Method for the Analysis of Non Steady State Thermal Behaviour of Buildings," *Build. Environ.*, vol. 23, pp. 19–24, 1988.

[243] W. Y. D. Yuen, "Transient temperature distribution in a multilayer medium subject to radiative surface cooling," *Appl. Math. Modell.*, vol. 18, pp. 93–100, 1994.

[244] R. I. Hickson, S. I. Barry, and G. N. Mercer, "Critical times in multilayer diffusion. Part 1: Exact solutions," *Int. J. Heat Mass Transfer*, vol. 52, pp. 5776–5783, 2009.

[245] R. I. Hickson, S. I. Barry, and G. N. Mercer, "Critical times in multilayer diffusion. Part 2: Approximate solutions," *Int. J. Heat Mass Transfer*, vol. 52, pp. 5784–5791, 2009.

[246] C. D. Shackelford, "Laboratory diffusion testing for waste disposal — A review," *J. Contam. Hydrol.*, vol. 7, pp. 177–217, 1991.

[247] G. Liu, L. Barbour, and B. C. Si, "Unified Multilayer Diffusion Model and Application to Diffusion Experiment in Porous Media by Method of Chambers," *Environmental Science & Technology*, vol. 43, pp. 2412–2416, 2009.

[248] C. D. Shackelford and S. M. Moore, "Fickian diffusion of radionuclides for engineered containment barriers: Diffusion coefficients, porosities, and complicating issues," *Eng. Geol.*, vol. 152, pp. 133–147, 2013.

[249] S. R. Yates, S. K. Papiernik, F. Gao, and J. Gan, "Analytical solutions for the transport of volatile organic chemicals in unsaturated layered systems," *Water Resour. Res.*, vol. 36, pp. 1993–2000, 2000.

[250] R. A. Siegel, "A Laplace transform technique for calculating diffusion time lags," *J. Membr. Sci.*, vol. 26, pp. 251–262, 1986.

[251] G. Pontrelli and F. de Monte, "Mass diffusion through two-layer porous media: an application to the drug-eluting stent," *Int. J. Heat Mass Transfer*, vol. 50, pp. 3658–3669, 2007.

[252] H. Todo, T. Oshizaka, W. R. Kadhum, and K. Sugibayashi, "Mathematical Model to Predict Skin Concentration after Topical Application of Drugs," *Pharmaceutics*, vol. 5, pp. 634–651, 2013.

[253] D. Mantzavinos and M. G. Papadomanolaki and Y. G. Saridakis and A. G. Sifalakis, "Fokas transform method for a brain tumor invasion model with heterogeneous diffusion in 1+1 dimensions," *Applied Numerical Mathematics*, vol. 104, pp. 47–61, 2016.

[254] D. W. Hahn and M. N. Ozisik, "One-Dimensional Composite Medium," in *Heat Conduction*, John Wiley & Sons, Inc., pp. 393–432, 2012.

[255] B. Gaveau, M. Okada, and T. Okada, "Second order differential operators and Dirichlet integrals with singular coefficients," *Tohoku Math. J.*, vol. 39, pp. 465–504, 1987.

[256] E. J. Carr and I. W. Turner, "A Semi-analytical Solution for Multilayer Diffusion in a Composite Medium Consisting of a Large Number of Layers," *Appl. Math. Modell.*, vol. 40, pp. 7034–7050, 2016.

[257] R. I. Hickson, S. I. Barry, H. S. Sidhu, G. N. Mercer, "Critical times in single-layer reaction diffusion," *Int. J. Heat Mass Transfer*, vol. 54, pp. 2642–2650, 2011.

[258] R. I. Hickson, S. I. Barry, H. S. Sidhu, G. N. Mercer, "A comparison of critical time definitions in multilayer diffusion," *The ANZIAM Journal*, vol. 52, pp. 333–358, 2011.

[259] M. Fukuda and H. Kawai, "Diffusion of low molecular weight substances into a fiber with skin-core structure—rigorous solution of the diffusion in a coaxial cylinder of multiple components," *Polymer Engineering & Science*, vol. 34, pp. 330–340, 1994.

[260] M. Fukuda and H. Kawai, "Diffusion of low molecular weight substances into a laminar film. I: Rigorous solution of the diffusion equation in a composite film of multiple layers," *Polymer Engineering & Science*, vol. 35, pp. 709–721, 1995.

[261] J. R. Miller and P. M. Weaver, "Temperature profiles in composite plates subject to time-dependent complex boundary conditions," *Compos. Struct.*, vol. 59, pp. 267–278, 2003.

[262] A. Biess, E. Korkotian, and D. Holcman, "Barriers to Diffusion in Dendrites and Estimation of Calcium Spread Following Synaptic Inputs," *PLoS Comput. Biol.*, vol. 7, pp. 1–14, 2011.

[263] S. Carranza and D. R. Paul and R. T. Bonnecaze, "Design Formulae for Reactive Barrier Membranes," *Chem. Eng. Sci.*, vol. 65, pp. 1151–1158, 2010.

[264] B. F. Gray, J. Dewynne, M. Hood, G. C. Wake, and R. Weber, "Effect of deposition of combustible matter onto electric power cables," *Fire Saf. J.*, vol. 16, pp. 459–467, 1990.

[265] A. Okubo and S. A. Levin, *Diffusion and Ecological Problems: Modern Perspectives*, Springer, New York, NY, 2001.

[266] A. B. Mann, A. J. Gavens, M. E. Reiss, D. Van Heerden, G. Bao, and T. P. Weihs, "Modeling and characterizing the propagation velocity of exothermic reactions in multilayer foils," *J. Appl. Phys.*, vol. 82, pp. 1178–1188, 1997.

[267] J.-C. Gachon, A. S. Rogachevn, H. E. Grigoryan, E. V. Illarionova, J.-J. Kuntz, D. Yu. Kovalev, A. N. Nosyrev, N. V. Sachkova, and P. A. Tsygankov, "On the mechanism of heterogeneous reaction and phase formation in Ti/Al multilayer nanofilms," *Acta Mater.*, vol. 53, pp. 1225–1231, 2005.

DMRI in multilayered geometries

[268] D. S. Grebenkov, "Pulsed-gradient spin-echo monitoring of restricted diffusion in multilayered structures," *J. Magn. Reson.*, vol. 205, pp. 181–195, 2010.

[269] J. E. Tanner, "Transient diffusion in a system partitioned by permeable barriers. Application to NMR measurements with a pulsed field gradient," *J. Chem. Phys.*, vol. 69, pp. 1748–1754, 1978.

[270] P. W. Kuchel and C. J. Durrant, "Permeability coefficients from NMR q-space data: Models with unevenly spaced semi-permeable parallel membranes," *J. Magn. Reson.*, vol. 139, pp. 258–272, 1999.

[271] J. G. Powles, M. J. D. Mallett, G. Rickayzen and W. A. B. Evans, "Exact analytic solutions for diffusion impeded by an infinite array of partially permeable barriers," *Proc. Royal Soc. Lond. A*, vol. 436, pp. 391–403, 1992.

[272] E. G. Novikov, D. van Dusschoten, and H. Van As, "Modeling of self-diffusion and relaxation time NMR in multi-compartment systems," *J. Magn. Reson.*, vol. 135, pp. 522–528, 1998.

[273] A. L. Sukstanskii, D. A. Yablonskiy, and J. J. H. Ackerman, "Effects of permeable boundaries on the diffusion-attenuated MR signal: insights from a one-dimensional model," *J. Magn. Reson.*, vol. 170, pp. 56–66, 2004.

Random walks and Brownian motion

[274] D. S. Grebenkov, "Partially Reflected Brownian Motion: A Stochastic Approach to Transport Phenomena," in *Focus on Probability Theory*, Ed. L. R. Velle, pp. 135–169 (Nova Science Publishers, 2006).

[275] W. Feller, *An Introduction to Probability Theory and Its Applications, volume 1*, Ed. John Wiley and Sons, 1968.

[276] B. Sapoval, "General formulation of laplacian transfer across irregular surfaces," *Phys. Rev. Lett.*, vol. 73, pp. 3314–3316, 1994.

[277] B. Sapoval, M. Filoche, E. R. Weibel, "Smaller is better—but not too small: A physical scale for the design of the mammalian pulmonary acinus," *PNAS*, vol. 99, pp. 10411–10416, 2002.

[278] D. S. Grebenkov, "Scaling properties of the spread harmonic measures," *Fractals*, vol. 14, pp. 231–243, 2006.

[279] K. Ito and H. P. McKean, *Diffusion Processes and Their Sample Paths*, Springer-Verlag, Berlin, 1965.

[280] M. Freidlin, *Functional Integration and Partial Differential Equations*, Annals of Mathematics Studies, Princeton University Press, Princeton, New Jersey, 1985.

[281] P. Lévy, *Processus Stochastiques et Mouvement Brownien* Gauthier-Villard, Paris, 1948–1965.

[282] D. S. Grebenkov, "Residence times and other functionals of reflected Brownian motion," *Phys. Rev. E*, vol. 76, p. 041139, 2007.

[283] D. S. Grebenkov, "Probability distribution of the boundary local time of reflected Brownian motion in Euclidean domains," *Phys. Rev. E*, vol. 100, p. 062110, 2019.

[284] D. S. Grebenkov, "Imperfect Diffusion-Controlled Reactions," in *Chemical Kinetics: Beyond the Textbook*, Eds. K. Lindenberg, R. Metzler, G. Oshanin, New Jersey: World Scientific, pp. 191-219, 2019.

[285] D. S. Grebenkov, M. Filoche, and B. Sapoval, "Spectral properties of the Brownian self-transport operator," *Eur. Phys. J. B.*, vol. 36, pp. 221–231, 2003.

First-exit time processes

[286] D. S. Grebenkov and J.-F. Rupprecht, "The escape problem for mortal walkers," *J. Chem. Phys.*, vol. 146, p. 084106, 2017.

[287] B. Meerson and S. Redner, "Mortality, Redundancy, and Diversity in Stochastic Search," *Phys. Rev. Lett.*, vol. 114, p. 198101, 2015.

[288] S. B. Yuste, E. Abad, and K. Lindenberg, "Exploration and Trapping of Mortal Random Walkers," *Phys. Rev. Lett.*, vol. 110, p. 220603, 2013.

[289] S. Redner, *A Guide to First-Passage Processes*, Cambridge University Press, 2001.

[290] R. Metzler, G. Oshanin, and S. Redner, *First-passage phenomena and their applications*, World Scientific Publishing, 2014.

[291] D. Holcman and Z. Schuss, "The Narrow Escape Problem," *SIAM Rev.*, vol. 56, pp. 213–257, 2014.

[292] D. S. Grebenkov, "Universal Formula for the Mean First Passage Time in Planar Domains," *Phys. Rev. Lett.*, vol. 117, p. 260201, 2016.

[293] J.-F. Rupprecht, O. Bénichou, D. S. Grebenkov, and R. Voituriez, "Exit Time Distribution in Spherically Symmetric Two-Dimensional Domains," *J. Stat. Phys.*, vol. 158, pp. 192–230, 2015.

[294] F. Crick, "Diffusion in Embryogenesis," *Nature*, vol. 225, p. 420, 1970.

[295] S. Alexander, J. Bernasconi, W. R. Schneider, and R. Orbach, "Excitation dynamics in random one-dimensional systems," *Rev. Mod. Phys.*, vol. 1981, pp. 175–198, 1981.

[296] Ya. G. Sinai, "The limiting behavior of a one-dimensional random walk in a random medium," *Theory Prob. Its Appl.*, vol. 27, pp. 256–268, 1983.

[297] J. Bernasconi and W. R. Schneider, "Diffusion in a one-dimensional lattice with random asymmetric transition rates," *J. Phys. A: Math. Gen.*, vol. 15, p. L729, 1982.

[298] M. Ya. Azbel, "Diffusion: A Layman's Approach and Its Applications to One-dimensional Random Systems," *Solid State Commun.*, vol. 43, pp. 515–517, 1982.

[299] B. Derrida, "Velocity and Diffusion Constant of a Periodic One-dimensional Hopping Model," *J. Stat. Phys.*, vol. 31, pp. 433–450, 1983.

[300] S. H. Noskowicz and I. Goldhirsch, "Average versus Typical Mean First-Passage Time in a Random Random Walk," *Phys. Rev. Lett.*, vol. 61, pp. 500–502, 1988.

[301] P. Le Doussal, "First-passage time for random walks in random environments," *Phys. Rev. Lett.*, vol. 62, p. 3097, 1989.

[302] K. P. N. Murthy and K. W. Kehr, "Mean first-passage time of random walks on a random lattice," *Phys. Rev. A*, vol. 40, pp. 2082–2087, 1989.

[303] K. W. Kehr and K. P. N. Murthy, "Distribution of mean first-passage times in random chains due to disorder," *Phys. Rev. A*, vol. 41, pp. 5728–5730, 1990.

[304] M. Raykin, "First-passage probability of a random walk on a disordered one-dimensional lattice," *J. Phys. A: Math. Gen.*, vol. 26, p. 449, 1993.

[305] P. Le Doussal, C. Monthus, and D. S. Fisher, "Random walkers in one-dimensional random environments: Exact renormalization group analysis," *Phys. Rev. E*, vol. 59, pp. 4795–4840, 1999.

[306] Y. Lanoiselée, N. Moutal, and D. S. Grebenkov, "Diffusion-limited reactions in dynamic heterogeneous media," Nature Commun., vol. 9, 4398, 2018.

[307] S. Havlin and D. Ben-Avraham, "Diffusion in disordered media," *Adv. Phys.*, vol. 51, pp. 187–292, 2002.

[308] J.-P. Bouchaud and A. Georges, "Anomalous diffusion in disordered media: Statistical mechanisms, models, and physical applications," *Phys. Rep.*, vol. 195, pp. 127–293, 1990.

Interpretation of Langevin equation

[309] I M. Sokolov, "Itô, Stratonovich, Hänggi and all the rest: The thermodynamics of interpretation," *Chem. Phys.*, vol. 375, pp. 359–363, 2010.

[310] P. F. Tupper and X. Yang, "A paradox of state-dependent diffusion and how to resolve it," *Proc. R. Soc. A*, vol. 468, pp. 3864–3881, 2012

[311] H. W. de Haan, M. V. Chubynsky, and G. W. Slater, "Monte-Carlo approaches for simulating a particle at a diffusivity interface and the "Ito-Stratonovich dilemma"," *ArXiv e-prints*, 2012. URL: `https://arxiv.org/abs/1208.5081`

[312] P. Hänggi, "Stochastic processe I: Asymptotic behaviour and symmetries," *Helv. Phys. Acta*, vol. 51, pp. 183–201, 1978.

[313] P. Hänggi, "Connection between deterministic and stochastic descriptions of nonlinear systems," *Helv. Phys. Acta*, vol. 53, pp. 491–496, 1980.

[314] P. Hänggi and H. Thomas, "Stochastic processes: Time evolution, symmetries and linear response," *Phys. Rep.*, vol. 88, pp. 207–319, 1982.

[315] Y. L. Klimontovich, "Ito, Stratonovich and kinetic forms of stochastic equations," *Physica A*, vol. 163, pp. 515–532, 1990.

[316] Y. L. Klimontovich, "Nonlinear Brownian motion," *Phys. Usp.*, vol. 37, p. 737, 1994.

[317] E. Wong and M. Zakai, "On the convergence of ordinary integrals to stochastic integrals," *Ann. Math. Stat.*, vol. 36, pp. 1560–1564, 1965.

[318] R. Kupferman, G. Pavliotis, and A. M. Stuart, "Itô versus Stratonovich white-noise limits for systems with inertia and colored multiplicative noise," *Phys. Rev. E*, vol. 70, p. 036120, 2004.

[319] M. Matsuo and S.-i. Sasa, "Stochastic energetics of non-uniform temperature systems," *Physica A*, vol. 276, pp. 188–200, 2000.

[320] M. San Miguel and J. M. Sancho, "A colored-noise approach to Brownian motion in position space. Corrections to the Smoluchowki equation," *J. Stat. Phys.*, vol. 22, pp. 605–624, 1980.

[321] J. M. Sancho, M. San Miguel, and D. Dürr, "Adiabatic elimination for systems of Brownian particles with nonconstant damping coefficients," *J. Stat. Phys.*, vol. 28, pp. 291–305, 1982.

[322] K. Sekimoto, "Temporal coarse-graining for systems of Brownian particles with nonconstant temperature," *J. Phys. Soc. Jpn.*, vol. 68, pp. 1448–1449, 1999.

[323] P. Arnold, "Langevin equations with multiplicative noise: Resolution of time discretization ambiguities for equilibrium systems," *Phys. Rev. E*, vol. 61, pp. 6091–6098, 2000.

[324] N. G. Van Kampen, *Stochastic Processes in Physics and Chemistry*, Elsevier Science, 1992.

Bloch waves in solid state physics

[325] F. Bloch, "Über die Quantenmechanik der Elektronen in Kristallgittern," *Zeitschrift für Physik*, vol. 52, pp. 555–600, 1929.

[326] C. Kittel, *Introduction to Solid State Physics*, John Wiley and Sons, 2004

[327] J. von Neumann and E. P. Wigner, "Über merkwürdige diskrete Eigenwerte," *Z. Physik*, vol. 30, pp. 465–467, 1929.

[328] D. Emin and C. F. Hart, "Existence of Wannier-Stark localization," *Phys. Rev. B*, vol. 36, pp. 7353–7359, 1987.

[329] G. H. Wannier, *Elements of Solid State Theory*, Cambridge University Press, London, 1959.

Mathematical methods

[330] S. Axelrod and P. N. Sen, "Nuclear magnetic resonance spin echoes for restricted diffusion in an inhomogeneous field: Methods and asymptotic regimes," *J. Chem. Phys.*, vol. 114, no. 15, pp. 6878–6895, 2001.

[331] D. S. Grebenkov, "Laplacian eigenfunctions in NMR. II. Theoretical advances," *Conc. Magn. Res. A*, vol. 34A, no. 5, pp. 264–296, 2009.

[332] E. B. Davies, *Heat Kernels and Spectral Theory*. Cambridge Tracts in Mathematics, Cambridge University Press, 1989.

[333] P. Gilkey, *Asymptotic Formulae in Spectral Geometry*. Chapman and Hall/CRC, 2003.

[334] S. Desjardins and P. Gilkey, "Heat content asymptotics for operators of Laplace type with Neumann boundary conditions," *Math. Z.*, vol. 215, pp. 251–268, 1994.

[335] J. Canosa and R. G. De Oliveira "A new method for the solution of the Schrödinger equation," *J. Comput. Phys.*, vol. 5, pp. 188–207, 1970.

[336] S. Pruess, "Estimating the eigenvalues of Sturm-Liouville problems by approximating the differential equation," *SIAM J. Numer. Anal.*, vol. 10, pp. 55–68, 1973.

[337] S. Pruess, "High order approximations to Sturm-Liouville eigenvalues," *Numer. Math.*, vol. 24, pp. 241–247, 1975.

[338] M. Marletta and J. D. Pryce, "Automatic solution of Sturm-Liouville problems using the Pruess method," *J. Comput. Appl. Math.*, vol. 39, pp. 57–78, 1992.

[339] S. Pruess and C. T. Fulton, "Mathematical software for Sturm-Liouville problems," *ACM Trans. Math. Software*, vol. 19, pp. 360–376, 1993.

[340] B. Helffer, *Spectral theory and its applications*, Cambridge University Press, 2013.

[341] N. Moiseyev, *Non-Hermitian quantum mechanics*, Cambridge University Press, 2011.

[342] P. Kuchment, *Floquet Theory for Partial Differential Equations*, Operator Theory Advances and Applications, vol. 60, Birkhaüser, 1993.

[343] M. Abramowitz and I. Stegun, *Handbook of Mathematical Functions*, 1964.

Publications by N. Moutal

[344] N. Moutal, I. Maximov, and D. S. Grebenkov, "Probing surface-to-volume ratio of an anisotropic medium by diffusion NMR with general gradient encoding," *IEEE Trans. Med. Imag.*, vol. 38, pp. 2507–2522, 2019.

[345] N. Moutal, M. Nilsson, D. Topgaard, and D. S. Grebenkov, "The Kärger vs bi-exponential model: Theoretical insights and experimental validations," *J. Magn. Reson.*, vol. 296, pp. 72–78, 2018.

[346] N. Moutal and D. S. Grebenkov, "Diffusion Across Semi-permeable Barriers: Spectral Properties, Efficient Computation, and Applications," *J. Sci. Comput.*, vol. 81, pp. 1630–1654, 2019.

[347] N. Moutal, K. Demberg, D. S. Grebenkov, and T. A. Kuder, "Localization regime in diffusion NMR: theory and experiments," *J. Magn. Reson.*, vol. 305, pp. 162–174, 2019.

[348] N. Moutal, A. Moutal, and D. S. Grebenkov, "Diffusion NMR in periodic media: efficient computation and spectral properties," *J. Phys. A*, 2020 (accepted).

[349] N. Moutal and D. S. Grebenkov, "The localization regime in a nutshell," *J. Magn. Reson.*, 2020 (submitted).

[350] N. Moutal, D. S. Grebenkov, S. Clerjon, G. Pages, and J.-M. Bonny, "Diffusion MRI in muscles at high b-values: towards a quantification of microscopic organelles," *ISMRM*, 2018.

[351] N. Moutal, D. S. Grebenkov, S. Clerjon, G. Pages, and J.-M. Bonny, "Quantifying the mitochondrial content with diffusion MRI," *ICMRM*, 2019.

ECOLE DOCTORALE

Titre: Étude de l'équation de Bloch-Torrey associée à l'Imagerie de Résonance Magnétique Nucléaire pondérée par diffusion

Mots clés: IRM, Diffusion, Bloch-Torrey, Localisation, Perméabilité, Anisotropie

Résumé: L'imagerie de résonance magnétique nucléaire pondérée par diffusion (dMRI) est une technique expérimentale qui a pour but d'identifier les propriétés microstructurales d'un échantillon bien en-dessous de la résolution conventionnelle de l'IRM "classique". Bien que cette technique ait été introduite et appliquée dans divers contextes depuis plusieurs décennies, de nombreux éléments théoriques restent à élucider, et ce d'autant plus avec l'amélioration constante des appareils d'imagerie et des techniques expérimentales. Notablement, les mécanismes de formation du signal d'IRM aux forts gradients sont encore largement incompris, malgré une tendance "naturelle" à l'augmentation des gradients pour sonder des échelles structurales de plus en plus fines.
Nous revisitons dans un premier temps les effets d'anisotropie géométrique. Tandis que l'anisotropie aux échelles micro- et macroscopiques a été l'objet de beaucoup d'attention ces dernières années, l'échelle intermédiaire, "mésoscopique", n'avait pas encore été étudiée systématiquement. Nous avons obtenu une généralisation de la formule de Mitra qui permet d'améliorer significativement l'estimation du rapport surface-volume de domaines arbitraires quelle que soit la séquence de gradient utilisée.
Dans un second temps, nous étudions les effets de perméabilité, qui sont cruciaux pour les applications biomédicales. Nous proposons une analyse critique de trois modèles classiques de l'effet de l'échange sur le signal d'IRM de diffusion. De plus, nous formulons une méthode numérique et théorique générale et flexible pour étudier la diffusion à travers plusieurs membranes perméables parallèles.
Le dernier chapitre constitue le coeur de la thèse et aborde l'étude non-perturbative de l'équation de Bloch-Torrey qui régit l'évolution du signal d'IRM de diffusion. Aux forts gradients, nous montrons théoriquement, numériquement, et expérimentalement l'universalité du phénomène de localisation, qui ouvre des perspectives prometteuses pour augmenter la sensibilité du signal d'IRM à la microstructure.

Title: Study of the Bloch-Torrey equation associated to diffusion magnetic resonance imaging

Keywords: MRI, Diffusion, Bloch-Torrey, Localization, Permeability, Anisotropy

Abstract: Diffusion magnetic resonance imaging (dMRI) is an experimental technique which aims at unraveling the microstructural properties of a sample well below the conventional spatial resolution of "classic" MRI. Although this technique has been proposed and applied in various contexts for several decades, many theoretical points remain to be clarified, even more with the permanent improvement of MRI scanners and experimental protocols. Notably, the understanding of the signal formation at high gradients is largely incomplete, in spite of the "natural" tendency to increase the gradient in order to probe finer and finer structural scales.
We first revisit anisotropy effects. While micro- and macroscopic anisotropy have been largely studied over past years, the intermediate, "mesocopic" scale had not been investigated in a systematic way. We have obtained a generalized Mitra formula which improves significantly surface-to-volume ratio estimations for arbitrary domains and gradient waveforms.
In a second chapter, we investigate permeability effects, that are crucial for biomedical applications. We critically revise three classical models of exchange for dMRI. Moreover, we obtain a general and flexible numerical and theoretical method to study diffusion trough several parallel permeable membranes.
The last chapter is the heart of the thesis and contains a non-perturbative study of Bloch-Torrey equation, which governs the evolution of dMRI signal. At high gradient strength, we reveal theoretically, numerically, and experimentally the universality of the localization phenomenon, which opens promising perspectives to improve the sensitivity of the signal to the microstructure.

Institut Polytechnique de Paris

91120 Palaiseau, France